

University of Nottingham
UK | CHINA | MALAYSIA

Sustainable Metal Organic Framework Thin-Films for Medical Sensing Applications

Jan Warfsmann

Thesis submitted to the University of Nottingham
for the degree of Doctor of Philosophy (PhD)

May 2019

Abstract

We spend more and more time indoors, and the monitoring of the concentration of CO_2 and volatile organic compounds (VOCs) is important to maintain comfort, productivity and health. Furthermore, can the long-time exposure to these compounds lead to medical issues like cancer and nerve damage. The accumulation of CO_2 and VOC takes place automatically indoors. CO_2 is produced by cellular respiration, while VOCs are often outgassed from e.g. paint or furniture. In order to maintain a comfortable indoor atmosphere without wasting energy by wrong heating or ventilation the real-time monitoring of CO_2 and VOC concentrations is needed.

Long period grating fibres (LPG) are known to be lightweight and low-cost sensors with extreme short response times, possibly in the microsecond scale, but the non-selective response to various stimuli like strain, temperature and refractive index change is problematic for the creation of a reliable real-time sensor system. The use of metal-organic frameworks (MOFs), a new class of hybrid porous materials with tuneable pore size and chemical properties, might be here able to provide selectivity and sensitivity towards specific target compounds as a thin-film coating on the LPG surface. However, MOFs are in general first prepared as powders, often at elevated temperatures and long reaction times. Furthermore is the transformation of a powder synthesis to a thin-film synthesis not trivial.

For this work, two promising MOFs, MIL-53(Al) and TIFSIX-3-Ni, have been identified and the possible coating of LPGs was separated into three steps. These are the optimisation of the powder synthesis regarding more sustainable conditions (e.g. shorter reaction times, lower reaction temperature and easier purification of the product), devolving of a thin-film synthesis for glass as support and the application of the most-promising thin-film coating techniques on LPGs. The real-time sensor performance of the MIL-53(Al) and TIFSIX-3-Ni coated LPGs towards CO_2 and selected VOCs was tested afterwards.

In summary, could be especially the powder synthesis for MIL-53(Al) and TIFSIX-3-Ni in comparison with the literature protocols be improved. It was possible to greatly reduce the reaction time of MIL-53(Al) from 220°C and 72 h to 150°C and 5 h using the low-weight alcohol methanol as solvent. Furthermore, does the MIL-53(Al) derivate prepared in methanol show porosity directly after the synthesis. A common disadvantage of MIL-53(Al) is that normally a time and energy consuming activation process is needed in order to access the internal porosity. For TIFSIX-3-Ni, the yield could be improved and the reaction time reduced in comparison with the literature protocol using N,N-dimethylformamide (DMF) as solvent.

For both MIL-53(Al) and TIFSIX-3-Ni new thin-film protocols could be developed for the successful coating of glass surfaces with homogenous and uniform thin-films, but still more research is needed in order to create a reliable and repeatable sensor response of these MOF-coated LPGs.

Table of Contents

ABSTRACT.....II

TABLE OF CONTENTS.....III

INDEX OF FIGURES.....VI

INDEX OF TABLES.....XVIII

1 INTRODUCTION **1**

2 BACKGROUND INFORMATION **5**

2.1 State of the art for CO_2 detection 5
2.2 State of the art for VOC detection 8
2.3 Optical fibre sensors 10
2.3.1 Introduction to optical fibres 10
2.3.2 Interferometer-type optical fibre sensors 11
2.3.3 Evanescent wave optical fibre sensors 13
2.4 Synthesis methods for MOFs 19
2.5 Thin-film preparation of MOFs 23
2.6 Porous materials for CO_2 capture and detection 30
2.7 Porous materials for VOC capture and detection 34
2.8 Conclusion 36

3 SYNTHESIS OF MIL-53(AL) IN LOW-WEIGHT ALCOHOLS **38**

3.1 Introduction 38
3.2 Experimental 40
3.2.1 Materials 40
3.2.2 Synthesis of MIL-53(Al) 40
3.2.3 Characteisation 41
3.3 Results and Discussion 42
3.3.1 Particle size and morphology 42
3.3.2 Crystallinity and porosity 46
3.3.3 Effect of synthesis conditions on crystallinity 53
3.3.4 Breathing effect 59
3.3.5 Measurement of water, CO_2 and VOC uptakes 64
3.3.6 Thermal stability 73
3.3.7 Morphology in alternative solvents 75
3.4 Conclusions and Future Work 79

4 THIN-FILM SYNTHESIS OF MIL-53(AL) ON GLASS **82**

4.1 Introduction 82
4.2 Experimental 84
4.2.1 Materials 84
4.2.2 MIL-53(Al) powder synthesis 84
4.2.3 Treatment of glass slides 84
4.2.4 In-situ coating 84
4.2.5 Dip-coating / seeding with MIL-53(Al) 84
4.2.6 Secondary growth 85
4.2.7 Layer-by-Layer approach (LbL) 85
4.2.8 Rapid-Thermal deposition (RTD) 85
4.2.9 Solvent-assisted epitaxy (SAE) 86

4.2.10 Characterisation 86
4.3 In-situ coating 86
4.4 Conditions during dip-coating approach 90
4.4.1 MIL-53(Al)(H_2O) in water 91
4.4.2 MIL-53(Al)(H_2O) in MeOH 95
4.4.3 MIL-53(Al)(DMF) in water 96
4.4.4 MIL-53(Al)(DMF) in MeOH 97
4.5 Secondary growth 99
4.6 Dip-coating of multiple layers 103
4.6.1 MIL-53(Al)(H_2O) in MeOH 103
4.6.2 MIL-53(Al)(DMF) in MeOH 104
4.7 Layer-by-Layer approach 107
4.8 Rapid-Thermal Deposition 115
4.9 Solvent assisted epitaxy 121
4.10 Discussion and summary of the results from this chapter 129

5 MIL-53(AL) COATINGS ON LPG FOR CO_2 AND VOC DETECTION 135

5.1 Introduction 135
5.2 Experimental 136
5.2.1 Materials 136
5.2.2 MIL-53(Al) powder synthesis 136
5.2.3 Coating of LPG by dip-coating 136
5.2.4 Coating of LPG by in-situ coating 136
5.2.5 Coating of LPG by SAE 137
5.2.6 Characterisation 137
5.3 Methods 137
5.4 Sensor results 142
5.4.1 Blank fibre 144
5.4.2 LPG coated with MIL-53(Al) by dip-coating 154
5.4.3 LPG coated with MIL-53(Al) by in-situ coating 161
5.4.4 LPG coated with MIL-53(Al) by SAE 166
5.5 Conclusions and Future work 173

6 A NOVEL HYBRID ULTRAMICROPOROUS MATERIAL AS COATING ON LPGS 177

6.1 Introduction 177
6.2 Experimental 181
6.2.1 Materials 181
6.2.2 Synthesis of $NiTiF_6$ 181
6.2.3 One-step powder synthesis 181
6.2.4 Single crystal synthesis of Ni-pyrazine-TiF_6 ($NiPyTiF_6$) 181
6.2.5 Two-step powder synthesis 182
6.2.6 Treatment of glass slides 183
6.2.7 Dip-Coating 183
6.2.8 Seeding and Secondary growth 183
6.2.9 Solvent-assisted epitaxy 183
6.2.10 Rapid thermal deposition 184
6.2.11 In-situ coating 184
6.2.12 Coating of LPG with TIFSIX by in-situ coating 184
6.2.13 Characterisation 184
6.3 Synthesis of TIFSIX powder 185
6.3.1 Synthesis of $NiTiF_6$ 185
6.3.2 One-step synthesis of TIFSIX 186
6.3.3 Two-step synthesis of TIFSIX 191

6.4 Thin Film Synthesis of TIFSIX 200
6.4.1 Dip-coating 201
6.4.2 Seeding and secondary growth 202
6.4.3 Solvent assisted epitaxy 203
6.4.4 Rapid thermal deposition 204
6.4.5 In-situ coating 206
6.5 Sensor experiments 211
6.5.1 In-situ coating; 5 h reaction time 212
6.5.2 In-situ coating; 15 h reaction time 219
6.6 Conclusions and Future work 229

7 CONCLUSIONS AND FUTURE WORK 233

8 REFERENCES 238

9 APPENDIX A: THIN-FILM SYNTHESIS OF MIL-53(AL) ON GLASS 252

10 APPENDIX B: A NOVEL HYBRID ULTRAMICROPOROUS MATERIAL AS COATINGS ON LPGS 261

Index of Figures

Figure 2-1:Schematic image of a typical metal oxide sensor (MOX) 6
Figure 2-2:Scheme of the working principle of a NDIR sensor. One tube is filled with reference gas, the other is the measurement cell. IR light is sent though both cells and the signals compared with each other. 7
Figure 2-3:Image of a single-mode optical fibre 10
Figure 2-4:Possible configurations to create an in-line Mach-Zehnder interferometer (light brown: core of the fibre; white: cladding): a) pair of periodic perturbations, b) core mismatch, c)air holes, d) adding of segments with larger core diameter e) segment of smaller core diameter f) tapering of fibre 12
Figure 2-5:Schematic image of a optical fibre Michelson-interferometer. The beam splitting was implemented here by a periodic perturbation..... 13
Figure 2-6:Working principle of a evanescent wave sensor at the example of a tapered fibre. Normally has the evanescence wave inside the core a shorter range than the cladding diameter and does not interact with the environment. With reduction of the cladding diameter, the evanescent wave has an intensity outside the cladding and can interact with the environment. 14
Figure 2-7:Comparison of LPG and FBG (Fibre Bragg grating) 14
Figure 2-8:Working principle of the LPG. The wavelength has some intensity outside of the cladding. 15
Figure 2-9:Calculated wavelength for the modes of lower order (a: 1-9) and higher order (b: 18-27) for LPG with varying grating period 17
Figure 2-10:Transmission spectrum of a LPG used for sucrose detection. The wavelength difference of the LP_{012} was used. With sucrose solutions of varying concentrations, resulting in different RIs of the solutions, the two bands of the LP_{012} mode have shifted to smaller wavelength (“blueshift”) and larger wavelength (“redshift”) 18
Figure 2-11:Structure of several different MOFs. The structures were calculated from existing crystal data. a) MIL-53(Al), b) HKUST-1, c) ZIF-8, d) MOF-5. 20
Figure 2-12:Formation of MOFs by self-assembly of MOF from metal salt (yellow ball) and linker (red rod) components from solvothermal synthesis. 21
Figure 2-13:Comparison of heating by conventional heating (top) and microwave heating (bottom). In conventional heating, the thermal energy has to be transferred from outside the reaction mixture leading to a temperature gradient from the wall of the vessel into the reaction mixture. In heating by microwave the reaction mixture is heated from within 21
Figure 2-14:Schematic formation of a thin-film on a support. Problems like formation of particles in the bulk solution can lead to thin-films which are less uniform and homogenous. 24
Figure 2-15:Optimisation of the synthesis conditions for the thin-film synthesis of ZIF-8 on glass by varying the metal/linker ratio and the concentration 25
Figure 2-16:Schematic image of the seeding and secondary growth approach for HKUST-1 26
Figure 2-17:Schematic description of the Layer-by-Layer approach for the formation of a MOF thin-films 27
Figure 2-18:Schematic diagram of a typical SAM and description of the function of the different parts..... 28
Figure 2-19:Slow formation of a thin-film by LbL regarding the film thickness and number of layers needed at the example of HKUST-1 recorded by QCM. Insert shows the growth of the thin-film with atomic precision. 28
Figure 2-20:Schematic image of possible electrochemical synthesis methods of MOFs 29

Figure 3-1:Visualization of the breathing phenomenon of MIL-53(Al) between the large-pore for (left) and the small pore form (right). Hydrogen atoms have been omitted for clarity. Structures calculated from crystal data. 38
Figure 3-2:Schematic reaction scheme for synthesis of MIL-53(Al) 40
Figure 3-3:SEM images of MIL-53(Al)(H_2O). The AsSyn sample is shown at low (a) and higher magnification (b). MIL-53(Al) grows in water to micrometre sized particles with orthorhombic shape. After activation, the overall size, morphology and crystallinity of the particles does not change, but cracks (d, green square) and breaking of intergrown crystals (d red square) was observed. 43
Figure 3-4:SEM images of MIL-53(Al)(DMF). For the AsSyn sample the agglomeration of particles is observed in low magnification. At higher magnification, the MIL-53(Al)(DMF) particles have a spherical shape and size of 41 ± 17 nm. After activation, (c for lower d for higher magnification) no difference was observed. 44
Figure 3-5:SEM images of MIL-53(Al)(MeOH). For the AsSyn sample agglomeration is observed in low magnification (a). In contrast to MIL-53(Al)(DMF), the nano-sized particles are a mixture of spherical particles with size of 34 ± 15 nm and rod-shaped particles with a length of 178±42 nm and a width of 33 ± 8 nm. After activation, (c for lower, d for higher magnification) particles size or morphology do not change... 45
Figure 3-6:XRD of MIL-53(Al) derivatives (in different solvents before and after activation) in comparison with calculated pattern form existing crystal data. 47
Figure 3-7:SEM images of MIL-53(Al)(EtOH)-AsSyn. The shown sample was activated at elevated temperature. The sample tends to agglomerate (left) and show similar particle morphology to MIL-53(Al)(MeOH) (right). 48
Figure 3-8:XRD-pattern of MIL-53(Al)(EtOH) before and after activation 48
Figure 3-9:N_2-isotherms of the as-synthesized MIL-53(Al) samples, prepared in different solvents. Adsorption: solid line; Desorption: dashed line. 49
Figure 3-10:N_2-isotherm of the activated MIL-53(Al) samples, prepared in different solvents 49
Figure 3-11:Ideal t-plots for a) mesoporous, b) nonporous, c) microporous and d) samples containing micro- and mesoporosity. 51
Figure 3-12:Comparison of the t-plots for MIL-53(Al)(H_2O)-Acti(black),MIL-53(Al)(DMF)-Acti (yellow) and MIL-53(Al)(MeOH)-Acti (purple). 52
Figure 3-13:Comparison of N_2-isotherm of MIL-53(Al)(H_2O)-AsSyn (black) with samples after several activation methods. 53
Figure 3-14:MIL-53(H_2O) with 1:1 ratio of the starting materials (black) in comparison with H_2BDC (red). 54
Figure 3-15:MIL-53(Al)(H_2O)-AsSyn washed with DMF (black) and without washing (grey). Peaks of H_2BDC are highlighted with asterisk. 55
Figure 3-16:Comparison of MIL-53(Al) samples prepared in DMF with varying reaction temperature and time 56
Figure 3-17:MIL-53(Al)(DMF) prepared at RT. Fresh reaction mixture (right) and after 3 weeks at RT (left). 56
Figure 3-18:MIL-53(Al)(DMF)-RT with lower (left) and higher magnification (right). 57
Figure 3-19:MIL-53(Al)(H_2O) samples prepared with varying reaction time and temperature 57
Figure 3-20:MIL-53(Al)(MeOH)-samples with varying reaction time and temperature... 58
Figure 3-21:SEM of sample prepared in MeOH at 220°C with 3 days reaction time. 59
Figure 3-22:Temperature -dependent XRD of MIL-53(Al)(H_2O)-Acti prepared at 150°C and 5 h reaction time. 60
Figure 3-23:Temperature-dependent XRD of MIL-53(Al)(DMF)-Acti prepared at 150°C and 5 h reaction time. 61
Figure 3-24:Temperature-dependent XRD of MIL-53(Al)(MeOH)-Acti prepared at 150°C and 5 h reaction time. 62

Figure 3-25:Environmental SEM images of MIL-53(Al)(MeOH)-Acti at 60% relative humidity (left) and 80% relative humidity (right). Particles start to fuse at higher humidity levels. Scale bar: 2 µm. 62
Figure 3-26:Environmental SEM images of MIL-53(Al)(DMF)-Acti at 60% relative humidity (left) and 80% relative humidity (right). No change of the particles was observed. Scale bar 2 µm..... 62
Figure 3-27:Temperature-dependent XRD of MIL-53(Al)(DMF)-Acti prepared at RT..... 63
Figure 3-28:Temperature-dependent XRD of MIL-53(Al)(DMF) prepared at 220°C and 72 h reaction time..... 63
Figure 3-29:H_2O-isotherms of MIL-53(Al)(H_2O)-Acti, MIL-53(Al)(DMF)-Acti and MIL-53(Al)(MeOH)-Acti measured at 25°C and ambient pressure. The isotherms were measured between 0.1 and 0.9 relative pressure. 64
Figure 3-30:XRD pattern of MIL-53(Al)(DMF) before and after measurement of the water isotherm. 66
Figure 3-31:XRD pattern of MIL-53(Al)(H_2O) before and after measurement of the H_2O isotherm. 66
Figure 3-32:XRD pattern of MIL-53(Al)(MeOH) before and after measurement of the H_2O isotherm. 67
Figure 3-33:IR of MIL-53(Al) samples prepared in different solvents. 68
Figure 3-34:Comparison of N_2-isotherms for MIL-53(Al)(DMF) before and after measurement of H_2O isotherm. 69
Figure 3-35:Comparison of N_2-isotherms for MIL-53(Al)(H_2O) before and after measurement of H_2O isotherm. 69
Figure 3-36:Comparison of N_2-isotherms for MIL-53(Al)(MeOH) before and after measurement of H_2O isotherm. 70
Figure 3-37:CO_2-isotherms for activated MIL-53(Al) samples. All samples were prepared at 150°C with 5 h reaction time. 71
Figure 3-38:Comparison of MeOH isotherms for the activated MIL-53(Al) samples, prepared at 150°C and 5 h reaction time. 72
Figure 3-39:Comparison of TGA for activated MIL-53(Al) samples. MIL-53(Al)(MeOH)-AsSyn is shown in addition as dashed line. 74
Figure 3-40:TGA of MIL-53(Al)(EtOH)-AsSyn. 75
Figure 3-41:DMSO mixture with aluminium nitrate at reaction mixture at RT (left) and 150°C (right). At 150°C, a residue of aluminium nitrate is visible and has settled as white solid powder at the bottom of the beaker. 76
Figure 3-42:XRD pattern of sample prepared in DMSO (MIL-68(Al)(DMSO); blue) in comparison with pattern of MIL-53(Al)(DMF)-Acti (black) and calculated XRD pattern of MIL-68(In) from existing crystal data 77
Figure 3-43:Crystal structure of MIL-68(In) calculated from existing crystal data. 77
Figure 3-44:Morphology of MIL-68(Al)(DMSO). The particles are rod-shaped and have a size ranging from 0.7 µm to 3 µm. 78
Figure 3-45:The exposure the rod-shaped MIL-68(Al)(DMSO) particles to the electron beam has led to a shrinkage of the particles 78
Figure 3-46: N_2-isotherm of MIL-68(Al)(DMSO)-Acti. 79
Figure 4-1: Schematic set-up of in-situ coating of glass slides with MIL-53(Al)..... 87
Figure 4-2: SEM images of glass slide coated with MIL-53(Al)(H_2O) in-situ. The glass slide remains mostly empty. One of the particles (white rectangle) was observed at higher magnification. It has the typical star-shape of MIL-53(Al)(H_2O)..... 88
Figure 4-3: SEM image glass slide coated in-situ with MIL-53(Al)(DMF) with 5 h reaction time at 150°C in lower (left) and higher magnification (right). Black strains on the surface imply areas with reduced coverage. 88

Figure 4-4:Cross-section of in-situ coated glass slide with MIL-53(Al)(DMF). The green lines are guidance for the eye and are projected by the SEM software to calculate the film thickness. The highest point of the film was chosen to measure the film thickness. 89
Figure 4-5:XRD pattern of glass slide covered in-situ with MIL-53(Al)(DMF) at 5h at 150°C. The visible peaks at 8.9° and 15.1° can be attributed to MIL-53(Al)(DMF) 89
Figure 4-6:Schematic set-up of dip-coating. The concentration of the dip-coating suspension was controlled by varying the weight ratio between MIL-53(Al) (water or DMF derivate) and the solvent (water or MeOH). 91
Figure 4-7:SEM image of a glass slide coated with a 0.1 wt% of MIL-53(Al)(H_2O) suspension in water. 92
Figure 4-8:SEM image of a glass slide coated with a 0.5 wt% coating suspension of MIL-53(Al)(H_2O) in water. 92
Figure 4-9:XRD patterns of glass slide covered with MIL-53(Al)(H_2O) with water as solvent. While for a glass covered with 0.1 wt% suspension (grey) no peaks are visible, on a glass slide covered from a 0.5 wt% suspension peaks at 9.5°, 12.5° and 16.01° can be identified 93
Figure 4-10:SEM images of a glass slide coated with a 1.0 wt% of MIL-53(Al)(H_2O) suspension in water. 93
Figure 4-11:SEM image of a glass slide, coated with a 0.5 wt% suspension of MIL-53(H_2O) in water, which was cleaned before in piranha acid. 94
Figure 4-12:SEM image of a glass slide coated with a 0.5 wt% suspension, of MIL-53(Al)(H_2O) in water, which was cleaned before with acetone and immersed in 0.1 M NaOH. 94
Figure 4-13:SEM image of glass slide covered with a 0.1 wt% suspension of MIL-53(Al)(H_2O) in MeOH. The surface is mostly empty with a few particles of MIL-53(Al)(H_2O) on the surface. 95
Figure 4-14:SEM image of a glass slide with was coated with a 0.5 wt% suspension of MIL-53(H_2O) in MeOH. The surface coverage is higher in comparison with glass slides coated with MIL-53(Al)(H_2O) which used water as solvent. 95
Figure 4-15:SEM image of a glass slide which was covered with a 1.0 wt% suspension of MIL-53(Al)(H_2O) in MeOH. No difference to a glass slide coated with 0.5 wt% suspension in MeOH was observed. 96
Figure 4-16:SEM image of glass slide covered with a 0.1 wt% suspension on MIL-53(Al)(DMF) in water. 96
Figure 4-17:SEM image of glass slide covered with 0.5 wt% suspension of MIL-53(Al)(DMF) with water as solvent. The surface coverage of the particles is higher in comparison with samples coated with MIL-53(Al)(H_2O) or samples coated with suspension of lower concentration. Furthermore, are no larger agglomerated clusters visible on the surface. 97
Figure 4-18:SEM images of glass slides covered with a 1.0 wt% suspension. At higher magnification (right side) the surface seems to have a higher and more homogenous coverage of particles, but the drawback is the formation of numerous agglomerated clusters on the surface. These might have a reduced interaction with the glass surface and make a possible coating rougher. 97
Figure 4-19:SEM image of a glass slide covered with a 0.1 wt% suspension of MIL-53(Al)(DMF) in MeOH. The surface is mostly empty and only in a few particles are visible on the surface. 98
Figure 4-20:SEM image of a glass slide covered with a 0.5 wt% suspension of MIL-53(Al)(DMF) in MeOH. 98
Figure 4-21:Comparison of slides covered with 0.5 wt% suspensions of MIL-53(Al)(DMF) in H_2O and MeOH. At increased magnification (10,000x) slides covered with MIL-53(Al)(DMF) from water show gaps in the coating. 98

Figure 4-22:SEM image of a glass slide covered by a 1.0 wt% suspension of MIL-53(Al)(DMF) in MeOH. The surface coverage is in comparison with coating from lower concentrated suspensions, but particles agglomerate to large cluster on the surface. 99
Figure 4-23:SEM images of glass slide covered with of MIL-53(Al)(H_2O) in MeOH before (a in lower magnification, b in higher magnification) and after (c in lower and d higher magnification) adhesion test in water at 150°C for 5 h. 100
Figure 4-24:SEM images of glass slide covered of MIL-53(Al)(DMF) in MeOH before (a in lower magnification, b in higher magnification) and after (c in lower and d in higher magnification) adhesion test in DMF at 150°C for 5 h. 100
Figure 4-25:Preparation of a ZIF-8 thin-film on glass, after 1 (a), 10 (b) and 40 (c) repetition of in-situ growth. With progress of the experiment, the individual particles start to intergrowth to larger particles, leading to a homogenous, nearly crack-free surface. Scale bar: 500 nm..... 101
Figure 4-26:SEM images of a glass slide seeded with a 0.5 wt% suspension of MIL-53(Al)(DMF) in MeOH, followed by secondary growth of MIL-53(DMF) at 150°C and 5 h reaction time..... 101
Figure 4-27:Cross-section image of a glass slide coated by seeding and secondary growth with MIL-53(Al)(DMF) at 150°C and 5 h reaction time. The thickness of the coating varies between 2.1 µm and 3.2 µm. 102
Figure 4-28:XRD pattern of glass slide covered by seeding and secondary growth with MIL-53(Al)(DMF). Peaks corresponding to MIL-53(Al)(DMF) are highlighted by asterisks. 102
Figure 4-29:SEM image of slide covered with 1 step of MIL-53(Al)(H_2O) in MeOH. 103
Figure 4-30:SEM image of slide covered with 2 steps of MIL-53(Al)(H_2O) in MeOH. 104
Figure 4-31:SEM image of slide covered with 5 steps of MIL-53(Al)(H_2O) in MeOH. 104
Figure 4-32:SEM image of slide covered with 10 steps of MIL-53(Al)(H_2O) in MeOH. ... 104
Figure 4-33:SEM image of glass slide covered with 1 step of MIL-53(DMF) from a 0.5wt% suspension. The surface was covered with areas of MIL-53(DMF), but holes in coating and larger agglomerated particles were also visible. 105
Figure 4-34:SEM image of glass slide covered with 2 step of MIL-53(DMF) form a 0.5 wt% suspension in MeOH. In comparison with the 1 step sample, the surface coverage was higher and more homogenous. Some gaps were still in the coating visible. 105
Figure 4-35:SEM image of glass slide covered with 5 step of MIL-53(Al)(DMF) from a 0.5 wt% suspension in MeOH. 106
Figure 4-36:SEM images of glass slide covered with 10 step of MIL-53(Al)(DMF) from a 0.5 wt% suspension in MeOH. The surface was mostly covered, but larger agglomerated clusters were embedded in the coating. 106
Figure 4-37:SEM image of a cross section of a glass slide covered with 5 step of MIL-53(Al)(DMF) from a 0.5 wt% suspension in MeOH. 106
Figure 4-38:XRD pattern of a glass slide covered with 5 step of MIL-53(Al)(DMF) in MeOH as solvent (black). For comparison, the XRD pattern of MIL-53(Al)(DMF) as powder is shown (grey). 107
Figure 4-39:Schematic description of the Layer-by-Layer approach. 108
Figure 4-40:XRD patterns of glass slides covered by LbL with 1 (blue), 2 (black) and 10 (grey) processing steps in DMF as solvent and with 30 min immersion time for metal and linker solution respectively. No peaks corresponding to MIL-53(Al) could be observed. 109
Figure 4-41:SEM images of glass slides coated by LbL with a) 1 step, b) 2 steps and c) 10 steps. In the lower right corner (d), a cross section of the glass slide covered with 2 steps is shown. In contrast to the top-down SEM images (a to c), the glass slide appeared in the cross-section image bright white, while the coating was grey. 110

Figure 4-42:SEM images of glass slides covered with 1 step of MIL-53(Al) with different immersion times for the metal and linker solution of a) 30 min, b) 60 min and c) 90 min. White boxes show areas with reduced coverage. 111
Figure 4-43:SEM images of 4 glass slides covered in LbL with 2 steps and 30 min immersion time in metal and linker solution. 112
Figure 4-44:SEM image of a glass slide, which was covered by a solution of $Al(NO_3)_3 \cdot 9\ H_2O$ in DMF with the same concentration of Al-salt used in the LbL approach. At lower magnification (left side) different morphologies were visible on the surface. At higher magnification (white square on the left side, right for higher magnification) these particles have irregular shape. 113
Figure 4-45:SEM image of a glass slide, which was covered by a solution of H_2BDC in DMF with the same concentration used in the LbL approach. In contrast to the samples covered with $Al(NO_3)_3 \cdot 9\ H_2O$, the surface was covered with only one type of particles. At higher magnification (the right image was taken at the position of the red marking in the left image) these particles appear as leaf-shaped particles with a size of ~3 µm. 113
Figure 4-46:XRD pattern of glass slide covered only with metal solution ($Al(NO_3)_3 \cdot 9\ H_2O$, grey) and linker solution in DMF (H_2BDC, black) in comparison with XRD of powder sample of the starting materials $Al(NO_3)_3 \cdot 9\ H_2O$ (blue) and H_2BDC (green)..... 114
Figure 4-47:SEM image (left) of a glass slide covered with two treatment steps by LbL and inverted order of immersion (first metal solution, than linker solution) show a surface covered with ellipse shaped particles. An XRD pattern of the surface (right) confirm the coating of the surface with H_2BDC. 114
Figure 4-48:Schematic mechanism of rapid thermal deposition (RTD) 115
Figure 4-49:SEM image of a glass slide covered with MIL-53(Al) in RTD approach. No difference between a glass slide that coated according to the original RTD approach (reaction at 150°C for 15 min with consecutive switching off oven for a total reaction time of 2 h) and a glass slide that was placed at 150°C for 2 h can be seen. In both cases the surface is covered with small particles of MIL-53(Al). 116
Figure 4-50:Comparison of the particle types found on RTD coated slides. Left: Glass slides coated with small particles, which intergrow on the surface (NEq, 5 h, 150°C). Right: slide covered with larger spherical particles (NEq, 1 h, 100°C)..... 118
Figure 4-51:XRD pattern of glass slide covered by RTD (black; NEq, 5 h, 150°C) which has shown small agglomerated particles on the surface (Figure 4-50, left). The broad peak at ~8.8° is in good correlation with the XRD powder pattern of MIL-53(Al)(DMF) (grey). 118
Figure 4-52:SEM images of glass slides covered by RTD approach with NEq solution with reaction time of a)1 h, b)3 h, c) 5 h and d) overnight (~17 h) at 150°C. 119
Figure 4-53:SEM image of glass slide covered by RTD approach (NEq, 1 h, 150°C), while in the red area crystalline particles are found (Figure 4-52a), the blue area is covered with petal shaped particles (see image below). 120
Figure 4-54:SEM image of glass slide covered in RTD approach (NEq, 1 h, 150°C, see blue area in Figure 4-53) and of a glass slide which was only covered with H_2BDC dissolved in DMF. 120
Figure 4-55:XRD of glass slide covered by RTD (NEq, 5 h, 100°C; grey) in comparison with XRD pattern of H_2BDC. 121
Figure 4-56:SEM image of glass slide coated only with $Al(NO_3)_3 \cdot 9H_2O$ in DMF (from Figure 4-44, left) in comparison with a slide covered by RTD (Lex, 3 h 150°C). 121
Figure 4-57:Schematic illustration (left) of set-up for the solvent-assisted evaporation (SAE) and image of the used experimental set-up (right). 122
Figure 4-58:SEM image of glass slide covered by SAE at 75°C with 5 h reaction time. The surface is only covered with particles of H_2BDC. 123

Figure 4-59:XRD pattern of glass slide covered by SAE at 75°C with reaction time of 5 h. Visible peaks at 17.57°, 25.19° and 27.95° (highlighted by asterisks) are in good agreement with peaks for H_2BDC. 123
Figure 4-60:SEM images of slide covered by SAE at 100°C with reaction time of 5 h. ... 124
Figure 4-61:XRD pattern of slide covered by SAE at 100°C with reaction time of 5 h.... 124
Figure 4-62:SEM image of slide covered by SAE at 125°C with 5 h reaction time. Surface is covered with flakes, with cracks between the particles. At higher magnification, it is visible that the surface is composed of agglomerated smaller particles. 125
Figure 4-63:XRD pattern of slide covered by SAE at 125°C with reaction time of 5 h. Peaks at 9.0°; 15.3° and 17.9° are in good agreement of MIL-53(Al)(DMF) 125
Figure 4-64:SEM image of slide covered by SAE at 150°C for 5 h. At lower magnification (left) is the surface completely covered and only at higher magnification (right) are small cracks visible in the coating. 126
Figure 4-65:XRD pattern of slide covered by SAE at 150°C with a reaction time of 5 h. 126
Figure 4-66:Cross-section image of glass slide covered with MIL-53(DMF) by SAE at 150°C with reaction time of 5 h. 127
Figure 4-67:SEM image of glass slide covered by SAE at 150°C and reaction time of 1 h. At lower magnification (top left) the surface seems to be only partly covered. At higher magnification, these particles might be identified as MIL-53(DMF) due to the spherical shape (top right). Not the whole surface is covered, instead some areas are just covered with a few clusters of agglomerated particles (bottom). 128
Figure 4-68:XRD pattern of slide covered by SAE at 150°C with reaction time of 1 h.... 128
Figure 4-69:SEM image of slide covered by SAE at 150°C and reaction time of 3 h. 129
Figure 4-70:XRD pattern of glass slide covered by SAE at 150°C with reaction time of 3 h. Peaks corresponding of MIL-53(Al)(DMF) are visible on the surface, but in contrast to other samples with longer reaction time the intensity is lower and the peaks less distinct. 129
Figure 4-71:SEM image of glass slides covered by dip-coating from a 0.5 wt% suspension of MIL-53(Al)(DMF) in THF (left) and MeOH (right). 131
Figure 4-72:SEM image of glass slides covered by dip-coating from a 0.5 wt% suspension of MIL-53(Al)(H_2O) in THF (left) and MeOH (right). 131
Figure 4-73:Image of freshly prepared 0.5 wt% coating suspension of MIL-53(Al)(DMF) in MeOH (left) and hexane (right). The position of the agglutinated MIL-53(Al)(DMF) in the vial was highlighted with a black marking 132
Figure 4-74:Photo of glass slides covered with MIL-53(Al)(DMF) with MeOH (left) and water (right) as solvent. 132
Figure 5-1:Schematic description of the LPG (red lines represent perturbations in the fibre). The small area with removed protective coating (~3 cm) will be coated with thin-film of MIL-53(Al). 138
Figure 5-2:Experimental set-up for the sensor measurement. 138
Figure 5-3:Image of the used CO_2-sensor (Senseair K33 ICB). The minimum response time is 20 s and the measurement principle is based on IR. 139
Figure 5-4:Rotameter for the control of the CO_2 gas flow..... 139
Figure 5-5:Measured CO_2-concentration during a sensor experiment. The data was taken from the IR-CO_2 sensor, which acts as control element. 140
Figure 5-6:Total spectrum of the blank fibre. The blue band is the LP_{018} and the green band the split LP_{019} band. 142
Figure 5-7:Image of the blank fibre. 144
Figure 5-8:CO_2-sensor experiment results for the blank fibre. Measured wavelengths of the LP_{018}-band. Red circles show wavelength range (~5 min) used to calculate the reported wavelength. 145
Figure 5-9:CO_2-sensor experiment results for the blank fibre. Measured wavelengths of the LP_{019L}-band. 146

Figure 5-10:CO_2-sensor experiment results for the blank fibre. Measured wavelengths of the LP_{019R}-band. 147
Figure 5-11:MeOH-sensor experiment results for the blank fibre. Measured wavelengths of the LP_{018}-band. 149
Figure 5-12:MeOH-sensor experiment results for the blank fibre. Measured wavelengths of the LP_{019L}-band. 151
Figure 5-13:MeOH-sensor experiment results for the blank fibre. Measured wavelengths of the LP_{019R}-band. 152
Figure 5-14:Image of a fibre immersed in 0.5 wt% dip-coating suspension. 155
Figure 5-15:Fibre coated with one step of MIL-53(Al)(DMF) from a 0.5 wt% dip-coating suspension in MeOH. 156
Figure 5-16:Fibre coated with 5 steps of MIL-53(Al)(DMF) from a 0.5 wt% dip-coating suspension in MeOH. 156
Figure 5-17:Total spectrum of LPG coated with 5 steps of MIL-53(Al)(DMF) by dip-coating from a 0.5 wt% suspension in MeOH. 157
Figure 5-18:CO_2-sensor experiment results for fibre coated with 5 steps of MIL-53(Al)(DMF) by dip-coating from 0.5 wt% suspension in MeOH. Measured wavelength for LP_{018}-band 157
Figure 5-19:CO_2-sensor experiment results for fibre coated with 5 steps of MIL-53(Al)(DMF) by dip-coating from 0.5 wt% suspension in MeOH. Measured wavelength for LP_{019}-band. 158
Figure 5-20:MeOH-sensor experiment results for fibre coated with 5 steps of MIL-53(DMF) by dip-coating from 0.5 wt% suspension in MeOH. Measured wavelength for LP_{018}-band. 160
Figure 5-21:Schematic image of the Teflon chamber for in-situ coating. 162
Figure 5-22:Photo of the Teflon chamber. 162
Figure 5-23:Fibre coated in-situ (5 h; 150°C) with MIL-53(Al)(DMF). 163
Figure 5-24:Total spectrum of LPG coated in-situ with MIL-53(Al)(DMF) at 150°C with 5 h reaction time 163
Figure 5-25:CO_2-sensor experiment results for fibre coated in-situ with MIL-53(Al)(DMF). Measured wavelength for LP_{018}-band. 164
Figure 5-26:MeOH-sensor experiment results for fibre coated in-situ with MIL-53(Al)(DMF). Wavelength for LP_{018}-band. 165
Figure 5-27:Schematic image of coating fibre by SAE 166
Figure 5-28:Fibre coated with MIL-53(Al) by SAE approach. 167
Figure 5-29:Total spectrum of LPG coated by SAE with MIL-53(DMF) at 150°C with 5 h reaction time 167
Figure 5-30:CO_2-sensor experiment results for fibre coated by SAE with MIL-53(Al)(DMF). Measured wavelength for LP_{018}-band. 168
Figure 5-31:Repetition CO_2-sensor experiment results for fibre coated by SAE with MIL-53(Al)(DMF). Measured wavelength for LP_{018}-band. 170
Figure 5-32:MeOH-sensor experiment results for fibre coated by SAE with MIL-53(Al)(DMF). Measured wavelength for LP_{018}-band. 171
Figure 5-33:Different fibre coated by SAE (bottom, c, fibre broke into two pieces), without DMF vapor (mid, b) and only DMF vapor (top, a). 172
Figure 6-1:a) Structure of MIL-101(Cr); b) PEI-MIL-101(Cr) (PEI = polyethyleneimine) has the same structure then MIL-101(Cr), but PEI is bound to the open-metal sites in MIL-101(Cr); c) Structure of HKUST-1 (structure calculated from existing crystal data); d) Structure of CPO-27(Mg) (structure calculated from existing crystal data). 177
Figure 6-2: a)Structure of the first prepared HUM containing zinc as metal ion, 4.4'-bipyridine as linker and the SiF_6^{2-}anions bridging ligand (structure calculated from existing crystal data); b) Structure of the tungsten containing, non-cubic HUM WOFOR-1-Co (H was omitted for clarity). 178

Figure 6-3:Examples of nitrogen containing linker (bipyridines) used for the synthesis of HUMs. Number in parenthesis show the number used to identify the linker in the HUMs. 179
Figure 6-4:Structure of SIFSIX-3-Ni, which has a very similar structure to TIFSIX-3-Ni. The structure was calculated from existing crystal data. View along the b-axis. The oxygen (red) in the pores represent water bound in the pores of SIFSIX-3-Ni before activation. Bonds in light red show stabilization of the framework by H···F hydrogen bonds. 180
Figure 6-5:XRD pattern of $NiTiF_6$ prepared from $Ni(CO_3)$ (black), $Ni(NO_3)_2$ (blue) in comparison with the starting $Ni(CO_3)$ (grey). No residue of starting material was observed in the product. Less crystalline product with impurities was prepared when MeOH was used as solvent (green). 186
Figure 6-6:XRD pattern of TIFSIX powder samples prepared in different solvents and reaction temperature. 188
Figure 6-7:TIFSIX samples, prepared in a) water at RT, b) water at 85°C, c) MeOH at RT and d) MeOH at 85°C. 188
Figure 6-8:Crystal structure of the Ni-pyrazine-TiF_6-compound ($NiPyTiF_6$). 189
Figure 6-9:TIFSIX prepared in MeOH at 85°C in one-step synthesis (left), after activation in vacuum at 120°C (mid) and after activation in vacuum at 160°C (right). 190
Figure 6-10:XRD pattern of TIFSIX prepared in a one-step reaction at 85°C (black). Activation in vacuum at 120°C (grey) and 160°C (blue). 190
Figure 6-11:Comparison of XRD pattern for TIFSIX samples prepared with varying solvent and reaction temperature. All samples used an excess of pyrazine during the reaction. 191
Figure 6-12:SEM images of TIFSIX samples prepared with different solvent and reaction temperature. The reaction mixture used excess of pyrazine. a) water at RT b) water at 85°C c) MeOH at RT d) MeOH at 85°C. 192
Figure 6-13:XRD pattern of TIFSIX samples prepared with various solvent and reaction temperatures. All reactions have used an equimolar reaction mixture. 194
Figure 6-14:SEM images of TIFSIX prepared with equimolar reaction mixtures a) water at RT, b) water at 85°C, c) MeOH at RT, d) MeOH at 85°C. 194
Figure 6-15:Left: Image of the reaction mixture in acetone after the reaction. Right: sample prepared in acetone (left) and in MeOH at 85°C (right). The acetone sample is grey, whereas a purple colour should be expected for TIFSIX 196
Figure 6-16:SEM image of sample, prepared in acetone at 85°C with lower (left) and higher (right) magnification. 196
Figure 6-17:XRD pattern of sample prepared in acetone at 85°C (black) and at RT (grey) in comparison with sample prepared in MeOH at RT (blue, see p. 185). Both patterns match, which shows that the product prepared in acetone is $NiPyTiF_6$. 196
Figure 6-18:TIFSIX prepared in DMF at 85°C in a two-step synthesis at lower (left) and higher (right) magnification. 197
Figure 6-19:XRD pattern of samples from the reaction in DMF with a one-step reaction at 85°C (black), two-step-reaction at RT and two-step reaction at 85°C 198
Figure 6-20:XRD pattern of TIFSIX prepared in DMF at 85°C AsSyn, after solvent exchange and heating in vacuum and after refluxing in DMF at 160°C 199
Figure 6-21:N_2-isotherms of TIFSIX prepared in DMF at 85°C AsSyn (black), after activation by solvent exchange and heating in vacuum at 120°C (blue) and after reflux in DMF at 160°C for 15 h (grey). Adsorption: solid line; Desorption: dashed line. 199
Figure 6-22:TGA comparing samples from different attempts at preparing TIFSIX. 200
Figure 6-23:SEM image of glass slide coated with 1 step of TIFSIX, prepared in DMF from 0.5 wt% suspension in MeOH at lower (left) and higher (right) magnification. 201

Figure 6-24:SEM image of glass slide coated with 2 layers of TFISIX, prepared in DMF from 0.5 wt% suspension in MeOH at lower and higher magnification. 202
Figure 6-25:XRD pattern after coating a glass slide with TIFSIX, from 0.5 wt% suspension in MeOH. Peaks corresponding to TIFSIX are highlighted with asterisk. 202
Figure 6-26:SEM image of a glass slide coated by seeding and secondary growth at low (left) and higher (right) magnification. The glass slide was seeded with 2 steps of TIFSIX prepared in DMF in a 0.5 wt% suspension with MeOH as solvent, followed by secondary growth at 85°C for 15 h. 203
Figure 6-27:XRD pattern of glass slide coated by seeding (0.5 wt% suspension in MeOH) and secondary growth (DMF at 85°C with 15 h reaction time). 203
Figure 6-28:Glass slide covered by product prepared using the SAE approach with DMF at 85°C 204
Figure 6-29:XRD pattern of TIFSIX product prepared using the SAE approach with DMF as solvent and 85°C reaction temperature. Starting material ($NiTiF_6$; highlighted by asterisk) and unknown impurities are visible. 204
Figure 6-30:Glass slide covered using the RTD approach in DMF at 85°C and 5 h reaction time. 205
Figure 6-31:XRD of glass slide coated using the RTD approach using DMF as solvent at 85 C and 5 h reaction time. 205
Figure 6-32:XRD pattern of glass slide covered in-situ with TIFSIX at 85°C with 1 h reaction time. Peak positions (highlighted with asterisks) and relative intensity of the peaks match pattern of typical TIFSIX powder samples. 206
Figure 6-33:Glass slide covered in-situ using DMF as solvent and 1 h reaction time, which lower (left) and higher (right) magnification. 207
Figure 6-34:SEM cross-section of glass slide covered by in-situ at 85°C with 1 h reaction time. Coating thickness is about 4.8 µm, but with gaps in the coating. 207
Figure 6-35:SEM image of glass slide covered in-situ with TIFSIX at 85°C and 5 h reaction time at lower (left) and higher (right) magnification. Only small cracks in the coating were visible 208
Figure 6-36:Side-view of a glass slide coated in TIFSIX in DMF in-situ for 5 h. The thickness of about 3.6 µm and the particles are more fused. No gaps in the coating are visible. 208
Figure 6-37:Glass slide with in-situ coating of TIFSIX in DMF with 15 h reaction time at lower (left) and higher magnification (right). 209
Figure 6-38:Side-view of a sample prepared in-situ with DMF as solvent and 15 h reaction time. 209
Figure 6-39:XRD pattern of glass slides covered by in-situ approach with TIFSIX at 85°C with 5 h (black) and 15 h (grey) reaction time. Both pattern were recorded before activation by solvent exchange. 210
Figure 6-40:XRD pattern of a glass slide covered by in-situ approach in DMF after 5 h reaction time before (black) and after solvent exchange in MeOH (grey). Glass coated in-situ with 5 h reaction time was used. 210
Figure 6-41:SEM image of a fibre coated with TIFSIX in-situ in DMF as solvent at 85°C with 5 h reaction time. 212
Figure 6-42:Image of fibre coated with TIFSIX in-situ with DMF as solvent at 85°C with 5 h reaction time. Shown is the highlighted is the area in Figure 6-41 with higher magnification. 213
Figure 6-43:Total spectrum recorded over the range 200-1100 nm for the LPG coated with TIFSIX in-situ at 85°C with 5 h reaction time. 213
Figure 6-44:CO_2-sensor experiment results for fibre coated in-situ with TIFSIX at 85°C with 5 h reaction time. Measurement for the LP_{018}-band. During the measurement, several fluctuations of the wavelength have been observed 214

Figure 6-45:CO_2-sensor experiment results for fibre coated in-situ with TIFSIX at 85°C with 5 h reaction time. Measurement for the LP_{019}-band. 215
Figure 6-46:MeOH-sensor experiment results for fibre coated in-situ with TIFSIX at 85°C and 5 h reaction time. Measured for LP_{018}-band. 217
Figure 6-47:MeOH-sensor experiment results for of fibre coated in-situ with TIFSIX at 85°C and 5 h reaction time. Measured for LP_{019}-band. 218
Figure 6-48:SEM image of the fibre coated in-situ with TIFSIX introduced at 85°C with 15 h reaction time. 220
Figure 6-49:Spectrum recorded over the range 200-1100 nm of the LPG coated with TIFSIX in-situ at 85°C with 15 h reaction time. The LP_{018}-band (blue) and the split LP_{019}-band (green) can be seen in the spectrum and will be used for the investigation of the sensor performance. 220
Figure 6-50:CO_2-sensor experiment results for fibre coated in-situ with TIFSIX at 85°C with 15 h reaction time. Results for LP_{018}-band. 221
Figure 6-51:Results of repeated CO_2-sensor experiment for fibre coated in-situ with TIFSIX at 85°C with 15h reaction time. Measured for LP_{018}-band. 222
Figure 6-52:CO_2-sensor experiment results for fibre coated in-situ with TIFSIX at 85°C with 15 h reaction time. Measured for LP_{019L}-band. 223
Figure 6-53:CO_2-sensor experiment results for for fibre coated in-situ with TIFSIX at 85°C with 15 h reaction time. Measured for LP_{019R}-band. 224
Figure 6-54:MeOH-sensor experiment results for fibre coated in-situ with TIFSIX at 85°C with 15 h reaction time. Measurement for LP_{018}-band. 226
Figure 6-55:MeOH-sensor experiment results for fibre coated in-situ with TIFSIX at 85°C with 15 h reaction time. Measurement for LP_{019L}-band. 227
Figure 6-56:MeOH-sensor experiment results for fibre coated in-situ with TIFSIX at 85°C with 15 h reaction time. Measurement for LP_{019R}-band. 228
Figure 9-1:SEM image and XRD pattern of glass slide covered by RTD with NEq solution at 100°C with reaction time of 1 h. 252
Figure 9-2:SEM image and XRD pattern of glass slide covered by RTD with NEq solution at 100°C with reaction time of 3 h. 252
Figure 9-3:SEM image and XRD pattern of glass slide covered by RTD with NEq solution at 100°C with reaction time of 5 h. 252
Figure 9-4:SEM image and XRD pattern of glass slide covered by RTD with NEq solution at 125°C with reaction time of 1 h. 253
Figure 9-5:SEM image and XRD pattern of glass slide covered by RTD with NEq solution at 125°C with reaction time of 3 h. 253
Figure 9-6:SEM image and XRD pattern of glass slide covered by RTD with NEq solution at 125°C with reaction time of 5 h. 253
Figure 9-7:SEM image and XRD pattern of glass slide covered by RTD with NEq solution at 150°C with reaction time of 1 h. 254
Figure 9-8:SEM image and XRD pattern of glass slide covered by RTD with NEq solution at 150°C with reaction time of 3 h. 254
Figure 9-9:SEM image and XRD pattern of glass slide covered by RTD with NEq solution at 150°C with reaction time of 5 h. 254
Figure 9-10:SEM image and XRD pattern of glass slide covered by RTD with NEq solution at 150°C with reaction time of ~17 h (overnight reaction) 255
Figure 9-11:SEM image and XRD pattern of glass slide covered by RTD with Mex solution at 100°C with reaction time of 1 h. 255
Figure 9-12: EM image and XRD pattern of glass slide covered by RTD with Mex solution at 100°C with reaction time of 3 h. 255
Figure 9-13:SEM image and XRD pattern of glass slide covered with Mex solution at 125°C with reaction time of 1 h. 256

Figure 9-14:SEM image and XRD pattern of glass slide covered by RTD with Mex solution at 125°C with reaction time of 3 h. 256
Figure 9-15:SEM image and XRD pattern of glass slide covered by RTD with Mex solution at 150°C with reacting time of 1 h. 256
Figure 9-16:SEM image and XRD pattern of glass slide covered by RTD with Mex solution at 150°C with reaction time of 3 h. 257
Figure 9-17:SEM image and XRD pattern of glass slide covered by RTD with Mex solution at 150°C with reaction time of 5 h. 257
Figure 9-18:SEM image and XRD pattern of glass slide covered by RTD with Lex solution at 100°C with reaction time of 1 h. 257
Figure 9-19:SEM image and XRD pattern of glass slide covered by RTD with Lex solution at 100°C with reaction time of 3 h. 258
Figure 9-20:SEM image and XRD pattern of glass slide covered by RTD with Lex solution at 125°C with reaction time of 1 h. 258
Figure 9-21:SEM image and XRD pattern of glass slide covered by RTD with Lex solution at 125°C with reaction time of 3 h. 258
Figure 9-22:SEM image and XRD pattern of glass slide covered by RTD with Lex solution at 150°C with reaction time of 1 h. 259
Figure 9-23:SEM image and XRD pattern of glass slide covered by RTD with Lex solution at 150°C with reaction time of 3 h. 259
Figure 9-24:SEM image and XRD pattern of glass slide covered by RTD with Lex solution at 150°C with reaction time of 5 h. 259
Figure 9-25:SEM image of glass slide covered with NEq reaction mixture at 150°C for 1 h. Only a small are is covered with agglomerated particles. Rest of the surface is covered with leaf-shaped of unreacted starting material (H_2BDC). 260
Figure 10-1:N_2-isotherm for TIFSIX prepared in one-step synthesis at RT with MeOH . 261
Figure 10-2:CO_2-isotherm of TIFSIX prepared in one-step synthesis at RT with MeOH . 261
Figure 10-3:N_2-isotherm of TIFSIX prepared in acetone at 85°C in two-step reaction... 262
Figure 10-4:N_2-isotherm of TIFSIX prepared in DMF at 85°C in a two-step reaction with excess of pyrazine. 262
Figure 10-5:N_2-isotherm of TIFSIX prepared in H_2O at RT with equimolar composition. 263
Figure 10-6:N_2-isotherm of sample prepared in one-step reaction in MeOH at 85°C. .. 263
Figure 10-7: XRD pattern of TIFSIX prepared in DMF at 85°C with equimolar reaction mixture (0.5 g $NiTiF_6$ and 0.356 g pyrazine). 264
Figure 10-8:TIFSIX prepared in water at reduced concentration at 85°C. At 50% concentration (0.25 g NiTiF6 and 0.178 g pyrazine in 10 ml water), only starting material with a few small product peaks can be seen (highlighted by asterisks). 264
Figure 10-9:XRD pattern of TIFSIX, prepared in water at RT, after activation by solvent exchange in MeOH and heating in vacuum at 120°C. The peaks at 12.58° and 17.72° are matching TIFSIX, but pattern was measured with very small amount (~12 mg) of sample, leading to the pattern with low intensities. 265
Figure 10-10:CO_2-isotherm of TIFSIX prepared in DMF at 85°C in a two-step synthesis. Measured with shorter (5 s, default, blue) and longer (60 s, black) equilibrium time for each point on the isotherm. 265
Figure 10-11:XRD of residue collected after evaporation of solvent from decanting process (black). Reaction was TIFSIX in two-step synthesis with excess of pyrazine at RT and water as solvent. XRD pattern of the starting material NiTiF6 (green) and pyrazine (grey) are shown for comparison. 266
Figure 10-12:Sample of $NiTiF_6$ after 1 day drying (left) and after 3 days (right) at 90°C. 266

Index of Tables

Table 2-1:Comparison of the different conditions for CO_2 capture applications 31
Table 2-2:Kinetic Diameter and Quadrupole momentum of typical molecules found in atmosphere and flue gas 32
Table 2-3:Comparison of several MOFs with their amine containing derivative regarding porosity, CO_2-capacity at different pressures and selectivity. Selectivity is given for the low-pressure region..... 33
Table 2-4:CO_2-uptake of different MOFs at low CO_2 concentration (2000 ppm) and flue-gas conditions (0.15 bar) 34
Table 3-1:Examples of applied conditions for the solvothermal synthesis of MIL-53(Al). The concentration is shown as concentration of the metal salt in the reaction mixture (n.s. = not specified). 40
Table 3-2:Comparison of the pKa for different solvents used. 45
Table 3-3:H_2BDC solubility at room temperature and at reaction temperature of 150°C (for MeOH solubility at 160°C). The values are given as g per 100 g solvent..... 46
Table 3-4:Comparison of BET and microporosity for different MIL-53(Al) derivatives 50
Table 3-5:Comparison of MIL-53(Al)(H_2O) after different activation methods 53
Table 3-6:Porosities of various MIL-53 samples after measurement of water isotherms 68
Table 3-7:Results of solubility experiment for $Al(NO_3)_3 \cdot 9\ H_2O$ in DMSO 76
Table 3-8:Tendencies affecting the particle size of MIL-53(Al) in different solvents 79
Table 4-1:Summary of used dip-coating suspensions. 85
Table 4-2:Summary of used conditions for the RTD approach (all reaction mixtures have been prepared in 30 ml DMF)..... 85
Table 4-3:Summary of the tested conditions for the dip-coating. 91
Table 4-4:Results of the RTD experiments..... 117
Table 5-1:Measured wavelength at different CO_2-concentrations for the blank fibre. Measured for the LP_{018} band. 145
Table 5-2:Measured wavelength shifts between different CO_2-concentrations and sum of the wavelength shifts for the blank fibre. Measured for the LP_{018}-band. 146
Table 5-3:Measured wavelength at different CO_2-concentrations for the blank fibre. Measured for the LP_{019L}-band. 146
Table 5-4:Measured wavelength shift between different CO_2-concentrations and sum of the wavelength shifts for the blank fibre. Measured for the LP_{019L}-band. 147
Table 5-5:Measured wavelength at different CO_2 concentrations for the blank fibre. Measured for the LP_{019R}-band. 148
Table 5-6:Measured wavelength shift between different CO_2-concentrations and sum of the wavelength shifts for the blank fibre. Measured for the P_{019R}-band. 148
Table 5-7:Measured wavelength shift between different CO_2-concentrations for the blank fibre. Difference of the wavelength between the LP_{019L}- and LP_{019R}-band. 148
Table 5-8:Measured wavelength at different MeOH concentrations for the blank fibre. Measured for the LP_{018}-band. 150
Table 5-9:Measured wavelength shift between different MeOH-concentrations and sum of the wavelength shifts for the blank fibre. Measured for the LP_{018}-band. 150
Table 5-10:Measured wavelength at different MeOH-concentrations for blank fibre. Measured for the LP_{019L}-band. 151
Table 5-11:Measured wavelength shift between different MeOH-concentrations and sum of the wavelength shifts for the blank fibre. Measured for the LP_{019L}-band. 151
Table 5-12:Measured wavelength at different MeOH concentrations for blank fibre. Measured for LP_{019R}-band. 152
Table 5-13:Measured wavelength shift between different MeOH-concentrations and sum of the wavelength shifts for the blank fibre. Measured for LP_{019R}-band. 153

Table 5-14:Measured wavelength shift between different MeOH concentrations for the blank fibre. Difference of the wavelength between the LP_{019L}-and LP_{019R}-band. 153
Table 5-15:Measured wavelength during CO_2 sensor test of fibre coated with 5 steps of MIL-53(Al) by dip-coating. Measured for LP_{018}-band..... 158
Table 5-16:Measured wavelength shift between varying CO_2-concentrations and sum of the wavelength shift for fibre coated with 5 steps of MIL-53(Al) by dip-coating. Measured for the LP_{018}-band 158
Table 5-17:Measured wavelength during CO_2 sensor test of fibre coated with 5 steps of MIL-53(Al) by dip-coating. Measured for LP_{019}-band. 159
Table 5-18:Measured wavelength shift between varying CO_2-concentrations and sum of wavelength shift for fibre coated with 5 steps of MIL-53(Al) by dip-coating. Measured for the LP_{019}-band. 159
Table 5-19:Measured wavelength during MeOH sensor test of fibre coated with 5 steps of MIL-53(Al) by dip-coating. Measured for LP_{018}-band. 160
Table 5-20:Measured wavelength shift between varying MeOH-concentrations and sum of the wavelength shift of fibre coated with 5 steps of MIL-53(Al) by dip-coating. Measured for the LP_{018}-band. 161
Table 5-21:Measured wavelength during CO_2 sensor test of fibre coated in-situ with MIL-53(Al)(DMF). Measured for the LP_{018}-band. 164
Table 5-22:Measured wavelength shift between varying CO_2-concentrations and sum of the wavelength change of fibre coated in-situ with MIL-53(Al)(DMF). Measured for the LP_{018}-band. 165
Table 5-23:Measured wavelength during MeOH sensor test of fibre coated in-situ with MIL-53(Al)(DMF). Measured for the LP_{018}-band. 165
Table 5-24:Measured wavelength shift between varying MeOH-concentrations and sum of the wavelength change of fibre coated in-situ with MIL-53(DMF). Measured for the LP_{018}-band. 166
Table 5-25:Measured wavelength during CO_2 sensor test of fibre coated by SAE with MIL-53(Al)(DMF). Measured for the LP_{018}-band. 169
Table 5-26:Measured wavelength shift between varying CO_2-concentrations and sum of the wavelength change of fibre coated by SAE with MIL-53(Al)(DMF). Measured for the LP_{018}-band. 169
Table 5-27:Measured wavelength during repeated CO_2 sensor test of fibre coated by SAE with MIL-53(Al)(DMF). Measured for the LP_{018}-band. 170
Table 5-28:Measured wavelength shift of repeated sensor experiment between varying CO_2-concentrations and sum of the wavelength change of fibre coated by SAE with MIL-53(Al)(DMF). Measured for the LP_{018}-band. 170
Table 5-29:Measured wavelength during MeOH sensor test of fibre coated by SAE with MIL-53(Al)(DMF). Measured for the LP_{018}-band. 171
Table 5-30:Measured wavelength shift between varying MeOH-concentrations and sum of the wavelength change of fibre coated by SAE with MIL-53(Al)(DMF). Measured for the LP_{018}-band. 171
Table 5-31:Summary of the sensor results for the blank fibre. The concentrations for CO_2 and MeOH were the highest measured concentration of the target compound during the sensor test and the wavelength shift was given as the sum of the wavelength shift 173
Table 5-32:Uncertainty of the measured wavelength during the CO_2 sensor experiment for the blank fibre. 173
Table 6-1:Comparison of the crystallographic data for SIFSIX-3-Ni and TIFSIX-3-Ni 179
Table 6-2:Crystallographic data of $NiPyF_6$..... 182
Table 6-3:Summary of the used reaction conditions during the Two-step synthesis. ... 183
Table 6-4:Combinations of reaction conditions for the one-step synthesis of TIFSIX.... 187

Table 6-5:Measured wavelength during CO_2 sensor test with fibre coated with TIFSIX at 85°C and 5 h reaction time. Measured for the LP_{018}-band. 214
Table 6-6:Measured wavelength shift between varying CO_2-concentrations and sum of the wavelength shift for fibre coated with TIFSIX at 85°C and 5 h reaction time. Measured for the LP_{018}-band. 214
Table 6-7:Measured wavelength during CO_2 sensor test with fibre coated with TIFSIX at 85°C and 5 h reaction time. Measured for the LP_{019}-band. 216
Table 6-8:Measured wavelength difference between varying CO_2-concentrations and sum of the wavelength shift for fibre coated with TIFSIX at 85°C and 5 h reaction time. Measured for the LP_{019}-band. 216
Table 6-9:Measured wavelength during MeOH sensor test with firer coated with TIFSIX at 85°C and 5 h reaction time. Measured for the LP_{018}-band. 217
Table 6-10:Measured wavelength difference between varying MeOH-concentrations and sum of the wavelength shift for the fibre coated with TIFSIX at 85°C and 5h reaction time. Measured for the LP_{018}-band. 218
Table 6-11:Measured wavelength during MeOH sensor test with fibre coated with TIFSIX at 85°C and 5 h reaction time. Measured for the LP_{019L}-band. 219
Table 6-12:Measured wavelength difference between varying MeOH-concentrations for fibre coated with TIFSIX at 85°C and 5 h reaction time. Measured for the LP_{019L}-band. 219
Table 6-13:Measured wavelength during CO_2 sensor test with fibre coated with TIFSIX at 85°c and 15 h reaction time. Measured for the LP_{018}-band. 221
Table 6-14:Measured wavelength shift between varying CO_2-concentrations and sum of the wavelength shift for fibre coated with TIFSIX at 85°C and 15 h reaction time. Measured for the LP_{018}-band. 222
Table 6-15:Measured wavelength during repeated CO_2 sensor test for fibre coated with TIFSIX at 85°C and 15 h reaction time. Measured for the LP_{018}-band. 223
Table 6-16:Measured shift between varying CO_2-concentrations and sum of the wavelength shift for fibre coated with TIFSIX at 85°C and 15 h reaction time during the repeated CO2-sensor test.. Measured for the LP_{018}-band. 223
Table 6-17:Measured wavelength during CO_2 sensor test for fibre coated with TIFSIX at 85°C and 15 h reaction time. Measured for LP_{019L}-band. 224
Table 6-18:Measured shift between varying CO_2-concentrations and sum of the wavelength shift for fibre coated with TIFSIX at 85°C and 15 h reaction time. Measured for LP_{019L}-band. 224
Table 6-19:Measured wavelength during CO_2 sensor test with fibre coated with TIFSIX at 85°C and 15 h reaction time. Measured for LP_{019R}-band. 225
Table 6-20:Measured shift between varying CO_2-concentrations and sum of the wavelength shift for fibre coated with TIFSIX at 85°C and 15 h reaction time. Measured for LP_{019R}-band. 225
Table 6-21:Measured wavelength difference between the split LP_{019}-band for fibre coated in-situ with TIFSIX at 85°C and 15 h reaction time. 225
Table 6-22:Measured wavelength during MeOH sensor test for fibre coated with TIFSIX at 85°c and 15 h reaction time. Measurement for LP_{018}-band. 226
Table 6-23:Measured wavelength shift between varying MeOH-concentrations and sum of the wavelength shift for fibre coated with TIFSIX at 85°C and 15 h reaction time. Measurement for LP_{018}-band. 227
Table 6-24: Measured wavelength during MeOH sensor test for fibre coated with TIFSIX at 85°c and 15 h reaction time. Measured for the LP_{019L}-band. 227
Table 6-25:Measured wavelength shift between varying MeOH-concentrations and sum of the wavelength shift for fibre coated with TIFSIX at 85°C and 15 h reaction time. Measured for LP_{019L}-band. 228

Table 6-26:Measured wavelength during MeOH sensor test for fibre coated with TIFSIX at 85°c and 15h reaction time. Measured for the LP_{019R}-band. 228
Table 6-27:Measured wavelength shift between varying MeOH-concentrations and sum of the wavelength shift for fibre coated with TIFSIX at 85°C and 15 h reaction time. Measured for LP_{019R}-band. 229
Table 6-28:Measured wavelength difference during MeOH sensor experiment between the LP_{019}-band for LPG coated in-situ with TIFSIX at 85°C and 15 h reaction time. .. 229

1 Introduction

In the most general sense, a sensor is a system, which transforms information from the environment into an analytically useful signal [1]. Sensor systems are needed in numerous applications ranging from control and automatization in manufacturing through to personal devices such as smart phones. However, the usage of sensors is required everywhere, where information from the environment is collected in order to react to external influences. Therefore has every living being has sensors ("sensory nervous system") in order to fulfil basic needs such as maintaining the organism (*e.g.* with food and water), warning from danger to interactions with other individuals [2].

Sensors can collect various information such as physical properties (*e.g.* temperature and pressure) through to chemical sensors which detect the concentration of a target compound or the composition of a system. However, the production of a chemical sensor is often more demanding than a physical sensor. The perfect chemical sensor should be an "inexpensive, portable, fool-proof device that responds with perfect and instantaneous selectivity to a particular target chemical substance (analyte) present in any desired medium in order to produce a measurable signal output at any required analyte concentration" [3].

Such a perfect chemical sensor system is far from existing and compromises must be made. In particular, sensor systems which can measure changes in chemical concentrations with short response times ("in-situ measurement") are some of the most demanding systems to be manufactured. Furthermore, the measurement process in a chemical sensor is often separated into different steps with the most important ones are being the recognition process and signal transduction. The recognition process identifies changes in the environment and is responsible for the sensitivity and selectivity of the sensor system. The signal transduction step translates the signal from the recognition element into an interpretable response. Only sensor systems where these steps are well matched can show a good sensor performance.

Existing in-situ sensor systems are often expensive, bulky and difficult to use and there is always a demand for improved in-situ chemical sensor systems.

One possible application, is the in-situ measurement of Volatile Organic Compounds (VOCs), which are in general considered as harmful for our health [4]. Typical sources of VOCs are outgassing from paints or furniture, and due to the origin of these sources, the concentration of VOCs is often a few times higher indoors than outdoors [5]. This has become increasingly a problematic issue, because we spend more and more times indoors (about 90% of our time [6]) and the direct measurement and control of VOCs concentration (known as "Central Heating Ventilation and Air-Conditioning" [7]) are necessary to maintain a comfortable atmosphere and to prevent long-term medical issues such as cancer and nerve damage. Even very low concentrations are considered a risk for our health and the air concentration for different VOCs like benzene or dichloromethane is limited to 10 ppb [8].

Another example is the measurement of CO_2-concentrations, best known for its role as a greenhouse gas. However at the same time, it is produced all the time by every living being

and increased concentration affects both well-being and productivity. Furthermore, the in-situ measurement of CO_2-concentration is of importance in fields, ranging from medicine [9] to process control of bioreactors [10].

Thus, new measurement principles and advances in sensor processing might lead to the development of sensors with improved performance [3].

Optical fibre sensors represent such a promising new approach to sensor systems. They are based on optical fibres, which have become the backbone of our globalised world by connecting different continents with internet and telephone [11]. However, in order to transport information over large distances optical fibres have a low attenuation loss and consequently interact minimally with the environment outside of the fibre, restricting their use as a sensor systems per se. Several possible modifications and working principles have been applied to increase the interaction of an optical fibre to environmental changes in order to create a sensor. Amongst the approaches long-period grating fibre sensors (LPGs) show advantages in comparison with other optical fibre sensors. They are small, lightweight, inexpensive, have extremely short response times, down to a few ms [12], are immune to electromagnetic interferences and are more mechanically robust than other optical fibre systems.

LPGs are a promising in-situ sensor platform, but, in general, they show low selectivity toward changes of the environment and the addition of a coating to act as a recognition system is needed to add sensitivity and selectivity. Several coatings have been applied to LPGs for the fabrication of sensors for the detection of target compounds as diverse as humidity [13], hydrogen [14], different VOCs (*e.g.* toluene [15] or acetone [16]) or to act as biosensors [17].

Metal-organic frameworks (MOFs), a new class of porous materials, have properties, which make them ideal for the application as a recognition layer on LPGs. They are composed of metal atoms or clusters linked by organic molecules and by variation of the starting material or reaction conditions the morphology and chemical properties can be precisely controlled. Even though they have a lot of potential and received attention in fields as diverse as gas separation and purification [18] or catalysis [19] they are barely commercialised. Despite the varying structures and properties of MOFs the most common synthesis protocols are still time and energy consuming, need large quantities of solvent and are difficult to scale [20]. Another problem is that MOFs are normally first prepared as powder samples, while the preparation as thin-films are mandatory for several applications for example as the above-mentioned recognition elements on LPGs. However, the transfer from powder synthesis to thin-film synthesis is not trivial and often laborious work is needed to prepare thin-films with the desired properties *e.g.* film thickness, morphology or uniformity.

Consequently there are only few reports of the successful application of MOFs for optical fibre sensor systems (especially LPGs) [21],[22].

The aim of this project is, therefore, the coating of LPGs with thin-films of MOFs and in order to investigate their performance as an in-situ sensor system for different target compounds such as CO_2 and selective VOCs. Further attention will be given to the

improvement of MOF powder synthesis in order to make the process more sustainable. The specific objectives include:

1) Identification of promising MOFs, which can act as a recognition layer on LPGs.

2) Investigation and possible improvement of the powder synthesis for these MOFs using more sustainable conditions.

3) Investigation of MOF thin-film synthesis on glass as a test system to control parameters which determine film thickness to morphology.

4) Application of the thin-film synthesis on LPGs.

5) Measurement of in-situ sensor response of MOF-coated LPGs to CO_2 and selected VOCs.

Structure of the thesis:

This thesis is composed of 7 main chapters, a brief summary of the chapters is given below:

Chapter 1: Introduction

This chapter gives a brief introduction and defines the aims and objectives of this research.

Chapter2: Background information

This chapter introduces the class of materials known as MOFs and show existing synthesis protocols for the formation of both powder samples and thin-film samples. The state of the art for CO_2 detection and VOC detection is presented. The role of MOFs for CO_2 and VOC sensor applications and possible ways to optimize the properties of a MOF for CO_2 capture and storage will be discussed. The measurement principles of several optical fibre sensors will be introduced and compared with the properties of LPGs.

Chapter3: Synthesis of MIL-53(Al) in low-weight alcohols

MIL-53(Al) was identified as a potentially interesting MOF for the coating of LPGs as a suitable recognition layer. The synthesis of MIL-53(Al) in low-weight alcohols is reported and the properties of these materials in comparison to existing synthesis protocols investigated.

Chapter 4: Thin-film synthesis of MIL-53(Al) on glass

As a preliminary study for the synthesis of MIL-53(Al) on LPGs, the synthesis of MIL-53(Al) on glass slides is described. Existing thin-film syntheses are applied and optimised or modified to create a thin-film of MIL-53(Al) with controllable thickness and morphology.

Chapter 5: MIL-53(Al) coatings on LPG for CO_2 and VOC detection

The thin-film coatings of MIL-53(Al), investigated in chapter 4, are applied to LPGs and the in-situ sensor response with respect to different concentrations of CO_2 and selected VOCs tested.

Chapter 6: A novel hybrid ultramicroporous material as coatings on optical fibre sensors

The ultramicroporous material TIFSIX-3-Ni, with unmatched CO_2 capacity and selectivity at low CO_2 concentration of 2000 ppm, is investigated as a potential material for a thin-film on LPGs for use as a recognition layer. Preliminary steps include the improvement of the

powder synthesis and development of a thin-film synthesis for TIFSIX-3-Ni. Investigated thin-film coatings will be applied on LPGs and the in-situ sensor response regarding different concentrations of CO_2 and selected VOCs tested.

Chapter 7: Conclusions and Future Work

This chapter summarises the results from the research conducted and gives suggestions for future work, beyond the scope of this project, and to further extent the field of MOF thin-film synthesis and optical fibre sensor systems.

Additional chapters provide details for chapter 4 “Thin-film synthesis of MIL-53(Al) on glass” and chapter 6 “A novel hybrid ultramicroporous material as coatings on optical fibre sensors”.

Authour’s published reseach paper and conference contributions

1. J. Warfsmann, B. Tokay, N. R. Champness (2016): “Sustainable Metal Organic Framework Thin-Films for Medical Sensing Application – An investigation of different thin film synthesis”, Poster Presentation at LINK16, Nottingham, 3. June 2016

2. J. Warfsmann, B. Tokay, N. R. Champness (2018): “Synthesis of hydrophobic MIL-53(Al) nanoparticles in low molecular weight alcohols: systematic investigation of solvent effects”, CrystEngComm, **20**, (32), pp. 4666-4675.

3. J. Warfsmann, B. Tokay, N. R. Champness (2018): “Synthesis of Hydrophobic MIL-53(Al)-Nanoparticles in Low Weight Alcohols: Systematic Investigation of Solvent Effects“, Poster Presentation at 7th EuCheMS, Liverpool, 26. – 30. Aug. 2018.

2 Background Information

The aim of this thesis is the identification of promising MOFs for selective and sensitive coatings on a special type of optical fibre sensors, the so called long-period grating fibre sensors (LPGs) in order to create in-situ CO_2 and VOC sensors. Background information about the state of the art of CO_2 and VOC detection, information about existing optical fibre sensors, the use of porous materials (especially MOFs) for the capture and detection of CO_2 and VOCs and how MOFs can be modified in order to increase their selectivity and capacity towards specific target compounds will be given. Furthermore are possible synthesis methods of MOFs as powder samples and thin films introduced.

2.1 State of the art for CO_2 detection

Due to the ubiquitous nature of CO_2 and the various number of possible applications, the concentration of CO_2 has to be measured at very different conditions and is of importance for example for air pollution measurement [23] or the process control of bioreactors [24]. CO_2 measurements at lower concentrations with high precision is especially important for medical applications and for indoor air quality investigations. Even comparably low CO_2 concentrations of 1400 ppm have negative impacts on health and productivity, with symptoms like headache and reduced concentration [25]. While in offices and schools, an increased CO_2 level leads mostly to discomfort, the observation of CO_2 levels can be vital in spaces with limited ventilation like mines [26] or submarines [27]. In medicine, is it possible to detect pulmonary diseases or asthma [9] by observing CO_2 levels in the breath and the in-situ measurement of CO_2 level for anaesthetized patients (capnography) is a standard procedure to immediately identify problems like leakage, oesophageal intubation or severe complications like malignant hyperthermia [28].

Due to the very different specifications needed for CO_2 sensing regarding measurable range, detection limit, response time and sensor size very different systems have been developed:

One CO_2 sensor type (the so-called Severinghaus electrode [29]) measures the pH change induced by CO_2, forming carbonic acid in an aqueous solution. However, the measurement depends on the diffusion of the CO_2, which limits the response time and gives typical problems of a pH-sensor such as cross-contamination by volatile gases and acid/basic compounds, temperature dependency [30] and the need for expensive maintenance and recalibration on a regular basis [24]. Still, this type of CO_2 sensor is commonly used for the detection of CO_2 in liquid samples, especially blood [31].

Other systems used for the detection of CO_2 are mass spectrometry (MS) and gas chromatography (GC) [32]. MS enables in-situ measurement, but is extremely expensive, due to high infrastructure and operating cost and needs experienced operators for the interpretation of the signals [22]. GC is less expensive, but has measurement times of ~10-20 min. Due to the disadvantages of pH-sensors, gas chromatography (GC) and mass spectrometry (MS); chemical and infrared (IR) sensors have been turned into the quasi-standard for most CO_2 sensing applications.

In general, chemical gas sensors are small, lightweight, robust and need only low power, but problems such as long-term stability, degradation of the detection limit and loss of sensitivity are often observed [33]. A typical chemical sensor contains a sensitive material, which adsorbs CO_2 and gives a specific signal and different measurement systems have been introduced like thermal, mass, electrochemical, potentiometric or conductive sensors [10]. Amongst the different chemical CO_2 sensors, the conductive metal oxide sensors (MOX) are the most common ones. The basic set-up of a metal oxide sensor can be seen in Figure 2-1. Electrodes are embedded into a semi-conductive metal oxide layer. The metal oxide of the surface can interact with the target molecule CO_2, which changes the conductivity of the metal oxide. Heating is necessary to enable a fast enough diffusion in the metal oxide [34]. However one problem about this sensor is that other reducing gases (*e.g.* ozone or different VOCs) or humidity might interfere with the measurement and a MOX sensor are prone to poisoning [35]. Compounds as diverse as sulphides, phosphates or organic halides can from passivating overlayers on the heated metal oxide surface of the sensor [36].

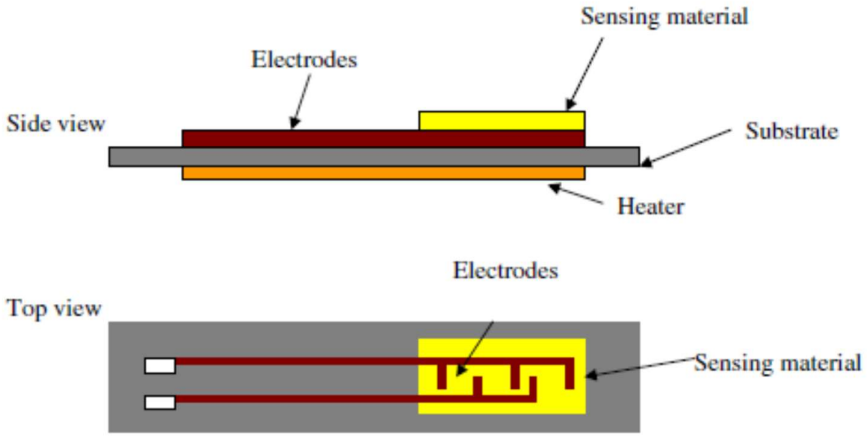


Figure 2-1: Schematic image of a typical metal oxide sensor (MOX) [37].

MOXs have a working range of normally 2,000-10,000 ppm [38] but sensitivities in ppb range have also been reported [39]. Different metal oxides have been introduced (*e.g.* SnO_2 [40] or $BaTiO_2{\cdot}LaCl_3$ [41]), but especially NASICON ($Na_{2.8}Zr_2Si_{1.8}P_{1.2}O_{1.2}$) [42] has proven the most promising system due to the lower susceptibility to influences such as humidity and increased long-term stability, but the disadvantage is still the need to heat the system up to 550°C [41].

The other common CO_2-sensor type is based on absorption of IR light in the target molecule. They are normally built as NDIR systems (non-dispersive infrared), the basic principles of which can be seen in Figure 2-2. The IR beam is emitted and guided through a measurement cell, which contains the sample gas. CO_2-sensors normally have a second cell with a non-absorbing reference gas (*e.g.* N_2) to compensate for external influences like temperature and to improve the detection limit, by using the reference cell as the blank value [37]. The measured intensity of the IR light is directly related to the concentration of

CO_2. For the measurement of CO_2, a wavelength of 2350 cm^{-1} is often used and wavelength filters remove other parts of the spectrum. This band is the strongest in the CO_2 spectrum and has the advantage that in the region between ~2000-3000 cm^{-1} very few other signals can be found [43]. However, water has a weak band in this region and can, when present, interfere at higher concentrations.

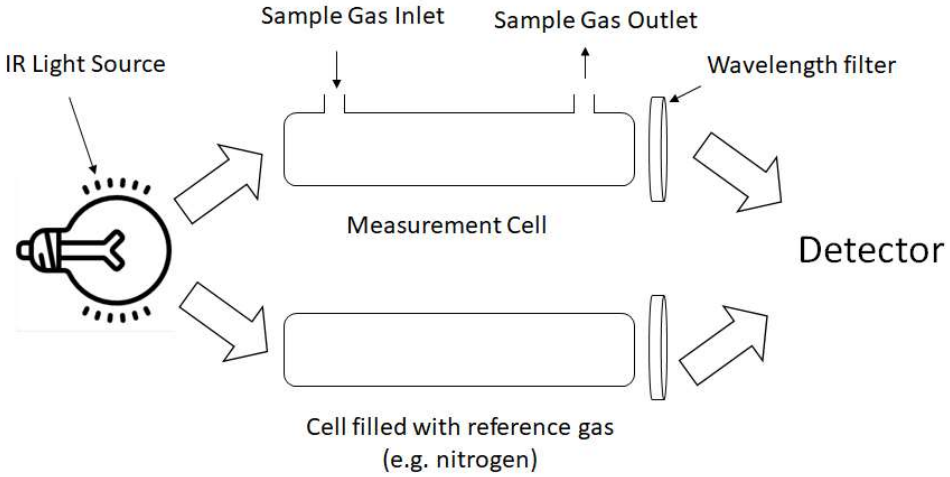


Figure 2-2: Scheme of the working principle of a NDIR sensor. One tube is filled with reference gas, the other is the measurement cell. IR light is sent though both cells and the signals compared with each other.

NDIR sensors are often easy to use, reliable and can, depending on the specifications, cover CO_2-concentrations between 200 ppm and 300,000 ppm with varying precision [44].

The use of a reference chamber reduces possible cross-sensitivity, but scattering particles like particulates or soot can still interfere with the measurement [37]. Another disadvantage is that an NDIR sensor can only be minimized in size to a certain degree. It is made up of several parts (*e.g.* light source, test chamber, detector) and often in-situ measurement is not possible. Commercial available NDIR sensors have response times ranging from 20 s to 120 s [45], and even 20 s might too slow for time-critical applications such as capnography. However active pumping (in contrast to passive diffusion) of the sample gas into the measurement cell can possibly reduce the response time [46].

Besides the CO_2-sensor types already introduced, several new measurement principles or improvements of the existing sensor types have been proposed in the literature.

One example is the introduction of a laser as the light source for the measurement [47]. In contrast to IR-light sources, lasers emit a powerful monochromatic light which makes the use of a wavelength filter unnecessary. Furthermore, laser sources are available ranging from UV to IR, whereas a wavelength range can be chosen, which does not have interaction with other compounds. This might improve the detection limit in the sub-ppm range without cross-contamination [48].

In addition, fibre optic sensors have been introduced for measurement of CO_2, where different measurement principles such as luminescence quenching [49] or photoluminescence [50] have been proposed. Another type of fibre optic CO_2-sensors measure the change of a pH-indicator embedded into a matrix. Even though these systems

are based on pH changes, the response time and sensitivity can be greatly increased in comparison with Servinghaus electrodes. For instance Liu *et.al.* [51] have coated a fibre tip sensor with thymol blue in a silica matrix which does not show temperature influence up to 40°C and has a response time of 17 s between 0-6% (~60,000 ppm) CO_2-concentration.

2.2 State of the art for VOC detection

VOCs can be emitted from various sources such as paint, cleaning agents or furniture. We are therefore in contract everyday with numerous VOCs and the concentration of VOCs are on average 2 to 5 times higher indoors than outdoors [5]. VOCs have been identified as a reason for the so-called sick-building syndrome [52]. Symptoms for the sick-building syndrome are short-time effects such as irritation, headaches, nausea and fatigue and long-time effects such as cancer and nerve damage [53].

The EU defines VOCs as any organic compound, which has a boiling point of ≤ 250°C at standard atmospheric pressure [54]. In contrast, the US defines VOCs as every carbon containing compound, besides CO, CO_2, carbonic acid and metal/ammonium carbides or carbonates, which can conduct photochemical reactions in the atmosphere [55].

Due to the extremely broad definition of VOCs, various compounds can be classified as VOCs, ranging from alcohols (*e.g.* methanol, ethanol), alkanes (*e.g.* hexane, octane), aromatics (*e.g.* benzene, xylene) or aldehydes (*e.g.* formaldehyde) to pesticides and fire retardants [56]. Consequently, VOCs have varying impact on the human health and the environment. While some are identified as carcinogenic, mutagenic or cause the formation of smog, others have less severe impact, but in general VOCs are regarded as harmful compounds [4]. Often several dozen VOCs can be measured in indoor air at one time, but each of them at concentrations in the ppm range. Despite this, the concentration can increase by several magnitudes for a short period of time after certain activities, such as painting of a room. Hence are methods needed, which detect small concentrations of VOCs. Their adsorption in porous material followed by extraction and detection is regarded the state of the art for VOC identification. In general, these methods can be separated into two classes: passive and active sampling.

The first class are passive flux samplers, which are chambers or patches filled with a porous material (*e.g.* a porous polymer [57]) where the target molecules will be adsorbed and later extracted and identified. Passive flux samplers have several advantages such as low cost, robustness and no need for supervision. They have therefore been used in different fields such as measurement of ground water contamination [57], or concentration of VOCs in indoor air [58]. However, the performance of a passive sampler is strongly dependent on the concentration of the target molecules, because the capture is done by diffusion into the porous material. Therefore, the necessary sampling time is between several hours and up to a week up for low concentrations of VOCs. During such prolonged sampling periods, back diffusion might occur [59], which leads to a mismatch between the measured concentration and the real concentration, especially for VOCs with high vapour pressure.

With active pumping, the measurement time can often be reduced, but a lot of experience and competence is needed to create reproducible and reliable results. This is because the air-flow used has a strong influence on the results and the identification of the optimum flow rate is case specific and difficult to assess [60]. Furthermore, active samplers are bulky and more expensive, because additional equipment, such as pumps, are needed. For the active flux methods, a few systems have emerged for the testing of different samples. The outgassing of VOCs from different samples can be detected in an emission field chamber (EFC). In an EFC, samples are placed in an enclosed chamber, where the outgassing can be precisely and reproducibly controlled with respect to temperature, flow rate etc. However an EFC is not portable, the test samples can have only a limited size and a measurement cannot be done directly on the test site [58]. An alternative for the on-site measurement of VOCs are field and laboratory emission cells (FLEC) [61]. FLEC are chambers made from an inert material (*e.g.* stainless steel), which are attached to the sample area such as flooring and air will be pumped through the system. The VOC from the test sample are adsorbed, often in a resin.

After both methods, the VOCs have to be extracted from the porous material (often with organic solvents) and identified, which is mostly done with a combination of gas chromatography and mass spectroscopy (GC-MS). This leads to precise results, but the high price of the equipment and the need for experienced operators for the interpretation of the results are common disadvantages. Some systems have been introduced as alternatives for MS. A photoionization detector (PID), is often faster and has lower cost, but has to be calibrated for each chemical separately and has possible problems with cross-contamination of other compounds and humidity [58]. An alternative to PID is a flame ionisation detector (FID), which can reach a high sensitivity especially for hydrocarbons (*e.g.* alkanes or alkanes), but has a reduced sensitivity for molecules containing heteroatoms [62].

Due to the very different chemical properties of the VOCs, different sampling methods (active or passive), sorbents, operational procedures and detectors, a precise documentation of the measurement process is necessary in order to make different results comparable. The process of VOC detection is further complicated by the fact that the results of VOC measurements are often not given as the concentration of the individual compounds, but as a summarised total value (TVOC) for the sake of convenience and comparability. This result can vary greatly regarding the measurement set-up used and which VOCs have been accounted for in the calculation of the TVOC [63].

While the established methods of VOC measurement by active or passive adsorption are able to detect even low ppm concentrations of VOC, often weeks pass between the sampling and the presentation of the results. This might not be problematic to identify long-time health risks, but they are far too slow for systems where an immediate result is necessary. For example, the identification of point sources of VOC emission or for the variable and automatized control of room air (Central Heating Ventilation and Air-Conditioning) [7] to improve health and working conditions. Some in-situ systems exist, such as conductive metal oxide sensors, IR or colorimetric methods. However, these in-

situ systems have to be calibrated on a regular basis and are often susceptible to cross-contamination.

2.3 Optical fibre sensors

2.3.1 Introduction to optical fibres

Optical fibres are mostly used for telecommunication and since the 1960s the performance of optical fibre has been improved. With new fabrication methods, it was possible to reduce the signal loss to less than 20 dB/km (20 dB corresponds to a reduction of signal intensity to 1%) [64] from former 1000 dB/km [65], which makes the transportation of information over longer distance possible. With reduced production cost, further improved signal loss (nowadays less than 0.1 dB/km [64]) and the possibility to transport about 65,000 times more information than a copper wire [65], they have become the backbone of our globalised world and connect different continents with internet and telephone [11]. Further improvement has led to the fabrication of fibre optics with low cost in high quality and the use of fibre optics was extended to sensor applications about 30 years ago [17]. As such, they are used for real-time detection of several parameters such as deformation of planes, ships and bridges [66] or oxygen measurement [17]. Having said this, optical fibre sensors are often a niche product, because they are still more expensive than other sensor types and complex processing steps are necessary to convert a normal telecommunication fibre into an optical fibre sensor. The set-up of such a basic optical fibre is shown in Figure 2-3.

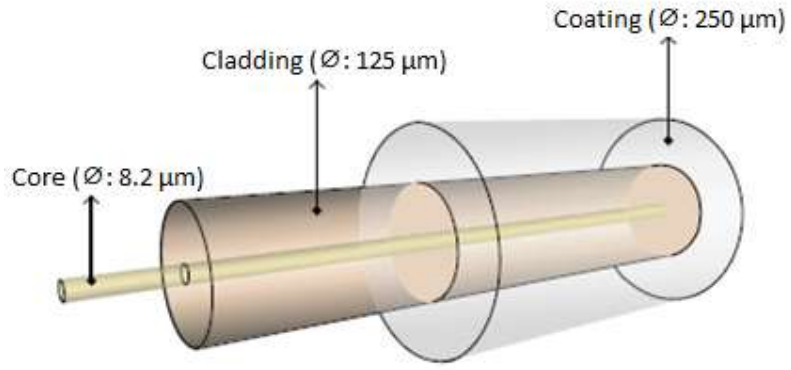


Figure 2-3: Image of a single-mode optical fibre [67].

An optical fibre is composed of a core, where the light is transported, usually consisting of silica with dopants, such as germanium, to fine tune the refractive index (RI), and a cladding of lower RI to keep the light inside the fibre by total internal reflection. In addition, a fibre normally has a coating around the cladding (often made from a polymer such as polyacrylate) for increased mechanical and chemical stability. In this basic set-up, a single mode optical fibre, one small core is inside the fibre and acts as a light guide. Other optical fibre types such as photonic crystal fibres [68] (fibre with a periodical hollow structure) have been introduced for sensor applications, but the single-mode fibre is the most commonly used type for the preparation of an optical fibre sensor.

As mentioned previously, these types of fibres are normally created for telecommunication, where a low signal loss is desired and consequently no interaction with the environment. However, in order to create an optical fibre sensor, interaction with the environment is necessary and an optical fibre has to be modified in some way in order to act as a sensor. Over the years, different measurement principles have emerged where systems are based on interferometry or evanescent waves are the most common ones.

2.3.2 Interferometer-type optical fibre sensors

In a typical interferometer, light from a single source is separated into two different beams which travel on individual optical paths before they later recombine and interfere with each other. Measurements based on interference are regarded as some of the most sensitive measurement set-ups available and have been used for instance for the measurement of gravitational waves [69]. In order to create an interferometer with an optical fibre, the light in the fibre has to be separated into different paths and recombined later. Instead of using a classical beam splitter (a semi-transparent mirror) in the pathway, the structure of the optical fibre has to be changed in a way that they can act as interferometer set-up, which further leads to miniaturisation of traditional bulky optical compounds.

One possible set-up is the Mach-Zehnder interferometer, where the light is split into a reference arm and a sensing arm. It is in theory possible to split the beam by splicing and adding a second fibre into the path, but these systems are difficult to fine-tune and have been replaced by the creation of in-line interferometer [70]. Different set-ups to create a Mach-Zehnder interferometer have been developed over the years (Figure 2-4).

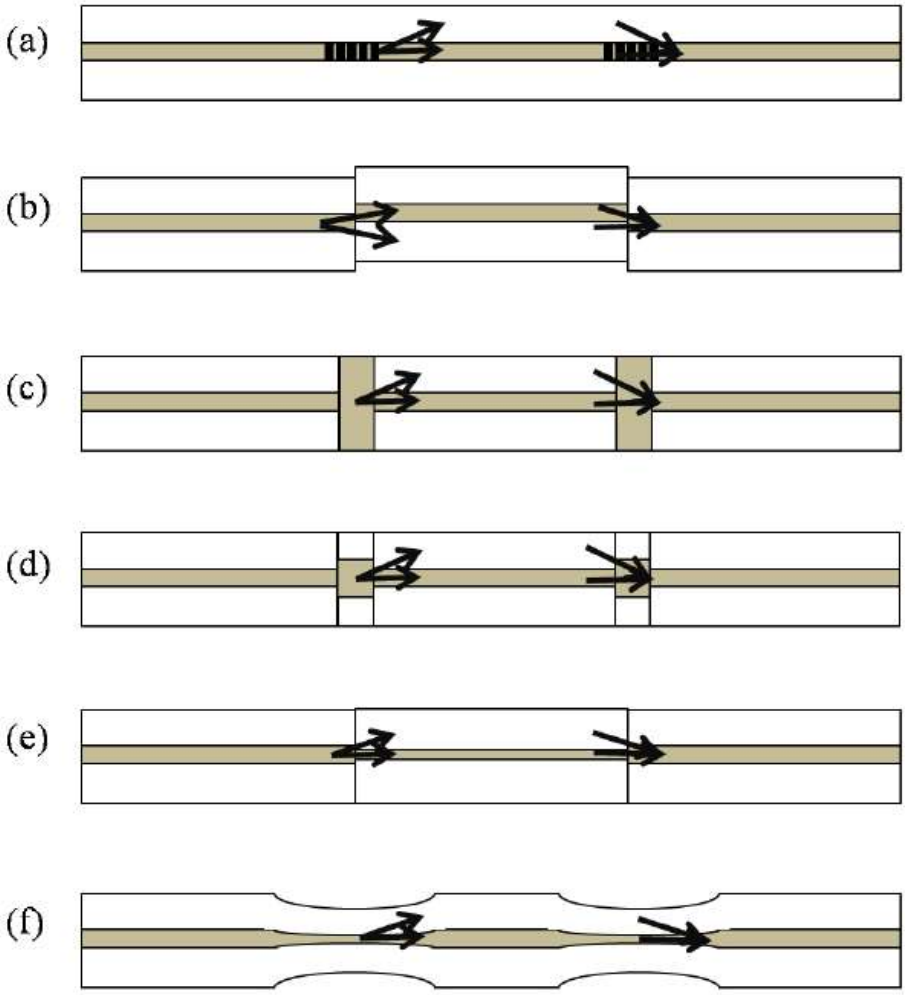


Figure 2-4: Possible configurations to create an in-line Mach-Zehnder interferometer (light brown: core of the fibre; white: cladding) [70]: a) pair of periodic perturbations, b) core mismatch, c) air holes, d) adding of segments with larger core diameter e) segment of smaller core diameter f) tapering of fibre.

Mach-Zehnder sensors have been used for the measurement of temperature changes [71], including the measurement of temperature and strain from the same fibre without cross-interference between the two results [72].

Another set-up is the Michelson-interferometer. In contrast to the above-mentioned Mach-Zehnder interferometer, the separation of the reference path and the sensor path is carried out with only one beam splitter in the fibre. The beam splitter can be added in similar ways than in the Mach-Zehnder interferometer (Figure 2-4). In a Michelson-interferometer, the beam reflected from a mirror at the tip of a fibre, which gives this interferometer a compact size and a higher mechanical stability, because no weakening modification is added in the middle of the fibre.

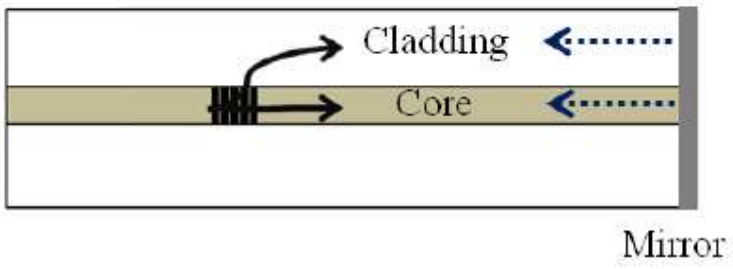


Figure 2-5: Schematic image of a optical fibre Michelson interferometer [70]. The beam splitting was implemented here by a periodic perturbation.

For a measurement, the tip has to be immersed into the measurement medium. A Michelson-interferometer shows similar influences to external stimuli in comparison with the Mach-Zehnder interferometer *e.g.* RI changes, strain and temperature. However, the Michelson-interferometer in general shows higher cross-sensitivity to temperature changes [73]. Due to the ease of fabrication and higher mechanical stability several Michelson-interferometers sensors have been published including sensors for the detection of humidity [74], CO_2-concentrations [51] or the measurement of vibrations [75]

Additional interferometer set-ups, such as the Sagnac-interferometer (the fibre is spliced into a loop and the light is transported in opposing directions [76]) or the Fabry-Perot-interferometer (two reflection surfaces are embedded into the fibre, which are separated by a certain distance [77]) have been also investigated, but these sensor types are less common than the previous mentioned Mach-Zehnder and Michelson-interferometers.

2.3.3 Evanescent wave optical fibre sensors

During the propagation inside an optical fibre the light (an electromagnetic wave) undergoes total internal reflection at the boundary between the core and the cladding. Even though the light is reflected, parts of its electric and magnetic field are able to reach outside of this boundary. This part of the light outside the boundary is called evanescent wave and has only a limited range. Normally the diameter of the cladding is larger than the potential range of the evanescent wave and no interaction with the environment takes place. This is desired in a telecommunication fibre, because interaction with the environment lead to a loss of energy and for the transportation of information over long distances the attenuation loss should be as low as possible. In order to have an interaction of the light with the environment, so it can act as a sensor system, the cladding is partly removed by either etching [78], polishing [79] or tapering [80]. With such a modification the evanescent wave can reach outside the fibre (Figure 2-6).

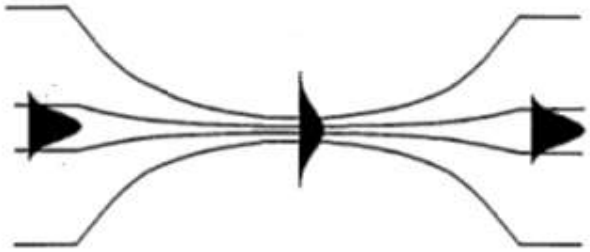


Figure 2-6: Working principle of a evanescent wave sensor at the example of a tapered fibre [80]. Normally has the evanescence wave inside the core a shorter range than the cladding diameter and does not interact with the environment. With reduction of the cladding diameter, the evanescent wave has an intensity outside the cladding and can interact with the environment.

Such a set-up has been used in several sensor set-ups to detect *e.g.* concentrations of HCl [81] or ammonia [82]. In this type of sensors, the evanescent wave interacts with the target compound and the intensity of the light is reduced depending on the concentration of the target compound [82]. However, their general problem is that part of the cladding has been removed, which reduces the mechanical stability. As a result, the fibre has to be attached in a supportive device [83] or embedded into a matrix [81] to make the sensor less fragile.

Another way to create an evanescent wave sensor is by adding periodic perturbations into the fibre, which can be done by different means such as laser radiation [84], etching, heating [85] or even mechanical force [86]. These perturbations interrupt the total reflection between the core and cladding and specific wavelength can be transported into the cladding. The cladding remains intact and therefore the mechanical stability is not affected. Two types of fibre with periodic perturbations can be identified, the short period gratings (often called fibre Bragg grating (FBG)) with a grating period (distance between the individual perturbations) of about 0.5 µm and the long period grating (LPG) with a grating period ranging up to several hundreds of µm [87].

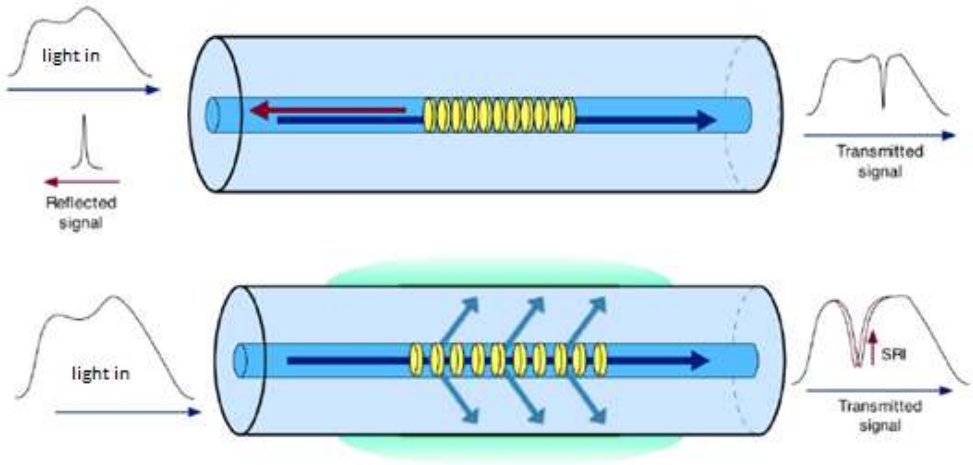


Figure 2-7: Comparison of LPG and FBG (Fibre Bragg grating) [88].

The different grating periods of the fibre leads to different direction of the coupled light (Figure 2-7). In the FBG, light of specific wavelength (the so-called Bragg wavelength) is reflected backwards and is missing in the transmission spectrum. The Figure 2-7 shows that in an FBG the light is mostly reflected without being transported into the cladding and therefore the light has nearly no interaction with the outside of the fibre. FBGs are therefore in general less useful as chemical sensors, but in contrast have a higher sensitivity to changes of physical properties such as strain, temperature or pressure [89]. The reflected wavelength can be calculated by a modified version of the Bragg's law (hence the name of the fibre):

$$\lambda = 2n_{eff}\Lambda \qquad \text{Eq.2-1}$$

Where n_{eff} is the effective RI of the core (composed of RI from core and cladding), Λ is the grating period and λ is the wavelength of the reflected light. Hence, only specific wavelength are reflected by the grating and a FBG can further act as an efficient wavelength filter [90].

In contrast, in an LPG the light is transported into the same direction in core and cladding. The transported wavelength into the cladding have a reduced intensity in the transmission spectrum, which can be seen as specific bands.

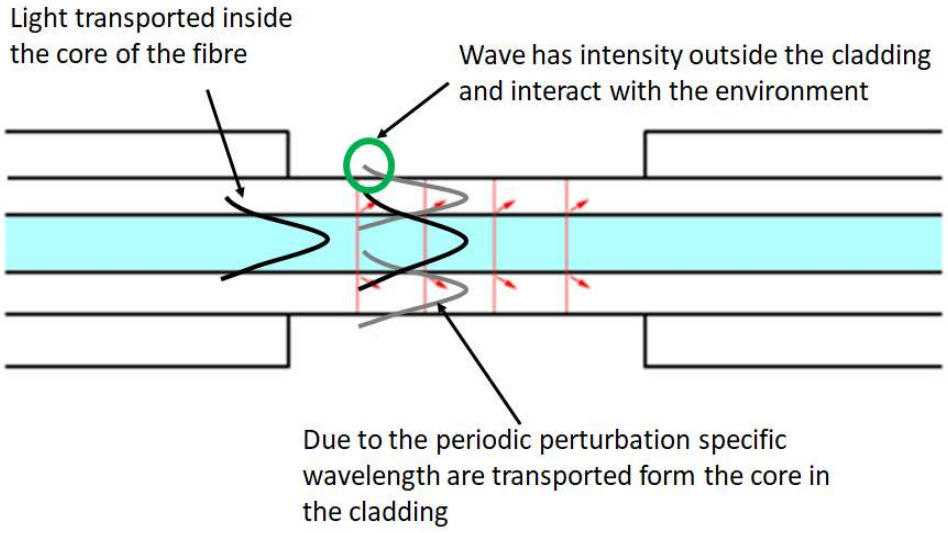


Figure 2-8: Working principle of the LPG. The wavelength has some intensity outside of the cladding. (blue: core).

The light, which has been transported into the cladding, has an intensity outside of the fibre and can have a direct interaction with the environment if the protective coating is removed (Figure 2-8). The wavelength of the different transported bands can be calculated by the following equation Eq 2-2 [84]:

$$\lambda_m = (n_{core} - n_{clad,m})\Lambda \qquad \text{Eq.2-2}$$

Where λ_m is wavelength of the *m*.th band, n_{core} is RI of the core, $n_{clad,m}$ the RI of the *m*.th order band of the cladding and Λ is the grating period, which in the distance between the

periodic perturbations. The propagating of light into the cladding has different *m* modes, for which several bands can be seen in the spectrum.

The exact position and wavelength of the bands in the transmission spectrum of an LPG depends on the grating period in the fibre and the RIs of the core and the cladding. However, these RIs are effective RIs. For instance, the effective RI of the cladding is composed of the RI of the cladding itself and the RI of the surrounding media. The formula further explains the sensitivity of LPG to outer stimuli such as temperature, strain and RI change. Strain, bending and temperature change (by thermal expansion and thermo-optic effects) leads to a change of the grating period, while a change of the RI of the surrounding media leads to a change of the effective RI of the cladding. Both effects lead to a change of the wavelength, which can be transported into the cladding and are consequently missing in the transmission spectrum. The measurement principle is therefore based on wavelength changes, which is one advantage of LPGs. Other optical fibre sensor systems (*e.g.* the above-mentioned evanescent wave sensors with tapered fibre; Figure 2-6) are often based on the measurement of intensity changes which is less robust. For instance the intensity of a light source can often vary over a period of time [91].

The RI of the core and the cladding are dependent on the used material for the fibre and cannot be changed during the measurement. With the exclusion of temperature and strain effects (*e.g*. by fixation of the fibre), a change of the wavelength of specific bands in the transmission spectrum is therefore only dependent on the RI in the surrounding medium. Different compounds have different RIs and this is further dependent on the concentration of the target compound. Hence, an LPG can act as an in-situ chemical or biochemical sensor.

In general, LPGs have a lower temperature and strain sensitivity in comparison to other sensor types such as FBGs [92], but large temperature shifts or vibrations can interfere with the measurement. However with the choice of appropriate materials for the preparation of the fibre, LPGs which are more insensitive to temperature change or strain can be constructed [93].

The above-mentioned equation (Eq 2-2) and coupled mode theory (a set of second order partial differential equations) can be used to model the wavelength of bands of different order dependent on the grating period of the LPG (Figure 2-9).

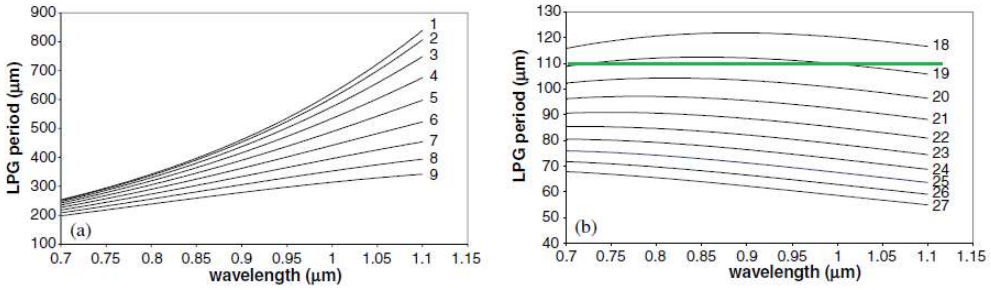


Figure 2-9 Calculated wavelength for the modes of lower order (a: 1-9) and higher order (b: 18-27) for LPG with varying grating period [94].

These images show that the observed wavelength and the order of band which can be reached is strongly dependent on the grating period of a fibre. It can be further seen, that at higher order the curve has a parabolic shape. It is therefore possible that in a transmission spectrum two observed bands are attributed to the same order. In Figure 2-9 b this is for instance shown for an LPG with a grating period of 110 µm (highlighted by a green line as guidance for the eye), where two wavelengths are attributed to the 18^{th} mode at ~0.75 µm and ~1 µm wavelength. This effect is called split band or dual response [95].

In theory, LPG shows the highest sensitivity at the vertex of such a curve, the so called phase match turning point (PMTP) and large changes of the observed wavelength occur even with small changes in outer stimuli [96]. It is however challenging to create an LPG, which exactly matches the PMTP because this is not only dependent on the grating period of the fibre, but also on other influences such as the RI of core and cladding or the diameter of the cladding. Therefore, LPG sensors often work close to the PMTP with two bands in the spectrum. An advantage of such a set-up is that the two bands show shifts to outer stimuli in opposite directions and the measurement of the wavelength difference between these two bands can be used to create high-sensitivity sensors.

For instance, Liu *et.al.* [97] coated an LPG with antibodies for the measurement of sucrose concentrations. The LPG has a grating period of 162 µm and the wavelength difference between the LP_{012}-band was used for the detection. Using the wavelength difference between the two split bands a detection limit of 0.7 mg dL^{-1} was reached (Figure 2-10). The LP stands here for "linearly polarized" and is a wave, whose field compounds (*e.g.* magnetic and electric field) are perpendicular orientated to the propagation direction of the wave, the typical wave form found in an optical fibre [98]. LP_{012} therefore means, that light is transported from the core to the 12^{th} mode of the cladding and is the typical labelling method used for different bands in an LPG transmission spectrum.

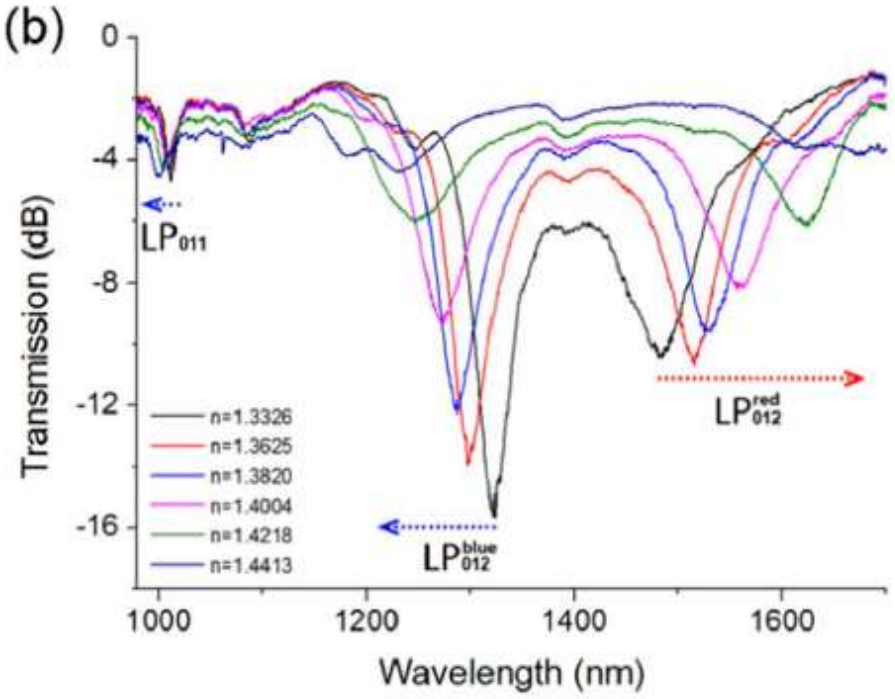


Figure 2-10Transmission spectrum of an LPG used for sucrose detection. The wavelength difference of the LP_{012}-band was used. With sucrose solutions of varying concentrations, resulting in different RIs of the solutions, the two bands of the LP_{012}-band have shifted to smaller wavelength ("blueshift") and larger wavelength ("redshift") respectively [97].

One general problem with LPGs is that they show sensitivity to any change of RI in the surrounding media. Blank LPGs can still be useful for the measurement of concentration differences in systems of known composition, such as monitoring the quality of olive oil [99] or to measure the concentration of aqueous NaCl or ethylene glycol solutions [100].

However, it is possible to add a coating on the LPG, which is the "environment" for the light wave. Such a coating can further act as a concentration element, which adsorbs target compound from the environment and improves the detection limit. If this film only adsorbs specific target molecules, selectivity can be added to the LPG sensor.

A general problem with such a modification by coating with a thin-film is that the measured wavelength of a LPG depends on the thickness and morphology of the coating [101]. Furthermore, the evanescent wave of an LPG has only a limited range in the environment outside the cladding of about 10% of the used wavelength [102]. Therefore, the film can only have a limited thickness for sufficient response and recovery times. For the measurement process, the target compound must diffuse close to the fibre surface in order to create a response and a thicker film often leads to no sensitivity or a sluggish response [103]. A good coating for an LPG sensor should therefore be homogeneous and smooth (that the response over the whole LPG compartment is comparable for sharp bands in the transmission spectrum) and show a fast change of RI upon interaction with the target compound. Regarding film thickness, normally films of up to several hundreds of nm are recommended for fast diffusion of the target molecules, but this is strongly

dependent on the chemical and physical properties of the coating and LPGs even with coatings up to 2 µm have been reported [21].

Due to the specific requirements for a coating on a LPG, such coatings are often made from SiO_2 [104] (with possible additives such as calixarene [105] or gold nanoparticles [106]), which has the advantage that the particles size can be precisely controlled [107] and established thin-film coated methods such as dip-coating [108] or Langmuir-Blodgett [101] could be applied.

With the improvement of possible coating techniques the range of materials applied for the coating on LPG have steadily increased and several other materials could be successfully coated on LPG such as graphene oxide [15], metal oxides, [109] zeolites [16] or even antibodies [97] and DNA fragments [110] for the detection of compounds as diverse as humidity [13], heavy metals [102], several VOCs [15] [16] or even large biological samples such as sucrose [97] or whole bacteria. [110].

Another advantage of the LPG is that it might be possible to create sensor systems, which can measure several parameters at the same time. As mentioned before, the response of an LPG is dependent on the grating period of the LPG. For instance, two LPGs, which are modified with the same coating and placed in the same conditions, will show responses at different wavelength, if the grating period of the used LPG is different. At the same time, it is possible to attach several LPGs in a series (with different coatings and grating periods) as long as the individual bands of the different grating periods are not overlapping in the resulting transmission spectrum. This approach has been used for instance by Hromadka *et.al.* [105] for the measurement of temperature, humidity and the concentration of VOCs at the same time.

2.4 Synthesis methods for MOFs

Metal-organic frameworks (MOFs) are hybrid materials comprising of metal atoms or clusters bridged by organic linkers. They are porous materials with one of the highest known internal surface area (up to 7000 $m^2 g^{-1}$ [111]) and their structure can be tailored in terms of pore size and chemical properties. By the combination of different metals and linkers as starting materials, MOFs with varying morphology can be prepared (Figure 2-11). With the further possibility to fine-tune their properties after the reaction (post-synthetic modification [112]) they show a greater synthetic flexibility than other porous materials, such as zeolites or activated carbon. Especially due to this flexibility they show promising properties for several applications where an accessible and controllable porosity is an important feature such as gas storage and separation [18], catalysis, [19], sensing [113] or controlled drug release [114].

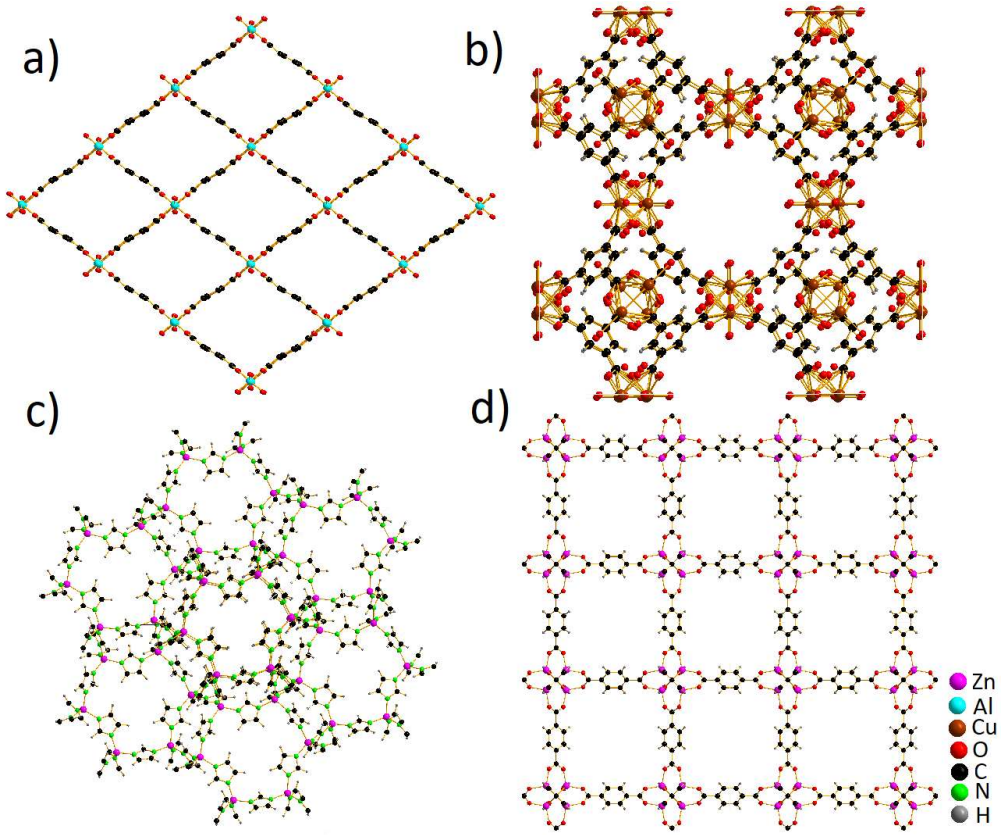


Figure 2-11: Structure of several different MOFs. The structures were calculated from existing crystal data. a) MIL-53(Al) [115] , b) HKUST-1 [116], c) ZIF-8 [117], d) MOF-5 [118].

The most common method for the preparation of MOFs is solvothermal synthesis, a synthesis approach which was adapted from the synthesis of zeolites. The starting materials are placed in solvent and the reaction mixture is heated (in some cases over 200°C) by conventional heating for prolonged reaction times (up to a week) and autogenous pressure. The MOF structures are formed by self-assembly of the starting materials (Figure 2-12). This synthesis method has only low technical demands (no sophisticated and expensive equipment is needed) and therefore can be widely applied, but often needs large quantities of solvent, is difficult to scale-up and has a high energy consumption [119]. In order to make MOF synthesis more sustainable, reduction of the reaction time and temperature is required and lower quantities of solvent are beneficial. Alternative synthesis routes have been developed such as the use of microwaves, ultrasonics or mechanochemical synthesis [120].

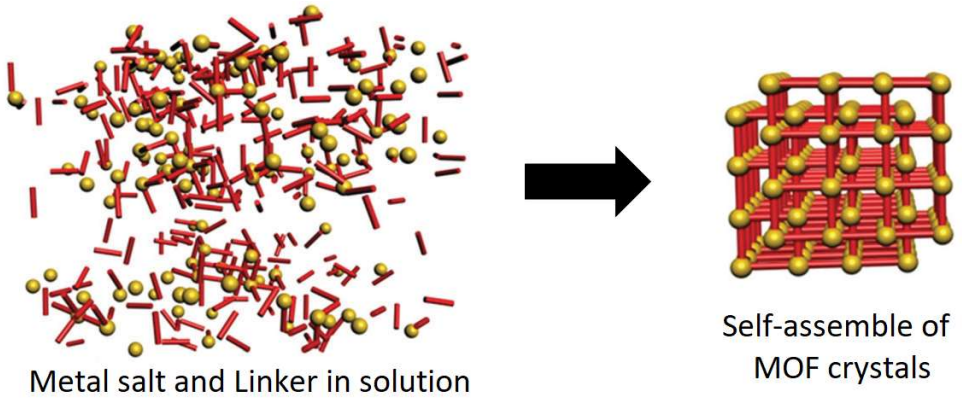


Figure 2-12: Formation of MOFs by self-assembly of MOF from metal salt (yellow ball) and linker (red rod) components from solvothermal synthesis (modified from [121]).

The use of microwaves leads to a more efficient use of energy in the reaction. In conventional heating, the thermal energy has to be transported through the reaction vessel, whereas microwaves interact directly with the reaction mixture and heat it from within (Figure 2-13). In conventional heating only about 60% of the energy is transferred into the reaction mixture, while with microwaves ~98% of the energy is used [122]. This leads to faster reaction times and it is possible to successfully prepare MOFs even in seconds [123].

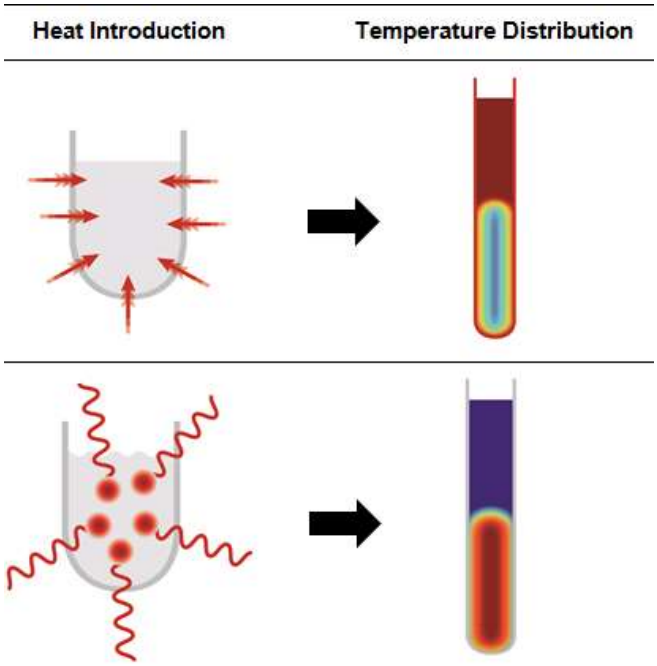


Figure 2-13: Comparison of heating by conventional heating (top) and microwave heating (bottom) [124]. In conventional heating, the thermal energy has to be transferred from outside the reaction mixture leading to a temperature gradient from the wall of the vessel into the reaction mixture. In heating by microwaves, the reaction mixture is heated from within (blue = lower temperature; red = higher temperature).

Another way to speed up the preparation of MOFs is the use of ultrasonication. During the synthesis, acoustic cavitations are formed inside the reaction mixture, which give hot-spots of extreme high temperature and pressure (~5000 K and ~1000 bar) [120]. This effect is used to both speed up the reaction and to control the particle size of MOFs by

changing the energy input of the ultrasonication [125]. For instance, it was possible to reduce the reaction time of the MOF HKUST-1 from 12 h at 180°C (using conventional solvothermal synthesis [116]) to 1 h at RT by the use of ultrasonic synthesis [126].

By the application of mechanochemical synthesis the amount of solvent can be reduced to catalytic quantities or even be completely solvent-free, often at RT. It is therefore not necessary to remove the solvent after the reaction from the product, which makes the clean-up process after the synthesis not only faster but also more sustainable. Furthermore is the mechanochemical synthesis potentially less energy consuming than other MOF synthesis (*e.g.* no energy for heating is needed). The application of mechanical forces in devices such as a ball-mill or screw-extruder leads to the breaking of intermolecular bonds in the starting material followed by a rearrangement to prototypical MOFs such as HKUST-1 or ZIF-8 [127],[128].

However, the optimisation of the synthesis conditions is only one aspect of more sustainable synthesis routes to MOFs. Another important step is the purification and separation of the product, which is often the most cost-intensive and time-consuming part [129],[130]. During the synthesis, solvent molecules or unreacted starting material can be trapped in the pores of the MOFs. These additional molecules can act as structure dictating agents during the formation of a MOFs, but must be removed after the reaction without damaging the porous structure. This has to be done in order to access the internal porosity and remove the trapped molecules, but sometimes the activation can be incomplete. This can be due to several reasons, such as retention of molecules or collapse of the porous structure upon removal of the supporting solvent molecules [131]. The most common methods to activate MOFs are heating at elevated temperatures for prolonged time or/and use of vacuum [115],[132], solvent-exchange [133] or refluxing in solvent [134] but all these methods are time and energy-consuming processes. Alternative activation methods have been applied such as the usage of supercritical CO_2 [135], which has an extremely low viscosity (0.09 mPa s at 25°C and typical working pressure of 35 MPa [136], in comparison with water of 0.89 mPa s at 25°C) and can effectively remove solvent molecules and starting material from the pores of a MOF. It is easily removed as gaseous CO_2 after the activation is complete and the working pressure reduced to ambient conditions, although the initial formation of supercritical CO_2 is energy intensive. Another attempt to reduce the effort needed for the activation was to improve the reaction conditions. For instance, Pan *et.al.* [137] prepared MIL-101(Cr) with a temperature program, preventing the trapping of linker molecules in the pores. Fischer *et.al.* [138] have prepared MIL-53(Al) in ionic liquids, where the porosity of the sample could be used without a thermal activation process. However, a disadvantage of ionic liquids is that they are extremely expensive, toxic and highly damaging to the environment [139]. Other groups have reported that for some MOFs simple washing with solvent and removal of the solvent molecules with a gas flow or even no activation process gives a MOF product with fully accessible internal porosity [140],[141].

2.5 Thin-film preparation of MOFs

The previously mentioned synthesis routes for MOFs usually lead to the formation of powders or highly crystalline samples. The use of MOFs as powder samples has been applied for several application such as gas storage or as selective adsorbent material [18]. For other applications the use of a thin-film with controllable chemical properties is advantageous, for example catalysis, where thin films have fewer mesopores and mass and heat transport can be better controlled [142]. Other possible applications of thin-films are MOF membranes, which can be used for continuous gas separation [143] or sensors where a thin-film can improve the signal transduction and sensitivity [144]. However, the production of MOF-thin films is often challenging. Besides the properties of a powder synthesis (*e.g.* morphology or particle size) additional properties such as film thickness, roughness, particle distribution or the interaction with the surface has to be controlled in order to produce a high quality thin-film. Depending on the application, the thickness of a "thin-film" can greatly vary from nanometre (100 nm film for a sensing application [145]) to micrometre (film exceeding 100 µm for gas separation [125]).

However due to the promising application of MOF thin-films, numerous reviews have discussed the possibilities, challenges and possible applications of such thin-films and a lot of work has been done in the area of MOF-thin-film synthesis in recent years [146]–[153].

The field of thin-film synthesis becomes even more diverse by the introduction of pure free-standing MOF films [154] or the usage of MOFs as a filler in polymer membranes ("mixed-matrix membranes"; MMM [155]), but often the combination of support and thin-film is important for the properties. In gas-separation (*e.g.* as membranes) the support adds mechanical stability. In sensing applications, the thin-film improves selectivity and the detection limit, while the response and signal transduction is created from the support [103]. The interaction between the thin-film and the support is therefore a crucial part of the system optimisation. The main goal is the deposition/growth of MOFs on substrates, while retaining the size, shape and chemical functionalisation of the MOFs [151].

As a relatively young class of compounds, many existing thin-film techniques have been applied from the toolbox of zeolite thin-films and the advances in both fields are continuously affecting each other [153]. However, slight modifications are required because MOFs are often prepared at lower temperatures.

The most direct thin-film synthesis method is the in-situ growth where a substrate is immersed into a MOF reaction mixture and the MOF grows on the surface to create a thin-film. The first MOF thin-film prepared in-situ was the formation of MOF-5 on an Al_2O_3 support [156], but the approach has been applied later for various other MOFs such as ZIF-8 [144] or CPO-27 [157], and on supports such as glass [144] or silicon [158]. Furthermore it is often possible to control thickness to a certain degree by repetition of the coating process [22],[144]. Alternative heating methods such as microwaves, could further reduce the necessary time for the thin-film synthesis [159].

Shah *et.al.* [160] further improved the in-situ growth by the introduction of the "rapid-thermal-deposition" (RTD) and successfully prepared thin-films of HKUST-1 and ZIF-8 on Al_2O_3. In this approach a support was wetted with reaction mixture by slip-coating or dip-coating and then placed in an oven at high temperature for short periods of time (*e.g.* for ZIF-8: 200°C for 15 min), before the oven was switched off and the sample cooled down inside the oven. The high temperature at the start is needed to accelerate the nucleation process, but the film-growth is slower at lower temperatures, which leads to the formation of a more homogenous film. Furthermore, RTD prevents a temperature shock, which can lead to the formation of cracks in the coating. An additional advantage of this technique are the small amounts of reaction mixture required, which speed-up the process in comparison to other in-situ methods and makes the process more sustainable.

While the in-situ formation has shown promising results for several applications achieving a good adhesion with the surface is often difficult. For most applications the film should be homogeneous, intergrown and free of cracks.

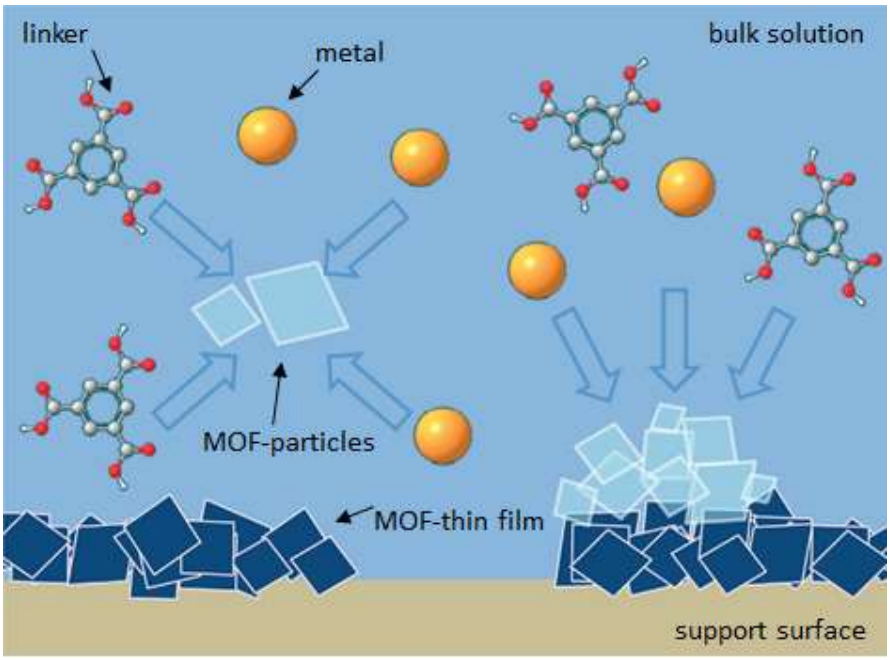


Figure 2-14: Schematic formation of a thin-film on a support [154]. Problems like formation of particles in the bulk solution can lead to thin-films which are less uniform and homogenous.

A general problem is the heterogeneous nucleation and growth process of MOFs [146]. In in-situ conditions crystals can grow in the bulk solution and sink down to the surface instead of growing directly on the surface, which leads to particles which are weakly to the surface. Furthermore, MOF crystals can preferably grow on existing MOF structures instead of growing on the support. This process often leads to a rough and less homogeneous coating (Figure 2-14).

Furthermore, the quality of a thin-film depends on numerous different properties such as the concentration and metal/linker ratio of the reaction mixture, reaction temperature and time or the activation process to name just a few. Consequently, the synthesis of a high-quality thin-film is very laborious. For instance Lu *et.al*. [141] investigated the in-situ

coating of ZIF-8 on glass, and even with the variation of only two parameters (concentration and metal/linker ratio) the quality of the thin-film varied greatly (Figure 2-15). While in some reaction attempts, the surface was only sparsely covered (*e.g.* 1/2 metal to linker ration, 25 mM concentration of reaction mixture), could a homogenous and well-intergrown surface be prepared by slightly changing the reaction conditions (*e.g.* 1/2 metal to linker ratio, 12.5 mM concentration of reaction mixture).

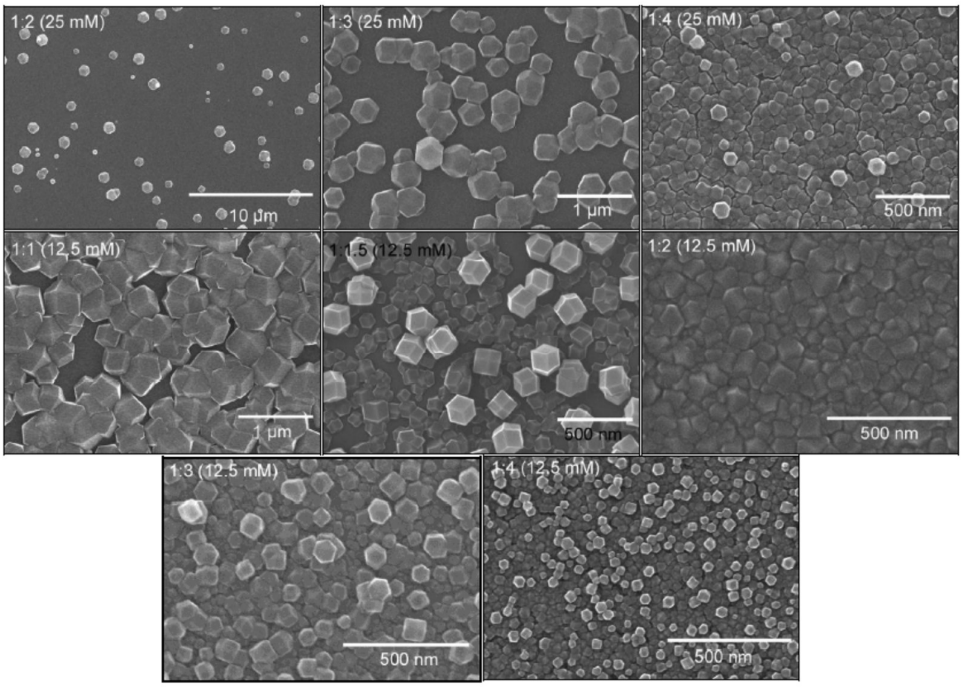


Figure 2-15: Optimisation of the synthesis conditions for the thin-film synthesis of ZIF-8 on glass by varying the metal/linker ratio and the concentration (in brackets) [141].

A possible method to overcome the problems of in-situ coating is the use of a seeding layer on the surface, followed by the thin-film growth in solvothermal conditions ("seeding and secondary growth", Figure 2-16). Due to seeding, the nucleation and film-growth can be separated in two steps. This enables, in general, a better control of the surface thickness, morphology and orientation and often better interaction with the support [161].

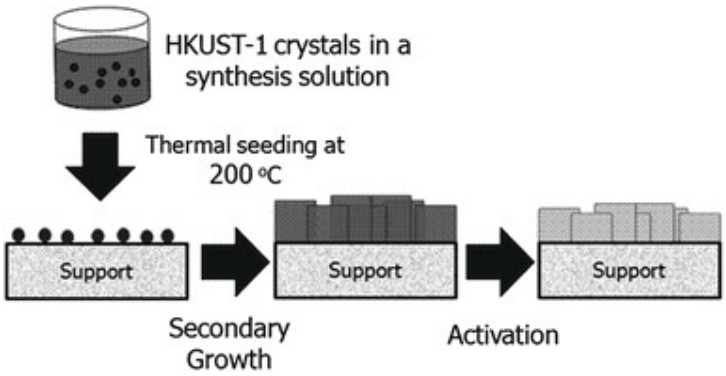


Figure 2-16: Schematic image of the seeding and secondary growth approach for HKUST-1 [162].

Comparative reports have shown the superior performance of the seeding and secondary growth to the non-seeded in-situ growth. Gascon *et.al.* [163] have grown HKUST-1 on an Al_2O_3 support by in-situ growth and on several seeded supports. The in-situ growth on a non-seeded surface led to a thin-film with random orientation and 2 µm thickness, while the growth on a seeded surface led in similar conditions a thin-film of 5 µm and increased orientation. Fan *et.al.* [164] have coated an Al_2O_3 membrane with NH_2-MIL-53(Al) by in-situ growth and on supports seeded by dip-coating. On the in-situ coated surface, more gaps and cracks in the coating were observed which led to reduced performance in a gas separation study.

For the seeding and secondary growth approach, different types of seeds have been applied. While most methods use small particles of the desired MOF, some groups seeded a surface with the starting material (metal or linker [165][166]) of the corresponding MOF. In addition to this, alternative seeds such as polymers [167] or even a different MOF [168] have been investigated. In some cases, the support itself has been used for the formation of seeds. For instance Zhang *et.al.* [169] treated an Al_2O_3 sheet with a mixture of H_3PO_4 and H_2O_2 in order to create seeds for the formation of MIL-53(Al). This direct seeding from the surface leads to a good interaction with the surface but is limited to very specific supports.

Due to the importance of seeding for the thin-film quality, very different approaches have been used for optimum control of the thin-film growth conditions. Possible seeding methods are the coating of a surface with a suspension of the MOF by dip-coating [164] or spin-coating [163] or even the solvent-free mechanical rubbing of MOF seeds onto a support surface [170]. Other reports have tried to increase the interaction of the seeds with the support by heating the support surface before the seeding process ("thermal seeding") [162] or to initiate the seeding by microwaves [171]. These seeding methods are normally followed by a secondary growth step in solvothermal conditions, but alternative methods such as microwave [171] have been introduced to speed-up the secondary growth.

For good film growth in the secondary growth step, the seeds need a good interaction with the surface (so they are not washed away during the secondary-growth) and should be equally distributed over the surface. Therefore, some of the seeding-methods are adopted

for the growth of a thin-film on surface without a subsequent secondary growth step. Such thin-films have been prepared for instance by redispersion of a powder sample in solvent and dip-coating [172] or the spray-coating of a suspension on a surface [173].

Still a general problem about the methods mentioned, the growing a thin-film from a MOF reaction mixture, is the difficulty in controlling film-thickness and morphology. Alternative methods of thin-film coating have been introduced to enable the control over the film-thickness with atomic resolution. Some earlier examples of controlled MOF thin-film growth in mild conditions and with controllable thickness, were carried out using the Langmuir-Blodgett technique [174], but this is often limited to specific MOFs. A more versatile approach is the Layer-by-Layer technique (LbL), which is also called liquid phase epitaxy [150]. For the LbL, a support is alternating immersed into compounds with opposite polarity and based on the electrostatic attraction and self-assembly of the compounds a thin-film is formed (Figure 2-17).

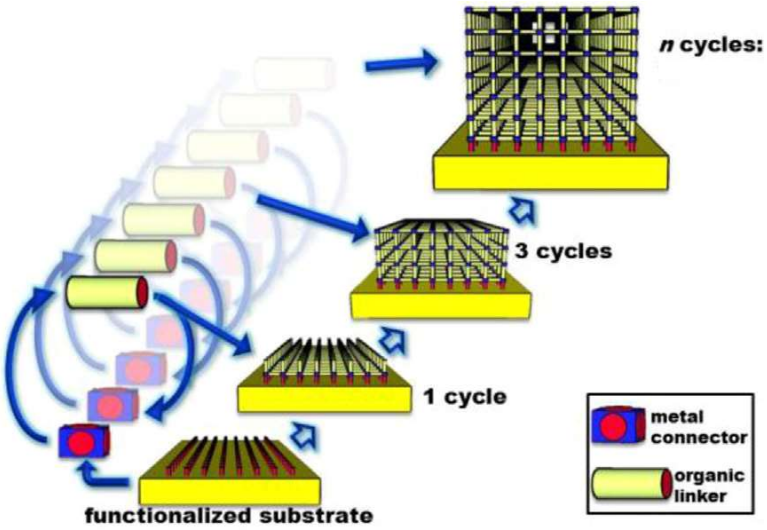


Figure 2-17: Schematic description of the Layer-by-Layer approach for the formation of a MOF thin-films [175].

Surfaces are often modified by immersing in basic solutions [97] or adding self-assembled monolayers (SAMs) onto the surface in order to add a starting point for the thin-film growth. These SAMs are normally long-chain thiolates, where the sulphur acts as an anchor to a gold-coated surface, while long alkyne chains enable the well-ordered orientation of the SAMs and the chemical properties are controlled by the terminal group of the SAM (Figure 2-18). Furthermore a SAM can even control the orientation of the film by using different terminal groups leading to MOF thin-film with different orientations [176].

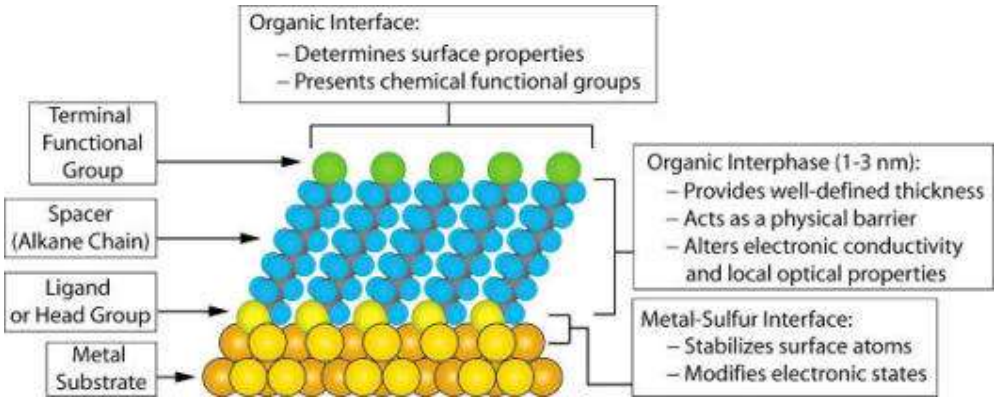


Figure 2-18: Schematic diagram of a typical SAM and description of the function of the different parts [177].

The LbL approach has first been introduced for isoreticular MOFs (IRMOFs [178]), but was soon applied to other MOFs such as ZIF-8 [179] or CPO-27 [180]. Furthermore, it was possible to prepare MOFs, which cannot be synthesised in solvothermal synthesis by the LbL approach. One example is the formation of MOFs with longer linker molecules, which is a possible method to increase the porosity of a MOF, but these MOFs have a tendency of framework interpenetration, which reduces the possible porosity again. By the LbL approach, long-chained MOFs could be successfully prepared on a surface without the risk of interpenetration [181]. The possibility to grow different MOFs on each other to create multifunctional thin-films further shows the flexibility of the LbL approach [182].

However, while the LbL approach enables the precise control of the properties of a thin-film, it is a time consuming process and the film thickness is often limited to about 100 nm, which is much too thin for some applications, such as membranes for gas separation [183].

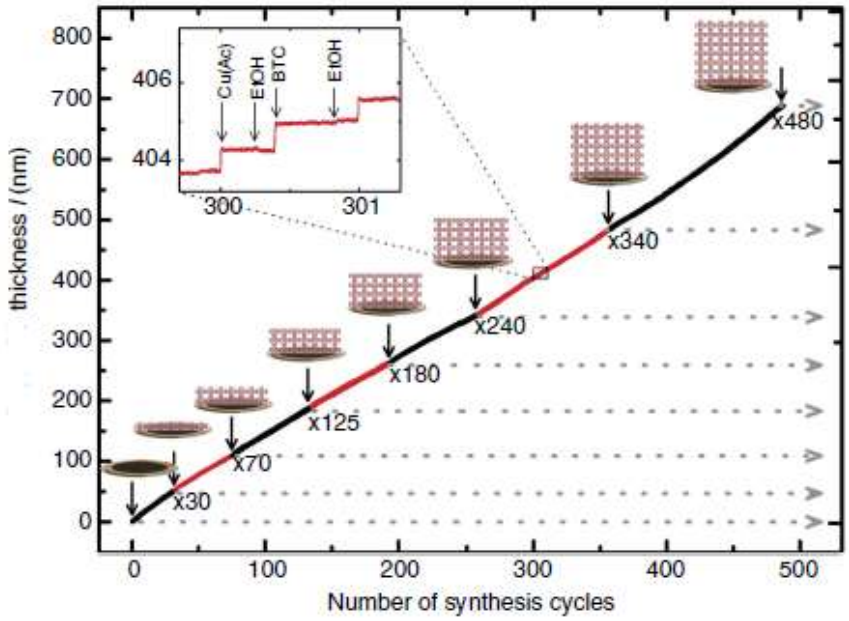


Figure 2-19: Slow formation of a thin-film by LbL regarding the film thickness and number of layers needed at the example of HKUST-1 recorded by a quartz-micro balance (QCM) [184]. Insert shows the growth of the thin-film with atomic precision.

This is further highlighted by Figure 2-19. For the growth of a 1 µm thick film about 700 cycles are necessary, which is only achieved after long reaction times. With the typical reaction times for HKUST-1 (30 min immersion in metal solution and 60 min in linker solution) [185] over 43 days are needed for the formation of a 1 µm film, not including additional steps such as gold coating, SAM formation or washing steps. Several improvements of the LbL approach such as automatization [186] and spray-coating [183] have been described. For instance, the spray-coating method reduced the synthesis times of HKUST-1 to only 10 s for the metal solution and 20 s for the linker solution for each cycle, which makes the use of LbL for the formation of thicker films more reasonable. Still, in general, the thin-film techniques from MOF reaction mixtures are useful for films in the micrometre range, while the LbL approach is aiming for the nanometre range.

Another method to create MOF thin-films uses electrochemical methods in an electrolytic cell, where the formation of a thin-film can be precisely controlled by alternating several parameters such as the concentration of the electrolyte, voltage and current. This approach, however, can only be applied for conductive supports. Three different methods have been applied so far: anodic, electrophoretic and cathodic deposition (Figure 2-20).

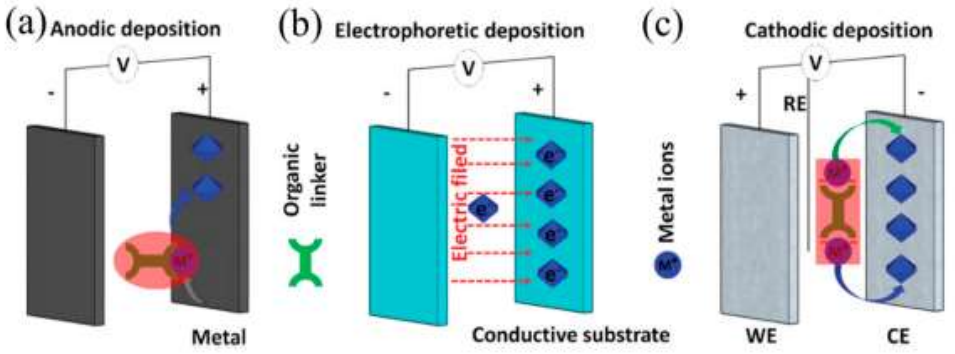


Figure 2-20: Schematic image of possible electrochemical synthesis methods of MOFs [147].

In anodic deposition (Figure 2-20 a), electric energy is used to oxidize a metal membrane, which acts as the metal source. The electrolyte contains the linker for the formation of the MOF and a thin-film of the MOF is formed on the anode. This approach was first applied for the synthesis of HKUST-1 from a copper electrode [187], but has also been applied for other MOFs such as MIL-100(Fe) [188].

In the electrophoretic deposition (Figure 2-20 b), solutions containing MOF particles are aligned in the electric field between two conductive electrodes forming a thin-film on the electrode surface and has been used for MOFs such as HKUST-1, MIL-53(Al), UiO-66 or NU-100 [189][190].

In the cathodic deposition (Figure 2-20 c), the electrodes are not used as reactants. Instead, they act as a source of electrons in the reaction. The electrolyte contains the starting materials for the formation of the MOF. The electrons deprotonate linker molecules, while forming hydrogen and react with the metal in the solution to form MOF particles for the formation of thin films [191].

The above-mentioned methods (coating from MOF reaction mixture, LbL and electrochemical methods) have already shown a large variety of possible approaches to prepare thin-films of MOFs, but there are several additional methods which have been reported in literature. These include counter-diffusion methods, where metal and linker solution diffuse into a porous membrane from two sides [192], or the hot-pressing method, where a powder mixture of metal and linker is placed on a surface and the solvent-free synthesis of a MOF thin-film is conducted by pressing with a heated stamp [193]. All these methods presented give an impression about the huge variety of MOF thin-film coating methods.

2.6 Porous materials for CO_2 capture and detection

As mentioned previously (chapter 2.1, p. 5), CO_2 is an ubiquitous gas and despite its biological, medical and economic importance, CO_2 is still best known for its role as a greenhouse gas. CO_2 levels in the atmosphere has increased from 280 ppm in pre-industrial times to about 400 ppm, due our dependency of fossil fuels for energy production and transportation. However, with growing global population and industrialization in developing countries, worldwide demand of energy is still increasing [194]. As a possible way to limit the global warming, the introduction of "negative emission" has been discussed [195]. For this, CO_2 has to be removed from atmosphere and stored in geological structures or underwater [195].

These attempts have been summarized as "Carbon Capture and Storage" (CCS) for reducing CO_2 emissions at points of large emission such as power plants and factories.

At the moment, three main approaches are investigated [196]:

- Post-combustion capture; where the CO_2 is removed from flue gas.
- Pre-combustion capture; where fuel is not burned directly but turned into syngas. In the syngas is the reaction shifted to H_2 and CO_2. While the H_2 is used as fuel, the concentrated CO_2 can be separated.
- Oxy-fuel; where the fuel is burned with pure oxygen and the resulting flue gas is composed of mostly water and CO_2.

As an additional technique, Direct Air Capture (DAC) has emerged [196], but is often considered not as a classical CCS technique. CCS aims to remove CO_2 at point sources, which only cover about 50% of total CO_2 emission [197]. The removal of CO_2 from smaller sources and directly from the atmosphere might cover this gap. For DAC to be successful, a technique needs to be developed with different performance parameters to classical CCS methods. For DAC, high CO_2 selectivity and capacities at low CO_2 concentrations (less than 1% CO_2 concentration in the atmosphere) and ambient pressure/temperatures must be achieved. Different DAC approaches have been investigated, which are mostly based on the absorption of CO_2 in basic compounds (*e.g.* NaOH) as carbonate. However these

processes suffer from low capacities and problems with desorption and recovery of the absorbent, which makes the process expensive and energy consuming [197].

However, CCS has until now only been used in some pilot-plants. Problems are the higher energy cost (energy is needed for the CCS which reduce the overall efficiency of the plant [198]) and often problematic implementation into existing plants. As shown in Table 2-1, the CCS techniques have different working conditions regarding temperature, pressure and CO_2 concentrations and different materials and instrumentations are needed for each technique.

Table 2-1: Comparison of the different conditions for CO_2 capture applications [196],[197].

Technique	Pre-Combustion	Post-Combustion	Oxy-Fuel	DAC
Pressure	Up to 5 bar	~1 bar	Up to 50 bar	~1 bar
Temperature	Over 100°C	~ 100°C	Less than 50°C	~25°C
CO_2 concentration	~35%	Up to 15%	Over 90%	<1%

The most common and technically mature technique to remove CO_2 is amine scrubbing, where an aqueous solutions of alkylamines (e.g. diethanolamine or ethanolamine) are used to capture CO_2 [199]. In an amine scrubber, the CO_2 is absorbed over a carbamate intermediate as a hydrogen carbonate [200]. The process is fully reversible, but the high heat capacity of the solvent (water) makes the recovery very cost intensive [201]. Another disadvantage is that the amines degenerate in these conditions with oxygen [202] and the highly corrosive nature of the alkylamines used.

Due to the disadvantages of the amine scrubber, alternative methods like membrane separations [203] or cryogenic distillation [204] have been investigated, but the use of porous sorbent materials is a particularly promising approach for CO_2 separation. In porous materials the gases are adsorbed instead of the chemical absorption that occurs in the amine scrubber. The adsorption is by 3 orders of magnitude faster than the absorption [205]. In addition, the heat of adsorption is lower, giving reduced energy demand for the recovery. Porous materials such as zeolites, silica and activated carbon have been used as adsorption beds for CO_2 in applications like PSA (pressure-swing adsorption) or TSA (temperature swing adsorption) [206]. In these techniques an adsorbent becomes saturated with the compound of higher affinity (often CO_2) and the gas is removed by reduction in pressure (PSA) or increase in temperature (TSA). A porous material for CO_2 adsorption and separation should have properties such as high selectivity for CO_2, good adsorption kinetics, high CO_2 capacity and be easily regenerated [207]. However, often trade-offs are necessary. For instance, a material with high selectivity for CO_2, often has a high heat of adsorption for CO_2, which leads to more difficult regeneration.

For most applications, a high selectivity and capacity for the target compound CO_2 is most important for the working performance of a separation system [208]. The linear molecule CO_2 has several unique properties in comparison with other common molecules found in flue gas or the atmosphere (*e.g.* N_2 or CH_4) including a smaller kinetic diameter and larger quadrupole momentum and polarizability (Table 2-2). Consequently, the selectivity can be

improved by increasing the polarizability or by controlling the pore size of the sorbent material ("sieving effect").

Table 2-2: Kinetic diameter and quadrupole momentum of typical molecules found in atmosphere and flue gas.

Molecule	Kinetic diameter (Å)[209]	Quadrupole momentum (D·Å)[210]
CH_4	3.80	0.02
N_2	3.64	1.54
CO_2	3.30	4.30
H_2O	2.65	2.30
Ar	3.40	0.00
CO	3.76	2.04
H_2	2.89	0.43

Previously zeolites, silica and activated carbon have been used extensively for these adsorption processes [207]. The polarity and polarization of zeolites can be controlled by different means *e.g.* the Al/Si ratio used during the synthesis [211] or impregnation with polar compounds after the synthesis [207]. Zeolites are robust, but high temperatures are needed (up to 400°C) to remove adsorbed material, which makes the recovery energy intensive. Activated carbons are often more cost-effective (regarding synthesis and recovery), but have lower capacities and the chemical and physical properties are difficult to optimize [212].

In this regard MOFs are promising alternatives for CO_2 capture. In contrast to the above-mentioned porous materials their morphology and chemical properties are more tuneable and several methods have been investigated to increase the selectivity of MOFs towards CO_2. The most common approach is to increase the polarizability, which can be done by adding polar groups, creating a charged framework or adding open-metal sites, which can act as Lewis-Basis.

The most common way to enhance the polarizability is to add amines to the framework, in order to mimic the condition of the anime-scrubbing used for carbon capture, while retaining the fast gas adsorption kinetics of a porous material. Different ways have been investigated to introduce amine groups into the framework. These range from impregnation with amines [213] or the use of linker containing amine groups and numerous amine modified MOFs have been reported [214]. However, as mentioned previously, several trade-offs have to be made.

To highlight this, several pristine MOFs and their amine derivates have been compared with each other regarding important process parameters for CO_2 separation: porosity, thermal stability, selectivity of CO_2 to N_2 and CO_2 capacity (Table 2-3). The CO_2 capacities are shown for two different pressure regions. The CO_2 low-pressure region at 0.15 bar can be typically found in flue gases, while the high-pressure region at 10 bar are conditions utilized during PSA, Oxy-Fuel or for gas storage. The results show, that the adding of additional amine groups to the MOFs increases the capacity at lower pressure and the selectivity. This is due to a stronger interaction of the amine groups with the CO_2 in

contrast to the non-modified MOFs. A measurement for the higher affinity is the heat of CO_2-adsorption in these MOFs. For instance, the amino modified MOF NH_2-MIL-53(Al) has a heat of adsorption of -45 kJ mol^{-1} to CO_2 [215], while the pristine MIL-53(Al) has a heat of adsorption of -26.4 kJ mol^{-1} [216]. However, the data from Table 2-3 implies that the introduction of the amine leads to reduced thermal stability of the MOF.

Table 2-3: Comparison of several MOFs with their amine containing derivative regarding porosity, CO_2-capacity at different pressures and selectivity. Selectivity is given for the low-pressure region (0.15 bar).

Material	S_{BET} (m^2 g^{-1})	Thermal stability (°C)	CO_2-capacity at 25°C and 0.15 bar (mmol g^{-1})	CO_2-capacity at 25°C and 10 bar (mmol g^{-1})	CO_2/N_2 selectivity
MIL-53(Al)	1140 [115]	500 [115]	2.4 [217]	3.7 [215]	10.1[216]
NH_2-MIL-53(Al)	840 [218]	400 [218]	1.7 [217]	2.8 [217]	30 [217]
UiO-66	1425 [219]	450 [220]	1.8 [221]	5.6 [222]	26 [223]
NH_2-UiO-66	1232 [219]	310 [220]	2.1 [221]	5.2 (5 bar)[224]	32 [224]
MIL-101(Cr)	2136 [225]	350 [225]	0.5 [213]	9 [226]	13.7 [226]
NH_2-MIL-101(Cr)	2001 [225]	300 [225]	1.9 [227]	8 [228]	16 [228]

These results further show, that the pristine compounds have a higher porosity and improved CO_2-capacity at higher pressure. Furthermore, these MOFs have in general a lower heat of adsorption, whereas less energy for the recovery is needed. Therefore MOFs with increased porosity has been discussed for CO_2 separation, but the need of often sophisticated linker makes their synthesis challenging and expensive [229]. Furthermore, Mason *et. al.* [208] have shown in a comparative study, that the usage of MOFs with higher selectivity can greatly improve the economic viability in comparison with MOFs with higher porosity, but lower selectivity. It is therefore not sensible to increase the porosity at the cost of selectivity.

While amines are the most common groups introduced to increase the CO_2 selectivity, MOFs with additional azo [230], triazole [231] or amide groups have been also investigated. Amides have a potential stronger interaction and selectivity than amines, because of additional interaction of the carboxylate group with the CO_2 [232].

Another type of MOF with high CO_2 capacity and selectivity use open-metal sites with a free electron pair in the framework to strongly polarize the CO_2 [233]. Typical MOFs with open-metal sites are HKUST-1 [234] and CPO-27 (or MOF-74) [233]. The magnesium derivate of CPO-27 is one of the MOFs with the highest known CO_2-capacity at lower pressure (at 0.15 bar and 25°C: 5.3 mmol g^{-1} [233]) and a high selectivity (CO_2/N_2 selectivity at 25°C and 1 bar: >100 [208]). However, the strong interaction with CO_2 makes the removal of the CO_2 difficult and more energy is needed for the recovery of the material. An additional disadvantage of MOFs with open-metal sites is that they are less water stable, which is pervasive in most systems [206]. The water compete with CO_2 for the

open-metal sites and regeneration of the compound often leads to a reduction of porosity, CO_2-capacity and long-term stability [235].

Most of the MOFs until now have used the high polarizability as a driving force for improved CO_2-selectivity and capacity. A new group of MOFs use the smaller kinetic diameter of the CO_2 in comparison with other molecules found in the atmosphere or flue gas for selective adsorption instead. These MOFs are called hybrid ultramicroporous materials (HUMs [236]) due to their pore size, with an aperture of less than 0.5 nm [237] in comparison with other MOFs (ZIF-8: 0.9 nm [238]; HKUST-1: 1-1.5 nm [239]; CPO-27: 1.1 nm [240]). HUMs are made from layers consisting of metal ions like copper [241] or nickel [242] and a bipyridine linker. By using anionic pillars such as hexafluorosilicate (SiF_6^-) or hexafluorotitanate (TiF_6^-) primitive cubic shaped materials are formed. However the class of HUMs has recently been further extended by using non-octahedral shaped anions [243]. For instance, the HUM SIFSIX-3-Cu (composed of copper(II) cations, pyrazine and SiF_6^-) has a pore size of 3.5 Å, which is only slightly larger than the kinetic diameter of CO_2 (3.3 Å). With a combination of the size-exclusive effect of the pores and the anionic pillars, which can polarize CO_2, a very high selectivity for CO_2 can be reached (CO_2/N_2: 1874 for the nickel derivative [235]). Investigations have shown, that the CO_2-capacity and selectivity at pressures, which can be found in typical flue gas concentrations (0.15 bar CO_2) is lower than MOFs containing open-metal sites and amine groups, but HUMs show a very high uptake at concentrations as low as 2000 ppm CO_2 (Table 2-4), which makes them a promising materials for DAC.

Table 2-4: CO_2 uptake of different MOFs at low CO_2 concentration (2000 ppm) and flue-gas conditions (0.15 bar).

Material	Uptake at 2000 ppm (mmol g^{-1})	Uptake at 0.15 bar (mmol g^{-1})
HKUST-1	0.9 [244]	3.5 [245]
CPO-27-Mg	0.5 [132]	5.3 [233]
UiO-66-NH_2	0.6 [132]	2.1 [221]
TIFSIX-3-Ni	2.0 [132]	2.6 [132]

2.7 Porous materials for VOC capture and detection

For the sorption methods, porous materials such as zeolites [246], resins [247] or activated carbon [248] have been used for the detection of VOCs and the implementation of alternative porous materials such as MOFs is an emerging topic.

MOFs have been applied for improvement of the active and passive sorption methods (see chapter 2.2, p. 8) for the detection of VOCs or the removal of harmful VOCs from the atmosphere. Their use has been investigated by several groups. For instance Britt *et.al.* [249] have compared several MOFs such as MOF-5, CPO-27 and HKUST-1 for the adsorption of different VOCs (*e.g.* benzene, dichloromethane and ethylene oxide) with the performance of commercially available activated carbon. HKUST-1 has shown a particularly improved performance. This was attributed to the interaction of the VOCs with the open-metal sites in HKUST-1, while a highly porous MOF (MOF-177 ; BET: 4508 $m^2\ g^{-1}$ [240]), but without open-metal sites and functionalisation, has shown an adsorption

performance inferior to activated carbon. The promising performance of HKUST-1 was confirmed in a study by Vellingiri *et.al.* [250], where several MOFs (*e.g.* HKUST-1 and MOF-5) were compared with zeolites and activated carbons for the sorption of a mixture of VOCs.

The importance of open-metal sites for the sorption of VOCs was also shown by Yang *et.al*. [251], who used MIL-101(Cr) as a MOF with a high porosity (BET-area: 2136 $m^2 g^{-1}$ [225]), and open-metal sites [140] for the sorption of numerous VOCs such as acetone, benzene or toluene. These reports show the adsorption performance of MOFs for a mixture of several VOCs. However, most reports about the sorption of VOC in MOFs only look at specific compounds, often for the removal of harmful substances. Examples are the usage of NH_2-UiO-66 for the adsorption of indole [252] or MOF-5 for the adsorption of formaldehyde [253].

While these reports have investigated the use of MOFs to improve the performance of sorption materials for VOC detection, the adsorption of VOCs in MOFs has been further used for the fabrication of novel in-situ sensor systems. These methods can, in general, be separated into three different classes: optical, mechanical and electrical methods [254].

Mechanical methods are often based on the adsorption of the target molecule in a thin-film on the sensor device. The devices used measure the vibration frequency of a quartz piece in a quartz crystal microbalance (QCM) or of a cantilever, similar to the tips used in atomic force microscopy (AFM). The adsorption of target molecules in the sensitive layer leads to an increased weight and a change of the vibration frequency, which can be detected. The sensitive thin-film enables at the same time the concentration of target molecules from the environment, which leads to an improvement of the detection limit [255]. In general, mechanical systems have a high sensitivity and good response times, but the sophisticated set-ups make the portable use complicated or impossible. Tu *et.al* [256] have coated QCMs with different ZIFs (*e.g.* ZIF-8, ZIF-67, ZIF-90) to detect several alcohols, aromatics and hexane-derivatives. Yamagiwa *et.al.* [257] have coated QCMs with MOF-5 and HKUST-1 and both MOFs have improved the sensor response to the VOCs (toluene, octane, acetone and ethanol) investigated with a detection limit of 1 ppm and a response time within seconds. Allendorf *et.al.* [145] have coated a cantilever with HKUST-1 for the detection of methanol and ethanol.

In contrast to the mechanical methods are the colorimetric/optical methods based on the colour change or luminescence during the adsorption of target molecules or to utilize the change of different optical properties such as the refractive index. These systems are often more robust than mechanical methods, but, depending on the used measurement systems, sometimes do not reach the sensitivity and response times of the mechanical methods.

Takashima *et al*. [258] adsorbed various benzene derivatives in a zinc-containing MOF and have observed the effects on the fluorescence depending on the target molecule used, but the adsorption of the target molecules into the pores of the MOFs takes several minutes. Lu *et.al.* [144] coated a silicon surface with a thin-film of ZIF-8 to create a device, which

showed colour changes depending on the amount of adsorbed alcohols. The colour change was measured in a reflective spectrum. This set-up was later further improved by Li *et.al*. [103]. They coated a silicon surface with hollow spheres of ZIF-8 instead of a homogenous thin-film. This improved device showed a linear response for several alcohols and aromatics between 1000 and 20,000 ppm with a response time of 2 s. Hromadka *et.al* [22] coated an optical-fibre sensor, which measure changes of the refractive index change in the coating, with a thin-film of ZIF-8 for the detection of several VOCs and have reached a detection limit of 1500 ppm with a response time of 3 min for methanol.

Electrical methods are based on changes of electrical properties such as resistance or capacitance, but reports based on this measurement systems are less common. MOFs in general are isolating materials and have to be modified by adding conducting salts or nanoparticles for the application in an electrical sensor system. One recent example of the successful application of electronical methods in a MOF is the impregnation of HKUST-1 with an ionic liquid in order to create a capacitive sensor [259]. This sensor was able to detect several VOCs with comparably low detection limits (*e.g.* 47 ppm for methanol), but with response times of ~10 min.

However, a general problem with most VOCs sensors is the limited possibility to control the selectivity of the sorbent materials. While this is not problematic, or could even be desired, if the porous materials are used as a sorbent material for passive or active flux, it can be problematic, if specific VOCs have to be detected from a mixture of compounds. While it is relatively easy to create sensors for water or CO_2, because these compounds show properties which are different from typical associated materials, many VOCs have similar chemical and physical properties. Larger compounds often show a weaker response (*e.g.* caused by slower diffusion) and a certain selectivity can be reached by size-exclusion. For instance MIL-101(Cr) has shown a reduced adsorption of *m*-xylene to ethylbenzene due to the larger kinetic diameter of *m*-xylene [251]. Having said this, it is still challenging to create a porous material which can selectively detect larger molecules (*e.g.* ethanol), while excluding smaller molecules with similar chemical properties (*e.g.* methanol). All of the above-mentioned MOF based sensor systems have shown cross-sensitivities to several VOCs. While the concentration of one compound can be detected after a calibration, it is nearly impossible the measure the concentrations of individual compounds from a mixture.

2.8 Conclusion

MOFs sometimes cannot be directly used for applications such as gas storage, separation or catalysis. For these applications, the internal porosity of the MOF must be accessible. However are directly after the synthesis solvent molecules and starting materials being trapped inside the porous structure. Such trapped species have to be removed in order to access the framework porosity. Synthesis and activation are time and energy consuming processes and there is still demand to make MOF synthesis more sustainable. MOFs are normally prepared at first as crystalline powders, but they may show their full potential as

thin-films coated on different supports for fields as diverse as catalysis or sensor applications. Different approaches have been introduced for the preparation of MOF thin-films but transfer of a powder synthesis to a thin-film synthesis is not trivial and numerous properties have to be considered for a high quality thin-film.

CO_2 is a hot topic in research because of its importance as greenhouse gas but has several other applications such as in medicine (*e.g.* for the detection of pulmonary diseases or the monitoring of anaesthetized patients). The reduction of CO_2 levels in the environment by carbon capture and storage has been introduced in this chapter and adsorption of CO_2 by porous materials has shown several advantages in comparison to established systems. MOFs have shown a lot of potential because of their tailorable structure and different ways have been shown to modify MOFs in order to increase the selectivity towards CO_2. Due to the importance of CO_2, several sensor systems for concentration measurement are available, but only very few show response times of less than 30 s, which might be too much for time-critical application *e.g*. the above-mentioned medical applications or process control of bioreactors.

The role of VOCs as a class of harmful compounds and our increased exposure to them has also been discussed. It is therefore of importance to measure the concentration of VOCs in different environments such as indoor air or ground water. However, most methods are still based on long-time adsorption. This makes the interpretation and reproducibility of the results complicated and the time between sampling and the presentation of the results can be several weeks. Hence, there is a demand for sensor systems with a much shorter response time for application such as the online control of room air, but existing in-situ system often show cross-sensitivity and problems with long-term stability.

As a new sensor platform, optical fibre sensor devices and their different possible measurement principles have been presented. Amongst them, the LPG has been identified as the most promising system. It has advantages such as low price, robustness, small size and very fast response times and has the potential to act as an in-situ sensor system. A further advantage of the LPG is that properties such as sensitivity and selectivity can be fine-tuned by adding a coating on the LPG. Several coatings have been already applied on LPGs to create chemical and biochemical sensors. For the usage as CO_2-sensors, MOFs are especially promising, as they have shown high sensitivity and capacity in DAC. For DAC, CO_2 adsorption at relatively low concentration is needed (at ~2000 ppm) and this concentration range is also typically observed in indoor air (*e.g.* office or schools). These materials might be therefore useful to crease sensor systems, which can be monitor the CO_2-concentrations in indoor air, which is of importance for our comfort and to prevent long-time health risk. In contrast, the identification of promising MOFs for the VOC detection is a more challenging task, because most VOCs have similar chemical and physical properties. However, most existing VOCs sensor systems struggle from cross-sensitivity issues and the use of LPG might reduce the sensing time drastically.

3 Synthesis of MIL-53(Al) in low-weight alcohols

3.1 Introduction

Metal-organic frameworks (MOFs) have received extensive interest due to their highly porous structure and their ability to act as efficient hosts for guest molecules. The possibility to tune pore dimensions and functionality has led to the application of MOFs in fields as diverse as gas adsorption [18], drug delivery [114], catalysis, [19], sensing [113] or controlled drug release [114].The MIL-53 class (MIL = Matériaux de l'Institut Lavoisier) of materials received much attention in recent years due to their unusual structural behaviour. Férey *et.al* [260] reported the first chromium-containing MIL-53, formed by $CrO_4(OH_2)$ octahedral clusters connected by 1,4-benzenedicarboxylic acid (H_2BDC; terephthalic acid) that lead to a porous material with one-dimensional rhombus-shaped channels. Numerous MIL-53 derivatives have been synthesized whilst preserving the overall structure by using different metal sources, *e.g.* Fe [261], Al [115] and Ga [262], and/or BDC^{2-} derivatives, *e.g.* amino [263], fluorine [264], chlorine, nitro or hydroxyl [265]. The possibility to employ post-synthetic modification [112] and using mixtures of metals [266] or ligands [267] in the same framework material further increase the variability of MIL-53. As a result, MIL-53 has been successfully applied in gas separation [268], storage [269] or heavy metal capture [270]. Besides the synthetic variability, MIL-53 is particularly notable for the so called breathing effect [115]. It has a flexible framework and the internal pore size and volume change by up to 33% [262] upon appropriate stimulation including guest molecule adsorption [115] or temperature variation [266]. For the aluminium and chromium derivatives, small and large pore forms (pore apertures are 0.26 nm x 1.36 nm and 0.85 nm x 0.85 nm respectively; Figure 3-1) are observed, while for the Fe [261] and Ga [262] derivatives several additional pore forms exists.

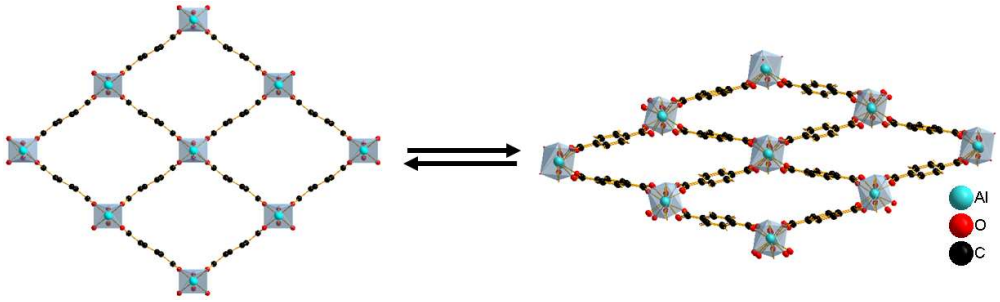


Figure 3-1: Visualization of the breathing phenomenon of MIL-53(Al) between the large-pore for (left) and the small pore form (right). Hydrogen atoms have been omitted for clarity. Structures calculated from crystal data. [115].

The breathing of the MIL-53-class is most commonly caused by adsorption of water or CO_2 and it adsorbs water from ambient air within minutes even at low relative humidity of 10% [115],[271]. Although, the adsorption of water is desired for some applications *e.g.* water capture from ambient conditions for usage as drinking water [272], this feature can limit the use of MIL-53 compounds for most industrial applications where adsorbed water has to be removed prior. Due to the ubiquity of humidity in ambient air, several studies investigated the usage of additional agents or synthesis methods in order to increase the

hydrophobicity of MIL-53, such as ionic liquids [271] or hydrophobic linkers [273], respectively during the synthesis. However, possible trade-offs can be extended synthesis times (up to one week) or a reduced pore volume. Although MIL-53 was synthesized by microwave radiation [123], ultrasound [274] or in continuous flow conditions [20], solvothermal synthesis at autogenous pressure and elevated temperatures still remains as the most common way to prepare MIL-53 employing *N,N*-dimethylformamide (DMF) and water as solvents [275]. Synthesis of MIL-53 in DMF has the advantages of high product yields (up to 100%) and the possible synthesis of nano-sized particles (< 1000 nm), but DMF is flammable, toxic and can cause congenital disorders [276]. Moreover, the low DMF vapour pressure prevents the easy removal of excess/residue DMF (at 20°C for DMF 0.377 kPa in comparison with 2.33 kPa for water and 12.9 kPa for MeOH [277]) from the pores. In addition, for several MOFs, including MIL-53, coordination of DMF to the MOF metal nodes was observed, which further complicates the purification/activation process [278]. Water would be a more sustainable alternative, but low yields remain a significant challenge [279]. Another challenge is the difficulty to prepare nano-sized particles in water, which is desirable for *e.g.* catalysts, electrode materials or medical applications [280],[281]. Ahnfeld *et.al.* [282] have shown by a high throughput synthesis in low weight alcohols *e.g.* methanol (MeOH) and ethanol (EtOH) that the synthesis of MIL-53(Al) is in principle possible. These solvents have several advantages such as low cost and ease of removal, making the synthesis of MIL-53 more sustainable. Until now, no reports of successful synthesis and characterization of MIL-53 in simple alcohols have been reported and this research will cover this topic for a more sustainable synthesis of MIL-53. The MIL-53 aluminium derivative, MIL-53(Al), was used as the test compound due to the known lower toxicity in comparison with other derivatives such as chromium [265] and the commercial availability (as Basolite A100®). Although some studies investigate the synthesis of MIL-53(Al) in water and DMF [279],[283] a wide range of applied synthesis conditions *e.g.* temperature, reaction time, concentration, metal-to-linker ratio and additives make the direct comparison of these results complicated (see Figure 3-2 and Table 3-1). Furthermore various aluminium salts such as nitrate [115], chloride [282], perchlorate [284] or sulphate [123] have been reported for the synthesis of MIL-53(Al).

The results of this chapter have been further published as: J. Warfsmann, B. Tokay and N. R. Champness, *CrystEngComm*, 2018, **20**, 4666-4675 (DOI: 10.1039/c8ce00913a).

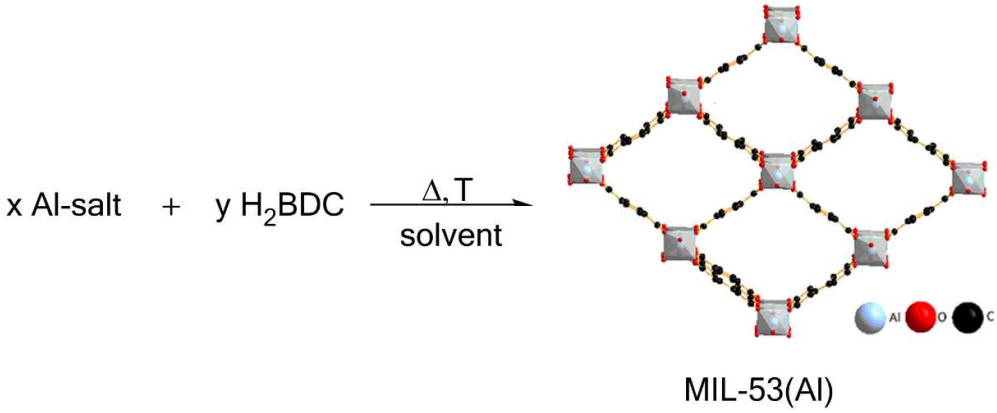


Figure 3-2: Schematic reaction scheme for synthesis of MIL-53(Al).

Table 3-1: Examples of applied conditions for the solvothermal synthesis of MIL-53(Al). The concentration is shown as concentration of the metal salt in the reaction mixture (n.s. = not specified).

Metal-to-Linker ratio (x/y)	Concentration (mol L^{-1})	Reaction temperature Δ (°C)	Reaction time T (h)	Solvent	
1/0.5	0.69	220	72	water	[115]
1/1	0.39	150	5	water	[164]
1/2.5	n.s.	120	72	DMF	[283]
1/1.5	0.08	110	24	DEF + EtOH	[214]
1/0.75	0.06	250	0.3	water	[20]

3.2 Experimental

3.2.1 Materials

Aluminium nitrate nonahydrate, $Al(NO_3)_3 \cdot 9\ H_2O$, and 1,4-benzenedicarboxylic acid (>98%) were purchased from Sigma Aldrich. *N,N*-dimethylformamide (DMF), methanol (MeOH), ethanol (EtOH), dimethyl sulfoxide (DMSO) and acetone were provided from Fisher-Scientific. All chemicals were used without further purifications. Deionised water (DI-water) was collected from a Millipore Direct-Q 5 UV water purification system.

3.2.2 Synthesis of MIL-53(Al)

MIL-53(Al) was synthesized according to a modified synthesis protocol [164]. Typically, a reaction mixture of $Al(NO_3)_3 \cdot 9\ H_2O$ (5.99 mmol; 2.246 g) and H_2BDC (5.38 mmol; 0.895 g), was prepared in 30 ml of solvent (DMF, water, MeOH or EtOH) and stirred vigorously at room temperature for 15 min and transferred to a 45 ml Teflon lined stainless steel autoclave. The reaction mixture was heated to 150°C for 5 h after which the product was separated by centrifugation (4500 rpm for 30 min). The solution was decanted, and the crystalline material washed with DMF (2 x 50 ml) and acetone (1 x 50 ml). The product, a white powder, was dried at 150°C for 17 h. Unreacted starting material and residue solvent were removed from the as-synthesized samples (referred as MIL53(Al)-AsSyn subsequently) by heating at 333°C for 3 days (referred as MIL-53(Al)-Acti subsequently) [115].

3.2.3 **Characteisation**

Scanning Electron Microscopy (SEM) was used to characterise the morphology and crystal size (from an average of 25 particles). Measurements were conducted, regarding the availability, with a JEOL JSM-7100F Field Emission Gun (FEG) instrument or a JEOL 6490LV. Measurements were conducted with a beam voltage of 15 kV. Samples were sputtered with a 10 nm iridium film by a Quorm Q150T ES coater in order to increase conductivity of the samples. Environmental SEM (ESEM) in varying relative humidity was measured using a FEI Quanta 650 ESEM at 15 kV. The samples were not coated prior to the measurement. X-Ray diffraction (XRD) measurement was done by a PANanalytical X'Pert Pro diffractometer operating at 40 kV and 40 mA and Cu Kα radiation (wavelength: 1.540598 Å) equipped with a PIXCell3D detector. The experiments were conducted in continuous scanning mode with the goniometer fixed in the theta/theta orientation. For the incident site and detector site a soller slit of 0.04 rad° and an incident beam mask of 15 mm was used. The irradiated length was 10.0 mm. In a typical experiment ~50 mg of powder sample was used and scans were conducted in a range of 5°-35° 2θ with a step size of 0.006565° and a scan time of 51 s per step, resulting in a total measurement time of ~14 min. For temperature dependant XRD measurements an AntonPaar HTK 1200N oven was used. For all measurements, the sample was heated between 25°C and 250°C (between 25°C and 200°C in 25°C steps with one additional measurement at 250°C) and then cooled down to 25°C. Additional diffractograms at 25°C were measured immediately after reaching 25°C again (0 min waiting time) and after waiting times of 30 min and 60 min respectively. All samples for the temperature dependant XRD measurements were kept in a saturated water atmosphere for 3 days prior to XRD measurements.

Thermal stability of the powder samples was investigated by thermogravimetric analysis (TGA) using a TA instruments Q500 thermal gravimetric analyser. Samples were heated up to 700°C under air flow (100 ml/min) with a heating rate of 5°C/min.

For the measurement of adsorption isotherms, the powder samples were degassed by heating at 80°C for 1 h in vacuum and at 150°C overnight in vacuum.

Sample porosity and BET area were determined by N_2-adsoprtion via Micrometrics Tristar II-adsorber. N_2-isotherms were measured at 77 K. Surface area was calculated by BET-theory. The pressure range between 0.05 and 0.35 p/p^0 of a N_2-isotherm measured at 77 K is deemed to be the quasi-standard for the application of the BET-theory in order to create comparable values for the porosity of various samples [285]. However especially microporous samples are known to be problematic for the application of the BET-theory for the calculation of the porosity. The BET-theory has to be applied to the linear part of the isotherm, which might be applied to different parts of the low-pressure region of a microporous material (0.05 – 0.35 p/p^0), leading to a variation of the porosity up to 30% [286]. Therefore, additional criteria for the application of the BET-theory have been used. Besides a positive C-value, it was ensured that the plot $n^a(p^0-p)$ is increasing with (p^0-p), which is the so-called Rouquerol criteria [286].

Water-isotherms were measured with a Micrometrics 3Flex adsorber at 25°C. The water vapour of different relative humidity was created by bubbling dry nitrogen though deionized water. Methanol isotherm were measured similar to the water isotherms with

Micrometrics 3Flex adsorber at 25°C. Different relative methanol vapour pressures have been created by bubbling dry nitrogen though MeOH. The used MeOH for the measurement of adsorption isotherms was of technical grade and directly used from the storage bottle without further purification.

CO_2-isotherms have been measured with a Micrometrics 3Flex adsorber. During the measurement, the temperature was kept at 25°C and the isotherm measured between 6 and 1013 mbar absolute pressure, whereas the equilibrium time for every step was in the default setting 5 s.

Fourier transformation infrared (FT-IR) spectroscopy was measured on a Bruker Alpha equipped with a Platinum ATR module. Spectra were measured with 4 cm^{-1} resolution collecting 50 consecutive measurements.

3.3 Results and Discussion

3.3.1 Particle size and morphology

The morphology of MIL-53(Al) powder samples synthesised using water, DMF and MeOH before and after activation are shown in Figure 3-3 to Figure 3-5. For simplification, these samples will be referred to as MIL-53(Al)(H_2O), MIL-53(Al)(DMF) and MIL-53(Al)(MeOH), respectively.

When water is used as the solvent for the synthesis, resulting in MIL-53(Al)(H_2O), micrometre sized (~3 µm), star-shaped particles were formed (Figure 3-3 a and b). This may indicate the intergrowth of orthorhombic crystals, which is the typical shape of MIL-53(Al) single crystals [169],[287]. Due to the blockage of the pores by unreacted starting material and solvent molecules after the reaction, an activation process has to be conducted after the synthesis. Such activation was done by heating at 333°C for 3 days [115]. However, after activation at high temperatures for prolonged time, cracks and broken intergrown particles were observed (Figure 3-3 d), presumably caused by thermal stresses during the activation process.

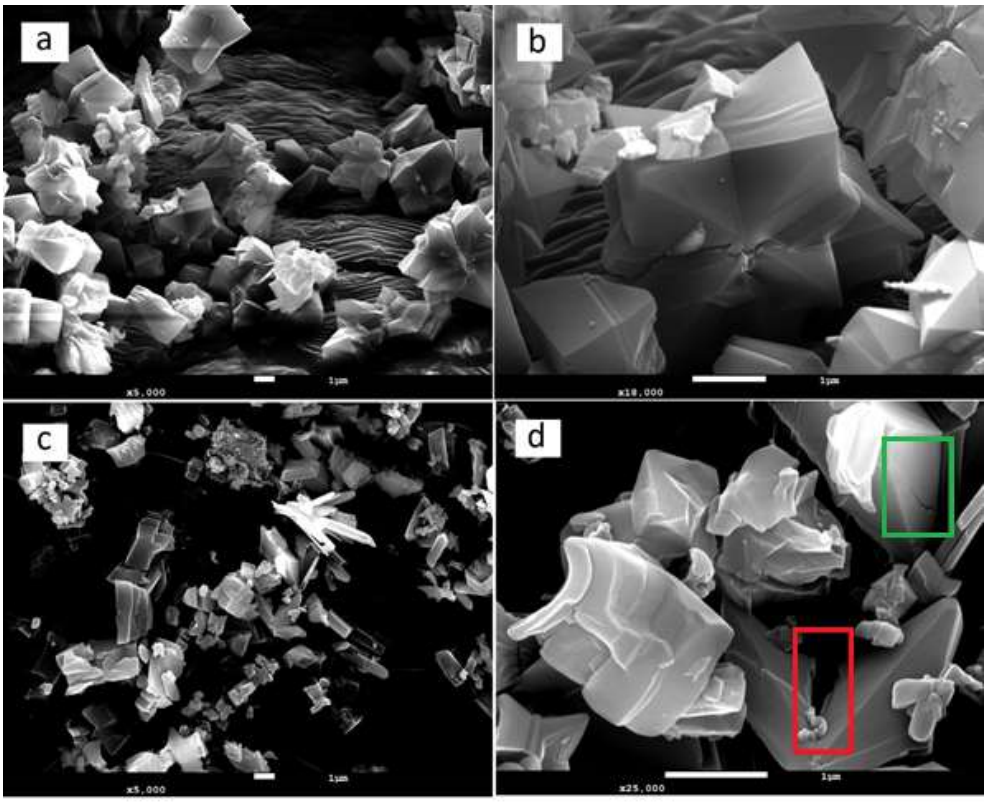


Figure 3-3: SEM images of MIL-53(Al)(H_2O). The AsSyn sample is shown at low (a) and higher magnification (b). MIL-53(Al) grows in water to micrometre sized particles with orthorhombic shape. After activation, the overall size, morphology and crystallinity of the particles did not change, but cracks (d, green square) and breaking of intergrown crystals (d, red square) were observed.

In contrast, the individual particles prepared in DMF (Figure 3-4) are spherical particles with a size of 41 ± 17 nm. These agglomerate to larger cluster with a size of several micrometre. This agglomeration can be partly explained with the drying process. Previous reports showed that the removal of the solvent can facilitate strong particle agglomeration [288]. In contrast to MIL-53(Al)(H_2O), activation did not cause any cracks in the particles' surface, which may be related to the smaller particle size of MIL-53(DMF)(Al). The particles of MIL-53(Al)(DMF) are relatively weakly attached to each other and the stress during the activation (*e.g.* by thermal expansion) might be for instance compensated by movement of the particles in relation to each other. In contrast, the larger crystals of MIL-53(H_2O)(Al) are not able to compensate the thermal stress and break or crack instead.

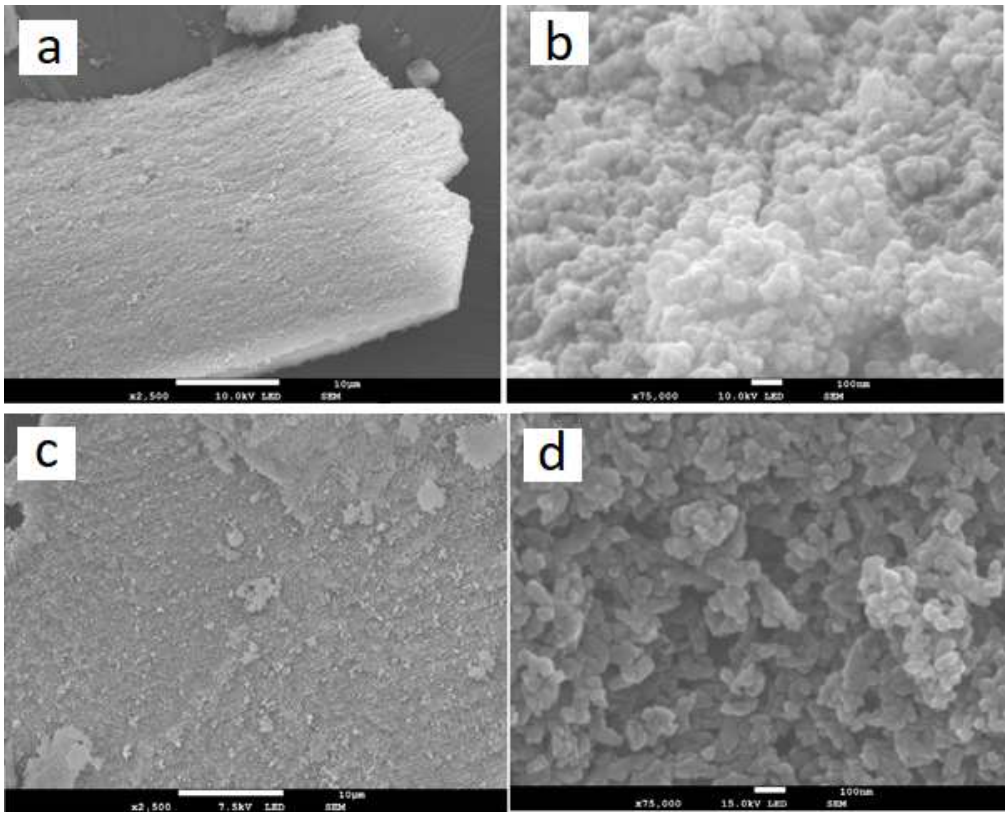


Figure 3-4: SEM images of MIL-53(Al)(DMF). For the AsSyn-sample the agglomeration of particles is observed in low magnification (a). At higher magnification, the MIL-53(Al)(DMF) particles have a spherical shape and size of 41 ± 17 nm. After activation, (c for lower and d for higher magnification) no difference was observed.

Two morphologies were observed when MeOH was used as the solvent (Figure 3-5). These are spherical particles with similar size and shape to MIL-53(Al)(DMF) and longer rod-shaped particles, with a diameter comparable to the spherical particles, but with substantially longer length (178 ± 42 nm) (Figure 3-5 d). Similar to MIL-53(Al)(DMF), in MeOH a tendency towards agglomeration to micrometre sized clusters was observed. Furthermore was no difference in morphology (*e.g.* cracks) before and after activation observed. Similar to MIL-53(Al)(DMF), the smaller particles of MIL-53(Al)(MeOH) might be better able to withstand the thermal stress during the activation process.

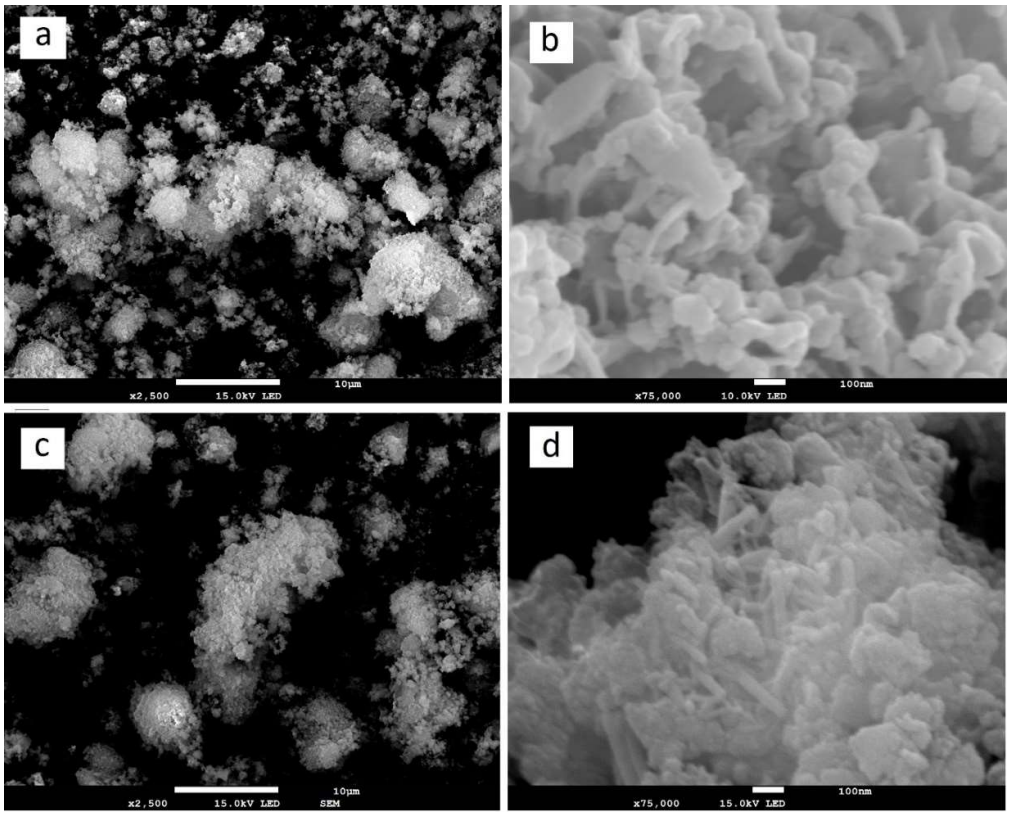


Figure 3-5: SEM images of MIL-53(Al)(MeOH). For the AsSyn-sample agglomeration was observed at low magnification (a). In contrast to MIL-53(Al)(DMF), the nano-sized particles are a mixture of spherical particles with size of 34 ± 15 nm and rod-shaped particles with a length of 178 ± 42 nm and a width of 33 ± 8 nm. After activation, (c for lower and d for higher magnification) particles size or morphology did not change.

Results show nanometre sized particles can be prepared using DMF and MeOH as solvent. Previous investigations explained the difference in particle size in different solvents by the varied deprotonation rate of the linker H_2BDC as the main reason [279]. During the reactions, the solvent acts as a base for the deprotonation of the linker. In general, a faster nucleation rate is expected to lead to the formation of smaller particles [289]. A good indicator for the basicity and in this regard for the deprotonation rate, is the p*K*a of the solvents used. (Table 3-2)

Table 3-2: Comparison of the pKa for different solvents used.

Solvent	p*K*a
Water	14 [290]
DMF	-0.30 [291]
MeOH	15.7 [291]

However, this suggests that MeOH is slightly more acidic than water and should, in principle, lead to the formation of even larger particles. It can be therefore assumed, that the particle size may also be dependent on other parameters. The solubility of the starting materials was identified here as one of the possible parameters affecting the particle size. The solubility of the linker H_2BDC in water, DMF and MeOH is shown in Table 3-3. At the reaction temperature of 150°C, the linker only dissolved partly in water and reacts with metal ions dissolved in water to form MIL-53(Al) seeds. Due to the star-shape of the MIL-53(Al)(H_2O) particles, it can be assumed that the growth from existing seeds may be

preferred over the nucleation of new seeds, which leads to the formation of particles exceeding several micrometres. In both solvents DMF and MeOH, the solubility at reaction temperature of 150°C is several orders of magnitude higher in comparison with water. The deprotonated BDC^{2-} is therefore fully dissolved, leading to a more likely interaction between the linker and metal ions in the solvent and a greater number of seeds. Consequently, more MIL-53(Al) particles are formed with a reduced size.

Table 3-3: H_2BDC solubility at room temperature and at reaction temperature of 150°C (for MeOH solubility at 160°C). The values are given as g per 100 g solvent

Solvent	Solubility at 25°C	Solubility at 150°C
Water	0.0065 [292]	0.0332 [293]
DMF	7.4 [294]	14.49 [295]
MeOH	0.11 [296]	2.9 [297]

The solubility of the linker may also affect the yield of the reaction, because in DMF a nearly complete conversion was observed, while the yields were significantly lower in MeOH (52%) and water (18%).

3.3.2 Crystallinity and porosity

The XRD patterns of samples synthesised in water, DMF and MeOH before and after activation are shown in Figure 3-6 and compared with patterns calculated from existing crystal data [115]. Three calculated patterns are shown, for an AsSyn sample with trapped linker in the pores, the activated large-pore form and the small pore form, respectively. The pattern of the prepared MIL-53(Al)(H_2O) are before and after activation in good agreement with the calculated pattern (Figure 3-6). During the synthesis, H_2BDC remains in the sample pores, which forces the pores into the large pore from (AsSyn) and reducing the available porosity. However, due to interaction of the H_2BDC in the pores with the pore walls, the pore diameter is slightly smaller (0.73 nm x 0.77 nm) in comparison with the activated large-pore form (0.85 nm x 0.85 nm) [115].

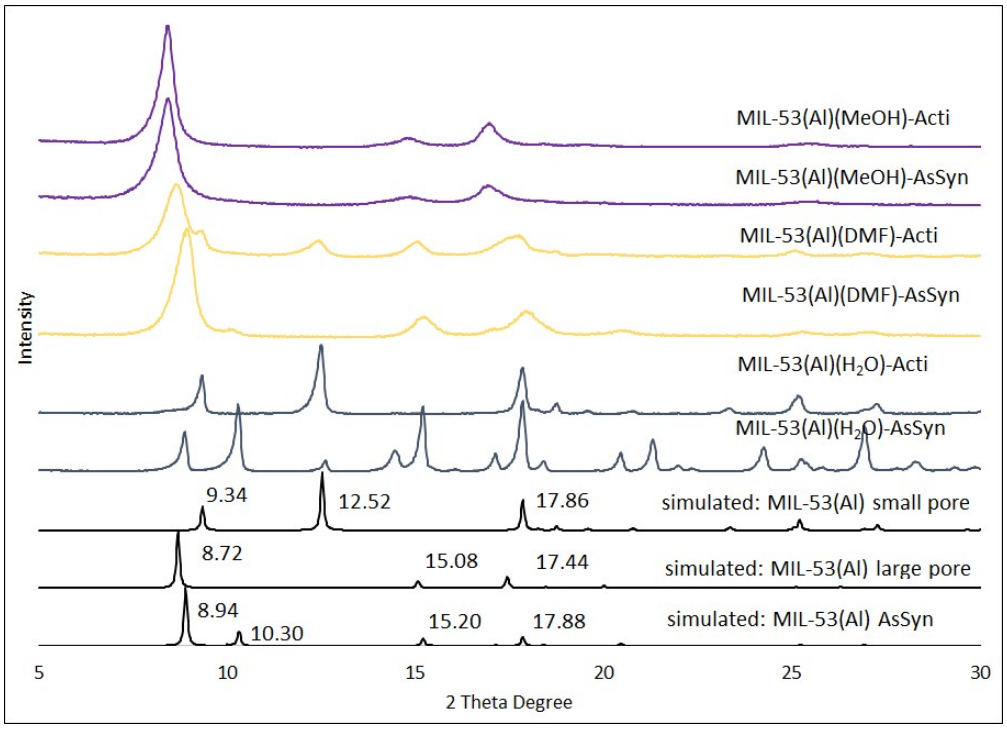


Figure 3-6:XRD of MIL-53(Al) derivatives (prepared in different solvents before and after activation) in comparison with calculated pattern form existing crystal data. [115].

The change of the pore size leads to an observable shift in the XRD (*e.g.* the peak in the calculated pattern at 2Theta = 8.94° shifts to 8.72° for the activated large-pore form; Figure 3-6). Activated MIL-53(Al)(H_2O), with removed H_2BDC, adsorbs moisture from ambient air, leading to a shrinkage of the pores (0.26 nm x 1.36 nm). The both forms (large and small pore form) can be distinguished by XRD, where the large pore form shows a peak at ~15°, while the small pore form is indicated by a peak at ~12°. The XRD pattern of MIL-53(Al)(DMF)-AsSyn matches with the calculated AsSyn pattern. The observed peaks of the XRD pattern from MIL-53(Al)(DMF) are broader in comparison with MIL-53(Al)(H_2O), which might be explained with the smaller particles size of MIL-53(Al)(DMF) in comparison with the water sample. After the activation process has the most intensive peak at ~9° shifted to smaller 2Theta values (from 8.99° to 8.72°). A similar shift was observed between the calculated pattern of MIL-53(Al)-AsSyn and the calculated pattern of MIL-53(Al) in the large pore form. Between these patterns has the peak shifted from 8.94° to 8.72°. The shift between the measured pattern of MIL-53(Al)(DMF)-AsSyn and MIL-53(Al)(DMF)-Acti might be therefore also imply the removal of H_2BDC from the pores. The pattern of MIL-53(Al)(DMF)-Acti show peaks at ~12° and ~15° with similar intensity, which may suggest equal proportions of the small and large pore forms in the sample. In contrast to the water and DMF sample, for MIL-53(Al)(MeOH), no peak at ~12° could be observed indicating the absence of the small pore form. Furthermore, the peak positions of MIL-53(Al)(MeOH)-AsSyn did not shift to lower 2Theta values and matches already to the activated form. This implies that MIL-53(Al)(MeOH)-AsSyn does not contain any unreacted starting material in the pores, which would have to be removed.

The synthesis of MIL-53(Al) was also performed in ethanol, leading to MIL-53(Al)(EtOH). The morphology of crystals prepared in EtOH is similar to MIL-53(Al)(MeOH), with small spherical particles and rod-shaped particles (Figure 3-7).

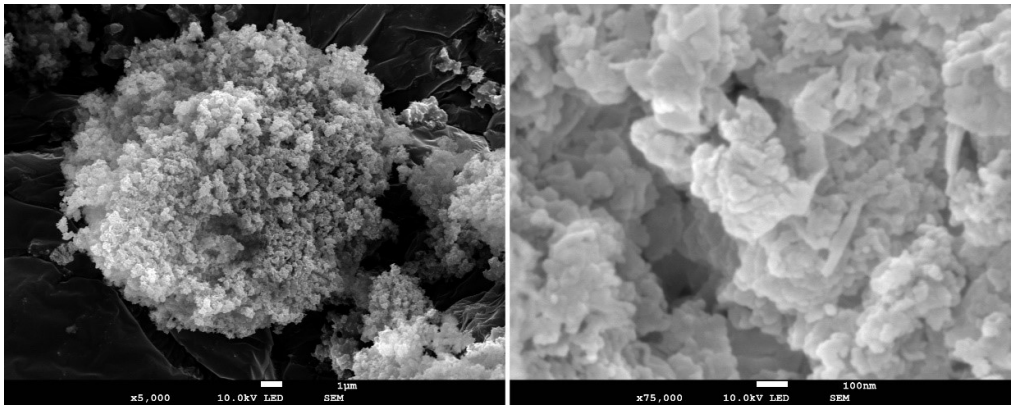


Figure 3-7: SEM images of MIL-53(Al)(EtOH)-AsSyn. The shown sample was activated at elevated temperature. The sample tends to agglomerate (left) and show similar particle morphology to MIL-53(Al)(MeOH) (right).

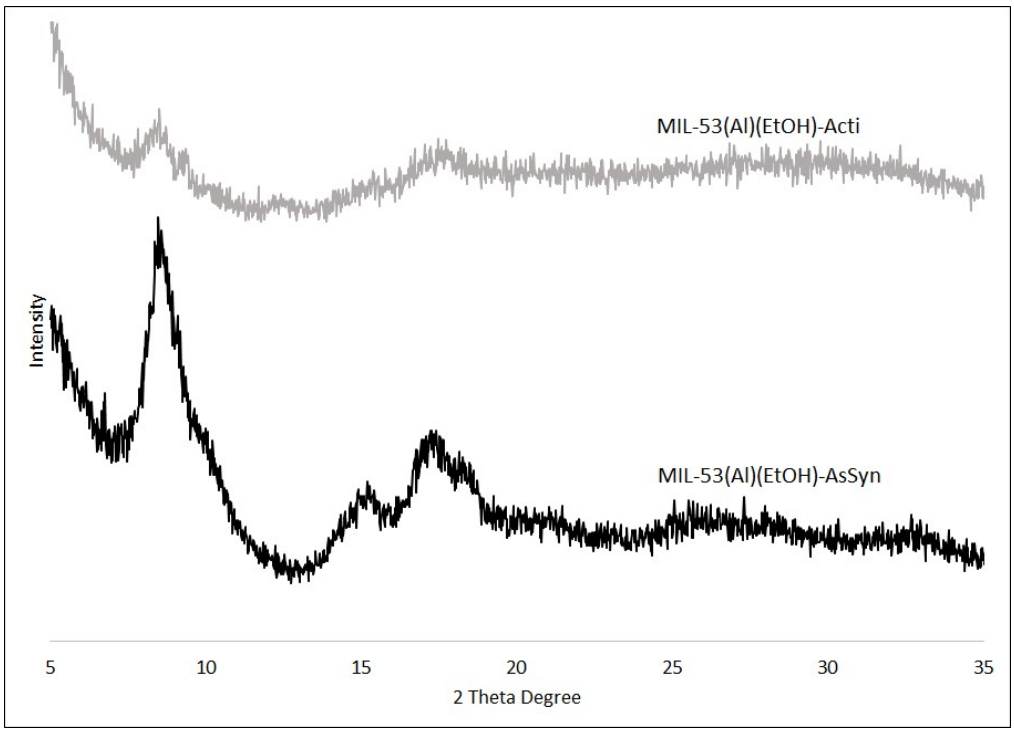


Figure 3-8: XRD-pattern of MIL-53(Al)(EtOH) before and after activation.

The XRD patterns (Figure 3-8), show characteristic peaks at 8.48°, 15.20° and 17.34°, which indicate the successful synthesis of MIL-53(Al). However, the greatly reduced intensity in comparison with the samples prepared in water, DMF and MeOH implies low crystallinity. After activation, the intensity of characteristic peaks was greatly reduced and an almost amorphous product was obtained. As a possible explanation could be the reduced thermal stability of MIL-53(Al)(EtOH) in comparison with MIL-53(Al) prepared in other solvents (a more in deep discussion can be found in chapter 3.3.6 (p. 73) during the investigation of the thermal stability of MIL-53(Al)). Due to the reduced crystallinity of MIL-53(Al)(EtOH), no further investigation of this sample was conducted.

The XRD patterns of the samples prepared in MeOH imply that the crystals are already in the activated large-pore form even without activation. In order to confirm this, the internal pore volumes and BET surface areas of AsSyn (Figure 3-9) and activated samples (Figure 3-10) were measured using N_2 adsorption isotherms at 77 K.

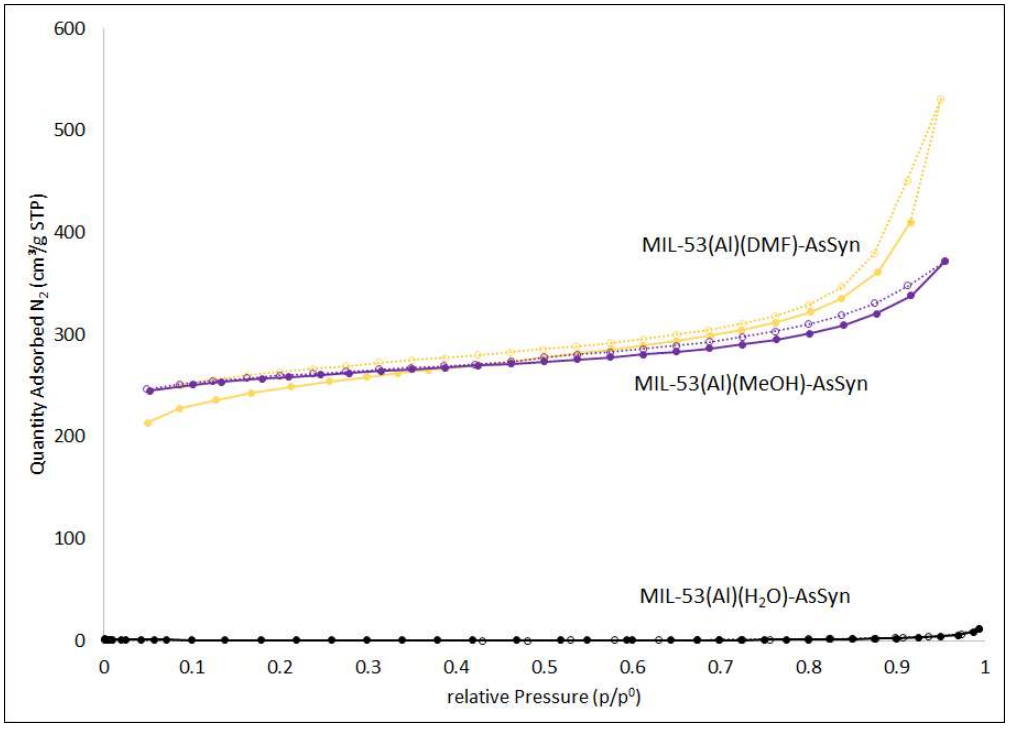


Figure 3-9: N_2-isotherms of the as-synthesized MIL-53(Al) samples, prepared in different solvents. Adsorption: solid line; Desorption: dashed line. STP: standard temperature and pressure

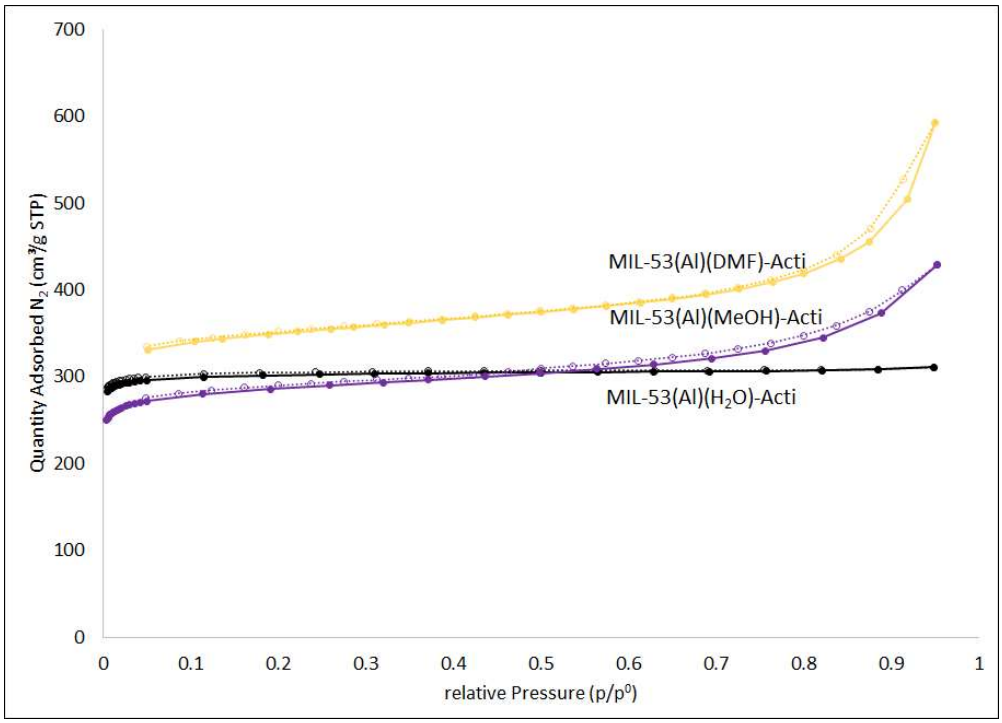


Figure 3-10: N_2-isotherm of the activated MIL-53(Al) samples, prepared in different solvents. Adsorption: solid line; Desorption: dashed line.

Table 3-4: Comparison of BET surface area and microporosity for the different MIL-53(Al) derivatives

Compound	S_{BET} ($m^2\ g^{-1}$)	t-plot micropore volume ($cm^3\ g^{-1}$)
MIL-53(Al)(H_2O)-AsSyn	/	/
MIL-53(Al)(H_2O)-Acti	1002 ± 18	0.44
MIL-53(Al)(DMF)-AsSyn	767 ± 24	0.23
MIL-53(Al)(DMF)-Acti	1084 ± 35	0.45
MIL-53(Al)(MeOH)-AsSyn	805 ± 26	0.35
MIL-53(Al)(MeOH)-Acti	895 ± 30	0.39

The measured BET-areas and microporosity for all samples are shown in Table 3-4. The value of the activated samples prepared in water (1002 $m^2\ g^{-1}$) and DMF (1084 $m^2\ g^{-1}$) are in good agreement with the previously reported data [115],[268], respectively. The measured BET surface area of MIL-53(Al)(MeOH)-Acti is slightly lower (895 $m^2\ g^{-1}$) than for the samples prepared in water and DMF. However, in case of MIL-53(Al)(MeOH) only a 10% difference between the AsSyn and the activated samples regarding the surface area and microporosity was observed. For MIL-53(Al)(DMF), the differences in surface area (~29%) and microporosity (~49%) are larger. For MIL-53(Al)(H_2O)-AsSyn, the N_2-adsorption measurement did not show any porosity. A possible reason might be that unreacted starting material (H_2BDC) and solvent molecules are blocking the pores of MIL-53(Al)(H_2O)-AsSyn and therefore no N_2 can be adsorbed.

This may indicate, combined with the results of the XRD measurements, that nearly no H_2BDC is trapped in the pores of MIL-53(Al)(MeOH) after the reaction and milder or even no activation might be necessary to access the framework porosity.

At the same time, the shape of the N_2-isotherms imply that the samples MIL-53(Al)(DMF) and MIL-53(Al)(MeOH) contain at least some mesoporosity (pores with size between 2-50 µm [298]). Mesoporosity show itself often as a hysteresis in the isotherm caused by capillary condensation in the mesopores, but the isotherms (Figure 3-9 and Figure 3-10) show nearly no hysteresis and the increase of adsorbed N_2 could be mainly observed at high relative pressure (< 0.8 p/p^0), which might also be caused by condensation in interparticle volume [299]. A possible alternative for identifying microporosity is the t-plot curve (plot of the quantity adsorbed vs. the thickness of the film adsorbed on the surface t), which is normally used for the identification of the microporosity of different samples [300]. From the shape of the t-plot, the type of porosity in the sample can be identified (Figure 3-11).

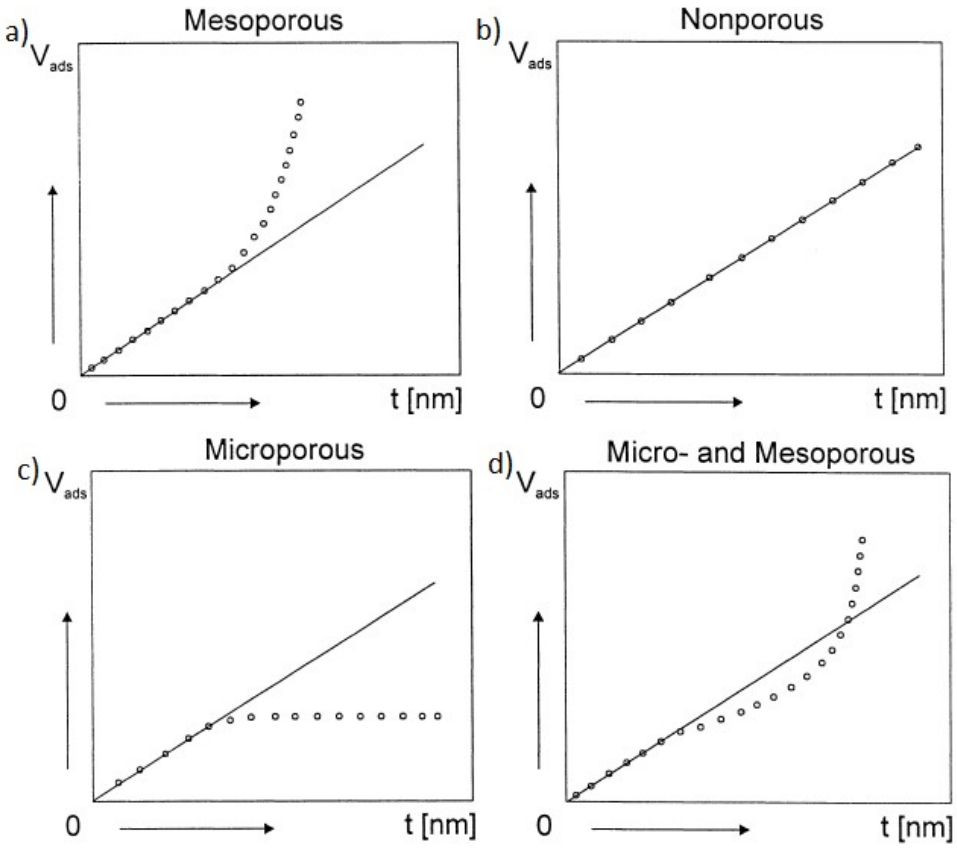


Figure 3-11: Ideal t-plots for a) mesoporous, b) nonporous, c) microporous and d) samples containing micro- and mesoporosity [301].

The existence of micro- or mesopores can be identified by the divergence of the t-plot curve from a nonporous sample of similar chemical composition as a reference sample. The t-plot curve of such a nonporous sample is a straight line passing though the origin. However especially for highly porous samples with a large microporous part (*e.g.* MOFs or zeolites), the usage of the t-plot might be problematic. For this type of materials, the t-plot reference curve does not intercept at or close to the origin [302]. Such a behaviour was also observed for the activated sample of MIL-53(Al) (Figure 3-12). The t-plot of MIL-53(Al)(H_2O)-Acti show a horizontal departure from the straight reference line, which implies that this samples only contains microporosity. In contrast show both samples prepared in DMF and MeOH first a horizontal departure from the reference, followed by a vertical departure. This behaviour resembles the ideal t-plot of a sample containing both micro- and mesopores (Figure 3-11 d). A possible reason might be the formation of defects during the synthesis and activation of MIL-53(Al). MIL-53(Al)(DMF) and MIL-53(Al)(MeOH) have in contrast to the water sample a particle size of ~100 nm (Figure 3-4 and Figure 3-5) and consequently a larger external surface area. The activation of these samples was done by heating at elevated temperature for prolonged time (333°C for 3 days) and it might be possible that the sample has been partly decomposed, while MIL-53(Al)(H_2O) might be less affected by the activation process due to the smaller surface area of the micrometre sized particles, even though cracks have been seen in the crystals after the activation process (Figure 3-3). Another possibility is that this mesoporosity might be also caused by interparticle volume. Due to the small size of the particles prepared in DMF and MeOH

(~100 nm), a part of the interparticle volume might be inside the domain of mesoporosity (2-50 µm).

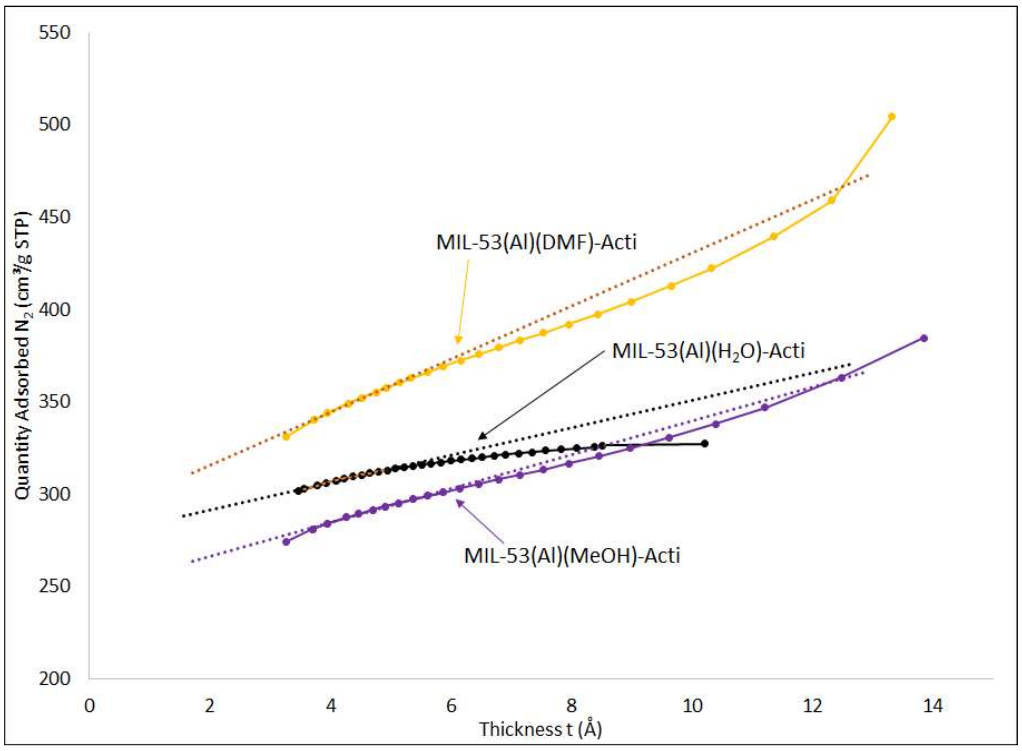


Figure 3-12: Comparison of the t-plots for MIL-53(Al)(H_2O)-Acti (black), MIL-53(Al)(DMF)-Acti (yellow) and MIL-53(Al)(MeOH)-Acti (purple). Reference: dotted line.

While the porosity of MIL-53(Al)(MeOH) might be mostly directly accessible, the activation is of great importance for MIL-53(Al)(DMF) and even more for MIL-53(Al)(H_2O). In MIL-53(Al)(DMF)-AsSyn, 70% of the porosity is available before activation whilst, for MIL-53(Al)(H_2O)-AsSyn all the pores were blocked before the activation. Therefore, the activation of MIL-53(Al) was investigated for the sample prepared in water.

In general, various ways of activation have been introduced in literature. The most common activation methods are heating at elevated temperature [115], refluxing in DMF [134] or solvent-exchange in DMF [133]. All these processes are time and energy consuming. Another problem of DMF are the strong interactions with the metal sites in the MOF, which makes the removal more complicated [278]. Therefore, additional methods have been tested here. One method, was heating the sample in vacuum at 150°C for 12 h [164]. Solvent exchange has been successfully applied for other MOFs whereas especially organic solvents with low boiling points and consequently high vapor pressure have proven effective for the activation [303]. Hence solvent exchange with MeOH was also tested for the activation of MIL-53(Al). After applying activation methods, the N_2-isotherms of the samples were measured. The quality of the activation methods was determined by the comparison of BET surface areas. The results are shown in Figure 3-13 and Table 3-5. While the activation by heating for prolonged time (3 days) at elevated temperature (333°C) and refluxing in DMF both lead to successful activation with similar S_{BET} (1002 $m^2 g^{-1}$ and 968 g m^{-1} respectively), the activation in vacuum was not successful (resulting BET area: 11 $m^2 g^{-1}$). The activation of MIL-53(Al) by solvent exchange in MeOH

led to an activation in a certain degree (742 $m^2 g^{-1}$), but not as effective as the heating at elevated temperature or the reflux in DMF, since the resulting BET-area is lower[1]. The activation in vacuum was applied in literature for thin-films [164], whilst it was not successful for powder samples and this makes the quality of this activation technique for MIL-53(Al) questionable. With regards to these results, the activation by heating at elevated temperature for 3 days was used as the standard approach for activation of MIL-53(Al), as a slightly better result (BET-area, Table 3-4) was observed in comparison with reflux in DMF and the sample is ready to use directly after the activation without additional processing steps (*e.g.* no DMF has to be further removed from the pores).

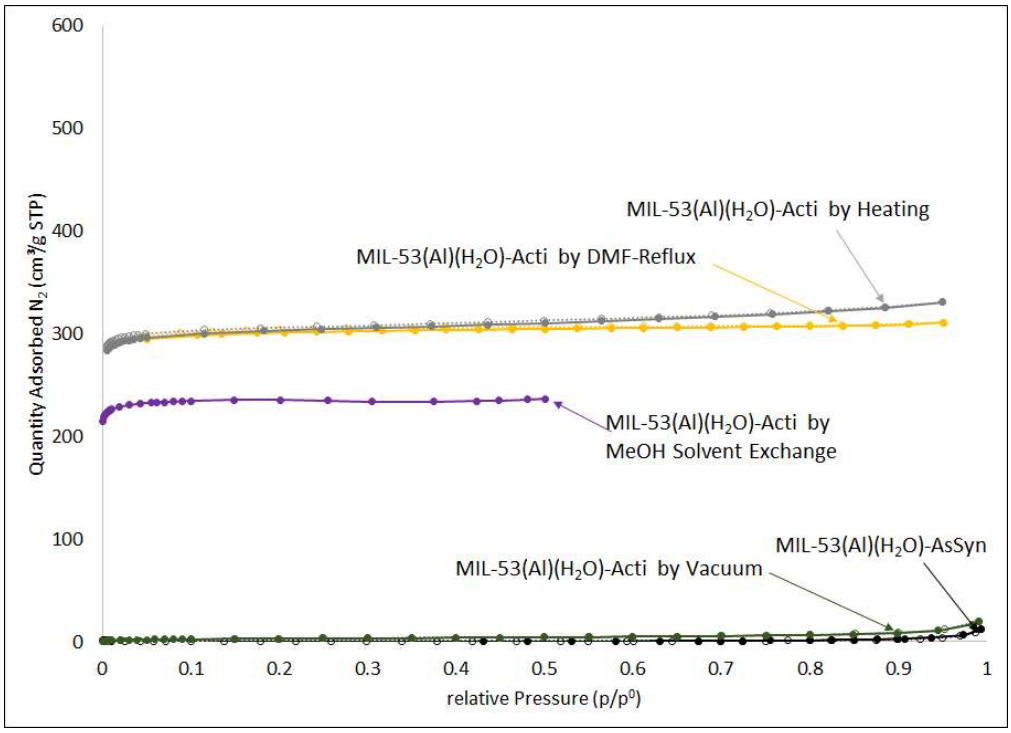


Figure 3-13: Comparison of N_2-isotherm of MIL-53(Al)(H_2O)-AsSyn (black) with samples after several activation methods. Adsorption: solid line; Desorption: dashed line.

Table 3-5: Comparison of porosity for MIL-53(Al)(H_2O) after different activation methods.

Activation Method	BET-area ($m^2 g^{-1}$)	t-plot micropore volume ($cm^3 g^{-1}$)
None (AsSyn)	/	/
Heating at 333°C	1002 ± 18	0.44
Reflux in DMF	968 ± 33	0.42
Heating at 150°C in Vacuum	11 ± 0.1	0.01
Solvent Exchange MeOH	742 ± 18	0.36

3.3.3 Effect of synthesis conditions on crystallinity

The standard synthesis protocol was introduced by Loiseau *et.al.* [115], who prepared MIL-53(Al) at 220°C for 3 days. In general, are for the synthesis of amino derivates lower

[1] The N_2-isotherm could be not successfully measured over the whole adsorption and desorption branch, due to technical problems, but the important range for the calculation of the BET-value (p/p^0 = 0.05 - 0.35) was available [304].

reaction temperature and shorter reaction times applied. Fan *et.al.* [164] have applied for the synthesis of NH_2-MIL-53(Al) 5 h reaction time at 150°C. The lower reaction temperature might be chosen as amino-derivates of MOFs have in general a lower thermal stability in comparison with the pristine compounds [218]. Furthermore, is the amino-group showing an inductive effect, which makes the deprotonation of the carboxyl-group easier. Consequently, lower reaction temperature and shorter reactions times might be sufficient needed in comparison to the pristine MOF. The results during this research show that the application of typical synthesis conditions for the amino compound (5 h; 150°C) are also sufficient for the synthesis of pristine MIL-53(Al). However, a slight variation to the synthesis protocol was necessary. For the amino-compound, a reaction mixture with a 1:1 ratio between metal and linker was used [164], but an equimolar reaction mixture has led for pristine MIL-53(Al) to residue of unreacted free H_2BDC (not trapped in the pores) during MIL-53(Al) synthesis, which can be shown in the XRD pattern of the sample (Figure 3-14). This problem could be avoided by adding a slight excess of metal to linker (1.1/1) to the reaction mixture.

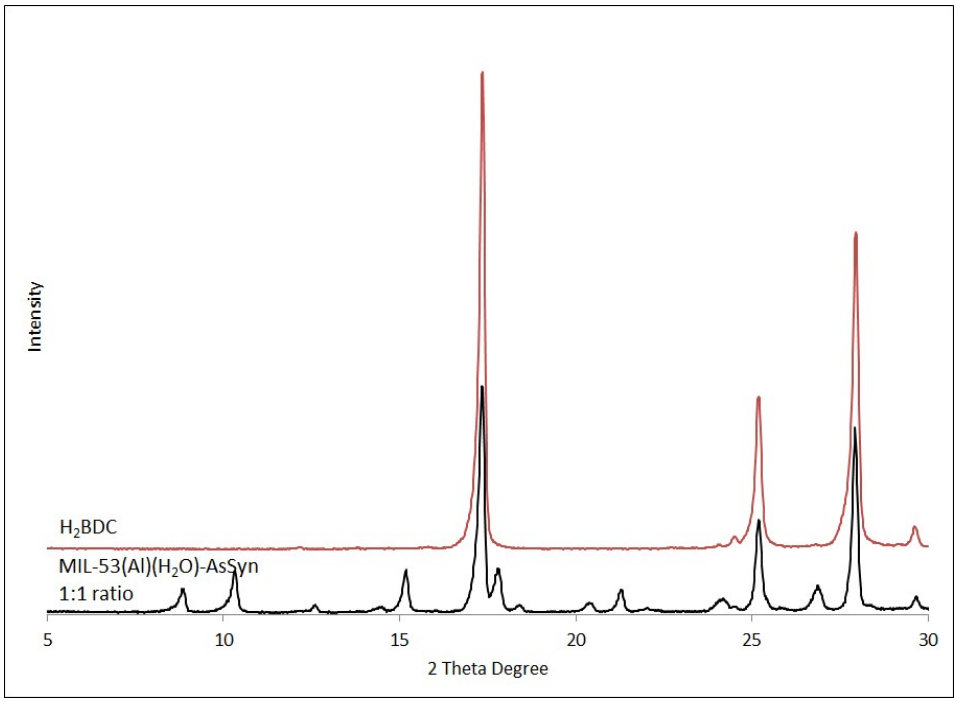


Figure 3-14: MIL-53(Al)(H_2O) with 1:1 ratio of the starting materials (black) in comparison with H_2BDC (red).

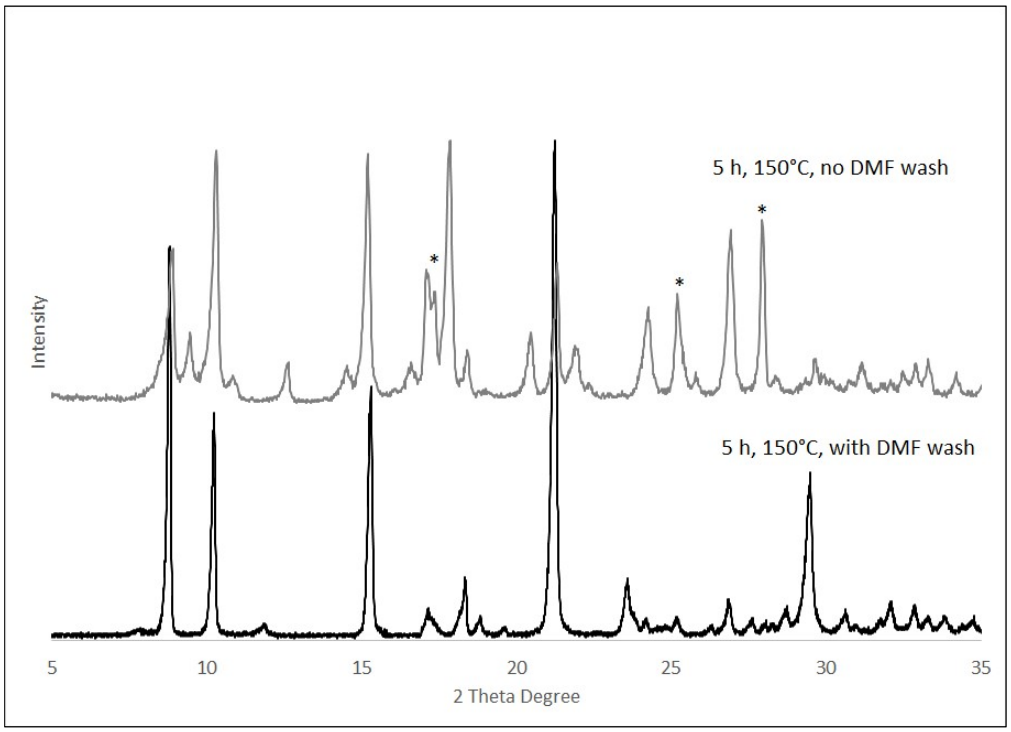


Figure 3-15: MIL-53(Al)(H_2O)-AsSyn washed with DMF (black) and without washing (grey). Peaks of H_2BDC are highlighted with asterisk.

In addition, the washing of the AsSyn-sample with copious DMF before activation was determined as an important step for the synthesis. In Figure 3-15, XRD pattern of a MIL-53(Al)(H_2O)-AsSyn sample is presented, that was washed with DMF in comparison with an unwashed sample. While the contamination of free linker H_2BDC is a less severe problem (lower relative intensity of H_2BDC in the XRD pattern) due to the improved reaction mixture with a 1.1/1 ratio of metal to linker, the XRD pattern still shows more impurity peaks. Unwashed samples also needed a longer time (7 days at 333°C) for activation since they showed impurities after 3 days of activation at 333°C.

During MIL-53(Al) synthesis, the minimum necessary reaction temperature and time depend on the solvent used was investigated. The reaction at 150°C for 5 h reaction time lead to the complete conversion (~100% yield) of the starting material to MIL-53(Al) in DMF as solvent. However, it was still possible to successfully prepare MIL-53(Al)(DMF) with lower reaction temperature (100°C) or shorter reaction time (1 h), but with reduced yield (<20%) (Figure 3-16). A possible reason for this might be the fast deprotonation rate of H_2BDC as the linker in the basic solvent DMF, which speeds up the synthesis [279]. MIL-53(Al)(DMF) was successfully prepared with a reduced reaction temperature (100°C) for a reasonable reaction time of 5 h. However, a further reduction of the reaction temperature needs much longer reaction times: It was possible prepare MIL-53(Al)(DMF) even at RT, but with a reaction time of several weeks.

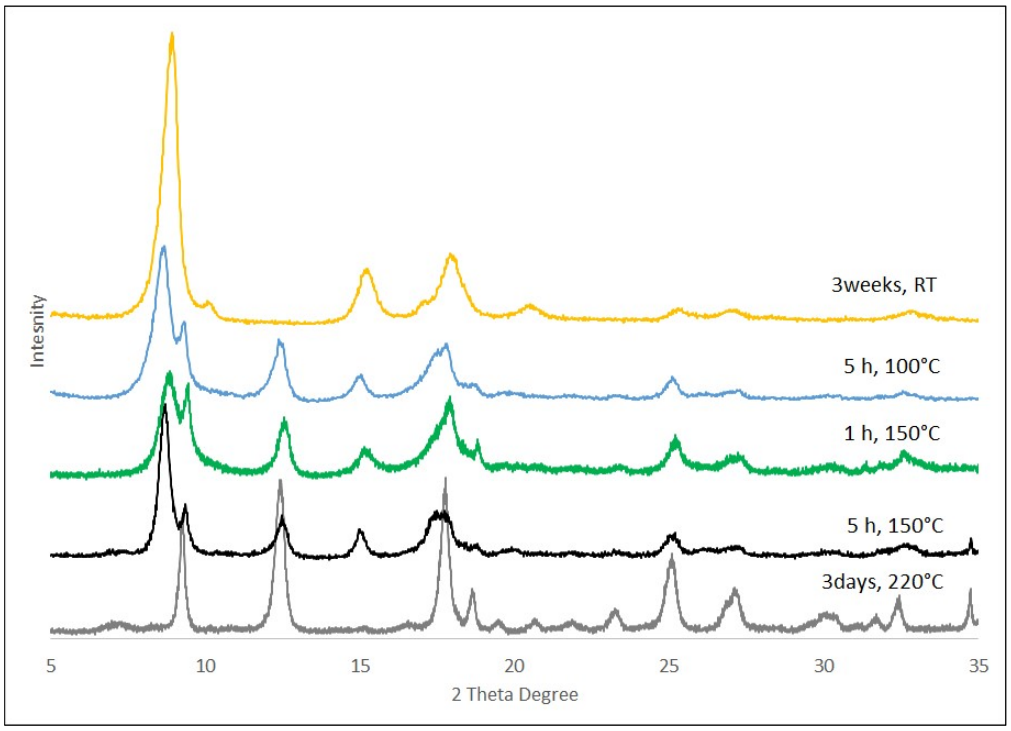


Figure 3-16: Comparison of MIL-53(Al) samples prepared in DMF with varying reaction temperature and time.



Figure 3-17: MIL-53(Al)(DMF) prepared at RT. Fresh reaction mixture (right) and after 3 weeks at RT (left).

A clear MIL-53(Al) reaction mixture turned cloudy after 3 weeks at RT (Figure 3-17). The collected product after reaction at RT (Figure 3-18) showed a similar morphology to MIL-53(Al)(DMF) prepared at 150°C for 5 h (Figure 3-4). All samples were identified as MIL-53(Al) by XRD, whilst several differences in the pattern were observed. As mentioned previously (Figure 3-6), the large and small pore forms of MIL-53(Al) can be identified with the peaks at ~12° and ~15°. Therefore is the sample prepared at 220°C completely in the small pore form, while the sample prepared at RT is completely in the large pore form (Figure 3-16). The other samples (5 h at 100°C; 1 h at 150°C; 5 h at 150°C) show varying ratio of these pore forms. This might imply different speed of the breathing phenomenon and degree of water adsorption from ambient air. This will be investigated later (chapter 3.3.4; p. 59).

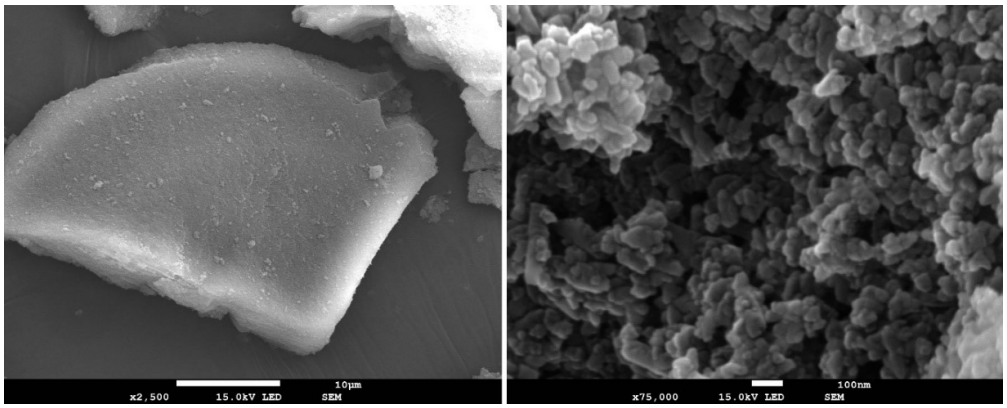


Figure 3-18: MIL-53(Al)(DMF)-RT with lower (left) and higher magnification (right).

The same set of experiments with reduced reaction time and temperature were conducted for water and MeOH as solvents. For water as solvent, in general, a stronger dependency on the reaction temperature for successful synthesis (Figure 3-19) was observed. Although MIL-53(Al) was synthesised at 150°C after only 1 h (with reduced crystallinity according to the XRD pattern; Figure 3-19), MIL-53(Al) did not form at 100°C even after 5 h reaction time. In addition, MIL-53(Al) in water at RT, even with prolonged reaction time of several weeks could be not prepared. Only the starting material H_2BDC was recovered.

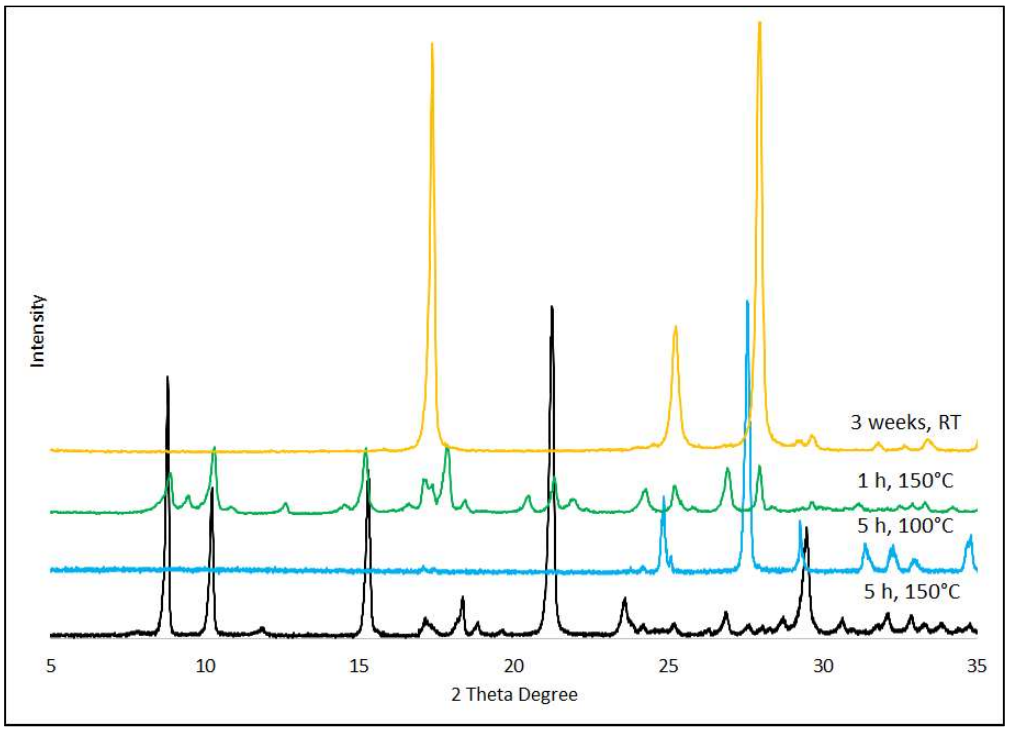


Figure 3-19: MIL-53(Al)(H_2O) samples prepared with varying reaction time and temperature.

Similar tendencies were identified for MeOH as solvent. Although MIL-53(Al)(MeOH) was prepared at 150°C for 5 h, only amorphous sample was obtained after 1 h synthesis at 150°C. In contrast to water as solvent, it was possible to prepare MIL-53(Al) a with reduced reaction temperature of 100°C and 5 h reaction time, but this sample has an even lower

crystallinity (in comparison with sample prepared at 150°C and 1 h reaction time) and is mostly composed of unreacted H_2BDC (Figure 3-20).

This investigation regarding reaction temperature and reaction time may also explain the reason of the lack of publication on MIL-53(Al)(MeOH). MIL-53(Al) in MeOH was prepared in the same conditions than the first published MIL-53(Al) by Loiseau *et.al.* [115] with 220°C reaction temperature and 72 h reaction time, but this has not turned out successful. The resulting XRD pattern (Figure 3-20) did not match the characteristic peaks of MIL-53(Al). In addition is the morphology different. Large spherical particles (dimeter between 1 and 3 µm) are prepared in MeOH with a reaction temperature of 220°C for 72 h (Figure 3-21) instead of nanometre-sized spherical or rod-shaped particles, which were prepared at 150°C reaction temperature and 5 h reaction time (Figure 3-5). As a side note, is the sample prepared in MeOH with 220°C reaction temperature and 72 h reaction time not similar to the sample prepared in water with 5 h reaction time and 100°C reaction temperature. The XRD pattern were not matching. The most intensive peaks of the sample prepared in water (5 h; 100°C) were at 24.9° and 27.6°, while the peaks of the MeOH sample (72°h; 220°C) were at 24.7° and 34.3°.

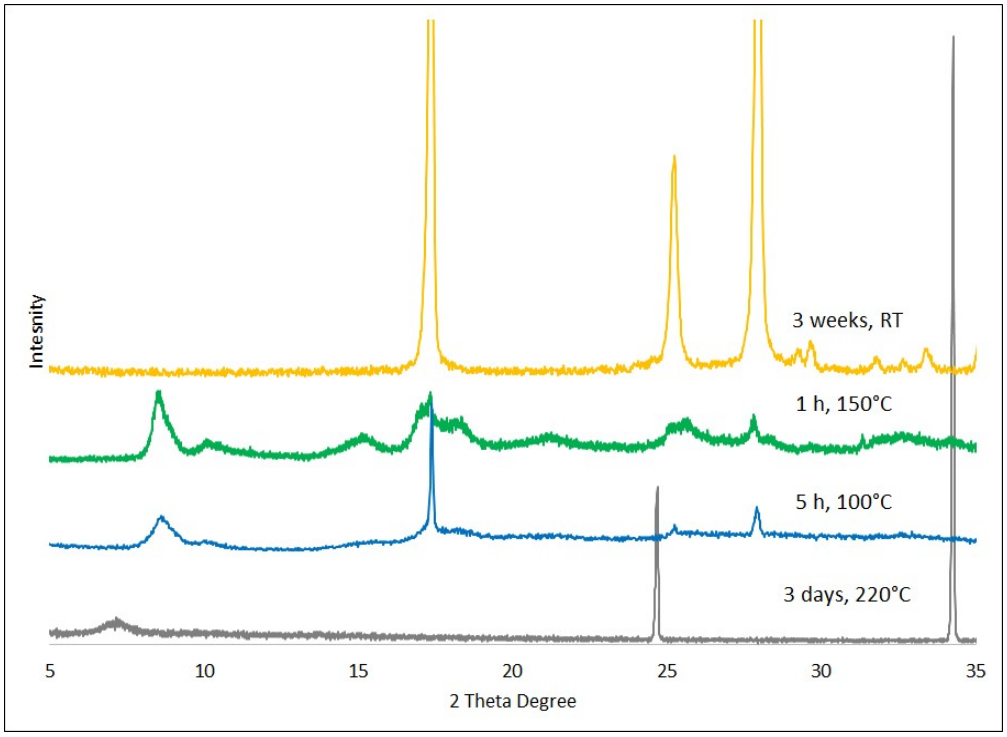


Figure 3-20: MIL-53(Al)(MeOH)-samples with varying reaction time and temperature.

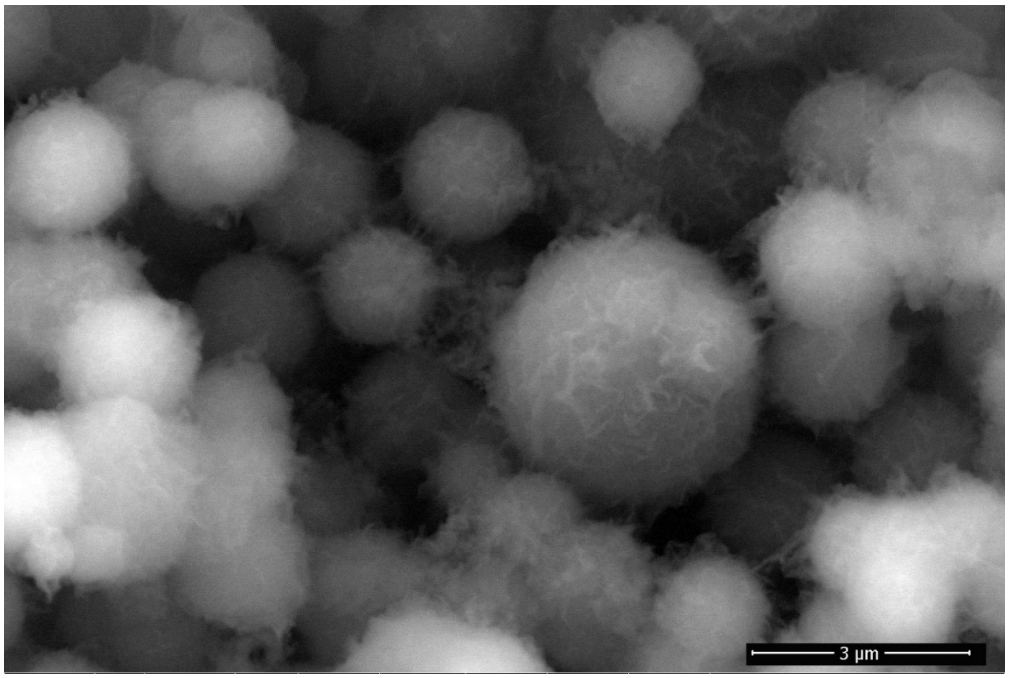


Figure 3-21: SEM image of sample prepared in MeOH at 220°C with 3 days reaction time.

3.3.4 **Breathing effect**

As previously mentioned, the small and large pore forms of MIL-53(Al) can be distinguished by XRD pattern and the change between the small and large pore forms is at ambient conditions mostly caused by adsorption of humidity from the atmosphere [115],[271]. After activation, MIL-53(Al) samples prepared in water, DMF and MeOH showed different ratios of the small and large pore forms, which may imply a difference in water adsorption kinetics which can be identified by the breathing of MIL-53(Al). To investigate the water adsorption kinetics further, temperature-dependent XRD measurements were conducted. In order to have a defined starting point, the samples were placed before the measurement in a saturated water atmosphere for 3 days at RT. The XRD pattern measured at different temperature are then used to investigate the removal of water from the pores and consequently the breathing phenomenon and kinetics.

Figure 3-22 shows the temperature-depended XRD pattern of MIL-53(H_2O)-Acti. Only a peak at ~12° was visible at 25°C and the sample was solely in the small pore form. At approximately 75°C, the small pore peak became broader and decreased in intensity, while the large pore at ~15° increased in intensity. From 150°C onwards, only the large pore form was identified. After cooling down to 25°C, a peak at ~12° could be identified, which can be attributed to the small pore form and the adsorption of water from the ambient air. The intensity of the small pore peak (~12°) peak increased whereas the intensity of the large pore form peak at 15° peak decreased at every consecutive waiting step (0 min, 30 min and 60 min), showing fast water adsorption from ambient air.

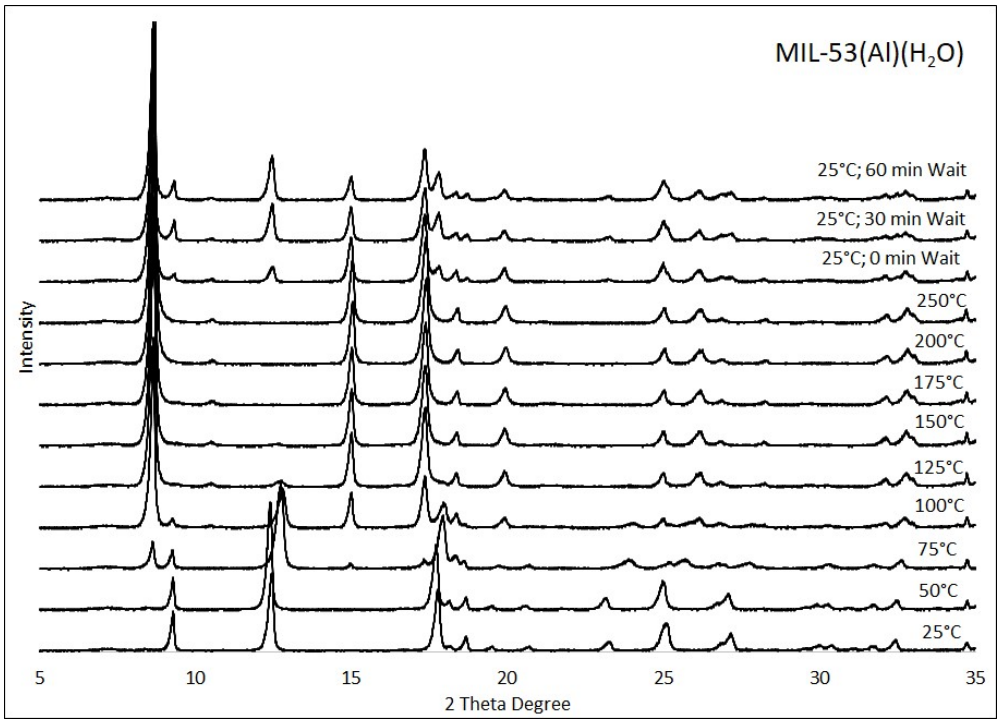


Figure 3-22: Temperature-dependent XRD of MIL-53(Al)(H_2O)-Acti prepared at 150°C and 5 h reaction time.

As shown in Figure 3-23, the sample structure of MIL-53(Al)(DMF) did not change completely into the small pore form after being exposed to a saturated water atmosphere. Instead the XRD pattern indicates a 1:1 ratio of the large to small pore form based on the peak intensities. During the heating process, the small pore peak at 12.51° shifts to larger 2Theta values when the temperature was increased from 25°C to 100°C with a shift up to 0.64°. For higher temperatures, this peak shifted back to the initial position while reducing in intensity until the peak disappears at 200°C. After cooling down the sample back to 25°C, a small peak at 12.49° appeared after 1 h period. Appearance of the peak only after 1 h and the 1:1 ratio between small and large pore form in the material after water saturation at the beginning of the experiment, may suggest slower water adsorption in comparison to MIL-53(Al)(H_2O).

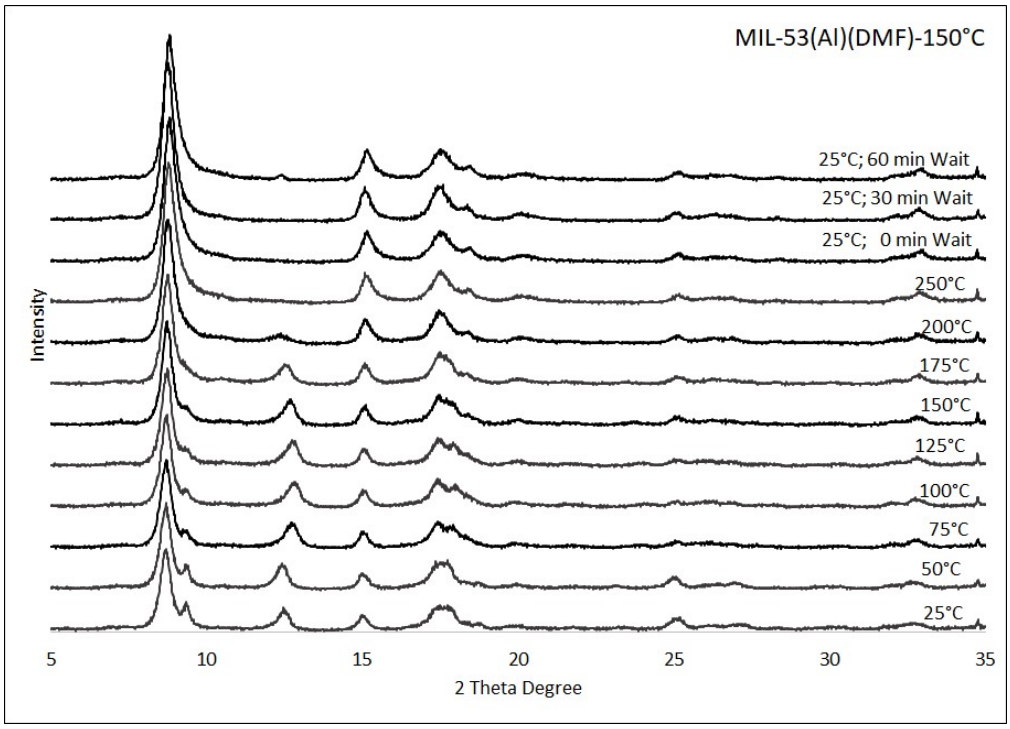


Figure 3-23: Temperature-dependent XRD of MIL-53(Al)(DMF)-Acti prepared at 150°C and 5 h reaction time.

In contrast, in the temperature-dependent XRD pattern of MIL-53(Al)(MeOH)-Acti (Figure 3-24) no small pore peak at ~12° or shift of the XRD peak positions during the whole experiment could be observed. This may imply that MIL-53(Al)(MeOH) does not show any breathing. However, in contrast to the other samples prepared in water and DMF, during the initial measurement at 25°C, the observed peaks in the whole pattern were considerably lower in intensity. In order to understand this effect environmental SEM measurements were employed with varying levels of humidity during the measurements. At higher humidity levels (>80%), particles of MIL-53(Al)(MeOH) started to fuse (Figure 3-25), which might lead to a lower crystallinity of the sample. MIL-53(Al)(DMF), which has a comparable morphology with nanometer-sized particles, did not show similar behaviour with humidity change (Figure 3-26). However the temperature-depended XRD showed that, in contrast to moisture sensitive MOFs *e.g.* HKUST-1 or MOF-5 [305], that the crystallinity of MIL-53(Al)(MeOH) can be restored after removal of water and thus that the process is reversible. With every consecutive temperature step and consequently the removal of water, the intensity of the ~12° has increased until returning at 100°C to the maximum intensity.

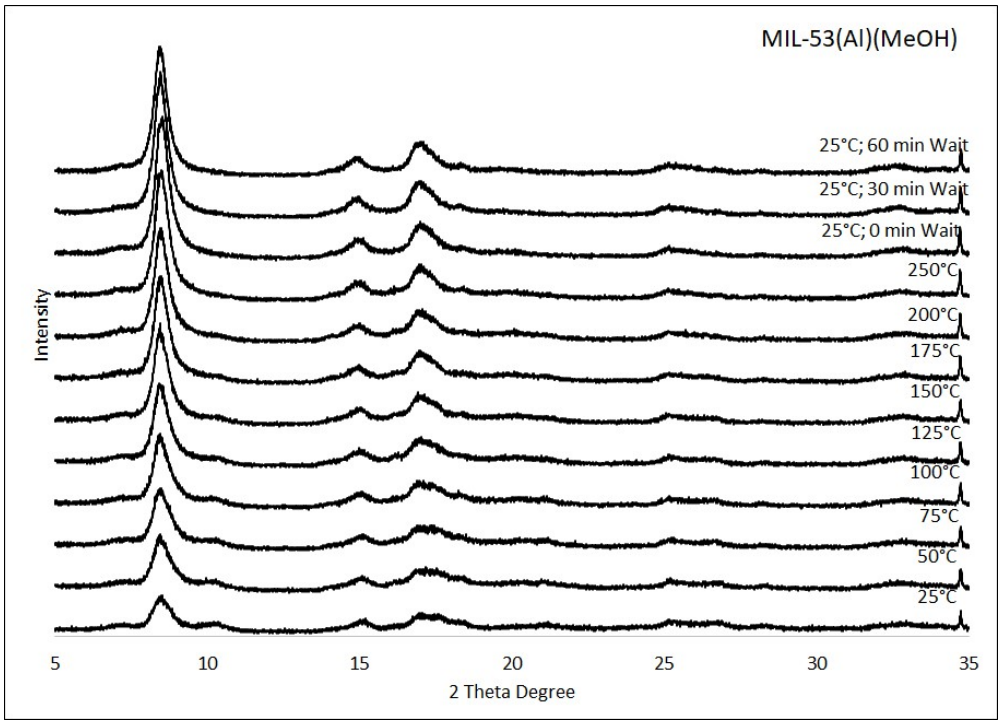


Figure 3-24: Temperature-dependent XRD of MIL-53(Al)(MeOH)-Acti prepared at 150°C and 5 h reaction time.

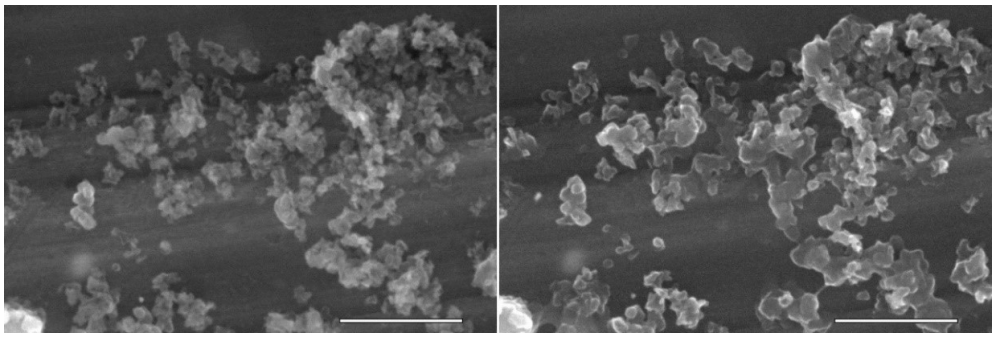


Figure 3-25: Environmental SEM images of MIL-53(Al)(MeOH)-Acti at 60% relative humidity (left) and 80% relative humidity (right). Particles start to fuse at higher humidity levels. Scale bar: 2 µm.

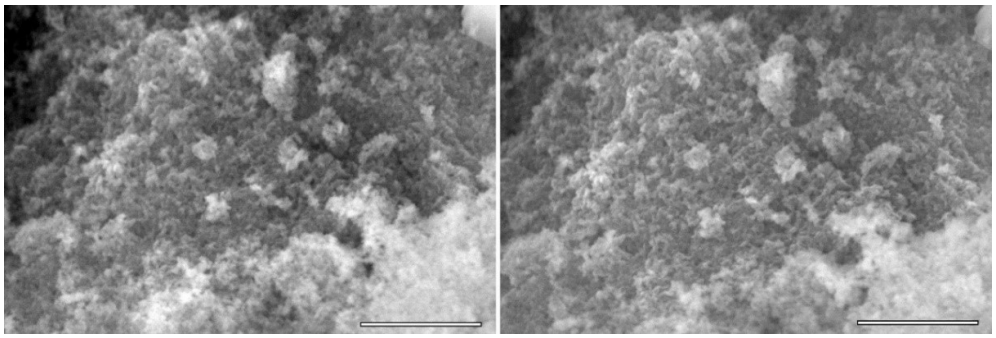


Figure 3-26: Environmental SEM images of MIL-53(Al)(DMF)-Acti at 60% relative humidity (left) and 80% relative humidity (right). No change of the particles was observed. Scale bar 2 µm.

A dependency between reaction temperature and breathing phenomenon in MIL-53(DMF) was reported previously [283]. Those dependencies could be successfully confirmed *via* temperature-dependent XRDs measured of MIL-53(Al)(DMF) samples prepared at 220°C and RT.

The temperature-dependent XRD pattern of MIL-53(Al)(DMF) prepared at RT is shown in Figure 3-27. The sample shows only a peak at ~15°, which implies that the sample is in the large pore form. During the experiment, no shift of the pattern was observed. The results look similar to MIL-53(Al)(MeOH), but the change of intensity at the start of the experiment was not observed, which further confirms the unique behaviour of MIL-53(Al)(MeOH) regarding the fusing of particles at high humidity levels.

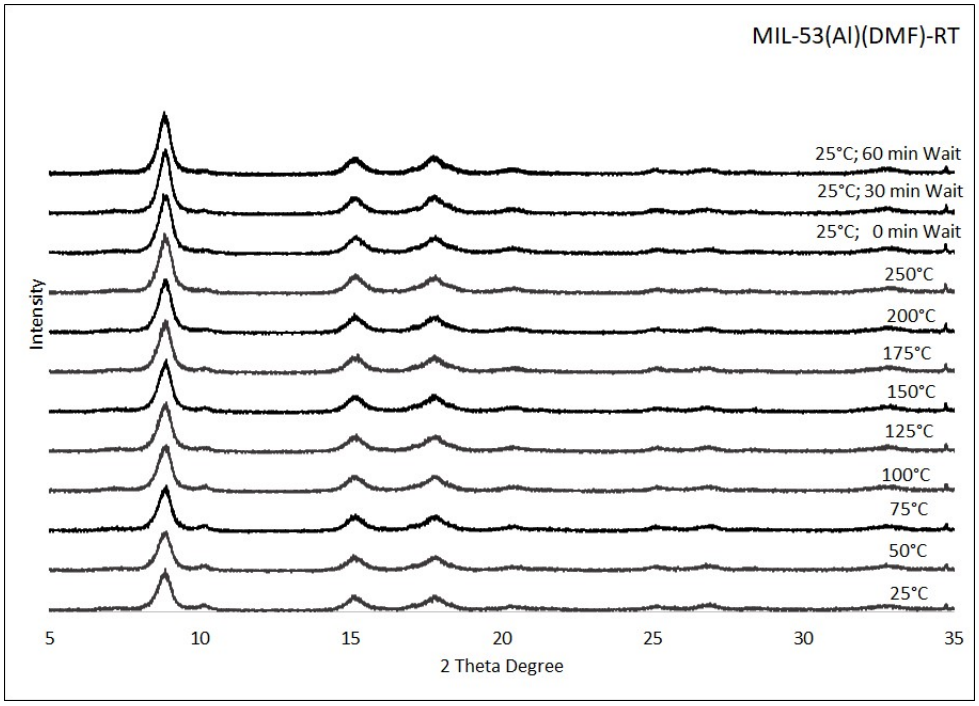


Figure 3-27: Temperature-dependent XRD of MIL-53(Al)(DMF)-Acti prepared at RT.

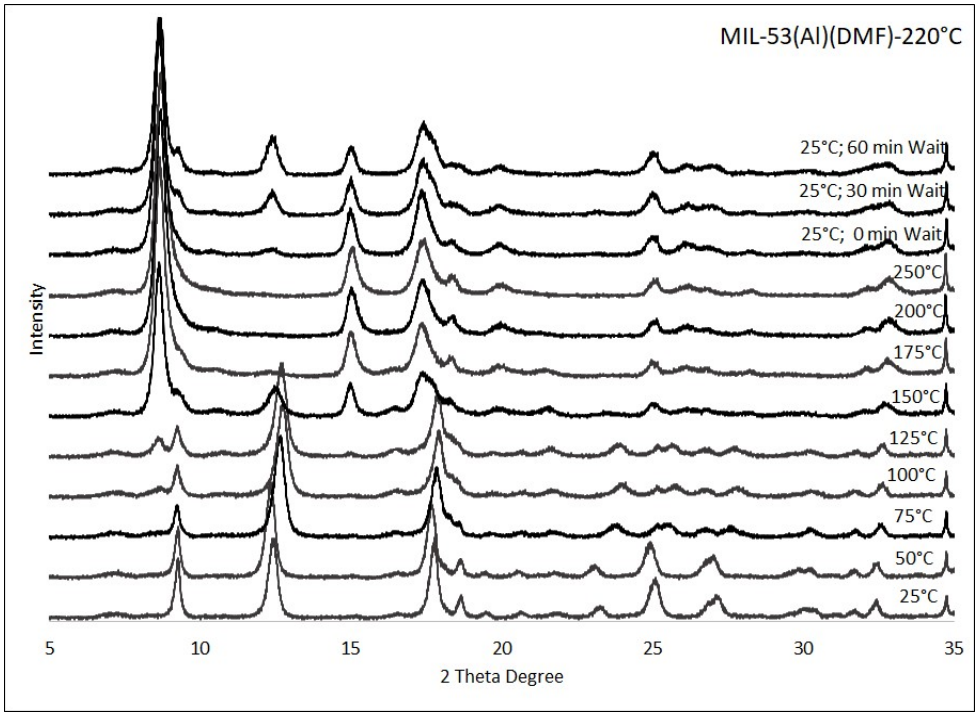


Figure 3-28: Temperature-dependent XRD of MIL-53(Al)(DMF) prepared at 220°C and 72 h reaction time.

In contrast to the RT sample, MIL-53(Al)(DMF) prepared at 220°C showed a distinct breathing effect (Figure 3-28). At RT, no peak at ~15° was observed, which may show that the sample is completly in the small pore form. At 150°C, the peak at 12° broadened and reduced in intensity, while the peak at 15° increased in intensity. After cooling the sample to RT, a small peak at 12° was observed immediately, which imply a fast adsorption of water and consequently fast breathing. This may suggest that the breathing of MIL-53(Al)(DMF) greatly depends on the reaction temperature. A sample prepared at RT does not show any breathing effect whereas samples prepared at 150°C show a slow (12° peak after 60 min waiting time) and MIL-53(Al)(DMF) prepared at 220°C fast breathing phenomenon (12° peak after 0 min waiting time), respectively. However, the breathing of MIL-53(Al)(DMF) prepared at 220°C is in comparison with the water sample (prepared at 150°C) slightly slower. MIL-53(Al)(H_2O) changed completely to the large pore form at 125°C, while MIL-53(Al)(DMF)-220°C had to be heated up to 175°C. This may be a result of varying morphologies of these samples. MIL-53(Al)(DMF) has nanometer sized particles which agglomerate, leading to a large interparticle volume and it might be more difficult for the water molecules to leave the pores of MIL-53(Al)(DMF) in the agglomerated clusters. In contrast is MIL-53(Al)(H_2O) is prepared as micrometre sized particles and water can directly leave the particles.

3.3.5 Measurement of water, CO_2 and VOC uptakes

The temperature-dependent XRD patterns proves that the MeOH sample does not show any breathing. This may bring up the question if this material is hydrophobic. Therefore, water adsorption isotherms were measured to determine the hydrophobicity of the MIL-53(Al) samples.

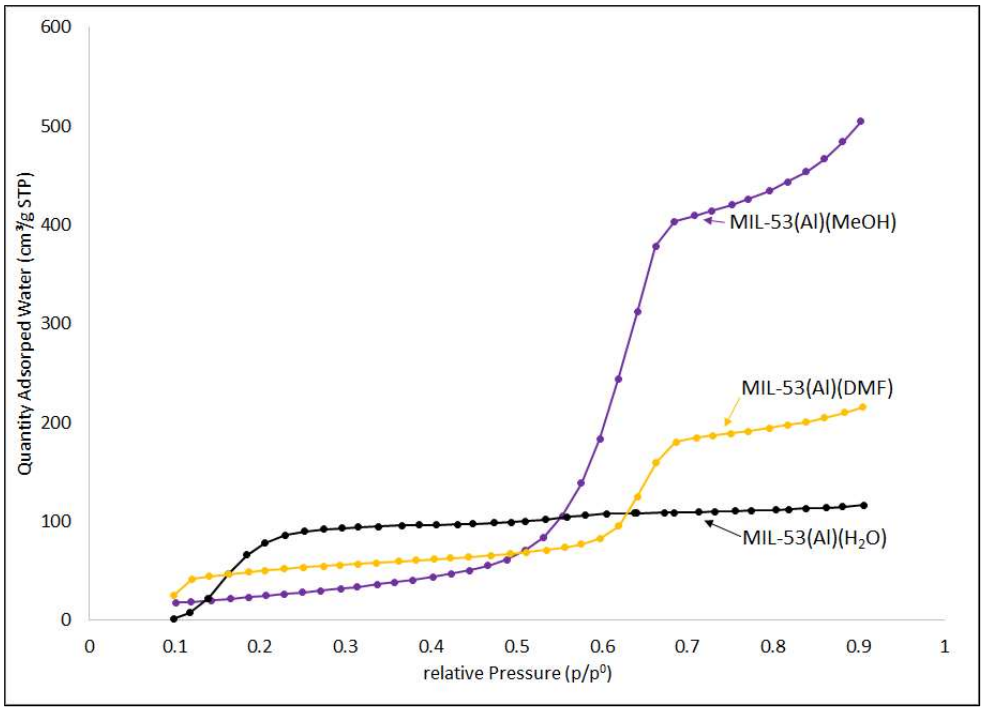


Figure 3-29: H_2O-isotherms of MIL-53(Al)(H_2O)-Acti (black), MIL-53(Al)(DMF)-Acti (yellow) and MIL-53(Al)(MeOH)-Acti (purple) measured at 25°C and ambient pressure. The isotherms were measured between 0.1 and 0.9 relative pressure.

All MIL-53(Al) samples have been heated at elevated temperature (up to 150°C) in vacuum overnight in order to remove possible residues from the pores (*e.g.* adsorbed water molecules from ambient air). The samples were therefore at the beginning of the sorption experiments in the activated large-pore form. The water adsorption isotherms (Figure 3-29) verify the difference in hydrophobicity. MIL-53(Al)(H_2O) showed a fast uptake of water at low relative pressure of 0.1 and reached a plateau at ~0.25 p/p^0 with an adsorbed water amount of 5 mmol g^{-1} (115 $cm^3\ g^{-1}$). The isotherm has Type-I shape, which implies strong interaction between the adsorbate and adsorbent at low relative pressures and a sample without macroporosity. With the adsorption of water molecules, the pores of MIL-53(Al)(H_2O) may contract into the small pore form, preventing further water adsorption. Both MIL-53(Al)(DMF) and MIL-53(Al)(MeOH) showed at first low uptake, followed by a sharp increase at relative pressure of 0.5 and 0.6 for MIL-53(Al)(MeOH) and MIL-53(Al)(DMF), respectively. At low relative pressure (< 0.5), the water uptake of MIL-53(Al)(MeOH) (~40 $cm^3\ g^{-1}$) is lower than MIL-53(Al)(DMF) (~60 $cm^3\ g^{-1}$). This was reserved at higher relative pressures. At relative humidity of 0.9, the total uptake for MIL-53(Al)(DMF) was measured as 10 mmol g^{-1} (210 $cm^3\ g^{-1}$) and 22 mol g^{-1} (480 $cm^3\ g^{-1}$) for MIL-53(Al)(MeOH). The water isotherm shape for both samples is similar to a Type-V isotherm, which indicates a weaker interaction at low relative pressure following with clustering of water molecules (pore condensation) at higher relative pressure. Above p/p^0 = 0.8, a further increase in the amount of adsorbed water may indicate the adsorption in the voids between the particles (macroporosity).

AS a side note, the XRD pattern measured of the samples after the water-isotherms have shown an interesting phenomenon for MIL-53(Al)(DMF). The peaks of MIL-53(Al)(DMF) have reduced in intensity, which imply a reduction in crystallinity (Figure 3-30), whereas the patterns of MIL-53(Al)(H_2O) (Figure 3-31) and MIL-53(Al)(MeOH) (Figure 3-32) remained similar. These results may suggest that MIL-53(Al)(DMF) has a reduced stability to humidity, which is surprising, because MIL-53(Al)(H_2O) is known to be highly water stable [306].

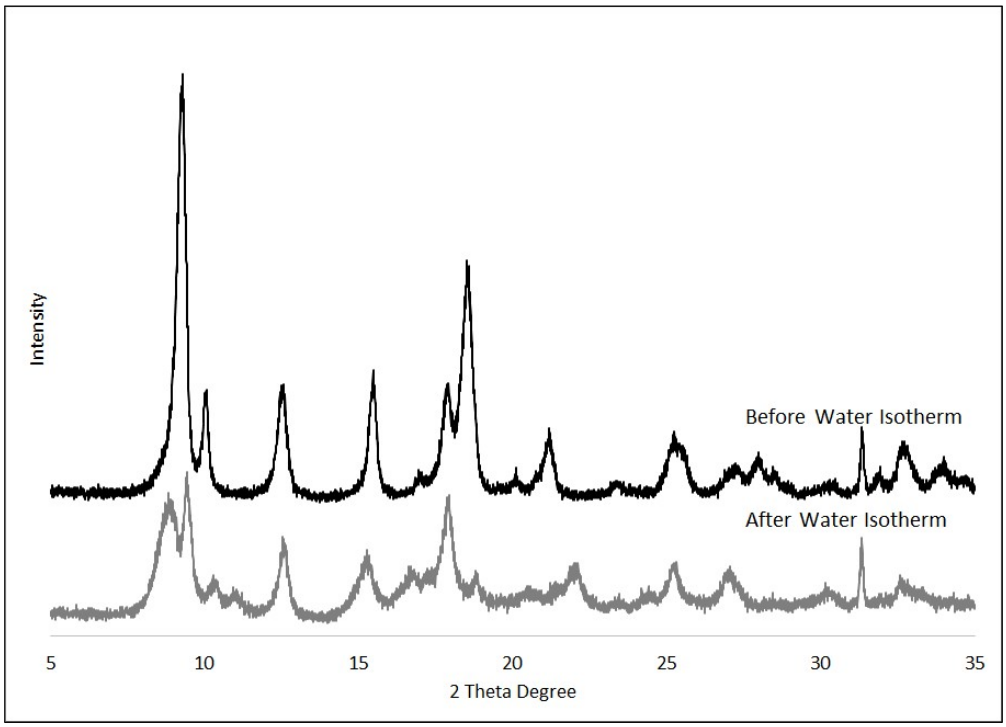


Figure 3-30: XRD pattern of MIL-53(Al)(DMF) before and after measurement of the H_2O-isotherm.

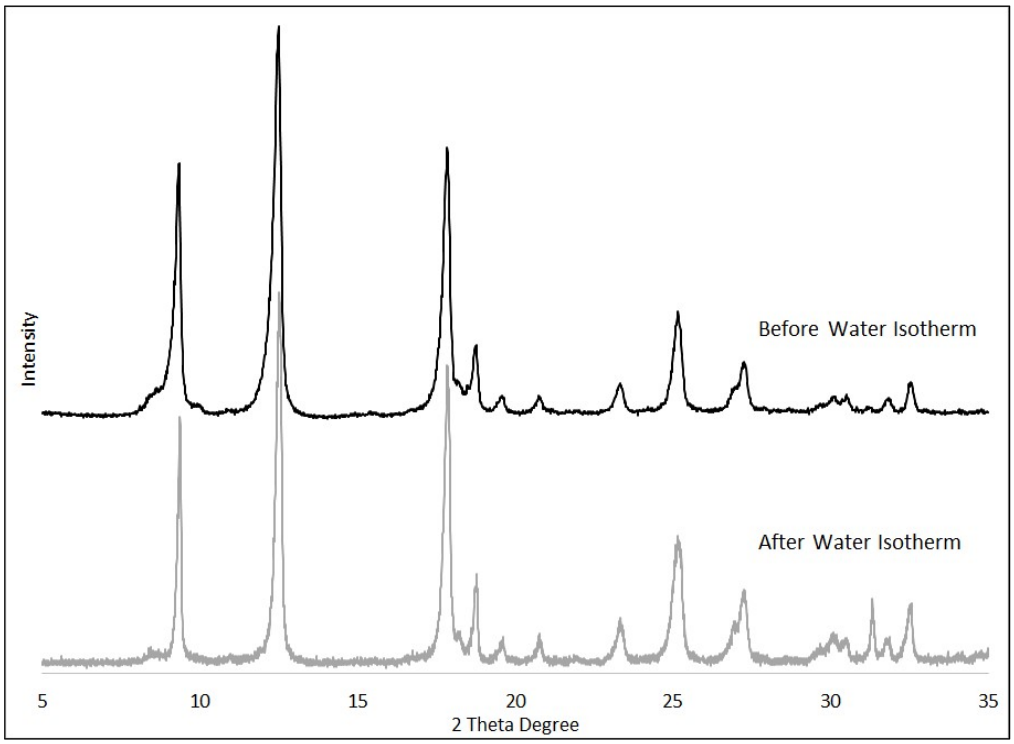


Figure 3-31: XRD pattern of MIL-53(Al)(H_2O) before and after measurement of the H_2O-isotherm.

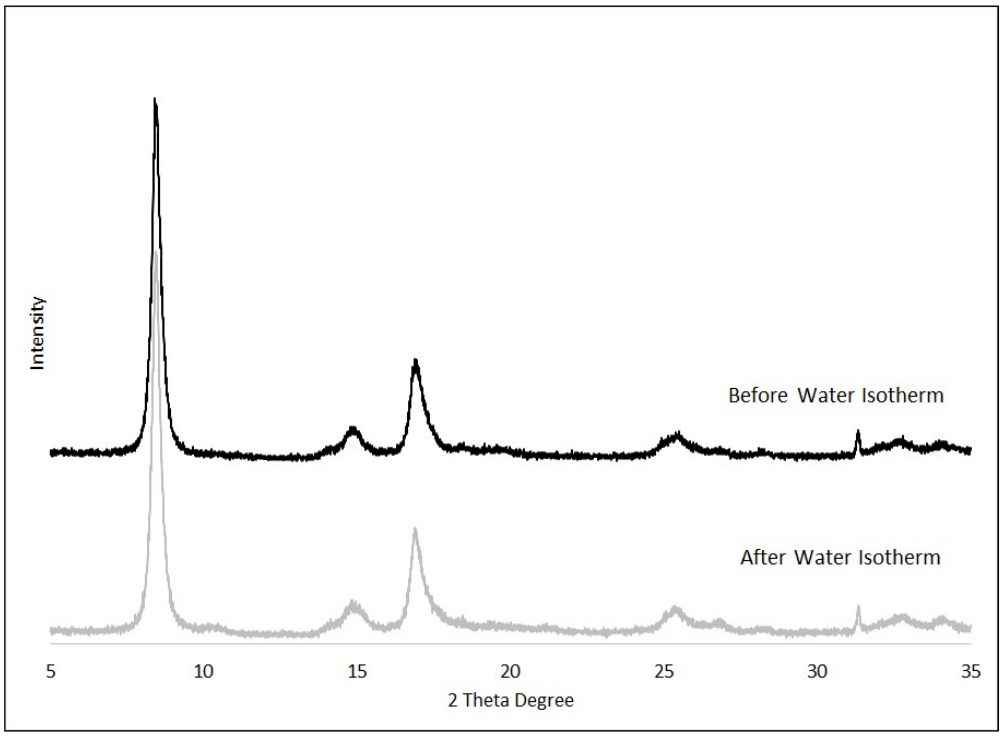


Figure 3-32: XRD pattern of MIL-53(Al)(MeOH) before and after measurement of the H_2O-isotherm.

The fast water uptake of MIL-53(Al)(H_2O) was also shown by FTIR of activated samples (Figure 3-33). Activated MIL-53(Al) samples were dried at 125°C overnight to remove the water from the pores. The samples were measured 5 min after removal from the oven. The FTIR spectra of the samples show peaks at 1414 cm^{-1} and 1510 cm^{-1}, which are attributed to the symmetrical and asymmetrical stretching of the framework carboxylate groups [307]. Peaks at 1120 cm^{-1}, 3463 cm^{-1} and 3610 cm^{-1} are only observed in the IR spectrum of MIL-53(Al)(H_2O). According to Salazar *et.al.* [307] can these peaks be attributed to interaction of the framework μ-OH group with water in the pores of MIL-53(Al). This indicates the fast adsorption of water from ambient air.

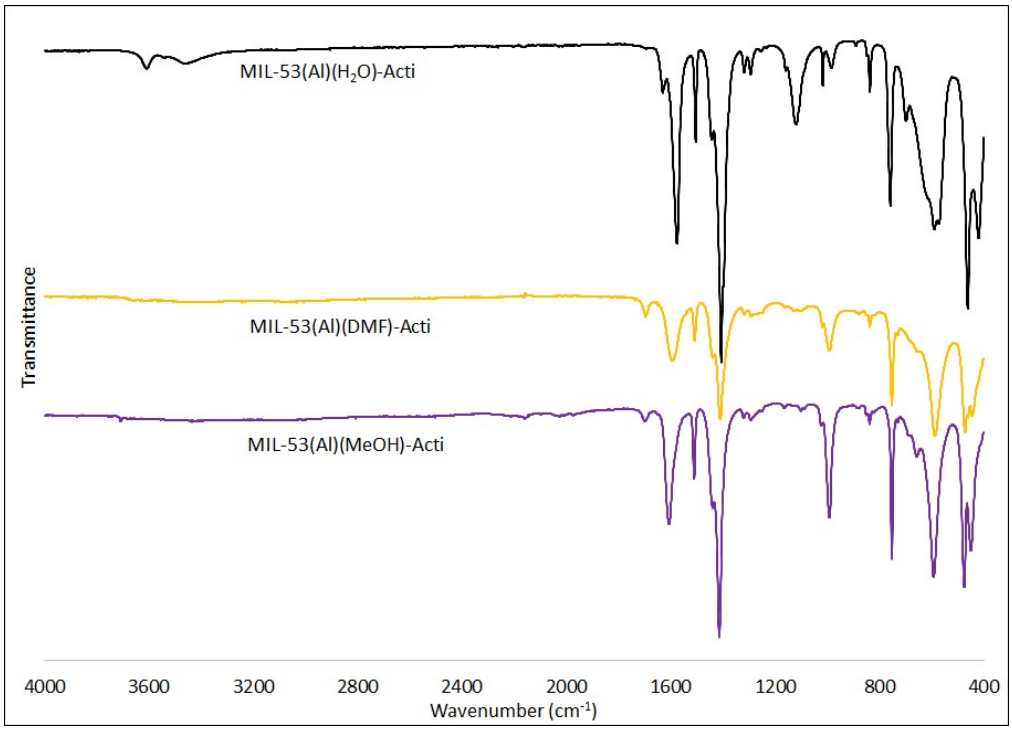


Figure 3-33: IR of MIL-53(Al) samples prepared in different solvents.

The XRD pattern before and after the measurement of water-isotherms has implied a reduced stability to humidity for MIL-53(Al)(DMF) in comparison to MIL-53(Al)(H_2O) and MIL-53(Al)(MeOH), respectively. This implication has been verified by measurement of N_2-isotherms followed by the calculation of the BET-area of these samples. The isotherms were measured for MIL-53(Al)(DMF) (Figure 3-34), MIL-53(Al)(H_2O) (Figure 3-35) and MIL-53(Al)(MeOH) (Figure 3-36) and directly compared with the results for the activated samples before the water isotherms. The degassing conditions were for all samples identical.

Table 3-6: Porosities of various MIL-53(Al) samples after measurement of H_2O-isotherms

Compound	S_{BET} ($m^2\ g^{-1}$)	t-plot micropore volume ($cm^3\ g^{-1}$)
Before H_2O-isotherm:		
MIL-53(Al)(H_2O)-Acti	1002 ± 18	0.44
MIL-53(Al)(DMF)-Acti	1084 ± 35	0.45
MIL-53(Al)(MeOH)-Acti	895 ± 30	0.39
After H_2O-isotherm:		
MIL-53(Al)(H_2O)-Acti	1021 ± 27	0.48
MIL-53(Al)(DMF)-Acti	377 ± 6	0.18
MIL-53(Al)(MeOH)-Acti	862 ± 17	0.34

The results are summarized in Table 3-6 and confirmed that MIL-53(Al)(DMF) has lost most of its porosity during the measurement of the water isotherm (S_{BET}: 1084 $m^2\ g^{-1}$ → 337 $m^2\ g^{-1}$). The porosity of MIL-53(Al)(MeOH) has only slightly decreased (895 $m^2\ g^{-1}$ → 862 $m^2\ g^{-1}$), while the porosity of MIL-53(Al)(H_2O) remained unchanged (inside the error tolerance). MIL-53(Al)(DMF) shows therefore reduced

stability to humidity, while MIL-53(Al)(H_2O) is known to be a water-stable MOF even at extreme pH-levels or at elevated temperature (up to 100°C) for at least a week [306]. This effect cannot be explained by the difference in morphology, because MIL-53(Al)(MeOH) remains stable.

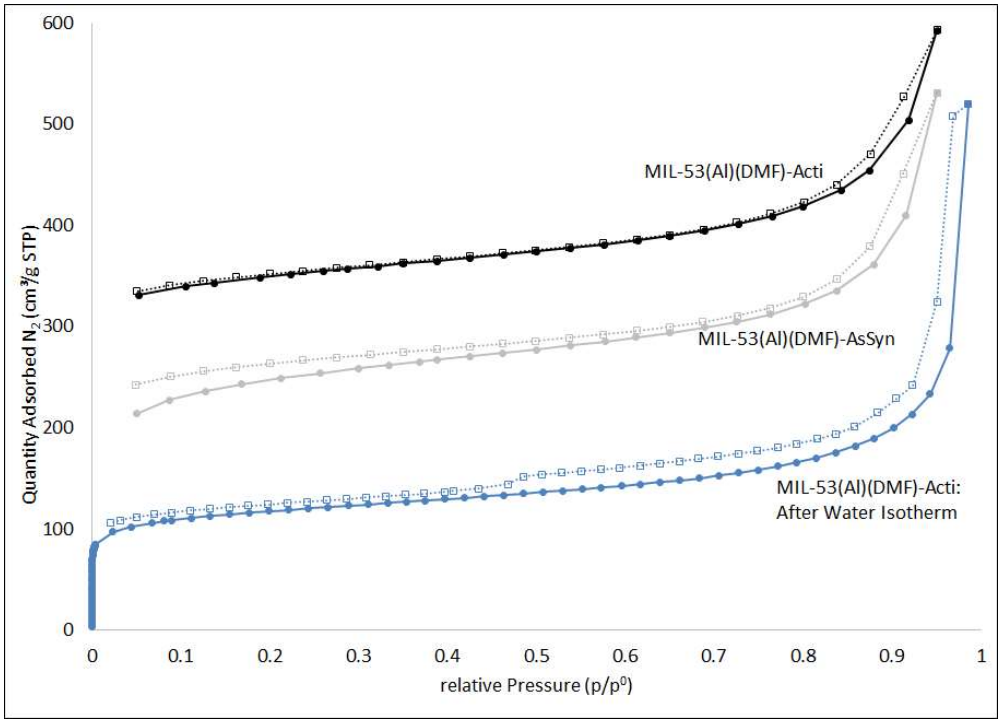


Figure 3-34: Comparison of N_2-isotherms for MIL-53(Al)(DMF) before and after measurement of H_2O-isotherms.

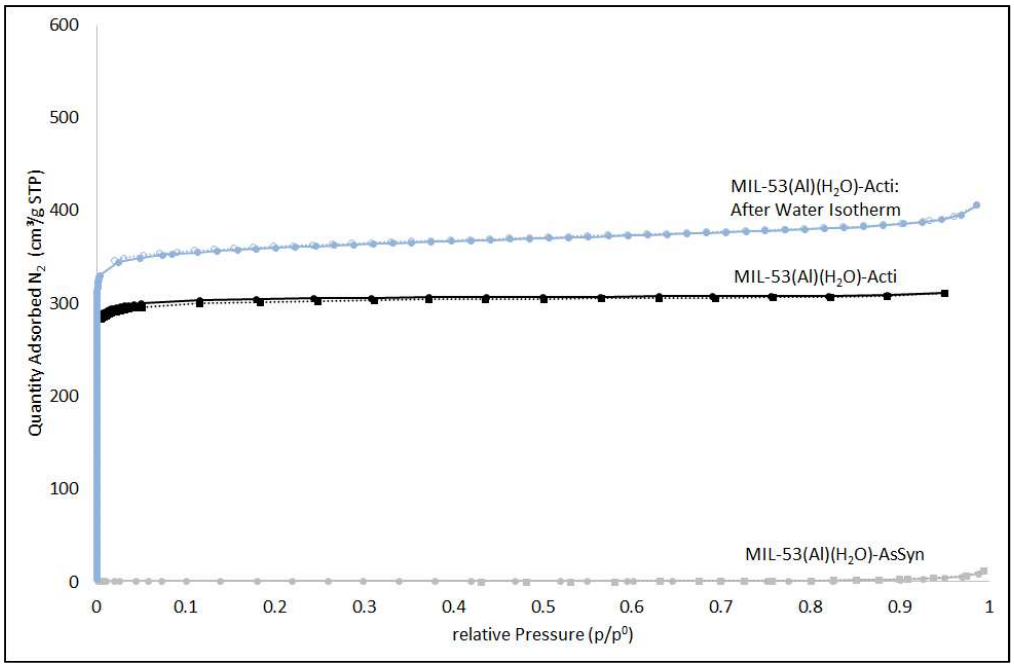


Figure 3-35: Comparison of N_2-isotherms for MIL-53(Al)(H_2O) before and after measurement of H_2O-isotherms.

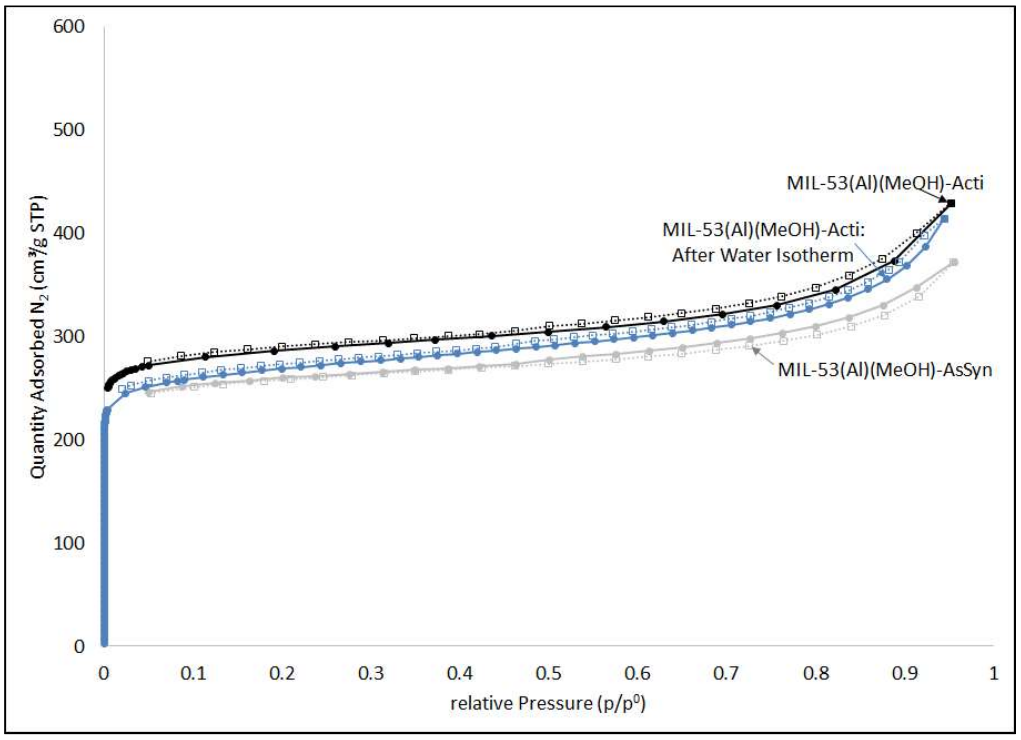


Figure 3-36: Comparison of N_2-isotherms for MIL-53(Al)(MeOH) before and after measurement of H_2O-isotherms.

Until now only the adsorption of N_2 (for the investigation of the porosity) and water (for investigation of the hygroscopicity) have been analysed. However, due to the great attention MIL-53-class compounds has received in the literature, the capacity for very different target compounds has been investigated. These are ranging from CO_2 [308], H_2 [138], CH_4, CO, O_2[216] to less common compounds such as various VOCs (*e.g.* heptane [309], MeOH or EtOH [310]) or even sulphur and nitrogen containing heteroaromatics [309]. In most cases these compounds have been investigated for gas separation and purification. To have an insight of the chemical properties of the various MIL-53(Al) derivates, the adsorption of the two compounds CO_2 and MeOH will be investigated. One aim of this research is the investigation possible MOFs for sensor applications and knowledge of *e.g.* adsorption capacity is of importance to assess the performance. CO_2 is most famous for its role as a greenhouse gas and is a typical contamination in natural gas, but keeping specific CO_2 levels are also important for a good indoor room atmosphere. MeOH is a typical example of the class of VOCs, which are in general known for possible negative impact in the human health (for more information about health impact of CO_2 and VOCs see chapter 2.1, (p. 5) and 2.2, (p. 8)).

CO_2-isotherms in literature were often reported for high pressure regions (up to 35 bar CO_2 pressure [311]). Such high pressures are for instance of interest for gas storage. For other applications *e.g.* gas separation or sensing, the low-pressure region (up to 1 atm) is of greater importance. Therefore were the CO_2-isotherms measured during this research at 25°C in the low-pressure region till 1 atm CO_2 pressure (Figure 3-37). This are conditions, which can be expected in typical sensor set-ups to detect CO_2-concentrations in room air or in medical applications.

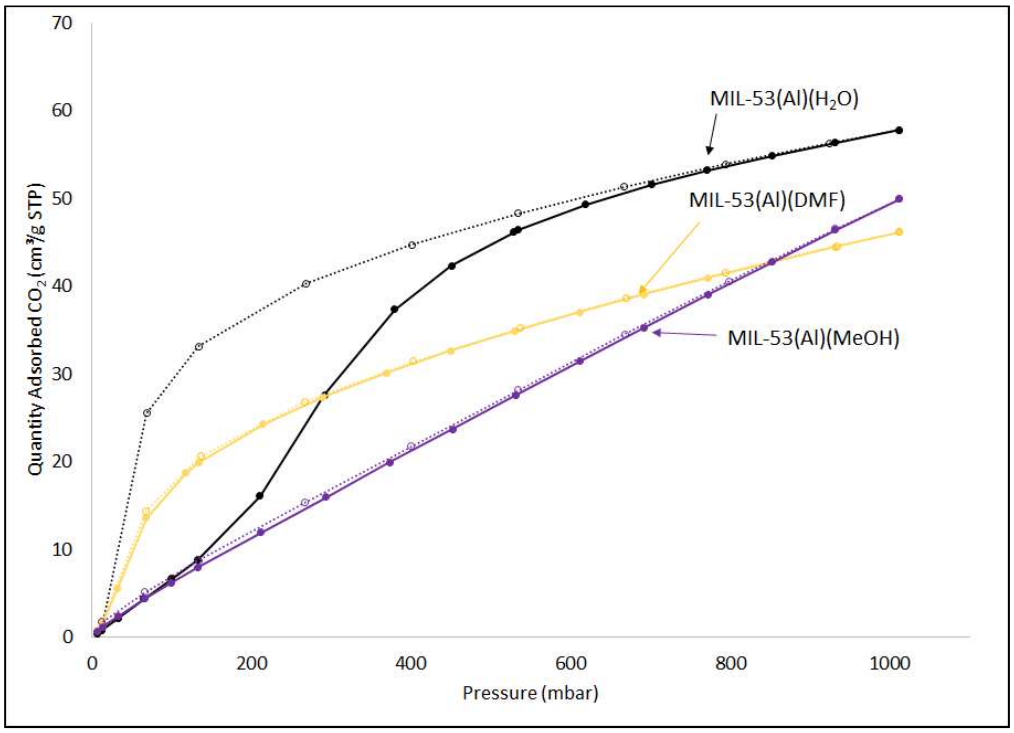


Figure 3-37: CO_2-isotherms for activated MIL-53(Al) samples. All samples were prepared at 150°C with 5 h reaction time. Adsorption: solid line; Desorption: dashed line.

The compound MIL-53(Al)(H_2O) (Figure 3-37, black) started to adsorb CO_2 at lower pressure, but above ~150 mbar the shape of the isotherm changed and the amount of adsorbed CO_2 increased until reaching at 1 atm an uptake of 55 $cm^3\ g^{-1}$ (2.57 $mmol\ g^{-1}$; 12 wt%). Rallapaili *et.al.* [216] have measured CO_2-isotherms of MIL-53(Al)(H_2O) at 15°C and 30°C. A CO_2-isotherm measured at 15°C has shown an total uptake (at 1 atm) of 57 $cm^3\ g^{-1}$, while the measurement at 30°C has led an uptake of 51 $cm^3\ g^{-1}$ at 1 atm. The CO_2-isotherm during this research was measured at 25°C and the uptake is between the uptakes measured at 30°C and 15°C and is therefore in good agreement with the literature data.

A striking difference during the measurement for the MIL-53(Al)(H_2O) CO_2-isotherm in contrast to the samples prepared in MeOH and DMF, is the hysteresis of the isotherm. The CO_2-adsorption isotherm for the low pressure region by Rallapaili *et.al.* [216] was measured for the adsorption branch only and therefore no comparison regarding hysteresis behaviour in the low-pressure region with the available literature was possible. Until now, such a hysteresis in a CO_2-isotherm was until now observed in the high-pressure region and was explained with the breathing of MIL-53(Al)(H_2O). CO_2 interacts, similar to water, with the μ-OH-framework group of MIL-53(Al) [215]. However, the changing of the cell dimensions is in comparison with a water-induced breathing smaller. A comparison of the unit cell parameters illustrates this. While the open-fore form has a c-value of 12.08 Å, the water-adsorbing small-pore form has a smaller value of c = 6.570 Å [115]. With CO_2, the pore dimension has changed (c = 10.38 Å) [215], but not in the same regard than for water adsorption. In the high-pressure region, additional CO_2 molecules force the pores open again, which causes another change of the cell parameters and consequently

breathing [312]. Breathing effect of MIL-53(Al) and hysteresis in the adsorption isotherms might be directly connected. A hysteresis could be only observed for MIL-53(Al)(H_2O). The measurement of the temperature-dependent XRD have already showed, that the breathing in MIL-53(Al)(H_2O), prepared at 150°C and 5 h reaction time, is faster than in MIL-53(Al)(DMF) and MIL-53(Al)(MeOH) in the same conditions.

In contrast to MIL-53(Al)(H_2O), MIL-53(Al)(DMF) (Figure 3-37, yellow) showed a Type-I isotherm without an observable hysteresis. At 1 atm, MIL-53(Al)(DMF) has an CO_2-uptake of 2.1 mmol g^{-1} (9wt% or 45 cm^3 g^{-1}).

The CO_2-isotherm of MIL-53(Al)(MeOH) (Figure 3-37, purple) is a straight line, without a hysteresis. At 1 atm is the uptake of MIL-53(Al)(MeOH) 50 cm^3 g^{-1} (2.2 mmol g^{-1}; 9 wt%). While MIL-53(Al)(MeOH) has a lower CO_2 adsorption capacity in comparison with MIL-53(Al)(DMF) at low CO_2 pressure (< 900 mbar), the shape of the isotherm further imply that the uptake might even surpass the uptake of MIL-53(Al)(H_2O) with further increase of CO_2-pressure. The isotherm has not shown a saturation point in the measured pressure range. The temperature-dependent XRD pattern already verified that MIL-53(Al)(MeOH) is not showing any breathing effect, even though it was able to adsorb target compounds such as CO_2 or water. The lack of breathing for MIL-53(Al)(MeOH) can be therefore not explained with the lack of adsorption capacity and must be caused by a different effect.

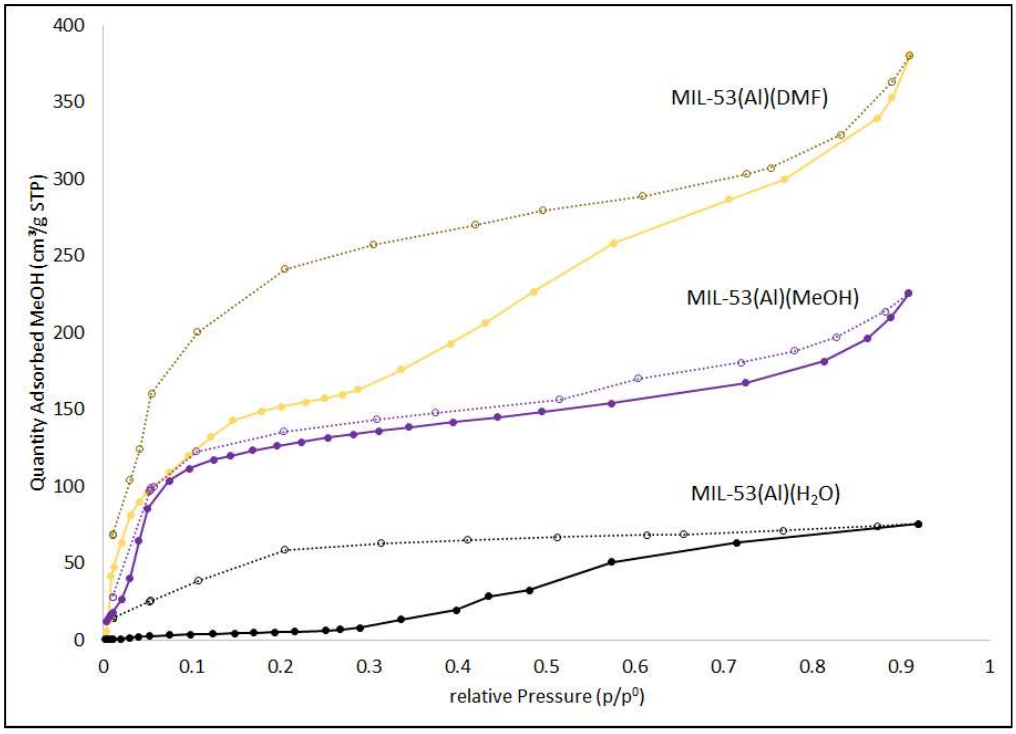


Figure 3-38: Comparison of MeOH-isotherms for the activated MIL-53(Al) samples, prepared at 150°C and 5 h reaction time. Adsorption: solid line; Desorption: dashed line.

The MeOH-isotherm were measured for the activated samples prepared in water, DMF and MeOH (Figure 3-38). MIL-53(Al)(DMF) showed the highest total capacity at p/p^0 = 0.9 of 380 cm^3 g^{-1} (16.7 mmol g^{-1}), while the capacities for MIL-53(Al)(MeOH) and MIL-53(Al)(H_2O) are lower with 225 cm^3 g^{-1} (10.1 mmol g^{-1}) and 75 cm^3 g^{-1} (3.37 mmol g^{-1}),

respectively. The isotherms showed for MIL-53(Al)(H_2O) and MIL-53(Al)(DMF) a certain hysteresis, which might be attributed to the breathing of MIL-53(Al). In contrast, MIL-53(Al)(MeOH) does not show breathing and consequently little hysteresis. The shape of all MeOH-isotherms and the uptakes show an unexpected behaviour, because the uptake is inverse to the behaviour during the water isotherm even though MeOH and water are both polar compounds. MIL-53(Al)(DMF) and MIL-53(Al)(MeOH) showed an uptake of MeOH at low relative pressure, while MIL-53(Al)(H_2O) only starts to adsorb MeOH at p/p^0 = ~0.3. The additional uptake for MIL-53(Al)(H_2O) and MIL-53(Al)(DMF) at high relative pressure (> 0.7) might be attributed to the intraparticle adsorption.

According to the measured isotherms, MIL-53(Al)(DMF) and MIL-53(Al)(MeOH) show a stronger interaction with MeOH than MIL-53(Al)(H_2O). A visible MeOH adsorption could be observed for MIL-53(Al)(H_2O) from 0.3 relative MeOH pressure onwards, while MIL-53(Al)(DMF) and MIL-53(Al)MeOH show uptake even below p/p^0 = 0.1. This is contrast to the behaviour known from literature [310], where MIL-53(Al)(H_2O), show large uptake at low relative pressure and reaching a plateau at p/p^0 = 0.2, which is similar to the behaviour known from water-isotherms [283]. One possible reason might be that the MeOH used for the measurement of the isotherm was not completely water-free (technical grade MeOH was used, the exact amount of water in the MeOH is not known). However, is such a measurement more feasible to determine the adsorption behaviour, because MeOH is hygroscopic and can be rarely found without traces of water. A possible explanation for the discrepancy of the shape of the measured MeOH-isotherms (Figure 3-38) for and the isotherm known from literature [283] might be as follows: MIL-53(Al)(H_2O) has a stronger interaction with water than with MeOH and readily absorbs the traces of water in the MeOH, which leads to a change into the small-pore form of MIL-53(Al). Larger relative pressure of MeOH (during this measurement <0.3 p/p^0) is then needed to replace the water molecules for MeOH in the pores and an adsorption of MeOH can take place. MIL-53(Al)(DMF) and MIL-53(Al)(MeOH) show in contrast at low pressure (< 0.5 relative water pressure) a reduced tendency for water adsorption (Figure 3-29) and consequently are they able to readily adsorb MeOH at low relative pressure even with traces of water.

3.3.6 **Thermal stability**

The analysis by thermogravimetric analysis (TGA) of the MIL-53(Al) samples (Figure 3-39) have shown that the thermal stability of MIL-53(Al)(DMF) and MIL-53(Al)(MeOH) are slightly reduced (~460°C) in comparison with MIL-53(Al)(H_2O) (~500°C). This might be caused by the smaller particle size and consequently the larger surface area of MIL-53(Al)(DMF) and MIL-53(Al)(MeOH) to MIL-53(Al)(H_2O). Even so, the thermal stability of MIL-53(Al) prepared in DMF or MeOH is still higher in comparison with other commercial available, carboxylate containing MOFs *e.g.* HKUST-1 (240°C [116]) or MOF-5 (400°C [313]), which is explained with the strong bond between aluminium and oxygen from the linker in the framework [314]. As mentioned before, was the dependency of the reaction temperature and the breathing phenomenon for MIL-53(Al)(DMF) already investigated. Mounfield *et.al.* [283] have attributed the increased hydrophobicity to

remaining DMF molecules in the framework after activation by DMF-reflux. However, here activation was conducted at elevated temperature (333°C for 3 days) to ensure the complete removal of any residue. The absence of weight loss steps between 100°C and 250°C (residue of DMF [283]) or 275°C and 420°C (residue of H_2BDC [115]) indicate the formation of a product free of any residual species in the pores. The TGA supports the observation from the XRD pattern (Figure 3-6). The most intensive peak of MIL-53(Al)(DMF) at ~9° has shifted from 8.99° to 8.72°. This shift could be also observed between calculated XRD pattern from crystal data of as-synthesized and activated MIL-53(Al).

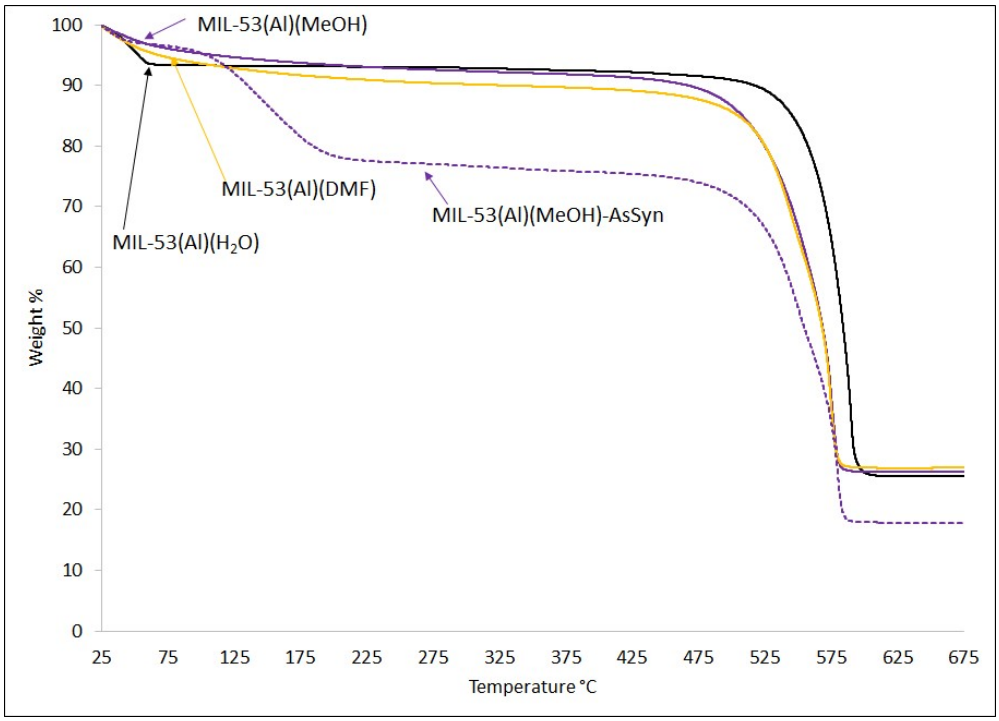


Figure 3-39: Comparison of TGA for activated MIL-53(Al) samples. MIL-53(Al)(MeOH)-AsSyn is shown in addition as dashed line.

The TGA of MIL-53(Al)(MeOH)-AsSyn (Figure 3-39) could further explain an observation, which was done in the XRD pattern of MIL-53(Al)(MeOH). While the XRD pattern has not shifted (the most intensive peak of MIL-53(Al)(OH) was observed for both the as-synthesized and activated form at 8.73°), has the BET value indicated a ~10% lower porosity for MIL-53(Al)(MeOH)-AsSyn (Table 3-4). In the TGA of this sample could be, in contrast to the activated samples, a weight loss between 100°C and 250°C clearly identified, which implied residue of DMF in the pores. Even though DMF was not used during the synthesis or the activation, washing with DMF is important for the removal of impurities from the sample such as unreacted free H_2BDC from the product (Figure 3-15). A sample without a washing step with DMF needed longer activation time (up to a week) and shows even after the prolonged activation more impurity peaks in the XRD-pattern (see chapter 3.3.3, p. 53). However, due to the known tendency of MIL-53(Al) to quickly adsorb DMF [315], DMF might be trapped in the pores before the activation process at elevated temperature. The adsorption of DMF in the pores of MIL-53(Al)(MeOH)-AsSyn

might be therefore a possible explanation for the difference in porosity for MIL-53(Al)(MeOH)-AsSyn and MIL-53(Al)(MeOH)-Acti (Table 3-4).

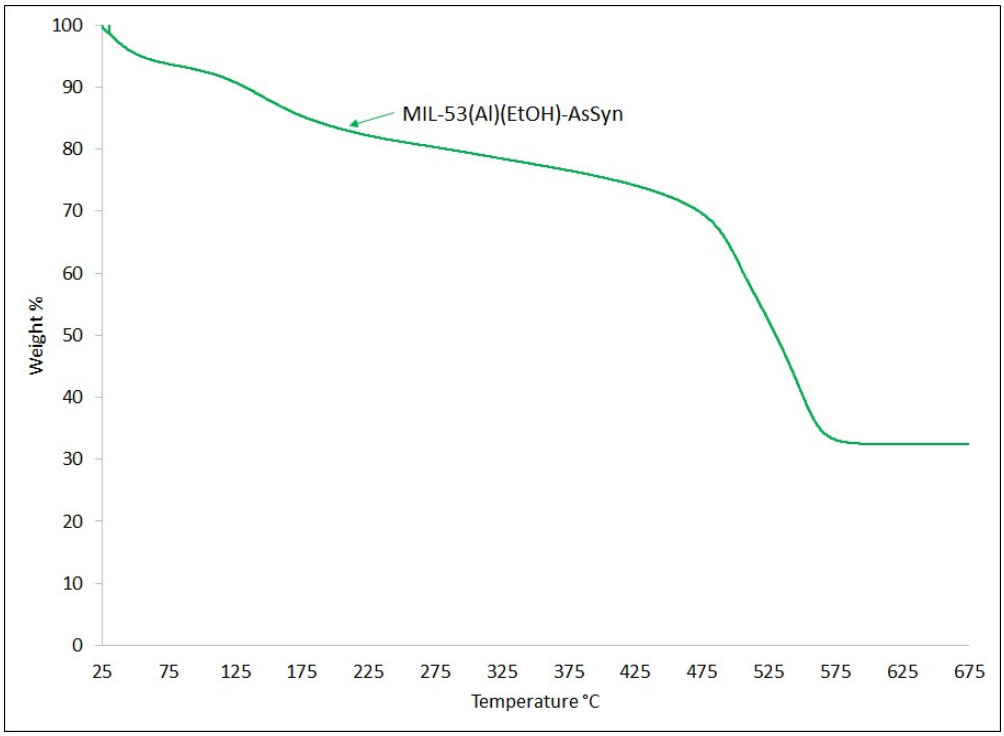


Figure 3-40: TGA of MIL-53(Al)(EtOH)-AsSyn.

XRD pattern showed (Figure 3-8) that the MIL-53(Al) samples prepared in EtOH had a reduced crystallinity in comparison to samples prepared in water, DMF and MeOH and has further decomposed to an amorphous sample after activation. This was further investigated with TGA. The decomposition temperature of MIL-53(Al)(EtOH)-AsSyn (Figure 3-40; TGA of MIL-53(Al)(EtOH)-Acti was not measured) is with ~450°C similar to the samples prepared in DMF and MeOH, but the TGA shows over the whole temperature range till the total decomposition a continuous weight loss, while other MIL-53(Al)-AsSyn samples (*e.g.* MIL-53(Al)(MeOH)-AsSyn in Figure 3-39) showed nearly no weight loss in the same temperature range. It might be therefore possible that MIL-53(Al)(EtOH) has slowly decomposed during the activation process at 333°C for 3 days, leading to the amorphous sample. However, the application of additional activation methods (e.g. reflux in DMF) for MIL-53(Al)(EtOH) has exceeded the scoop of this research.

3.3.7 Morphology in alternative solvents

Until now only the formation of MIL-53(Al) was conducted in the commonly used solvents water and DMF and in addition in low-weight alcohols MeOH and EtOH. Investigation of the morphologies led to the theory that the solubility of the linker H_2BDC is of importance for the particle size of the synthesized MIL-53(Al) (see chapter 3.3.1, p. 42). However, only the solubility of the linker was investigated, but the solubility of the metal salt might also influence the crystal morphology. The existing data regarding the solubility for the starting material aluminium nitrate in water (68.9 g/100 g in water at RT [277] and 160 g/100 g at 100°C [316]) and MeOH (11.46 g/100 g at RT [316]) imply a complete solubility of the

starting material even at temperatures lower than the used reaction temperature of 150°C. Consequently, the prepared metal solutions in water, MeOH and DMF were clear solutions without residue. To investigate the dependency of the metal salt to the morphology of MIL-53(Al) a solvent has to be found, which dissolves H_2BDC at the reaction conditions, but not aluminium-nitrate. Dimethyl sulfoxide (DMSO) was identified as a possible candidate. While it has a high solubility for H_2BDC (20 g/100 g solvent [317]) solubility experiments have shown that the used amount of sample for a standard powder synthesis (2.246 g aluminium nitrate in 15 ml solvent) cannot be completely dissolved even at 150°C (Figure 3-41).

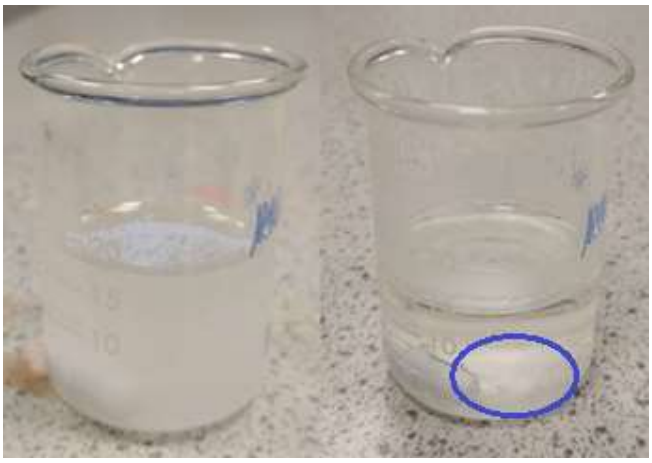


Figure 3-41: DMSO mixture with aluminium nitrate at reaction mixture at RT (left) and 150°C (right). At 150°C, a residue of aluminium nitrate is visible and has settled as white solid powder at the bottom of the beaker (highlighted by blue marking).

In order to investigate the solubility of aluminium nitrate in DMSO at reaction conditions, a simple solubility experiment was conducted. A saturated solution of aluminium nitrate was prepared and heated to 150°C. After 30 min, 10 ml clear DMSO solution was extracted with a pipette, while preventing the transfer of any solid aluminium nitrate residue. The DMSO was evaporated and the weight of the residue measured. With the density of DMSO at 150°C (δ = 0.974 g ml^{-1} [317]) the solubility can be calculated. This measurement was repeated three times.

Table 3-7: Results of solubility experiment for $Al(NO_3)_3 \cdot 9\ H_2O$ in DMSO

	Dissolved $Al(NO_3)_3 \cdot 9\ H_2O$ (g)
Experiment 1	0.1641
Experiment 2	0.1824
Experiment 3	0.1732

The resulting mean value of the dissolved aluminium nitrate is 0.1732 g in 9.7 g DMSO at 150°C, which leads to a solubility of ~1.7 g/100 g DMSO at 150°C. This quick experiment demonstrated, that the solubility of aluminium nitrate in DMSO is a magnitude lower than in the other used solvents water, MeOH or DMF.

A powder sample was prepared in DMSO according to the standard synthesis protocol (2.246 g aluminium nitrate and 0.895 g H_2BDC in 30 ml solvent) at 150°C reaction temperature and 5 h reaction time, followed by thermal activation (heating at 333°C for 3

days). The measurement of the XRD pattern (Figure 3-42) has shown that the pattern was not matching MIL-53(Al). Instead could the sample be identified as MIL-68(Al)(DMSO) after comparison with calculated XRD pattern from existing crystal data [318].

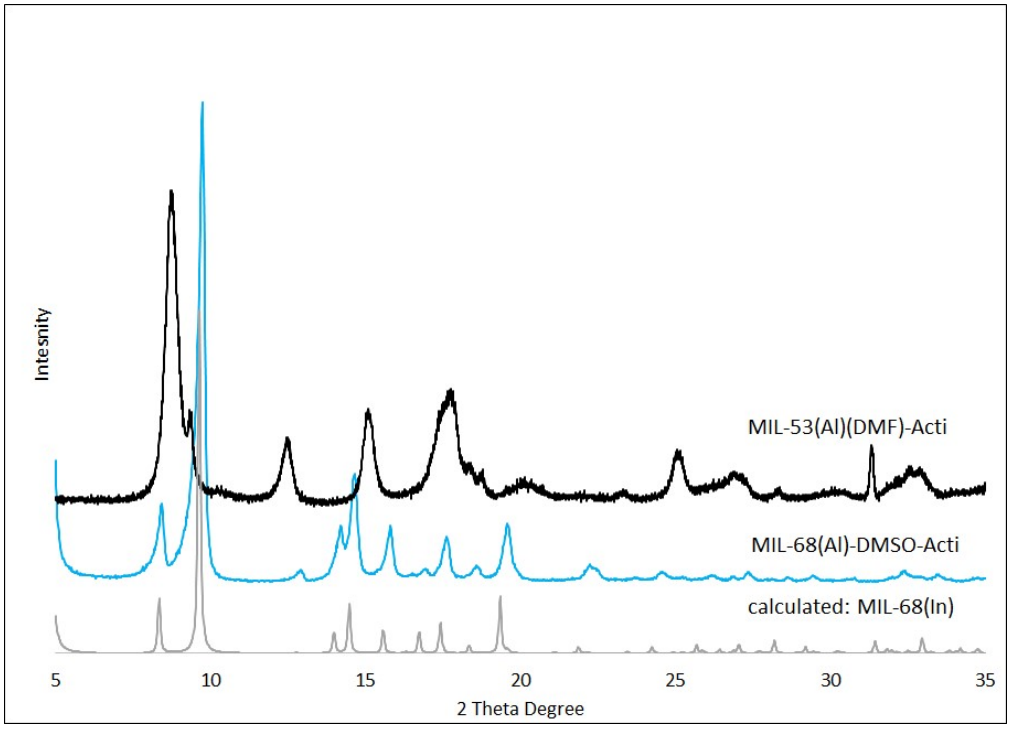


Figure 3-42: XRD pattern of sample prepared in DMSO (MIL-68(Al)(DMSO); blue) in comparison with pattern of MIL-53(Al)(DMF)-Acti (black) and calculated XRD pattern of MIL-68(In) from existing crystal data [318].

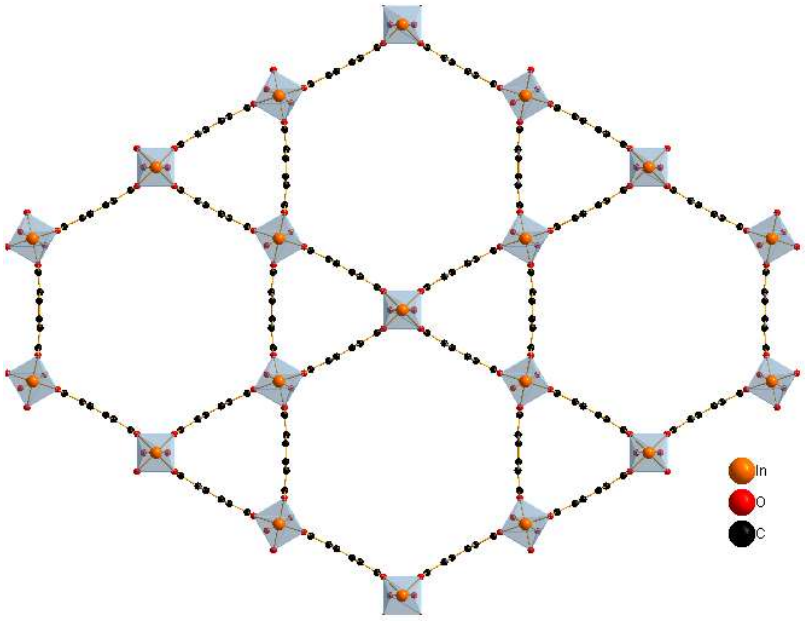


Figure 3-43: Crystal structure of MIL-68(In) calculated from existing crystal data [318].

MIL-68 is composed of a one-dimensional channel structure, but in contrast to MIL-53, two different shaped channels (triangular and octagonal) can be identified leading to a so-called Kagomé structure (Figure 3-43). The morphology of MIL-68(Al)(DMSO) has been further investigated by SEM (Figure 3-44). Rod-shaped particles are prepared with a length

ranging from 0.7 µm to 3 µm and a width of 401 ± 131 nm. As a side-note, was a shrinkage of the MIL-68(Al)(DMSO) particles observed (Figure 3-45). The particles might be heated up by the exposure to the electron beam of the SEM causing the shrinkage of the particles. MIL-68 is known for a negative thermal expansion effect [319].

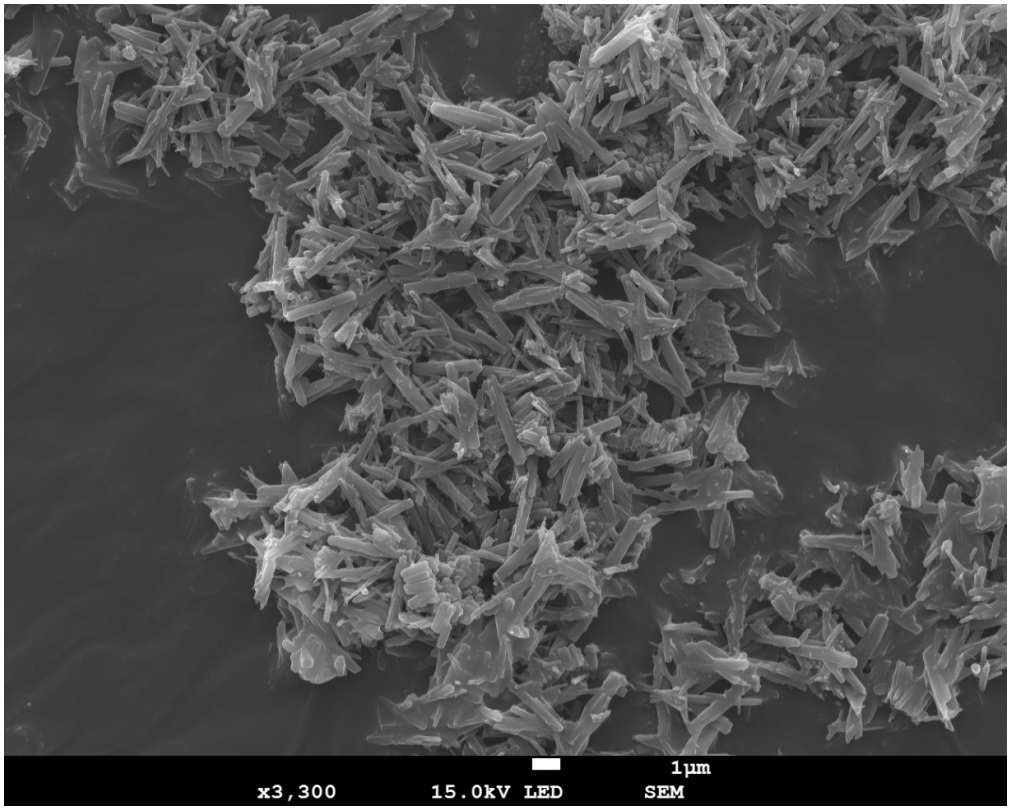


Figure 3-44: Morphology of MIL-68(Al)(DMSO). The particles are rod-shaped and have a size ranging from 0.7 µm to 3 µm.

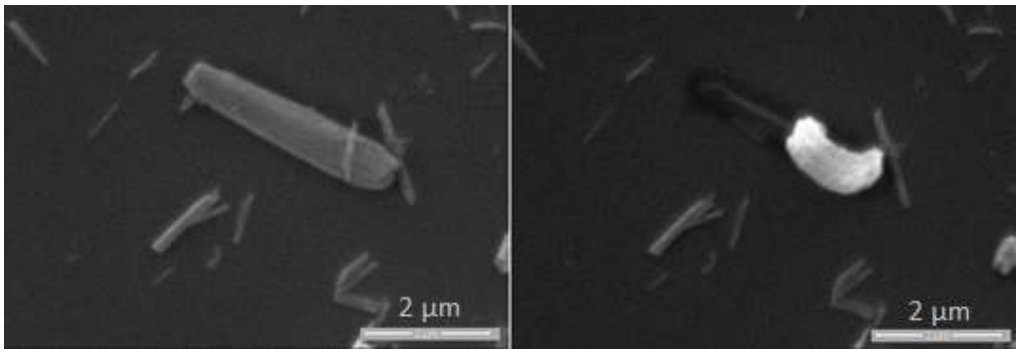


Figure 3-45: The exposure the rod-shaped MIL-68(Al)(DMSO) particles (left) to the electron beam has led to a shrinkage of the particles (right, after 1 min exposure).

Even though the sample prepared in DMSO was identified as MIL-68(Al), both sample are known to be convertible into each other by a state transformation [320]. It might be therefore possible to extent the results for the dependency between solubility of the starting materials and the particles size to the metal salt. Only if both starting materials (metal salt and the linker H_2BDC) were completely dissolved in the reaction mixture, nanometer-sized particles can be prepared. In solvents (DMF and MeOH), which were able

to completely dissolve both starting materials, the metal salt and H_2BDC, nanometer sized particles have been prepared (~100 nm), while in water and DMSO (incomplete dissolution of H_2BDC or the metal salt respectively) the prepared particles have a size of up to 3 µm. The results have been summarized in Table 3-8, whereas high solubility is referring to the complete dissolution of the corresponding starting material (>1 g/100 g solvent for H_2BDC and >5 g/100 g solvent for the used metal salt aluminium nitrate).

Table 3-8: Tendencies affecting the particle size of MIL-53(Al) in different solvents

Solvent	Solubility of metal	Solubility of linker	Particle size
Water	High	Low	µm-range
DMF	High	High	nm-range
MeOH	High	High	µm-range
DMSO#	*Low*	*High*	*nm-range*

#The sample in DMSO has been identified as MIL-68(Al), but MIL-53(Al) and MIL-68(Al) can be converted into each other by state transformation [320].

Additional data was collected by measurement of the porosity of the prepared MIL-68(Al)-DMSO. A N_2-isotherm was measured at 77 K with a sample, which has been activated by heating at 333°C for 3 days (Figure 3-46). The resulting BET-value was calculated as 1304 $m^2 g^{-1}$, which is a higher porosity than other MIL-68 samples known from literature (746 $m^2 g^{-1}$ for MIL-68(In) [318] and 1121 $m^2 g^{-1}$ for MIL-68(Al) [320]).

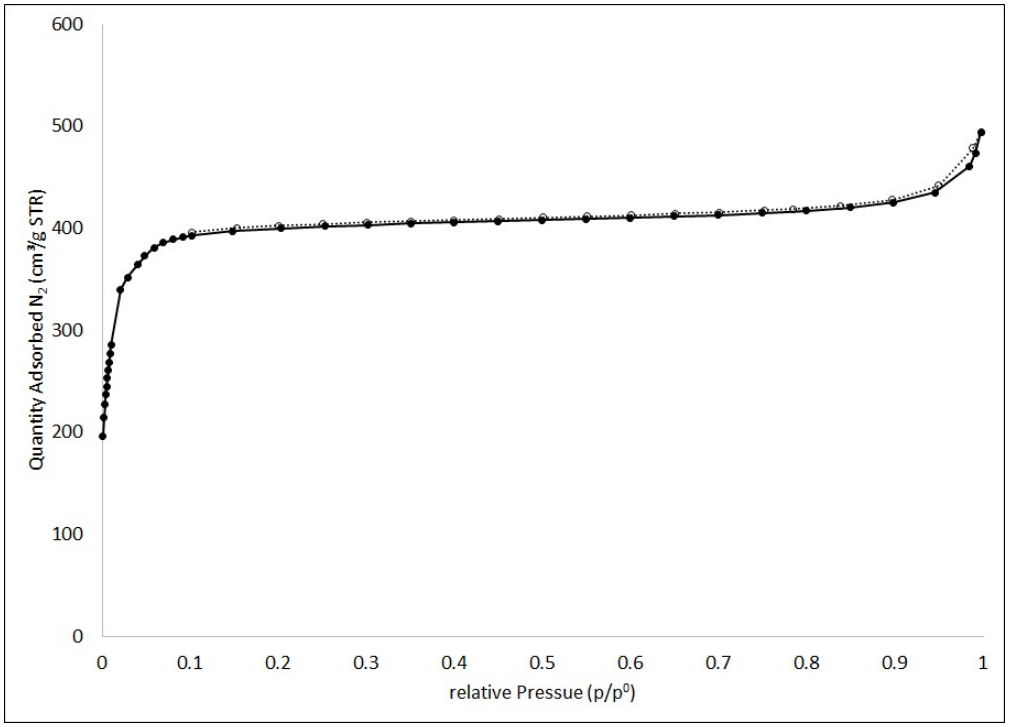


Figure 3-46: N_2-isotherm of MIL-68(Al)(DMSO)-Acti. Adsorption: solid line; Desorption: dashed line.

3.4 Conclusions and Future Work

This research has investigated the possibility to synthesize MIL-53(Al) by solvothermal synthesis in low-weight alcohols such as MeOH and EtOH and directly compared these

properties with samples of MIL-53(Al) prepared in the well-established solvents water and DMF. The investigation showed the successful synthesis of porous MIL-53(Al) in MeOH at lower temperature and time than the standard protocol established by Loiseau *et.al.* [115] (72 h; 220°C). All samples were prepared at 150°C and 5 h reaction time. A possible reason for the shorter needed reaction time and lower needed reaction time for the successful synthesis of MIL-53(Al) might be that the protocol used for the synthesis of MIL-53(Al) was the same protocol used than for the first prepared chromium derivate of MIL-53 [321]. Millange *et.al.* [322] have investigated the reaction rate of various MIL-53 derivates showed that MIL-53(Al) has a faster reaction rate than MIL-53(Cr). Consequently, the reaction time and reaction temperature could be successfully decreased for the synthesis of MIL-53(Al) in comparison with MIL-53(Cr). The results from chapter 3.3.3 (p. 53) have further implied that the used reaction time of 5 h and reaction temperature of 150°C are the lower limit of a successful synthesis of MIL-53(Al) in different solvents. The further reduction of the reaction time to 1 h or the reaction temperature to 100°C has led in H_2O and MeOH to samples with reduced crystallinity, more impurities (additional peaks in XRD pattern and lower intensity of the MIL-53(Al) peaks) and reduced yields (< 10 %). In contrast was the synthesis of MIL-53(Al) in DMF as solvent still possible at the reduced reaction temperature and shorter reaction time, but also with a reduced yield of < 20 %. A nearly complete conversion (~100% yield) of MIL-53(Al)(DMF) was possible at 5 h reaction time and 150°C reaction temperature. The results further imply that the synthesis of MIL-53(Al)(MeOH) might be not even possible at the established reaction conditions of 220°C and 3 days, which might explain why the successful synthesis of MIL-53(Al) prepared in MeOH was not reported until now.

In contrast to the samples prepared in water and DMF, MIL-53(Al)(MeOH) showed some unique traits. For instance, MIL-53(Al)(MeOH) does not show any breathing phenomenon, which is an archetypical effect of the MIL-53 class. The porosity of MIL-53(Al)(MeOH) is slightly lower then MIL-53(Al)(H_2O) or MIL-53(Al)(DMF), but is in contrast accessible with milder or even no time and energy consuming activation process. Furthermore, showed MIL-53(Al)(MeOH) a tendency of particle fusing at high humidity (> 80% relative humidity). However, in contrast to other moisture-sensitive MOFs, does this not lead to a collapse of the framework and the crystallinity can be restored after removal of the water. Such a fusing was not observed for any other MIL-53(Al) sample.

Different existing activation techniques have been investigated for MIL-53(Al) at the example of the sample prepared in water. The activation of MIL-53(Al)(H_2O) is of uttermost importance, because it has not shown any porosity without an activation process. In contrast has MIL-53(Al)(DMF)-AsSyn already shown 70% of the final porosity (in comparison with the activated sample), while for MIL-53(Al)(MeOH), as mentioned above, nearly no activation was required to access the porosity. The most common activation techniques were reflux in DMF for 1 day [134] or heating at elevated temperature for prolonged time (333°C for 3 days) [115] have shown similar results regarding BET porosity (1002 $m^2 g^{-1}$ and 986 $m^2 g^{-1}$ respectively) and the use of either techniques is more depended on personal preferences. The reflux in DMF has a shorter activation time (1 day in comparison with 3 days) but it needs additional processing steps (*e.g.* the removal of

the DMF from the pores). While both activation techniques were successful for powder samples, the conditions might be too harsh *e.g.* for thin-films or membranes made from MIL-53(Al) on different supports. Fan e*t.al.* [164] have introduced for such type of samples an activation technique in vacuum at 150°C, but the vacuum activation has not proven successful during this research at least for powder samples. The calculation of the BET-area has only led to a value of 11 $m^2 g^{-1}$. The newly introduced activation by solvent exchange in MeOH (1 day at RT, followed by removal of MeOH at 100°C for 1 day) was less successful (S_{BET}: 742 $m^2 g^{-1}$) than heating at elevated temperature or reflux in DMF, but might be a possible alternative for sensitive samples such as the above-mentioned thin-films on supports.

Furthermore, it has still to be investigated, why the usage of EtOH as solvent has led to a product with reduced thermal stability and crystallinity despite similar chemical properties to MeOH. MIL-53(Al)(EtOH) was activated by heating at elevated temperature for prolonged times comparable to samples prepared in water, DMF and MeOH. It might be still possible to prepare a more crystalline product of MIL-53(Al)(EtOH) when alternative activation techniques such as refluxing in DMF or solvent exchange in MeOH are being applied. Further was until now only the synthesis in the low-weight alcohols MeOH and EtOH investigated. A possible future research might investigate the synthesis of MIL-53(Al) in longer alcohols (*e.g. n*-butanol) or branched alcohols (*e.g.* iso-propanol). The length of the alkyl chain of the alcohol might have an impact on the crystallinity of MIL-53(Al). Furthermore, the solubility of the starting materials in the reaction solvent has been identified as an important factor controlling the particles size of the prepared MIL-53(Al). According to the theory, should the usage of MeOH lead to particles which are even larger than in water, because MeOH is even slightly more acidic than water, which slows down the deprotonation of H_2BDC. However, have both, DMF and MeOH, showed a solubility of H_2BDC at the reaction temperature which is several magnitudes higher in comparison with water. This leads to faster nucleation and crystal growth. As a result, nanometer-sized particles have been prepared in both DMF and MeOH in contrast to the micrometer-sized particles prepared in water. The investigation of the solubility has been further extended to the usage of DMSO, which is able to completely dissolve H_2BDC, while the solubility of aluminium nitrate is reduced. As a matter of fact, larger micrometer sized particles have been prepared in DMSO, but further investigation has shown that MIL-68(Al) has been prepared instead of MIL-53(Al). Both MOFs are known to be interconvertible, but further research might be necessary to identify the reason why the synthesis in DMSO led to the formation of MIL-68(Al), while in the other investigated solvents (H_2O, MeOH, EtOH and DMF) MIL-53(Al) has been prepared in otherwise identical reaction conditions such as concentration, reaction time or reaction temperature.

4 Thin-Film synthesis of MIL-53(Al) on glass

4.1 Introduction

The use of MOFs as powder samples is often limited to specific applications. In contrast might the use of MOFs as thin-films on different supports further extent the application spectrum of MOFs. For more information about MOF thin-films and possible thin-film coating techniques the reader might referred to chapter 2.5 (p. 23).

This chapter will therefore act as a preliminary study for the possible application of MIL-53(Al) as a coating on LPGs for highly selective and sensitive in-situ sensors (see chapter 2.3.3, p. 13). LPGs are modified glass fibres, which is accompanied by specific problems. Glass is used in applications ranging from windows to labware or the above-mentioned optical glass fibre. While an inert surface is desired for some applications due to its ease of cleaning, the chemical and physical stability [323] (*e.g.* as protective layers on solar cells [324]) or to preventing biofouling [325], coating of glass surfaces is difficult. For thin-film application, a strong interaction between the MOF and the surface is needed [148]. Often thin films are applied on supports *e.g.* Al_2O_3 [164] or fibre mats [326]. These porous supports are used after coating with a MOF in applications such as catalysis [327] or in gas separation [164]. The rough surface and the chemical nature of the above-mentioned porous supports helps to create a MOF thin film. The MOF particles can better interact with the surface or are attached in pores of the support [164]. Consequently are reports of thin-film coating on flat surfaces like glass, silicon or stainless steel [328] more sparse.

Especially the coating of glass surfaces is often done by annealing at high temperature (up to 550°C [324]), or by modifying the glass surface with a self-assembled monolayer (SAM). Such a SAM can help to fine-tune the chemical properties of the surface, to increase the interaction between thin-film and surface and even enable the control the growth direction of MOFs and zeolites on the surface [176],[329]. In most cases, the use of an additional layer on the surface such as a SAM does not interfere with the application. Examples might be quartz crystal microbalance (QCM) or atomic force microscopy (AFM). In these applications, a thin-film on top of the device selective adsorbs analyte, leading to a weight increase and a change of vibration frequency [327],[330]. However, in optical fibre applications such as the above-mentioned LPG [94] the interaction between the support and the coating is also important. The coating with a SAM adds an additional non-sensitive layer between the support and the sensitive thin film (*e.g.* MOF or zeolite). In an LPG, the light has only a short range outside of the fibre (about 10% of the used wavelength [102]). With a SAM, the evanescent wave in an LPG might not reach the sensitive coating. Another problem is the anchoring of the SAM to the support surface. SAMs are typically composed of linear long-chain alcohols or carboxylic acids, which contains a thiol as an anchor group. Sulphur is able to form a strong bond to gold. Therefore, supports are often coated with a gold layer. However, reports show that coating an optical fibre with a metal film can remove the sensitivity to change of refractive index (RI), which is the

measurement principle for LPGs [331],[332]. Another possible disadvantage is the often low temperature stability (<100°C) of SAMs [333]. The resulting low temperature during the thin-film synthesis and consequently a slow film growth may lead to the formation of well-ordered films, but with reaction times of several days [334]. Annealing of films after coating can increase the attachment to the surface, whilst this has the risk of crack formation in the coating [335]. Higher temperatures are also for optical fibre sensors problematic: while glass is highly temperature stable (between 500°C and 1500°C depending of the composition of the glass [336],[337]), the protective coating of glass fibres (often composed of acrylate polymer, which is important for the mechanical stability of the optical fibre), has a much lower thermal stability. While the protective coating is stable at 150°C for over 50 h, it decomposes at 200°C in less than 1 h making the fibre brittle [338].

A MOF thin-film coating technique for fibre optical application, should therefore fulfil the following conditions:

- No use of SAM or additional coatings
- Temperature should not exceed 150°C to prevent decomposition of the protective coating.
- Reaction time should be less than a day.

Furthermore, the desired thin-film should be ideally homogenous (without cracks and gaps in the coating), smooth (small height difference of the coating) and have a thickness of less than 1 µm.

Although reports have shown fibre optical sensor with coatings to improve sensitivity and selectivity as diverse as graphene oxide [339], modified polyethylene glycol [340], or even biological coatings such as antigens [97], the number of studies with MOF coatings is far more sparse [21],[22]. Amongst the many MOF candidates, the MIL-53-class combine several advantages as possible coatings on LPGs. One advantage is the synthetic flexibility, whereas different linker or metal salts can be used as starting material while preserving the overall structure (see chapter 3.1, p. 38). A successful thin-film coating of pristine MIL-53, can therefore act as a template. Changing the functional group of the linker or changing the metal source might be applied to increase the selectivity for specific target compounds (*e.g.* has the amino derivate of MIL-53(Al) improved selectivity towards CO_2 in comparison with the pristine MIL-53(Al) [217]), while retaining the applied synthesis protocol. Similar to chapter 3 (p. 38), the pristine MIL-53(Al) will be used due to lower toxicity in comparison with the other derivatives and the commercial material (as Basolite A100®). For this chapter, glass slides made from soda-lime glass are used as test-system for thin-film coating on glass. Optical fibre sensors (*e.g.* LPGs) are mostly made from doped silica, but the chemical properties of different glass types are similar [337] and the usage of soda-lime glass enables a more cost-efficient scanning of possible coating techniques. Furthermore, have glass slides, in comparison with glass fiber, a larger surface area, which makes the usage of characterisation techniques (*e.g.* XRD) easier.

4.2 Experimental

4.2.1 Materials

Aluminium nitrate nonahydrate, $Al(NO_3)_3 \cdot 9H_2O$, and 1,4-benzenedicarboxylic acid (>98%) (terephthalic acid, H_2BDC) were purchased from Sigma Aldrich. DMF, MeOH, THF, acetone, 35% aqueous H_2O_2 solution and conc. H_2SO_4 were provided by Fisher-Scientific. All chemicals were used without further purification. Deionised water (DI-water) was collected from a Millipore Direct-Q 5 UV water purification system. For every instance water is mentioned during this research, DI-water was used.

4.2.2 MIL-53(Al) powder synthesis

MIL-53(Al) was prepared according to an already existing synthesis protocol [164] and slightly modified. Briefly, $Al(NO_3)_3 \cdot 9H_2O$ (5.99 mmol; 2.246 g) was dissolved in 15 ml solvent (water or DMF) and added to H_2BDC (5.38 mmol; 0.895 g) in 15ml solvent (water or DMF). After stirring vigorously at room temperature for 15 min, the reaction mixture was transferred to a 45 ml Teflon lined stainless steel autoclave (Paar Instruments 4744 General Purpose Acid Digestion Vessel) and heated to 150°C for 5 h. The reaction mixture was cooled down naturally to RT and the product separated by centrifugation. The solution was decanted, and the precipitate washed with DMF (2 x 50 ml) and acetone (1 x 50 ml). The product, a white powder, was dried at 150°C for 17 h. Unreacted starting material und residue solvent was removed by heating the as-synthesized product at 333°C for 3 days to create an activated sample.

4.2.3 Treatment of glass slides

The glass slides (soda-lime-glass microscope slides, Fischer Scientific Menzel Glaser) were cut into pieces of 1 x 1 cm and cleaned with piranha acid [144] (7:3 mixture of conc. H_2SO_4 and 35% aqueous H_2O_2 solution) for 30 min. Alternatively, the glass slides were immersed in acetone [97] and cleaned by ultrasonication for 30 min. The glass slides were washed with water and dried in N_2-flow. The glass slides were either directly used or placed for 1 h in a 1 M NaOH solution, washed with water and dried in N_2-flow.

4.2.4 In-situ coating

A cleaned glass slide was mounted vertically in a Teflon lined stainless steel autoclave and filled with 30 ml of a typical reaction mixture (2.246 g $Al(NO_3)_3 \cdot 9H_2O$ and 0.895 g H_2BDC in 30 ml solvent) used for MIL-53(Al) powder synthesis (see chapter 4.2.2, p.84) and the reaction conducted at 150°C with reaction time of 5 h. The reaction vessel was cooled down naturally (storing at RT for 5 h. The coated glass slide was picked up from the reaction vessel and cleaned with MeOH to remove loose particles from the surface. The washed glass slide was dried at 150°C for 2 h.

4.2.5 Dip-coating / seeding with MIL-53(Al)

To create suspension for dip-coating, MIL-53(Al)(H_2O)-Acti or MIL-53(Al)(DMF)-Acti are grounded for 10 min with mortar and pestle. To prepare a 0.5 wt% suspension 0.05 g MIL-53(Al) and 9.95 g solvent (water or MeOH) are placed in a beaker. The resulting suspension was placed for 10 min in an ultrasonic bath and then vigorously stirred for

10 min. To prepare other suspensions (0.1 wt% and 1.0 wt%), the ratio between MIL-53(Al) powder and solvent was varied accordingly (Table 4-1).

Table 4-1: Summary of used dip-coating suspensions.

Suspension	MIL-53(Al) (g)	Solvent (g)
0.1 wt%	0.01	9.99
0.5 wt%	0.05	9.95
1.0 wt%	0.10	9.90

For the coating process, the glass slides were placed in the suspension and after 1 min vertically extracted from the suspension. The glass slides were placed on a petri dish and the solvent evaporated for 2 h at 150°C. To add additional treatment steps, the procedure was repeated as required.

4.2.6 Secondary Growth

For the secondary growth, a glass slide coated with 1 layer of a 0.5 wt% suspension of MIL-53(Al) in MeOH was mounted vertically in a Teflon lines stainless steel vessel, filled with 30 ml of a reaction mixture used for MIL-53(Al) powder (2.246 g $Al(NO_3)_3 \cdot 9H_2O$ and 0.895 g H_2BDC in 30 ml solvent) and the reaction conducted at 150°C with a reaction time of 5 h. The reaction vessel was cooled down naturally (storing at RT for 5 h and the glass slides removed from the vessel. Loose powder was removed by washing the glass slide with MeOH from a wash bottle and dried for 2 h at 150°C.

4.2.7 Layer-by-Layer approach (LbL)

In a typical experiment, a cleaned glass slide was alternatingly placed in linker solution (0.490 g; 2.95 mmol H_2BDC in 15ml DMF) and metal solution (1.123g; 2.95mmol $Al(NO_3)_3 \cdot 9H_2O$ in 15ml DMF) for 30 min at RT. Between immersion in metal and linker solution, the glass slide was placed for 5 min in fresh DMF to remove unreacted starting material. After the glass slide was coated with the desired number of layers, the glass slide was dried in oven at 150°C for 2 h.

4.2.8 Rapid-Thermal Deposition (RTD)

In a typical synthesis, a cleaned glass slide was dip-coated in MIL-53(Al) reaction mixture containing $Al(NO_3)_3 \cdot 9H_2O$ (5.99 mmol; 2.246 g) and H_2BDC (5.38 mmol; 0.895g) in 30 mL DMF leading to a nearly equimolar composition of the reaction mixture (called NEq subsequently). Reaction mixtures with excess of metal (Mex) and excess of linker (Lex) were also investigated (Table 4-2).

Table 4-2: Summary of used conditions for the RTD approach (all reaction mixtures have been prepared in 30 ml DMF)

Name	Metal/linker ratio	$Al(NO_3)_3 \cdot 9H_2O$ (g)	H_2BDC (g)
NEq	1.1 / 1	2.246	0.895
Mex	2 / 1	2.246	0.498
Lex	1 / 2	1.011	0.895

The mixture was stirred for 15 min at RT, the glass slide immersed for 1 min in the reaction mixture and vertically extracted. To remove excess reaction mixture, the glass slide was

held vertical and slightly shaken, remaining a film of reaction solution on the surface. The coated glass slide was placed horizontal in oven at different temperature (100°C, 125°C and 150°C) and varying reaction time (1 h, 2 h and 5 h).

4.2.9 Solvent-assisted epitaxy (SAE)

Glass slides were coated with MIL-53(Al) reaction mixture in DMF (see RTD) and placed on a grid in a crystallisation dish. A porcelain evaporation dish, which act as stand for the mesh and reservoir, was filled with 10 ml DMF and the vessel closed with a petri dish (Figure 4-57 for image of the experimental set-up). In a typical experiment, the enclosed vessel was placed in oven at 150°C. After 5 h reaction time, the vessel was removed from the oven and the vessel opened to let excess solvent evaporate from the glass surface for 10 h at RT.

4.2.10 Characterisation

Scanning Electron Microscopy (SEM) was used to characterise the morphology and crystal size (from an average of 25 particles). Measurements were conducted, regarding the availability, with a JEOL JSM-7100F Field Emission Gun (FEG) instrument, a JEOL 6490LV or Philips XL30 FEG ESEM. Measurements were conducted with a beam voltage of 15 kV. For top-view images, samples were attached horizontal on a SEM sample holder with carbon tape. For cross-section images, the glass slides were cut in half and mounted vertically by a Buehler SamplKlip© on a SEM sample holder with carbon tape. All samples were sputtered with a 10 nm iridium film by a Quorm Q150T ES coater in order to increase conductivity of the samples.

X-Ray diffraction (XRD) were measured using a Bruker D8 advance diffractometer operated at 40 kV and 35 mA and Cu Kα radiation (wavelength: 1.540598 Å) with 0.6 mm exit slit, diffracted beam 0.12° soller-slit collimator and scintillation counter X-ray detector. The measurement of coated glass slides was done in a step-by-step fashion, with a step size of 0.02° and a measurement time of 30 s per step over a range of 5°-35° 2θ, leading to a measurement time of ~15 h.

4.3 In-situ coating

For the in-situ coating, glass supports were immersed in MIL-53(Al) reaction mixture (similar to the powder synthesis at 150°C and 5 h reaction time) with no further modification of the supports (Figure 4-1). As solvent have been water and DMF investigated.

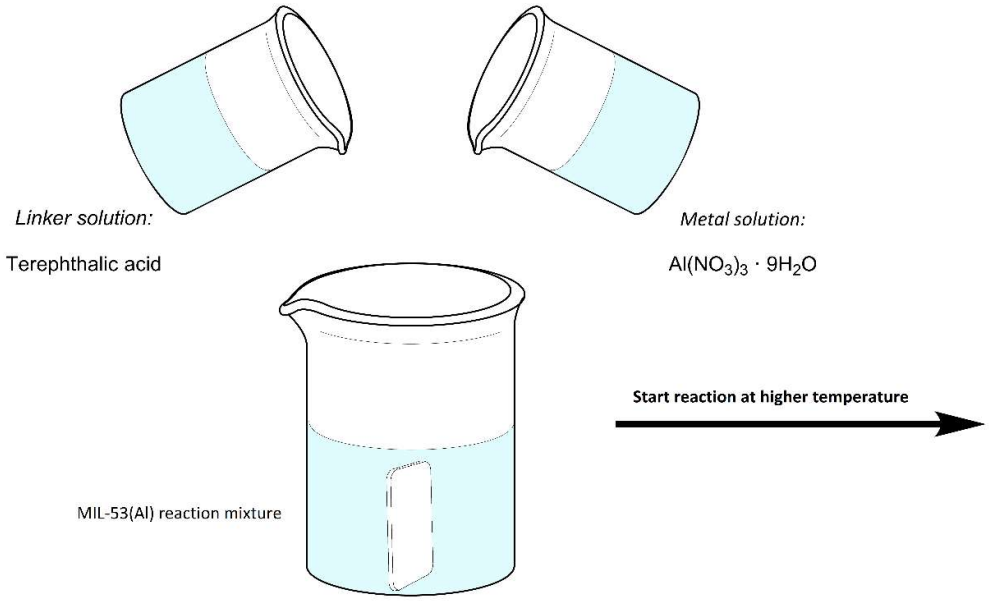


Figure 4-1: Schematic set-up of in-situ coating of glass slides with MIL-53(Al).

In contrast to other MOFs *e.g.* ZIF-8 [141], coating of MIL-53(Al) cannot be done at RT in solvothermal conditions due to the slow reaction rate of MIL-53 at RT (see chapter 3.3.3, p. 53). Due to the varying morphology of MIL-53(Al), depending on the solvent used, in-situ coating was fabricated using water and DMF as solvents. The results from the powder synthesis (see chapter 3.3.1, p. 42) have identified varying morphologies depending on the used solvent for the reaction. In water, the resulting MIL-53(Al) particles have a star-shape of about ~3 µm size, whereas in DMF particles have a spherical shape of ~100 nm. To ensure that the particles have grown on the surface and are not powder precipitate the samples were mounted vertical (with a Buehler SamplKlip©) during the reaction. The surface coverage was investigated using SEM. According to Figure 4-2, the interaction between glass slide and MIL-53(Al)(H_2O) seems to be weak. The glass slide is mostly empty and only individual particles are visible on the surface.

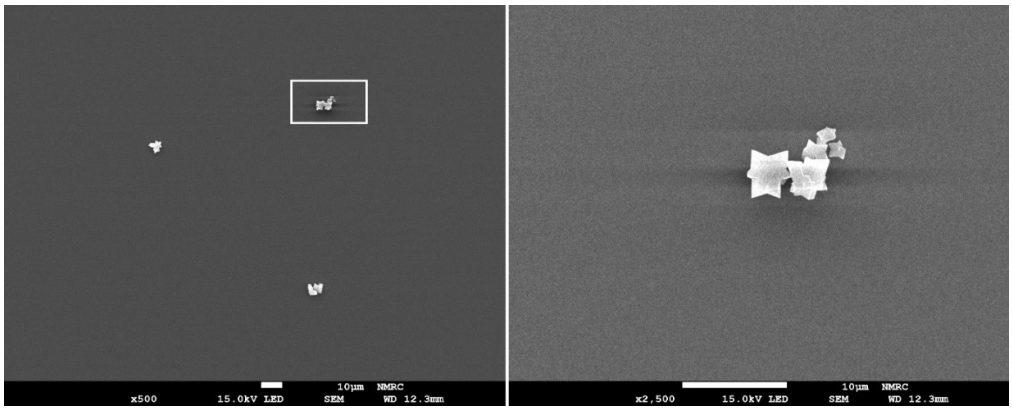


Figure 4-2: SEM images of glass slide coated with MIL-53(Al)(H_2O) in-situ. The glass slide remains mostly empty. One of the particles (white rectangle) was observed at higher magnification. It has the typical star-shape of MIL-53(Al)(H_2O).

In contrast to MIL-53(Al)(H_2O), a glass slide was successfully coated with MIL-53(Al)(DMF). SEM images show that the surface is mostly covered. (Figure 4-3, right). However, at lower magnification darker strains on the surface are visible (Figure 4-3, left), which are areas of lower surface coverage. A cross-section image of the glass slide shows the film-thickness of about 1.9 µm. (Figure 4-4). XRD was used to confirm the successful coating of the surface with MIL-53(Al). The XRD pattern of this sample (Figure 4-5) shows peaks ~8.9° and 15.1°, which matches the peaks of a MIL-53(Al)(DMF) powder sample. The broad peak between ~20° and ~35° is caused by the amorphous glass support.

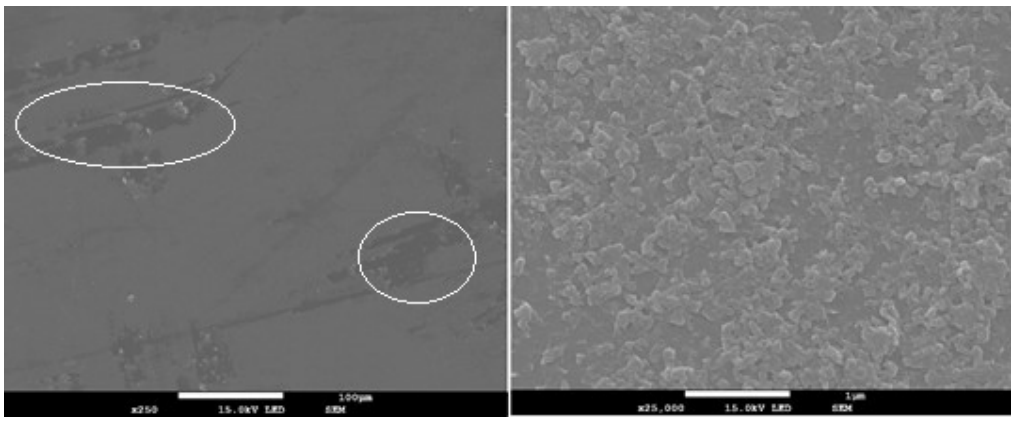


Figure 4-3: SEM image glass slide coated in-situ with MIL-53(Al)(DMF) with 5 h reaction time at 150°C in lower (left) and higher magnification (right). Black strains (highlighted by white markings) on the surface imply areas with reduced coverage.

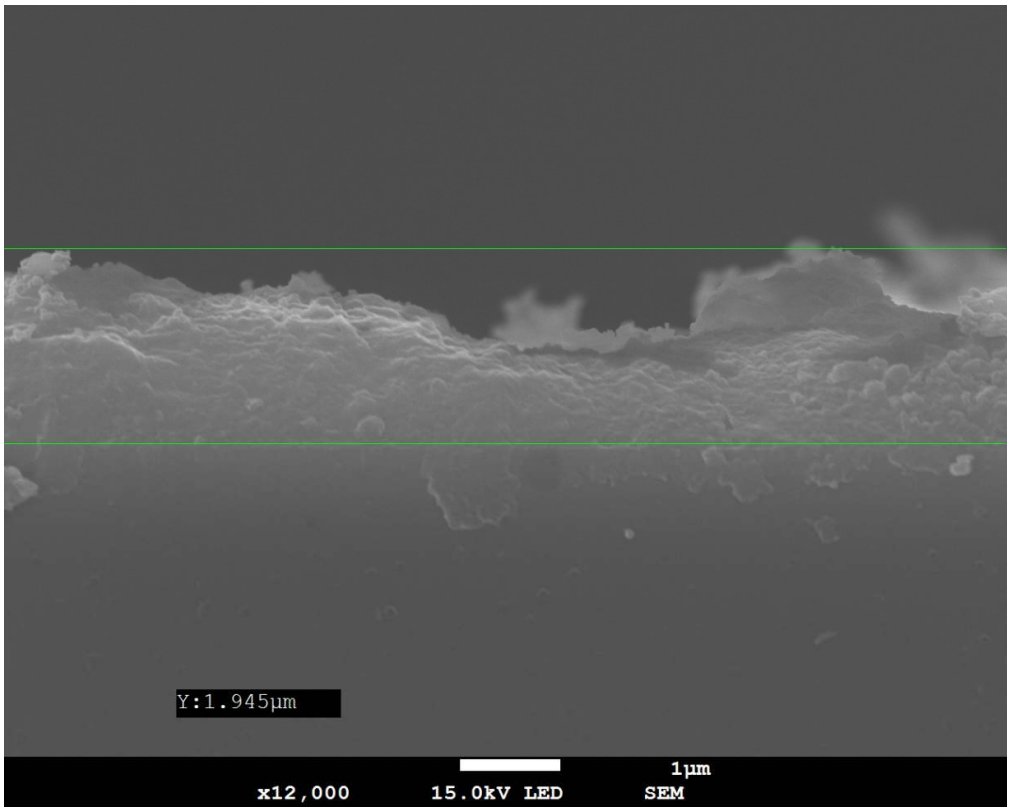


Figure 4-4: Cross-section of in-situ coated glass slide with MIL-53(Al)(DMF). The green lines are projected by the SEM operation software to calculate the film thickness. The highest point of the film was chosen to measure the film thickness.

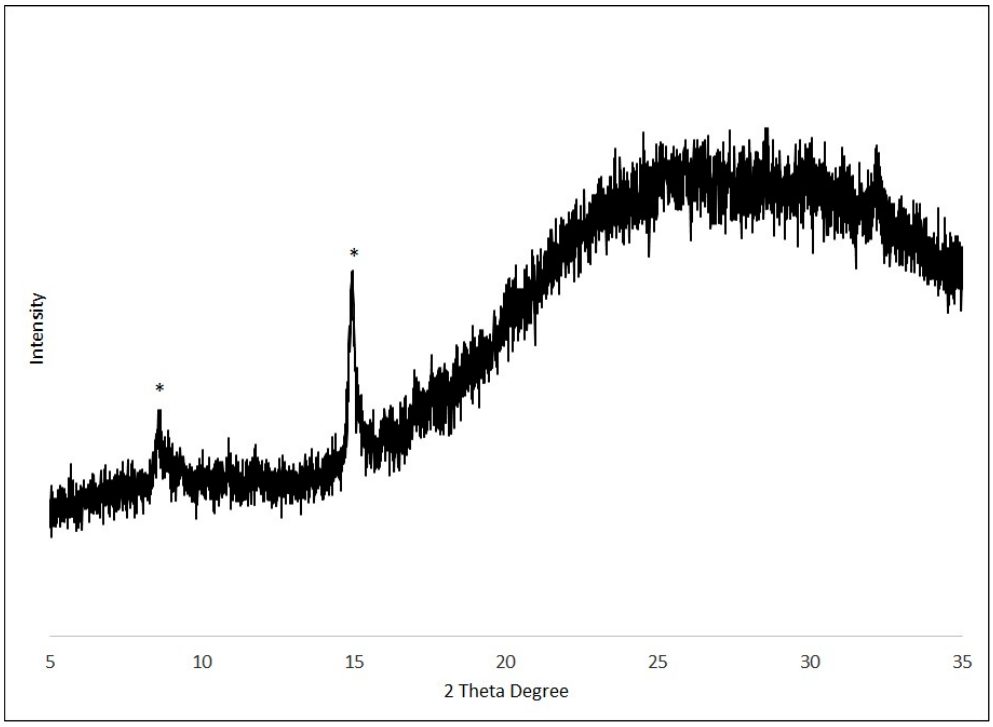


Figure 4-5: XRD pattern of glass slide covered in-situ with MIL-53(Al)(DMF) at 5h at 150°C. The visible peaks at 8.9° and 15.1° can be attributed to MIL-53(Al)(DMF) (highlighted by asterisks).

4.4 Conditions during dip-coating approach

In literature, various ways to conduct dip-coating have been tested, while the most common ways are a powder synthesis of MOFs followed by a redispersion in solvent [341] or the direct coating from a colloidal suspension without interim separation of the particles [342]. A coating can be created on a support by dip-coating and the attached particles can act as seeds for further growing of a thin-film by seeding and secondary growth [343]. The so-called seeding and secondary growth approach help to better control the surface thickness, morphology and orientation in comparison with a direct in-situ growth on the surface [161].

The process of dip-coating to create a thin-film of NH_2-MIL-53(Al) was already successfully applied by Fan *et.al.* [164]. They have used the dip-coating as seeds for a subsequent secondary growth on porous α-Al_2O_3 membranes for gas separation. The support α-Al_2O_3 has the advantage that MIL-53(Al) particles can interact with hydroxyl groups of the support [165]. In addition, the MIL-53(Al) particles can be "trapped" in the small pores of the support and facilitate the further growth of a thin-film on top [164]. In contrast, are glass surfaces dominated by more inert Si-O-Si bonds [344], which makes the interaction between MIL-53(Al) and the glass surface complicated.

For the seeding, Fan *et.al.* [164] has investigated seeding suspensions with concentrations ranging from 0.1 wt% to 1.0 wt%. The 0.1 wt% seeded membranes of Fan et.al. have a slightly lower permeability (attributed to a thinner coating), while 0.5 wt% and 1.0 wt% seeded membranes has a slightly higher H_2/CO_2 selectivity.

However, in contrast to α-Al_2O_3 membranes, glass has a flat and nearly inert surface and the results for α-Al_2O_3 supports cannot be directly transferred to glass supports. Therefore, a scanning of the different concentrations was applied for the glass slides to optimise the conditions. While Fan *et.al.* [164] have only used the water derivate of MIL-53(Al), the results of in-situ coating in chapter 4.3 (p. 86) showed that MIL-53(Al)(DMF) has a possible stronger interaction with the glass slides, leading to a higher surface coverage. Furthermore only water was used as solvent for the suspension by Fan *et.al. [164]*, but for instance MeOH [345] or acetone [346] are possible alternatives for solvents in dip-coating suspension due to their higher vapour pressure, lower surface tension and viscosity. This might lead to faster evaporation of the solvent and better coverage of the surface in comparison with water. Another possible problem is that glass is hydrophobic and water droplets might be formed on the surface [347], which further reduce the surface coverage when water is used as solvent for coatings. To investigate the relationship between particle morphology, solvent and concentration for the coverage and quality of the coatings both MIL-53(Al)(H_2O) and MIL-53(Al)(DMF) were used in combination of water

and MeOH as solvent at concentrations of 0.1 wt%, 0.5 wt% and 1.0 wt% (Table 4-3). The schematic set-up of the dip-coating can be further seen in Figure 4-6.

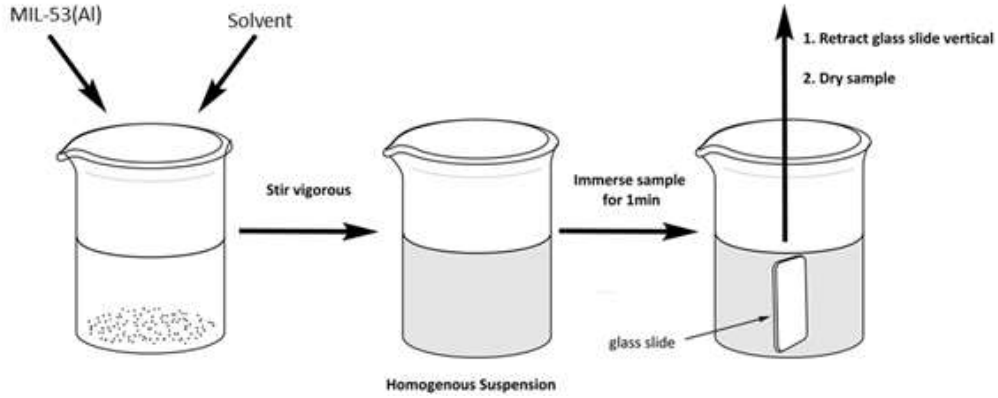


Figure 4-6: Schematic set-up of dip-coating. The concentration of the dip-coating suspension was controlled by varying the weight ratio between MIL-53(Al) (water or DMF derivate) and the solvent (water or MeOH).

Table 4-3: Summary of the tested conditions for the dip-coating.

MIL-53 derivate	Weight % of suspension	Solvent
MIL-53(Al)(H_2O)	0.1	Water
	0.5	
	1.0	
MIL-53(Al)(H_2O)	0.1	MeOH
	0.5	
	1.0	
MIL-53(Al)(DMF)	0.1	water
	0.5	
	1.0	
MIL-53(Al)(DMF)	0.1	MeOH
	0.5	
	1.0	

DMF was not used as solvent. The lower vapour pressure (in comparison with water and MeOH) and the known strong interaction with MIL-53(Al) [315] might make the removal of the solvent after the coating more complicated.

4.4.1 MIL-53(Al)(H_2O) in water

The result of the coating from the coating suspension with the lowest tested concentration of 0.1 wt% is shown in Figure 4-7. The coverage of the surface with particles is not homogenous and areas with various agglomerated particles can be observed. The surface is mostly empty in between agglomerated clusters of particles.

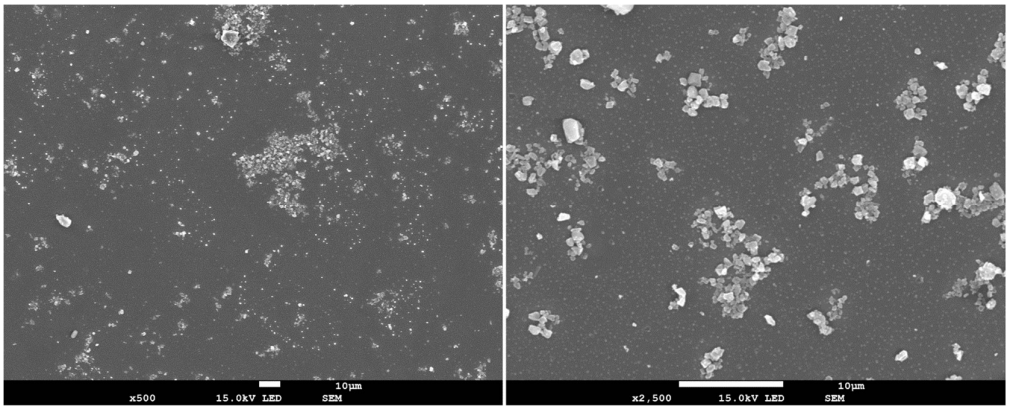


Figure 4-7: SEM image of a glass slide coated with a 0.1 wt% coating suspension of MIL-53(Al)(H_2O) in water.

With a 0.5 wt% coating suspension (Figure 4-8), the surface coverage is higher than for the 0.1 wt% sample, but gaps between the particles are visible. The XRD patterns (Figure 4-9) of the glass slides verify the better coverage of the glass slide coated from a 0.5 wt% suspension with characteristic peaks obtained at 9.5°, 12.5° and 17.0°, which are in good correlation with the small pore form of MIL-53(Al)(H_2O). On a glass slide coated using a 0.1 wt% suspension, no peaks corresponding to MIL-53(Al) could be observed. This is in good correlation with the results from the SEM images, which imply a reduced surface coverage of the 0.1 wt% in comparison with the 0.5 wt% sample.

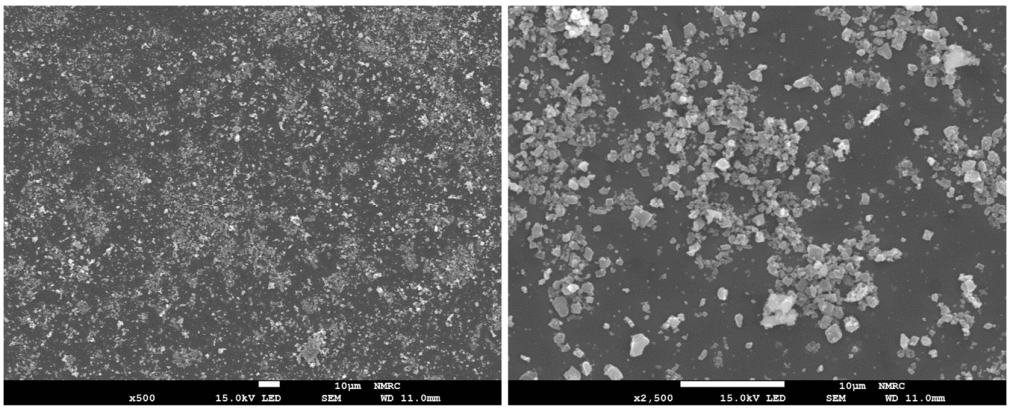


Figure 4-8: SEM image of a glass slide coated with a 0.5 wt% coating suspension of MIL-53(Al)(H_2O) in water.

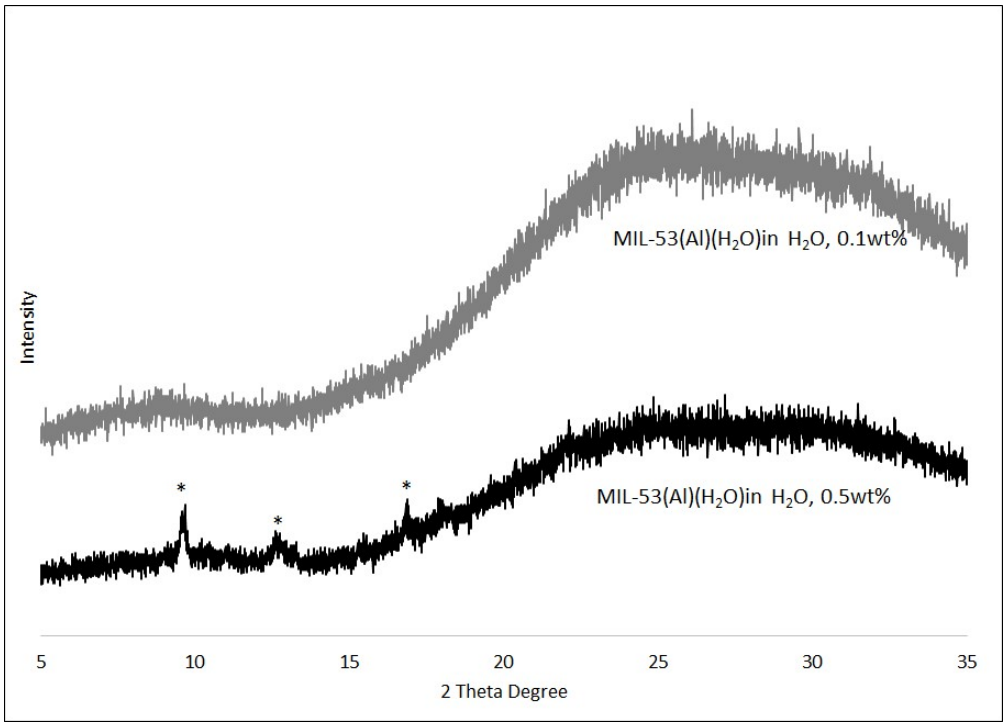


Figure 4-9: XRD patterns of glass slide covered with MIL-53(Al)(H_2O) with water as solvent. While for a glass covered with 0.1 wt% suspension (grey) no peaks are visible, on a glass slide covered from a 0.5 wt% suspension peaks at 9.5°, 12.5° and 16.01° can be identified (highlighted with asterisks).

In contrast, the surface of the sample covered with a 1.0 wt% suspension was covered with large cluster of MIL-53(Al)(H_2O) particles, while empty areas were also visible. The higher concentration of the coating suspension may lead to the agglomeration of the particles. In the SEM image of the surface (Figure 4-10) the clusters appear brighter, even though the glass samples were coated similar to the 0.1 wt% sample and 0.5 wt% sample with a 10 nm iridium film to improve the conductivity. This may be a result of SEM beam charging up the agglomerated particles and due to an inadequate connection with the surface. The charge of the electronic beam cannot be dispersed [348]. A possible reason is that this is caused by weak interaction of the large clusters with the glass surface. However, further tests to investigate the interaction between glass surface and MIL-53(Al)(H_2O) have to be conducted.

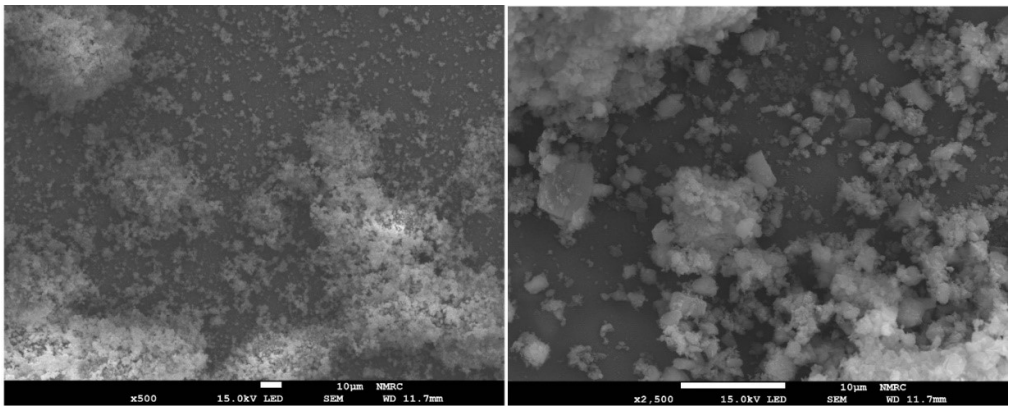


Figure 4-10: SEM images of a glass slide coated with a 1.0 wt% of MIL-53(Al)(H_2O) suspension in water.

The influence of surface cleaning/modification for the surface coverage was also investigated at this point. Before coating, glass surfaces are often cleaned by using of piranha acid [141]. Although some groups used piranha acid often solely for removing of organic residues [144], piranha acid might be also strong enough to etch glass and break Si-O bond on the surface, adding silanol groups [349] to make the surface more hydrophilic and thus increase the interaction between glass and coating [350]. Another method to increase the hydrophilicity of the glass surface may be cleaning in organic solvents such as acetone or isopropanol followed by immersion in a base (*e.g.* NaOH [97]). Both methods were tested for the coating of a glass slide in a 0.5 wt% suspension of MIL-53(Al)(H_2O) in water. After cleaning with piranha acid (Figure 4-11) or acetone + NaOH (Figure 4-12), no difference regarding surface coverage and particle distribution was observed. Even slides which were only cleaned in acetone have shown a similar surface coverage (Figure 4-8). Using highly corrosive piranha acid and time-consuming additional steps seems to not improve the surface coverage. Therefore, in the following experiments, the glass slides were only washed with acetone.

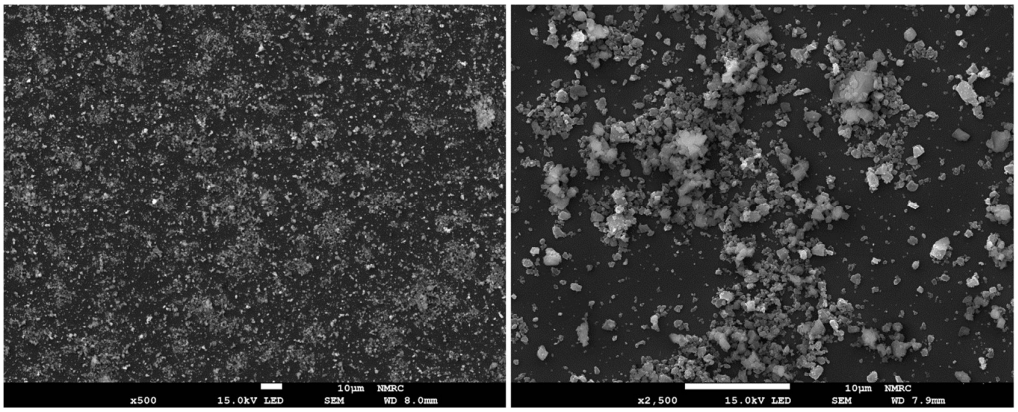


Figure 4-11: SEM image of a glass slide, coated with a 0.5 wt% suspension of MIL-53(Al)(H_2O) in water, which was cleaned before in piranha acid.

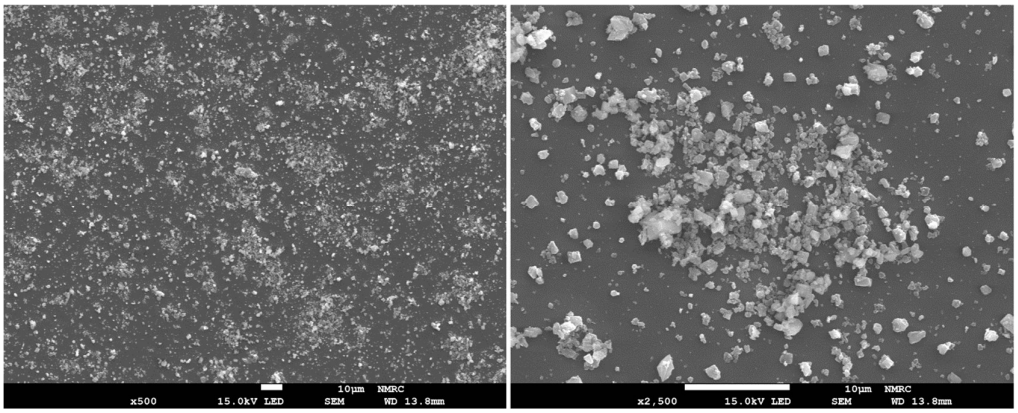


Figure 4-12: SEM image of a glass slide coated with a 0.5 wt% suspension, of MIL-53(Al)(H_2O) in water, which was cleaned before with acetone and immersed in 0.1 M NaOH.

4.4.2 **MIL-53(Al)(H_2O) in MeOH**

Until now, the glass slides coated with suspensions in water have not shown a homogenous coverage of the surface. MeOH will be therefore introduced here as an alternative solvent with lower viscosity and surface tension. However, the glass slides coated with a 0.1 wt% suspension in MeOH (Figure 4-13) still showed a sparse coverage comparable to the suspension in water with similar concentration. At higher concentrations of 0.5 wt% (Figure 4-14) the surface coverage is increased, but at lower magnification gaps in the coating were still visible.

In contrast to water used as solvent, no difference between surfaces coated from a 0.5 wt% or 1.0 wt% (Figure 4-15) suspension in MeOH can be identified. The coated surface of both samples was not charged during the SEM measurements, which implies a stronger interaction and better distribution of particles with the surface in comparison with the sample coated with water as solvent (see chapter 4.4.1, p. 91). A possible reason might be that MeOH is better able to separate the agglomerated clusters of the MIL-53(Al) powder samples into individual particles.

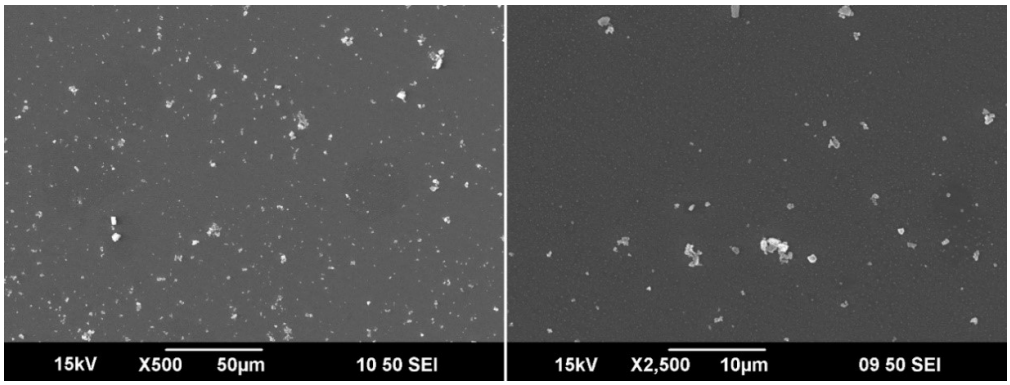


Figure 4-13: SEM image of glass slide covered with a 0.1 wt% suspension of MIL-53(Al)(H_2O) in MeOH. The surface is mostly empty with a few particles of MIL-53(Al)(H_2O) on the surface.

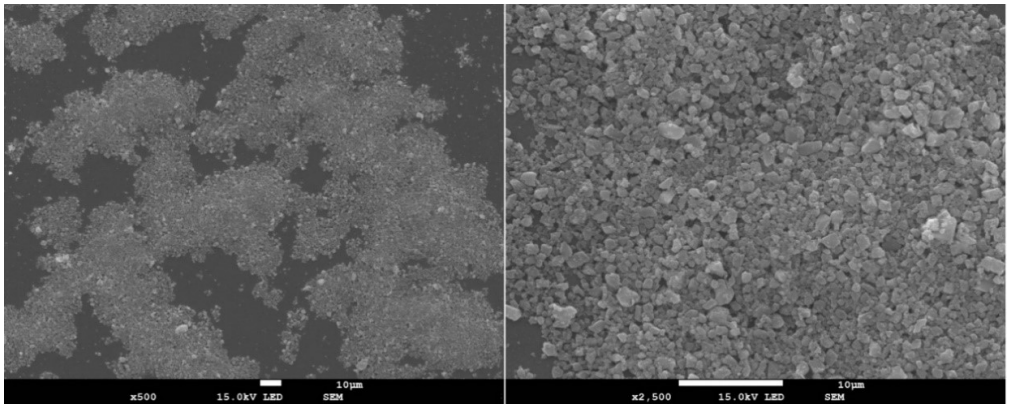


Figure 4-14: SEM image of a glass slide with was coated with a 0.5 wt% suspension of MIL-53(Al)(H_2O) in MeOH. The surface coverage is higher in comparison with glass slides coated with MIL-53(Al)(H_2O) which used water as solvent.

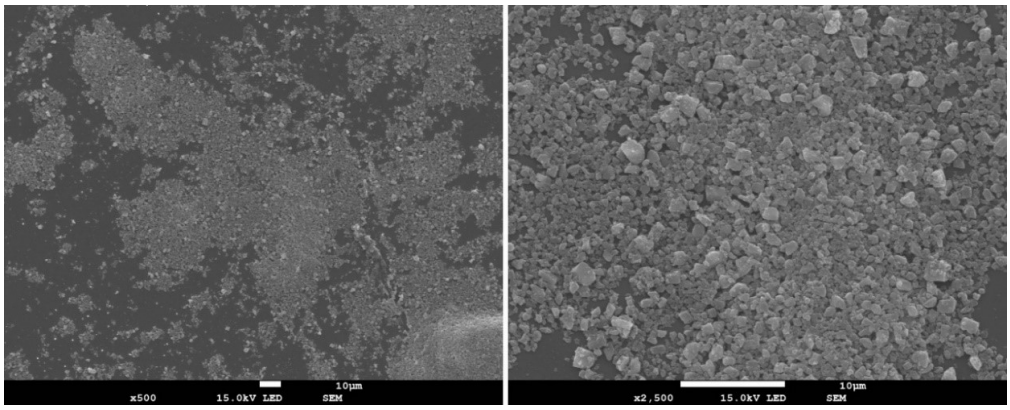


Figure 4-15: SEM image of a glass slide which was covered with a 1.0 wt% suspension of MIL-53(Al)(H_2O) in MeOH. No difference to a glass slide coated with 0.5 wt% suspension in MeOH was observed.

4.4.3 **MIL-53(Al)(DMF) in water**

As mentioned previously, MIL-53(Al)(DMF) and MIL-53(Al)(H_2O) have varying morphologies in powder samples and the effect of the morphology to the surface coverage was first investigated with water as solvent. The results show, that at low concentration of 0.1 wt% (Figure 4-16) surface coverage was low, comparable with the glass slide covered before at similar concentration with MIL-53(H_2O) in water (Figure 4-7) or MeOH (Figure 4-13) as solvent. Only few particles were visible on the glass surface.

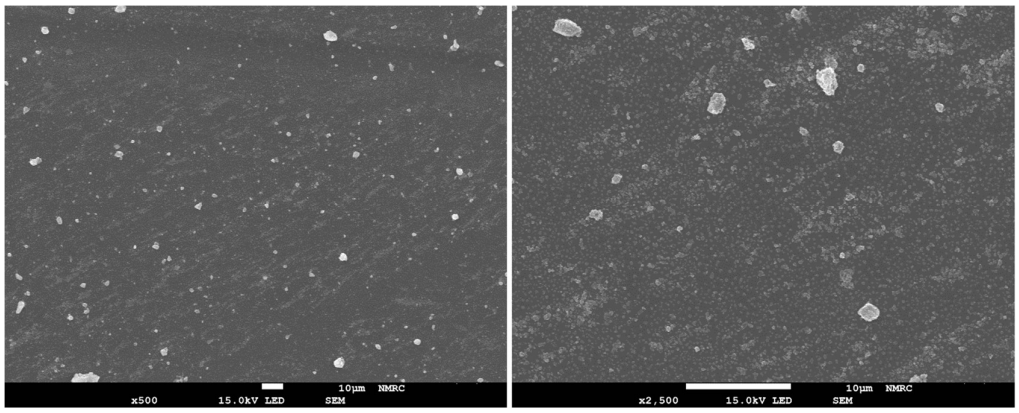


Figure 4-16: SEM image of glass slide covered with a 0.1 wt% suspension on MIL-53(Al)(DMF) in water.

The surface coverage was higher for the 0.5 wt% sample (Figure 4-17) in comparison to the 0.1 wt% coated glass slide. The surface coverage at higher magnification (Figure 4-17, right) has verified a surface coated with only small gaps between the individual particles. However, at lower magnification areas with reduced coverage became apparent (Figure 4-17, left), which were visible as dark strains.

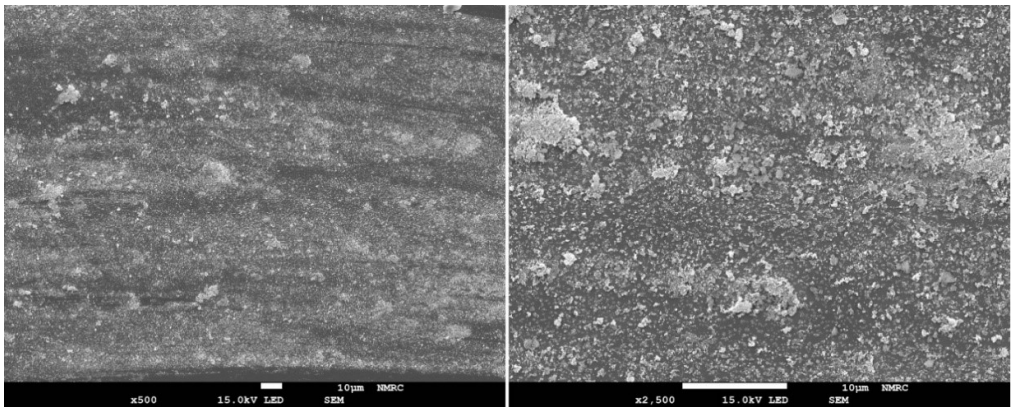


Figure 4-17: SEM image of glass slide covered with 0.5 wt% suspension of MIL-53(Al)(DMF) with water as solvent. The surface coverage of the particles is higher in comparison with samples coated with MIL-53(Al)(H_2O) or samples coated with suspension of lower concentration. Furthermore, are no larger agglomerated clusters visible on the surface.

The glass slide coated with 1.0 wt% suspension, shows a less homogenous coating in comparison with the samples coated with MIL-53(Al)(DMF) from water at 0.1 wt% and 0.5 wt% suspension. In some areas, the surface is covered with particles and even at higher magnification nearly no gaps between the particles were visible (Figure 4-18, green). However other areas have shown a reduced surface coverage (Figure 4-18, red). In addition, were larger cluster visible on the surface, likely caused by agglomeration of MIL-53(Al)(DMF) particles at the increased concentration in the coating suspension.

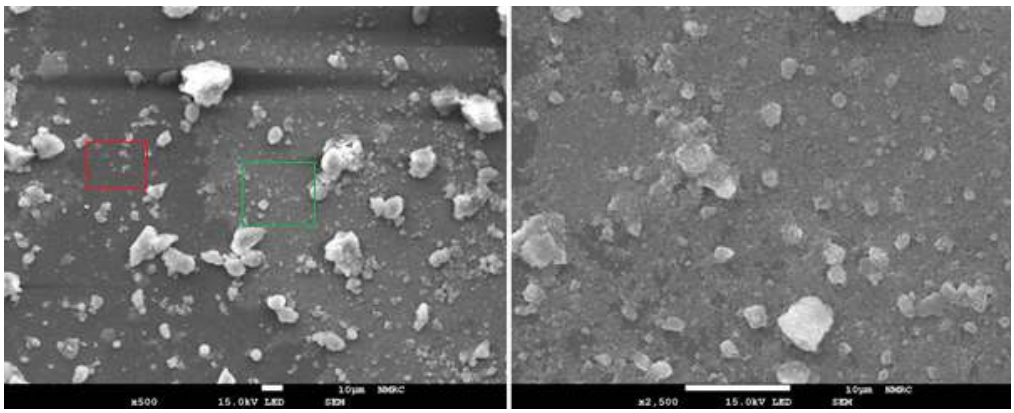


Figure 4-18: SEM images of glass slides covered with a 1.0 wt% suspension. At higher magnification (right side) the surface seems to have a higher and more homogenous coverage of particles, but the drawback is the formation of numerous agglomerated clusters on the surface. These might have a reduced interaction with the glass surface and make a possible coating rougher.

4.4.4 MIL-53(Al)(DMF) in MeOH

Comparable with the glass slides manufactured previously, only few particles of MIL-53(Al)(DMF) were visible on the surface and low coverage was achieved using a 0.1 wt% suspension (Figure 4-19) In contrast to the 0.1 wt% coated glass slide, glass slides coated with a 0.5 wt% suspension (Figure 4-20) showed a better coverage of the surface with a homogenous coating and less gaps in the coating. The coverage was also higher in comparison with glass slides coated by a 0.5 wt% suspension in water (Figure 4-21). Samples coated with a 1.0 wt% suspension (Figure 4-22) show the agglomeration of clusters of the surface. In general, seem to be the coverage more homogenous than with

MIL-53(Al)(H_2O) in MeOH. A possible reason might be the lower particle size of MIL-53(Al)(DMF) in comparison with the water sample. The nanometre-sized particles of MIL-53(Al)(DMF) were separated by the solvent in the suspension and are distributed over the glass surface, while the micrometre-sized particles of MIL-53(Al)(H_2O) were forming cluster on the surface.

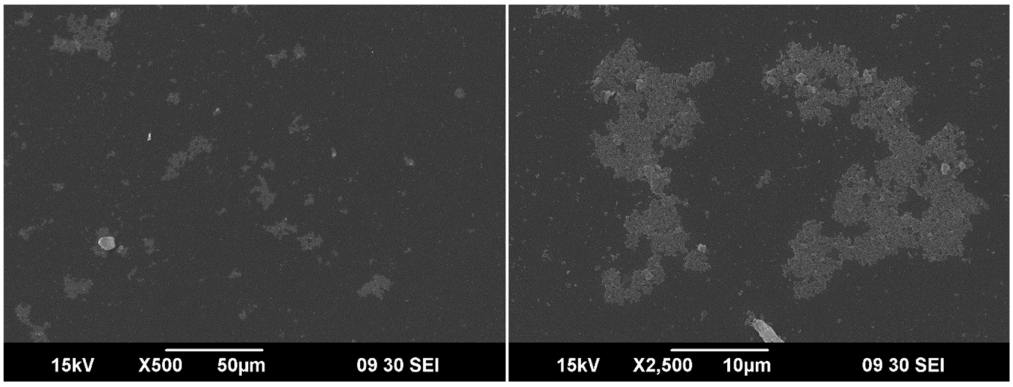


Figure 4-19: SEM image of a glass slide covered with a 0.1 wt% suspension of MIL-53(Al)(DMF) in MeOH. The surface is mostly empty and only in a few particles are visible on the surface.

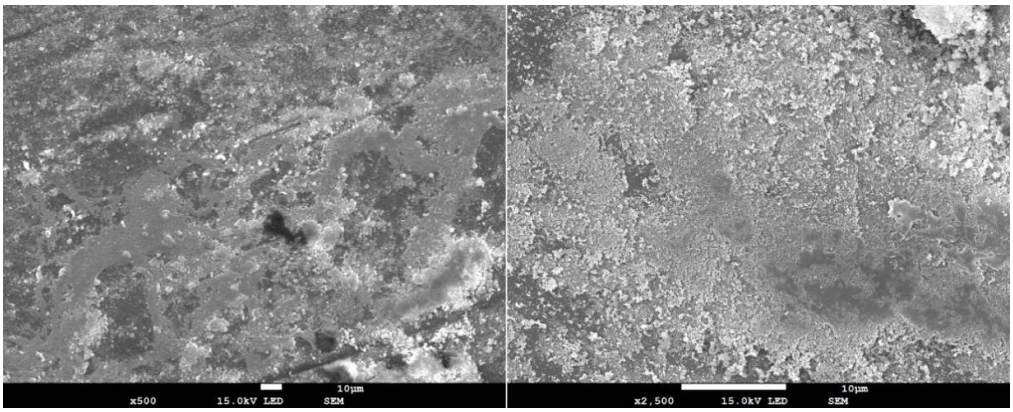


Figure 4-20: SEM image of a glass slide covered with a 0.5 wt% suspension of MIL-53(Al)(DMF) in MeOH.

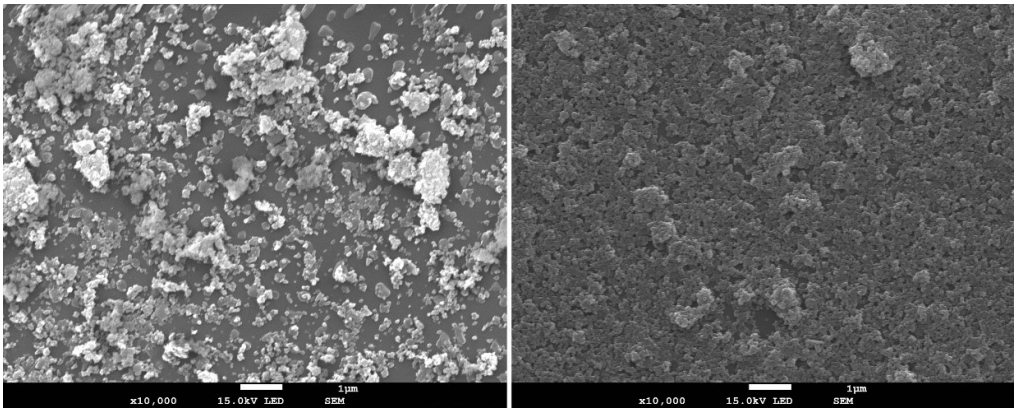


Figure 4-21: Comparison of glass slide covered with 0.5 wt% suspensions of MIL-53(Al)(DMF) in water (left) and MeOH (right) as solvent. At increased magnification (10,000x) glass slides covered with MIL-53(Al)(DMF) from water as solvent show gaps in the coating.

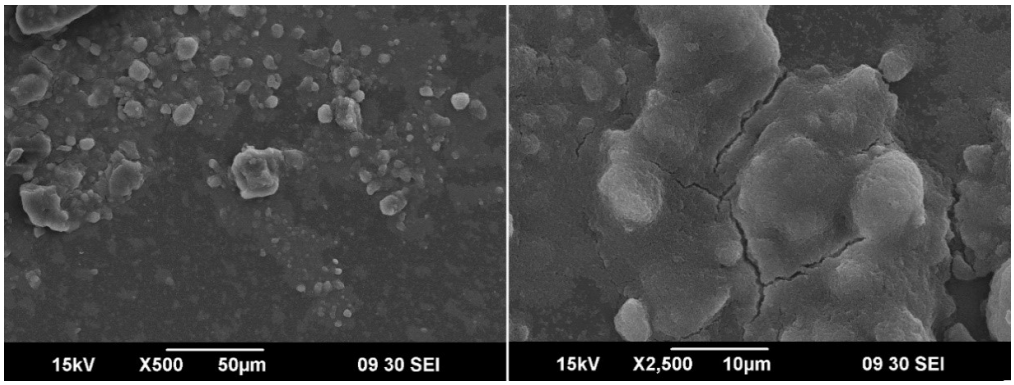


Figure 4-22: SEM image of a glass slide covered by a 1.0 wt% suspension of MIL-53(Al)(DMF) in MeOH. The surface coverage is similar in comparison with coating from lower concentrated suspensions, but particles agglomerate to large cluster on the surface.

4.5 Secondary growth

As mentioned before, a support surface can, coated by dip-coating, act as a seeding for subsequent secondary growth to create a thin-film. In the secondary growth, the sample is placed in the reaction mixture for the MOF in solvothermal conditions. This mechanism is therefore a combination of the approaches from chapter 4.3 (placing glass slides in a MIL-53(Al) reaction mixture, p. 86) and chapter 4.4 (coating of glass slides by dip-coating, p. 90). These seeds on the support are possible starting points for the crystal growth on the surface and help to better control the thickness and orientation of the film [161]. The results until now have shown that the seeding of the surface with a 0.5 wt% with MeOH as solvent gives the best results as a coating of the surface. Glass slides coated with a lower concentration of 0.1 wt% were only sparsely covered with particles, while glass slides covered with a 1.0 wt% suspension have shown a tendency of particle agglomeration and weaker adhesion with the glass surface. The used glass slides were therefore first seeded with MIL-53(Al) from a 0.5 wt% suspension and then vertically mounted in the reaction vessel. The reaction conditions during the secondary growth were similar to a powder synthesis, with a reaction temperature of 150°C and 5 h reaction time.

Fan *et.al.* [164] have conducted a similar approach for the coating of porous α-Al_2O_3 supports. However, can these results not bet directly transferred to the coating of glass slides by seeding and secondary growth, because glass supports have a flat surface and weaker interaction with the MIL-53(Al) particles. For the secondary growth, a good adhesion of the seeding particles with the support surface is of importance. The seeds have to stay on the surface during the secondary growth step. If the interaction between seeds and support surface is too weak, the seeds will be washed away from the surface before they can facilitate the film growth. As a preliminary test, glass slides coated with 0.5 wt% dip-coating suspension of MIL-53(Al)(H_2O) and MIL-53(Al)(DMF) in MeOH were placed in pure solvent for 5 h at 150°C mimicking the reaction conditions during a possible secondary-growth formation of MIL-53(Al). During the test, the coating of MIL-53(Al)(H_2O) was completely removed (Figure 4-23), while the surface covered with MIL-53(Al)(DMF) remained nearly unchanged (Figure 4-24).

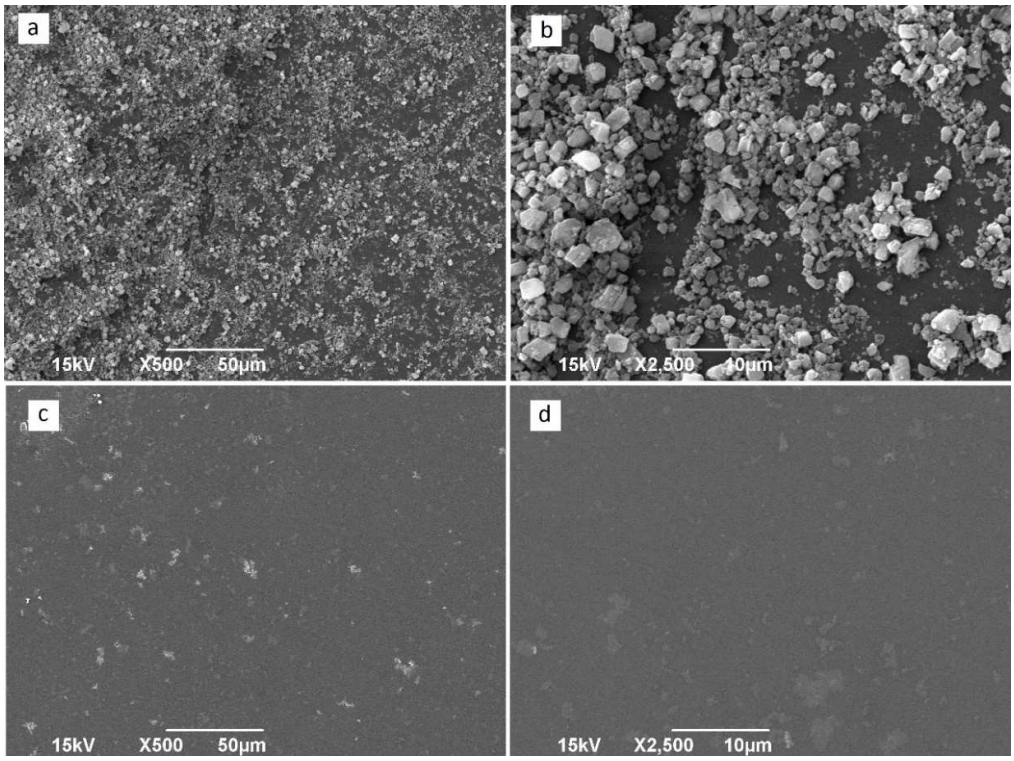


Figure 4-23: SEM images of glass slide covered with of MIL-53(Al)(H_2O) in MeOH before (a in lower magnification, b in higher magnification) and after (c in lower and d higher magnification) adhesion test in water at 150°C for 5 h.

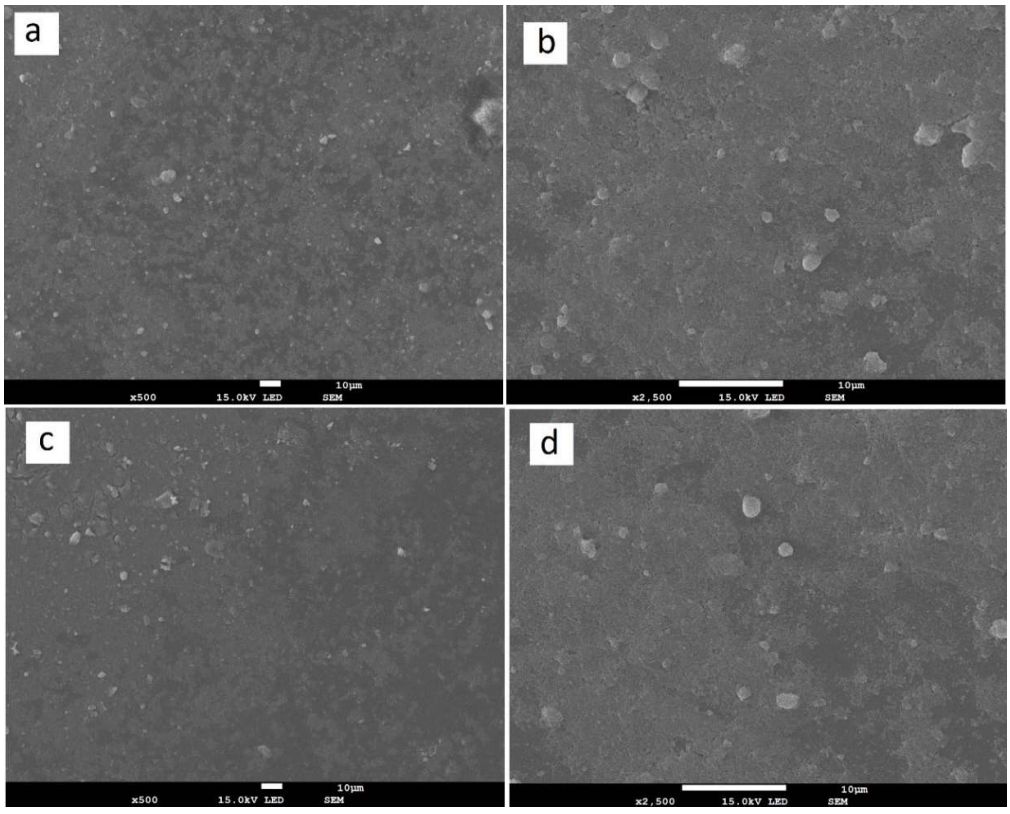


Figure 4-24: SEM images of glass slide covered of MIL-53(Al)(DMF) in MeOH before (a in lower magnification, b in higher magnification) and after (c in lower and d in higher magnification) adhesion test in DMF at 150°C for 5 h.

These tests have shown, that MIL-53(Al)(H_2O) particles have only a weak interaction with the glass surface, which makes their use not reasonable. Consequently, only the secondary growth for MIL-53(Al)(DMF) was investigated.

The surface (Figure 4-26) is completely covered after the secondary growth step. For the application of as a thin film on LPGs, a homogenous and smooth coating is desired. An example for the desired properties will be given as the results of Lu *et.al.* [144], which have done repetitive in-situ growth of ZIF-8 on glass to prepare a MOF thin-film. This technique which was also adopted by Hromadka *et.al.* [22] for the preparation of an MOF coated LPG.

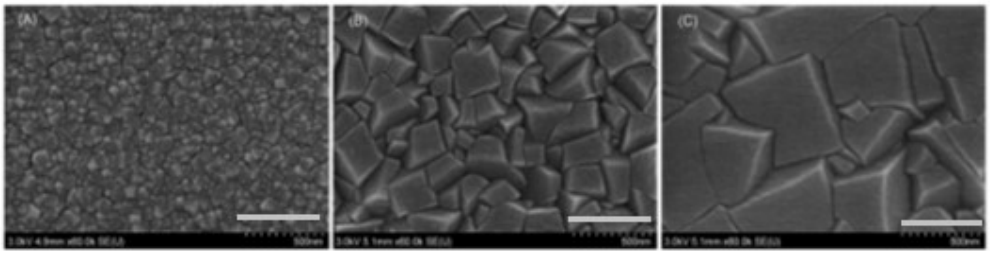


Figure 4-25: Preparation of a ZIF-8 thin-film on glass, after 1 (a), 10 (b) and 40 (c) repetition of in-situ growth. With progress of the experiment, the individual particles start to intergrowth to larger particles, leading to a homogenous, nearly crack-free surface. Scale bar: 500 nm [144].

In comparison to this literature example (Figure 4-25), have the particles of MIL-53(Al)(DMF) not fused to a homogeneous film and individual particles on the surface can be still identified (Figure 4-26). A cross-section image of the coating (Figure 4-27) shows that the thickness of the coating varies between 2.1 µm and 3.2 µm. The measurement of XRD pattern (Figure 4-28) of the glass slide further confirms the successful coating with MIL-53(Al)(DMF). Peaks were measured at 8.7°, 12.0°, 15.2° and 17.3° and correspond to a powder sample of MIL-53(Al)(DMF).

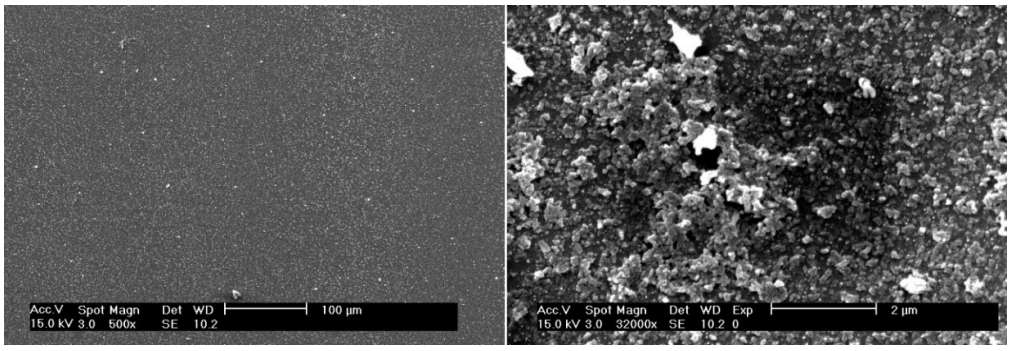


Figure 4-26: SEM images of a glass slide seeded with a 0.5 wt% suspension of MIL-53(Al)(DMF) in MeOH, followed by secondary growth of MIL-53(DMF) at 150°C and 5 h reaction time.

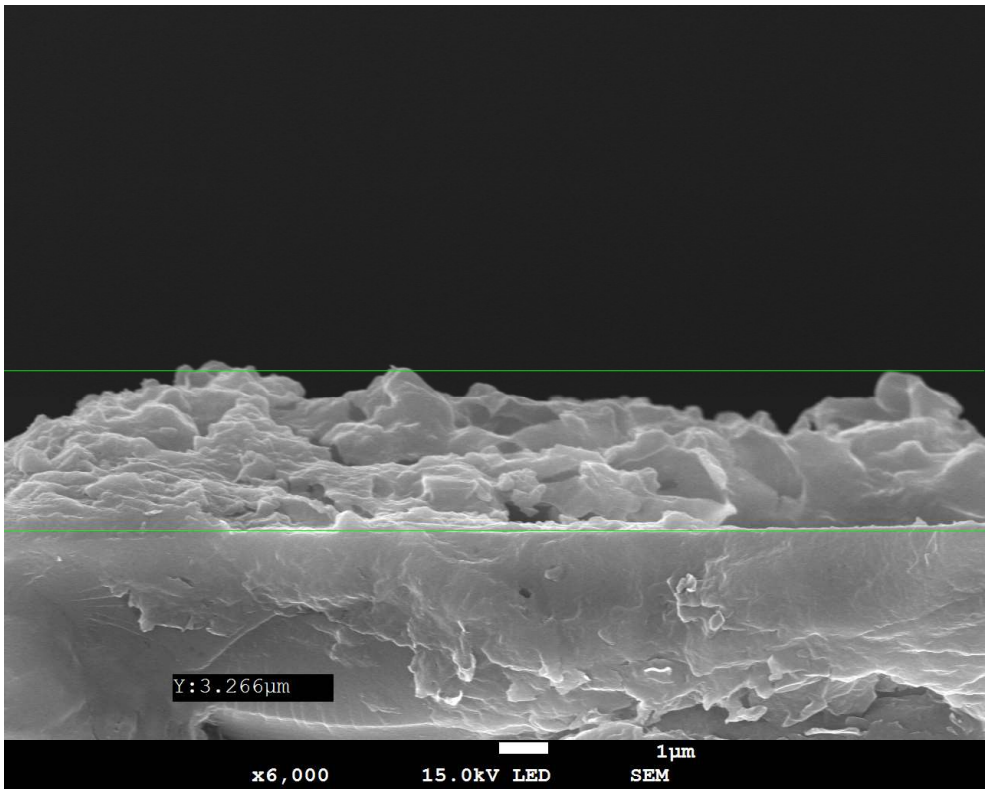


Figure 4-27: Cross-section image of a glass slide coated by seeding and secondary growth with MIL-53(Al)(DMF) at 150°C and 5 h reaction time. The thickness of the coating varies between 2.1 µm and 3.2 µm.

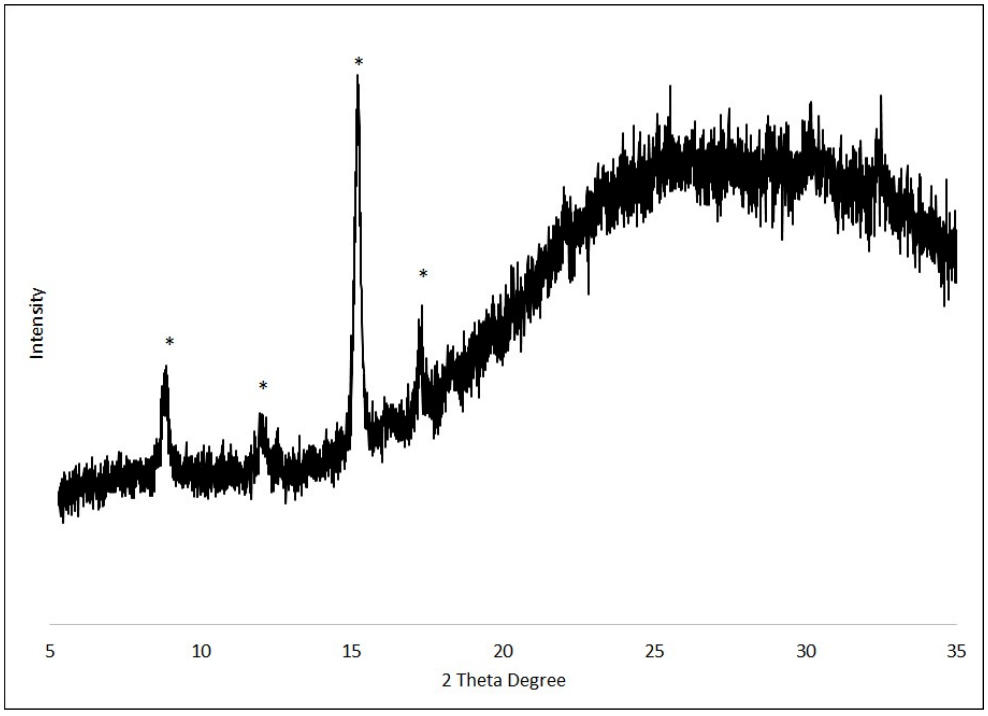


Figure 4-28: XRD pattern of glass slide covered by seeding and secondary growth with MIL-53(Al)(DMF). Peaks corresponding to MIL-53(Al)(DMF) are highlighted by asterisks.

4.6 Dip-coating of multiple layers

After secondary growth, it was possible to coat the surfaces completely with MIL-53(Al), but the resulting coatings had a large variation of coating thickness (ranging between 2.1 µm and 3.2µm) and far thicker than desired for a possible sensor application (ideally <1 µm).

Besides the secondary growth, a straight-forward approach to coat the support surface is the repetition of the dip-coating process in order to add several "layers" on the surface. [351]. To determine the ideal number of repetitions (referred to as layers subsequently), glass slides were coated with 1 (corresponding to the results from the chapter 4.4, p. 90), 2, 5 and 10 layers by using a 0.5 wt% suspension with MIL-53(Al)(H_2O) and MIL-53(Al)(DMF) in MeOH. The quality of the coated surfaces (thickness, morphology, coverage etc.) was investigated by SEM. The results from the seeding have already shown that coatings from suspensions using water as solvent formed less homogeneous coatings in comparison with MeOH. Hence, the dip-coating with water as solvent was not further investigated.

4.6.1 MIL-53(Al)(H_2O) in MeOH

After coating of 1 layer of MIL-53(Al) (Figure 4-29) large empty spaces were visible on the surface, but the surface coverage was improved with additional layers. Although the 2-layer sample was mostly covered (Figure 4-30), some areas of the surface were still identified as darker areas on the surface, which imply a lower surface coverage. In contrast, on a 5-layer sample (Figure 4-31) a nearly homogenous coating of the surface was observed. However, some gaps between the particles still remain and that the surface is covered with a mixture of particles with varying size (ranging from 0.5 to 3 µm). Between a 5-layer and a 10-layer covering (Figure 4-32) no difference regarding the surface coverage can be identified, which makes coating the surface with more than 5 layers not reasonable. On the 5-layer and 10-layer sample, some clusters were brighter in the SEM images. This may imply charging of the particles and consequently a weaker interaction with the surface.

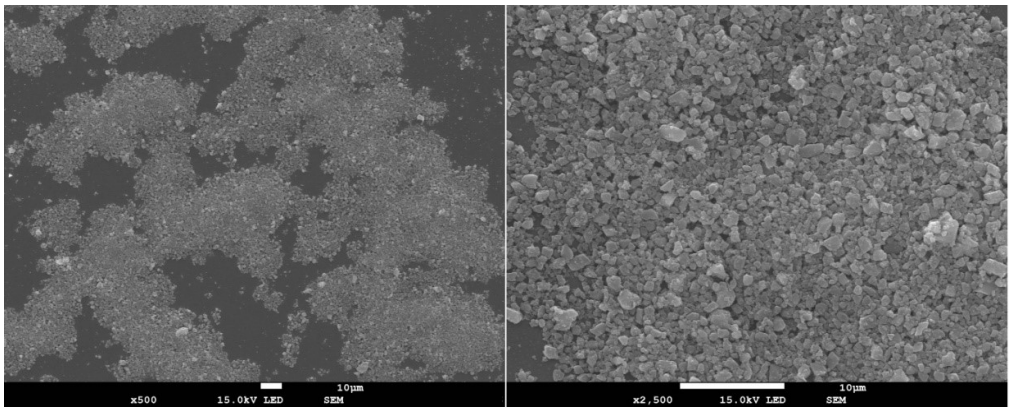


Figure 4-29: SEM image of glass slide covered with 1 layer of MIL-53(Al)(H_2O) in MeOH.

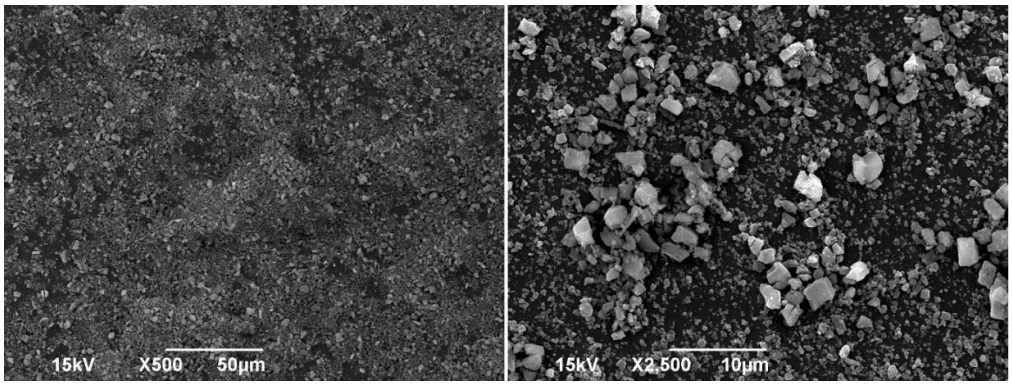


Figure 4-30: SEM image of glass slide covered with 2 layers of MIL-53(Al)(H_2O) in MeOH.

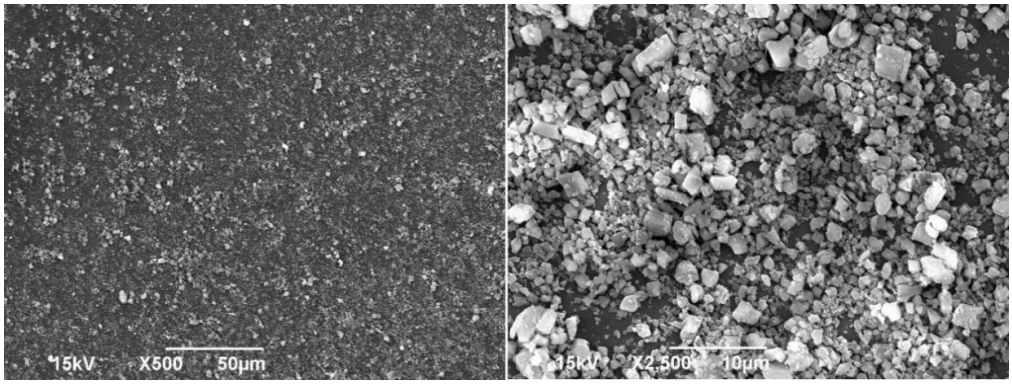


Figure 4-31: SEM image of glass slide covered with 5 layers of MIL-53(Al)(H_2O) in MeOH.

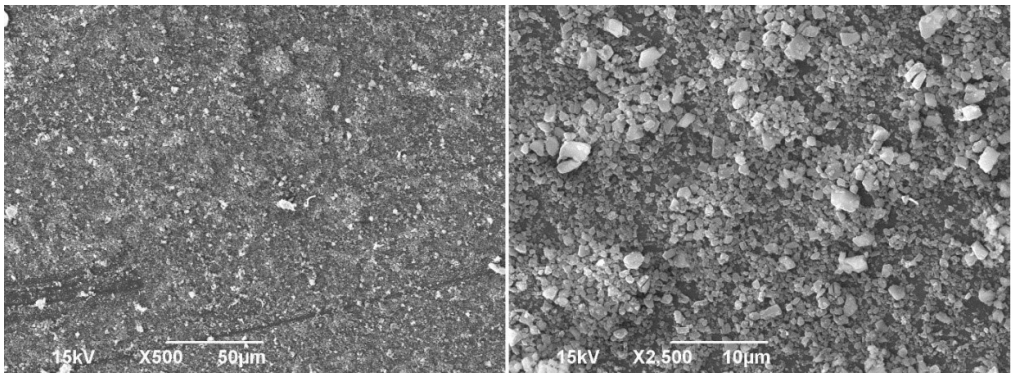


Figure 4-32: SEM image of glass slide covered with 10 layers of MIL-53(Al)(H_2O) in MeOH.

4.6.2 **MIL-53(Al)(DMF) in MeOH**

The glass surface coated with 1 layer of MIL-53(Al)(DMF) in MeOH as solvent (Figure 4-33) was coated with particles, but darker areas on the surface imply that the surface was not completely covered after only 1 layer. After 2 layers, (Figure 4-34) the surface coverage was increased. Black areas were still visible on the surface, but to a lesser extent. At higher magnification the particles are fused to a nearly crack-free coating, which is different to the MIL-53(Al)(H_2O) coated glass slides. The smaller spherical particles of MIL-53(Al)(DMF)

have fused to a homogenous film (Figure 4-34), while the larger micrometre-sized MIL-53(Al)(H_2O) particles, could be still identified as individual particles (Figure 4-30).

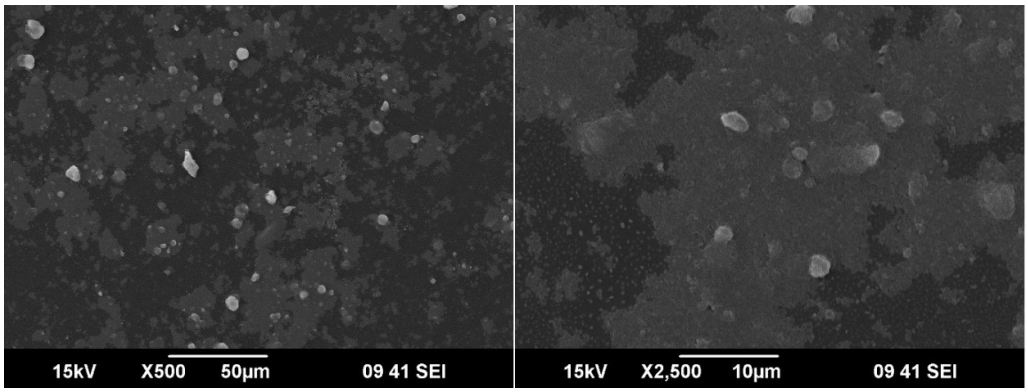


Figure 4-33: SEM image of glass slide covered with 1 layer of MIL-53(Al)(DMF) from a 0.5 wt% suspension. The surface was covered with areas of MIL-53(Al)(DMF), but holes in coating and larger agglomerated particles were also visible.

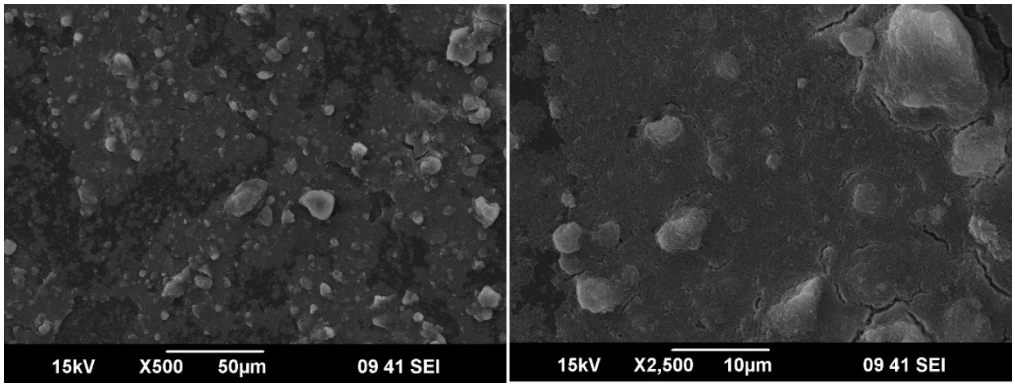


Figure 4-34: SEM image of glass slide covered with 2 layers of MIL-53(Al)(DMF) form a 0.5 wt% suspension in MeOH. In comparison with the 1-layer sample, the surface coverage was higher and more homogenous. Some gaps were still in the coating visible.

After 5 layers (Figure 4-35), the surface coverage was further increased could and nearly no dark areas were visible. At higher magnification, the particles have intergrown to from a crack-free coating, while a few larger clusters are embedded into this coating. A cross-section image (Figure 4-37) of this sample showed that this leads to a rough coating with a thickness between 301 nm and 828 nm. However, in comparison is this coating thinner than the coating after seeding and secondary growth (2.1 µm – 3.2 µm; Figure 4-27). The XRD pattern verifies the successful coating of the glass surface with a thin-film of MIL-53(Al)(DMF) (Figure 4-38). Peaks measured from the coated surface were matching the XRD pattern from a MIL-53(Al) powder sample. Coating the glass surface with more than 5 layers did not further improve the surface coverage and (Figure 4-36) more clusters were embedded into the coating on a 10-layer coated glass slide.

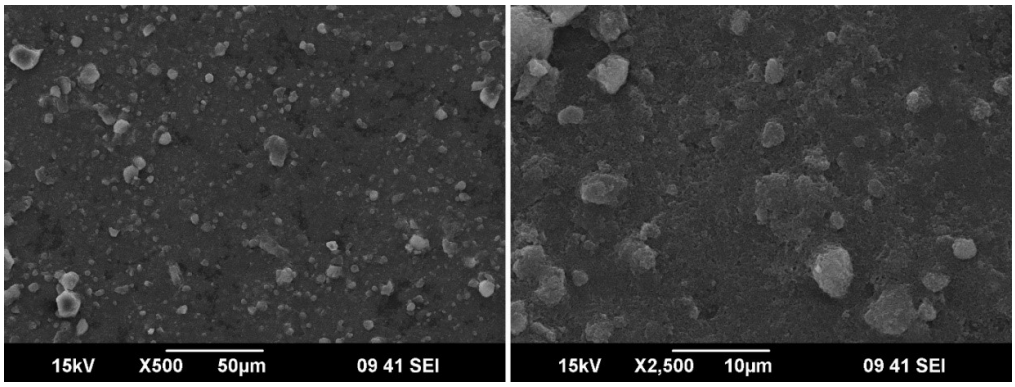


Figure 4-35: SEM image of glass slide covered with 5 layers of MIL-53(Al)(DMF) from a 0.5 wt% suspension in MeOH.

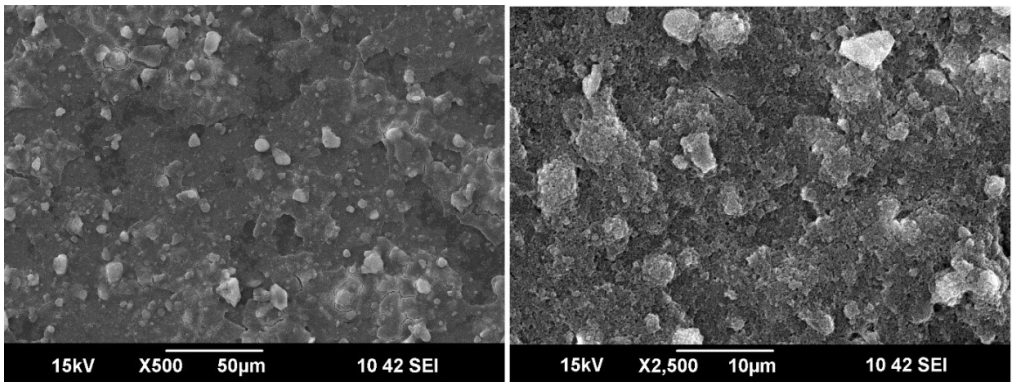


Figure 4-36: SEM images of glass slide covered with 10 layers of MIL-53(Al)(DMF) from a 0.5 wt% suspension in MeOH. The surface was mostly covered, but larger agglomerated clusters were embedded in the coating.

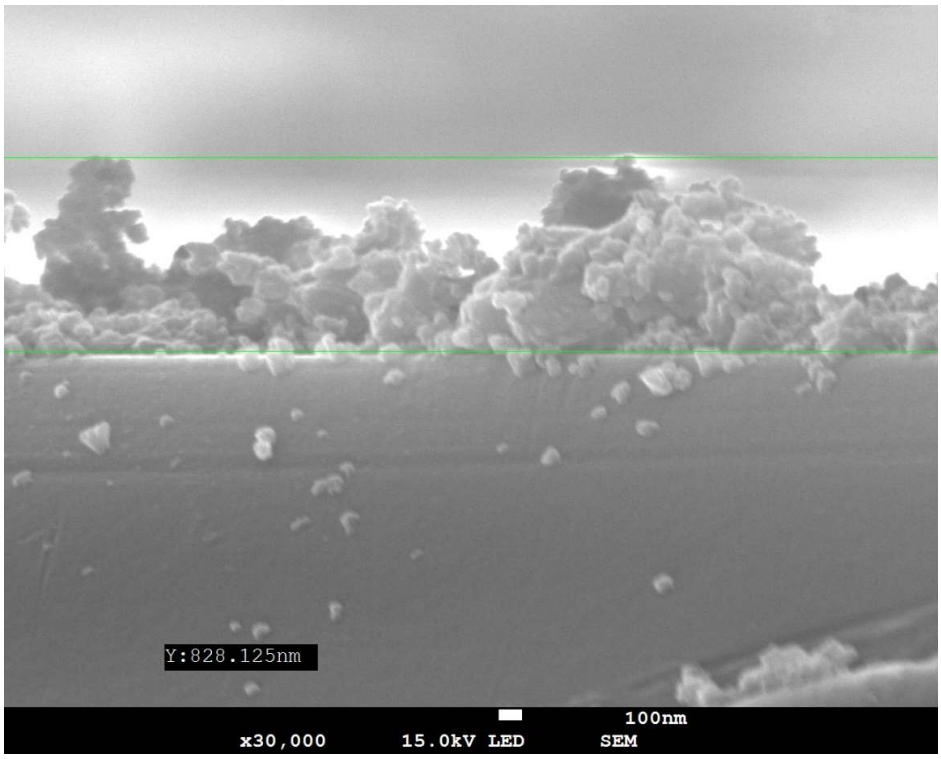


Figure 4-37: SEM image of a cross section of a glass slide covered with 5 layers of MIL-53(Al)(DMF) from a 0.5 wt% suspension in MeOH.

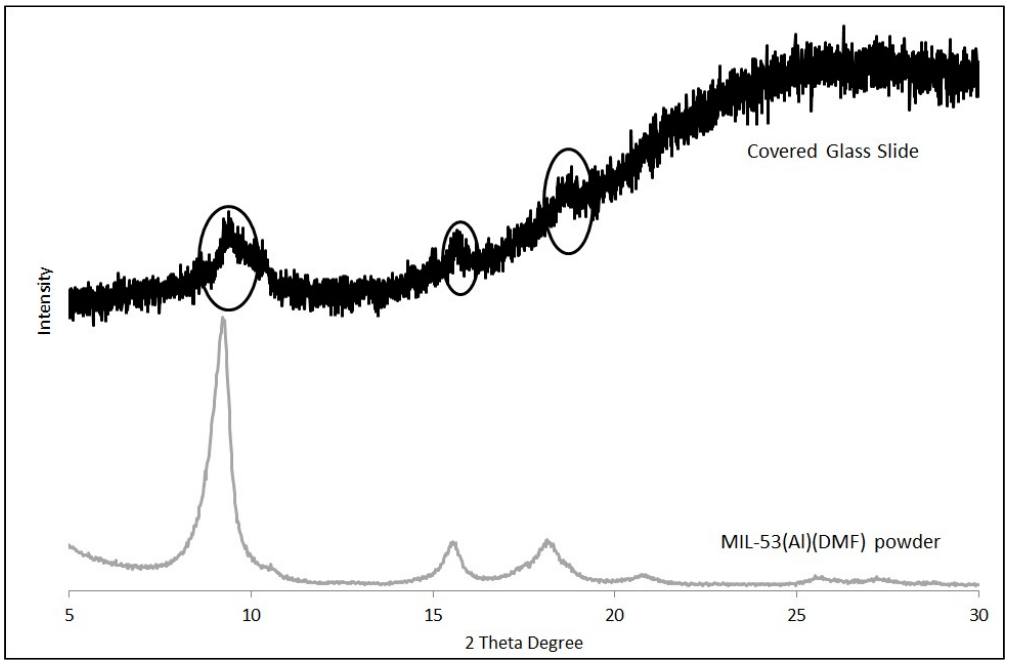


Figure 4-38: XRD pattern of a glass slide covered with 5 layers of MIL-53(Al)(DMF) in MeOH as solvent (black). For comparison, the XRD pattern of MIL-53(Al)(DMF) as powder is shown (grey).

4.7 Layer-by-Layer approach

In the Layer-by-Layer approach (LbL) [151], a thin-film of a MOF will grow step-by-step by alternated immersion of a support in metal and then linker solution (Figure 4-39). As mentioned before in chapter 2.5 (p. 23), such a support will be often functionalized with a SAM, which not only provides a starting point for the growth of MOFs on the surface, but also can act as a structure-dictating agent for the formation of well-ordered thin films [352].

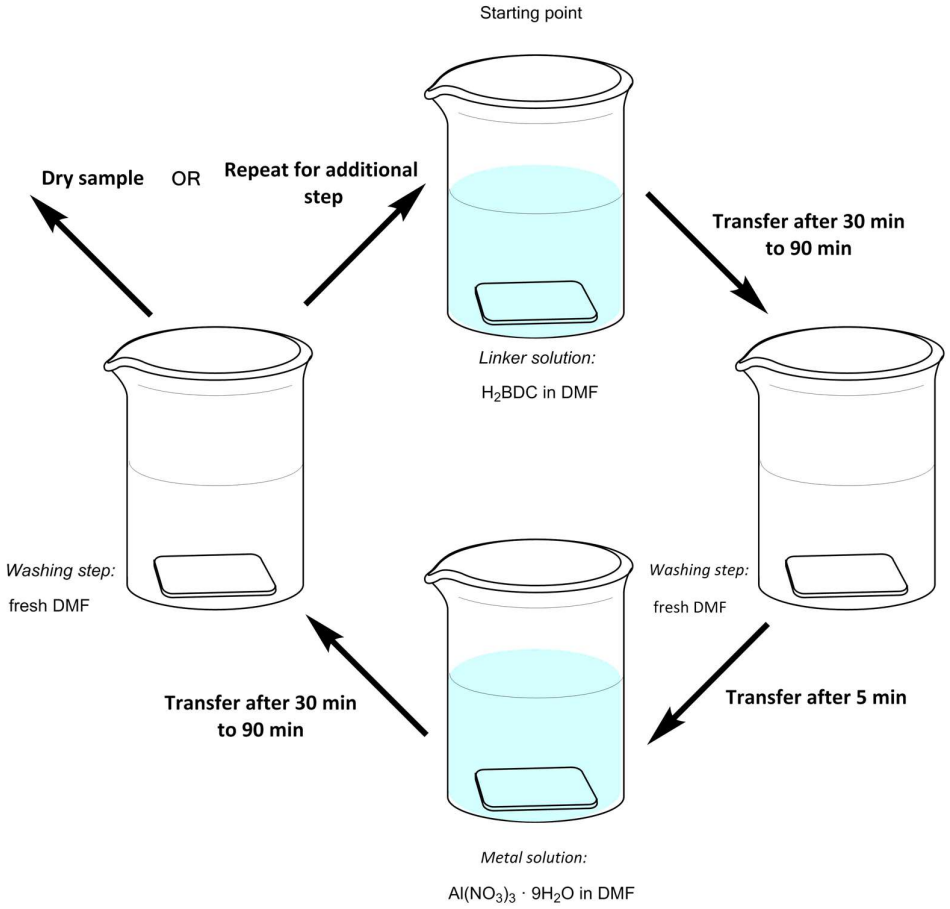


Figure 4-39: Schematic description of the Layer-by-Layer approach.

Due to the nature of this technique, the LbL-approach was often used for square shaped MOFs such as MOF-5 [353] or HKUST-1 [185], but there are reports of LBL used for other MOFs *e.g.* CPO-27 [180], which is composed of 1D-hexagonal channels. As mentioned before in the introduction of this chapter, SAM can be a possible interference for future applications, such as the coating of MOFs on an LPG. Therefore LbL techniques, which coat the surface only with MOF without relying on SAMs are therefore preferred here [180].

To the best of our knowledge, no LbL coating of MIL-53(Al) was reported until now and consequently, no data which can act as a starting point for the investigation was available. However, the immersion time of the sample in the metal or linker solution and the number treatment steps has been identified as possible parameters affecting the surface coverage [181],[354]. For this investigation, different immersion times (30, 60 and 90 min, followed by immersion for 5 min in clean solvent to remove weakly attached particles), which are typical immersion times for the synthesis of MOF thin-films by LbL through alternating immersion in metal and linker solutions [180],[353],[355]. These immersion times has been used as starting point for the investigation of LbL for the formation of MIL-53(Al) thin-films. Samples have been prepared here with up to 10 treatment steps, whereas a treatment step will be defined here as a complete cycle of immersion in metal and linker solution with washing steps in between. Comparable to other applications of LbL, the coating was done at RT. While it might be possible to prepare MIL-53(Al) in solvothermal

synthesis with solvents that are not able to completely dissolve the starting material *e.g.* water, for the LbL-approach both the linker and metal must completely dissolved, thus DMF (H_2BDC solubility: 7.4 g/100 g solvent at RT [294]) was used for the synthesis of MIL-53(Al) by LbL approach.

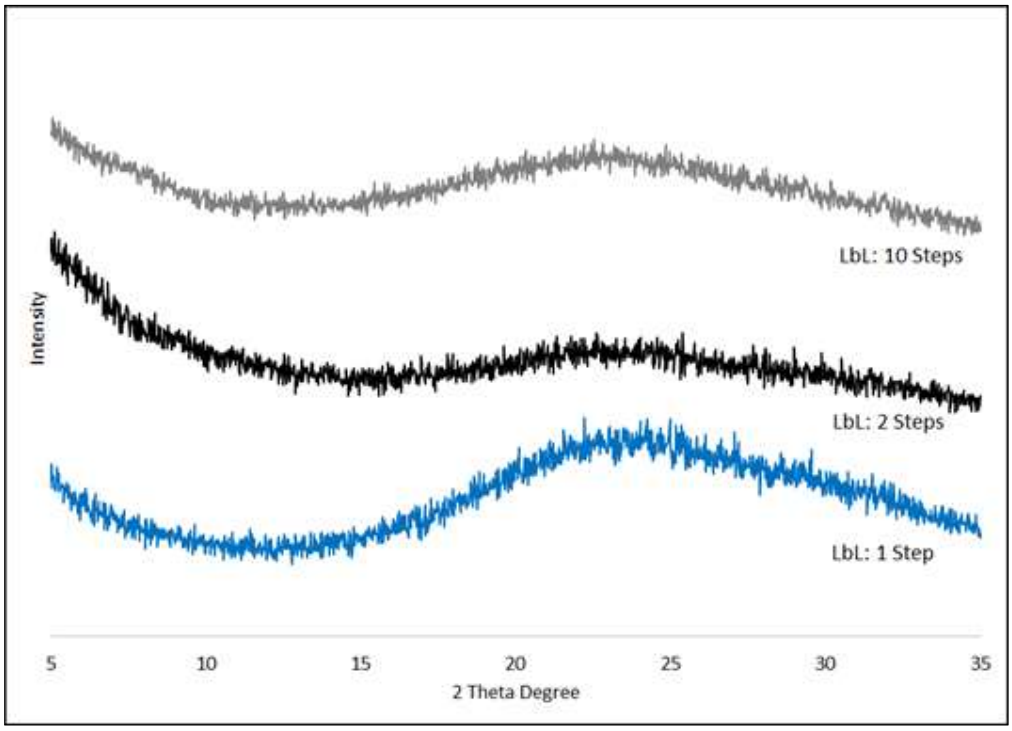


Figure 4-40: XRD patterns of glass slides covered by LbL with 1 (blue), 2 (black) and 10 (grey) processing steps in DMF as solvent and with 30 min immersion time for metal and linker solution respectively. No peaks corresponding to MIL-53(Al) could be observed.

In a first attempt, the immersion time for the metal and linker solution was set to 30 min and the treatment of the glass slides with metal and linker solution repeated up to 10 times leading to 10 processing steps. However, was it not possible to confirm the successful coating of the surface with MIL-53(Al). The XRD pattern of the LbL coated glass slides (Figure 4-40) did not show any peaks with could be attributed to MIL-53(Al), even though the measurement time for the XRD pattern have been largely increased in comparison with powder samples. The total XRD measurement time for the glass slides was up 15 h, while the measurement time of MIL-53(Al) powder samples was ~4 h.

The SEM images of the samples (Figure 4-41) might explain, why no signal could be detected by XRD. The glass surface was covered after 1 step with small irregular shaped particles, while after two steps, the surface seems to be mostly covered with nearly no gaps between the particles. However, a cross-section of the glass slides (Figure 4-41 d) covered with two steps imply that the coating thickness might be with ~200 nm too thin for the possible detection by XRD. After 10 processing steps (Figure 4-41c), the overall particle size had slightly increased (from 233 ± 88 nm from the 2-step sample to 320 ± 124 nm for the 10 step sample), but still individual amorphous shaped particles are visible on the surface. A further increase of treatment steps might be therefore necessary to create a thin-film, where the individual particles fuse to a homogenous and crack-free film.

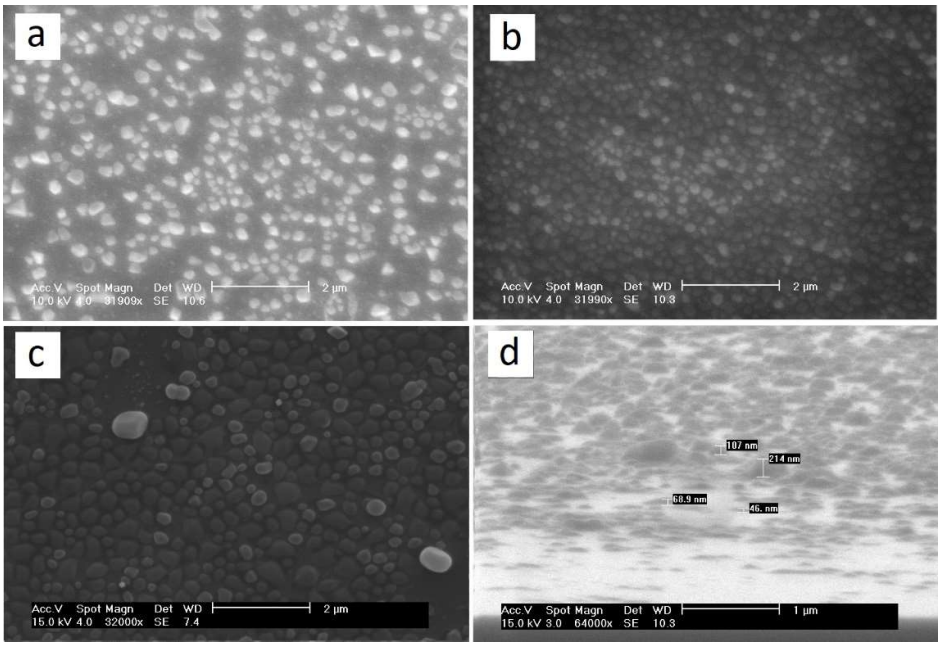


Figure 4-41: SEM images of glass slides coated by LbL with a) 1 step, b) 2 steps and c) 10 steps. In the lower right corner (d), a cross section of the glass slide covered with 2 steps is shown. In contrast to the top-down SEM images (a to c), the glass slide appeared in the cross-section image bright white, while the coating was grey.

A further investigation has implied, that for the LbL approach immersion time and number of treatment steps are exchangeable to a certain degree. Figure 4-42 shows the SEM images of glass slides, which have been coated with one treatment step. The immersion times were increased from 30 to 60 and 90 min. The results show that the surface coverage has increased after 60 min immersion time and that after 90 min the surface was nearly completely covered with only small gaps in the coating (Figure 4-42c, white boxes highlight the gaps).

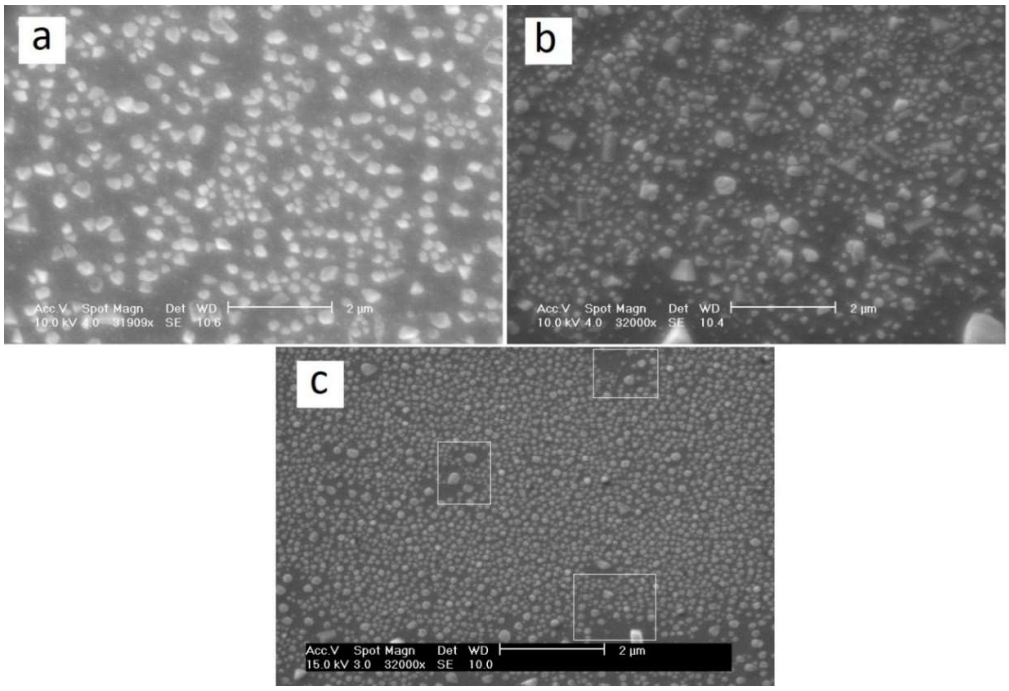


Figure 4-42: SEM images of glass slides covered with 1 step of MIL-53(Al) with different immersion times for the metal and linker solution of a) 30 min, b) 60 min and c) 90 min. White boxes show areas with reduced coverage.

While the results before had implied that it might be in principle possible to create a thin-film on the glass surface by LbL with an immersion time of 30 min and further increase of treatment steps several severe problems have been identified during this study. One of them was the repeatability of the results. For instance, was one experiment conducted in total 4 times using the same conditions (2 treatment steps, 30 min immersion time in metal and linker solution). SEM images of the samples show in Figure 4-43, that the coating was varying regarding particle size, surface coverage or particles shape with each repetition of the experiment.

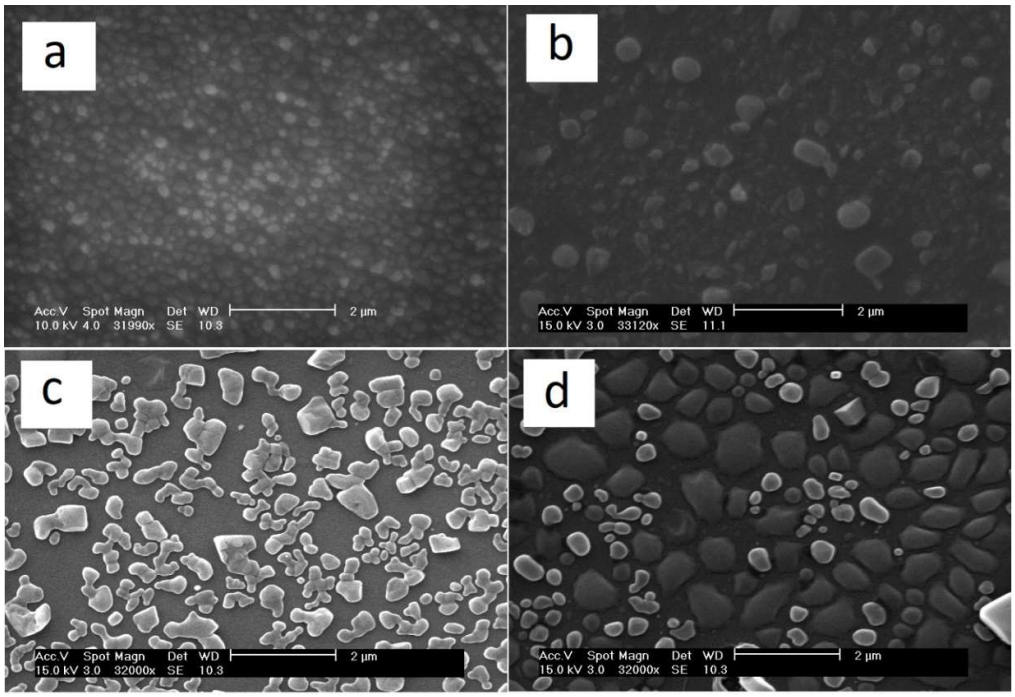


Figure 4-43: SEM images of 4 glass slides covered in LbL with 2 steps and 30 min immersion time in metal and linker solution.

Figure 4-43 d even share similarities regarding particles site and shape (amorphous particles with ~350 nm size) with the glass sample coated with 10 treatment steps (Figure 4-41 c) and it might be therefore possible, that the larger particle size of the 10-step sample is not caused by the growth of the particles during repetition of the reaction (as expected by the LbL), but inside the uncertainty of the experiment.

A further literature search and results from chapter 3.3.3 (p. 53) might further explain the observations for the LbL approach on glass slide (no detectable MIL-53(Al) pattern by XRD; problematic repeatability of the LbL coating). Kahn *et.al.* [356] have determined a strong dependency between the nucleation rate, crystal growth and reaction temperature for the formation of different MIL-53 samples. This was already proven for the powder synthesis of MIL-53(Al) in DMF (see chapter3.3.3, p. 53) that several weeks were required for MIL-53(Al) growth, whilst at 150°C MIL-53(Al) can be synthesised in hours. However, the LbL was during this research, similar to most literature examples until now, conducted at RT. The application of LbL at higher reaction temperature makes the experimental set-up more complicated and specially custom-made experimental set-ups are required [357]. Furthermore, the formation of MIL-53(Al) film might be hindered by the flat and inert glass surface with a weak interaction between crystals and the surface.

A possible theory is therefore now, that the formation of MIL-53(Al) was not possible because the metal and linker were not able to stick to the surface and have been mostly washed away from the surface during the washing step in DMF. Possible small remains off starting material on the surface were furthermore not able to form MIL-53(Al) during the short immersion time (between 30 min and 90 min) on the surface at RT.

To confirm this theory, a glass slide was coved covered only with $Al(NO_3)_3 \cdot 9\ H_2O$ in DMF (metal) or H_2BDC in DMF (linker) in the same concentration than used in the LbL-

experiments. Figure 4-44 show the results for a glass slide coated with a solution of $Al(NO_3)_3 \cdot 9\ H_2O$ in DMF. Various morphologies were obtained on the glass slide. One type of particles resembled flakes (Figure 4-44; yellow box), whereas other particles have an irregular shape (Figure 4-44; white box). These particles resemble particles which are observed on some LbL-samples (Figure 4-43 c and d) and on the 10-Layer glass slide (Figure 4-41 c). In contrast to the glass slide coated with metal salt solution, only one type of particles could be observed on the glass slides, which have been coated with a linker solution in DMF (Figure 4-45). Verification, that the glass surfaces are covered with $Al(NO_3)_3 \cdot 9\ H_2O$, was not possible by XRD (Figure 4-46). $Al(NO_3)_3 \cdot 9\ H_2O$ is a crystalline salt and has a characteristic XRD pattern, but decomposition may take place at elevated temperatures [358] (the DMF used to dissolve the $Al(NO_3)_3 \cdot 9\ H_2O$ and H_2BDC was removed by evaporation at 150°C for 24 h) possibly leading to an amorphous product. In contrast, a verification by XRD was possible when the surface was covered with the linker H_2BDC. Due to the similar shape of the particles on the surfaces covered by LbL (*e.g.* Figure 4-43 c and d) and glass slide only covered with $Al(NO_3)_3 \cdot 9\ H_2O$ (Figure 4-44) it can be implied that no reaction to MIL-53(Al) has taken place on any LbL sample. Instead, the glass slides were only covered with metal starting material.

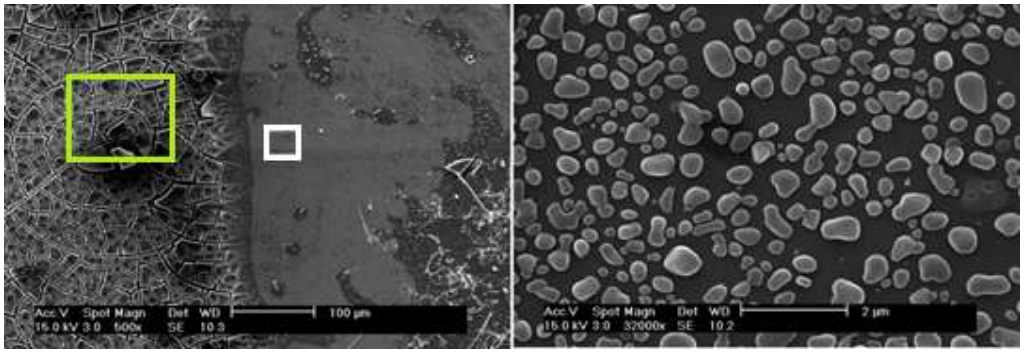


Figure 4-44: SEM image of a glass slide, which was covered by a solution of $Al(NO_3)_3 \cdot 9\ H_2O$ in DMF with the same concentration of Al-salt used in the LbL-approach. At lower magnification (left side) different morphologies were visible on the surface. At higher magnification (white square on the left side, right for higher magnification) these particles have irregular shape.

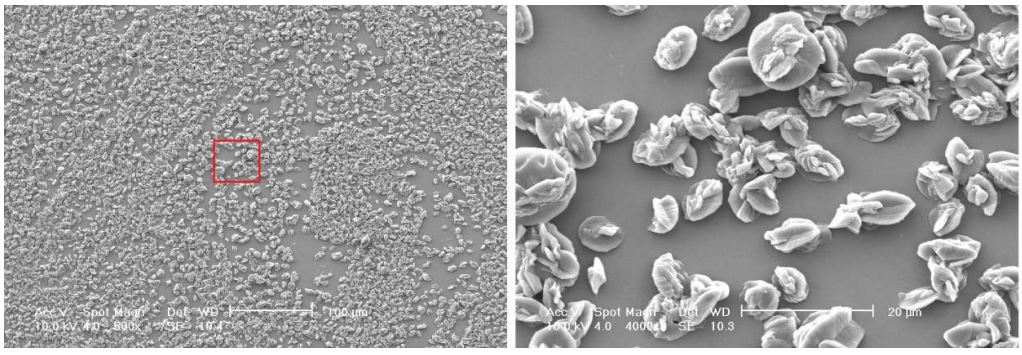


Figure 4-45: SEM image of a glass slide, which was covered by a solution of H_2BDC in DMF with the same concentration used in the LbL approach. In contrast to the samples covered with $Al(NO_3)_3 \cdot 9\ H_2O$, the surface was covered with only one type of particles. At higher magnification (the right image was taken at the position of the red marking in the left image) these particles appear as leaf-shaped particles with a size of ~3 µm.

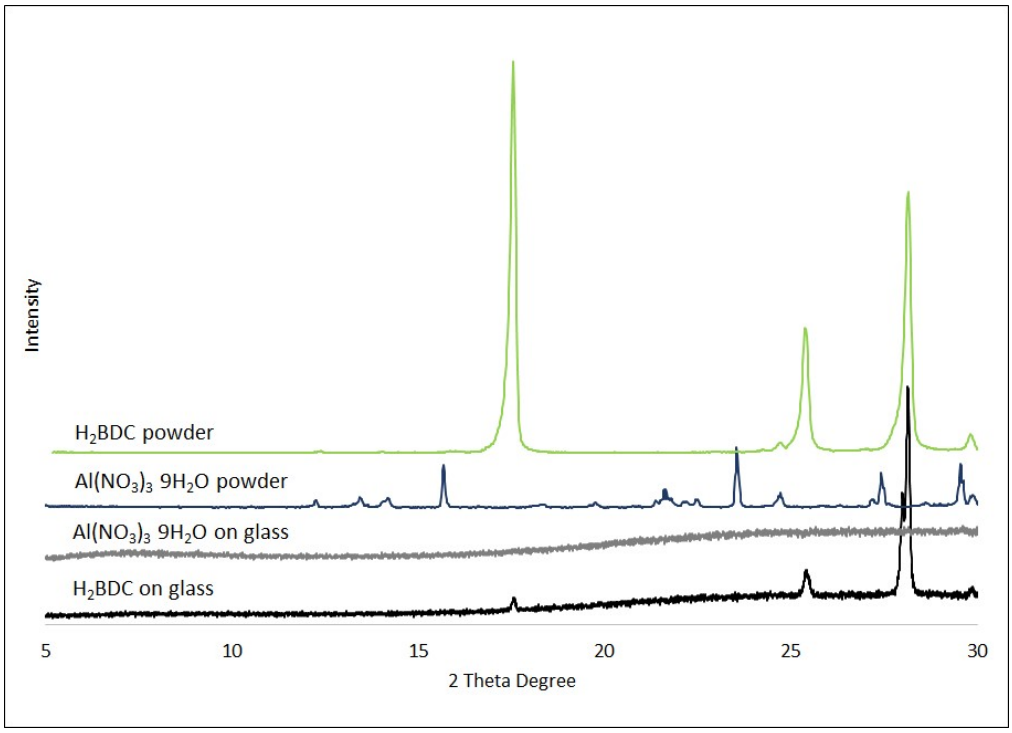


Figure 4-46: XRD pattern of glass slide covered only with metal solution ($Al(NO_3)_3 \cdot 9\,H_2O$, grey) and linker solution in DMF (H_2BDC, black) in comparison with XRD of powder sample of the starting materials $Al(NO_3)_3 \cdot 9\,H_2O$ (blue) and terephthalic acid (green).

For comparison, a glass slide has been coated with 2 treatment steps by LbL, but in contrast to the glass slides before the sequence of the LbL coating have been changed. The glass slide was first immersed in metal solution, followed by immersion in linker solution. The results further confirm the assumption, that during the LbL approach, no reaction has taken place and that instead only unreacted starting material remained on the surface. On the glass slide, were immersion in H_2BDC was the last processing step, ellipse shaped particles have been observed on the surface (Figure 4-47, left). While these particles are less distinct than the leaf-shaped particles observed before (Figure 4-45), could the coating of the surface with H_2DBC confirmed by XRD pattern (Figure 4-47, right).

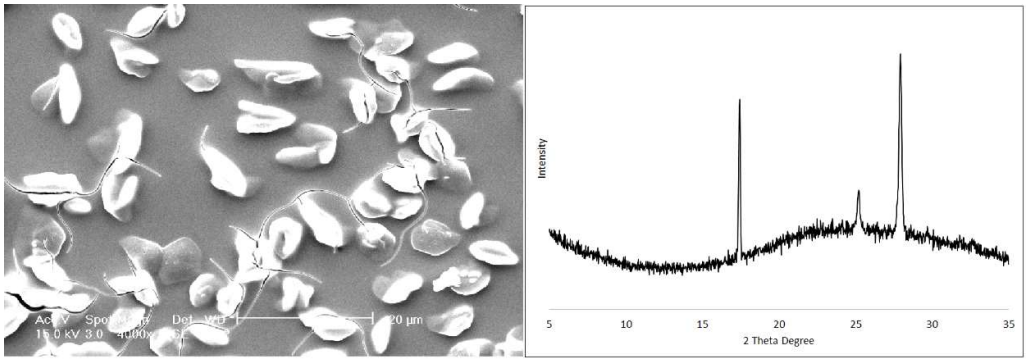


Figure 4-47: SEM image (left) of a glass slide covered with two treatment steps by LbL and inverted order of immersion (first metal solution, than linker solution) show a surface covered with ellipse shaped particles. An XRD pattern of the surface (right) confirm the coating of the surface with H_2BDC.

4.8 Rapid-Thermal Deposition

One possible disadvantage of the investigated thin-film growth techniques until now is that they are based on the heterogenous growth of MOFs and are often directly derived from the thin-film synthesis of zeolites [359] and thus often not take into account, the differences in the growth mechanism of MOFs in comparison with zeolites [147],[360],[361]. These differences have led to rough coatings or poor reproducibility.

The rapid-thermal deposition approach (RTD) is a new approach for MOF thin-film synthesis introduced by Shah *et.al.* [160] for ZIF-8 and HKUST-1. In this technique, the surface is coated with reaction mixture of the desired MOF by slip-coating or dip-coating and the thin-film growth induced by the evaporation of solvent [160],[342]. RTD has already found successful applications [362],[363] and in this part investigation of its application to MIL-53(Al) will be presented. For the RTD approach, the surface was coated with reaction mixture and the reaction starts at elevated temperature in order to evaporate the reaction solvent, which stimulates the formation and crystallisation of the MOF (Figure 4-48). Therefore, only DMF was used as solvent since both linker and metal salt can be completely dissolved in DMF. Other solvents such as water or MeOH are not able to dissolve the linker.

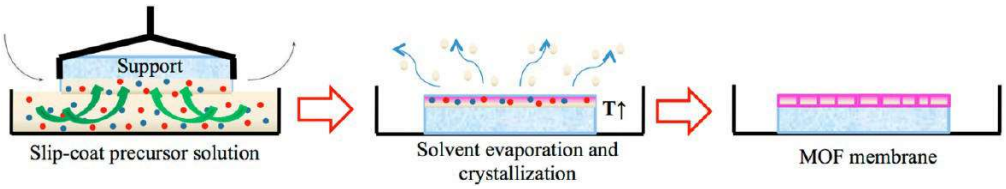


Figure 4-48: Schematic mechanism of rapid thermal deposition (RTD) [160].

In the original report, the evaporation of the solvent was controlled by switching off the oven after a certain time (for HKUST-1 and ZIF-8: 15 min [160]). Shah *et.al.* chose this time as a compromise between the evaporation of the solvent and formation of the crystals. If the timescale for the evaporation is too short, no crystals will be formed and if the timescale for evaporation is too long, the crystals are more distributed and well-grown films cannot be formed. At first, a high temperature is chosen to enable a fast evaporation of the solvent and enhance the formation of crystals. After switching oven off, the temperature decreases and the evaporation speed also decreases. At the same time, the homogenous crystallisation rate of the MOF increase. The slow cool-down in an oven help to from a homogenous intergrown thin-film, while the “temperature shock” of placing the sample directly from an oven to RT might make the film less homogenous or lead to cracks in the coating.

However, for the growth of MIL-53(Al), the synthesis was slightly modified. In the RTD approach, Shah *et.al.*[160] removed excess reaction mixture from the surface by wiping away with paper towel. The film was formed from residue of reaction mixture in the pores of the used porous support [137],[160], which was not possible for a flat surface such as glass. During the experiments, the glass slides were tilted after immersion in reaction

mixture to let the excess reaction mixture run off. A solvent film remained on the glass surface.

Shah *et.al.* [160] have stressed out the importance of switching off the oven and slow cool down inside of the oven during RTD. However, for MIL-53(Al), no improvement of the surface coverage or morphology was observed by switching off the oven during the experiment. Two glass slides were covered with MIL-53(Al) reaction mixture in DMF. One of the slides was placed in oven at 150°C for 2 h. The other glass slide was placed in oven at 150°C for 15 min and then the oven switched off and the sample left in oven for 105 min. Both glass slides have therefore a total reaction time of 2 h. However, no difference between the two glass slides was observed (Figure 4-49). Consequently, in the following RTD experiments the oven was not switched off and the samples kept at the same reaction time for the whole experiment.

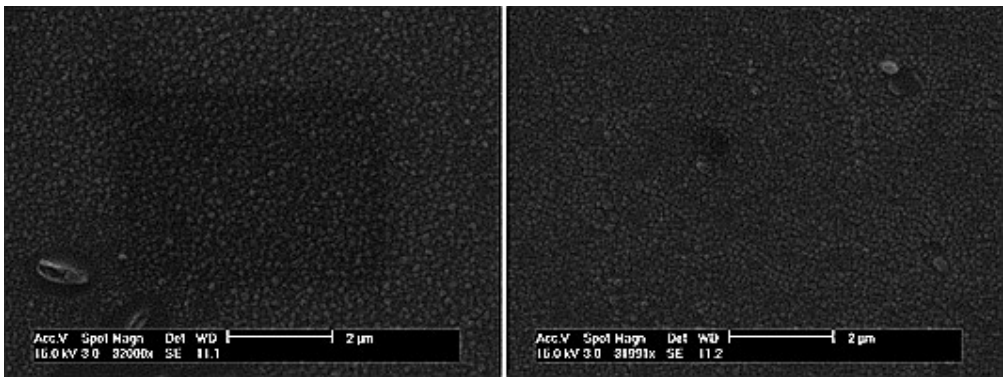


Figure 4-49: SEM image of a glass slide covered with MIL-53(Al) in RTD approach. No difference between a glass slide that coated according to the original RTD approach (reaction at 150°C for 15 min with consecutive switching off oven for a total reaction time of 2 h, left) and a glass slide that was placed at 150°C for 2 h (right) can be seen. In both cases the surface is covered with small particles of MIL-53(Al).

In order to find the optimum reaction conditions for MIL-53(Al) thin-film preparation, samples were synthesised with varying temperatures (100°C to 150°C), reaction times (1 to 5 h) and reactant ratio. These reaction times and reaction temperatures have been chosen because in chapter 3.3.3 (p. 53), 1 h reaction time and 100°C have been identified as possible lower boundaries for the successful formation of MIL-53(Al) in DMF, while 150°C was identified as a critical temperature for the mechanical stability of a glass fibre [338] (this investigation is a preliminary study for the coating of LPG fibre). Further, the metal to linker ratio of the reaction mixture was identified by Lu *et.al.* [141] as an important parameter affecting the quality of a MOF thin-film. Therefore, three metal-linker ratios were used during the experiments: (I) nearly equimolar concentrations (similar to the MIL-53(Al) powder synthesis; NEq; 1.1/1), (II) excess of metal (Mex; 2/1) and (III) excess of linker (Lex; 1/2). An overview of the results for the investigated conditions for the RTD approach can be seen in Table 4-4.

Table 4-4: Results of the RTD experiments

Reaction mixture	Time (h)	Temp (°C)	Morphology	XRD signal at ~8.8° for MIL-53(Al)	SEM image / XRD pattern
NEq (1.1/1)	1	100	Spherical	No signal	Figure 9-1
	3	100	Spherical	No signal	Figure 9-2
	5	100	Spherical	No signal	Figure 9-3
	1	125	Agglomerated	Yes	Figure 9-4
	3	125	Agglomerated	Yes	Figure 9-5
	5	125	Agglomerated	Yes	Figure 9-6
	1	150	Agglomerated	No signal	Figure 9-7
	3	150	Agglomerated	Yes	Figure 9-8
	5	150	Agglomerated	Yes	Figure 9-9
	~17h	150	Agglomerated	Yes	Figure 9-10
Mex (2/1)	1	100	Spherical	No signal	Figure 9-11
	3	100	Spherical	No signal	Figure 9-12
	1	125	Spherical	No signal	Figure 9-13
	3	125	Spherical	No signal	Figure 9-14
	1	150	Spherical	No signal	Figure 9-15
	3	150	Spherical	No signal	Figure 9-16
	5h	150	Spherical	No signal	Figure 9-17
Lex (1/2)	1	100	Spherical	No signal	Figure 9-18
	3	100	Spherical	No signal	Figure 9-19
	1	125	Spherical	No signal	Figure 9-20
	3	125	Spherical	No signal	Figure 9-21
	1	150	Agglomerated	Yes	Figure 9-22
	3	150	Agglomerated	Yes	Figure 9-23
	5	150	Agglomerated	Yes	Figure 9-24

The observed shapes of particles during the RTD can be divided into two types (Figure 4-50). One type of particles are smaller angular particles, which have a size of around 100 nm and agglomerate to form larger covered areas. The other type of particles only sparsely covered the surface. They had a larger spherical shape and a size between 100 and 300 nm. However, only for glass slides which show the angular particles on the surface, a broad peak around ~8.7° was visible in the XRD pattern, that can be correlated with the most intensive peak of MIL-53(Al) (Figure 4-51). Other peaks of MIL-53(Al) might be too small to be seen in the XRD pattern of the glass slides. For glass slides which are only covered with the larger spherical particles, no peaks in XRD pattern were visible even

after prolonged XRD measurement times (up to 15 h). This may indicate, that the glass slides, which show only spherical particles on the surface, are not covered with MIL-53(Al) or that the surface coverage is not good enough to show a peak in XRD. SEM images and XRD patterns of all samples are presented in the appendix (appendix A; Figure 9-1 to Figure 9-24).

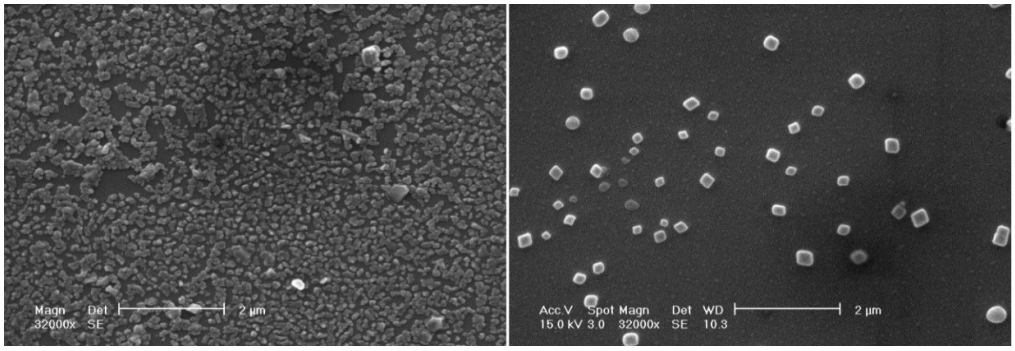


Figure 4-50: Comparison of the particle types found on RTD coated glass slides. Left: Glass slides coated with small particles, which intergrow on the surface (NEq, 5 h, 150°C). Right: Glass slide covered with larger spherical particles (NEq, 1 h, 100°C).

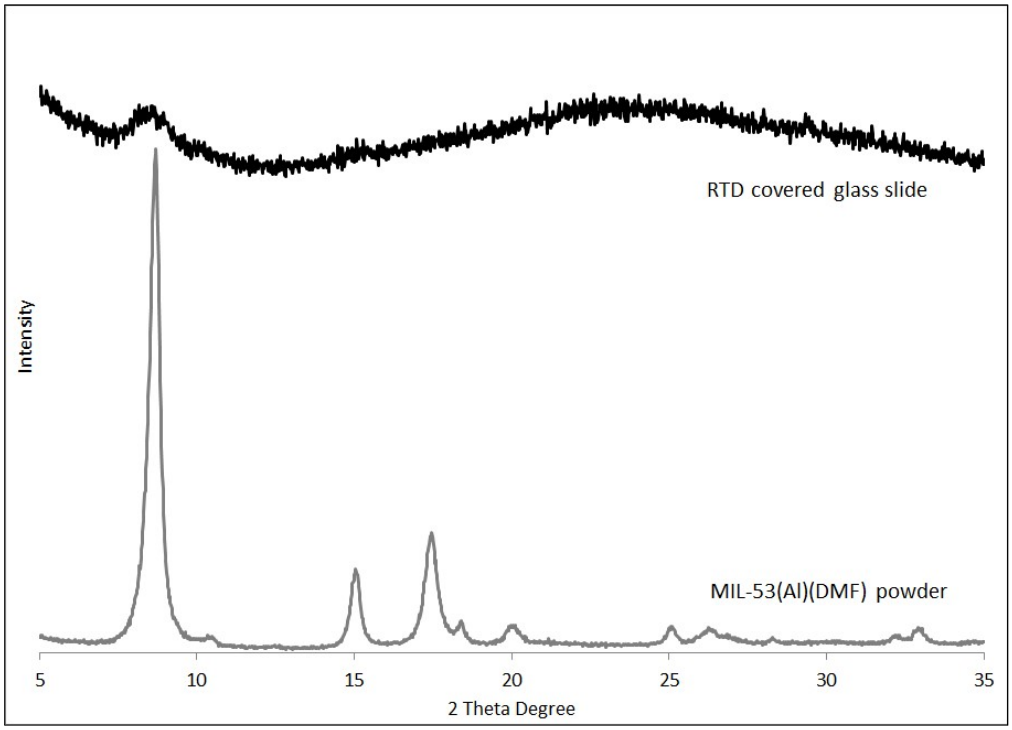


Figure 4-51: XRD pattern of glass slide covered by RTD (black; NEq, 5 h, 150°C) which has shown small agglomerated particles on the surface (Figure 4-50, left). The broad peak at ~8.8° is in good correlation with the XRD powder pattern of MIL-53(Al)(DMF) (grey).

The results of the RTD study have shown correlations between the reaction time and the surface coverage. A comparison of the surface coverage of glass slides prepared at 150°C with a NEq-reaction mixture is shown in Figure 4-52. Samples with 1 h and 3 h reaction time have a similar surface coverage, but larger triangular particles are also visible. After 5 h reaction time, these larger particles are not visible on the surface anymore, but at the expense of a slightly lower surface coverage. The nature of these triangular particles could

be not identified. A speculation is that they are residue of starting martial. With shorter reaction times (<3 h) they remain on the surface. After longer reaction times (5 h) they have reacted to MIL-53(Al), but left small gaps in the coating. For comparison, one sample was also coated by RTD, but with prolonged time reaction time (overnight; ~17h). For this sample increased surface coverage (no gaps) and no triangular shaped particles were observed.

Further, the results from Table 4-4 may suggest, that the reaction time has a less important effect onto the formation of MIL-53(Al) particles of the surface. If the temperature was high enough (125°C), the formation of MIL-53(Al) on the surface was possible even after 1 h. Below 125°C no agglomerated particles were visible on the surface of NEq samples. The only exception is the sample with was with reaction time of 150°C for 1 h. In the SEM images, agglomerated particles were observed, but the XRD pattern did not show any signal which can be attributed to MIL-53(Al). This might be explained with the low surface coverage of this sample (Figure 9-25).

On the contrary, the ratio of the reaction mixture strongly influences the formation of the different morphologies. With excess of metal (Mex), it was not possible for any sample to prepare the smaller agglomerating particles on the surface. In the meantime, for excess of linker (Lex), the minimum temperature required to prepare the angular particle type was increased to 150°C.

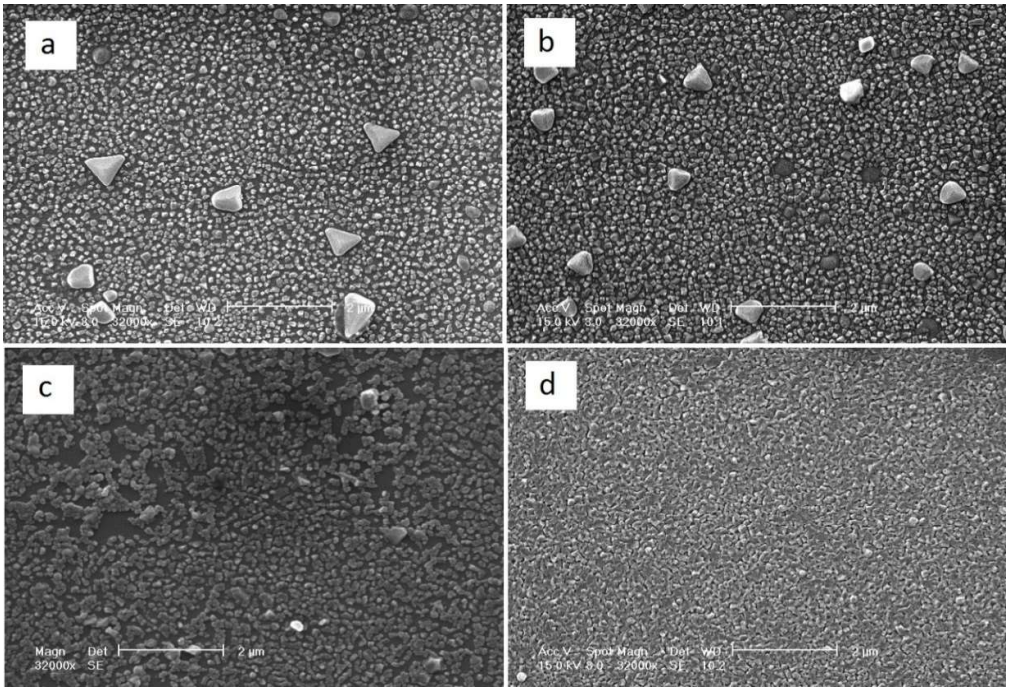


Figure 4-52: SEM images of glass slides covered by RTD approach with NEq solution with reaction time of a)1 h, b)3 h, c) 5 h and d) overnight (~17 h) at 150°C.

Although it was partially possible to coat glass slides with MIL-53(Al) by this approach, the surface coverage of the glass slides remained problematic (Figure 4-53). Large parts of the surface were coated with particles which resemble petals (*e.g.* NEq, 1 h, 150°C). The shape of these particles is similar to the shape of the particles of a glass slide which was only

coated with H_2BDC in DMF (Figure 4-54). In addition, peaks of H_2BDC could be seen in the XRD pattern of some RTD coated glass slides (Figure 4-55).

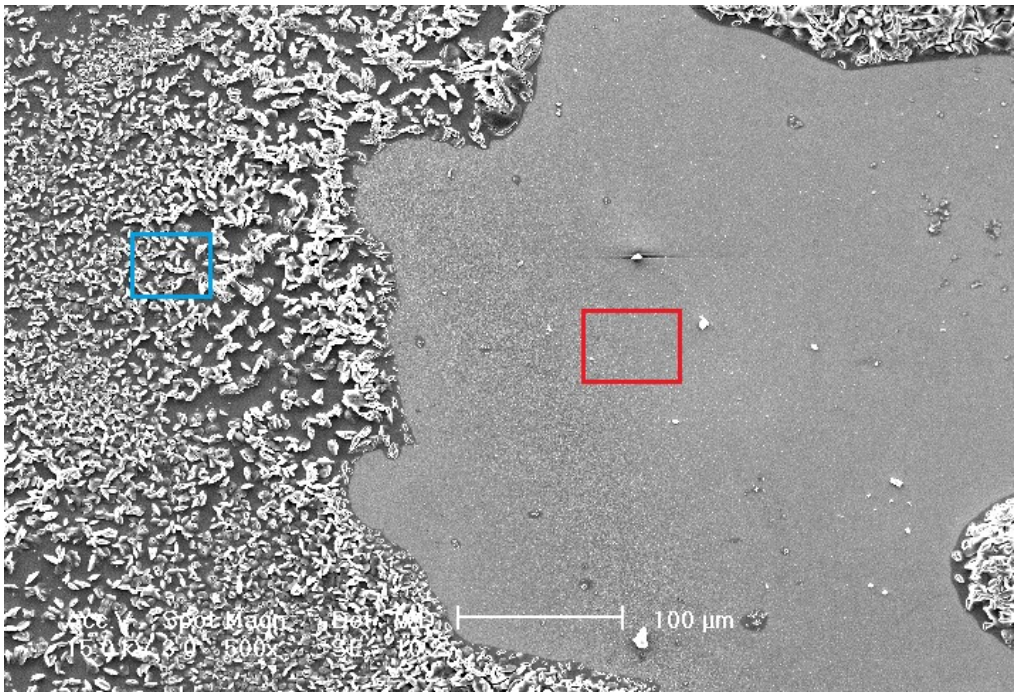


Figure 4-53: SEM image of glass slide covered by RTD approach (NEq, 1 h, 150°C), while in the red area crystalline particles are found (Figure 4-52 a), the blue area is covered with petal shaped particles (see image below).

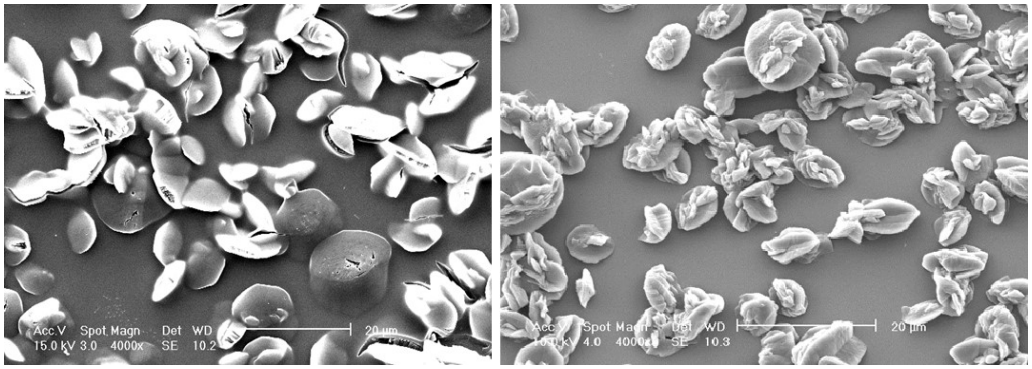


Figure 4-54: SEM image of glass slide covered in RTD approach (NEq, 1 h, 150°C, see blue area in Figure 4-53) and of a glass slide which was only covered with H_2BDC dissolved in DMF.

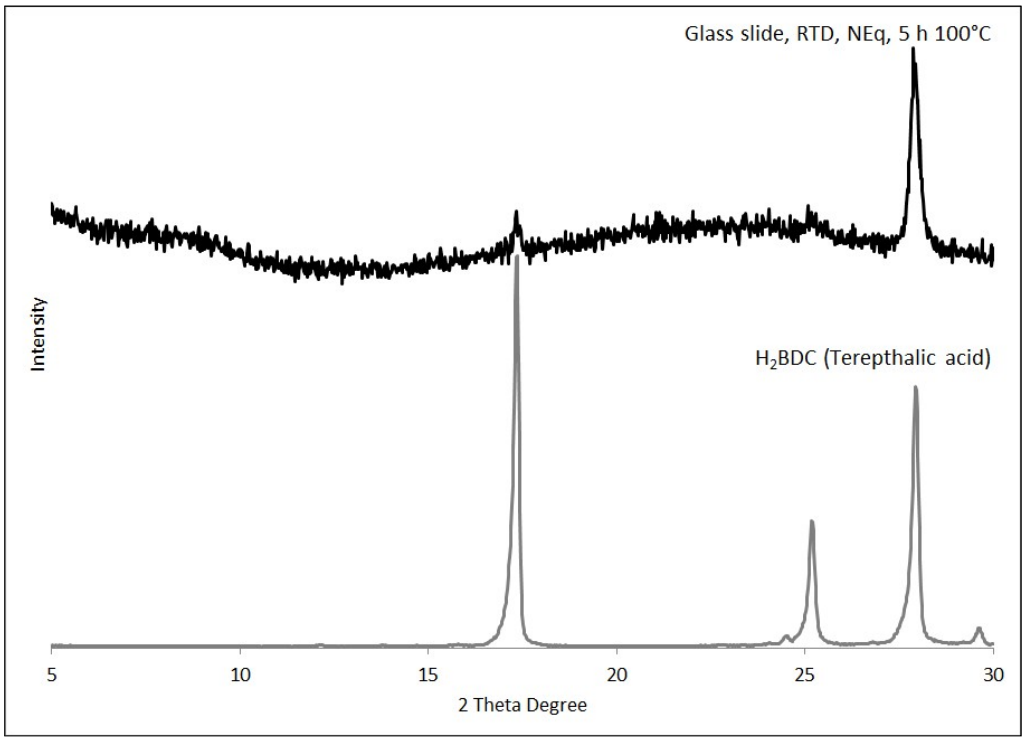


Figure 4-55: XRD of glass slide covered by RTD (NEq, 5 h, 100°C; black) in comparison with XRD pattern of H_2BDC.

On other RTD glass slides (*e.g.* Lex, 3h 150°C), the coating has a flake-like appearance (Figure 4-56). They show in the SEM images a type of exfoliation, which resemble the coating of a glass slide which was coated only with $Al(NO_3)_3 \cdot 9H_2O$ in DMF. Results from chapter 4.7 (p. 107) has shown, that residue of metal does not show peaks in XRD pattern and can only verified by SEM images.

In summary most glass slides coated by the RTD approach, were mostly covered with unreacted starting material of $Al(NO_3)_3 \cdot 9H_2O$ or H_2BDC and only small areas of the surfaces were covered with MIL-53(Al).

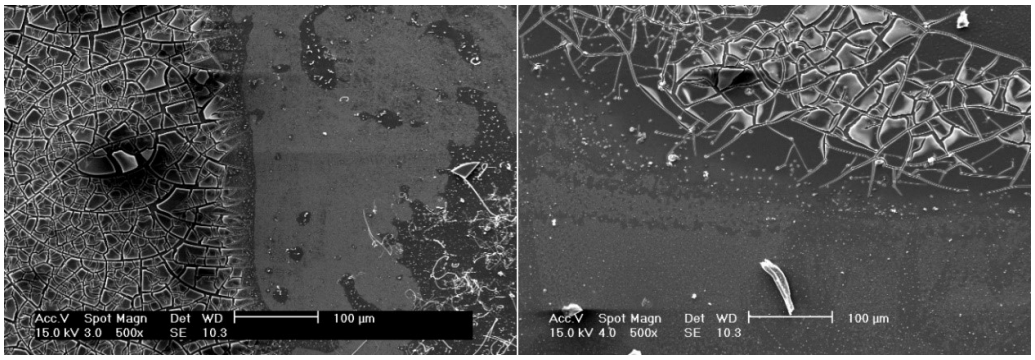


Figure 4-56: SEM image of glass slide coated only with $Al(NO_3)_3 \cdot 9H_2O$ in DMF (from Figure 4-44, left) in comparison with a glass slide covered by RTD (Lex, 3 h 150°C).

4.9 Solvent assisted epitaxy

The RTD coated glass slides have only shown a low coverage of MIL-53(Al) and the surface was mostly covered with unreacted starting material (both metal and linker). In contrast

to RTD, which was reported for HKUST-1 [160] and ZIF-8 [364], the thin-film growth of MIL-53(Al) seems to be not induced by the controlled removal of solvent. On the opposite, the complete formation of a MIL-53(Al) seems to be prevented. The results from the RTD coatings imply, that due to the evaporation of the solvent, the thin-film growth stops before a homogenous film can be formed and starting material starts to precipitate. It might be therefore possible to prevent the evaporation of the solvent and stimulate the growth of MIL-53(Al) films by placing a sample, covered with MIL-53(Al) reaction mixture, in a saturated atmosphere of solvent. If the reaction is performed in a closed vessel with a saturated atmosphere, the solvent from the reaction mixture on the glass slide cannot evaporate. Metal and linker cannot precipitate anymore, and they might react to MIL-53(Al) on the support. Since the growth of the film on the surface will be assisted by solvent vapour, which might prevent the precipitation of the starting materials, this approach will be called solvent-assisted epitaxy or SAE for short, in the following section.

For SAE, the following experimental set-up (Figure 4-57) was developed. The glass slide was wetted with a MIL-53(Al) reaction mixture in DMF and placed in a larger crystallizing dish on a mesh. The mesh was placed on a porcelain evaporation dish, which acted both as support for the mesh and as reservoir for DMF. The crystallisation dish was covered with a lid and placed in an oven for the reaction. At elevated temperature, DMF evaporates and created a saturated solvent atmosphere. This experimental set-up was not completely tight sealing, but by choosing the right temperature (up to 150°C, Bp of DMF: 153°C) and adding sufficient DMF to the reservoir, a saturated atmosphere was maintained during the experiment.

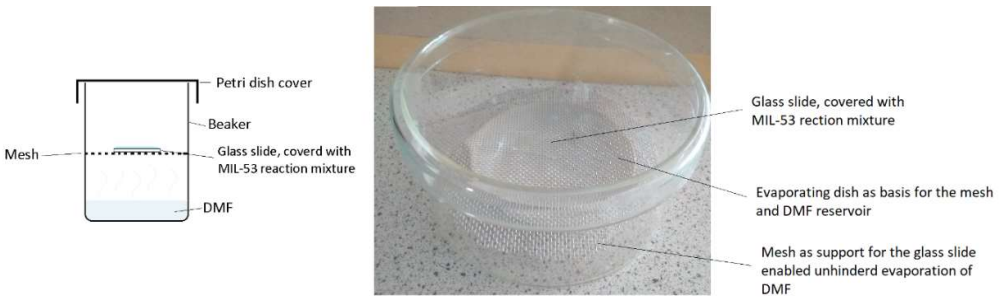


Figure 4-57: Schematic illustration (left) of set-up for the solvent-assisted evaporation (SAE) and image of the used experimental set-up (right).

During the RTD experiments, the reaction mixture of near equimolar composition (NEq) will act as starting point for the SAE experiments. The effect of reaction temperature and time will be investigated for the performance of SAE.

To investigate the influence of the reaction temperature, glass slides were coated at varying temperatures (ranging from 75°C to 150°C) with a given reaction time of 5 h and comparable to the RTD approach, a minimum temperature seemed to be necessary for the formation of MIL-53(Al). At 75°C, the surface was only covered with larger particles (~5 µm diameter) (Figure 4-58) interrupted by large gaps between these particles. At higher magnification, these particles looked like petals, which was found during the coating of glass slides by RTD and LbL and imply residue of unreacted linker on the surface.

These particles were more fused than the particles found during RTD or LbL, but the XRD pattern (Figure 4-59) of the surface confirm that the surface is only covered by H_2BDC.

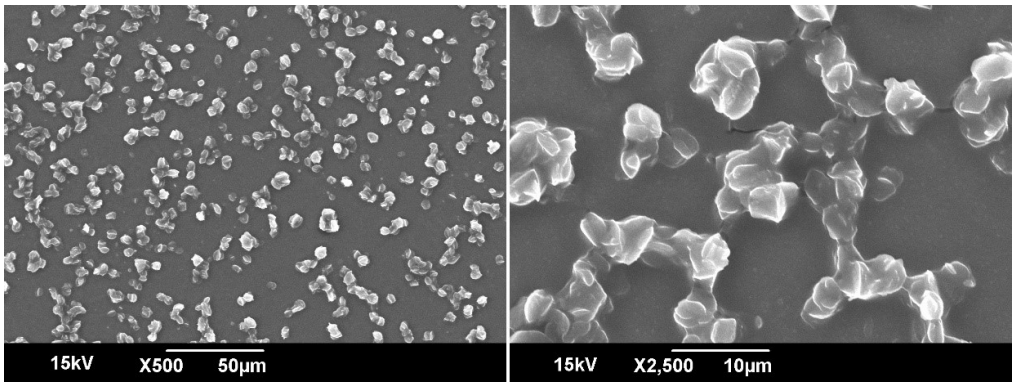


Figure 4-58: SEM image of glass slide covered by SAE at 75°C with 5 h reaction time. The surface is only covered with particles of H_2BDC.

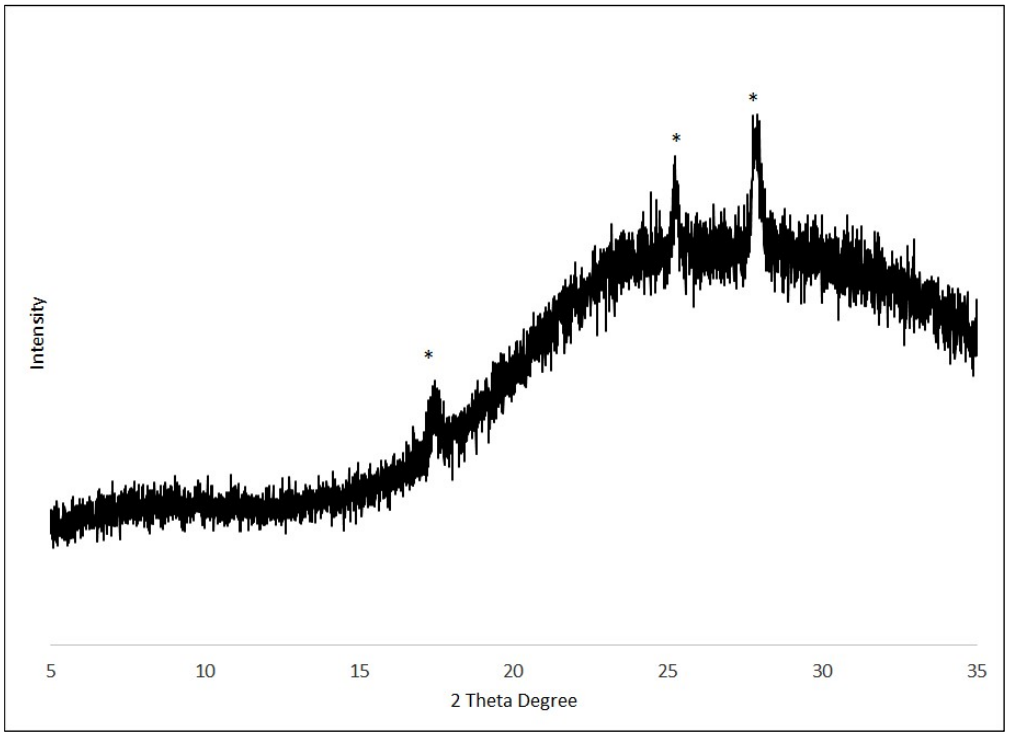


Figure 4-59: XRD pattern of glass slide covered by SAE at 75°C with reaction time of 5 h. Visible peaks at 17.57°, 25.19° and 27.95° (highlighted by asterisks) are in good agreement with peaks for H_2BDC.

At 100°C reaction temperature, the surface was covered with flake-like particles on the surface (Figure 4-60), with larger gaps between the individual flakes. For glass slides covered only with metal starting material ($Al(NO_3)_3 \cdot 9H_2O$), flake-like particles were found on the surfaces which have a smooth surface (Figure 4-44). However, higher magnification of the flakes in Figure 4-60 showed, that they are agglomerated clusters of smaller particles. MIL-53(DMF)(Al) powder samples have shown a tendency of agglomeration before, which may imply that these flakes on the surface are also composed of agglomerated cluster of MIL-53(Al). However the XRD pattern (Figure 4-61) has not shown

any peaks which can be attributed to MIL-53(Al). This might be caused by the gaps between the flakes on the surface and the resulting low surface coverage.

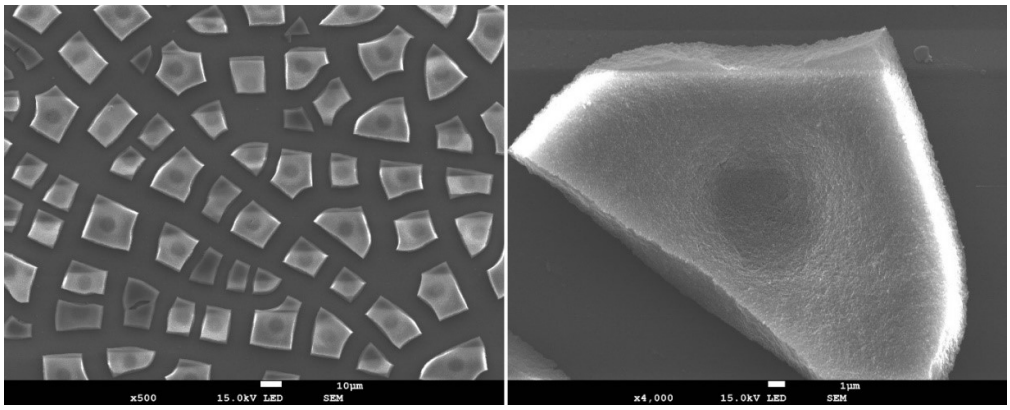


Figure 4-60: SEM images of glass slide covered by SAE at 100°C with reaction time of 5 h.

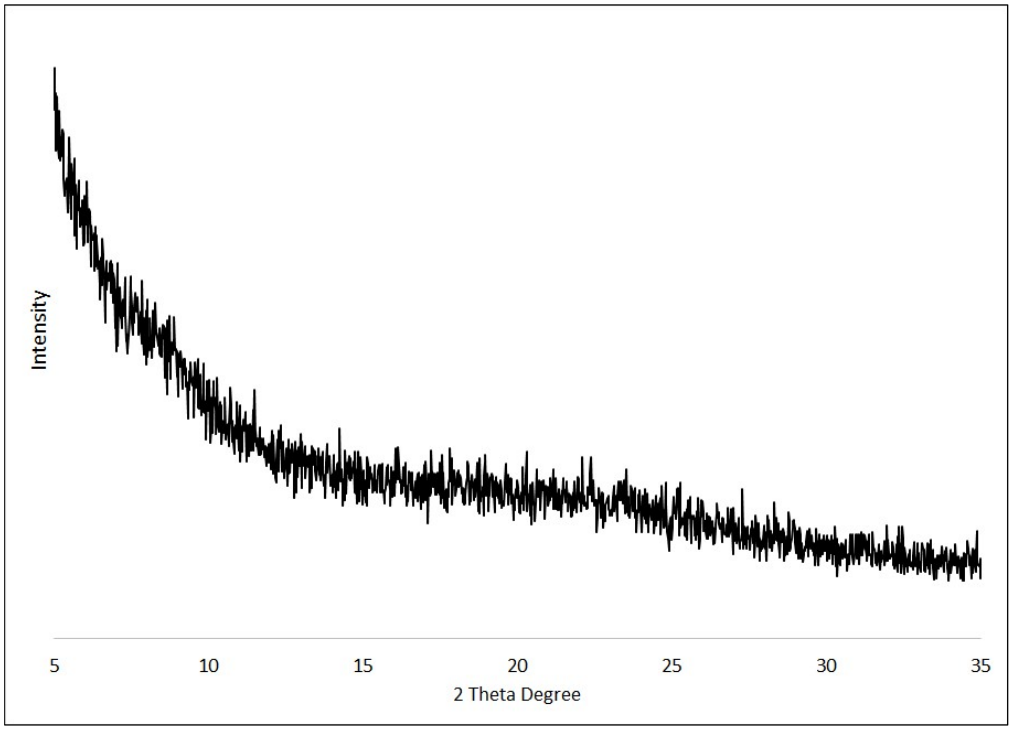


Figure 4-61: XRD pattern of glass slide covered by SAE at 100°C with reaction time of 5 h.

At 125°C, the surface is covered with particles (Figure 4-62), which resemble the larger flakes of the SAE-coated glass slide at 100°C and 5 h reaction time (Figure 4-60), but with smaller gaps between the individual flakes. Probably due to the higher surface coverage, the successful coating with MIL-53(Al) could be verified by XRD (Figure 4-63). This might further confirm that the particles on the glass slide covered at 100°C are also composed of MIL-53(Al), but the lower temperature has prevented intergrowth to a film on the surface.

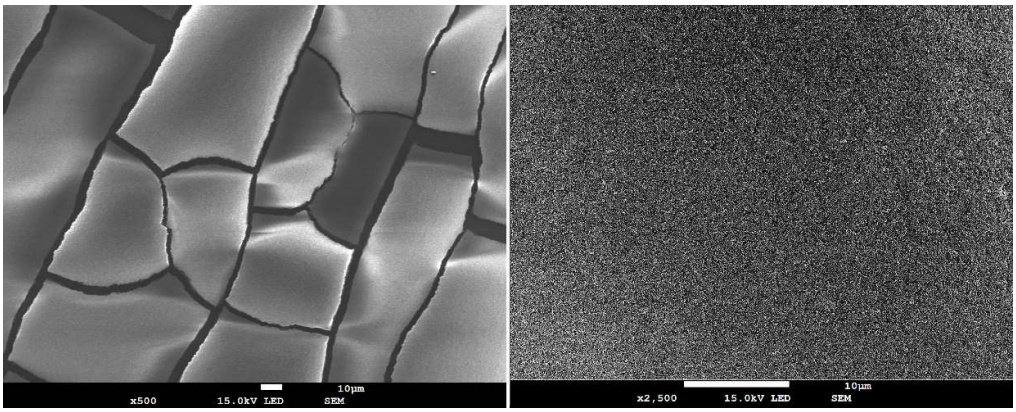


Figure 4-62 SEM image of glass slide covered by SAE at 125°C with 5 h reaction time. Surface is covered by flakes, with cracks between the particles. At higher magnification, it is visible that the surface is composed of agglomerated smaller particles.

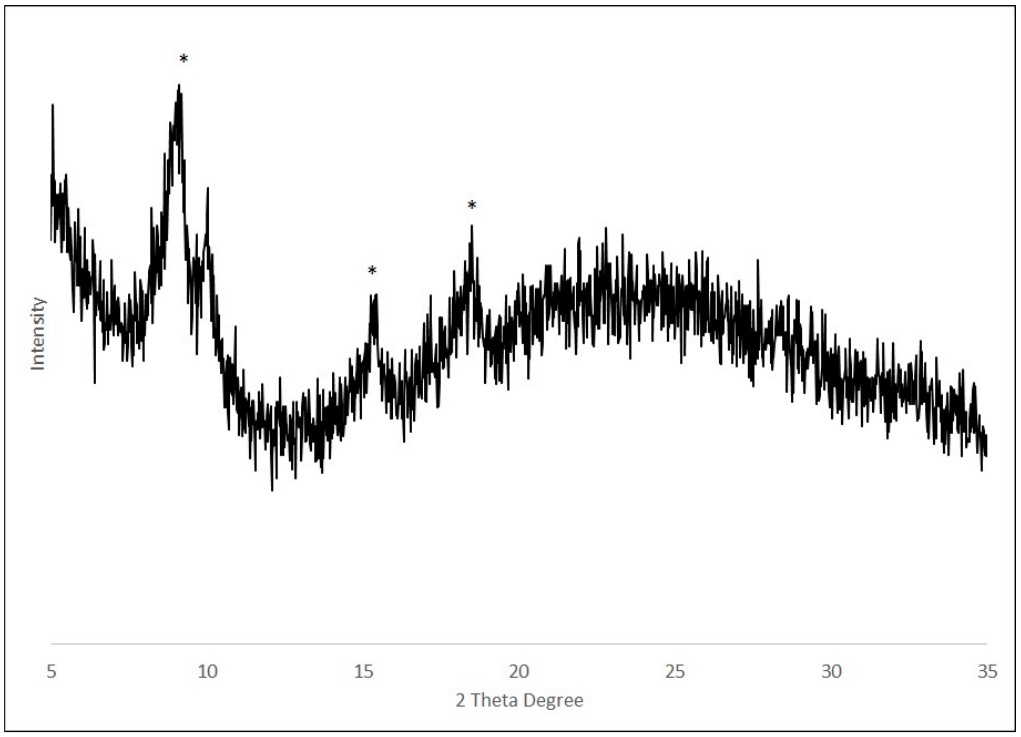


Figure 4-63: XRD pattern of glass slide covered by SAE at 125°C with reaction time of 5 h. Peaks at 9.0°; 15.3° and 17.9° are in good agreement of MIL-53(Al)(DMF) (highlighted by asterisks).

At a higher reaction temperature of 150°C, the surface was completely covered (Figure 4-64) and only at higher magnification, small cracks in this coating were visible. The XRD pattern of the coated glass slide further confirmed the successful coating with MIL-53(Al) (Figure 4-68). This further implies that a high enough temperature of 150°C and resulting high reaction rate is necessary for the intergrowth of the particles to form a homogenous film on the surface. Another advantage of this SAE approach seems to be that the resulting coatings are much more homogenous in comparison with coatings (*e.g.* prepared in-situ or by RTD) prepared before in this chapter. The SAE at 150°C and 5 h reaction temperature, results in coating with a thickness of about 4 µm and the cross-section image (Figure 4-66) showed between the highest and thinnest point of the surface only ~0.01 µm difference.

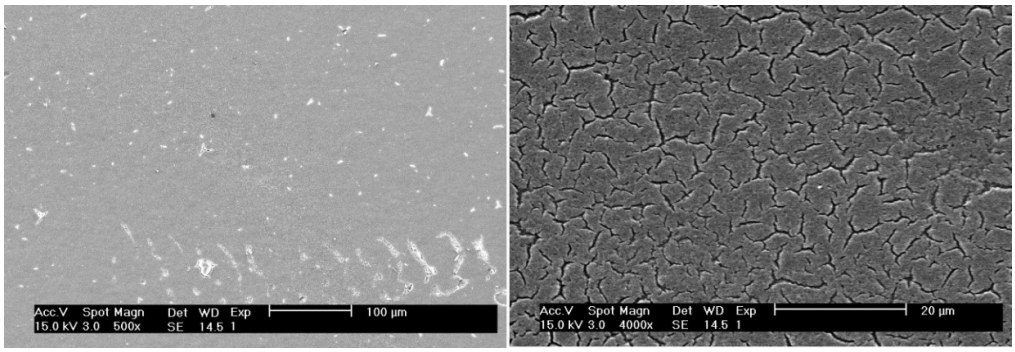


Figure 4-64: SEM image of glass slide covered by SAE at 150°c for 5 h. At lower magnification (left) is the surface completely covered and only at higher magnification (right) are small cracks visible in the coating.

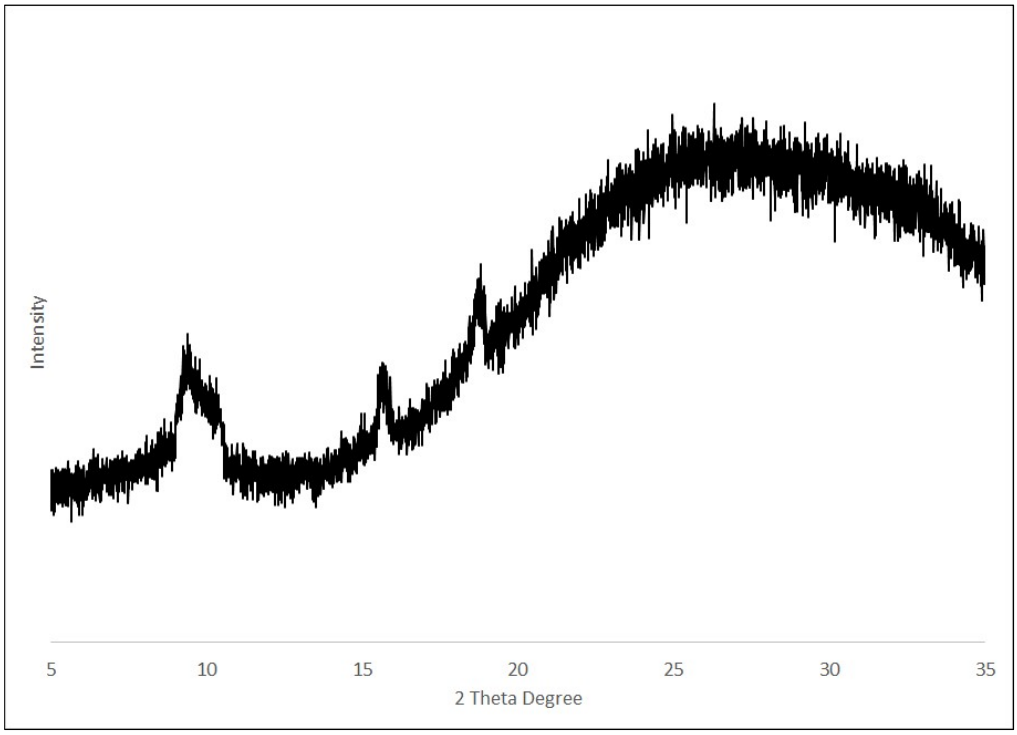


Figure 4-65: XRD pattern of glass slide covered by SAE at 150°C with a reaction time of 5 h.

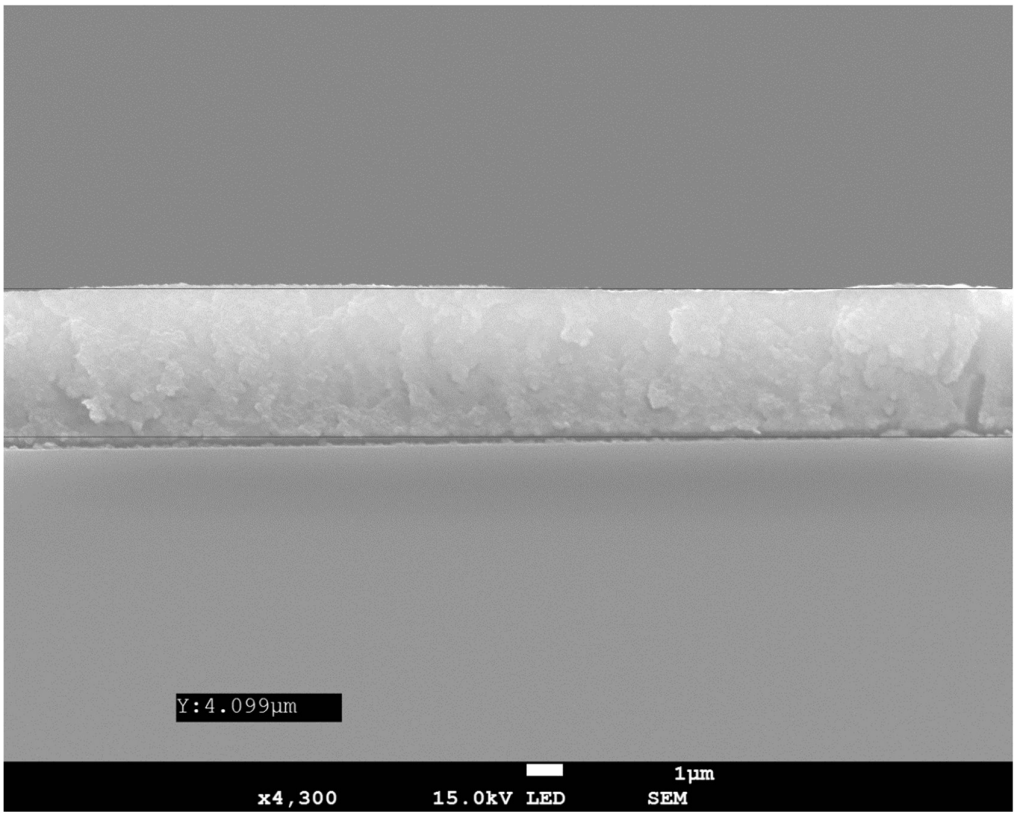


Figure 4-66: Cross-section image of glass slide covered with MIL-53(Al)(DMF) by SAE at 150°C with reaction time of 5 h.

For the investigation of the reaction time (1 h to 5 h) to the surface coverage, the temperature was kept at 150°C. In the section before, the glass slide covered at 150°C was covered complete and nearly crack-free with MIL-53(Al) (Figure 4-64) and it was deemed reasonable to use this reaction temperature to investigate the effect of the reaction time. In Figure 4-67, the result after 1 h reaction time is presented. The surface was only partly coated and this coating is composed of agglomerated individual particles, but in contrast to glass slides coated for 5 h the agglomeration was less homogenous, because individual particles can be still identified and have not fused. Furthermore, the surface was only partly covered with MIL-53(Al) coating. Consequently, the overall surface coverage might be too low to show peaks the XRD pattern of this glass slide (Figure 4-68) which can be attributed to MIL-53(Al).

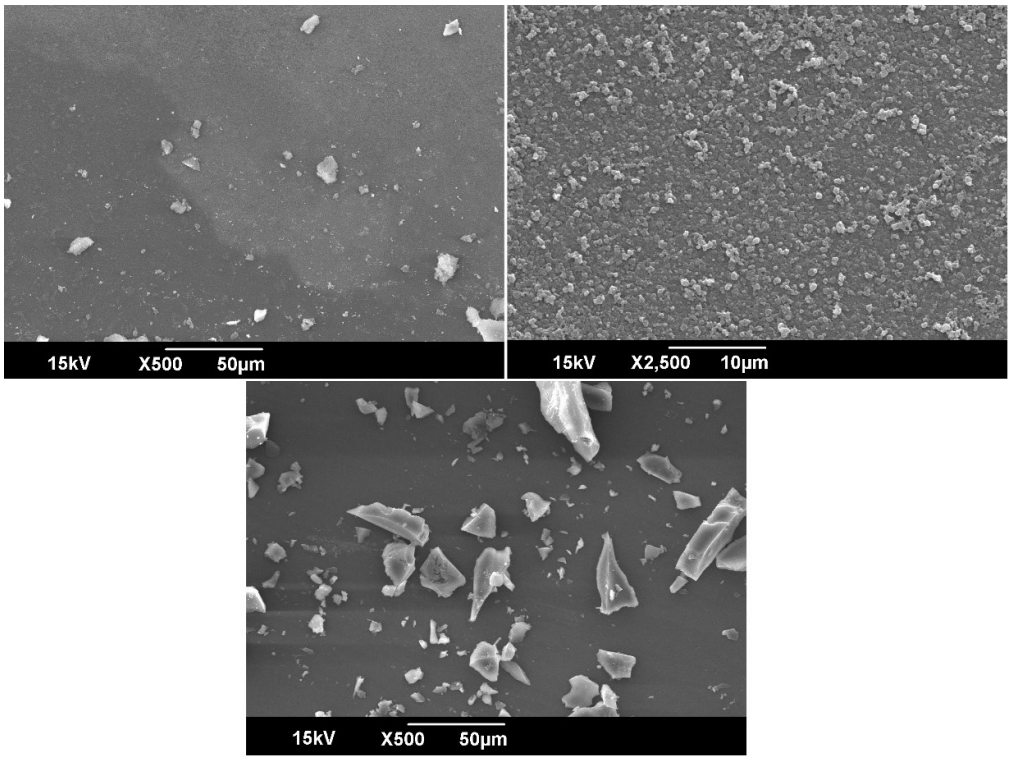


Figure 4-67: SEM image of glass slide covered by SAE at 150°C and reaction time of 1 h. At lower magnification (top left) the surface seems to be only partly covered. At higher magnification, these particles might be identified as MIL-53(Al)(DMF) due to the spherical shape (top right). Not the whole surface is covered, instead some areas are just covered with a few clusters of agglomerated particles (bottom).

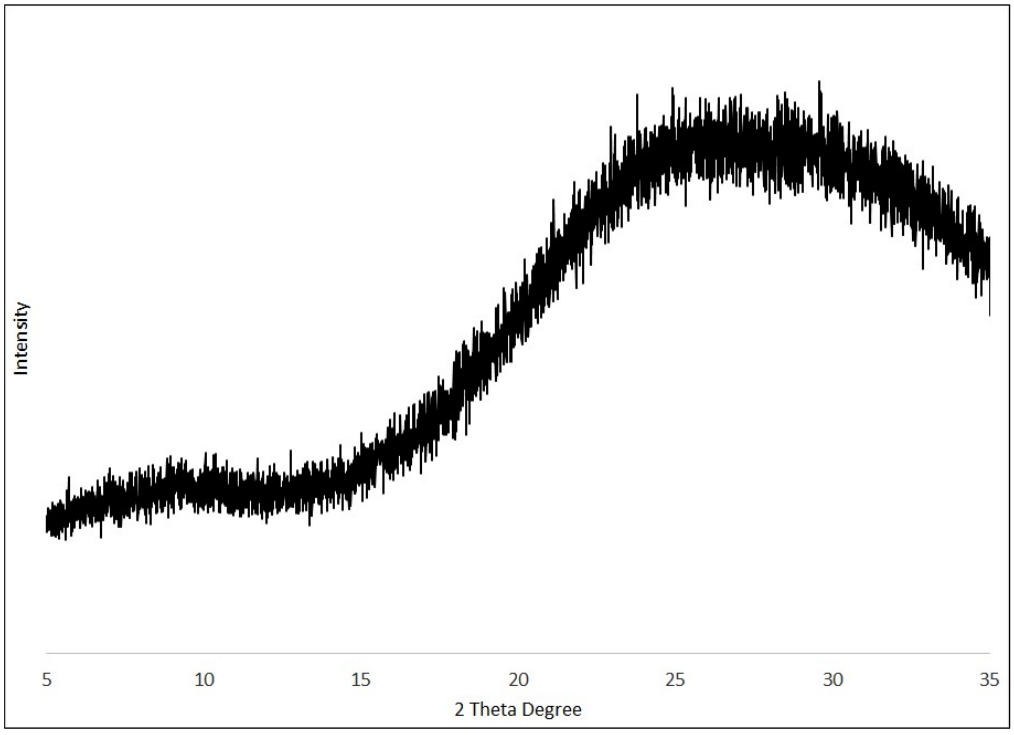


Figure 4-68: XRD pattern of glass slide covered by SAE at 150°C with reaction time of 1 h.

In contrast, the glass slide treated for 3 h at 150°C showed a higher surface coverage than the 1 h sample. In Figure 4-69, the surface was mostly coated, but with small areas of lower

coverage (as darker strains). At higher magnification the particles were, in contrast to the 1 h sample, fused which leads to a smoother surface of the coating. XRD pattern of the glass slide could further confirm the successful coating of the surface with MIL-53(Al) (Figure 4-70).

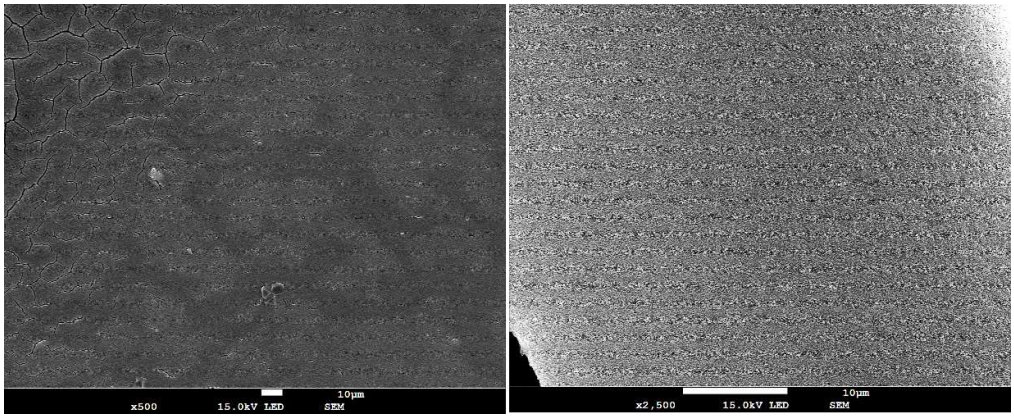


Figure 4-69: SEM image of glass slide covered by SAE at 150°C and reaction time of 3 h.

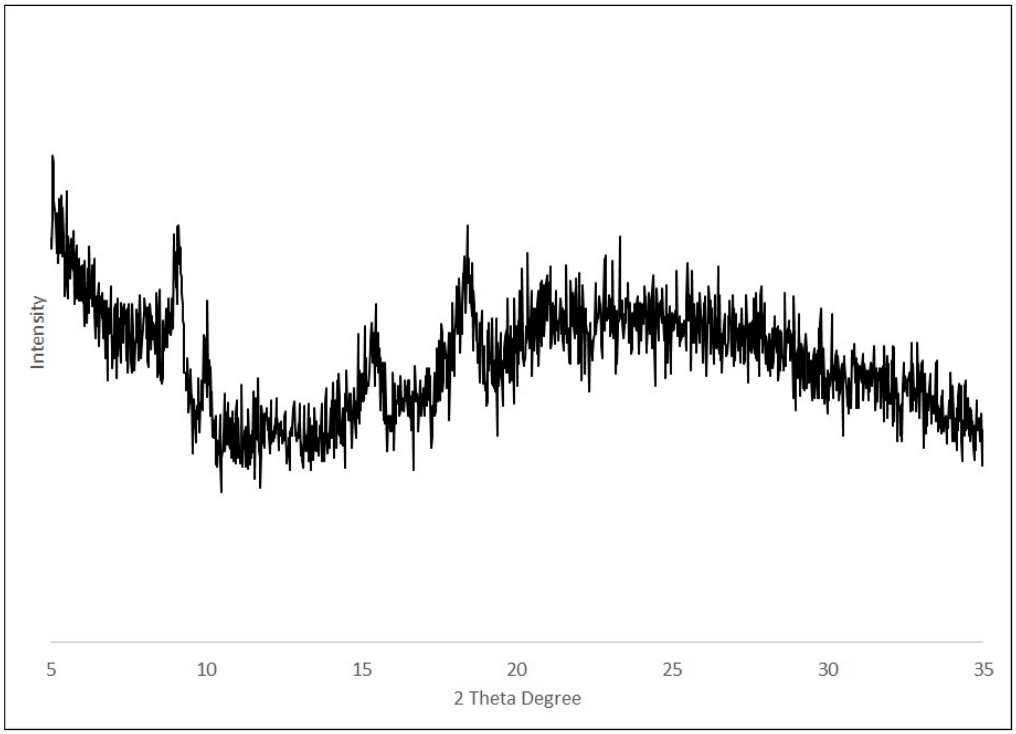


Figure 4-70: XRD pattern of glass slide covered by SAE at 150°C with reaction time of 3 h. Peaks corresponding of MIL-53(Al)(DMF) are visible on the surface, but in contrast to other samples with longer reaction time the intensity is lower and the peaks are less distinct.

4.10 Discussion and summary of the results from this chapter

For the most straightforward approach, the in-situ coating, the results are dependent on the used derivative of MIL-53(Al). While for MIL-53(Al)(H_2O) no particles could be attached to the surface, for MIL-53(Al)(DMF) the surface was mostly covered with particles, but gaps in the coating were visible. However, one advantage of this technique was the ease of

usage. The support can be placed in a reaction mixture similar to a powder synthesis and no additional preparation steps have to be done to the support for the thin-film coating.

Another approach during this research was the seeding and secondary growth approach. In this approach the surface was coated with smaller particles which act as seeds for a subsequent film- growth. The seeds help to control the thickness and morphology of the film on the surface. The investigation regarding this approach can be separated into the seeding part and the secondary growth part. Since a flat and inert glass surface was coated, only coating from a suspension by dip-coating could be applied. Other possible seeding approaches *e.g.* rubbing [170] of particles onto the surface can be only applied for rough surfaces, where the seeds remain in the pores. For the dip-coating of the surface, an extensive study was done, where the effect of the used solvent, concentration of the suspension and the used MIL-53(Al) derivative was investigated. While for lower concentration of 0.1 wt% the surface was only sparsely covered, for higher concentrations of 1.0 wt% problems like agglomeration of the particles or a weak attachment to the surface was observed. A 0.5 wt% suspension has shown the best results, especially in MeOH as solvent. A glass slide coated from a 0.5 wt% suspension of MIL-53(Al)(DMF) in MeOH was is completely covered with particles of MIL-53(Al) without the formation of larger agglomerated clusters. The coverage was lower when MIL-53(Al)(H_2O) was used. This can be partly explained with the morphology of MIL-53(Al)(DMF) in comparison to MIL-53(Al)(H_2O) and the properties of the used solvent. MIL-53(Al)(DMF) is composed of smaller spherical particles with a size of about 100 nm, which tend to agglomerate to larger particles, while MIL-53(Al)(H_2O) is composed of particles with size of several micrometer [346]. The results show that it was in MeOH possible to better separate the agglomerated cluster of MIL-53(Al) into individual particles in comparison with water. Glass slides coated from suspensions with MeOH as solvent have shown a uniform coverage of the surface. On the contrary, glass slides coated from suspension with water as solvent were covered with agglomerated cluster of MIL-53(Al) making the coating less homogenous (Figure 4-21). A possible reason might be that water is a highly polar solvent, while MeOH is composed of a polar hydroxyl group with an additional methyl group, which gives the molecule a nonpolar part. While MIL-53(Al) is in total a hydrophilic compound [365], it is composed of hydrophilic and hydrophobic parts (*e.g.* π-π interaction of the linker terephthalic acid) in close proximity [366]. We therefore speculate, that MeOH is able to separate the agglomerated cluster, because it can both interact with the hydrophilic and hydrophobic parts of MIL-53(Al), while water only interacts with the hydrophilic parts and forms a solvation shell around the MIL-53(Al) cluster with only a limited capacity to separate the individual particles. In order to further test this assumption, glass slides were coated with an alternative solvent, which contains both hydrophilic and hydrophobic parts. The coating in such a solvent might lead to a coating which look similar to the results of MeOH. The used solvent was tetrahydrofuran (THF), which contains as a cyclic ether a polar group and a nonpolar alkyl part. The results of the dip-coating in comparison with glass slides coated from MeOH as suspension for MIL-53(Al)(DMF) (Figure 4-71) and MIL-53(Al)(H_2O) (Figure 4-72) are shown below.

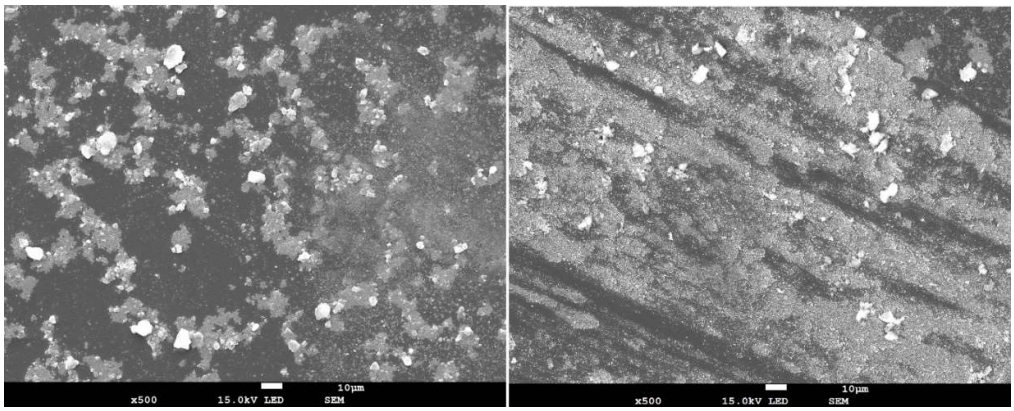


Figure 4-71: SEM image of glass slides covered by dip-coating from a 0.5 wt% suspension of MIL-53(Al)(DMF) in THF (left) and MeOH (right).

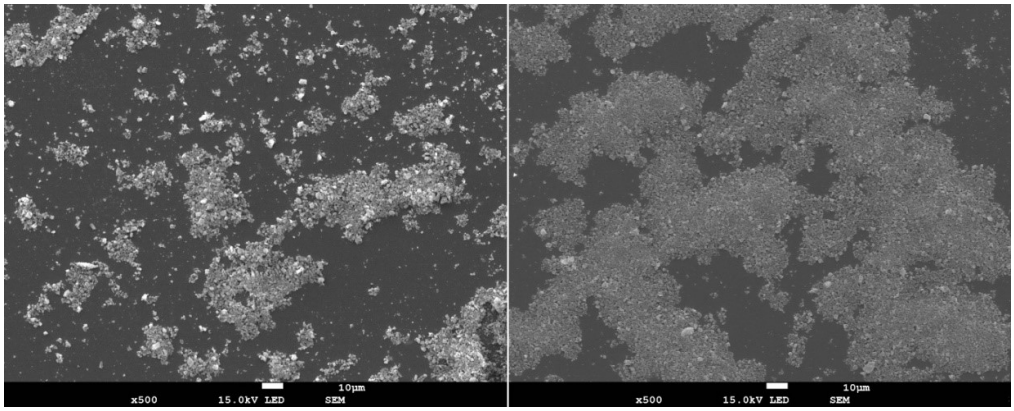


Figure 4-72: SEM image of glass slides covered by dip-coating from a 0.5 wt% suspension of MIL-53(Al)(H_2O) in THF (left) and MeOH (right).

The surface coverage of the suspensions containing THF was higher in comparison with water-suspensions (Figure 4-8 for MIL-53(Al)(H_2O) and Figure 4-17 for MIL-53(Al)(DMF)), but lower than with MeOH-suspensions. One possible explanation might be the difference in polarity of the different solvents. Water was, during this investigation, the solvent with the highest polarity of 1.85 D (Debye) [277] and only partly able to separate the agglomerated cluster of MIL-53(Al). THF has with 1.75 D [277] a slightly higher polarity than MeOH (1.70 D [277]). MeOH was better able to separate the agglomerated clusters of MIL-53(Al) to individual particles in the suspension which leads to a more homogenous coating of the surface. However, a certain polarity of the solvent is needed for the suspensions. A coating with nonpolar solvents like hexane was not found to be possible. In hexane, the particles do not form a suspension but stuck together (Figure 4-73).

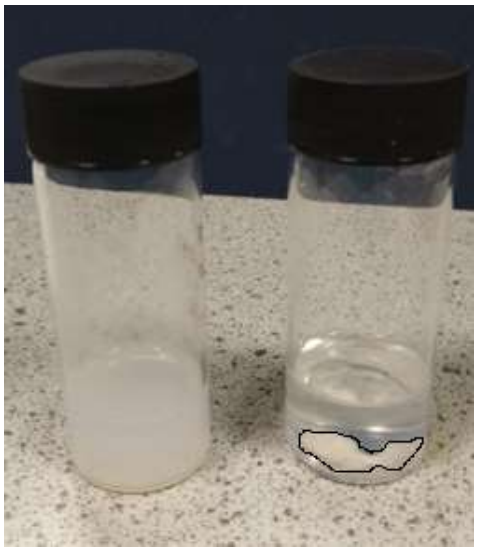


Figure 4-73: Image of freshly prepared 0.5 wt% coating suspension of MIL-53(Al)(DMF) in MeOH (left) and hexane (right). The position of the agglutinated MIL-53(Al)(DMF) in the vial was highlighted with a black marking

Other solvents with slightly lower polarity than MeOH might create an even more homogenous coating but MeOH already represents a good choice due to its low-cost and ease of removal. Another advantage of the usage of MeOH instead of water is the difference in surface tension and viscosity. The suspension in water as solvent formed a dome of suspension of the surface, which makes a homogenous coating of the surface difficult (Figure 4-74), which is known as coffee-stain effect [367].

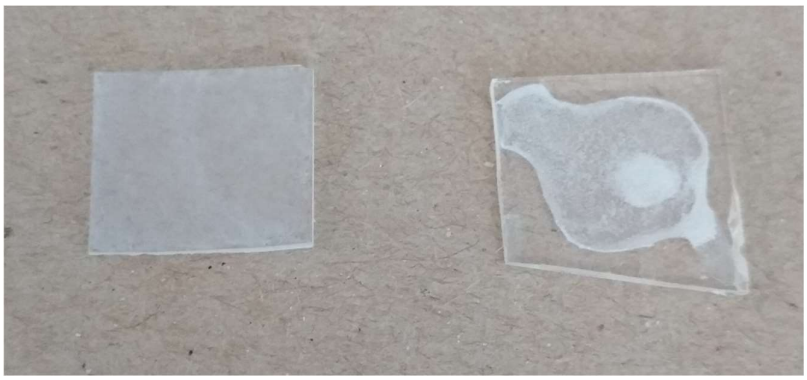


Figure 4-74: Photo of glass slides covered by dip-coating with MIL-53(Al)(DMF) with MeOH (left) and water (right) as solvent.

These coated glass slides by dip-coating from a 0.5 wt% suspension in MeOH were then used for secondary growth. However, the secondary growth has mostly led to a rough coating with large gaps (Figure 4-26). The coating with MIL-53(Al)(DMF) has a thickness between 2.1 µm and 3.2 µm (Figure 4-27).

Furthermore, was the effect on the surface treatment for the quality of the thin-film coating investigated. Several techniques have been used in literature, which not only remove contamination from the surface, but make the glass surface more polar at the same time to increase the interaction between the thin-film coating and the glass surface. One possibility the treatment of the surface with piranha acid, which can break Si-O groups

in order to add silanol groups. Another technique removes organic impurities by immersion of the support in an organic solvent with high vapour pressure (*e.g.* acetone or isopropanol) followed by immersion in a base (*e.g.* 0.1 M NaOH). Both techniques (piranha acid: Figure 4-11; acetone + NaOH: Figure 4-12) have been compared with glass slides, which have been only cleaned with acetone in order to remove possible organic impurities from the glass surface (Figure 4-8). However, no improvement of the surface coverage could be observed for glass slides which have been treated with piranha acid or NaOH. Consequently, were the glass slides in this chapter only cleaned with acetone, which prevents the use of highly corrosive compounds or time-consuming additional treatment steps.

As an alternative to the secondary growth, the repetition of the dip-coating to create a thin-film of MIL-53(Al) on the surface was also investigated. For the adding of several layer by dip-coating a suspension of 0.5 wt% in MeOH was used, which has shown the best results during the investigation of the seeding. The surface covered was with MIL-53(Al) without cracks and formation of agglomerated cluster (Figure 4-20). The dip-coating was repeated between 1 and 10 times to create "layers" of MIL-53(Al) on the glass surface. A repetition of the dip-coating process 5 times (creating 5 layers) was found to be sufficient for a homogenous coating of the surface. The glass slide has shown a homogenous coating of the surface without cracks and a resulting thickness between 338 nm and 821 nm (Figure 4-37), which is thinner compared to the coatings after seeding and secondary growth (2.1 µm to 3.2 µm; Figure 4-27). The results show that it seems to be not possible to create a much thicker coating by adding more layers. After repetition of the dip-coating 10 times with a 0.5 wt% suspension of MIL-53(Al)(DMF) in MeOH as solvent, the glass surface was covered with several agglomerated clusters, instead of the formation on a homogenous thin-film (Figure 4-36). The surface coating has become more rough. One advantage of the dip-coating approach was that already activated MIL-53(Al) was used. The solvent from the suspension can be easily removed by heating the sample at ~100°C before further application. In the other approaches, MIL-53(Al) was prepared in-situ, whereas unreacted starting material such as H_2BDC is trapped in the pores and has to be removed by methods such as reflux in DMF [368] or heating at elevated temperature (333°C for 3 days) [115]. While these conditions can be applied for powder samples, such harsh conditions might create cracks in the thin-film or destroy the support. Alternatives such as solvent exchange have to be sought and the results from the previous chapter 3.3.2 (p. 46, Table 3-5) have implied, that solvent exchange in MeOH is a suitable alternative for activation of MIL-53(Al) thin-films.

In contrast to the approaches before (in-situ, dip-coating, seeding + secondary growth) the Layer-by-Layer approach could be not successfully applied for MIL-53(Al) on glass. In this approach, the support was alternately immersed in metal and linker solution to stepwise grow a thin-film on the surface. Different reaction times and numbers of repetitions were investigated, but surface coverage and reproducibility of the results were problematic. A possible reason might be a low interaction between the starting materials and the glass surface. The starting material was washed away during the washing step with fresh solvent

and consequently no reaction could take place. Another possible reason is the low reaction rate at RT. The strong correlation between temperature and reaction rate of MIL-53(Al) was already investigated [356] and the chosen reaction times were not enough to enable the successful synthesis of MIL-53(Al) at RT. LbL synthesis at elevated temperature might be more difficult to apply.

The next investigated coating technique, rapid-thermal deposition, was successfully applied to different MOFs such as HKUST-1 or ZIF-8, but it was less successful for the preparation of thin films of MIL-53(Al). Although the RTD was extensively investigated regarding reaction temperature, reaction time and metal/linker ratio of the reaction mixture, it was not possible to create a homogenous thin-film of MIL-53(Al). The low surface coverage remains problematic for the RTD approach of MIL-53(Al). Further investigation has shown, that surfaces were only partly covered with MIL-53(Al), while most areas were covered with unreacted starting material. A possible reason was that the solvent evaporates faster than the metal and linker can react to MIL-53(Al) and the starting material precipitate on the glass surface.

Based on this observation (precipitation of the starting material), a new film coating method for MIL-53(Al) was developed, the solvent assisted epitaxy. In this approach, the glass slides were coated with a reaction mixture of MIL-53(Al) in DMF and placed in a saturated atmosphere of DMF, which prevents the precipitation of the starting material. The reaction conditions were optimised regarding reaction time and temperature and a nearly crack-free and homogenous coating could be successfully prepared at 150°C after 5 h reaction time. In addition, the SAE approach has led to a very smooth coating. A cross section verified, that the surface is covered with a film of 4.1 µm thickness and between the thinnest and thickest point of the surface is a difference off less than 20 nm (Figure 4-66).

In summary, the coating of glass with a thin-film of MIL-53(Al) by various different coating techniques has been investigated and especially the in-situ coating, dip-coating and solvent assisted epitaxy have shown promising results for the application as functional coatings on systems such as LPGs.

5 MIL-53(Al) coatings on LPG for CO_2 and VOC detection

5.1 Introduction

While the chapters before have aimed to solve typical problems of MOF synthesis *e.g.* to make the synthesis more sustainable (chapter 3; p. 38) or the formation of thin-films (chapter 4, p. 82), this chapter is trying to convert the obtained research results into an possible application, in this case the use of MOFs as sensor systems. An LPG will act as sensor platform, which has amongst the discussed fibre sensor systems several advantages such as being light-weight, low-cost and not affected by electromagnetical interferences. Furthermore have they response times, which are much shorter than existing commercial sensor systems [369]. For more information about LPGs (*e.g.* the working principle) the reader will be referred to chapter 2.3 (p. 10).

While LPGs are a promising real-time sensor system, is the problem that the measurement principle is based on changes of RI of the surrounding media. Some LPG sensor systems have been used as blank fibres, but this is often only possible for specific systems with known compositions, where a change of RI can be directly attributed to changes of concentrations in the target system. In these cases, the LPG has shown higher sensitives than classical measuring instruments like an Abbe-refractometer [100].

In contrast to blank LPG fibres, coating of LPG with a thin-film can both improve the sensitivity and selectivity of the sensor system by acting as both an adsorbent to concentrate the target compound on the surface and as a material, whose RI changes with concentrations [84]. These coatings are often made from nanoparticles such as SiO_2 nanoparticles (often modified, *e.g.* with calixarene as a weakly adsorbing systems for fast recovery [105]), because well-established methods of thin-film coating exist and the size of the nanoparticles can be easily controlled [107]. LPGs used in biological systems often use very sophisticated coatings including antibodies [370] or enzymes [350] to have specific responses.

While there are already several reports of LPGs sensors coated with alternative porous materials such as zeolites [371], it is surprising, that nearly no reports exist of LPG coated with MOFs, even though controllable pore size and chemical environment makes them promising systems for the usage of selective and sensitive LPG coatings. However, for the usage on LPGs, MOFs have several disadvantages. For instance the growth mechanism of MOFs is less well understood than that of zeolites [329], which is partly caused by the large diversity of existing MOF-structures. In addition MOFs are often only available as powders and the conversion to thin-film synthesis is not trivial [372]. Furthermore, due to the small size of the fibre and the cylindrical shape, some thin-film coating procedures cannot be directly used. For the sensor performance good control over the thickness while creating uniform films at the same time is of importance [327]. The thickness of the coating on a LPG is also important for the sensitivity [101]. Consequently, only two known MOF coated LPGs based on ZIF-8 [22] and HKUST-1 [21] have been reported.

In the previous chapter 4 (p. 82), the formation of thin-films of MIL-53(Al) on glass surfaces has been comprehensively investigated and the most promising approaches will be

adopted for the coating of an LPG and the real-time sensor performance towards to CO_2 and VOC tested. In total 4 fibres will be investigated. These are one blank fibre (as reference value) and 3 LPGs coated with MIL-53(Al) by in-situ coating (chapter 4.3, p. 86) dip-coating (chapter 4.4, p. 90), and solvent assisted epitaxy (chapter 4.9, p. 121). Especially VOC are known to affect human health leading to different illnesses [373], but lacking at the same time sensitive and selective real-time sensors. CO_2 is mostly known as the most prominent cause for the green-house effect and global warming, but is an also an indicator for indoor room quality [374] and even comparably low CO_2-concentrations of 1400 ppm have negative impacts on health and productivity [25]. For more information such as the state of the art of CO_2 detection and VOC detection or their possible effects on the human health, the reader will be referred to chapter 2.1 (p. 5) and 2.2 (p. 8) respectively.

5.2 Experimental

5.2.1 Materials

Aluminium nitrate nonahydrate, $Al(NO_3)_3 \cdot 9H_2O$, and 1,4-benzenedicarboxylic acid (>98%) (terephthalic acid, H_2BDC) were purchased from Sigma Aldrich. DMF, MeOH and acetone were provided by Fisher-Scientific. All chemicals were used without further purification.

5.2.2 MIL-53(Al) powder synthesis

MIL-53(Al) was prepared according to an already existing synthesis protocol [164] and slightly modified. Briefly, $Al(NO_3)_3 \cdot 9H_2O$ (5.99 mmol; 2.246 g) was dissolved in 15 ml DMF and added to H_2BDC (5.38 mmol; 0.895 g) in 15ml DMF. After stirring vigorously at room temperature for 15 min, the reaction mixture was transferred to a 45 ml Teflon lined stainless steel autoclave (Paar Instruments 4744 General Purpose Acid Digestion Vessel) and heated to 150°C for 5 h. The reaction mixture was cooled down naturally to room temperature and the product separated by centrifugation. The solution was decanted, and the precipitate washed with DMF (2 x 50 ml) and acetone (1 x 50 ml). The product, a white powder, was dried at 150°C for 17 h. Unreacted starting material und residue solvent was removed by heating the as-synthesized product at 333°C for 3 days to create an activated sample.

5.2.3 Coating of LPG by dip-coating

To create suspension for coating, MIL-53(Al)(DMF)-Acti was grounded for 10 min with mortar and pestle. To prepare a 0.5 wt% suspension, 0.05 g MIL-53(Al) and 9.95 g MeOH was placed in a beaker. The resulting suspension was placed for 10 min in an ultrasonic bath and then vigorously stirred for 10 min. The suspension was filled into a petri dish and an fixed LPG placed into the dip-coating suspension (Figure 5-14). After 1 min, the LPG was extracted and solvent removed from the coating by heating the LPG for 1 h at 100°C. This process was repeated up to 5 times.

5.2.4 Coating of LPG by in-situ coating

An LPG was placed in a custom-made Teflon chamber (Figure 5-22) and the chamber filled with MIL-53(Al)(DMF) reaction mixture (1.685 g $Al(NO_3)_3 \cdot 9H_2O$, 0.671 g H_2BDC in 10 ml

DMF), the chamber closed and was placed in oven at 150°C for 5 h. After the reaction, residual reaction mixture was poured out of the chamber and weakly attached MIL-53(Al) removed by washing with DMF from wash bottle (1 x ~10 ml). Activation of the coating was done by solvent exchange in MeOH (24 h at RT) and solvent residue from the activation process removed by heating at 100°C overnight (~17 h) before the sensor experiments.

5.2.5 Coating of LPG by SAE

An LPG was placed in a custom-made Teflon chamber (Figure 5-22) and the chamber filled with MIL-53(Al)(DMF) reaction mixture (1.685 g $Al(NO_3)_3 \cdot 9H_2O$, 0.671 g H_2BDC in 10 ml DMF). After 1 min, the reaction mixture was poured out of the chamber, leaving a film of MIL-53(Al)(DMF) reaction mixture on the LPG. The chamber was filled with 3 ml DMF, the chamber closed and placed in oven at 150°C for 5 h. After the reaction, the chamber was opened and the fiber let naturally cool down to RT (~10 h). Activation of the coating was done by solvent exchange in MeOH (24 h at RT) and solvent residue from the activation process removed by heating at 100°C overnight (~17 h) before the sensor experiments.

5.2.6 Characterisation

Scanning Electron Microscopy (SEM) was used to characterise the morphology of the coatings on the LPGs. Measurements were conducted with a JEOL JSM-7100F Field Emission Gun (FEG) instrument and with a beam voltage of 15 kV. For top-view images, the coated area of the LPGs was cut out by a razor blade after the sensor experiments. A ~2 cm long fibre piece was placed on a SEM sample holder with carbon tape. All samples were sputtered with a 10 nm iridium film by a Quorm Q150T ES coater in order to increase conductivity of the samples.

5.3 Methods

The measurement equipment to investigate the sensor performance of LPGs and the LPGs themselves (grating period: 109.5 µm) were provided by the Applied Optics Groups from the Department of Electronical and Electrical Engineering. The LPGs used had an area of removed protective coating (3 cm long) with added periodical perturbations in the middle of the fibre (total length~80 cm). The possible sensors are coated in this area of the fibre with a thin-film of MIL-53(Al) (Figure 5-1).

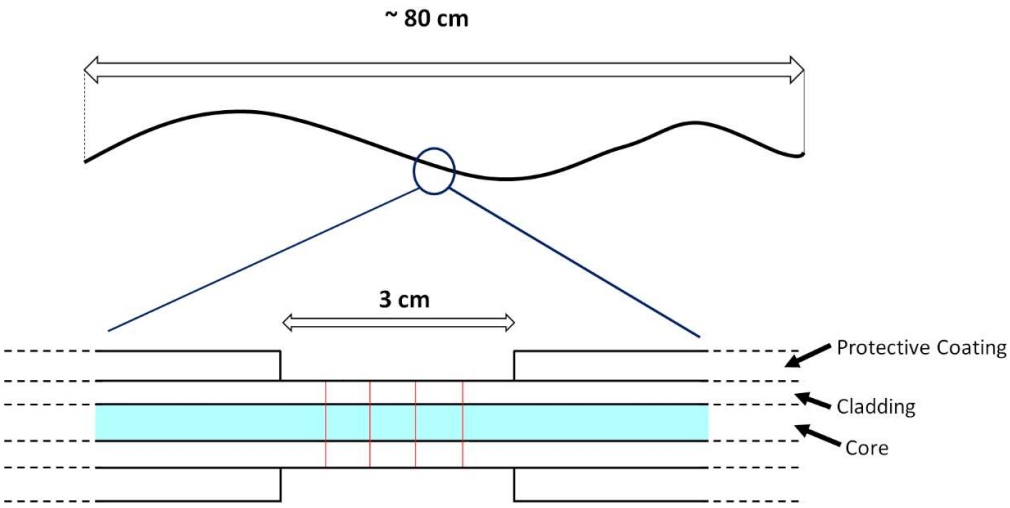


Figure 5-1: Schematic description of the LPG (red lines represent perturbations in the fibre). The small area with removed protective coating (~3 cm) will be coated with thin-film of MIL-53(Al).

The equipment used for the sensor measurement is shown in Figure 5-2. It is composed of a light source, a sealable PMMA box (cubic box with edge length of 15 cm, total volume 3.375 L) to create a controllable atmosphere during the measurement and a spectrometer to detect the wavelength. The light source used is an Ocean Optics HL-2000-LL Tungsten-Halogen lamp, with a range between 360 nm - 1400 nm, with the light of highest intensity emitted as visible light. The spectrometer used for detection is an Ocean Optics HR 4000, which can detect light between 200 nm and 1100 nm and has an optical resolution of 0.02 nm.

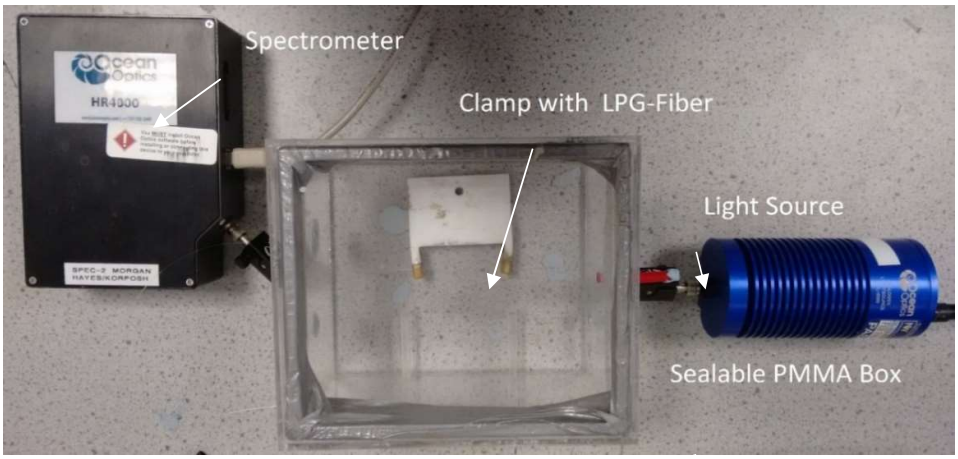


Figure 5-2: Experimental set-up for the sensor measurement.

In a typical sensor experiment, an LPG fibre was placed in a clamp with two crocodile clips on a Teflon board to prevent bending during the measurement and the ends of the fibre connected though small holes in the box with the light source and spectrometer. The spectrometer is connected to a PC, where the current spectrum of the LPG fibre is recorded every 10 s. Afterwards, the recorded raw-data was processed using a program named SIR (Spectrum Interrogation Routine) [85] to create data with time-resolution.

Before every experiment, the sealed box (the holes through which the target compound is introduced and the holes for the LPG are sealed with Blu-tack©), was flushed with N_2 from a pressurized gas cylinder for about 10 min to create a starting value of 0 ppm for the

measurement and to give the light source time to stabilize (about 10 min of warm-up time is needed to reach a stable light spectrum). Every LPG was tested for two different target compounds, CO_2 and MeOH as an example of the large class of VOCs. The set-ups for both CO_2 and MeOH are slightly different.

During CO_2-measurements, a commercial CO_2-sensor was placed in the box to control the CO_2 level in the chamber. The sensor used can be seen in Figure 5-3, whose measurement principle is based on IR and has a response time of 20 s.



Figure 5-3: Image of the used CO_2-sensor (Senseair K33 ICB). The minimum response time is 20 s and the measurement principle is based on IR.

The CO_2 was added into the box through a small hole in the side of the box (red plug at the side of the chamber in Figure 5-2) from a pressurized gas cylinder containing 5% CO_2 in Argon (MIG-shield gas). The CO_2 gas mixture was added directly from the bottle and the flow controlled with a rotameter (Figure 5-4).

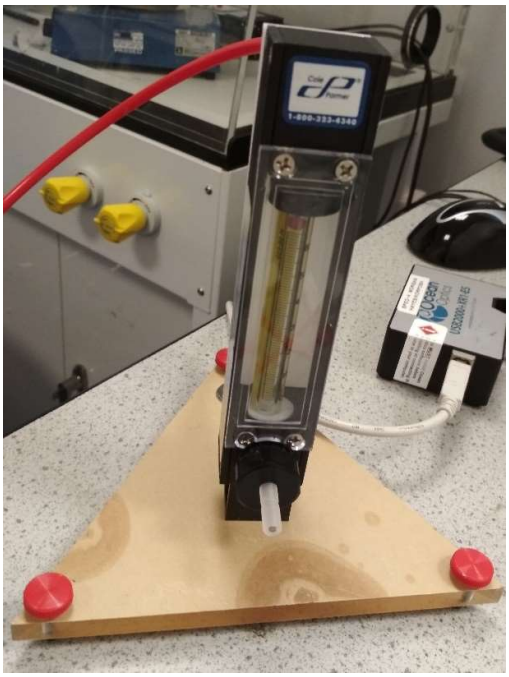


Figure 5-4: Rotameter for the control of the CO_2 gas flow.

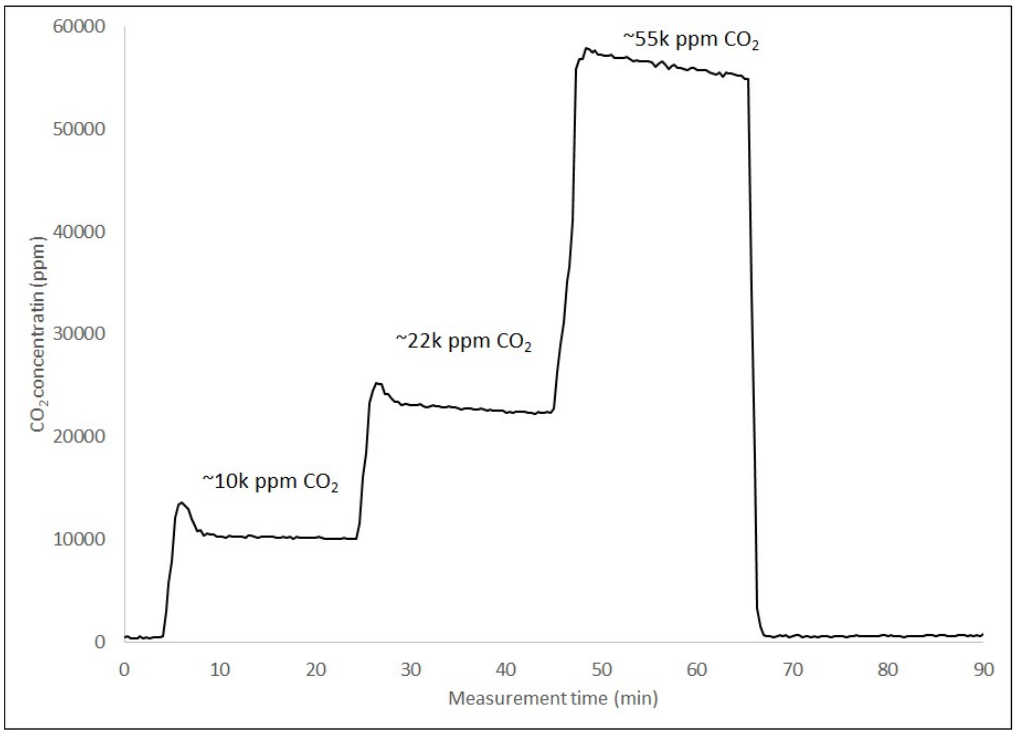


Figure 5-5: Measured CO_2-concentration during a sensor experiment. The data was measured by the IR-CO_2 sensor, which acts as control element.

Figure 5-5 shows the progression of CO_2-concentrations during a typical experiment. At first, the CO_2 is not equally distributed, and the IR sensor overestimates the CO_2-concentration in the chamber. The measured concentrations are therefore found to be higher initially before reaching a slightly smaller true concentration. In addition, the CO_2 mixture is coming directly from a bottle with high pressure, which leads to vibration of the fibre and a temperature change in the box (Joule-Thompson effect). Because an LPG reacts to external stimuli, *e.g.* strain and temperature, approximately 10 min of waiting time are necessary, until both temperature and CO_2-concentration have stabilized and the wavelength is measured to investigate the sensor performance of the LPG. The true measured concentrations during the CO_2-measurement by the IR-CO_2 sensor (Figure 5-5) were 10150 ppm – 10246 ppm; 22256 ppm – 23024 ppm and 54188 ppm – 56410 ppm. For simplification, these values are rounded, and the concentrations are recorded as 10k ppm CO_2, 22k ppm CO_2 and 55k ppm CO_2 in the experiments. It has to be admitted at this point, that the slow response time of the IR-CO_2 sensor of 20 s and the use of the available rotameter makes the precise control of the CO_2-concentration in the measurement box challenging. With the rotameter, the CO_2 flow can be only roughly controlled and during the 20 s measurement steps, the concentration in the box can change in a large degree. As mentioned previously (see chapter 2.1, p. 5) can CO_2 have a negative impact on the human health, but a possible future application for the LPG-CO_2 sensor is depended on the detectable CO_2 concentration. For instance are CO_2-concentrations of about ~2000 ppm considered low room quality where longer stay can lead to symptoms such as headache or reduced concentration [25]. A concentration of 8000 ppm can be fatal after ~30 min exposure [25]. However is at the same time the CO_2-concentration of exhaled air about

28,000 ppm [375]. The applicable CO_2-concentrations in the experimental set-up therefore represent typical concentrations, which can be found in medical applications such as for the detection of pulmonary diseases or the in-situ monitoring of anaesthetized patients *e.g.* as a part of a tracheal tube [376].

For the MeOH-measurement, no real-time sensor was available and therefore the concentration was directly calculated from the amount of added target compound. Nitrogen gas, was used to set the starting value to 0 ppm and to remove impurities. A gas can be treated as an ideal gas if the pressure is much lower than the critical pressure and if the temperature is much higher than the critical temperature. Nitrogen has a critical pressure of p_c = 33.96 bar and a critical temperature of T_c = -146.95°C [277]. The room used for the sensor measurements was air-conditioned (temperature set to 22°C) and the pressure was subjected to typical fluctuations caused by the weather (~1 bar). It was assumed that these conditions were sufficient to threat nitrogen as an ideal gas.

The ideal gas law was used to calculate the number of particles of N_2 (the moles of N_2) in the box (p = pressure, v = volume, n = amount of substance, R = ideal as constant, T = temperature):

$$pv = nRT \qquad \text{Eq.5-1}$$

$$\frac{pv}{RT} = n \qquad \text{Eq.5-2}$$

$$\frac{1.01325 \cdot 10^5\ Pa \cdot 3.375 \cdot 10^{-3}\ m^3}{8.314472 \frac{J}{mol\ K} \cdot 298.15\ K} = 0.137\ mol \qquad \text{Eq.5-3}$$

The number of particles of MeOH in the box were calculated from the known added volume of MeOH, the density and molar mass of MeOH. This is shown with the example of the addition of 50 µL of MeOH to the chamber (V = added volume, δ = density, m = mass, M = molar mass, n = amount of substance):

$$V \cdot \delta = m \qquad \text{Eq.5-4}$$

$$0.05\ ml \cdot 0.7918\ \frac{g}{ml} = 3.395 \cdot 10^{-2}\ g \qquad \text{Eq.5-5}$$

$$\frac{m}{M} = n \qquad \text{Eq.5-6}$$

$$\frac{3.395 \cdot 10^{-2}\ g}{32.042\ \frac{g}{mol}} = 1.232 \cdot 10^{-3} mol \qquad \text{Eq.5-7}$$

$$\frac{n_{N2}}{n_{MeOH}} \cdot 10^6 = mole\ fraction\ of MeOH\ in\ ppm \qquad \text{Eq.5-8}$$

$$\frac{0.137\ mol}{1.232 \cdot 10^{-3} mol} \cdot 10^6 = 8978\ ppm \qquad \text{Eq.5-9}$$

Thus, the addition of 50 µL MeOH leads to a MeOH concentration in the sensor chamber of ~9k ppm MeOH.

Similar to the CO_2-experiments, ~10 min was given to let the MeOH evaporate and distribute equally in the box before the measured wavelength of the LPG was used.

The tested MeOH concentrations during the LPG performance test (between 1.8k ppm and 22.5k ppm) were far higher than the typical observable concentration of VOCs in room air (about 0.3 ppm [377]). The LPG sensor test for MeOH act therefore as a proof of concept

for the real-time detection of VOCs with MIL-53(Al) coated LPGs. The observable MeOH concentrations might be only applicable for specific cases *e.g.* the monitoring of patients with methanol intoxication [378].

5.4 Sensor results

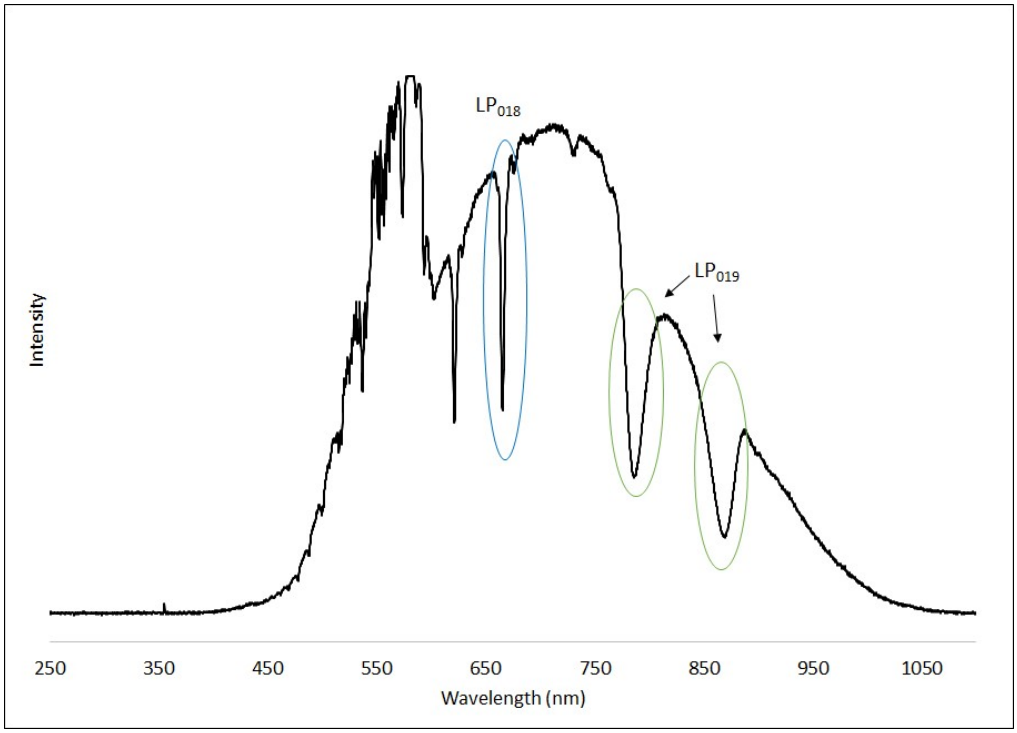


Figure 5-6: Total spectrum of the blank fibre. The blue band is the LP_{018}-band and the green band the split LP_{019}-band.

The first set of experiments were performed with a blank fibre for comparison with the MIL-53(Al) coated fibre and the response to different CO_2 and MeOH concentrations recorded. Starting from the first cladding mode, these bands are numbered consecutively. A total spectrum of a blank LPG (Figure 5-6) show the bands in the range of the spectrometer used. For the sensor, the LP_{018}-band (band caused by the coupling between the core mode of the fibre and the 18. cladding mode, Figure 5-6 in blue) [94] and the LP_{019}-band, which is separated into two individual bands (Figure 5-6 in green) were used. The LP_{018}-band can be seen at ~665 nm, while the split LP_{019}-band appears at ~787 nm and ~869 nm. Both the LP_{018}- and the LP_{019}-band were already successfully used for sensor applications [22]. In general, bands with a higher index number have the advantage of a higher sensitivity to external influences, but these bands are at the same time broader and therefore prone to be more noisy [96]. It might be especially difficult, therefore, to identify small wavelength shifts with bands of large index number.

As the LP_{019}-band separates into two individual bands, an increased sensitivity can be expected [97]. Both parts of the separated band show shifts in different directions, if they are exposed to external influences. Hence an increased sensitivity can be achieved by the measurement of the wavelength difference between these two bands.

A perfect measurement always produces consistent results, but in reality, a measured result always has a small error. These could be random errors or systematic errors. For instance, during the measurement it was observed, that the different bands in the spectrum have a specific broadness, and that the measured wavelength shifted slightly, in a random manner, during the measurement.

To determine the quality of a sensor measurement two limitations were used. One limitation of the system is the detector used, which has a spectral resolution of 0.02 nm. If a measured wavelength shift is smaller or close to this value it can be assumed, that the system is not showing any response.

In other cases, the system might show some response, but the variation of the signal measured at the same time is very high. In such a case it is difficult to decide if the system has measured a signal change or if the measured difference is background noise of the signal. The criteria for this decision are based on the limit of detection (LOD) [379], which is defined as:

$$LOD = \bar{x} + 3\sigma_x \qquad \text{Eq 5-10}$$

Whereas $\bar{x}$ is the mean of the blank value (the measured value with no target compound in the chamber, in this case the value at 0 ppm concentration CO_2 or MeOH) and σ_x is the standard deviation of this blank value. This means that even if an observed wavelength shift is larger than the spectral resolution of the detector, it should be at least 3 times larger than the standard deviation of the measured wavelength to count as a response. However, within the limit of detection only a qualitative answer is given (is there any target compound or not). The limit of quantification (LOQ), to detect the amount of target compound, uses the same formula as above, but with a factor 10 and not 3. Furthermore, should the wavelength shift have a specific direction. If the wavelength shifts into different directions, there might be no correlation between target compound concentration and wavelength shift of the LPG bands.

In order to have an idea about expected wavelength shifts of the LPG, the results of previous measurements for MOF-coated LPG will be shown here. For an LPG, coated with ZIF-8, at 20k ppm MeOH a shift for the LP_{018}-band (~665 nm) of ~2 nm was observed, while for the difference between the LP_{019L}- and LP_{019R}-band a wavelength difference of over 5 nm was measured. At lower concentrations, the sensor response was lower: At 9k ppm MeOH a wavelength difference of 2.2 nm was measured for the difference of the split LP_{019}-bands [22].

An LPG coated with HKUST-1 shows a varying sensor response to CO_2, depending on the coating technique used. A HKUST-1 fibre coated with 40 layers (thickness ~55 nm) by a Layer-by-Layer technique showed a wavelength shift of 0.4 nm at 15k ppm CO_2 and a shift of 0.7 nm at 30k ppm CO_2. A fibre coated with HKUST-1 by rapid-thermal-deposition (RTD) (thickness ~2 µm) has been reported to shows a response of 0.5 nm at 5k ppm [21]. All mentioned shifts from literature for the CO_2-experiment were observed for the LP_{018}-band.

5.4.1 **Blank fibre**

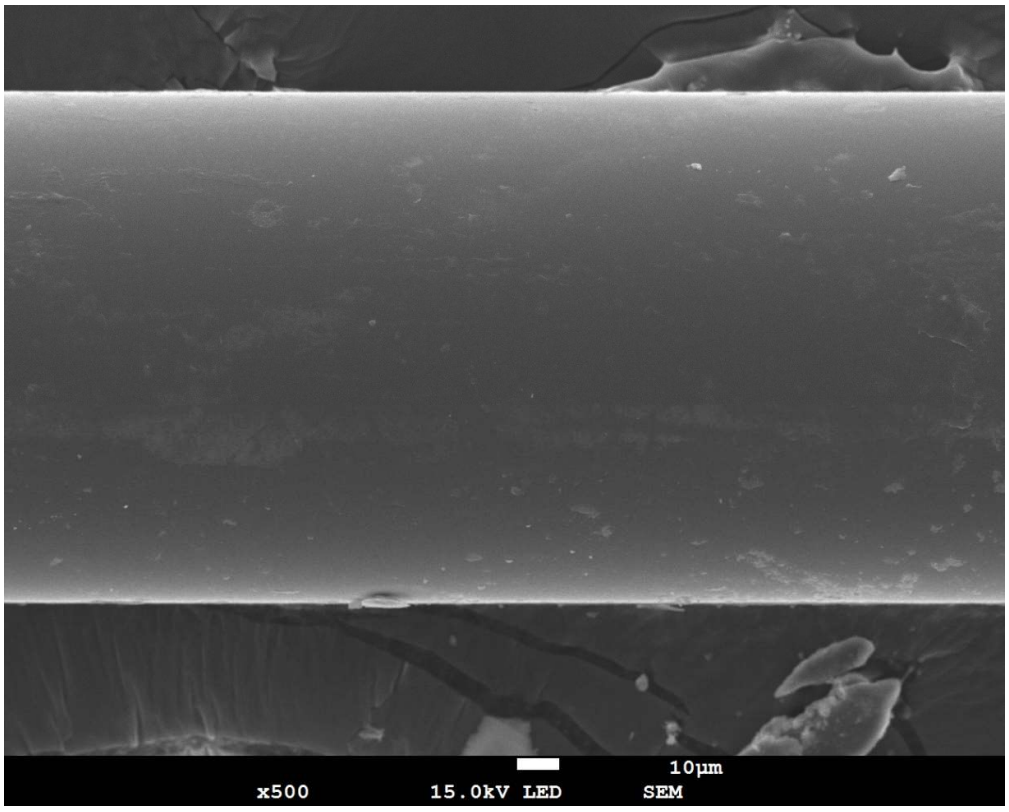


Figure 5-7: Image of the blank fibre.

In the total spectrum of the blank fibre (Figure 5-6) the LP_{018}-, LP_{019L}- and LP_{019R}-bands are visible. The results of the sensor are given as the measured wavelength at different concentrations of the target compound and the wavelength shift between different concentrations. Figure 5-7 shows the SEM image of a blank LPG fibre in order to have a comparison for the MIL-53(Al) coated fibre. The image shows, that the surface is not completely blank, but small residues are visible on the surface. The protective coating of the fibre has to be removed by a mechanical stripper and these particles might be residues of the stripping process.

The measurement of the sensor performance of the LPGs has shown some characteristic challenges. Figure 5-8 shows the measured wavelength during a CO_2-sensor sensitivity test run for the LP_{018}-band. The measured wavelength of this band in the spectrum and its changes were recorded during the whole run. The variation of wavelength of the observed band is shown on the y-axis, while the progress of the experiment in time is shown on the x-axis. The points where the CO_2-concentration was changed are highlighted by black arrows and the adjected text shows the measured total concentration in the chamber. The addition of CO_2 leads to vibrations of the LPG caused by the gas flow, a temperature change (Joule-Thompson-effect) and an uneven CO_2-concentration in the chamber. Even though an LPG is less sensitive to exterior physical influences like temperature and strain [92] in comparison with other fibre types, the addition of gas to the chamber can be clearly identified by drastic changes in wavelength. Approximately 10 min were allowed to stabilize the conditions. The measured wavelength of the different bands slightly varies

during the measurements, even after stabilization of the measurement. The wavelength recorded for different concentrations of target compound was, therefore, reported as the mean value over 5 min, before the concentration in the chamber was changed (red circles in Figure 5-8).

For the LP_{018}-band at ~665 nm, the measured (mean) wavelength at different CO_2-concentrations are given in Table 5-1. However, to assess the sensor performance, the wavelength shift between the different CO_2-concentrations are important and not the absolute measured wavelength themselves. The wavelength differences for the LP_{018}-band recorded for the blank fibre and the sum of the wavelength change are given in Table 5-2. For lower concentrations (0 ppm → 5k ppm) the shift was -0.008 nm. This is lower than the spectral resolution. The next two steps (5k ppm → 10k ppm and 10k ppm → 25k ppm) showed larger wavelength shifts of -0.040 nm and -0.045 nm. At higher concentrations (25k ppm → 60k ppm) a shift of-0.121 nm was observed. The variation of the measured wavelength was quite low. At 0 ppm a wavelength of 665.394 ± 0.007 nm (σ = 0.0058 nm) was observed.



Figure 5-8: CO_2-sensor experiment results for the blank fibre. Measured wavelengths of the LP_{018}-band. Red circles show wavelength range (~5 min) used to calculate the reported wavelength.

Table 5-1: Measured wavelength at different CO_2-concentrations for the blank fibre. Measured for the LP_{018}-band.

CO_2 concentration (ppm)	Wavelength (nm)
0	665.394
5k	665.386
10k	665.346
25k	665.301
60k	665.180

Table 5-2: Measured wavelength shifts between different CO_2-concentrations and sum of the wavelength shifts for the blank fibre. Measured for the LP_{018}-band.

CO_2 concentration change (ppm)	Wavelength shift (nm)	Σ Wavelength shift (nm)
0 → 5k	-0.008	-0.008
5k → 10k	-0.040	-0.048
10k → 25k	-0.045	-0.093
25k → 60k	-0.121	-0.214

The sensor response of the LP_{019L}-band at ~785 nm is shown in Figure 5-9. The measured wavelength shifts for the LP_{019L}-band (Table 5-7) are larger than the shifts for the LP_{018}-band (Table 5-2), but the variation of the measured wavelength is also larger, which is probably caused by the broader bands in the spectrum at larger wavelength (0 ppm of LP_{019L}-band: 786.321 ± 0.141 nm; σ = 0.0766 nm). Again, the largest wavelength shifts could be observed at higher CO_2-concentrations between 10k ppm → 25k ppm and 25k ppm → 60k.

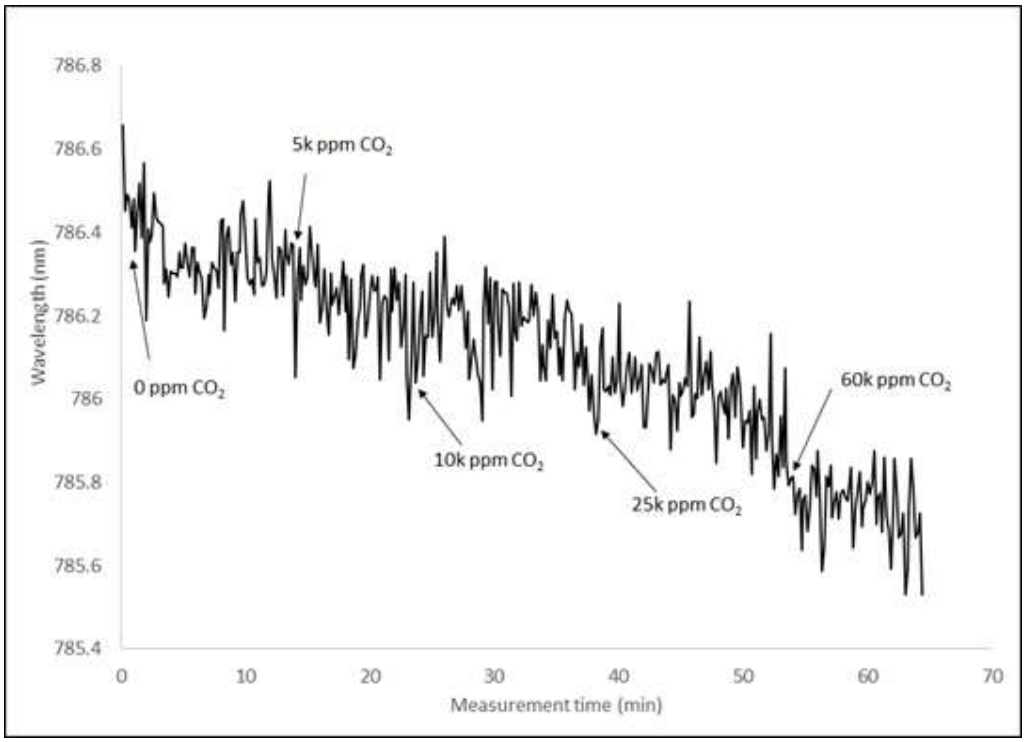


Figure 5-9: CO_2-sensor experiment results for the blank fibre. Measured wavelengths of the LP_{019L}-band.

Table 5-3: Measured wavelength at different CO_2-concentrations for the blank fibre. Measured for the LP_{019L}-band.

CO_2 concentration (ppm)	Wavelength (nm)
0	786.321
5k	786.217
10k	786.168
25k	785.985
60k	785.736

Table 5-4: Measured wavelength shift between different CO_2-concentrations and sum of the wavelength shifts for the blank fibre. Measured for the LP_{019L}-band.

CO_2 concentration change (ppm)	Wavelength shift (nm)	Σ Wavelength shift (nm)
0 → 5k	-0.104	-0.104
5k→ 10k	-0.049	-0.153
10k → 25k	-0.183	-0.336
25k → 60k	-0.249	-0.585

The results for the LP_{019R}-band are shown in Figure 5-10, while the measured wavelength is given in Table 5-5 and the wavelength shifts are shown in Table 5-6. The variation for the LP_{019R}-band is larger than for the LP_{018}- and LP_{019L}-bands, because this band is located at larger wavelength than the other two bands and is broader. The wavelength changes, which can be attributed to the addition of CO_2 to the chamber cannot be clearly identified anymore. This band shows a shift to larger wavelength in contrast to the LP_{018}- and LP_{019L}-bands. Split bands (in this case LP_{019}) typically show shifts in opposing directions. The absolute value of the wavelength shifts with different CO_2-concentrations is in the range of the LP_{019L}-band, but with a higher variation of the measured wavelength (0k ppm CO_2 of LP_{019R}-band 869.078 ± 0.339 nm σ = 0.137 nm). Table 5-7 additionally shows the total wavelength difference between the LP_{019L}- and LP_{019R}-band and represents the separation between these two bands at different CO_2-concentrations.

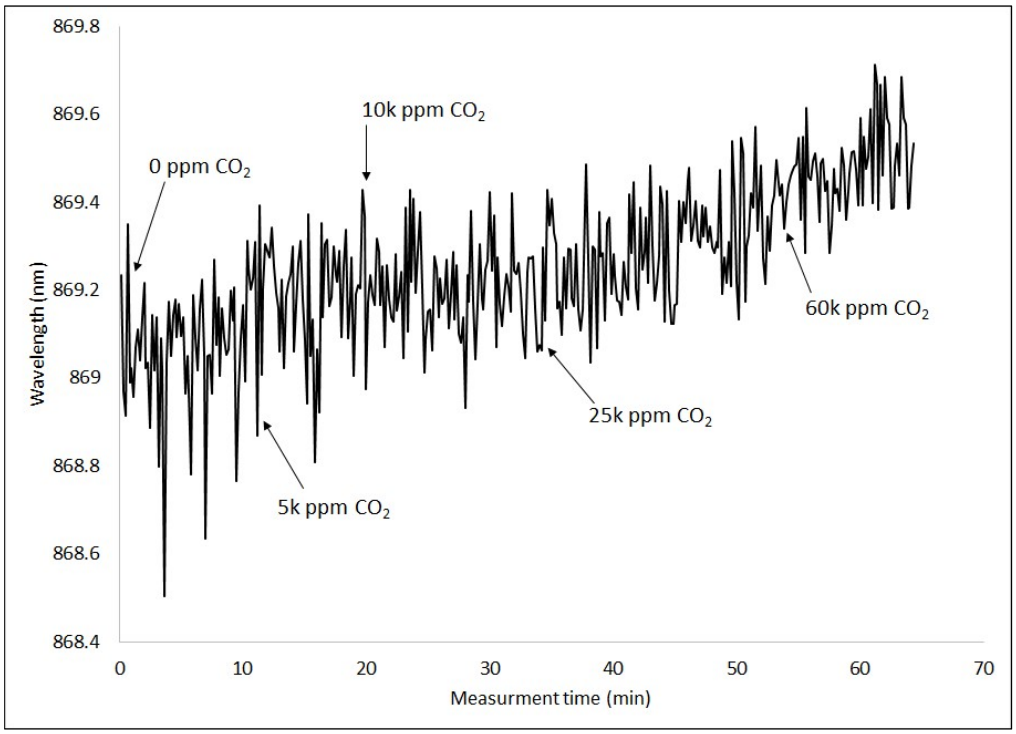


Figure 5-10: CO_2-sensor experiment results for the blank fibre. Measured wavelengths of the LP_{019R}-band.

Table 5-5: Measured wavelength at different CO_2-concentrations for the blank fibre. Measured for the LP_{019R}-band.

CO_2 concentration (ppm)	Wavelength (nm)
0	869.078
5k	869.213
10k	869.221
25k	869.344
60k	869.528

Table 5-6: Measured wavelength shift between different CO_2-concentrations and sum of the wavelength shifts for the blank fibre. Measured for the P_{019R}-band.

CO_2 concentration change (ppm)	Wavelength shift (nm)	Σ Wavelength shift (nm)
0 → 5k	+0.135	+0.135
5k → 10k	+0.008	+0.143
10k → 25k	+0.113	+0.256
25k → 60k	+0.184	+0.440

Table 5-7: Measured wavelength shift between different CO_2-concentrations for the blank fibre. Difference of the wavelength between the LP_{019L}- and LP_{019R}-band.

CO_2 concentration change (ppm)	ΔWavelength LP_{019} (nm)
0 → 5k	0.239
5k→ 10k	0.057
10k → 25k	0.296
25k → 60k	0.433

During the CO_2-measurements, the largest shift for the LP_{018}-band was observed at higher CO_2-concentrations (25k ppm → 60k ppm: -0.121 nm). For the LP_{018}-band a blank value (at 0 ppm) of 665.394 ± 0.007 nm and σ = 0.0058 nm was measured. After a wavelength shift of 0.058 nm (10 times the standard derivation of the blank value) the limit of quantification (LOQ) is reached, and precise CO_2-concentration can be measured. This limit is passed between 25k ppm and 60k ppm. Below that, only a qualitative measurement (is there CO_2 or not) was possible. It is therefore reasonable to measure CO_2-concentrations of >30k ppm with a blank fibre by the wavelength shift of the LP_{018}-band. For the LP_{019L}- and LP_{019R}-bands larger shifts were observed, but at the same time values with larger standard deviation of the measured wavelength: The LP_{019L}-band has shown a value of 786.321 nm (σ = 0.076 nm) at 0 ppm CO_2 and under the same conditions the LP_{019R}-band has a blank value of 869.078 nm (σ=0.137 nm). Even though the measured absolute values of the LP_{019}-band shifts are larger than for the LP_{018}-band (25k ppm CO_2 → 60k ppm; For LP_{019L}: -0.249 nm and LP_{019R}: +0.184 nm), the limit of detection was not passed during the whole experiment. The total observed shifts for the LP_{018L}- and LP_{019R}-bands (0 ppm → 60k ppm CO_2) are -0.585 nm and +0.440 nm, but to reach the LOQ shifts of 0.76 nm and 1.37 nm were needed, respectively. It is therefore not reasonable to use the LP_{019}-band for the detection of CO_2. The difference between the split LP_{019}-bands might have a higher total response than the individual bands, because the wavelength shifts are in different directions. However, due to the propagation of uncertainty, the error of the individual bands has to be also added.

The MeOH sensor performance (Table 5-11) was tested with the same blank fibre as that used for the CO_2-measurement. Between the CO_2 and the MeOH-measurement, the chamber was flushed for 10 min with N_2 to remove possible residues of CO_2 from the CO_2 experiment. Wavelength measurement was stopped during the flushing process and restarted before the MeOH-experiments.

In contrast to the CO_2-measurements, no distinct wavelength drop was observed during the addition of MeOH. The MeOH was added to the chamber by pipette through a small hole at the side of the PMMA-chamber, which did not cause vibration of the fibre or a temperature change. After addition of MeOH, approximately 10 minutes time was given for the MeOH to evaporate and distribute equally in the chamber. Again, the measured wavelength at different MeOH concentrations is reported as a mean value over 5 min (not highlighted in the figures from now on).

The largest wavelength shifts were observed at low concentrations of MeOH in the chamber (Table 5-8 for the measured wavelength at different MeOH concentrations and Table 5-9 for the shift between different concentrations): For the LP_{018}-band a shift of +0.371 nm was observed after addition of the first dose of MeOH (0 to 1.8k ppm MeOH). However, with further increasing the concentration (7.2k ppm → 14.3k ppm and 14.3k ppm → 21.4k ppm) the shift becomes smaller and drops below 0.02 nm. We assume that this was caused by saturation of the chamber with MeOH. The measurement principle of the LPG is based on changes of RI and at higher MeOH concentrations (14.3k ppm and 21.4k ppm) further addition of MeOH does not change the RI of the vapour in the test chamber anymore. Again, the measured wavelength for the LP_{018}-band has a low variation (0 ppm MeOH: 664.784 ± 0.007 nm; σ = 0.011 nm).

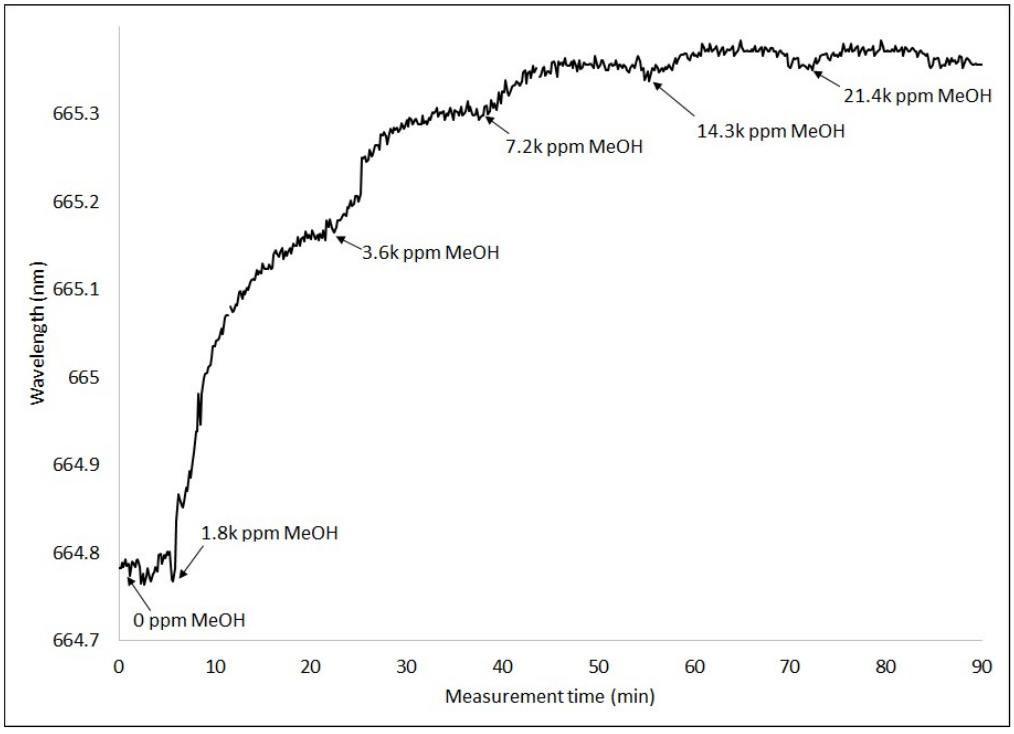


Figure 5-11: MeOH-sensor experiment results for the blank fibre. Measured wavelengths of the LP_{018}-band.

Table 5-8: Measured wavelength at different MeOH-concentrations for the blank fibre. Measured for the LP_{018}-band.

MeOH-concentration (ppm)	Wavelength (nm)
0	664.784
1.8k	665.155
3.6k	665.301
7.2k	665.355
14.3k	665.362
21.4k	665.368

Table 5-9: Measured wavelength shift between different MeOH-concentrations and sum of the wavelength shifts for the blank fibre. Measured for the LP_{018}-band.

MeOH-concentration change (ppm)	Wavelength shift (nm)	Σ Wavelength shift (nm)
0 → 1.8k	+0.371	+0.371
1.8k → 3.6k	+0.146	+0.517
3.6k → 7.2k	+0.054	+0.571
7.2k → 14.3k	+0.007	+0.578
14.3k → 21.4k	+0.006	+0.584

The measured wavelength during the experiment for the LP_{019L}-band is shown in Figure 5-12, whereas the individual measured wavelength at varying MeOH concentrations and the measured wavelength shifts are shown in Table 5-10 and Table 5-11, respectively. The measured wavelength has in comparison with the LP_{018}-band a higher variation (0 ppm MeOH: 784.462 ± 0.102 nm; σ = 0.099 nm), but the measured wavelength shift is with +1.156 nm at low concentrations (0k ppm → 1.8k ppm) the largest shift observed in this set of experiments. Similar to the LP_{018}-band the shifts become smaller with higher MeOH concentrations (1.8k ppm → 3.6k ppm: +0.294 nm; 3.6k ppm → 7.2k ppm: +0.135 nm) in the chamber and fall below the spectral resolution for the highest concentrations (14.3k ppm → 21.4k ppm: +0.010 nm).

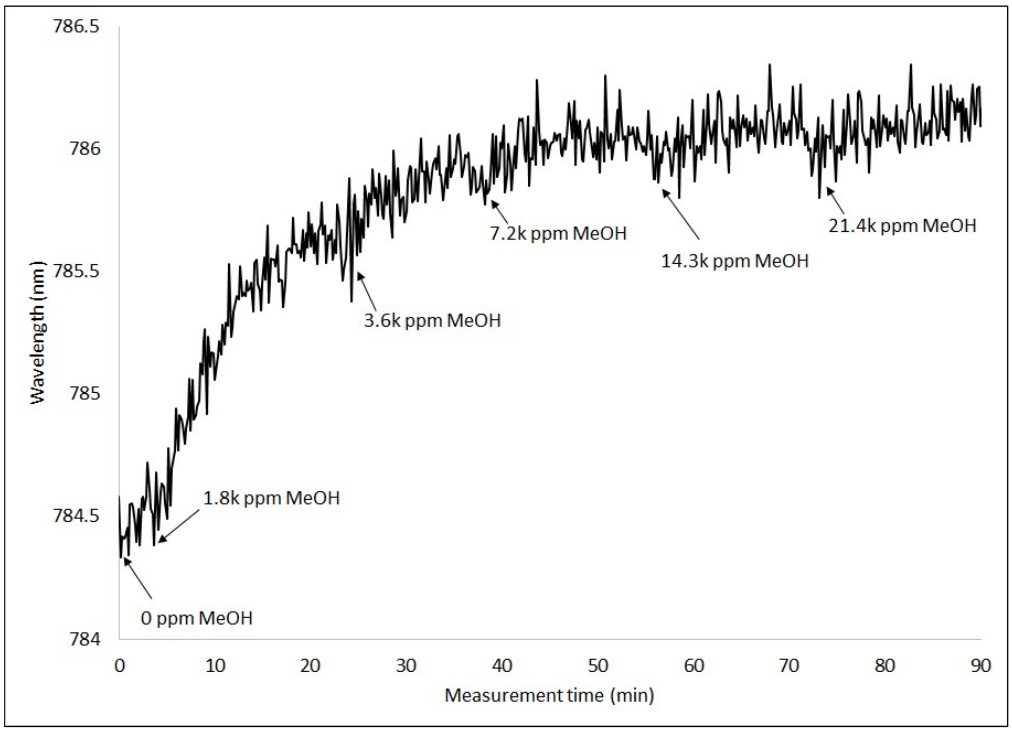


Figure 5-12: MeOH-sensor experiment results for the blank fibre. Measured wavelengths of the LP_{019L}-band.

Table 5-10: Measured wavelength at different MeOH concentrations for blank fibre. Measured for the LP_{019L}-band.

MeOH-concentration (ppm)	Wavelength (nm)
0	784.462
1.8k	785.618
3.6k	785.912
7.2k	786.047
14.3k	786.101
21.4k	786.111

Table 5-11: Measured wavelength shift between different MeOH-concentrations and sum of the wavelength shifts for the blank fibre. Measured for the LP_{019L}-band.

MeOH concentration change (ppm)	Wavelength shift (nm)	Σ Wavelength shift (nm)
0 → 1.8k	+1.156	+1.156
1.8k → 3.6k	+0.294	+1.450
3.6k → 7.2k	+0.135	+1.585
7.2k → 14.3k	+0.054	+1.639
14.3k → 21.4k	+0.010	+1.649

Result of the MeOH sensor experiments for the LP_{019R}-band are shown in Figure 5-13, while the measured wavelength for different MeOH concentrations and wavelength shift between different concentrations in are shown in Table 5-12 and Table 5-13, respectively. The wavelength shifts have an opposing direction to the other two bands investigated (due to its nature of being a split band) and a slightly higher variation of the measured wavelength (0 ppm MeOH: 870.728 ± 0.175 nm; σ = 0.115 nm) due to being at larger wavelength. While the absolute value for the first measured shift of the LP_{019R}-band

(0k ppm → 1.8k ppm) is smaller (LP_{019L}: +1.156 nm to $LP_{019R:}$ -0.648 nm), the measured wavelength shifts for the other concentrations are in the same range observed for the LP_{019L}-band. The measured wavelength difference between the LP_{019L}- and LP_{019R}-band (the ΔLP_{019} value) and consequently the sensor response (Table 5-14), especially at lower MeOH concentrations (0k ppm → 1.8k ppm: 1.804 nm and 1.8k ppm → 3.6k ppm: 0.683 nm), is larger than any observed wavelength shift than during the CO_2-sensor test (Table 5-7). The largest observed value ΔLP_{019} for the CO_2-sensor experiment was 0.433 nm between 25k ppm CO_2 and 60k ppm CO_2.

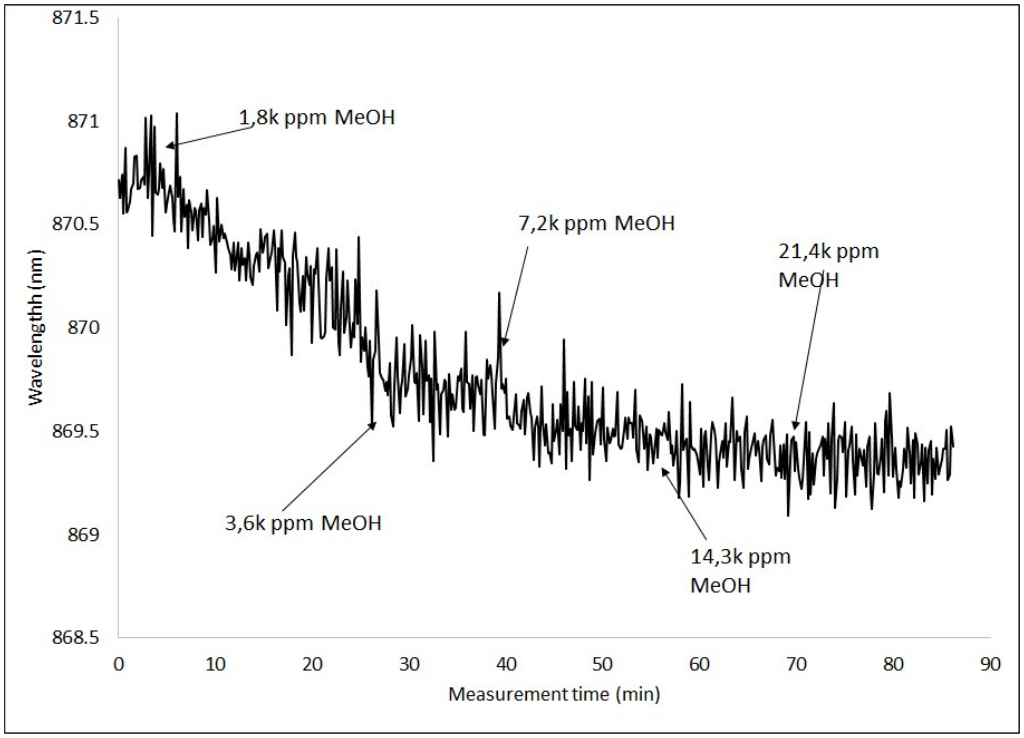


Figure 5-13: MeOH-sensor experiment results for the blank fibre. Measured wavelengths of the LP_{019R}-band.

Table 5-12: Measured wavelength at different MeOH concentrations for blank fibre. Measured for LP_{019R}-band.

MeOH-concentration (ppm)	Wavelength (nm)
0	870.728
1.8k	870.080
3.6k	869.691
7.2k	869.485
14.3k	869.405
21.4k	869.339

Table 5-13: Measured wavelength shift between different MeOH-concentrations and sum of the wavelength shifts for the blank fibre. Measured for LP_{019R}-band.

MeOH concentration change (ppm)	Wavelength (nm)	Σ Wavelength shift (nm)
0→ 1.8k	-0.648	-0.648
1.8k→ 3.6k	-0.389	-1.037
3.6k → 7.2k	-0.206	-1.243
7.2k → 14.3k	-0.080	-1.323
14.3 k→ 21.4k	-0.066	-1.383

Table 5-14: Measured wavelength shift between different MeOH-concentrations for the blank fibre. Difference of the wavelength between the LP_{019L}-and LP_{019R}-band.

MeOH concentration change (ppm)	ΔWavelength LP_{019} (nm)
0 → 1.8k	1.804
1.8k → 3.6k	0.683
3.6k → 7.2k	0.341
7.2k → 14.3k	0.134
14.3k → 21.4k	0.076

In contrast to the CO_2 results, the blank fibre has shown the highest wavelength shifts at low MeOH concentrations (< 7.2k ppm), before the shift drops at high concentrations (> 7.2k ppm). For the LP_{018}-band at 0 ppm MeOH a wavelength blank value of 664.784 ± 0.007 nm (σ = 0.011 nm) was observed. Even during the first addition of MeOH (0 ppm → 1.8k ppm) a wavelength shift of +0.371 nm was observed, which exceeds the LOQ. It is therefore plausible to detect MeOH with the blank fibre between 0 ppm and ~10k ppm MeOH. At higher MeOH concentrations (< 10k ppm) the wavelength shift drops below the spectral resolution of the spectrometer. For the LP_{019}-band, larger shifts but also larger standard deviations were observed in comparison with the LP_{018}-band (at 0 ppm MeOH: LP_{019L}:784.462 ± 0.102 nm; σ = 0.099 nm LP_{019R}: 870.728 ± 0.175 nm; σ = 0.115 nm). Between 0 ppm and 1.8k ppm MeOH, the largest shifts for the whole experiment were observed with +1.156nm for the LP_{018L}-band and -0.648 nm for the LP_{019R}-band. For the LP_{019}-band, it might be therefore reasonable to a detect even higher MeOH-concentrations in comparison with the LP_{018}-band (up to ~15k ppm MeOH). Again, at higher MeOH-concentrations the wavelength shifts drop below the spectral resolution. For the wavelength difference ΔLP_{019} it might be even reasonable to detect MeOH concentrations up to ~22k ppm.

For the blank fibre (total spectrum of the fibre Figure 5-6) a response for CO_2 at higher concentrations (> 25k ppm) and for MeOH at lower concentrations (< 7.2k ppm) was observed. Such a result was expected, because the chamber was filled with N_2 (to reach 0 ppm CO_2 or MeOH) before the target compounds were added. N_2 has a different RI to MeOH or CO_2 and an LPG is sensitive to RI change. However, an LPG is not selective for specific compounds and any RI change will be detected. The results of the blank fibre also show the different sensitivities for the LP_{018} and $LP_{019L/R}$ band.

The sensitivities for CO_2 at higher concentrations and for lower MeOH concentrations can be explained with the different RI of the compounds. An LPG is sensitive to RI changes of the surrounding medium, but CO_2 was not added as a pure compound, but as an Ar/CO_2 mixture. The RI of argon and nitrogen are close to each other (RI_{N2}: 1.000280 [380]; RI_{Ar}:1.000265 [381]; RI_{CO2}: 1.000443 [382]). Therefore, almost no shift was observed at low CO_2-concentrations (< 25k ppm) and only at higher concentrations of CO_2 (>25k ppm) does the RI difference between N_2/Ar and CO_2 have an impact. The RI of MeOH (RI_{MeOH}: 1.32303 [383]) is much higher than that of N_2. Even at low concentrations (~1.8k ppm), a large difference in RI could be observed. At higher concentrations of MeOH (> 7.2k ppm), the measurement chamber is already filled with MeOH and the RI difference between the different concentrations is not as large, which leads to a smaller measured wavelength shift.

5.4.2 LPG coated with MIL-53(Al) by dip-coating

The results above verify, that even a blank fibre shows a response for CO_2 or MeOH at different concentrations. However, a comparison with literature data shows that the response of MOF coated LPGs is still larger. HKUST-1 has shown a shift of 0.7 nm for the LP_{018}-band at 40k ppm CO_2 [21] (blank fibre in chapter 5.4.1: 0.21 nm) and a ZIF-8 coated fibre has shown a shift of 5.5 nm for the ΔLP_{019} [22](blank fibre in chapter 5.4.1: 3.03 nm) at 20k ppm MeOH. Not only did the above-mentioned MOF-coated fibres show larger wavelength shifts (corresponding to better sensor responses), the blank LPG does not show selectivity toward RI change, temperature or strain, and it cannot be said what the underlying reason for an observed wavelength shift is. As mentioned in the introduction, only in controlled environments can the wavelength shift be used in isolation to identify different concentrations of target compounds [99]. The results of the LPG sensors from literature imply, that in most cases a modification of the LPG fibre is needed to improve the selectivity towards specific compounds and modification of the surface can further help to concentrate the target compound on the fibre by specific adsorption, increases the wavelength shift and hence the sensor response [21],[22]. In the chapter 4 (p. 82) before, the thin-film coating of MIL-53(Al) has been investigated for coating of glass surfaces and the most promising approaches have been modified to coat a LPG with thin-films of MIL-53(Al).



Figure 5-14: Image of a fibre immersed in 0.5 wt% MIL-53(DMF) dip-coating suspension.

For the dip-coating approach, a fibre was placed in a clamp, which is made of a Teflon board, with two crocodile clips attached. Fixing on the board prevents bending of the LPG during the coating process. The fibre was cleaned before the dip-coating process by immersion in acetone for 30 min followed by drying in a N_2-flow. For the coating process a 0.5 wt% suspension of MIL-53(Al)(DMF)-Acti in MeOH was used. This suspension was chosen, because it has shown the best surface coverage while preventing the formation of agglomerated cluster on the surface (see chapter 4.4.4, p. 97). The coating suspension was created by adding 0.5 g MIL-53(Al)(DMF)-Acti powder (ground with mortar and pestle for 10 min) into 9.95 g MeOH and the mixture distributed by ultrasonication for 10 min. The mixture was poured into a petri-dish and the fibre placed in the suspension for 1 min (Figure 5-14). Residual solvent was removed by heating the fibre for 1 h at 100°C. The process was repeated in total 5 times (Figure 5-16). The repetition of the dip-coating process is important to archive coverage of the surface. For comparison, Figure 5-15 shows an image of a fibre coated with only one treatment step by dip-coating. The surface of the fibre is only sparsely covered with particles.

Before the sensor experiments, the fibre was heated overnight at 100°C to remove any impurities (*e.g.* humidity from the environment or MeOH solvent) from the coating. As in the blank fibre experiments, the recording of the wavelength was started after the CO_2/MeOH level was reduced to 0 ppm by flushing the chamber with N_2 for 5 min and additional 10 min waiting time to stabilize the conditions in the chamber. In contrast to the blank fibre, the chamber was flushed with N_2 after the sensor experiments to reach 0 ppm again. This step was introduced to investigate whether it is possible to recover the fibre directly after the experiment [22]. For a blank fibre, such a step was not introduced, because it does not contain a layer which has the ability to adsorb CO_2 or MeOH on the fibre.

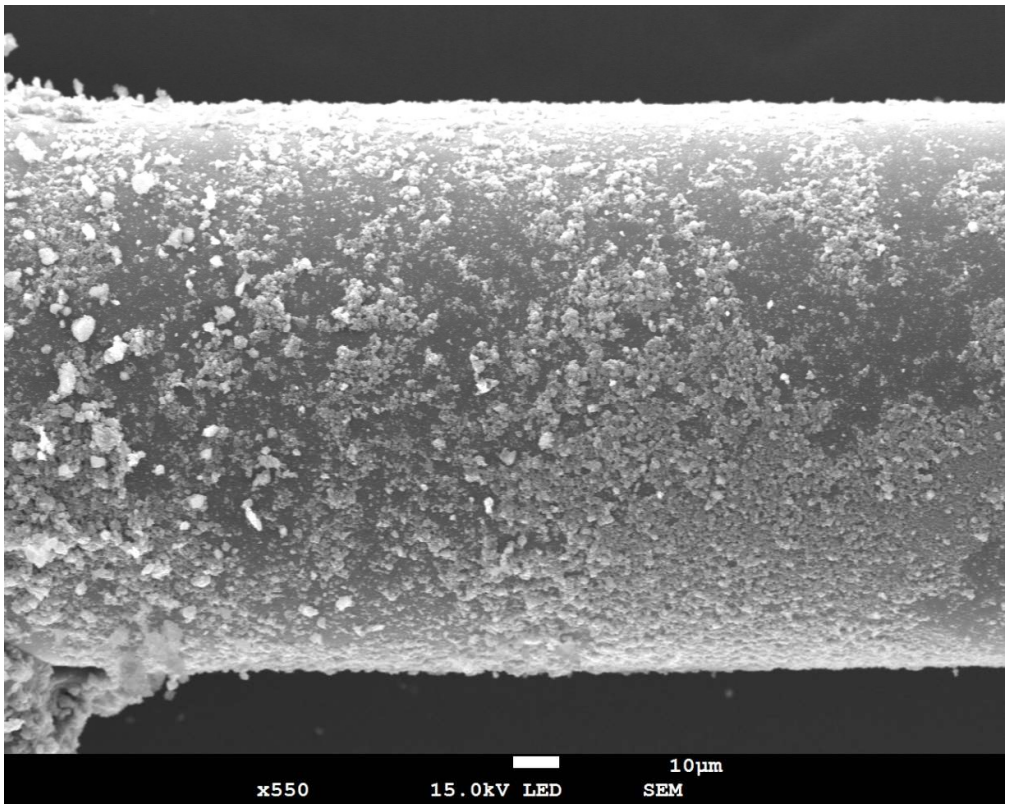


Figure 5-15: Fibre coated with one step of MIL-53(Al)(DMF) from a 0.5 wt% dip-coating suspension in MeOH.

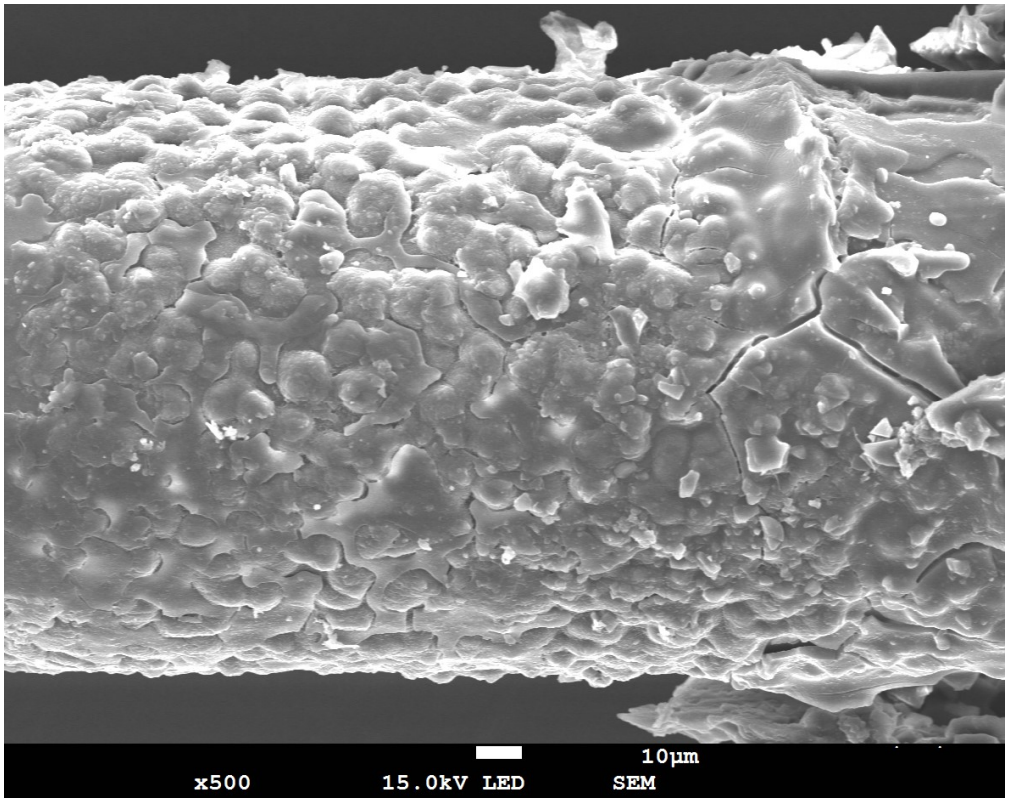


Figure 5-16: Fibre coated with 5 steps of MIL-53(Al)(DMF) from a 0.5 wt% dip-coating suspension in MeOH.

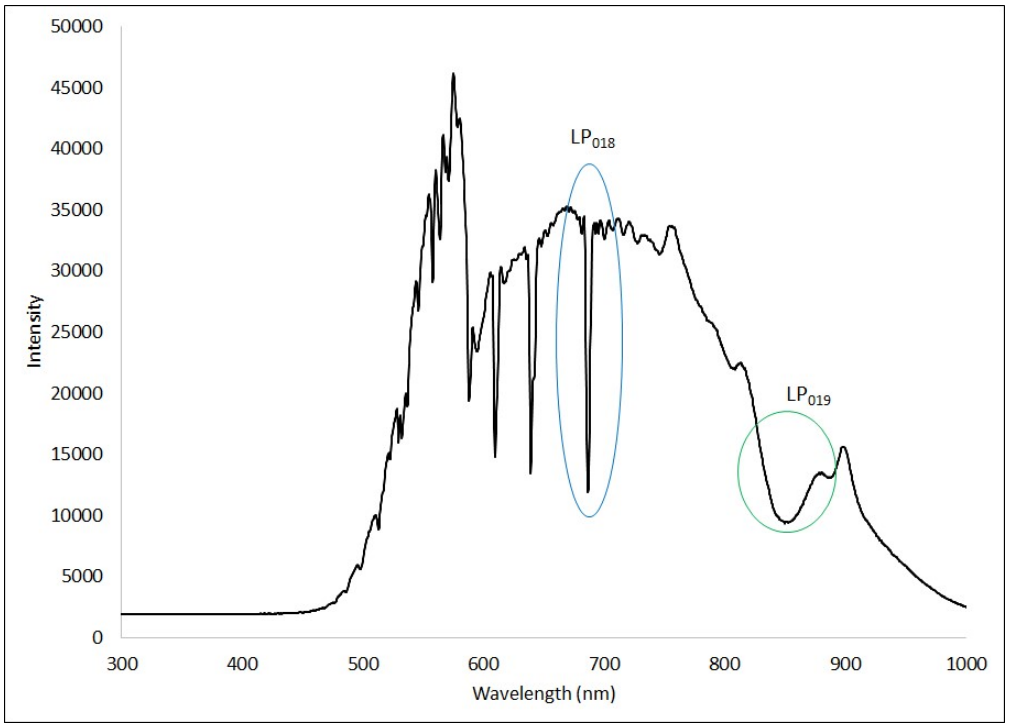


Figure 5-17: Total spectrum of LPG coated with 5 steps of MIL-53(Al)(DMF) by dip-coating from a 0.5 wt% suspension in MeOH.

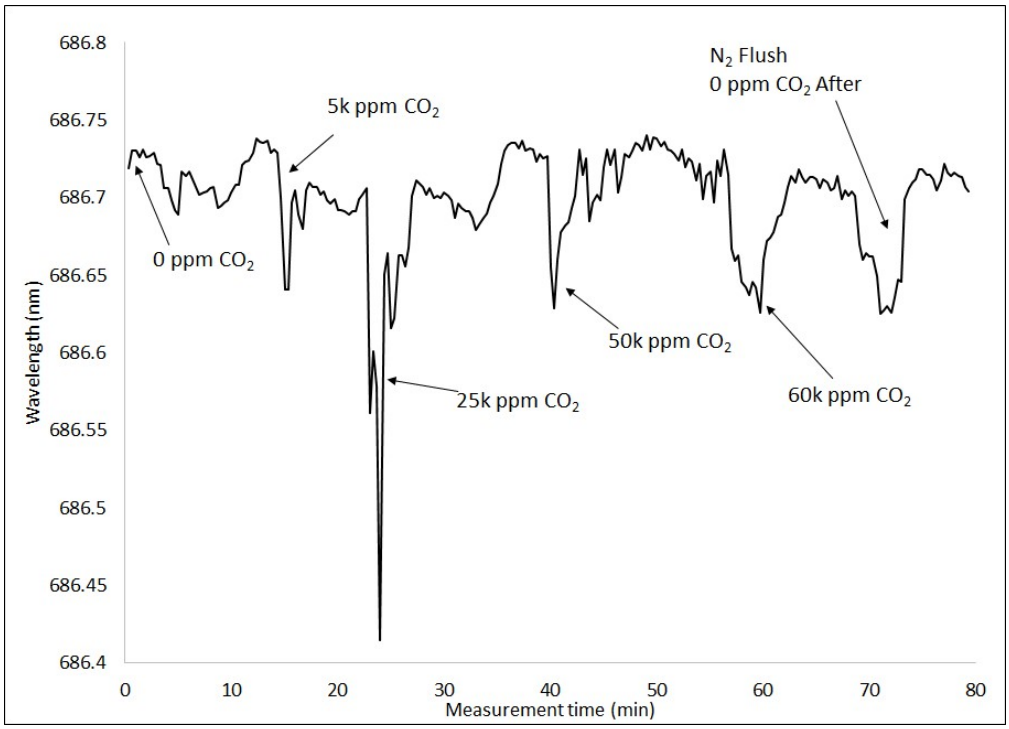


Figure 5-18: CO_2-sensor experiment results for fibre coated with 5 steps of MIL-53(Al)(DMF) by dip-coating from 0.5 wt% suspension in MeOH. Measured wavelength for LP_{018}-band.

Table 5-15: Measured wavelength during CO_2-sensor test of fibre coated with 5 steps of MIL-53(Al)(DMF) by dip-coating. Measured for LP_{018}-band.

CO_2 concentration (ppm)	Wavelength (nm)
0	686.714
5k	686.696
25k	686.730
50k	686.721
60k	686.707
0 after experiment	686.711

Table 5-16: Measured wavelength shift between varying CO_2-concentrations and sum of the wavelength shift for fibre coated with 5 steps of MIL-53(Al)(DMF) by dip-coating. Measured for the LP_{018}-band

CO_2 concentration change (ppm)	Wavelength shift (nm)	Σ wavelength shift (nm)
0→ 5k	-0.018	-0.018
5k → 25k	+0.034	+0.016
25k → 50k	-0.009	+0.007
50k → 60k	-0.014	-0.007
60k → 0 after experiment	+0.004	-0.003

The results of the CO_2-sensor measurement are shown in Figure 5-18. The points of added CO_2 (or N_2 for returning to 0 ppm CO_2 after the experiment) are visible as a wavelength drop. In contrast to the blank fibre, no clear response was observed during the experiment. Most of the wavelength shifts (Table 5-16) display variable directions and are, apart from the shift for 5k ppm → 25k ppm CO_2, below the spectral resolution of the detector. Furthermore, after flushing the chamber with N_2, the wavelength does not return to the starting value.

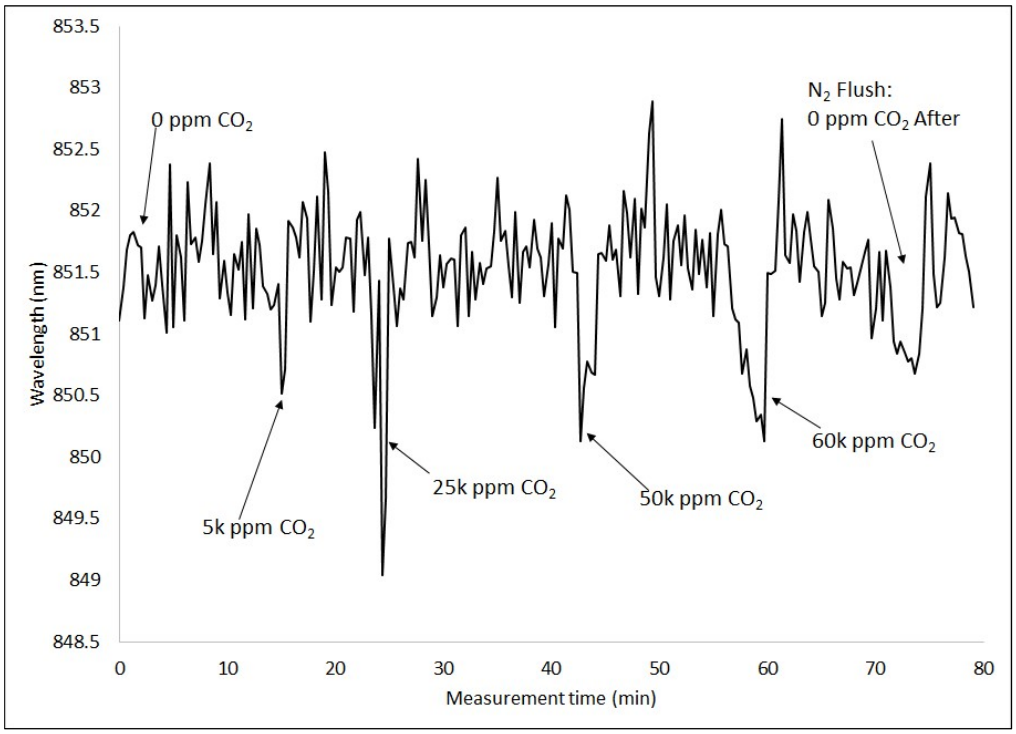


Figure 5-19: CO_2-sensor experiment results for fibre coated with 5 steps of MIL-53(Al)(DMF) by dip-coating from 0.5 wt% suspension in MeOH. Measured wavelength for LP_{019}-band.

Table 5-17: Measured wavelength during CO_2-sensor test of fibre coated with 5 steps of MIL-53(Al)(DMF) by dip-coating. Measured for LP_{019}-band.

CO_2 concentration (ppm)	Wavelength(nm)
0	851.652
5k	851.717
25k	851.624
50k	851.664
60k	851.589
0 after experiment	851.681

Table 5-18: Measured wavelength shift between varying CO_2-concentrations and sum of wavelength shift for fibre coated with 5 steps of MIL-53(Al)(DMF) by dip-coating. Measured for the LP_{019}-band.

CO_2 concentration change (ppm)	Wavelength shift(nm)	Σ Wavelength shift (nm)
0→ 5k	+0.065	+0.065
5k → 25k	-0.093	-0.028
25k → 50k	+0.040	+0.012
50k→60k	-0.075	-0.063
60k → 0 after experiment	+0.092	+0.029

In contrast to the blank fibre, the LP_{019}-band did not separate into two individual bands (Figure 5-17). Without this separation, the band is broader which leads to a more inaccurate measurement of the wavelength (0 ppm: 851.652 ± 0.478 nm; σ = 0 .294 nm) and the potential to use the wavelength difference between the LP_{019L}- and LP_{019R}-band is not available. The measured wavelength shifts have variable directions and the shift is far lower than the LOQ. To reach the LOQ, a shift of 2.94 nm is needed.

For the MeOH-measurement, the same LPG that was used for the CO_2-measurement was employed again. Before the measurement, the fibre was heated overnight at 100°C to remove possible residues from the CO_2-sensor measurement.
The reuse of the LPG has different reasons. One reason is the strong dependency of the coating of influences like coating thickness or roughness. By employing the same fibre, the fibre has the potential same sensor performance and results of the CO_2 and MeOH experiments can be directly compared. Furthermore, can be investigated to which degree the LPG can be recovered or if *e.g.* the coating of the fiber starts to disintegrate or target compound is trapped in the coating of the fiber (leading to a "single-use sensor"). Another important reason for reusing an coated LPG are of economical nature. The blank LPGs were provided by a different working group and due to the time-consuming manufacturing process only a limited number of blank LPGs were provided for this reseach.
The results of the MeOH-sensor measurement are shown in Figure 5-20, while the measured wavelength for different MeOH-concentrations are shown in Table 5-19 and the resulting wavelength shift between different concentrations in Table 5-20. As expected for MeOH-sensor measurements, the points where MeOH was added are not directly visible in the recording of the sensor measurement (Figure 5-20). None of the measured wavelength shifts is larger than the spectral resolution of the spectrometer (0.02 nm).

The results of the CO_2-measurement have shown, that a non-split LP_{019}-band does not show a reasonable sensor response. The results until now (from the blank fibre and the dip-coated LPG) have led to the observation, that the response of the LP_{019}-band can be predicted to a certain degree from the results of the LP_{018}-band, because they were recorded at the same time from the same fibre. Neither the LP_{018}-band or LP_{019}-band results of the CO_2-sensor experiment, nor the LP_{018}-band MeOH-sensor results have shown any sensor response of the dip-coated LPG. The LP_{019}-results for MeOH have been therefore not further investigated.

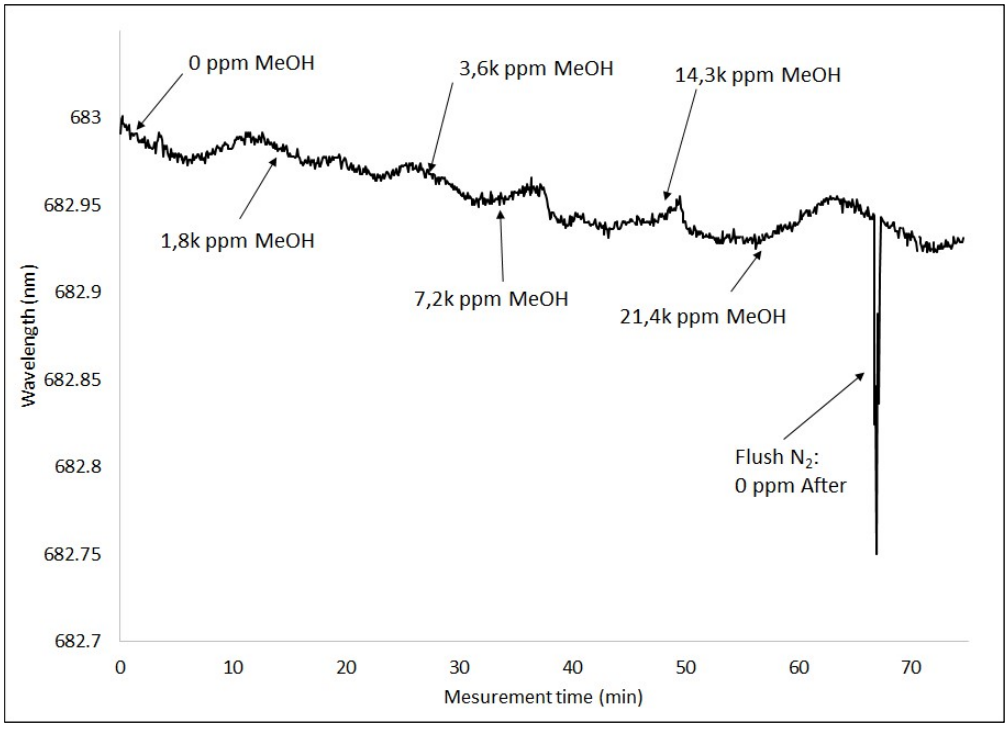


Figure 5-20: MeOH-sensor experiment results for fibre coated with 5 steps of MIL-53(Al)(DMF) by dip-coating from 0.5 wt% suspension in MeOH. Measured wavelength for LP_{018}-band.

Table 5-19: Measured wavelength during MeOH sensor test of fibre coated with 5 steps of MIL-53(Al)(DMF) by dip-coating. Measured for LP_{018}-band.

MeOH concentration (ppm)	Wavelength(nm)
0	682.991
1.8k	682.971
3.6k	682.960
7.2k	686.942
14.3k	686.930
21.4k	686.944
0 after experiment	686.928

Table 5-20: Measured wavelength shift between varying MeOH-concentrations and sum of the wavelength shift of fibre coated with 5 steps of MIL-53(Al)(DMF) by dip-coating. Measured for the LP_{018}-band.

MeOH concentration change (ppm)	Wavelength shift(nm)	Σ Wavelength shift(nm)
0 → 1.8k	-0.020	-0.020
1.8k → 3.6k	-0.011	-0.031
3.6k → 7.2k	-0.018	-0.049
7.2k → 14.3k	-0.012	-0.061
14.3k → 21.4k	+0.014	-0.047
21.4k → 0 after experiment	-0.016	-0.063

5.4.3 LPG coated with MIL-53(Al) by in-situ coating

While dip-coating can be carried out in a petri-dish, a more sophisticated approach has to be used for the in-situ coating of the LPG. For the in-situ coating, an environment which resembles the powder synthesis (5 h at 150°C) and prevents the fast evaporation of the solvent is required. While for a glass slide coating, discussed in chapter 4.3 (p. 86), a commercially available Teflon lined stainless steel autoclave can be used, the dimensions of the LPG prevent the usage of such a vessel. The 80 cm long LPG has to be kept straight during the coating (the LPG is sensitive to strain) and therefore cannot be coiled during the preparation. The stress of coiling up the fibre during the synthesis might further reduce the stability of the fibre and lead to breaking. Hence, for the in-situ coating a Teflon chamber was developed (Figure 5-22). A schematic image is shown in Figure 5-21. The LPG was fed through the chamber through small holes, with a diameter of 300 µm. This is only slightly larger than the diameter of an LPG with intact protective coating (~250 µm). This small difference between the holes and the diameter of the fibre mostly prevents leakage during the experiments and the holes are in addition sealed with adhesive (Blu-Tack®) during the experiment. Furthermore, a tight-fitting lid prevents evaporation of reaction mixture during the reaction time of 5 h.

For the in-situ coating, an LPG was placed in the chamber and washed with acetone for 30 min. The acetone was removed, and the fibre dried by N_2-flow. The MIL-53(Al) reaction mixture was added to the chamber. The amount of reaction mixture was chosen (1.685 g Ni-nitrate, 0.671 g H_2BDC, 10 ml DMF) to immerse the fibre in MIL-53(DMF) reaction mixture but prevents complete filling of the chamber. The reaction mixture used for the in-situ coating in the Teflon chamber has the same concentration than the MIL-53(Al) reaction mixture used for in-situ coating on glass. The volume is reduced, because the Teflon chamber is smaller in comparison with a Teflon lined stainless steel autoclave used in chapter 4.3 (p. 86). After reaction at 150°C for 5 h, the chamber was opened, and the reaction mixture removed. The coated fibre was washed with MeOH to remove loose particles from the fibre and the coating activated by solvent exchange in MeOH (24 h at RT). The fibre was dried in oven at 100°C overnight, before the sensor performance of the fibre was tested.

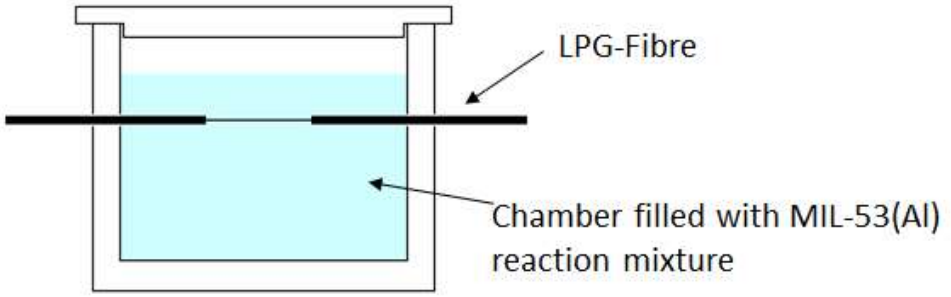


Figure 5-21: Schematic image of the Teflon chamber for in-situ coating.



Figure 5-22: Photo of the Teflon chamber.

SEM imaging of the fibre (Figure 5-23) shows that it was possible to coat the fibre with a homogenous film of MIL-53(Al). However, in contrast to dip-coating the resulting spectrum of the fibre (Figure 5-24) did not show a LP_{019}-band. Thus, only the results for the LP_{018}-band (~687nm) can be studied.

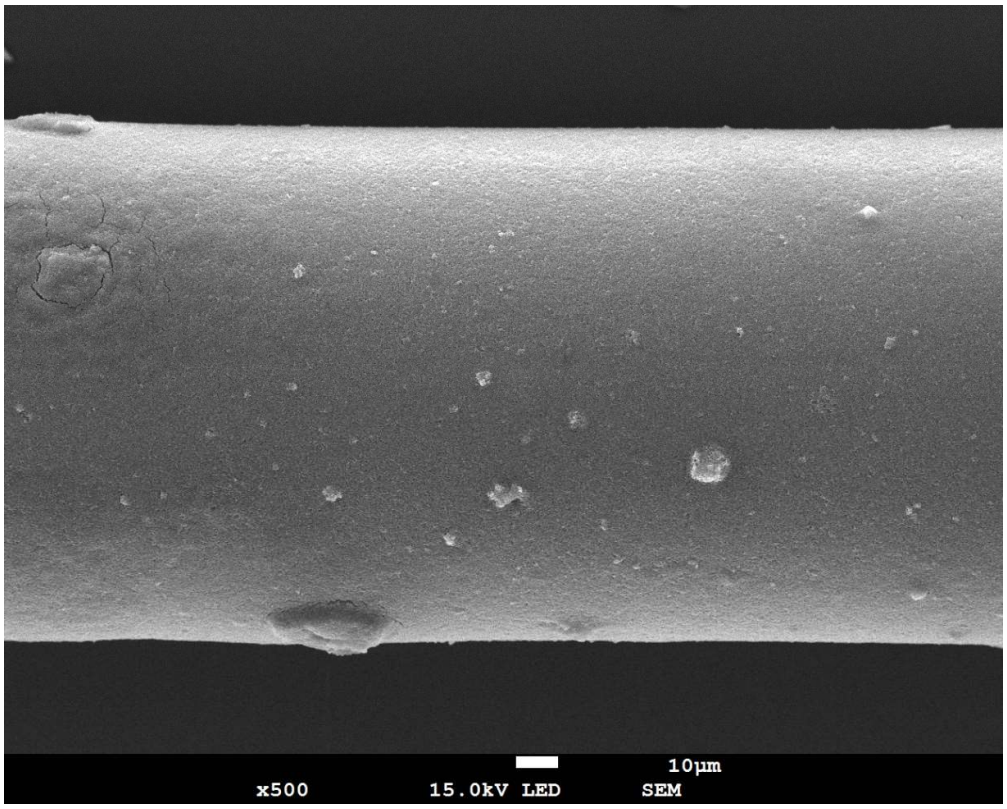


Figure 5-23: Fibre coated in-situ (5 h; 150°C) with MIL-53(Al)(DMF).

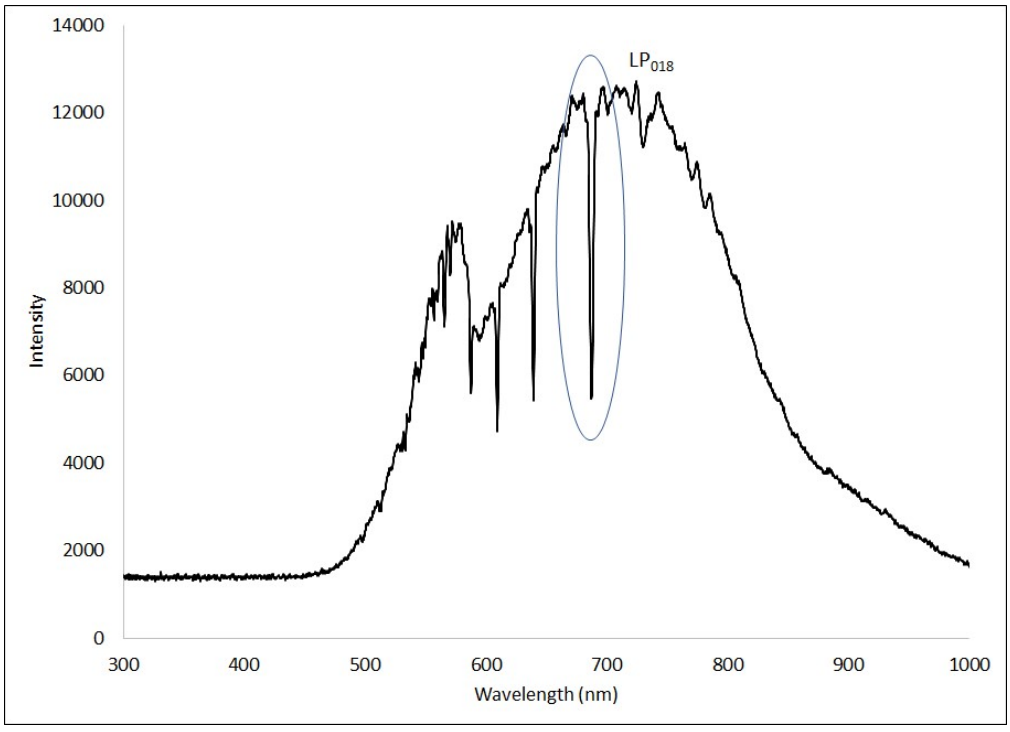


Figure 5-24: Total spectrum of LPG coated in-situ with MIL-53(Al)(DMF) at 150°C with 5 h reaction time.

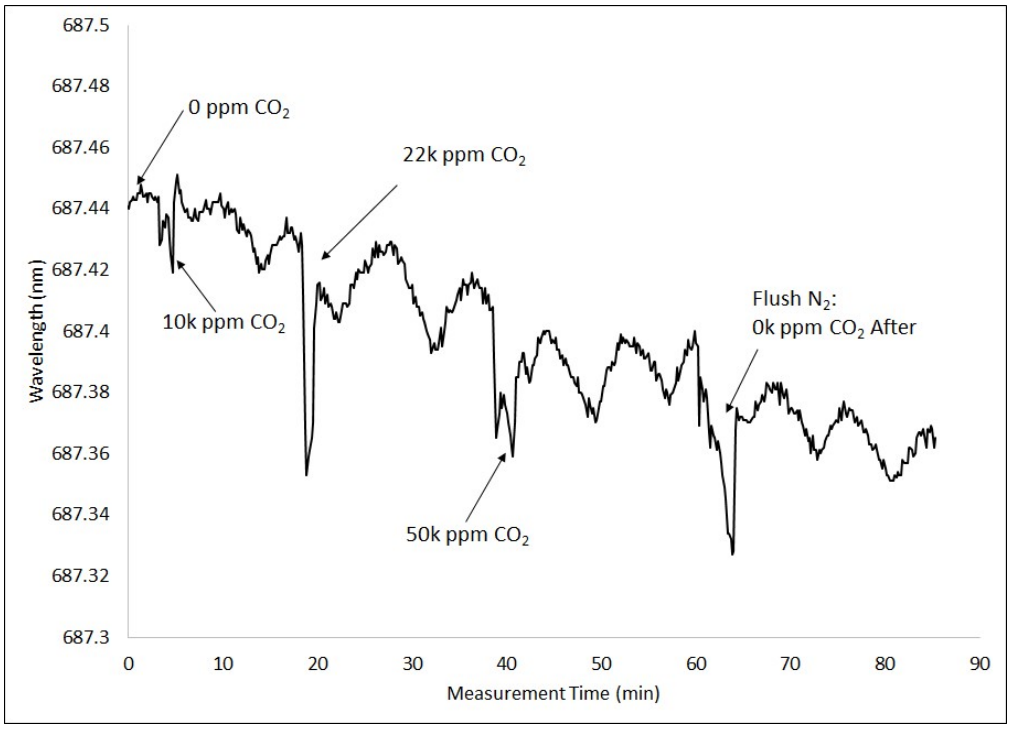


Figure 5-25: CO_2-sensor experiment results for fibre coated in-situ with MIL-53(Al)(DMF). Measured wavelength for LP_{018}-band.

The results of the sensor measurement are visible in Table 5-25, while the measured wavelength at different CO_2-concentration and the resulting wavelength shifts between different concentrations are shown in Table 5-21 and Table 5-22, respectively. The positions, where CO_2 or N_2 were added are visible in the spectrum as seen by wavelength changes in the spectrum. The blank value was measured before any CO_2 was added (0 ppm CO_2: 687.442 ± 0.011 nm σ = 0.0016 nm). The measured wavelength shifts between the different CO_2-concentrations (see Table 5-22 above) are close to or below the spectral resolution (0.02 nm) of the spectrometer. Furthermore, is the wavelength, after flushing the chamber with N_2 and returning the CO_2 value to 0 ppm, not returning to the starting value, but instead further decreasing (-0.027 nm). This imply that the LPG has no sensitivity to different CO_2-concentrations. If the LPG have shown sensitivity to the CO_2-concentration, the wavelength should have increased with the flushing of the chamber and the reduction of the CO_2-concentration. Another possibility is that the CO_2 was trapped in the coating and cannot be removed by simply flushing with N_2.

Table 5-21: Measured wavelength during CO_2-sensor test of fibre coated in-situ with MIL-53(Al)(DMF). Measured for the LP_{018}-band.

CO_2 concentration (ppm)	Wavelength (nm)
0	687.442
10k	687.432
22k	687.408
55k	687.387
0 after experiment	687.360

Table 5-22: Measured wavelength shift between varying CO_2-concentrations and sum of the wavelength change of fibre coated in-situ with MIL-53(Al)(DMF). Measured for the LP_{018}-band.

CO_2 concentration change (ppm)	Wavelength (nm)	Σ Wavelength shift (nm)
0 → 10k	-0.010	-0.010
10k → 22k	-0.024	-0.034
22k → 55k	-0.021	-0.055
55k → 0 after experiment	-0.027	-0.082

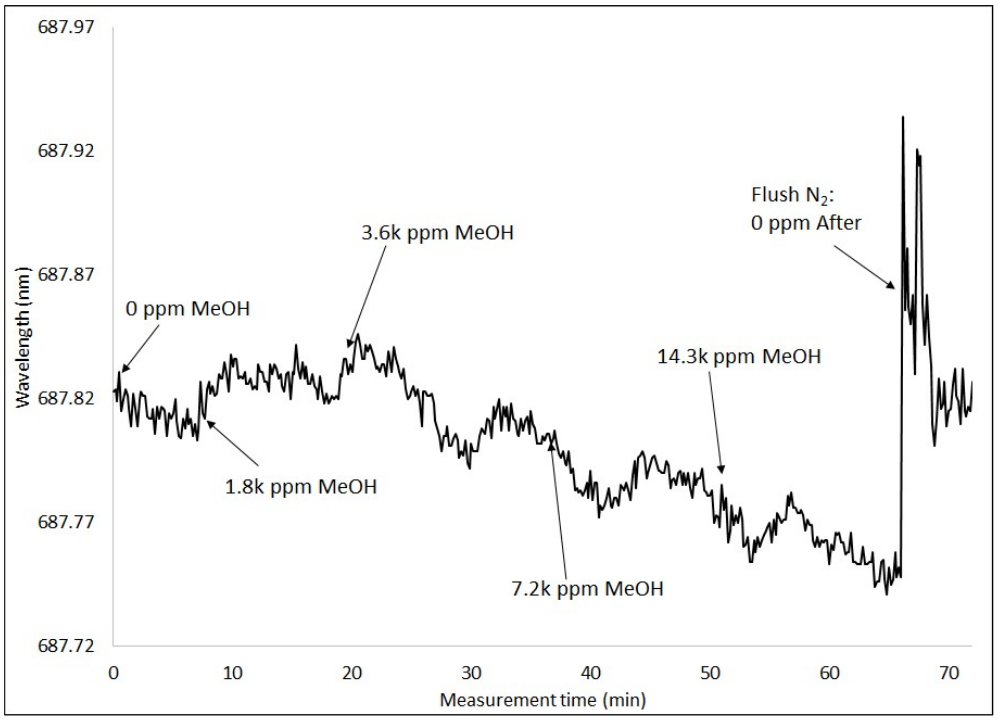


Figure 5-26: MeOH-sensor experiment results for fibre coated in-situ with MIL-53(Al)(DMF). Wavelength for LP_{018}-band.

Similar to the experiments described above, the same fibre employed for the CO_2 experiments was used to investigate the sensitivity towards MeOH. The fibre was placed overnight in oven at 100°C to remove possible residues and impurities from the fibre.

Table 5-23: Measured wavelength during MeOH sensor test of fibre coated in-situ with MIL-53(Al)(DMF). Measured for the LP_{018}-band.

MeOH concentration (ppm)	Wavelength(nm)
0	687.813
1.8k	687.827
3.6k	687.810
7.2k	687.789
14.3k	687.756
0 after experiment	687.821

Table 5-24: Measured wavelength shift between varying MeOH-concentrations and sum of the wavelength change of fibre coated in-situ with MIL-53(DMF). Measured for the LP_{018}-band.

MeOH concentration change (ppm)	Wavelength shift (nm)	Σ Wavelength shift (nm)
0→ 1.8k	+0.014	+0.014
1.8k → 3.6k	-0.017	-0.003
3.6k → 7.2k	-0.021	-0.024
7.2k →14.3k	-0.033	-0.057
14.3 → 0 after experiment	+0.065	-0.008

As with the results for the CO_2-response, the observed shifts for the MeOH sensor experiment are in the range or below (*e.g.* 0 → 1.8k ppm: +0.014 nm; 3.6k ppm → 7.2k ppm: -0.021 nm) the spectral resolution of the spectrometer (0.02 nm). Furthermore, the first shift (0k ppm → 1.8k ppm MeOH) moves to larger wavelength, while the wavelength shifts during the following concentration changes shifts to smaller values (see Table 5-24). After flushing the chamber with N_2 to return to 0 ppm, the measured wavelength shifts to larger wavelength, but the value is even higher than the starting value.

In summary has the LPG coated with MIL-53(Al) by in-situ coating give rise to wavelength shifts in varying direction during both the CO_2 and MeOH measurements. The measured shifts are close to or even below the spectral resolution of the spectrometer. It can, therefore, be assumed, that the fibre used has not shown a response for neither CO_2 or MeOH.

5.4.4 LPG coated with MIL-53(Al) by SAE

To coat an LPG by the SAE (solvent assisted epitaxy) approach, the same Teflon chamber used for the in-situ approach (Figure 5-22) was employed. Similar to the in-situ approach, the fibre was immersed in MIL-53(Al)(DMF) reaction mixture, but immediately removed from the reaction mixture. This process leaves only a small film of MIL-53(Al)(DMF) reaction mixture on the fibre. The saturated DMF atmosphere required for the experiment was established by adding fresh DMF to the chamber (~3 ml) but preventing direct contract with the fibre (Figure 5-27). The reaction was conducted at 150°C with 5 h reaction time. A SEM image of the fibre shows that the surface was successfully covered with MIL-53(Al), with a few cracks in the coating (Figure 5-28). The coating of this LPG fibre was activated by solvent exchange in MeOH for 1 day and the fibre was heated at 100°C overnight before the sensor experiment.

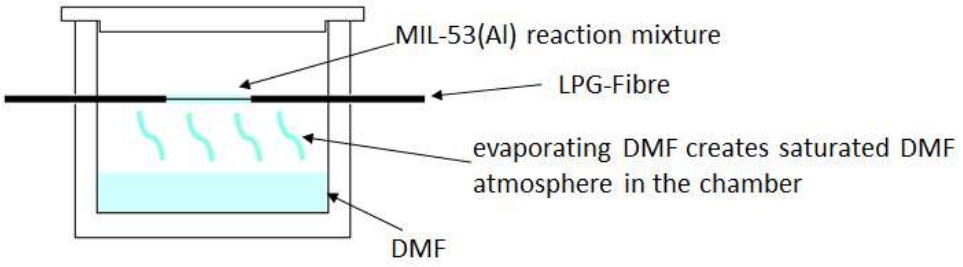


Figure 5-27: Schematic image of coating fibre by SAE

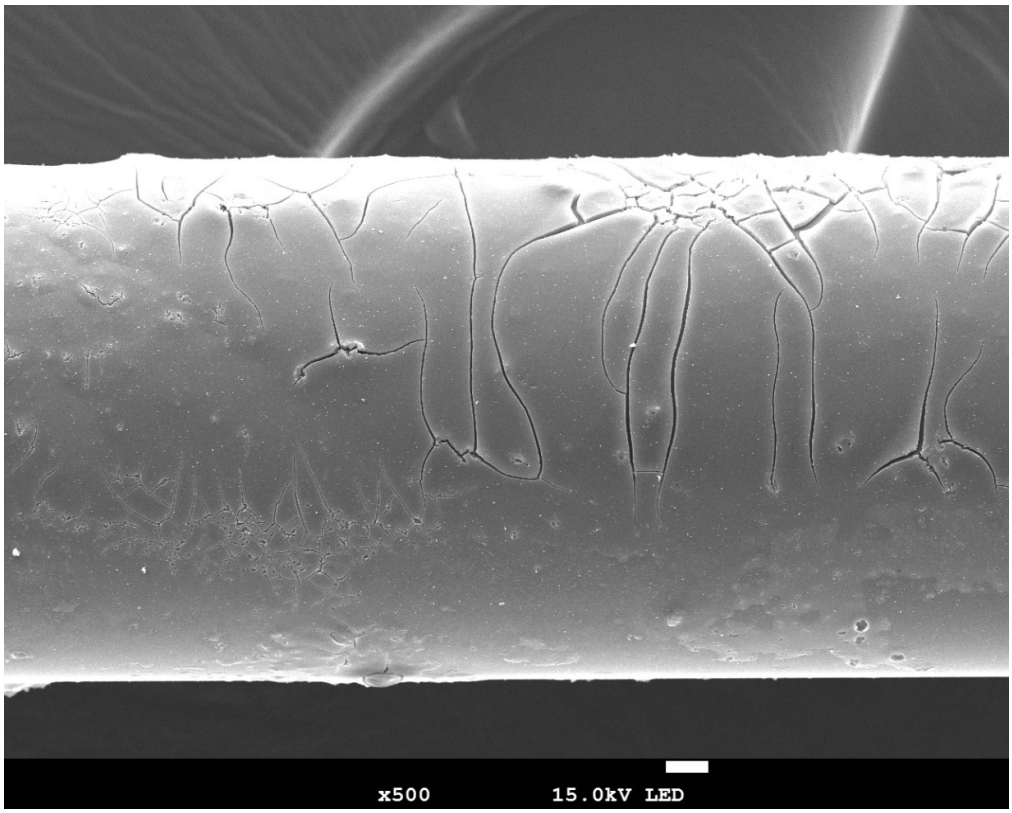


Figure 5-28: Fibre coated with MIL-53(Al)(DMF) by SAE approach.

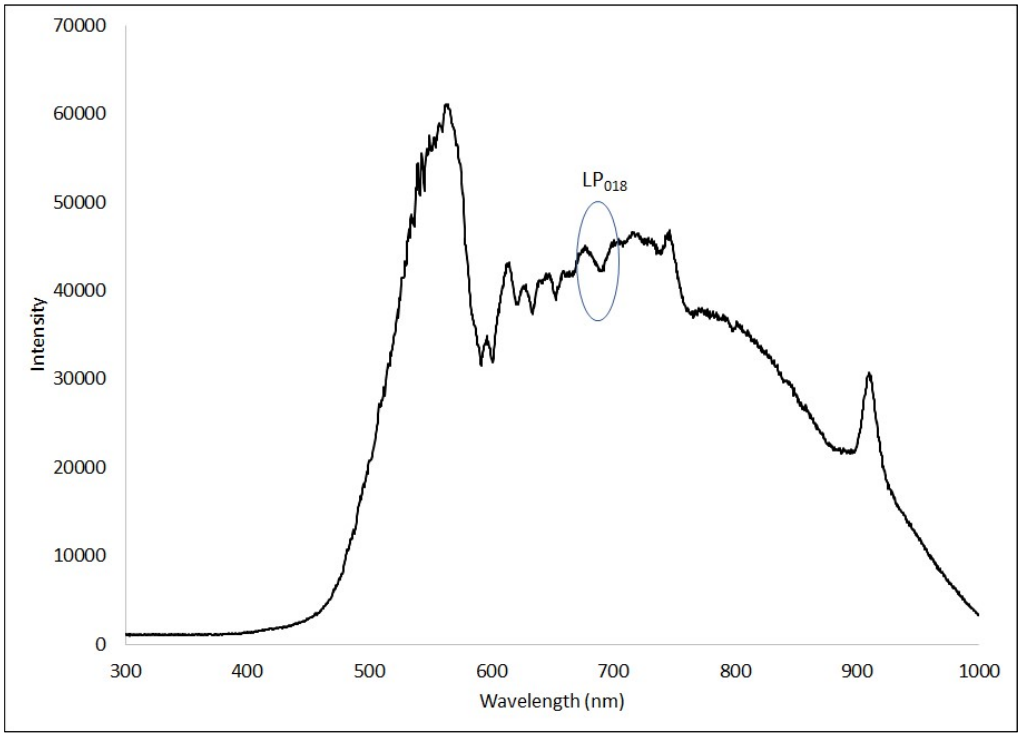


Figure 5-29: Total spectrum of LPG coated by SAE with MIL-53(Al)(DMF) at 150°C with 5 h reaction time.

The wavelengths measured during the sensor tests are shown in Figure 5-30, while the measured wavelengths at different CO_2-concentrations are shown in Table 5-25. The corresponding wavelength shifts are shown in Table 5-26. One noticeable difference to the

in-situ coated LPG and dip-coated LPG, is that the observed bands are less distinct (Figure 5-29). This leads at the same time to a larger variation of the measured wavelengths (0 ppm CO_2: 690.416 ± 0.141 nm; σ = 0.0846 nm). Furthermore, the LP_{019}-band is split into two individual bands, but the bands are not distinct enough, preventing the identification of the bands by the SIR program. The sensor response for the LP_{019}-band therefore could not be investigated further. At first (0 ppm → 15k ppm CO_2) a wavelength shift of +0.442 nm could be observed, but this shift was only observed during the first adding of CO_2 to the chamber. During the consecutive steps the absolute value of the wavelength shift is smaller and furthermore exhibits shifts in opposing directions (*e.g.* 15k ppm → 30k ppm: +0.096 nm; 30k ppm → 45k ppm: -0.045 nm; see Table 5-26).

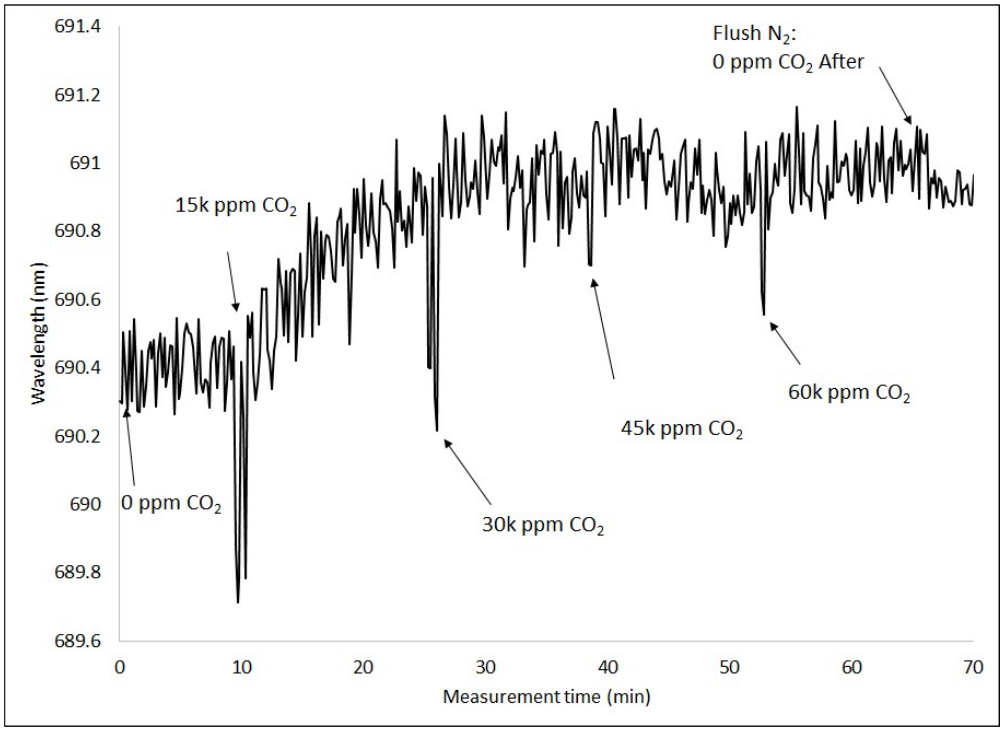


Figure 5-30: CO_2-sensor experiment results for fibre coated by SAE with MIL-53(Al)(DMF). Measured wavelength for LP_{018}-band.

Table 5-25: Measured wavelength during CO_2-sensor test of fibre coated by SAE with MIL-53(Al)(DMF). Measured for the LP_{018}-band.

CO_2 concentration (ppm)	Wavelength (nm)
0	690.416
15k	690.858
30k	690.954
45k	690.911
60k	690.998
0 after experiment	690.907

Table 5-26: Measured wavelength shift between varying CO_2-concentrations and sum of the wavelength change of fibre coated by SAE with MIL-53(Al)(DMF). Measured for the LP_{018}-band.

CO_2 concentration change (ppm)	Wavelength (nm)	Σ Wavelength shift (nm)
0 → 15k	+0.442	+0.442
15k → 30k	+0.096	+0.538
30k → 45k	-0.045	+0.493
45k → 60k	+0.087	+0.580
60k → 0 after experiment	-0.091	-0.489

The SAE coated fibre showed at first a promising wavelength shift of +0.442 nm between 0 and 15k ppm CO_2 (Table 5-26). It was therefore tested if this wavelength shift can be observed again in a subsequent experiment. Thus, the test chamber was flushed with N_2 for 20 min directly after the first experiment (during the step of flushing with N_2 the wavelength was not recorded) and the LPG exposed again to varying CO_2-concentrations to investigate the wavelength shift. The measured wavelengths during the experiments can be seen in Figure 5-31, while the measured wavelengths at different CO_2-concentrations are visible in Table 5-27 and the resulting wavelength shifts in Table 5-28. In contrast to the first CO_2-experiment, the wavelength shift at low CO_2-concentrations was not repeatable (0 ppm → 10k ppm CO2: -0.002 nm). In contrast, at higher concentrations a wavelength shift was observed (45k ppm → 60k ppm CO_2: +0.168 nm), but this shift is lower than the LOQ (σ = 0.0871 nm; LOQ is therefore 0.871 nm). However, at the same time it might be possible that the CO_2 has a too strong interaction with the MIL-53(Al) coating and cannot be removed by simply flushing with N_2. The coating might be therefore already saturated with CO_2 and cannot show any sensor response.

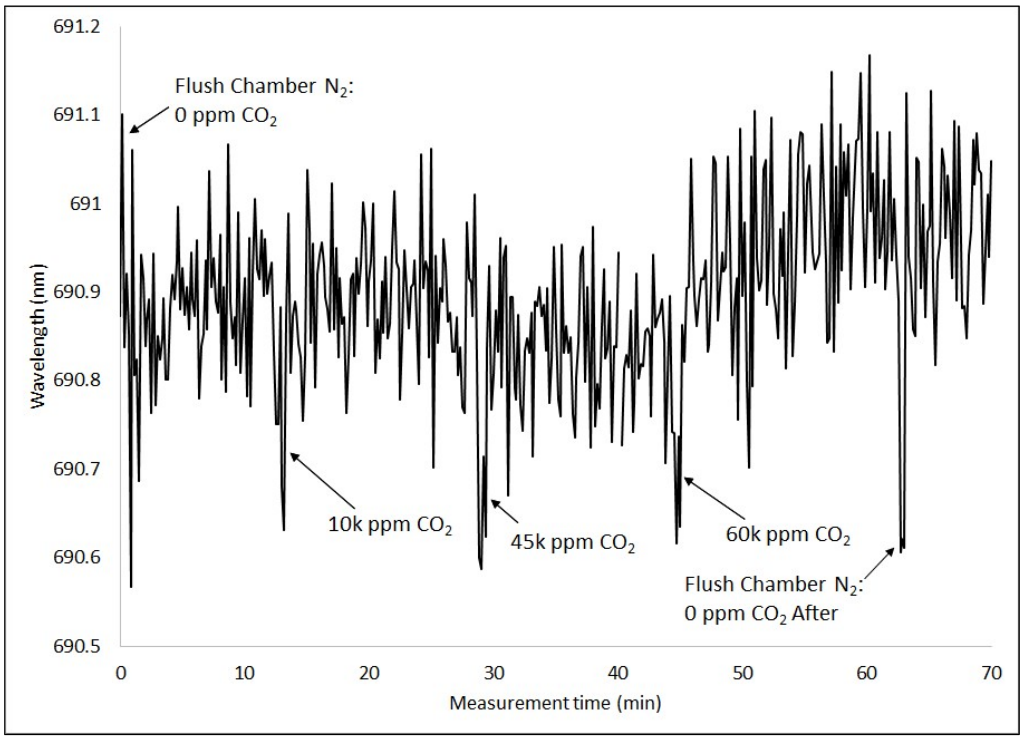


Figure 5-31: Repetition CO_2-sensor experiment results for fibre coated by SAE with MIL-53(Al)(DMF). Measured wavelength for LP_{018}-band.

Table 5-27: Measured wavelength during repeated CO_2-sensor test of fibre coated by SAE with MIL-53(Al)(DMF). Measured for the LP_{018}-band.

CO_2 concentration (ppm)	Wavelength (nm)
0	690.887
10k	690.885
45k	690.837
60k	691.004
0 after experiment	690.998

Table 5-28: Measured wavelength shift of repeated sensor experiment between varying CO_2-concentrations and sum of the wavelength change of fibre coated by SAE with MIL-53(Al)(DMF). Measured for the LP_{018}-band.

CO_2 concentration change (ppm)	Wavelength shift (nm)	Σ Wavelength shift (nm)
0 → 10k	-0.002	-0.002
10k → 45k	-0.048	-0.050
45k → 60k	+0.168	+0.118
60k → 0 after experiment	-0.006	+0.112

In contrast to the other LPG experiments until now, it was not possible to conduct the experiments for the MeOH sensitivity with the same fibre that was used during the CO_2-experiments. In comparison with the other LPGs before, the mechanical stability of the SAE coated fibre was reduced, and it broke after removal of the LPG from the sensor box (more information on page 172). Instead, a fibre, coated in similar conditions to the first fibre, was used for the MeOH experiment.

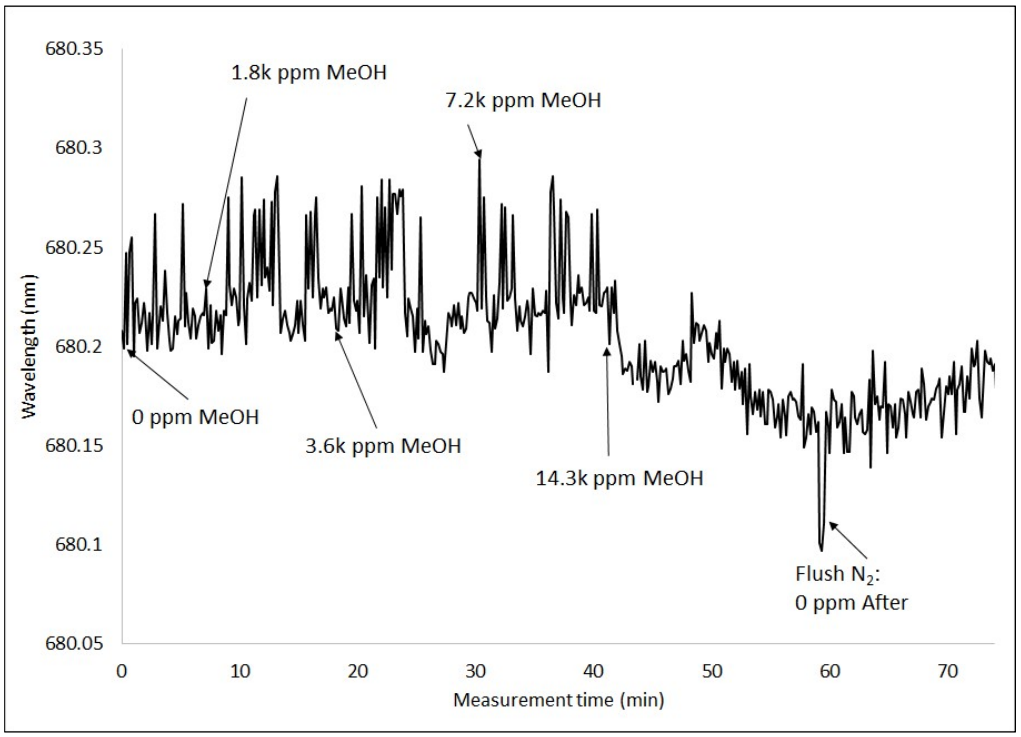


Figure 5-32: MeOH-sensor experiment results for fibre coated by SAE with MIL-53(Al)(DMF). Measured wavelength for LP_{018}-band.

Table 5-29: Measured wavelength during MeOH-sensor test of fibre coated by SAE with MIL-53(Al)(DMF). Measured for the LP_{018}-band.

MeOH concentration (ppm)	Wavelength (nm)
0	680.215
1.8k	680.232
3.6k	680.209
7.2k	680.229
14.3k	680.171
0 after experiment	680.179

Table 5-30: Measured wavelength shift between varying MeOH-concentrations and sum of the wavelength change of fibre coated by SAE with MIL-53(Al)(DMF). Measured for the LP_{018}-band.

MeOH concentration change (ppm)	Wavelength shift (nm)	Σ Wavelength shift (nm)
0 → 1.8k	+0.017	+0.017
1.8k → 3.6k	-0.023	-0.006
3.6k → 7.2k	+0.020	+0.014
7.2k →14.3k	-0.058	-0.044
14.3k → 0 after experiment	+0.008	-0.036

The wavelength measured during the MeOH sensor experiment is shown in Figure 5-32, while the measured wavelength at different concentrations and the resulting wavelength shifts are shown in Table 5-29 and Table 5-30, respectively. Apart from 7.2k ppm → 14.3k ppm MeOH (-0.058 nm), the shifts were found to be below the spectral resolution of the spectrometer and shift in opposite directions. The variation of the measured wavelength is lower than that for the CO_2-experiment (0 ppm MeOH: 680.215 ± 0.049 nm; σ = 0.0177 nm; First CO_2 sensor experiment first: σ = 0.0846 nm; Repetition of CO_2 sensor

experiment: σ = 0.0871 nm, all for LP_{018}-band), but still higher than the variations measured during the MeOH experiments for the other coated fibres (For Dip-Coating: σ = 0.0044 nm; For In-situ coating: σ = 0.0057 nm, all for LP_{018}-band).

A huge problem of the SAE coated fibre was is the repeatability of the results. While the fibre has shown a wavelength shift between 0 ppm CO_2 and 15k ppm CO_2 during the first measurement (+0.442 nm), the shift during a consecutive measurement (0 ppm → 10k ppm) was negligible (-0.002 nm).

Another problem observed during the SAE process, might further explain the less distinct peaks in the overall spectrum. While neither the dip-coating or the in-situ coating have changed the mechanical properties of the fibre, the LPG became brittle during the SAE coating process and only one of five coated LPGs survived the coating process. This was why different LPGs were used for the CO_2 and MeOH measurement. The SAE-coated LPG broke after the CO_2-sensor experiments. The LPG fibre are too small to conduct typical material tests such as tensile testing, but some further tests on the fibre were done to investigate this behaviour.

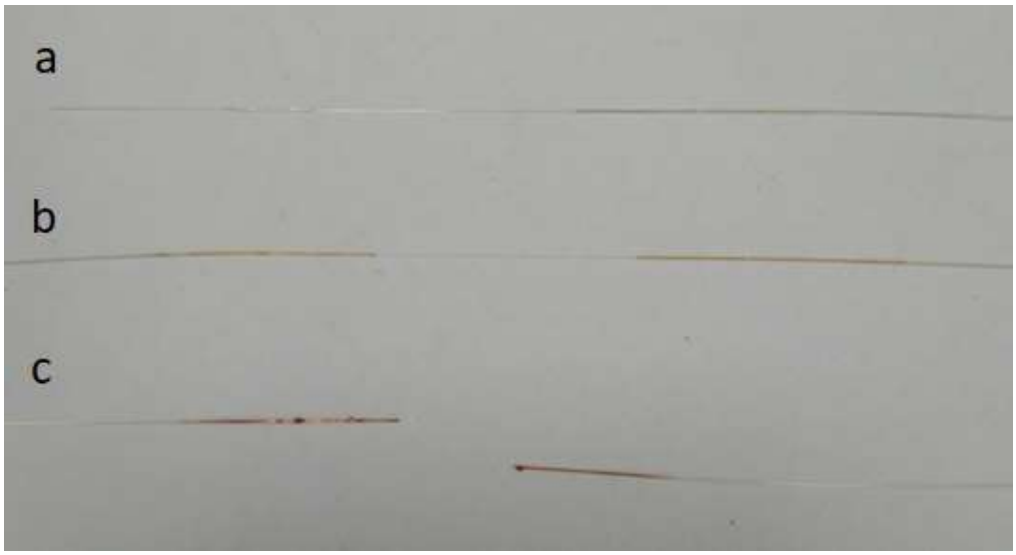


Figure 5-33: Different fibre coated by SAE (bottom, c, fibre broke into two pieces), without DMF vapor (mid, b) and only DMF vapor (top, a).

In Figure 5-33, three fibre are shown. For the fibre stability test, the SAE approach was separated into two steps. The fibre on top (Figure 5-33 a), was placed in the Teflon chamber and the chamber filled with DMF to create a saturated atmosphere during the synthesis. However, the fibre was not wetted with reaction mixture. After the experiment, the colour of the protective coating did not change, but it was observed that the coating (made from an acrylate polymer) became soft and can be easily stripped from the fibre. After drying, the mechanical stability has returned to its original state. The fibre shown in the middle (Figure 5-33 b), was placed in the Teflon chamber and wetted with MIL-53(Al)(DMF) reaction mixture, but no DMF was added to the chamber to create a saturated atmosphere. After the reaction, the colour of the protective coating has changed to yellow, but the mechanical properties did not change. The fibre at the bottom (Figure 5-33 c) was coated using the SAE-approach. The fibre was wetted with MIL-53(Al)(DMF) reaction mixture and the chamber filled with DMF to create a saturated atmosphere. The

protective coating turned brown and started to decompose (droplets of the coating were seen). Furthermore, this fibre broke during the removal from the chamber after the experiment. Most SAE coated fibres, like this, tend to break at the point between the protective coating and the start of the LPG coating, where the protective coating was removed, most likely caused by leverage at this point. The results of these experiments imply that a combination of the softening of the protective coating by the DMF-vapor and a reaction of the MIL-53(Al) with the weakened protective coating lead to a brittle LPG.

5.5 Conclusions and Future work

In total 4 fibres (one blank and 3 coated with MIL-53(Al) using different approaches) were tested for sensor response to CO_2 and MeOH.

For the blank fibre, the results were measured for the LP_{018}-band at ~665 nm and the split LP_{019}-band ($LP_{019L:}$ ~786 nm; LP_{019R}: ~863 nm). The blank fibre showed a response to CO_2 at high concentrations (60k ppm CO_2: 0.214 nm; for the LP_{018}-band), which is larger than the spectral resolution of the used detector (0.02 nm). However, this response is much lower than for previously reported MOF coated LPGs: Hromadka *et.al.* [21] have reported an LPG coated with HKUST-1 by a Layer-by-Layer approach, which has shown even at 5k ppm CO_2, a response of 0.5 nm (for the LP_{018}-band). However, a higher response can be expected for the LP_{019}-band (independent on the target molecule) and especially for the difference between the LP_{019L}- and LP_{019R}-band, because split bands show a response in opposing direction to external stimuli. Consequently, the ΔLP_{019} value has shown an even higher response than the LP_{018}-band for the blank fibre in the CO_2 and MeOH sensor experiments respectively (Table 5-31).

Table 5-31: Summary of the sensor results for the blank fibre. The concentrations for CO_2 and MeOH were the highest measured concentration of the target compound during the sensor test and the wavelength shift was given as the sum of the wavelength shift (the shift between 0 ppm and the specified concentration).

Measured concentration (ppm)	Observed band	Wavelength shift (nm)
60k ppm CO_2	LP_{018}	0.214
60k ppm CO_2	ΔLP_{019}	1.025
21.4k ppm MeOH	LP_{018}	0.584
21.4k ppm MeOH	ΔLP_{019}	3.032

However, bands at larger wavelength have a higher uncertainty (the fluctuation of the measured wavelength is larger) and the measured shift has not exceeded the LOQ (Table 5-32). It was therefore not reasonable to use the LP_{019}-band for the detection of CO_2.

Table 5-32: Uncertainty of the measured wavelength during the CO_2-sensor experiment for the blank fibre.

Observed band	σ of the measured wavelength (nm)	LOQ (nm)
LP_{018}	0.0058	0.058
LP_{019L}	0.0766	0.766
LP_{019R}	0.1372	1.372

In contrast, for MeOH even at lower concentrations (~1.8k ppm MeOH) a distinct wavelength shift was observed for the blank fibre (0 ppm → 1.8k ppm MeOH: +0.371 nm). This shift became smaller at higher concentrations (*e.g.* 7.2k ppm → 14.3k ppm: +0.007 nm), due to saturation effects. For the MeOH-experiments, the LP_{019}-band (and the

difference ΔLP_{019}) showed also a higher uncertainty for the wavelengths in comparison with the LP_{018}-band (LP_{018}: σ = 0.011 nm; LP_{019L}: σ = 0.099 nm; LP_{019R}: σ = 0.115 nm), but at the same time a larger shift was observed. Hence, both the LP_{018}- and LP_{019}-bands can be used for the detection of different MeOH-concentrations. However, in comparison with a MOF-coated fibre the response of the blank fibre was smaller. While the blank fibre displayed a response of 0.578 nm for the LP_{018}-band at ~20k ppm MeOH, a ZIF-8 coated fibre has shown a shift of ~2 nm at similar MeOH concentrations [22].

The blank fibre displayed surprisingly good results for the CO_2- and MeOH-detection (the measured wavelength shift was larger than the LOQ), but the problem with a blank fibre is that the LPG reacts to different external stimuli and the source of the wavelength shift cannot be clearly identified. A MOF-coated LPG might, therefore, be not only increasing the measured shift (by concentration of the target compound in the coating) but also making the response more selective. The chemical environment and pore size of a MOF can be controlled and only specific target molecules might be adsorbed in a MOF thin-film. With such selectivity (provided by the MOF thin-film) the wavelength shift can be therefore directly attributed to external stimuli such as “concentration change of target compound”.

While LPGs have previously been coated with ZIF-8 to create a VOC-sensor and HKUST-1 for a CO_2-sensor, other MOFs might be also applied for coatings. The coating of MIL-53(Al) on glass was investigated in the previous chapter 4 (p. 82) and the most promising approaches used for the coating of an LPG and the sensor response investigated towards CO_2 and MeOH. The approaches used are dip-coating 5 times from a 0.5 wt% suspension in MeOH as solvent, direct in-situ synthesis at 150°C and 5 h reaction time and solvent assisted epitaxy (SAE) in saturated DMF atmosphere at 150°C and 5 h reaction time.

However, none of these approaches led to a reasonable sensor response to either CO_2 or MeOH, whereas a reasonable sensor response will be a wavelength shift which is at the same time larger than the spectral resolution of the detector (0.02 nm) and larger than the LOQ. The LPG coated in-situ or by dip-coating showed wavelength shifts below the spectral resolution and in varying directions and can therefore be discarded.

The SAE coated fibre has shown a larger wavelength shift (0 ppm → 15k ppm CO_2: 0.448 nm) in comparison with the in-situ or dip-coated LPG, but stability of the fibre was a problem. The coating process has made the LPG brittle so that most fibres broke during the coating process. Furthermore was the above-mentioned initial large wavelength shift of 0.448 nm not reliable. For the SAE coated fibre, the wavelength measured has a large uncertainty, which leads to a wavelength with a large standard derivation (during CO_2 experiment: blank fibre: σ = 0.0058 nm, SAE: σ = 0.0846 nm, both values for the LP_{018}-band). The resulting wavelength measured for the SAE coated fibre is therefore below the LOQ cannot to be used for the measurement of different CO_2-concentrations. Furthermore, the results could not be not repeated for consecutive measurement. In addition, the SAE-coated fibre did not show a response to MeOH.

Therefore, it seems that the MIL-53(Al) does not improve the sensor results, but instead the coating protects the LPG from a sensor response. In order to identify the possible

reason for the lack of sensor response for the MIL-53(Al) coated LPGs different possible contributing effects will be discussed.

One problem might be the quality and thickness of the coating. The in-situ approach led to a coating with a thickness of ~2.9 µm, the dip-coating approach a thickness of ~900 nm and the SAE to a coating of about 4 µm (the thickness were measured for the test systems on glass slides in chapter 4, p. 82). A very thick coating (in general >1 µm) reduces the sensitivity of a LPG [94],[101], but this depends on the system used. For instance both films of ~2 µm and 50 nm of HKUST-1 show a sensor response to CO_2 [21]. For MIL-53(Al) a coating of 900 nm appears to be still too thick and methods have to be found, which lead to coatings thinner than 900 nm, while retaining a homogenous coating of the surface.

The SAE approach led to the thickest coating and it might be therefore possible that the noisy signal of the SAE-coated fibre is partly caused by the coating thickness of ~4µm. It might be possible to control the film thickness by not using a one-step synthesis at 150°C and 5 h reaction time, but a repeated coating with shorter reaction time or reduced reaction temperature (*e.g.* 3 separate reaction at 150°C with 1 h reaction time). In the case of SAE investigations are required to establish how such a repeated process would affect the stability of the fibre and homogeneity of the coating. It is still unclear whether it would be worthwhile to try to improve the dip-coating and in-situ coating methods as both approaches have not shown any sensor response.

Another potential problem might be the adsorption capacity or kinetics of MIL-53(Al). If MIL-53(Al) has slow kinetics or low capacity, an insufficient sensor response would be expected. While the adsorption kinetics of CO_2-adsorption by MIL-53(Al) is fast (it can reach its maximum CO_2-capacity even after short contact times of 10 min) [384], the CO_2-capacity especially at low pressure might be problematic. While MIL-53(Al)(DMF) can adsorb ~0.3 mmol g^{-1} CO_2 at low pressures of 50 mbar (~50k ppm CO_2, Figure 3-9), HKUST-1 reaches adsorption of ~2 mmol g^{-1} at the same concentration [244]. The problem might be that MIL-53(Al) is not a MOF with open-metal sites like HKUST-1 [245] which in general have strong interactions with polarisable compounds like CO_2. Another possible way to increase the CO_2-capacity is to use MOFs containing amine groups. It might be possible in principle to increase the capacity of the coatings by using with the amino-derivative NH_2-MIL-53(Al), which is known to have much higher capacity for CO_2, up to 6 times higher capacity in comparison with the pristine MIL-53(Al) [385]. However, until now, only the unfunctionalized MIL-53(Al) was used to investigate the preparation of thin-films on glass and for sensor performance as coatings on an LPG. It might be plausible to transfer a working thin-film coating from the unfunctionalized MIL-53(Al) to other derivatives due to a similar morphology of the MIL-53-class. However, the use of derivatives has exceeded the scope of this research.

In contrast to the CO_2-capacity, the MeOH-capacity for MIL-53(Al) can be assumed to be sufficiently high. Under the conditions of sensor measurements (~20k ppm MeOH), both ZIF-8 and MIL-53(Al) show similar capacities. These capacities were measured for powder samples. Adsorption capacity measurement for MOF thin-films are very sparse in literature and the results of powder samples are better comparable with each other. While MIL-53(Al) has a capacity of ~7 mmol g^{-1}, ZIF-8 shows a capacity at the same relative

pressure of 8 mmol g^{-1} [386]. At least regarding capacity, MIL-53(Al) should have shown a similar sensor response to MeOH. However, no data regarding the adsorption kinetics towards MeOH could be found and the adsorption of MeOH in MIL-53(Al) might be slower than that in other MOFs, *e.g.* ZIF-8.

Another possible challenge might be the porosity of the thin-films studied. Even with an adequate theoretical capacity for CO_2 or MeOH no sensor response is expected for thin-films, which are not porous. While this was of lesser importance for the dip-coating approach (already activated MIL-53(Al) was used) it might be problematic for the in-situ coating and SAE. Unreacted starting material and solvent residue is trapped in the pores of MIL-53(Al) after the synthesis reducing the available porosity. The common ways to activate MIL-53(Al) powders are refluxing with DMF [288] or heating at 330°C for 3 days [115]. Both activation methods would destroy the LPG. Therefore, the LPG fibres were activated by solvent exchange in MeOH overnight and dried at 100°C to remove possible solvent residue. This method proven at least for the powder samples as a sufficiently effective activation method. For the MeOH solvent exchanged sample a BET-area measured of 832m^2 g^{-1}, while the classical heating at 330°C lead to a porosity of 1002 m^2 g^{-1}. Furthermore MIL-53(Al)(DMF) was used. The results from chapter 3 (p. 38) have shown that MIL-53(Al)(DMF) has 70% of its final porosity available without an activation step.

In summary the coating of MIL-53(Al) on glass had been investigated in the previous chapter 4 (p. 82) and the most promising methods were chosen for LPG coating. A more precise control of the thickness necessary for an LPG coating would be beneficial. For other MOFs previously used for the coating of LPGs, ZIF-8 and HKUST-1, methods to more precisely control coating thickness were used in literature. ZIF-8 shows several advantages over MIL-53(Al) such as fast reaction even at RT (30 min), hydrophobic pores (*e.g.* water cannot enter the pores of ZIF-8 and blocking the pores for the target compound), easy activation (removing of solvent molecules after reaction possible in a N_2-flow) and reduced agglomeration of ZIF-8 particles leading to homogenous thin-films [141]. The results show that it is complex to apply a given MOF to an LPG in order to create a sensor and that more research is necessary to better understand thin-film coating mechanism for MOFs in general.

6 A novel hybrid ultramicroporous material as coating on LPGs

6.1 Introduction

As mentioned previously in chapter 2.6 (p. 30), different attempts have been applied in order to improve the selectivity of MOFs towards CO_2. This is often done by using MOFs which contain amine groups or uncoordinated open metal sites, which have an improved interaction to CO_2, but at the same time typical drawbacks. MOFs with additional amino groups have often reduced porosity and lower thermal stability than the pristine compounds [218] and MOFs with open metal sites have often problems with humidity, where water competes with CO_2 for the open-metal sites and regeneration of the compound often leads to a reduction of porosity and CO_2 capacity [387] and the long-term stability of the samples [388].

Hence, a new class of compounds are tackling the problem of obtaining high CO_2-capacities at low pressures, using strong interactions based on tight fitting. High selectivity for linear molecules such as CO_2 and ethylene are achieved by a combination of size-exclusion effects, polarization of the target molecules and a strong chemical interaction between the target molecules and the framework, typically due to strongly electronegative cations/atoms (*e.g.* Ti or Si). This leads to CO_2-capacities at low partial pressure of 0.15 bar (*e.g.* SIFSIX-3-Ni: 2.65mmol g^{-1} [389]) comparable to MOFs with open metal sites or amine groups (*e.g.* PEI-MIL-101(Cr): 4.2mmol g-1 [213], HKUST-1: 3.5mmol g-1 [245], CPO-27-Mg: 5.3mmol g^{-1} [233]; Figure 5-1).

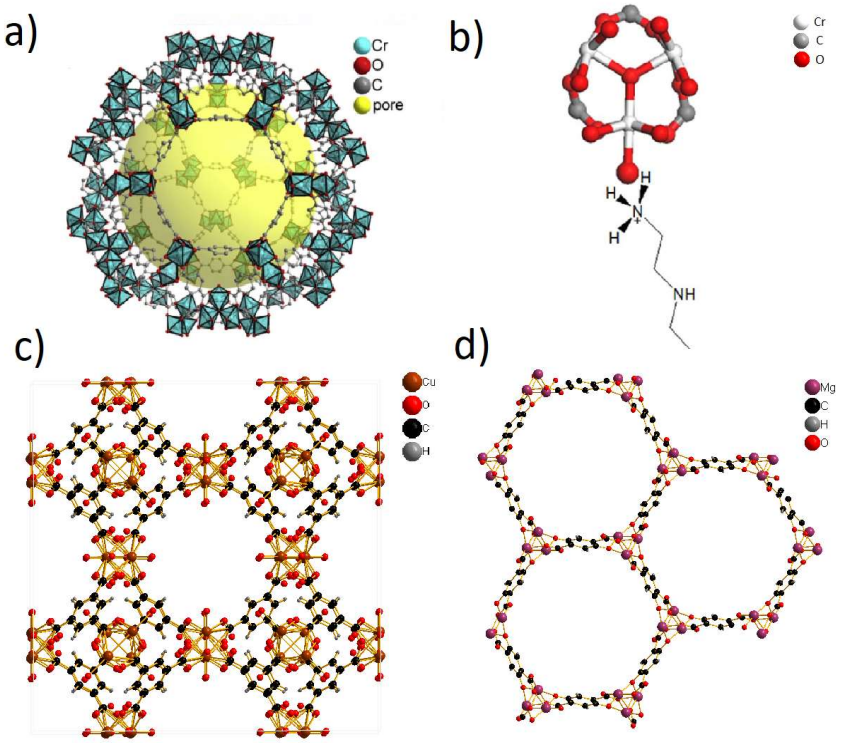


Figure 6-1: a) Structure of MIL-101(Cr) [390]; b) PEI-MIL-101(Cr) (PEI = polyethyleneimine) has the same structure then MIL-101(Cr), but PEI is bound to the open-metal sites in the MIL-101(Cr) [213]; c) Structure of HKUST-1 (structure calculated from existing crystal data [116]); d) Structure of CPO-27(Mg) (structure calculated from existing crystal data [391]).

While the CO_2-capacity at CO_2 partial pressures of 0.15 bar of these compounds is often slightly lower than for amine-containing or open-metal site MOFs, these MOFs have some of the highest known capacities at very low pressures, *e.g.* 2 mbar CO_2 (~2000 ppm CO_2) [132], which makes them promising materials for direct air capture (DAC, more information about DAC see p. 30) [196]. This new type of MOFs are known as hybrid ultramicroporous materials (HUMs) [236], because they have pore apertures which are small in comparison with other MOFs, often less than 0.5 nm [237] (*e.g.* ZIF-8: 0.9 nm [238]; HKUST-1: 1.0 - 1.5 nm [239]). HUMs are composed of three parts: metal cations, linear organic linker with nitrogen containing groups (bipyridines) and an inorganic anionic pillar. The properties of these MOFs can be therefore changed at three positions to create libraries with similar properties to fine-tune the MOFs for given applications; an approach which is known as crystal engineering [392].

The first example of the expanding class of HUMs has a cubic framework, composed of zinc as metal cation, 4.4'-bipyridine as linker and the octahedral anion hexafluorosilicate (SiF_6^{2-})[393] (Figure 6-2 a).

Since then, HUMs have been prepared with different metals including copper [241], nickel [242] or cobalt [389], anions containing tin [241], titanium [132] or niobium [237] and linker compounds including 1,2-bis(4-pyridyl)acetylene,[394] pyrazine [395], 1,4-bis(4-pyridyl)benzene [396] or 1,2-bis(4-pyridy)diazene [397], leading to an ever expanding number of existing HUMs. Even though most prepared HUMs have a primitive cubic topology, the group has been further extended by using non-octahedral anions like dichromate [243], tungsten or molybdenum oxides [398] introducing angularity (non-linearity) to the framework structures (Figure 6-2 b).

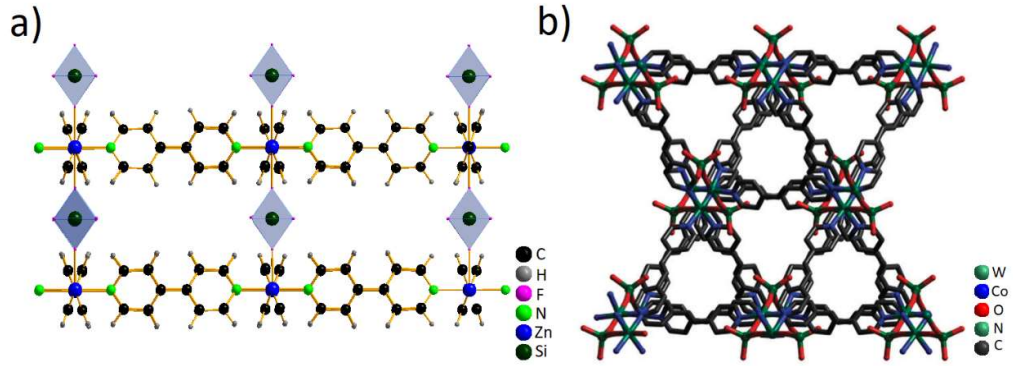
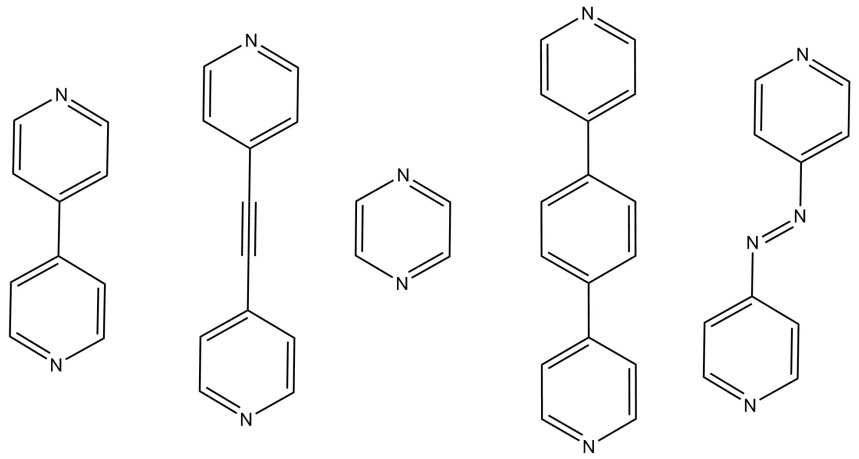


Figure 6-2: a) Structure of the first prepared HUM containing zinc as metal ion, 4.4'-bipyridine as linker and the SiF_6^{2-}anion bridging ligand (structure calculated from existing crystal data [394]); b) Structure of the tungsten containing, non-cubic HUM WOFOR-1-Co (H was omitted for clarity [398]).

The names given to HUMs are of systematic nature. The first part of the name identifies the inorganic anion used (*e.g.* SIFSIX for SiF_6^{2-}, TIFSIX for TiF_6^{2-} or NbOFFIVE for $NbOF_5^{2-}$), while the number characterizes the nitrogen containing linker (Figure 6-3). The metal cation is given as its elemental symbol. According to this scheme, the first ever synthesized HUM is for instance SIFSIX-1-Zn [393].



[1] [2] [3] [4] [14]

Figure 6-3: Examples of nitrogen containing linker (bipyridines) used for the synthesis of HUMs. Number in parenthesis show the number used to identify the linker in the HUMs.

HUMs have been investigated for their potential usage in commercial applications such as the purification of propene [237], acetylene [243], direct CO_2 capture from air and flue gases [399] or removal of toxic gases such as SO_2 [400]. Most of these potential applications are based on the high tendency for the adsorption of linear molecules like CO_2 at low partial pressure. This, and the hydrophobic nature of the HUMs, [389] makes them also promising candidates for the usage as a coating for CO_2-sensitive LPG sensors. From the numerous existing HUMs, TIFSIX-3-Ni was chosen the most promising candidate. TIFSIX-3-Ni has one of the highest CO_2-capacities of the HUMs at low CO_2-pressure [132]. The niobium containing NbOFFIVE-1-Ni displays a slightly higher uptake at low CO_2-pressure (40 $cm^3\ g^{-1}$ for TIFSIX-3-Ni and 42 $cm^3\ g^{-1}$ for NbOFFIVE-1-Ni at 2 mbar CO_2 pressure [132]) than TIFSIX-3-Ni, but due to the necessary usage of expensive starting material like Nb(V)-oxide and toxic hydrofluoric acid, the investigation with TIFSIX-3-Ni is preferred. The structure of the silicon derivate SIFSIX-3-Ni (due to the lack of crystal data for TIFSIX-3-Ni in literature) can be seen in Figure 6-4, a structure whose crystal parameters are close to those reported for TIFSIX-3-Ni (Table 6-1).

Table 6-1: Comparison of the crystallographic data for SIFSIX-3-Ni [242] and TIFSIX-3-Ni [132]. The values for a and b are equal.

	SIFSIX-3-Ni	TIFSIX-3-Ni
Space group	P4/mmm	P4/mmm
a (Å)	7.0148(4)	6.99007(18)
c (Å)	7.5655(7)	7.81267(21)
V ($Å^3$)	372.28	381.735

In the structure is the nickel cation is surrounded by 4 pyrazine groups through Ni-N bonds. The linear shape of pyrazine lead to the formation of a cubic primitive cell. The two remaining octahedral positions around nickel are occupied with by TiF_6^{2-} anions, separating the layers composed of nickel and pyrazine. The different pyrazine motifs are stacked in a coplanar manner and the framework is stabilized by hydrogen bonds between the hydrogen of the pyrazine and fluorine anionic pillars (highlighted as pale red bonds in

Figure 6-4). The structures of SIFSIX-3-Ni and TIFSIX-3-Ni are mostly similar, but titanium is a more electronegative atom than silicon, which leads to a shorter M-F bond (M = metal used in the inorganic anion) in TIFSIX in comparison with SIFSIX (Ti--F: 1.67 Å; Si--F: 1.81 Å) This leads to smaller pores and a tighter fit of CO_2 in comparison to SIFSIX-3-Ni, which further increases the selectivity towards CO_2 and the adsorption at low CO_2-pressures [132]. CO_2 is adsorbed linearly in the pores between the hexafluoro-anion pillars and the pore size of ~3.5 Å [395] is only slightly larger than the kinetic diameter of CO_2, which is 3.3 Å [210].

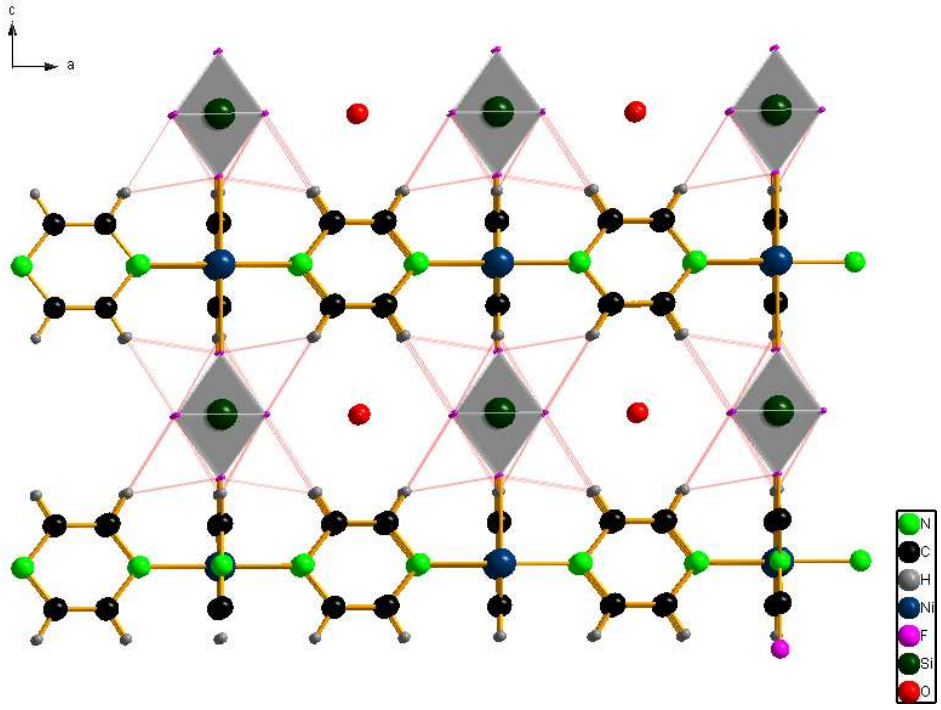


Figure 6-4: Structure of SIFSIX-3-Ni, which has a very similar structure to TIFSIX-3-Ni. The structure was calculated from existing crystal data [242]. View along the b-axis. The oxygen (red) in the pores represent water bound in the pores of SIFSIX-3-Ni before activation. Bonds in light red show stabilization of the framework by H···F hydrogen bonds.

Another advantage of TIFSIX in comparison to SIFSIX and the usage of nickel as the metal cation instead of copper, zinc or cobalt, is as improved thermal stability [389],[401], as a result of strong Ni-N and Ti-F bonds.

HUMs like TIFSIX and SIFSIX have mostly been investigated for applications such as gas separation and purification, investigations which are conducted with powder samples. In addition, the materials are recently discovered, which lead to the observation that to the best of our knowledge no thin-film synthesis of a HUM has yet been published. However for the preparation of a coating on a LPG, a thin-film synthesis has to be conducted and powder synthesis often does not directly convert to the synthesis on thin-films [327], a factor further complicated by the usage of the inert and non-porous support glass.

Thus, for the application of TIFSIX (for simplification TIFSIX-3-Ni, will be shorted to TIFSIX from now on) as a coating on an LPG sensor, the investigation will be divided into three consecutive steps:

- Replication /optimization of the powder synthesis of TIFSIX.
- Development of thin-film synthesis of TIFSIX on glass.
- Coating of LPG fibres and investigation of sensor performance.

6.2 Experimental

6.2.1 Materials

Nickel nitrate hexahydrate ($Ni(NO_3)_2{\cdot}6H_2O$), nickel carbonate basic hydrate ($NiCO_3{\cdot}2Ni(OH_2){\cdot}4H_2O$), pyrazine and H_2TIF_6 (60 wt% in water) were purchased from Sigma Aldrich. The solvents N,N-Dimethylformamide (DMF), acetone and methanol (MeOH) were purchased from Fischer Scientific. All chemicals were reagent grade and used as received. Deionised water was received from Millipore Direct-Q 5 UV water purification system.

6.2.2 Synthesis of $NiTiF_6$:

In a typical reaction, $NiCO_3{\cdot}2Ni(OH_2){\cdot}4H_2O$ (3 g, 4.93 mmol) was added to 15 ml water and the suspension stirred for 15 min at RT. 1.5 g H_2TiF_6 (as 60% solution in water, 10.98 mmol) were added and the reaction mixture stirred for additional 5 min. The reaction mixture was stored at RT for 2 days. After filtration, the solvent was evaporated for 1 day at 90°C resulting in a green, highly hygroscopic solid. Drying at 90°C was continued until a solid green product was formed. After 3 days drying time, 2.152 g (87% yield) of $NiTiF_6$ was collected.

ATR FTIR: ν (cm^{-1}) = 3422, 1640, 853, 700, 476.

6.2.3 One-step powder synthesis

The one-step synthesis was conducted according to an already existing synthesis protocol [402] and slightly modified. Briefly, $Ni(NO_3)_2{\cdot}6H_2O$ (5 mmol, 1.453 g), H_2TIF_6 (as 60 wt% solution in water, 5 mmol, 1.365 g) and pyrazine (10 mmol, 0.801 g) were stirred in 10 ml solvent (water, MeOH or DMF) and stored for 3 days at RT or 85°C respectively. The purple-blue precipitate was collected by filtration, washed with water (1 x 50 ml) and MeOH (2 x 50 ml), stored in MeOH for 1 day and dried for 1 day at 100°C.

6.2.4 Single crystal synthesis of Ni-pyrazine-TiF_6 ($NiPyTiF_6$)

For the single crystal synthesis, $Ni(NO_3)_2{\cdot}6H_2O$ (0.369 g, 1.23 mmol) and H_2TiF_6 (60% in water) (0.335 g, 1.23 mmol) were dissolved in 2 ml MeOH and stirred at RT for 15min. This mixture was layered over a solution of pyrazine (0.195g, 2.43 mmol) in 2 ml MeOH. The container, a test tube, was sealed with a rubber plug with a small hole to enable slow solvent evaporation. After 3 weeks at RT, purple crystals were collected.

ATR FTIR: ν (cm^{-1}) = 3323, 3112, 1645, 1427, 1161, 1124, 1068, 818, 623, 524, 476.

Table 6-2:Crystallographic data of $NiPyTiF_6$.

Empirical formula	$C_8H_8N_4O_2F_6TiNi$
Formula weight (g/mol)	412.726
Crystal colour	Pale purple
Measurement temperature	120 K
Space group	$P2_1/n$ (14)
Crystal system	monoclinic
Z	4
Unit cell parameter a (Å)	7.11450 (10)
Unit cell parameter b (Å)	14.0820 (2)
Unit cell parameter c(Å)	13.0033 (2)
Unit cell angle α (°)	90
Unit cell angle β (°)	90
Unit cell angle γ (°)	97.749 (1)
Cell Volume (Å³)	1290.86(5)
Number total reflections	2437
Reflections used in refinement	2395
θ Range of data collection	4.65° - 69.99°
R	0.0485
Goodness of fit	1.169

6.2.5 **Two-step powder synthesis**

The two-step synthesis was conducted according to an already existing synthesis protocol and slightly modified [132]. $NiTiF_6$ (0.5 g, 2.22 mmol) and pyrazine (1 g, 12.48 mmol for excess pyrazine or 0.356 g, 4.44 mmol for equimolar reaction) were dissolved in 5 ml of solvent (water, MeOH, acetone or DMF) each and stirred at RT. After 15 min, the pyrazine solution was added to the $NiTiF_6$ solution and stirred for additional 15 min. The reaction mixture was poured into a 50 ml beaker and covered with a lid (for RT reaction) or poured into a 45 ml Teflon lined stainless steel autoclave (Paar Instruments 4744 General Purpose Acid Digestion Vessel) (for 85°C reaction). In total 13 different experimental conditions have been tested (Table 6-3).

Table 6-3: Summary of the used reaction conditions during the two-step synthesis.

	Solvent	Reaction temperature
Equimolar reaction	water	RT
	water	85°C
	MeOH	RT
	MeOH	85°C
	DMF	85°C
Excess pyrazine	water	RT
	water	85°C
	MeOH	RT
	MeOH	85°C
	DMF	RT
	DMF	85°C
	acetone	RT
	acetone	85°C

After 24 h reaction time (for reaction in DMF at 85°C: 15 h), the product was separated by centrifugation at 4000 RPM for 30 min and the solvent decanted. The product was washed with water and activated by solvent exchange in MeOH for 3 days. The product was obtained as purple powder after heating in vacuum at 120°C for 24 h.

6.2.6 Treatment of glass slides

The glass slides (soda-lime-glass microscope slides, Fischer Scientific Menzel Glaser) were cut into pieces of 1 x 1 cm, immersed in acetone [97] and cleaned by ultrasonication for 30 min. The glass slides were washed with water and dried in an N_2-flow.

6.2.7 Dip-Coating

TIFSIX-3-Ni (0.5 g) prepared in DMF at 85°C (chapter 6.2.5, p. 182) was ground for 10 min with mortar and pestle and added to MeOH (9.95 g). The resulting suspension was placed in an ultrasonic bath for 10 min and then vigorously stirred for 10 min at RT. A cleaned glass slide was immersed into the suspension for 1 min and vertically extracted from the suspension. The glass slide was placed on a petri dish and solvent evaporated for 2 h at 100°C. To add additional treatment steps, the procedure was repeated as required.

6.2.8 Seeding and Secondary growth

A seeded glass slide after two treatment steps (chapter 6.2.7, p. 183) was mounted vertically by a Buehler SamplKlip© and placed in a Teflon lined stainless steel autoclave filled with 10 ml of TIFSIX reaction mixture (0.5 g $NiTIF_6$ and 1 g pyrazine in 10 ml DMF). The reaction mixture was placed in an oven at 85°C for 15 h. The reaction vessel was slowly cooled to RT (storing at RT for 5 h) and the glass slide removed from the vessel. Loose powder was removed by washing the glass slide with MeOH from wash bottle and the sample dried for 17 h at 100°C.

6.2.9 Solvent-assisted epitaxy

A cleaned glass slide was placed for 1 min in TIFSIX reaction mixture in DMF as solvent DMF (0.5 g $NiTIF_6$ and 1 g pyrazine in 10 ml DMF) vertically extracted and then placed on a grid in a crystallization dish (see Figure 4-57). A porcelain evaporation dish, acting as

stand for the grid and reservoir, was filled with 10 ml DMF and the vessel closed with a petri dish as lid. The closed vessel was placed in oven at 85°C for 15 h. After removal from the oven the lid was removed to let excess solvent evaporate from the glass surface for 15 h at RT.

6.2.10 **Rapid thermal deposition**

A cleaned glass slide was placed for 1 min in TIFSIX reaction mixture (0.5 g $NiTIF_6$ and 1 g pyrazine in 10 ml DMF), vertically extracted, placed on a petri dish and the reaction conducted at 85°C for 15 h.

6.2.11 **In-situ coating**

A cleaned glass slide was placed vertically (by a Buehler SamplKlip©) in a in a Teflon lined stainless steel autoclave filled with 10 ml of TIFSIX reaction mixture (0.5 g $NiTIF_6$ and 1 g pyrazine in 10 ml DMF) and placed in oven at 85°C with varying reaction times (15 h, 5 h or 1 h). After the reaction, the vessel was cooled to RT (by storing at RT for 5 h) and the glass slide picked up from the vessel. Loose powder was removed from the glass slide by washing with MeOH from wash bottle. For activation by solvent-exchange, the sample was placed in a beaker with 10 ml MeOH for 1 day and dried in oven at 100°C overnight (~17 h).

6.2.12 **Coating of LPG with TIFSIX by in-situ coating**

An LPG was placed in a custom-made Teflon chamber (Figure 5-22) and the chamber filled with TIFSIX reaction mixture (0.5 g $NiTIF_6$ and 1 g pyrazine in 10 ml DMF). The chamber was closed and placed in oven at 85°C for 15 h or 5 h respectively. After the reaction, residual reaction mixture was poured out of the chamber and weakly attached TIFSIX removed by washing with MeOH from wash bottle (1 x ~10 ml). Activation of the coating was done by solvent exchange in MeOH (24 h at RT) and solvent residue from the activation process removed by heating at 100°C overnight (~17 h) before the sensor experiments.

6.2.13 **Characterisation**

Scanning Electron Microscopy (SEM) was used to characterise the morphology and crystal size (from an average of 25 particles). Measurements were conducted, regarding the availability, with a JEOL JSM-7100F Field Emission Gun (FEG) instrument or a JEOL 6490LV. In general, the measurements were conducted with a beam voltage of 15 kV. Powder samples have been dispersing on carbon tape on SEM sample holder and loose powder was removed by blasts of compressed air. Glass samples were attached on a SEM sample holder with carbon tape. For cross-section images, the glass slides were cut in half and mounted vertically by a Buehler SamplKlip© on a carbon tape. Images of LPGs were taken after measurement of sensor performance. A ~2 cm long piece was cut from the coated area and attached on a SEM sample holder with carbon tape. All samples were sputtered with a 10 nm iridium film by a Quorm Q150T ES coater in order to increase conductivity of the samples.

X-Ray diffraction (XRD) measurement was done by a PANanalytical X'Pert Pro diffractometer operating at 40 kV and 40 mA and Cu Kα radiation (λ: 1.540598 Å) equipped with a PIXCell3D detector. The experiments were conducted in continuous scanning mode with the goniometer fixed in the theta/theta orientation. For the incident site and detector

site a soller slit of 0.04 rad° and an incident beam mask of 15 mm was used. The irradiated length was 10.0 mm. In a typical experiment ~50 mg of powder sample was used, and scans were conducted in a range of 5°-40° 2θ with a step size of 0.006565° and a scan time of 51 s per step, resulting in a total measurement time of ~17 min. For glass slide samples, the scan time per step was increased to 440 s leading to a total measurement time of ~2 h. Single crystal diffraction data was collected on Oxford SuperNova CCD area detector diffractometer at 120 K using Cu-Kα radiation (λ: 1.540598 Å). The data refinements were done using OLEX2 [403] crystallographic software with the SHELXTL refinement package [404] using Least Squares minimisation. All cif-files have been visualised using Diamond 3.2 software.

Thermal stability of the powder samples was investigated by TGA using a TA instruments Q500 thermal gravimetric analyser. Samples were heated up to 700°C under air flow (100 ml/min) with a heating rate of 5°C/min.

For the measurement of absorption isotherms, the powder samples were degassed by heating at 80°C for 1 h in vacuum and at 100°C overnight in vacuum.

Sample porosity and BET area were determined by N_2-adsoprtion via Micrometrics Tristar II-adsorber. N_2-isotherms were measured at 77 K. Surface area was calculated by BET-Theory. Similar to the BET measurement in chapter 3 (p. 41) it was ensured, that both the C-value was positive and that the Rouquerol criteria was fulfilled [286].

CO_2-isotherms have been measured with a Micrometrics 3Flex adsorber. During the measurement, the temperature was kept at 25°C and the isotherm measured between 6 and 1013 mbar absolute pressure, whereas the equilibrium time for every step was in the default setting 5 s.

Fourier transformation infrared (FT-IR) spectroscopy was measured on a Bruker Alpha equipped with a Platinum ATR module. Spectra were measured with 4cm^{-1} resolution collecting 50 consecutive measurements.

6.3 Synthesis of TIFSIX powder

For the synthesis of TIFSIX, only one synthesis protocol has been published previously, which uses $NiTiF_6$ and pyrazine as starting material, using water as solvent and a prolonged reaction time (48 h) at RT [132]. However, several other reaction protocols exist for the silicon derivative SIFSIX using other solvents than water (Shekhah *et.al.* [395] have used MeOH) or reaction at elevated temperatures of 85°C [389]. It will be investigated if the synthesis of TIFSIX can be improved (*e.g.* with shorter reaction time or higher yield) by applying known SIFSIX reaction conditions to the synthesis of TIFSIX.

6.3.1 Synthesis of $NiTiF_6$

For the synthesis of TIFSIX, $NiTiF_6$ is a necessary starting material, which can be prepared for instance by reacting nickel carbonate and titanium dioxide in concentrated hydrofluoric acid [405], but due to the high toxicity of hydrofluoric acid alternative methods, such as the synthesis of $NiTiF_6$ directly from H_2TiF_6 and $Ni(CO_3)$ are preferred [406]. The usage of $Ni(CO_3)$, which is commerical avaiable as a basic hydrate $Ni(CO_3)\cdot 2Ni(OH_2)\cdot 4H_2O$, has in contrast to other nickel-sources like $Ni(NO_3)_2 \cdot 6H_2O$ a low

solubility in water [407]. An excess of $Ni(CO_3)$ during the synthesis has the advantage that, in theory, a complete conversion of the H_2TiF_6 can be achieved (outgassing of CO_2 shifts rection to product side) and after the reaction, the product can be filtered to remove possible impurities from the product.

Filtration and removal of the solvent after the reaction at elevated temperature leads to a green crystalline product, which is highly hygroscopic (Figure 10-12). It is anticipated that the hexahydrate of $NiTiF_6$ is initially prepared [408] and several days of drying at elevated temperature (3 days at 90°C) are needed to remove the water of crystallisation. The resulting anhydrous $NiTiF_6$ is, in contrast to the hexahydate, not hygroscopic and can be stored at ambient conditions. In contrast with a product, which was produced with $Ni(NO_3)_2{\cdot}6H_2O$, the resulting $NiTiF_6$ has less impurities as verified by XRD (Figure 6-5). However, control of the pH of the reaction mixture is important. If the pH of the mixture becomes acidic, the $Ni(CO_3)$ will be dissolved and impurities cannot be removed by filtration anymore. Different solvents like MeOH were investigated for the synthesis of $NiTiF_6$, but these attempts led to products with reduced purity and crystalinity.

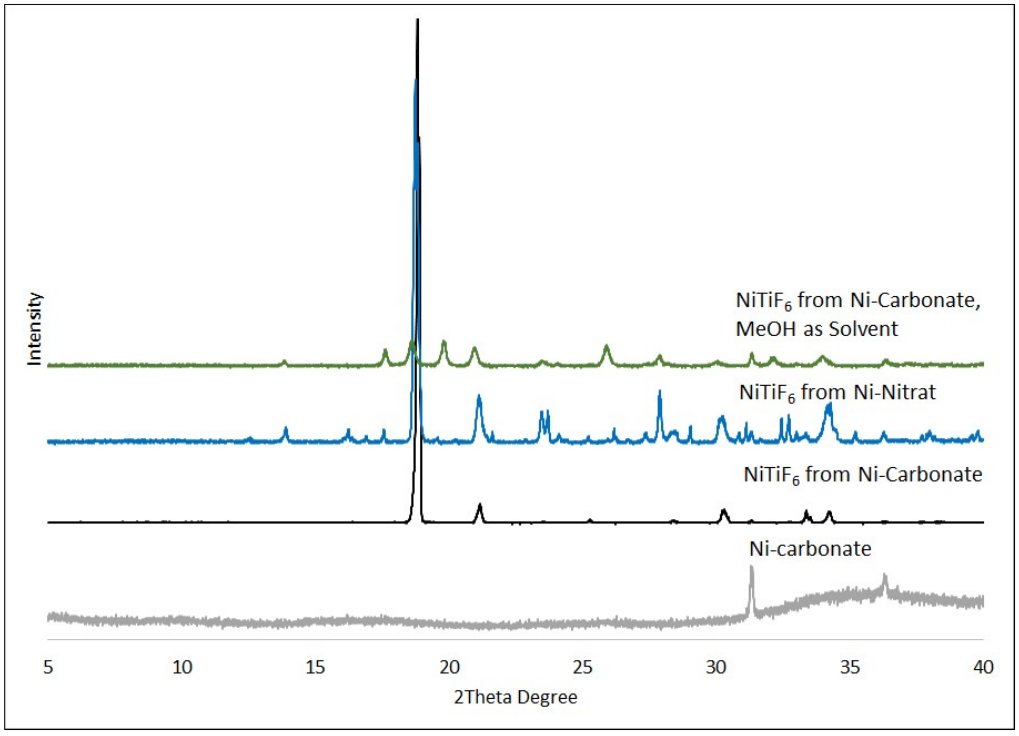


Figure 6-5: XRD pattern of $NiTiF_6$ prepared from $Ni(CO_3)$ (black), $Ni(NO_3)_2$ (blue) in comparison with the starting $Ni(CO_3)$ (grey). No residue of starting material was observed in the product. A less crystalline product with impurities was prepared when MeOH was used as solvent (green).

6.3.2 One-step synthesis of TIFSIX

Due to the time-consuming synthesis of $NiTiF_6$, which includes a drying step of several days, it was antipicated that a direct one-step synthesis would decrease the necessary synthesis time. In the case of SIFSIX, a sucessful direct synhtesis from $Ni(NO_3)_2{\cdot}6H_2O$, $(NH_4)_2TiF_6$ and pyrazine [402] has been reported. Hence, a similar approach was investigated for the synthesis of TIFSIX, using different combinations of temperature and solvent to optimize the possible reaction conditions. Kumar *et.al* [132] have reported the

use of water as solvent at RT, while Elsaidi *et.al* [389] have prepared the analogon SIFISIX in MeOH at 85°C. In total, with the reported use of water and MeOH solvents and reaction temperatures of RT and 85°C, 4 different reaction conditons were investiagted for the one-step synthesis (Table 6-4).

Table 6-4: Used combinations of reaction conditions for the one-step synthesis of TIFSIX

Solvent	Reaction temperature
water	RT
water	85°C
MeOH	RT
MeOH	85°C

The resulting XRD pattern (Figure 6-6) for the samples prepared in water at RT and 85°C and in MeOH at RT look similar with peaks at 13.45°, 15.08° and at 18.38° in 2Θ. Only the XRD pattern of the sample preared in MeOH at 85°C show different peaks at 12.53°, 14.11° and 18.21°.

The morphology of the prepared particles was invesitgated by SEM and it was found to vary for all reaction conditions (Figure 6-7). In water at RT, the particles have a cubic shape with edge lengths ranging from 400 to 900 nm. In water at 85°C, larger cuboid particles (edge length between 4.5 µm and 6.4 µm) with cut-off edges have been preapred.

In MeOH as solvent and at RT, the particles resemble cubic particles, fused from smaller components. The cubic particles have sizes ranging between 4 and 5 µm. In MeOH at 85°C two different types of particles are prepared: larger tiles and small spherical particles. While the larger tiles have a height of 6.5 µm - 8.5 µm and width of 0.9 - 1.5 µm, the smaller particles have a size between 500 nm and 750 nm.

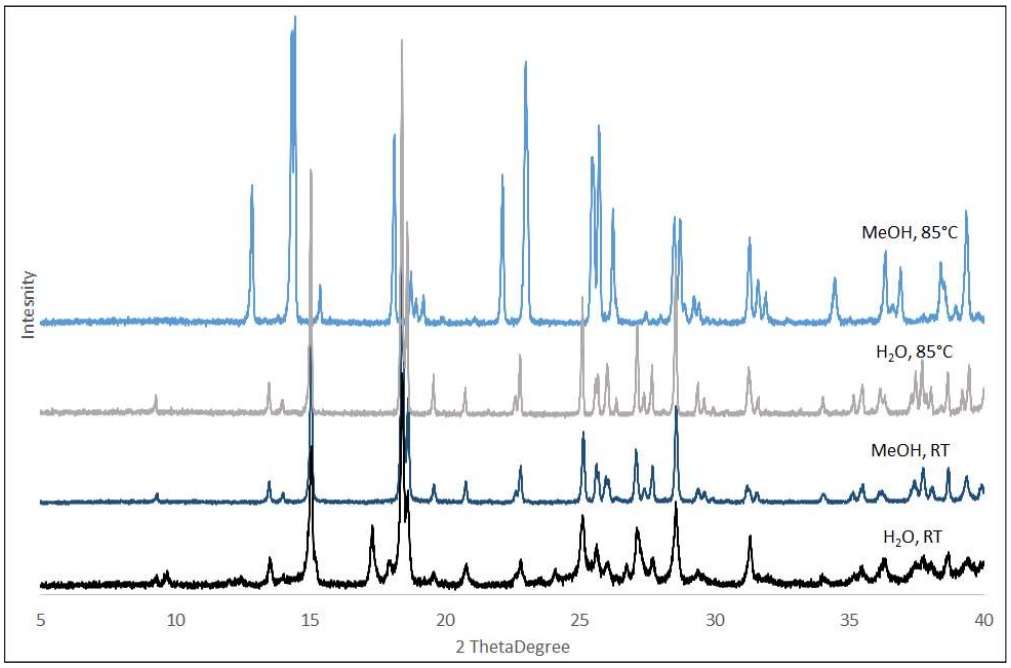


Figure 6-6: XRD pattern of powder samples prepared in different solvents and reaction temperature in a one-step synthesis.

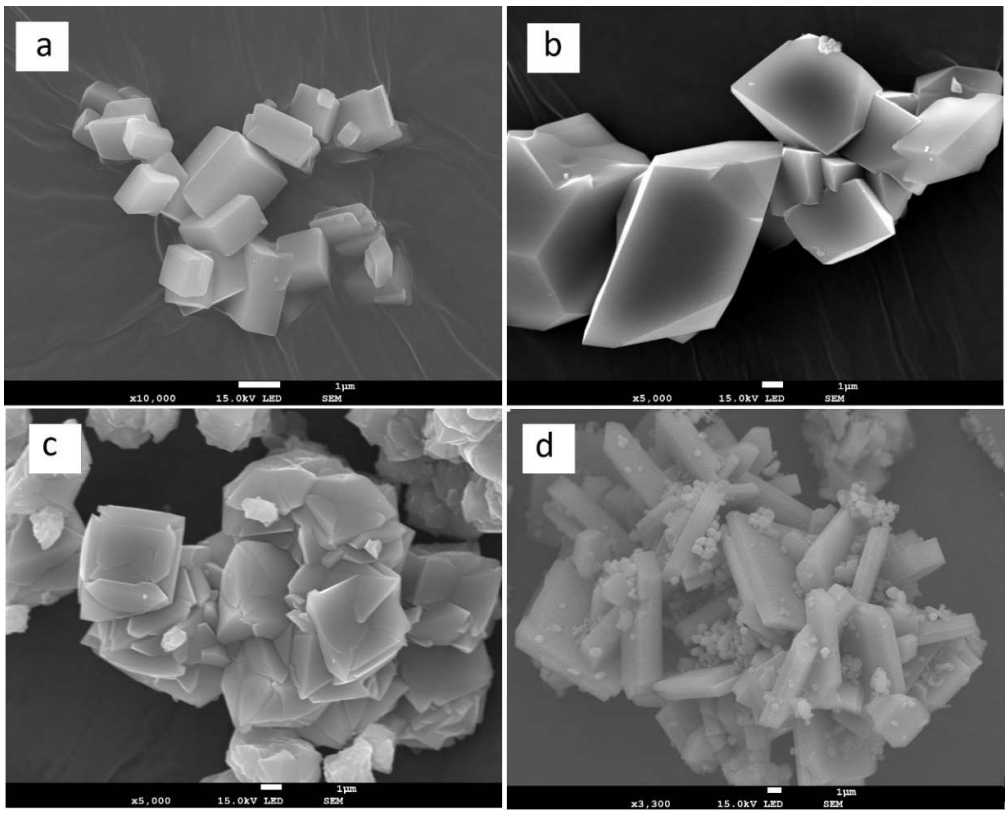


Figure 6-7: One-step samples, prepared in a) water at RT, b) water at 85°C, c) MeOH at RT and d) MeOH at 85°C.

However, according to Kumar *et.al.* [132], the XRD peaks of TIFSIX, which are expected at ~12° and ~18°, do not match with the XRD pattern of the samples prepared in a one-step synthesis. A peak at ~12° is missing for most samples. To identify this product, a single-

crystal measurement was conducted and show that the resulting product is a compound composed of nickel cations, pyrazine linkers and TiF_6^{2-} anions. This compound has the molecular formula $C_8H_8N_4O_2F_6TiNi$ and contains in each unit cell 1 eq of nickel, 1 eq of TiF_6^{2-} and 2 eq of pyrazine with additional crystallization water. The compound is composed of chains of nickel and pyrazine. However in contrast to already known Ni-pyrazinate [409], which is composed of linear chains, in the new compound the chains are interlinked by pyrazine. The nickel atoms are surrounded with three water molecules and three pyrazine molecules in a *mer*-arrangement. Between the chains, the TiF_6^{2-} is incorporated as a counterion (Figure 6-8). For simplification, the product will be called $NiPyTiF_6$. An N_2-isotherm followed by BET measurement (Figure 10-1) show that this compound is not porous. The sample has a low porosity of 8.8 $m^2\ g^{-1}$ and displays negligible CO_2-adsorption (Figure 10-2). With CO_2 adsorption capacity of 0.6 $cm^3\ g^{-1}$ (~0.026 mmol g^{-1}) (at $p/p^0 = 0.9$) the adsorption is much lower in comparison with literature reported TIFSIX [132], which has a CO_2-adsorption capacity of 55 $cm^3\ g^{-1}$ (~2.6 mmol g^{-1}) at similar partial pressure. Notably the striking high CO_2-adsorption at low concentrations of about 2000 ppm or 0.2 kPa CO_2-pressure of TIFSIX (40 $cm^3\ g^{-1}$ [132]) was not observed for $NiPyTiF_6$ having a CO_2-adsorption of only 0.013 $cm^3\ g^{-1}$ at 0.2 kPa CO_2 pressure.

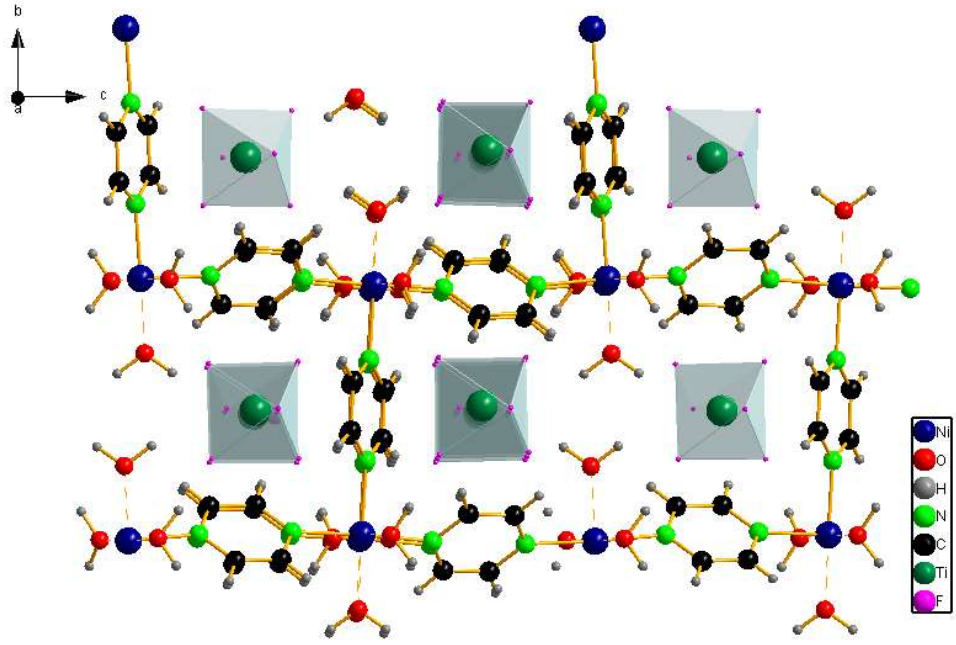


Figure 6-8: Crystal structure of the Ni-pyrazine-TiF_6-compound ($NiPyTiF_6$).

The sample prepared in a one-step synthesis at 85°C in MeOH show peaks at 12.52°, 14.43° and 18.21° and matches in principle the XRD-pattern of TIFSIX [132], although the peak at ~ 14° is an impurity and needs to be removed prior to subsequent use. In the literature, impurities of the product were removed by heating at 160°C in vacuum and solvent exchange in MeOH [132]. However, it was not possible to remove the impurity peak at 14° by this activation procedure. Instead, the product was decomposed in the process leading to an amorphous sample (Figure 6-10). Reducing the purification temperature was also

not successful. The sample becomes amorphous (the intensities of the peaks decrease), while the relative intensities of the peaks does not change. The different degree of decomposition can be seen by the colours of the samples (Figure 6-9). While the AsSyn product has a blue-purple colour, the amorphous product has a light-green colour. The sample activated at 120°C has a darker green colour, an intermediate between the AsSyn and amorphous product.



Figure 6-9: Sample prepared in MeOH at 85°C in one-step synthesis (left), after activation in vacuum at 120°C (mid) and after activation in vacuum at 160°C (right).

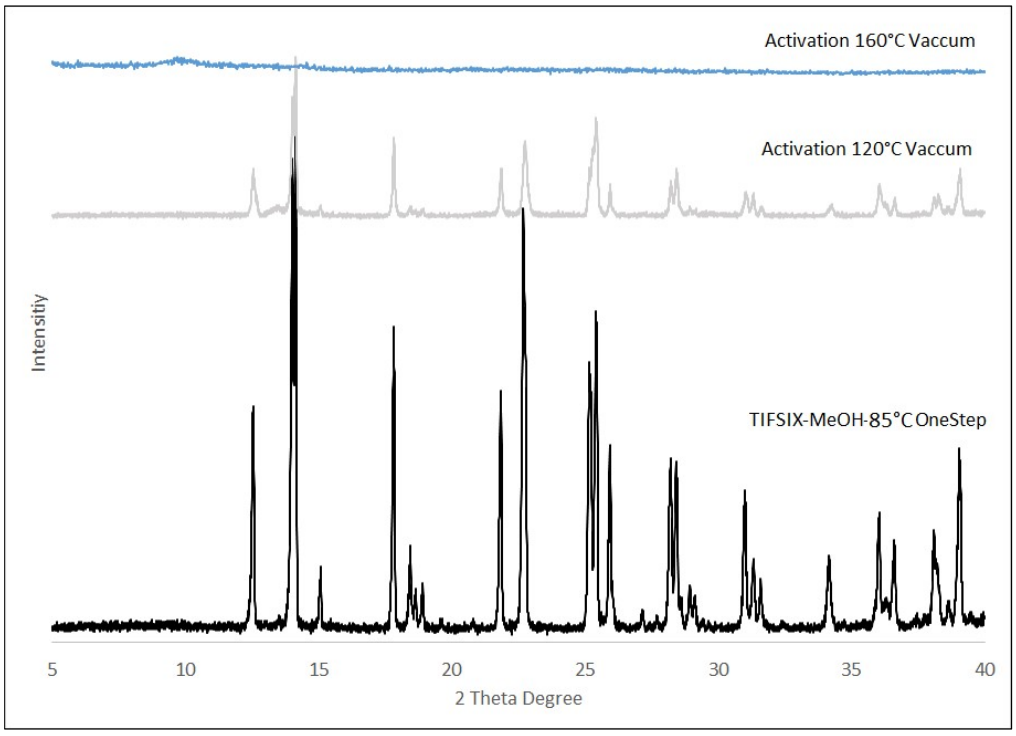


Figure 6-10: XRD pattern of sample prepared in a one-step reaction at 85°C (black). Activation in vacuum at 120°C (grey) and 160°C (blue).

In summary, the sample prepared in MeOH at 85°C in a one-step synthesis is decomposing during the activation (implying a lower thermal stability) and the XRD pattern (in TIFSIX, the ~12° should have a higher intensity than the ~18° peak) [132] are different to the data known from literature. While the sample prepared at RT in MeOH could be successfully identified by a single crystal measurement, a single crystal could be not prepared for the

second sample (MeOH at 85°C) and therefore the exact nature of this product is still unknown.

6.3.3 Two-step synthesis of TIFSIX

The two-step synthesis is based on the reaction of from $NiTiF_6$ and pyrazine. First, $NiTiF_6$ has to be prepared (see chapter 6.3.1, p. 185) from $Ni(CO_3)$ and H_2TiF_6 and then reacted with pyrazine to prepare TIFSIX. The known synthesis protocol uses a large excess of pyrazine for the reaction. Kumar *et.al* [132] have used a 13.4 times excess of pyrazine to $NiTIF_6$ in their reported procedure.

Again, in this set of experiments different solvents (water and MeOH) and reaction temperature (RT and 85°C) were used, which leads in total to 4 different experimental conditions, similar to the one-step synthesis (Table 6-4). The reaction time was set to 48 h. The concentration of the reaction mixture was not modified. At lower concentrations, the reaction rate is further reduced, which leads to a product composed mostly of unreacted starting material (Figure 10-8), while at higher concentrations, the starting material $NiTiF_6$ could be not fully dissolved.

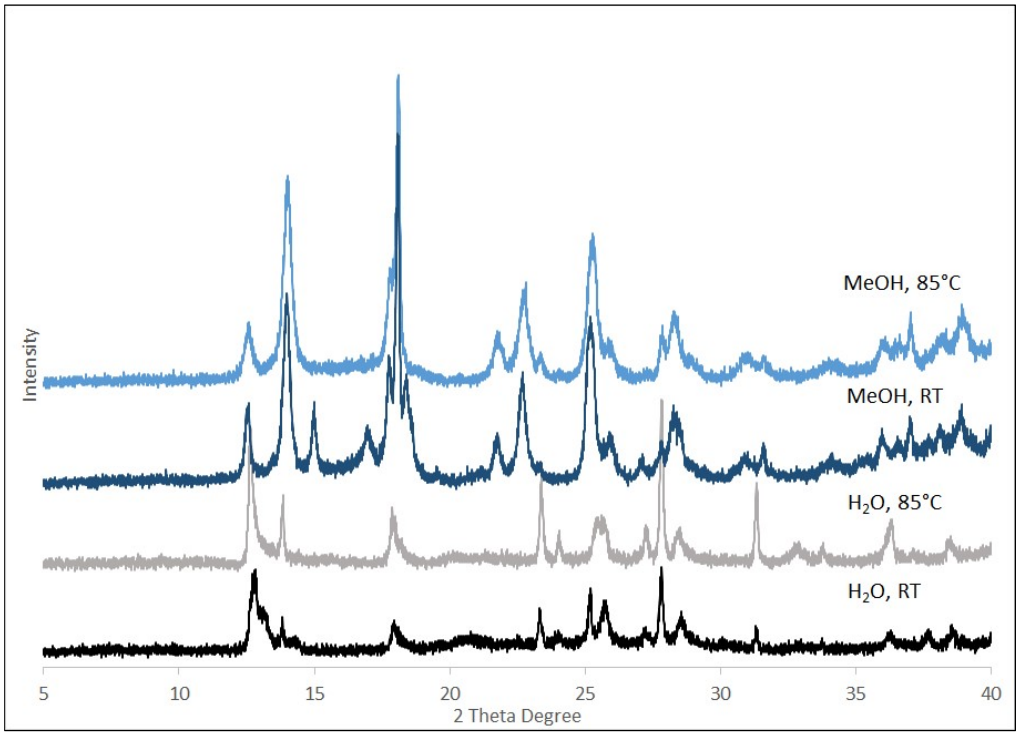


Figure 6-11: Comparison of XRD pattern for samples prepared in a two-step synthesis with varying solvent and reaction temperature. All samples used an excess of pyrazine during the reaction.

For the first set of experiments, a reaction mixture containing an excess of pyrazine was used. The samples prepared in water show similar XRD patterns (Figure 6-11) with peaks at 12.62°, 13.92° and 17.70°. The "impurity peak" at 13.92° and the second product peak at 17.70° have both different positions than in the sample prepared in MeOH at 85°C in the one-step synthesis. This implies that the samples prepared in the two-step synthesis and the sample prepared in the one-step synthesis in MeOH at 85°C have different compositions. Hence, in contrast to the reactions described above, it was possible to activate the products by solvent exchange in MeOH and heating in vacuum at 120°C,

leading to a product which matches the XRD pattern of TIFSIX (Figure 10-9). However, the sample prepared at RT have slightly broader peaks compared with the sample prepared at 85°C with lower intensity, which might imply a sample with lower crystallinity or caused by the very low yield of the reaction. During the reaction only 13 mg of sample could be prepared at RT (2% yield) and 65 mg at 85°C (9% yield). This is possibly explained by a slow reaction rate. The solvent from the reaction was collected after decantation and the water evaporated. The solid residue was investigated by XRD and showed a mixture of unreacted starting material $NiTiF_6$ and pyrazine (Figure 10-11).

The samples prepared in MeOH show peaks at similar positions to those observed for samples prepared in water, but in comparison with larger amounts of impurities. For the sample prepared in MeOH at 85°C, the peak at ~14° has the highest intensity in the spectrum, while for the MeOH at RT sample even additional peaks at ~15° and ~16° are observed. In addition, two peaks are visible at 17.76° and 18.14°. This implies a mixture of the two different products.

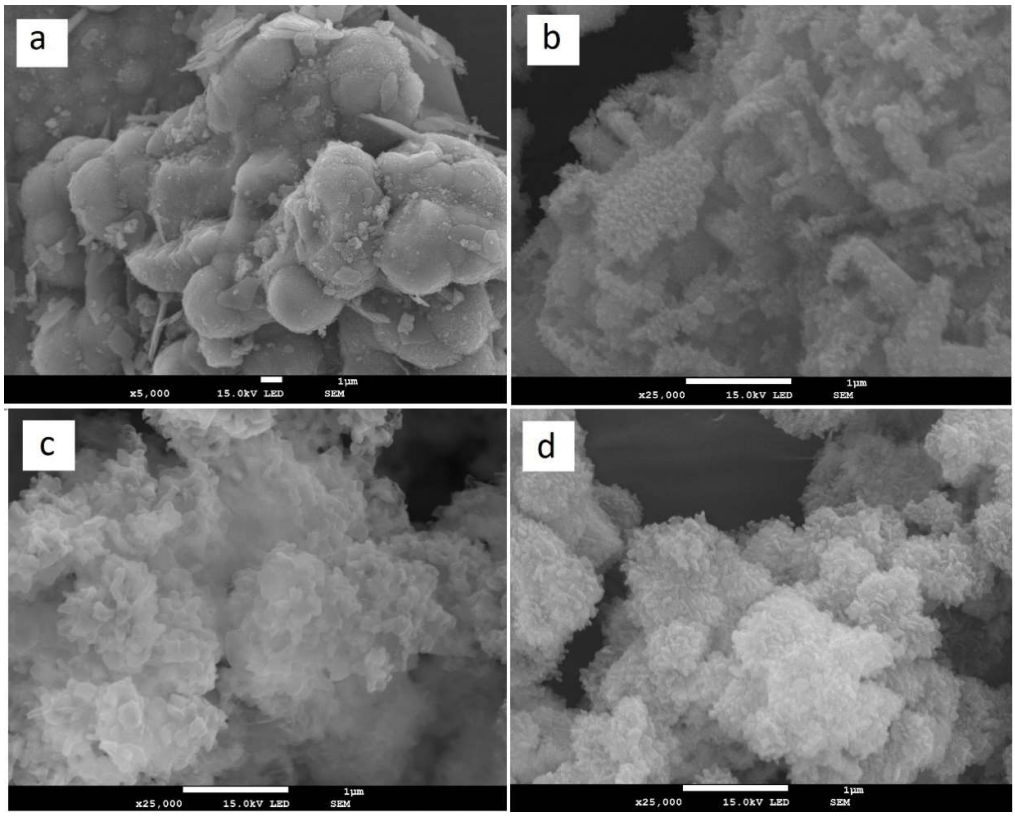


Figure 6-12: SEM images of samples prepared in two-step synthesis with different solvent and reaction temperature. The reaction mixture used excess of pyrazine. a) water at RT b) water at 85°C c) MeOH at RT d) MeOH at 85°C.

The morphology of the prepared samples is different from the samples of the one-step synthesis (Figure 6-12). Agglomeration of particles was observed in all samples. During the reaction at RT in water, the particles agglomerate to larger cluster with sizes ranging between 3 and 6 µm. In comparison with the sample prepared in water at 85°C, fewer small particles are visible, implying that the particles have fused or that at the lower reaction temperature no larger distinct particles can be formed. In the sample prepared in

water at 85°C, particles with a size of 75 ± 13 nm are observed, which agglomerate to cluster with a size ranging between 1 and 2 µm.

The particles prepared in MeOH have shown similar morphology to the sample prepared in water at 85°C, with nanometre sized particles agglomerating into larger cluster of ~1 µm diameter. Comparable with the corresponding sample prepared in water, the sample prepared in MeOH at RT show a higher degree of fusing. While the particles prepared in MeOH at 85°C were thick rods with a length of 78 ± 16 nm, the shape of the particles prepared in MeOH at RT is less distinct and the edges of the particles more rounded. These particles have a size of 146 ± 51 nm.

While the synthesis of TIFSIX using excess pyrazine have been investigated previously, reports show successful synthesis for SIFSIX with equimolar reaction mixtures. For such an equimolar reaction mixture, a ratio of 1/2 between $NiTiF_6$ and pyrazine is needed [389]. The reaction using an equimolar reaction mixture was attempted and the crystallinity of the sample investigated by XRD (Figure 6-13), while the morphology was investigated by SEM images (Figure 6-14). All samples show peaks at 12.6°, 13.8° and 18.2° and therefore at the same positions than the sample prepared in a one-step reaction in MeOH at 85°C. In comparison to the samples prepared with excess of pyrazine (Figure 6-11), the intensity of the peaks is reduced, implying a sample with lower crystallinity. Another problem was the reduced yield of the samples prepared with equimolar reaction mixtures for the reactions in MeOH. During the reaction with excess pyrazine in MeOH at 85°C 312 mg of sample could be prepared, whereas the same reaction with equimolar composition only leads to 129 mg sample. This sample (equimolar, MeOH at 85°C) show peaks at 17.78° and 18.2° and seems to be, similar to the product prepared in MeOH at 85°C with excess pyrazine, a mixture of the two different products.

The amount of sample prepared in water remains at the same low level compared to the reaction with excess of pyrazine. Both reactions in water lead to particles resembling rods (Figure 6-14), but the particles prepared at RT are smaller with length of 101 ± 31 nm in comparison with 228 ± 87 nm for particles prepared at 85°C. Again, the morphology of the samples prepared in MeOH vary with the reaction temperature. While at 85°C longer needles with a length of 680 ± 161 nm and a width of 213 ± 37 nm were observed, the particles prepared at RT are round particles of 710 ± 203 nm.

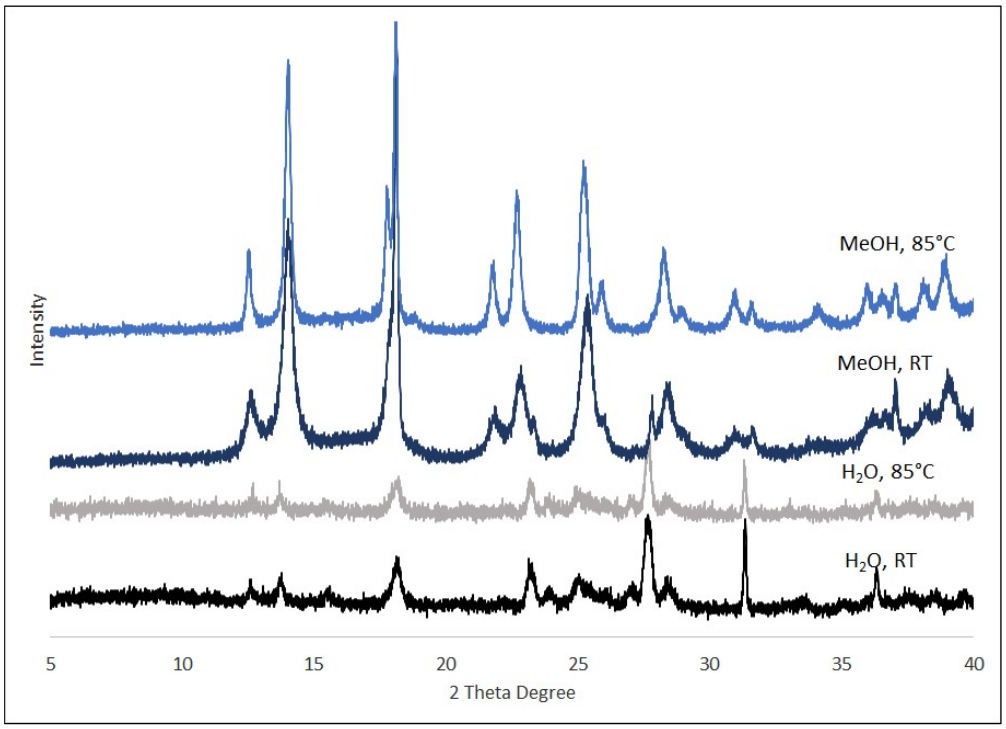


Figure 6-13: XRD pattern of samples prepared in two-step synthesis with various solvent and reaction temperatures. All reactions have used an equimolar reaction mixture.

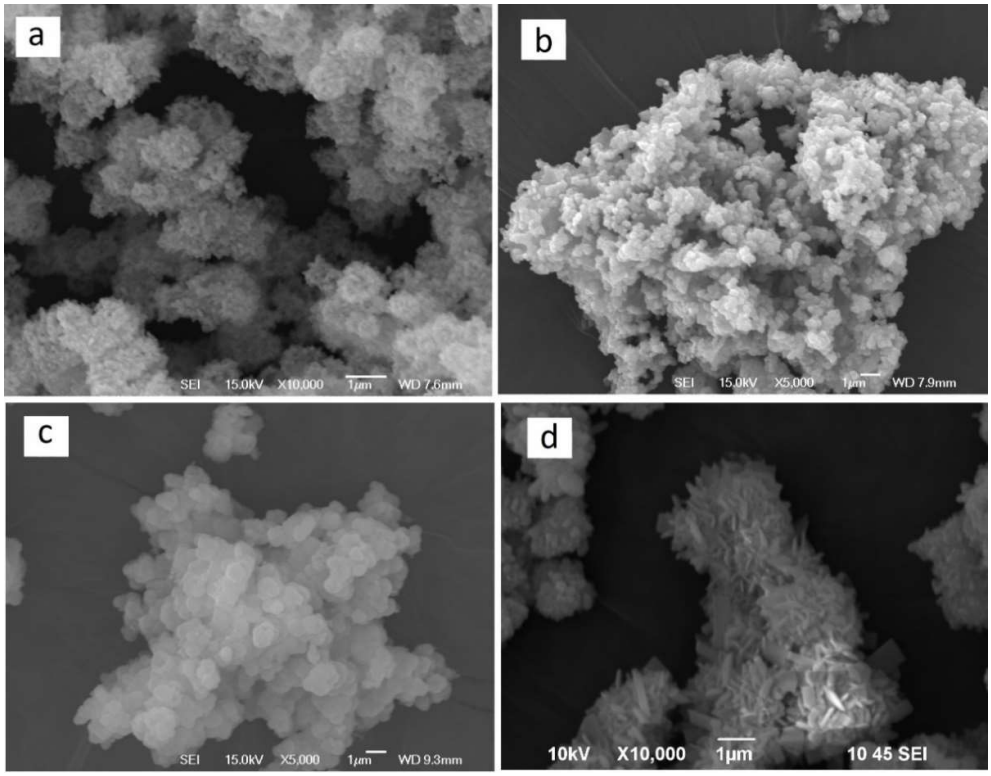


Figure 6-14: SEM images of samples prepared in two-step synthesis with equimolar reaction mixtures a) water at RT, b) water at 85°C, c) MeOH at RT, d) MeOH at 85°C.

Different synthesis protocols have been reported in the literature to prepare TIFSIX or the silicon-analog SIFSIX with variations regarding the solvent, metal-to-linker ratio and the reaction temperature used. However, we found that it was not possible to use these

methods to prepare TIFSIX in acceptable yields. In one-step reactions, a non-porous product was prepared, which contains of nickel cation and pyrazine in a framework, where TiF_6^{2-} is bound in the pores ($NiPyTiF_6$). Reactions using the two-step synthesis have led to products with varying crystallinities, where peaks are visible at ~12°, as desired, but also at ~13° and ~18.2°. However, it was not possible to remove the impurity by vacuum activation, preceded by solvent exchange in MeOH. The samples collapsed to an amorphous product. This might imply that the resulting sample is not TIFISIX, which should have peaks at ~12° and ~17.8° and a higher thermal stability. The sample prepared in water with excess pyrazine led to a product which is most likely TIFSIX, but with a very low yield of less than 10%.

The reaction was therefore also tried in different solvents. One of the solvents used was acetone. The reaction was tested using the two-step reactions process at RT and 85°C. For all reactions an excess of pyrazine was used. The results until now have implied, that with excess of pyrazine the yield and purity of TIFSIX can be improved (Figure 6-11 and Figure 6-13). The reaction using acetone as solvent, resulted in the reaction mixture turning brown with an gaseous product evaporating after the reaction. Even after the clean-up process, the product maintained a grey colour, while a purple colour is expected for TIFSIX (Figure 6-15).The XRD pattern (Figure 6-17) shows that the resulting sample is $NiPyTiF_6$, while the crystallinity of the sample prepared at 85°C is higher than the sample prepared at RT (higher intensity of peaks in XRD pattern). The brown colour and gaseous product imply, that in acetone a decomposition process is taking place. The decomposition of the material during the reaction might explain, why the reaction to TIFSIX was not successful in acetone. As a side note, BET was measured for the samples of $NiPyTiF_6$ prepared in acetone, showing with capacity of 17 $m^2 g^{-1}$ a slightly higher porosity than $NiPyTiF_6$ prepared in water or MeOH (Figure 10-3). The morphology of this product was different to the samples prepared in water or MeOH with SEM images (Figure 6-16) showing particles of no distinct shape and size of 1-2 µm, agglomerating to larger clusters exceeding 10 µm for this sample.



Figure 6-15: Left: Image of the reaction mixture in acetone after the reaction. Right: sample prepared in acetone (left) and in MeOH at 85°C (right). The acetone sample is grey, whereas a purple colour should be expected for TIFSIX [410].

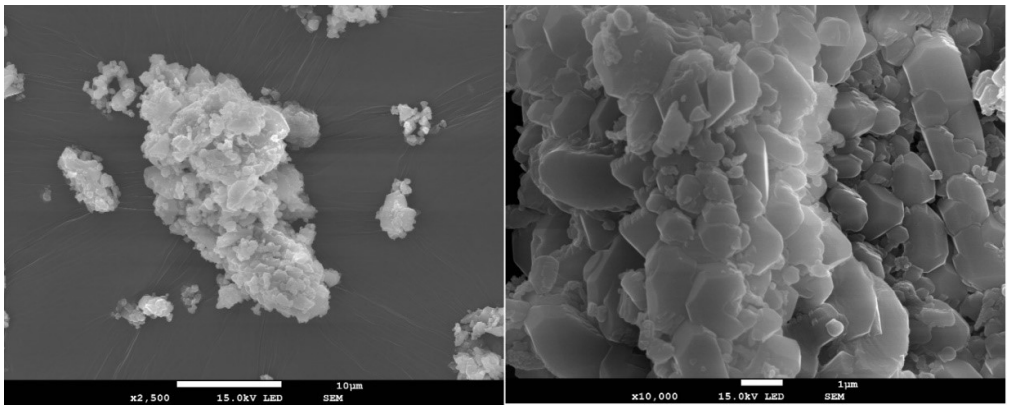


Figure 6-16: SEM image of sample, prepared in acetone at 85°C with lower (left) and higher (right) magnification.

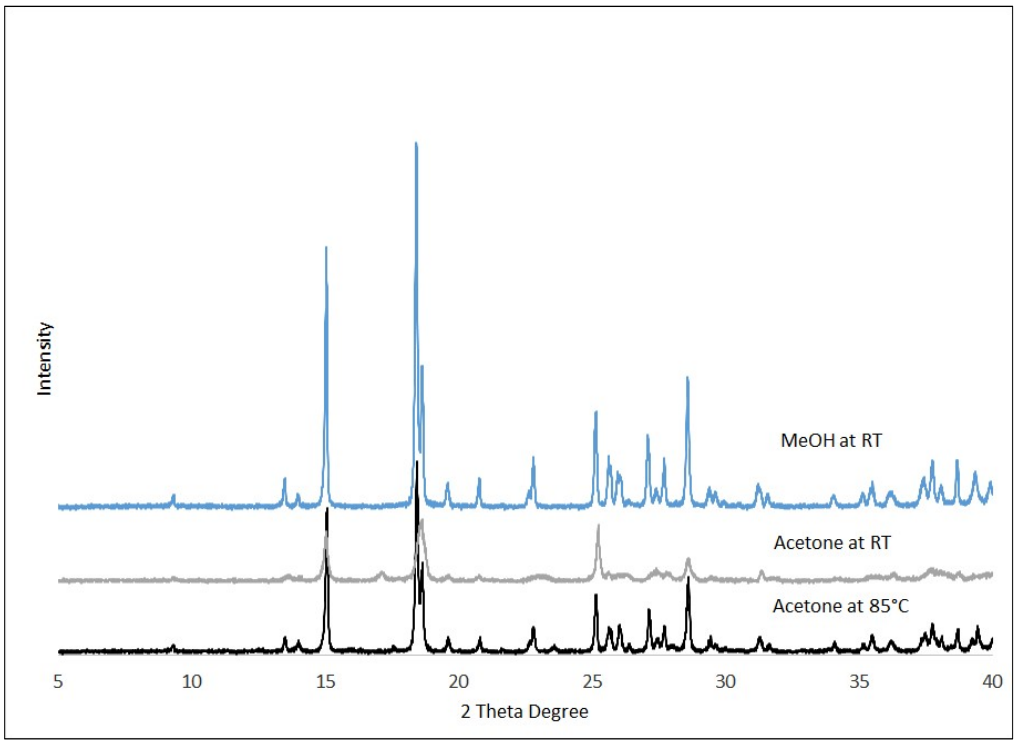


Figure 6-17: XRD pattern of sample prepared in acetone at 85°C (black) and at RT (grey) in comparison with sample prepared in MeOH at RT (blue, see page 188). Both patterns match, which shows that the product prepared in acetone is $NiPyTiF_6$.

In contrast, the use of DMF as solvent improves both the quality and yield of the product. Different reactions with excess pyrazine were conducted. A one-step reaction at 85°C and two-step reactions with $NiTiF_6$ at RT and 85°C were investigated. The XRD patterns (Figure 6-19) show that, depending on the reaction conditions, different products were prepared. In the one-step synthesis, peaks at 14.98° and 18.38° imply that only $NiPyTiF_6$ was synthesized. The product, prepared in a two-step at RT, resembles the unknown product, with peaks at 12.57°, 15.61° and 18.25°. The product prepared in DMF at 85°C shows only two peaks at 12.52° and 17.75° and therefore matches the pattern of TIFSIX [132]. The relative peak intensities of the pattern of the sample prepared in DMF at 85°C further

match the literature data [132]: The ~12° peak is the most intense peak while the peak at ~17.8° has about 25% of the intensity from the 12° peak [132]. As a side note, the reaction of TIFSIX in DMF at 85°C was repeated with an equimolar reaction mixture. The resulting product had a similar XRD pattern to the sample prepared with excess pyrazine (Figure 10-7), but with reduced yield (28% for the reaction at equimolar composition and 61% for with excess of pyrazine). Regarding the reaction time, no difference in sample quality or yield was observed after reducing the reaction time from 48 h [132] to 24 h or even 15 h. The morphology of the particles prepared in DMF is also different to the other samples studied until now. A SEM image (Figure 6-18) shows two different types of particles with larger needle-shaped particles and small cubic particles. However, images at higher magnification show that the larger needle shaped particles are formed from small cubic particles as building blocks.

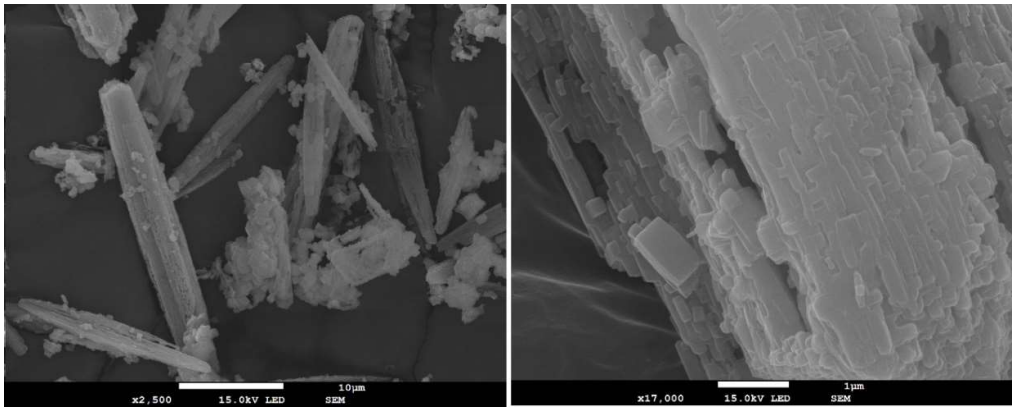


Figure 6-18: TIFSIX prepared in DMF at 85°C in a two-step synthesis at lower (left) and higher (right) magnification.

Although the XRD pattern matches the literature pattern, the measured BET-area is with 58 $m^2 g^{-1}$ lower than the literature data. No data has been published for TIFSIX until now, but for the analogous SIFSIX a BET area of 223 $m^2 g^{-1}$ was reported [402]. The porosity of the DMF sample is in the same range as the samples prepared in water at RT (56 $m^2 g^{-1}$; Figure 10-5), which further implies that both are similar samples.

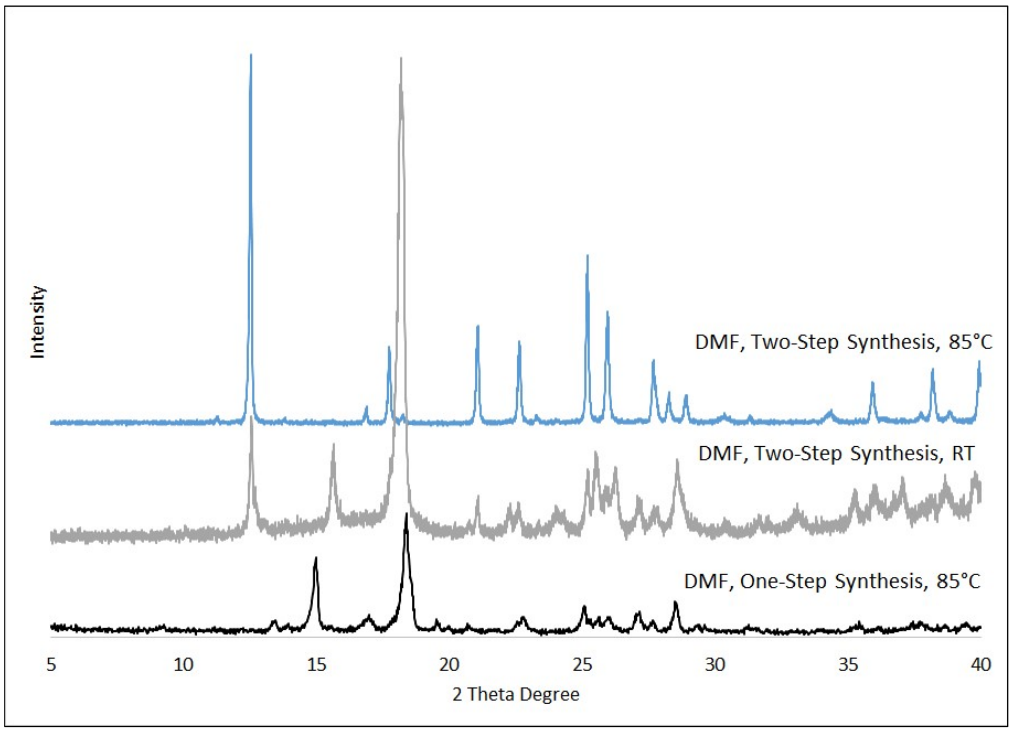


Figure 6-19: XRD pattern of samples from the reaction in DMF with a one-step reaction at 85°C (black), two-step-reaction at RT (grey) and two-step reaction at 85°C (blue).

For the sample prepared in DMF at 85°C, similar to MIL-53(Al) (Table 3-5) different activation methods were investigated in order to find activation conditions, which are faster or can be conducted in less harsh conditions. The activation method in literature are composed of two steps, solvent exchange in MeOH and heating at elevated temperature in vacuum, which is a time-consuming process. This activation needs several days. An activation by refluxing in DMF for 15 h might be able to speed up this process. The XRD pattern (Figure 6-20) and porosity of the samples (Figure 6-21, AsSyn: 21 $m^2 g^{-1}$, SolventExchange + Vacuum: 58 $m^2 g^{-1}$ DMF-Reflux: 56 $m^2 g^{-1}$) are similar for both activation methods. The sample activated by reflux has an increased adsorption at high relative pressure, which implies an increased mesoporous volume, which is often attributed to interparticle volume.

In comparison with the sample activated by DMF-Reflux, the XRD pattern shows higher peak intensities for the sample activated by solvent-exchange and vacuum heating (Figure 6-20). This implies a higher crystallinity and solvent-exchange + vacuum heating was chosen as the standard activation method for TIFSIX.

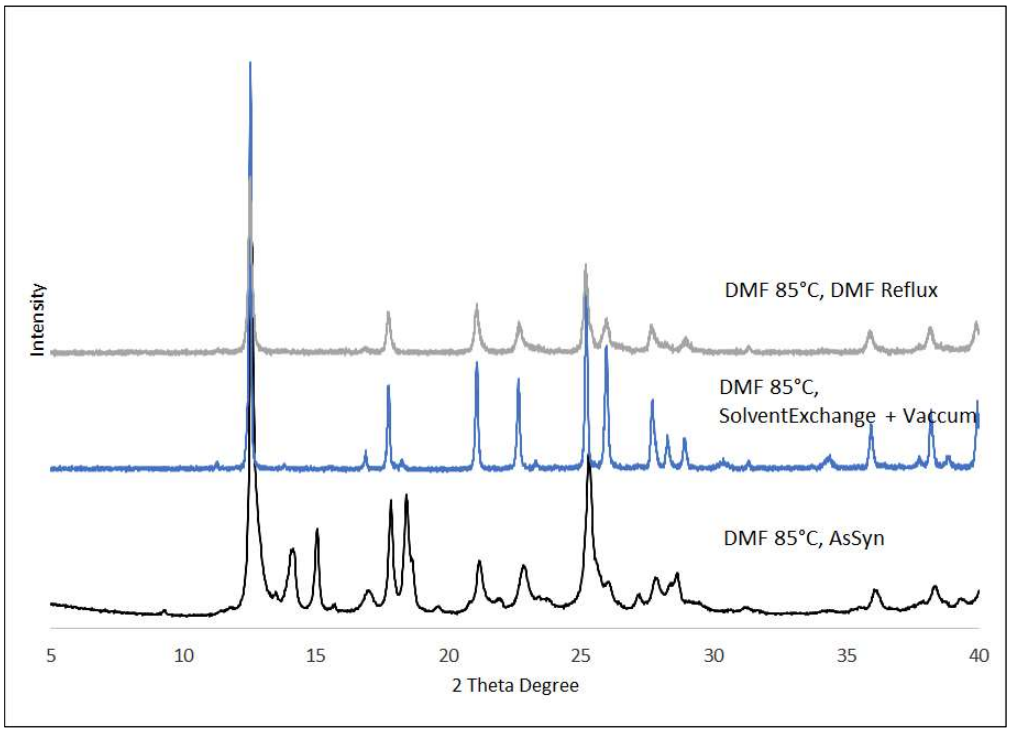


Figure 6-20: XRD pattern of TIFSIX prepared in DMF at 85°C AsSyn (black), after solvent exchange and heating in vacuum (blue) and after refluxing in DMF at 160°C (grey).

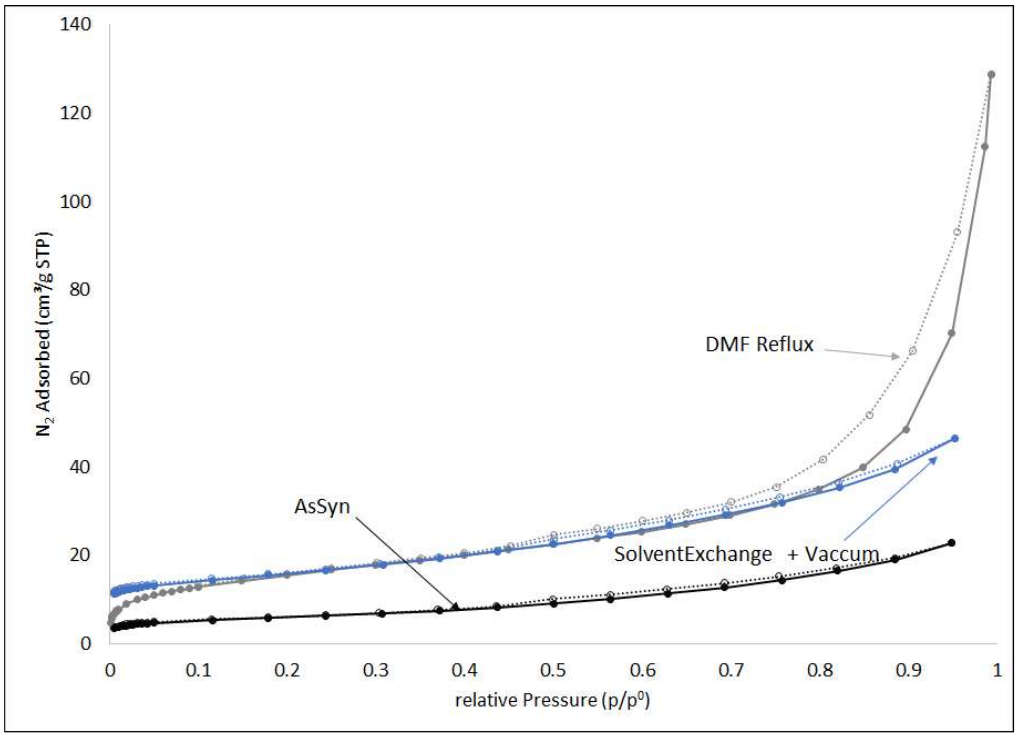


Figure 6-21: N_2-isotherms of TIFSIX prepared in DMF at 85°C AsSyn (black), after activation by solvent exchange and heating in vacuum at 120°C (blue) and after reflux in DMF at 160°C for 15 h (grey). Adsorption: solid line; Desorption: dashed line.

The thermal stability of the different samples, prepared during the TIFSIX synthesis, was investigated by TGA. Three different samples were measured: those prepared in water at RT in a one-step reaction ($NiPyTiF_6$), prepared in MeOH at 85°C in a one-step reaction (peak

at 18.2°) and prepared in DMF at 85°C in two-step reaction (peak at 17.7°). The sample prepared in DMF at 85°C in a two-step reaction start to decompose around 250°C (~17.7° peak; Figure 6-22, black), which is in good agreement with the literature data [132]. The sample prepared at 85°C in MeOH by a one-step synthesis (~18.2° peak; Figure 6-22, grey) has a lower thermal stability than TIFSIX (~225°C) and shows even before the decomposition a constant weight loss, which might explain the formation an amorphous sample during activation at elevated temperature in vacuum (Figure 6-10). This sample exhibits a negligible porosity of 2.9 $m^2 g^{-1}$ (Figure 10-6). This might further confirm that a sample with peak at 18.2° is not identical with TIFISIX. $NiPyTiF_6$ (sample in water at RT in one-step reaction; Figure 6-22, blue) shows a weight loss of 12% at 100°C which might be due to the crystallization water in the sample. After that, the sample shows a continuous weight loss until complete decomposition at ~250°C and hence a lower thermal stability than TIFSIX.

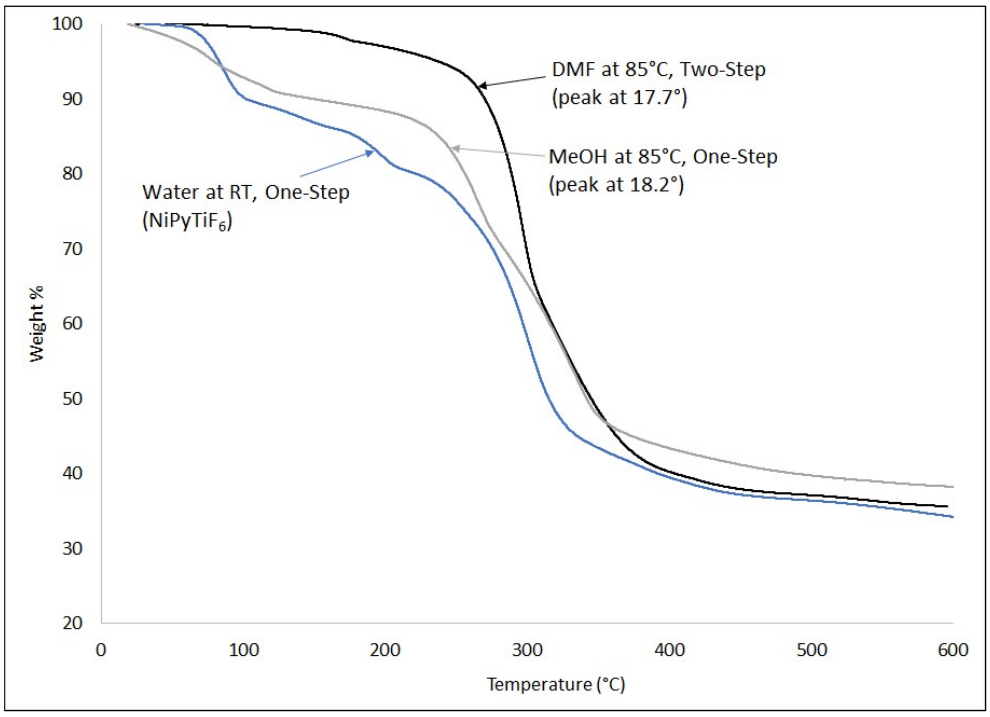


Figure 6-22: TGA comparing samples from different attempts preparing TIFSIX.

6.4 Thin Film Synthesis of TIFSIX

Even though, according to the literature reports, TIFSIX (or the silicon derivative SIFSIX) is prepared in water or MeOH, it was not possible, even after alternating several synthetic parameters (*e.g.* reaction temperature or metal to linker ratio), to prepare TIFSIX in acceptable yield. Sufficient yields could be only achieved after changing the reaction solvent to DMF. Therefore, the DMF sample, prepared from $NiTiF_6$ and pyrazine ("two-step synthesis"; excess pyrazine) will act as the basis for the investigation of different thin-film techniques. TIFSIX is a completely novel compound, where no thin-film synthesis has yet been published. Due to the limitations of the target support, including a non-porous and

inert glass surface, coating techniques, which have been already introduced during thin-film investigations of MIL-53(Al) in chapter 4 (p. 82), have been modified for the synthesis of TIFSIX. Similar to the thin-film synthesis of MIL-53(Al) pieces of soda-lime glass will act as test systems. The most promising thin-film approaches will be adopted to the coating of LPG fibres.

6.4.1 Dip-coating

For the dip-coating approach, TIFSIX was prepared as a powder in DMF and then a suspension created in MeOH. For the suspension a TIFSIX powder sample, which was prepared in DMF at 85°C using a reaction time of 15 h and excess pyrazine, was used. Water was not investigated here as a solvent for the suspension. Due to the high surface tension of water a "coffee-strain effect" [367] is anticipated instead of forming a homogeneous film. DMF was not used due to the higher boiling point (Bp: 156°C) and the expected more complicated removal of the solvent from the thin-film after the coating process. For now, only a 0.5 wt% suspension was prepared in MeOH as solvent and glass slides were coated with one (Figure 6-23) or two treatment steps (Figure 6-24). For the one-step glass slide, the surface coverage is low, and particles are sparsely visible on the surface. The TIFSIX prepared in DMF powder has a needle shaped morphology composed of smaller nanosized, cubic particles (Figure 6-18). However, in the SEM images after dip-coating, no larger needle shaped particles could be identified. A possible reason is that in the solvent the interaction between the individual particles is lower than in a powder sample and the needles may have disintegrated during the preparation of the coating suspension [288]. This separation might be further assisted by the usage of ultrasound to prepare a homogeneous suspension.

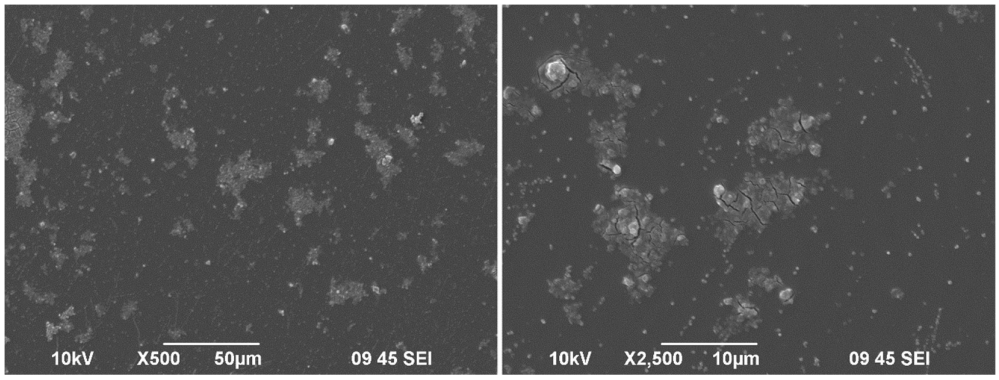


Figure 6-23: SEM image of glass slide coated with 1 step of TIFSIX, prepared in DMF from 0.5 wt% suspension in MeOH at lower (left) and higher (right) magnification.

After adding an additional step, the surface coverage was increased, but still large gaps on the surface were visible (Figure 6-24). XRD of the samples (Figure 6-25) were measured to verify the successful coating of the surface. Only for the 2-step sample, peaks at 12.61° and 17.75° were visible. These are the same positions expected for a TIFSIX powder sample. Adding additional steps to the surface might increase the surface coverage, but it is questionable if this will lead to a more homogeneous coating or if the TIFSIX particles tend to agglomerate with each other leading to non-homogeneous coating and a rough surface. The results from an earlier chapter with dip-coating of MIL-53(Al) on glass (chapter 4.4, p. 90) has shown, that the repeated dip-coating of a glass surface does not

lead to a more homogeneous coating, but to the agglomeration of the particles on the surface. Furthermore has an in deep investigation of the dip-coating approach for TIFSIX exceeded the scoop of this research. Therefore, for now, no further investigation to increase the surface coverage in terms of number of treatment steps on the surface or changing the concentration of the suspension were investigated.

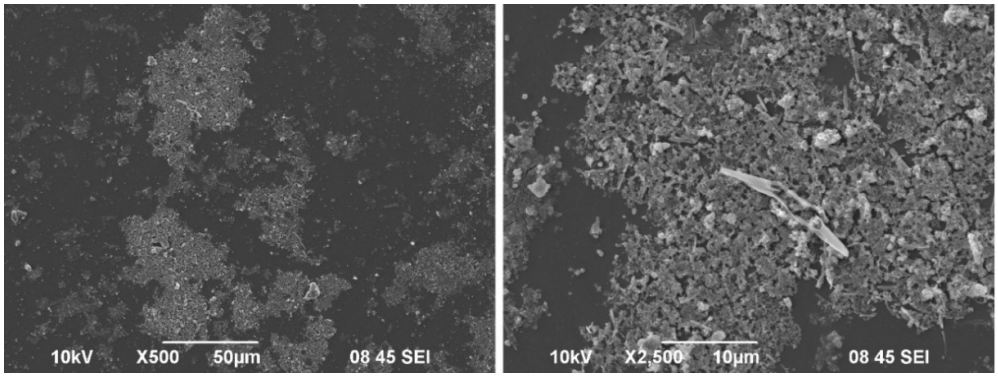


Figure 6-24: SEM image of glass slide coated with 2 steps of TFISIX, prepared in DMF from 0.5 wt% suspension in MeOH at lower (left) and higher (right) magnification.

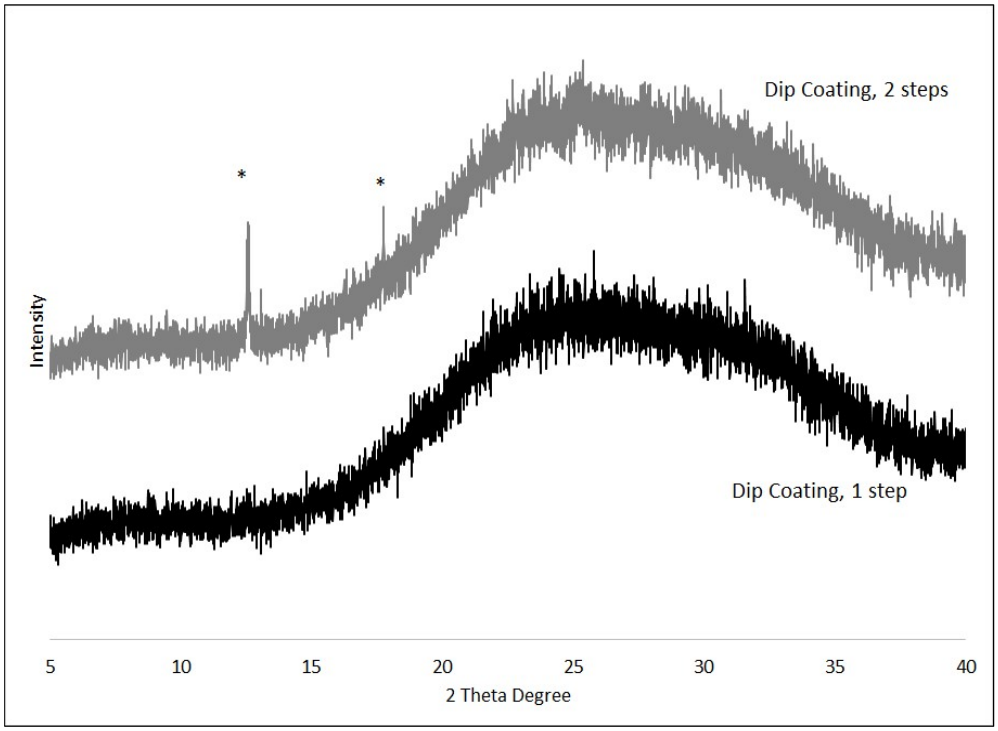


Figure 6-25: XRD pattern after coating a glass slide with TIFSIX, from 0.5 wt% suspension in MeOH as solvent. Peaks corresponding to TIFSIX are highlighted with asterisk.

6.4.2 Seeding and secondary growth

Besides the repetition of the dip-coating to create thicker coatings on the surface, another way is to conduct a secondary growth in reaction conditions after the dip-coating. The particles on the surface added by the dip-coating act as seed for the subsequent thin-film growth. For the seeding and secondary growth approach, a glass slide was coated with 2 steps of TIFSIX with a 0.5 wt% suspension in MeOH and the glass slide vertically placed in TIFSIX reaction mixture with DMF as solvent and the reaction conducted at 85°C and 15 h reaction time. SEM images and XRD pattern were measured for the sample. The SEM

image (Figure 6-26) shows that the surface is completely covered with particles, but at higher magnification gaps in the coating are visible. The XRD pattern of the sample (Figure 6-27) show peaks at ~12° and ~17.8°, but additional peaks imply a sample with impurities. It might be possible to remove these impurities by additional activation methods like solvent exchange or heating in vacuum at elevated temperature, but this was not further investigated, because of the non-uniform structure of the coating.

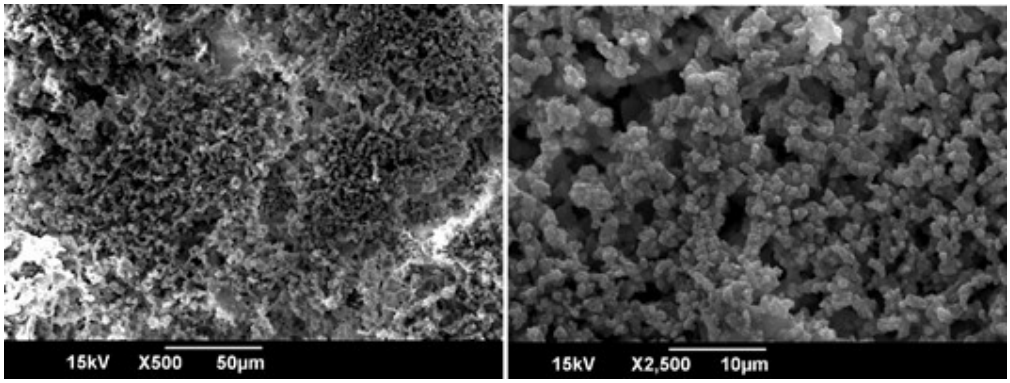


Figure 6-26: SEM image of a glass slide coated by seeding and secondary growth at low (left) and higher (right) magnification. The glass slide was seeded with 2 steps of TIFSIX prepared in DMF in a 0.5 wt% suspension with MeOH as solvent, followed by secondary growth at 85°C for 15 h.

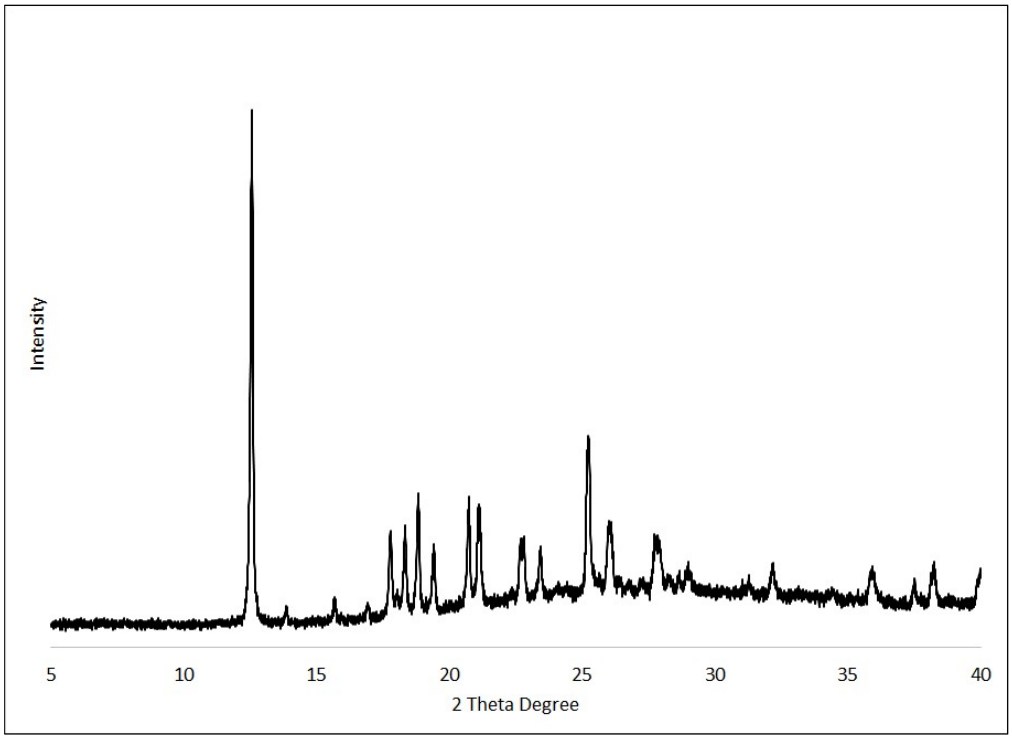


Figure 6-27: XRD pattern of glass slide coated by seeding (0.5 wt% suspension in MeOH) and secondary growth (DMF at 85°C with 15 h reaction time).

6.4.3 **Solvent assisted epitaxy**

The solvent-assisted epitaxy (SAE) was tested for TIFSIX using DMF as solvent. Similar to the SAE experiments of MIL-53(Al) (chapter 4.9, p. 121) the reaction conditions were

chosen similar to the powder synthesis conditions. In the case of TIFSIX, this was a reaction temperature of 85°C and a reaction time of 15 h.

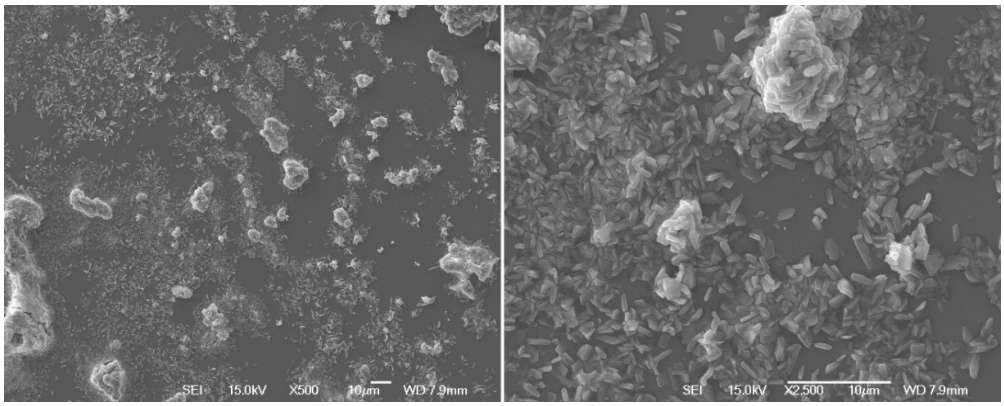


Figure 6-28: Glass slide covered by product prepared using the SAE approach with DMF at 85°C.

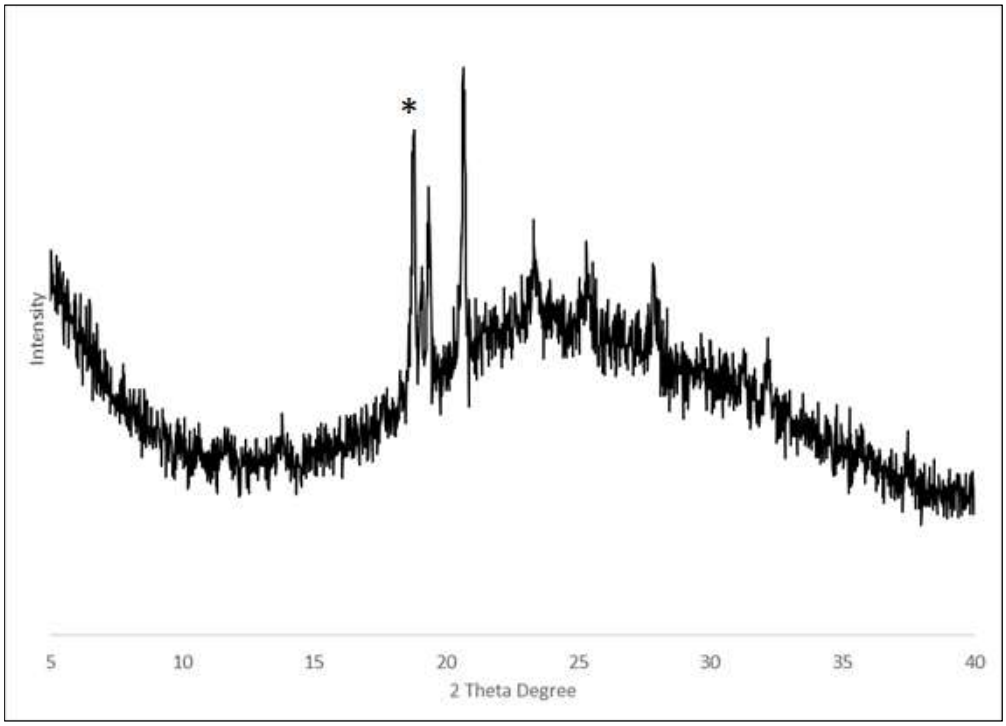


Figure 6-29: XRD pattern of TIFSIX product prepared using the SAE approach with DMF as solvent and 85°C reaction temperature. Starting material ($NiTiF_6$; highlighted by asterisk) and unknown impurities are visible.

However, after the synthesis, the surface (Figure 6-28) was only sparsely covered with particles. These are rod-shaped at higher magnification and does not resemble the known TIFSIX particles. During the powder synthesis in DMF at 85°C, smaller cubic particles which agglomerate to larger micrometre shaped needles were expected (Figure 6-18). The identification of these particles as TIFSIX was not possible. The XRD pattern (Figure 6-29) show peaks at 18.76°, 19.34° and 20.68°, which does not resemble any known product.

6.4.4 Rapid thermal deposition

For the RTD approach, the glass slides were covered with a thin-film of reaction mixture and placed in an oven at 85°C. The reaction conditions were tested using DMF as solvent and a reaction time of 5 h at 85°C, a reduced reaction time in comparison to the powder

synthesis. Due to the nature of the RTD technique (thin-film growth caused by the evaporation of solvent) much shorter reaction times can be applied for the RTD in contrast to solvothermal powder synthesis [160].

The surface covered using the RTD approach was not homogeneously covered. SEM images of the surface (Figure 6-30) show particles on the surface at lower magnification, but with larger inter-particle gaps. At higher magnification, these particles do not have a cubic or needle shape as observed for sampled from powder synthesis (Figure 6-18), rather they are fused particles with varying shape. According to the XRD pattern (Figure 6-31) the successful synthesis of TIFSIX was not possible in these conditions. The peak positions (12.58°, 15.60° and 18.33°) and relative intensities match the product prepared in DMF at RT and the product prepared in the one-step reaction in MeOH at 85°C and is therefore most likely not TIFSIX.

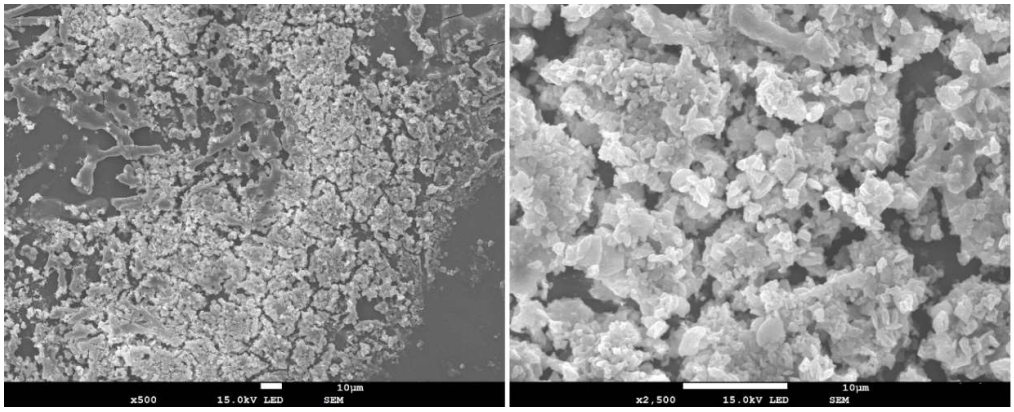


Figure 6-30: Glass slide covered using the RTD approach in DMF at 85°C and 5 h reaction time.

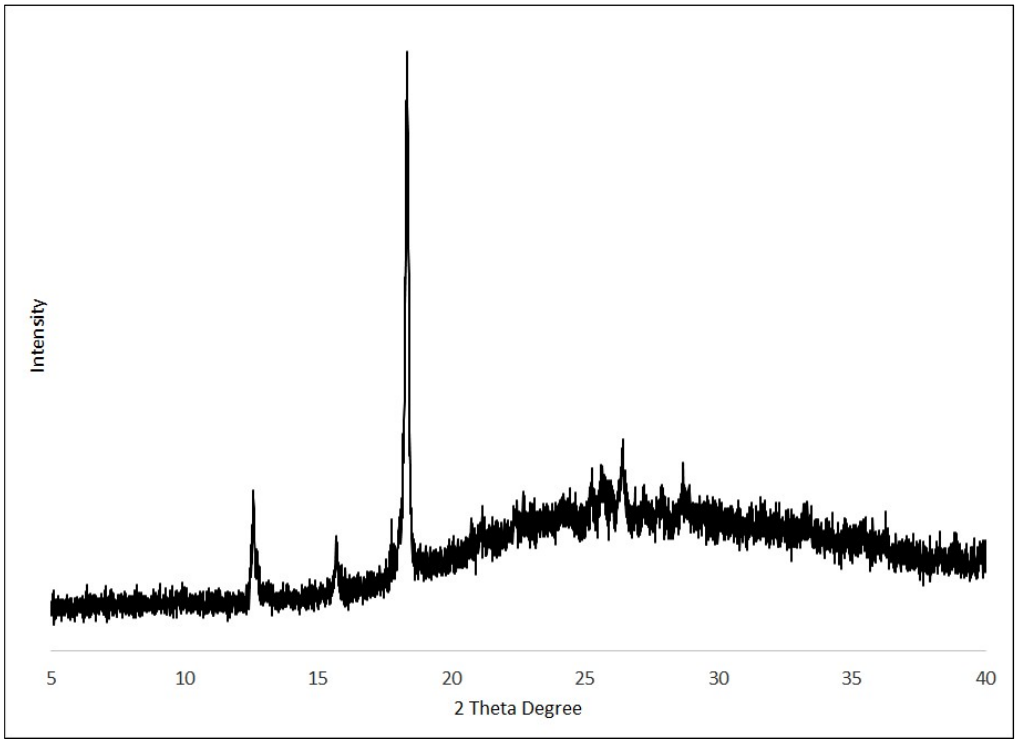


Figure 6-31: XRD of glass slide coated using the RTD approach using DMF as solvent at 85°C and 5 h reaction time.

6.4.5 **In-situ coating**

In-situ coating of the glass slide was achieved by placing the slide vertically in the reaction mixture in solvothermal conditions similar to the conditions used for the powder synthesis. Again, only DMF was used as solvent. The reaction temperature for the in-situ coating was set to 85°C and the influence of different reaction times for the coating was investigated using reaction times of 15 h (same reaction time used for the powder synthesis), 5 h and 1 h.

Even after 1 h reaction time, the XRD pattern (Figure 6-32) show peaks at 12.59° and 17.87°, matching the peaks observed for TIFSIX. However, the intensity of the peaks was low, in comparison with the background signal of the glass. A possible explanation for the low intensity of the peaks might be identified by the SEM images of the coated glass surface. The images (Figure 6-33) show that the surface could be not completely covered and gaps between the coating are visible implying a reduced surface coverage. A cross-section of the surface (Figure 6-34) shows that the coating has a thickness of about 4.8 µm, but with the coating is not uniform and large gaps in the coatings are visible.

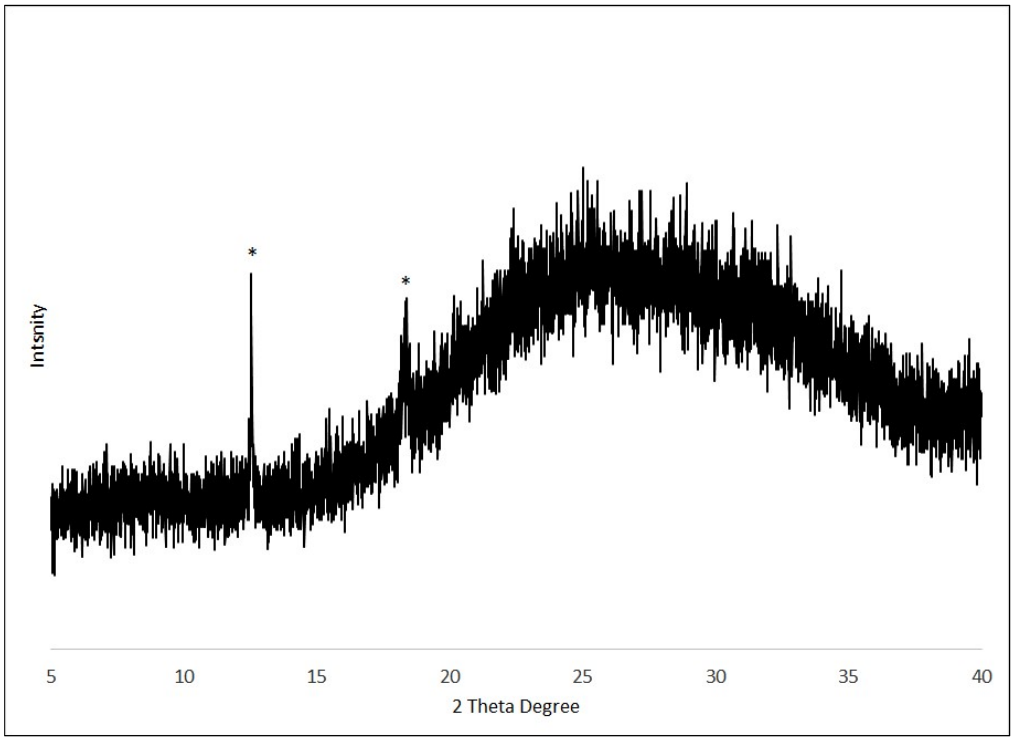


Figure 6-32: XRD pattern of glass slide covered in-situ with TIFSIX at 85°C with 1 h reaction time. Peak positions (highlighted with asterisks) and relative intensity of the peaks match pattern of typical TIFSIX powder samples.

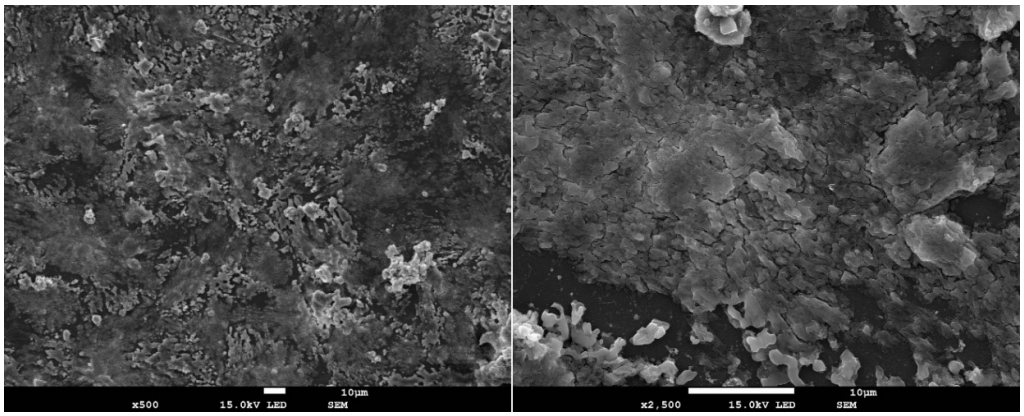


Figure 6-33: Glass slide covered in-situ using DMF as solvent and 1 h reaction time, which lower (left) and higher (right) magnification.

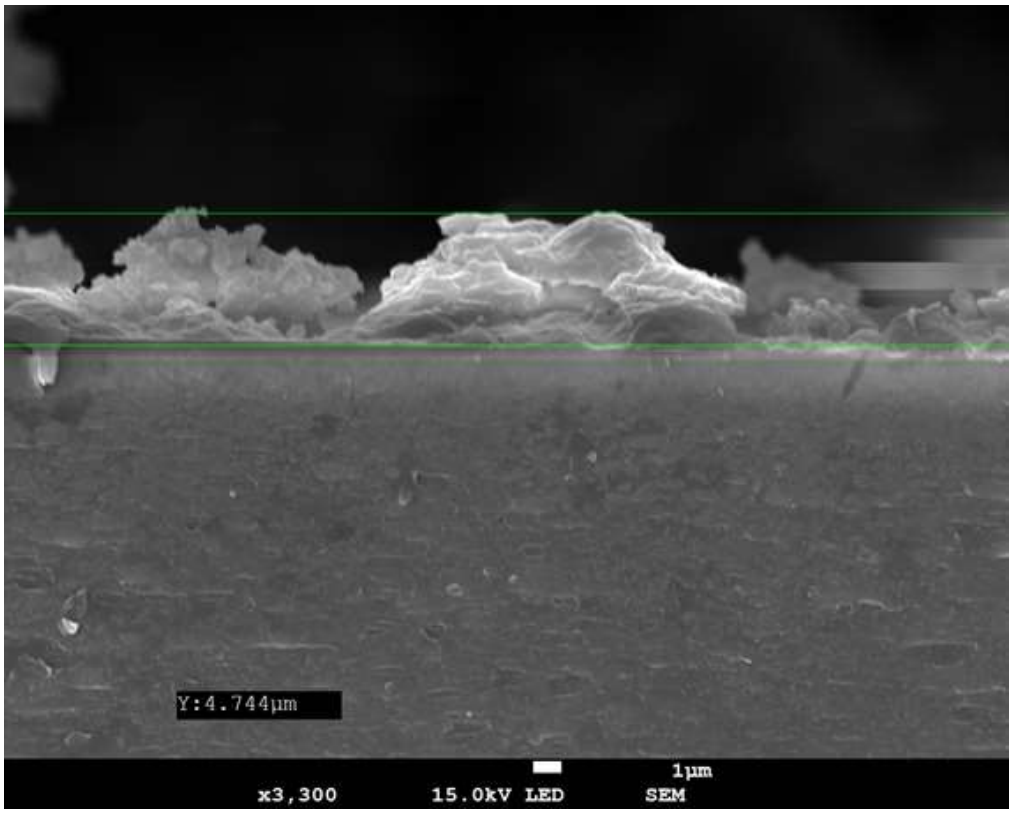


Figure 6-34: SEM cross-section of glass slide covered by in-situ at 85°C with 1 h reaction time. Coating thickness is about 4.8 µm, but with gaps in the coating.

While it was possible to coat the surface with TIFSIX after 1 h of reaction time, the SEM images of the surface show that this coating is not homogeneous. By increasing the reaction time, the surface coverage could be improved. After 5 h reaction time (Figure 6-35) the surface of the glass slide is mostly covered and only small gaps in the coating are visible. Larger agglomerated particles are also visible on the surface. At higher magnification, the surface is covered with small cubic particles and the larger agglomerated particles are mostly needle shaped. This resembles the powder samples prepared in DMF. A cross section of the sample (Figure 6-36) shows that the coating of the surface is thinner (3.9 µm) and more homogeneous and smooth (probably caused by

fusing of particles) than the coating after 1 h. No gaps can be identified in the cross-section image of the coating after 5 h reaction time.

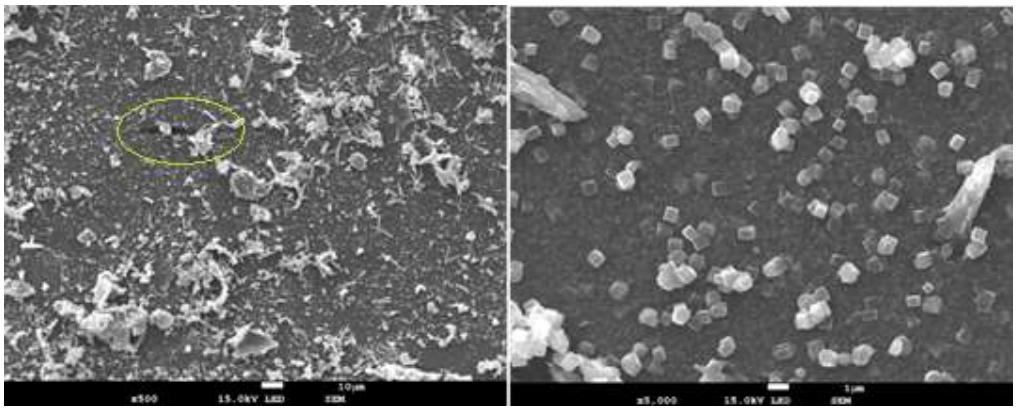


Figure 6-35: SEM image of glass slide covered in-situ with TIFSIX at 85°C and 5 h reaction time at lower (left) and higher (right) magnification. Only small cracks in the coating were visible (yellow marking).

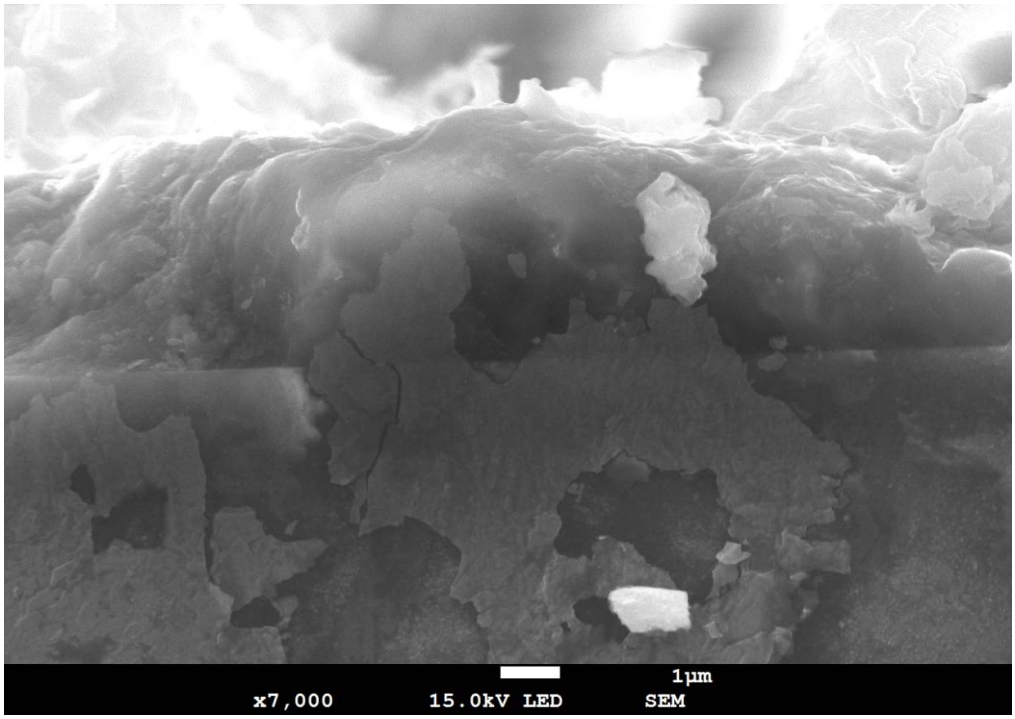


Figure 6-36: Side-view of a glass slide coated in TIFSIX in DMF in-situ for 5 h. The thickness of about 3.6 µm and the particles are more fused. No gaps in the coating are visible.

The SEM image shows (Figure 6-37) that after 15 h reaction time at 85°C the surface is completely covered with needle shaped particles. Such needle-shaped particles were observed for the powder synthesis of TIFSIX in DMF before (Figure 6-18). At higher magnification, these particles are composed of smaller cubical particles and resemble the morphology of TIFSIX prepared in DMF during the powder synthesis. A cross-section of the surface (Figure 6-38) show that with longer reaction time the coating is with 6.9 µm, thicker and rougher than the coating prepared after 5 h reaction time. Still, in contrast to the 1 h sample, the surface is completely covered without gaps.

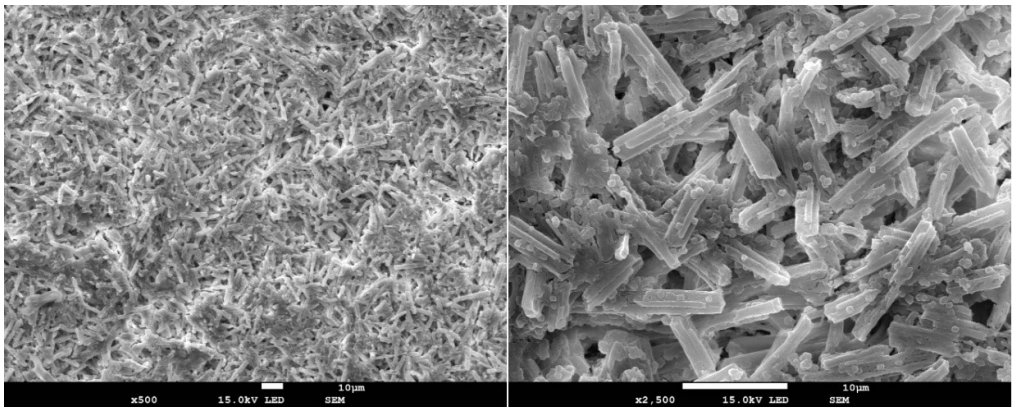


Figure 6-37: Glass slide with in-situ coating of TIFSIX in DMF with 15 h reaction time at lower (left) and higher magnification (right).

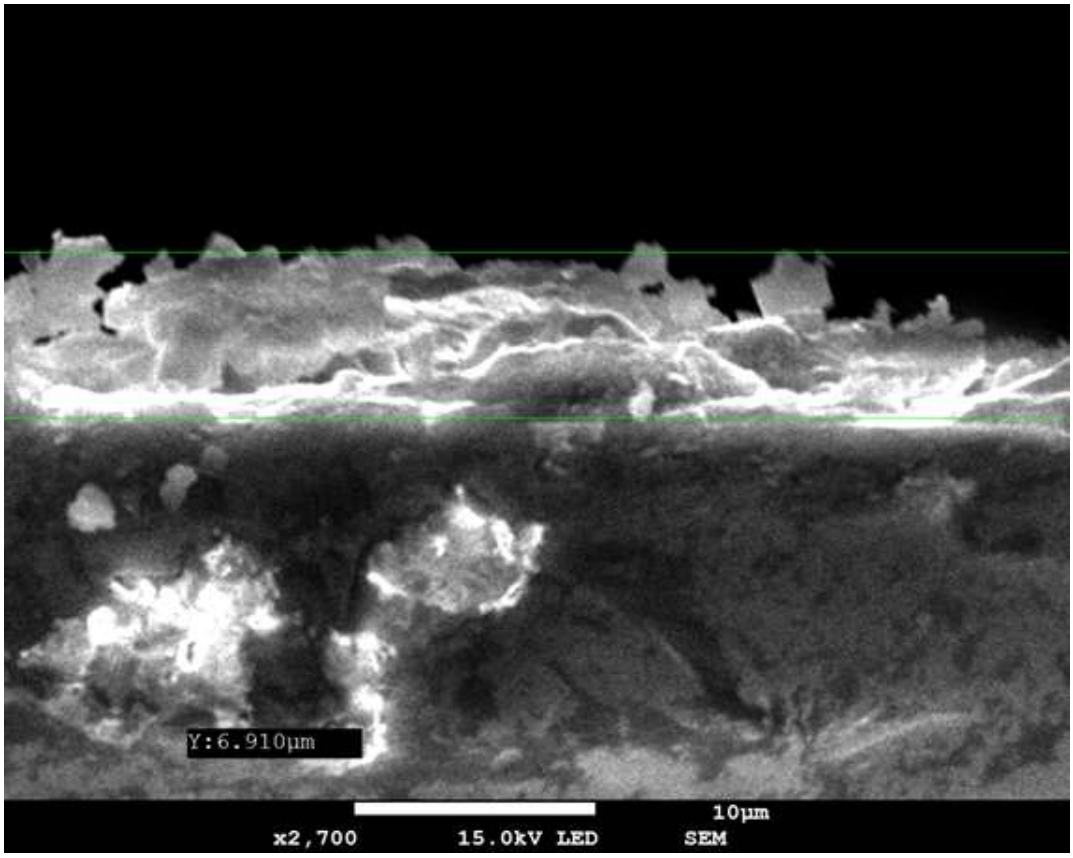


Figure 6-38: Side-view of a sample prepared in-situ with DMF as solvent and 15h reaction time.

XRD measurement (Figure 6-39) were performed for the in-situ coated glass slides. Both patterns after 5 h reaction time and 15 h reaction time look similar with slightly lower intensity of the peaks for the 5 h sample, perhaps by the thinner coating after 5 h reaction time. While peaks at 12.58° and 17.82° confirm the successful coating with TIFSIX, additional peaks at 15.75° and 18.69° show that the coating still contains impurities. Similar to the powder synthesis in DMF (Figure 6-20), these impurities could be mostly removed by solvent exchange in MeOH for 1 day. The XRD pattern (Figure 6-40) show that peak at 15.75° could be completely removed and the peak at 18.69° (which might be unreacted starting material $NiTiF_6$) reduced in intensity.

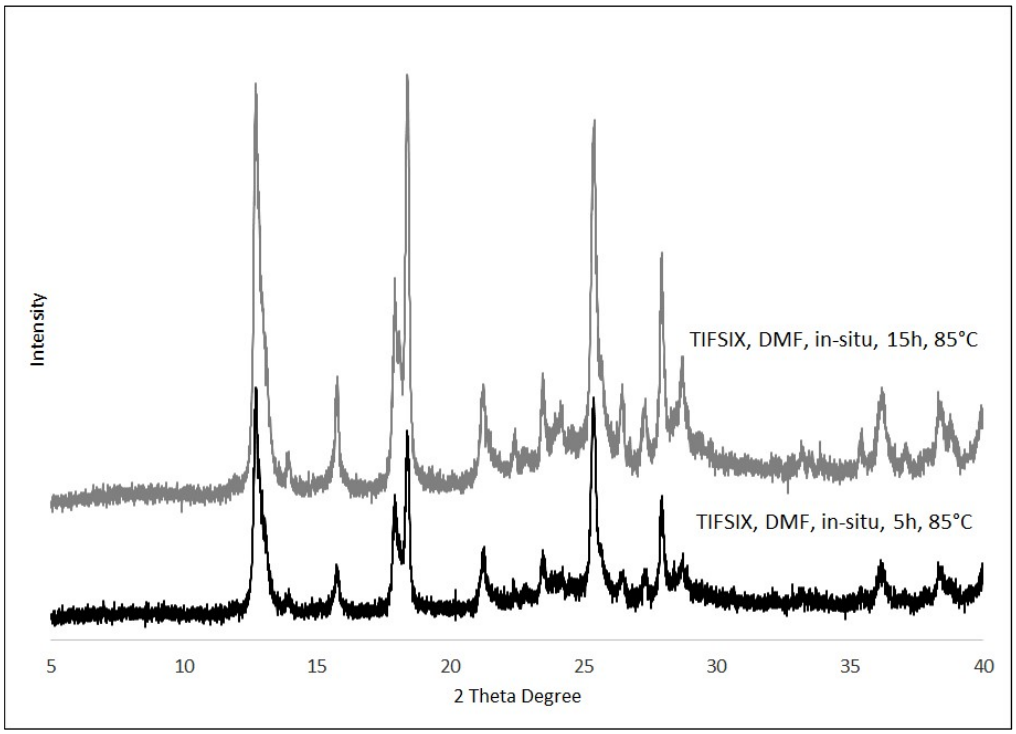


Figure 6-39: XRD pattern of glass slides covered by in-situ approach with TIFSIX at 85°C with 5 h (black) and 15 h (grey) reaction time. Both patterns were recorded before activation by solvent exchange.

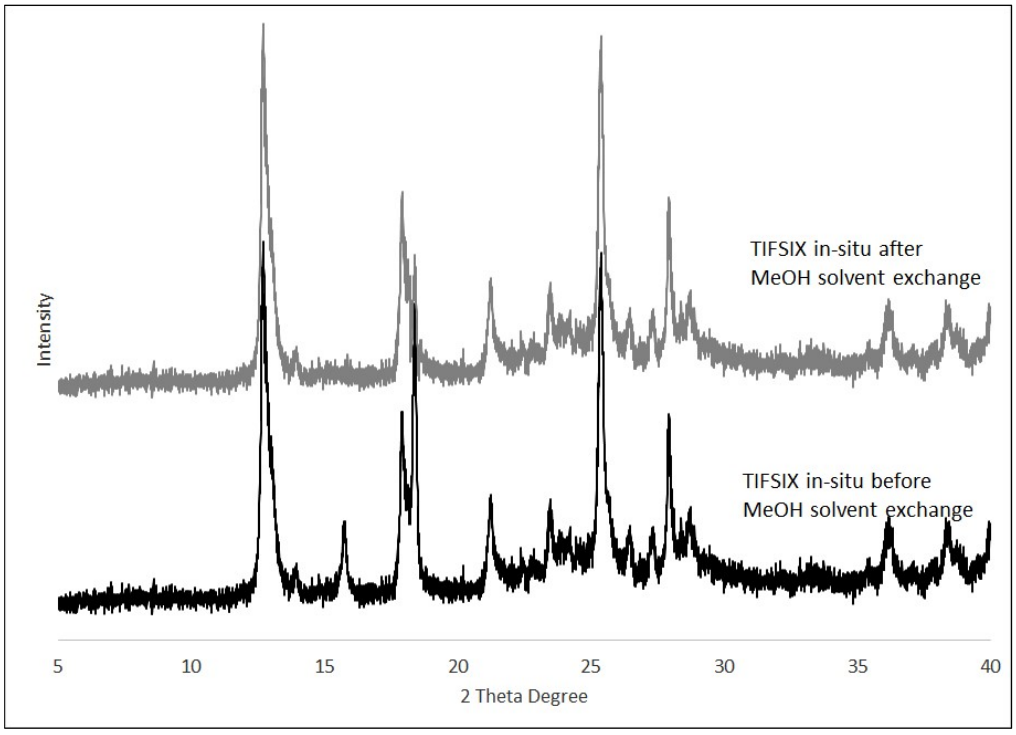


Figure 6-40: XRD pattern of a glass slide covered by in-situ approach in DMF after 5 h reaction time before (black) and after solvent exchange in MeOH (grey). Glass coated in-situ with 5 h reaction time was used.

6.5 Sensor experiments

During the thin-film synthesis, it was only possible to coat the surface with a homogenous film of TIFSIX using in-situ coating in DMF with reaction times of 5 h and 15 h respectively. The in-situ coating with 5 h and 15 h reaction times were applied to coat an LPG and sensor measurements were conducted for CO_2 and MeOH. The sensor measurement was conducted similar to the sensor experiments for MIL-53(Al)-coated fibre in an acrylic glass box (Figure 5-2). For more information about the sensor measurement process and expected wavelength shifts for published MOF coated LPGs, the reader will be referred to chapter 5.3 (p. 137). In short, the CO_2-concentration in the chamber was controlled with a commercial CO_2 sensor and the MeOH-concentration calculated according to the known volume of the chamber and the volume of added MeOH. After adding the target compounds, samples were left for ~10 min in order to stabilize the environmental conditions (*e.g.* temperature and distribution of the target compound in the chamber) and the wavelength measured as a mean value over a 5 min period.

Similar to the in-situ coating of MIL-53(Al) (chapter 5.4.3; p. 161), the LPG fibres were coated inside the custom-made Teflon chamber. The fibre was attached inside the box and the box filled with TIFSIX reaction mixture in DMF until the fibre was immersed. The chamber was placed in oven at 85°C and the reaction conducted for 5 h and 15 h respectively. Loose powder was removed by washing with MeOH. To remove impurities, solvent exchange in MeOH was conducted for a day and the fibre dried at 100°C overnight before sensor measurements were performed.

It was anticipated that both compounds (CO_2 and MeOH) should exhibit some adsorption. TIFSIX has one of the highest known CO_2-capacities at low and ambient pressure, which was emphasized in publications referring to TIFSIX and SIFSIX [235]. For MeOH, no isotherms or data regarding the capacity and adsorption selectivity have yet been published and, unlike CO_2, it is not a linear molecule. However, MeOH has been used to activate TIFSIX and SIFSIX by solvent-exchange and therefore must be able to enter the pores of TIFSIX. MOFs are known to exhibit framework flexibility, which enables adsorption of target molecules which are larger than the nominal pore size of the MOF [411].

Similar to criteria to those used for the MIL-53(Al) sensor experiments were used to determine the quality of the sensor response. One limitation of the experiment is the spectral resolution of the spectrometer, which is 0.02 nm. Another criterion, which must be considered is the limit of quantification (LOQ). The LPG should act as a sensor system to quantify and distinguish different concentrations of CO_2 and MeOH and the signal of the measurement must be clearly separated from the background noise of the system. This is especially problematic for measurements, which have large signal fluctuations. The limit of quantification is defined as [379]:

$$LOQ = \bar{x} + 10\sigma_x \qquad \text{Eq 6-1}$$

Whereas $\bar{x}$ is the mean value of the blank (the measured value with no target compound in the chamber, in this case the value at 0 ppm concentration CO_2 or MeOH) and σ_x is the standard deviation of this blank value. The measured wavelength should therefore be 10

times larger than the standard deviation of the blank value to be counted as a sensor response. Furthermore, should the wavelength shift have a specific direction. If the wavelength shifts into different directions, there might be no correlation between target compound concentration and wavelength shift of the LPG bands.

6.5.1 In-situ coating; 5 h reaction time

A SEM image of the fibre (Figure 6-41) shows successful coating of the surface. The surface is covered with a homogeneous film, with several needle shaped particles embedded in the coating and resemble the glass slide coated using similar conditions (Figure 6-35). However, at higher magnification (Figure 6-42) between the larger needle shaped particles the surface is not completely covered and gaps in the coatings are visible. A spectrum of the LPG over the range 200-1100 nm is shown in Figure 6-43, the LP_{018}-band (~665 nm) and the LP_{019L}-band (783 m) are both visible. The LP_{019}-band is in split into two bands (LP_{019R}-band at ~880 nm), but the resolution of the LP_{019R}-band band was not good enough to be clearly identified by the SIR program to create time-resolved data of the band wavelength. Hence the LP_{018}-band and the LP_{019L}-band were used to investigate the sensor performance of this fibre in response to CO_2 and MeOH.

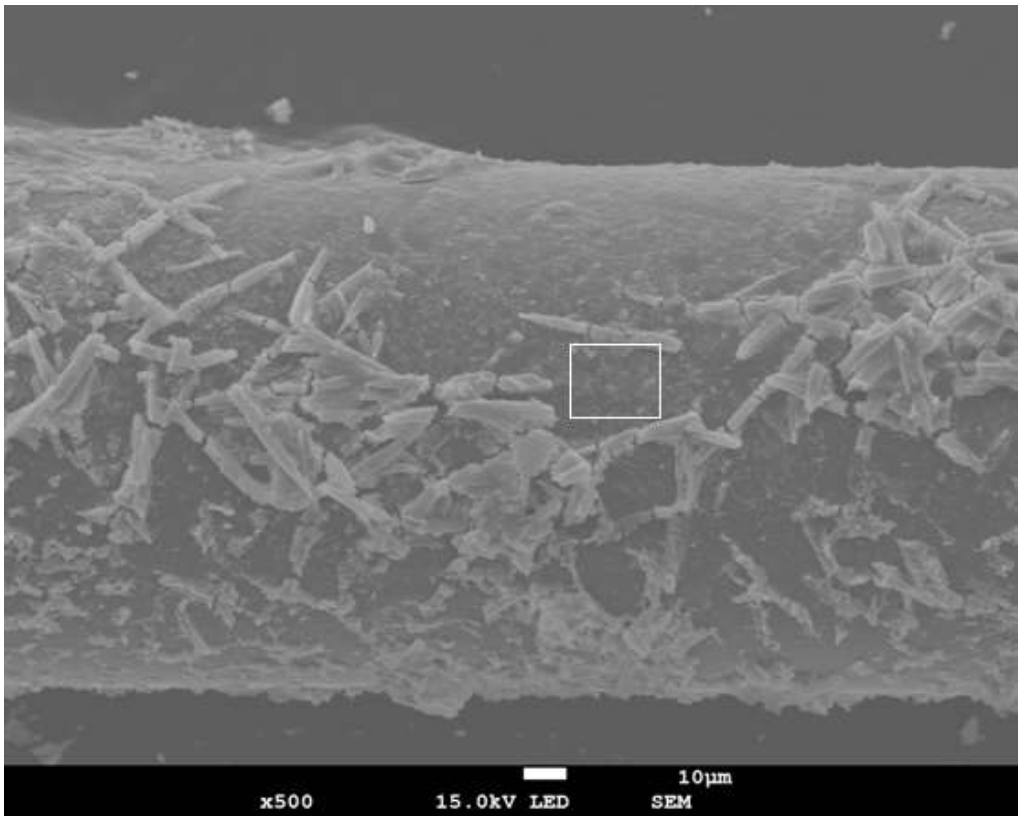


Figure 6-41: SEM image of a fibre coated with TIFSIX in-situ in DMF as solvent at 85°C with 5 h reaction time.

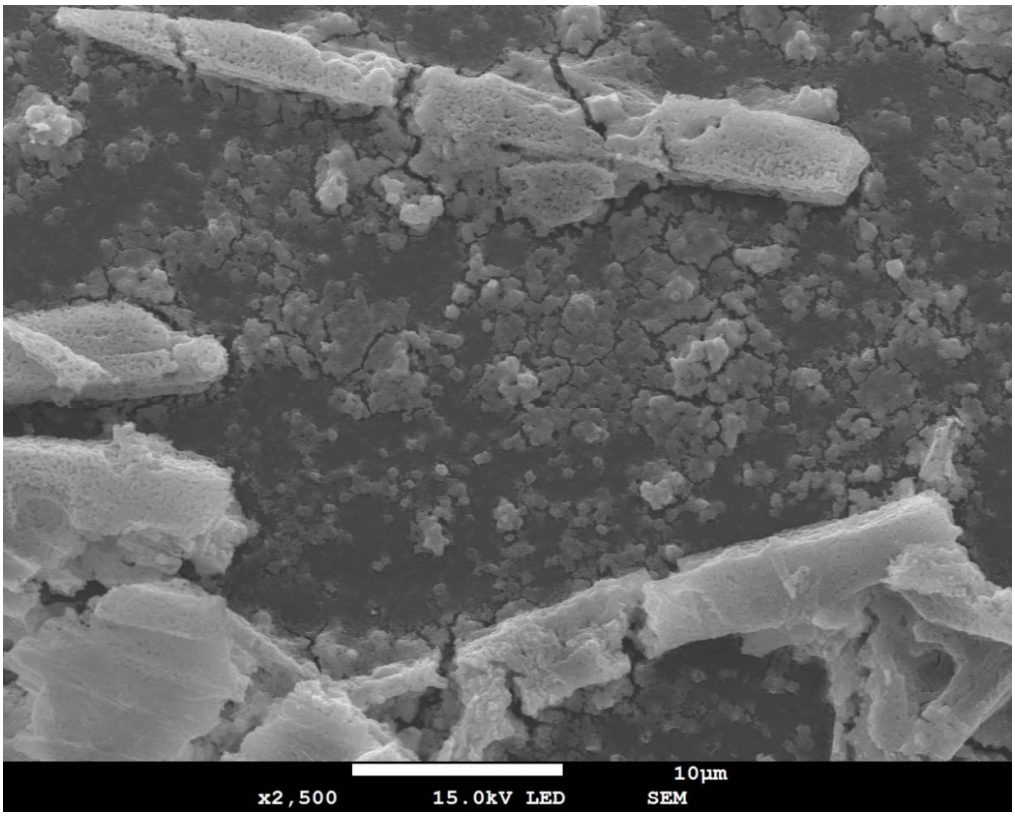


Figure 6-42: Image of fibre coated with TIFSIX in-situ with DMF as solvent at 85°C with 5 h reaction time. Shown is the highlighted is the area in Figure 6-41 with higher magnification.

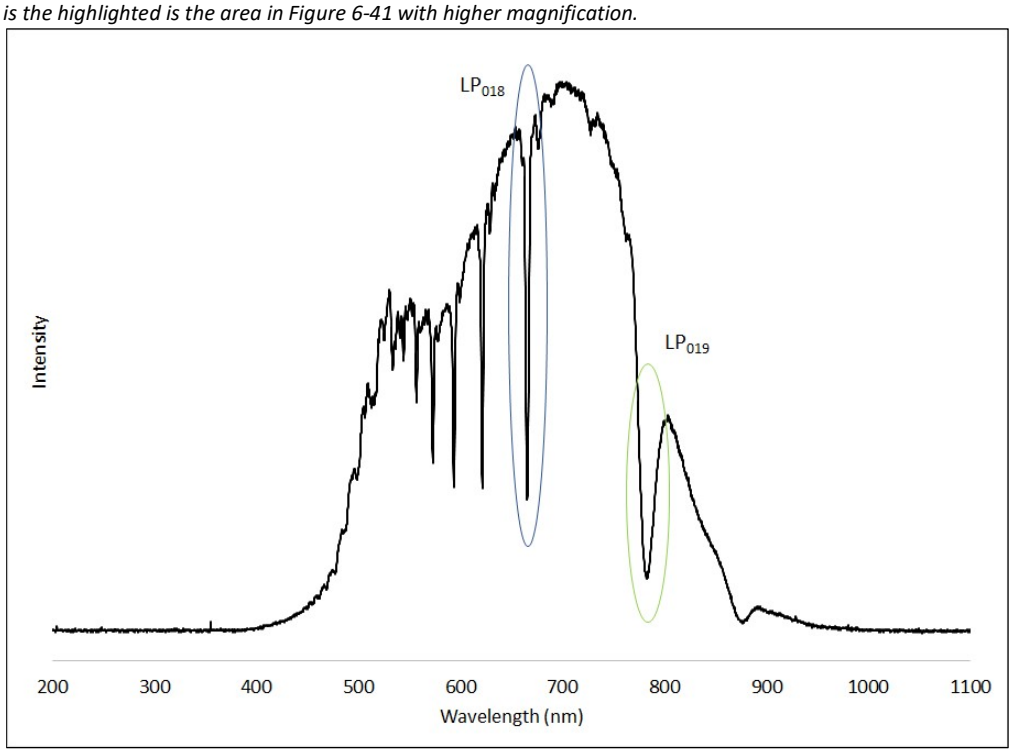


Figure 6-43: Total spectrum recorded over the range 200-1100 nm for the LPG coated with TIFSIX in-situ at 85°C with 5 h reaction time.

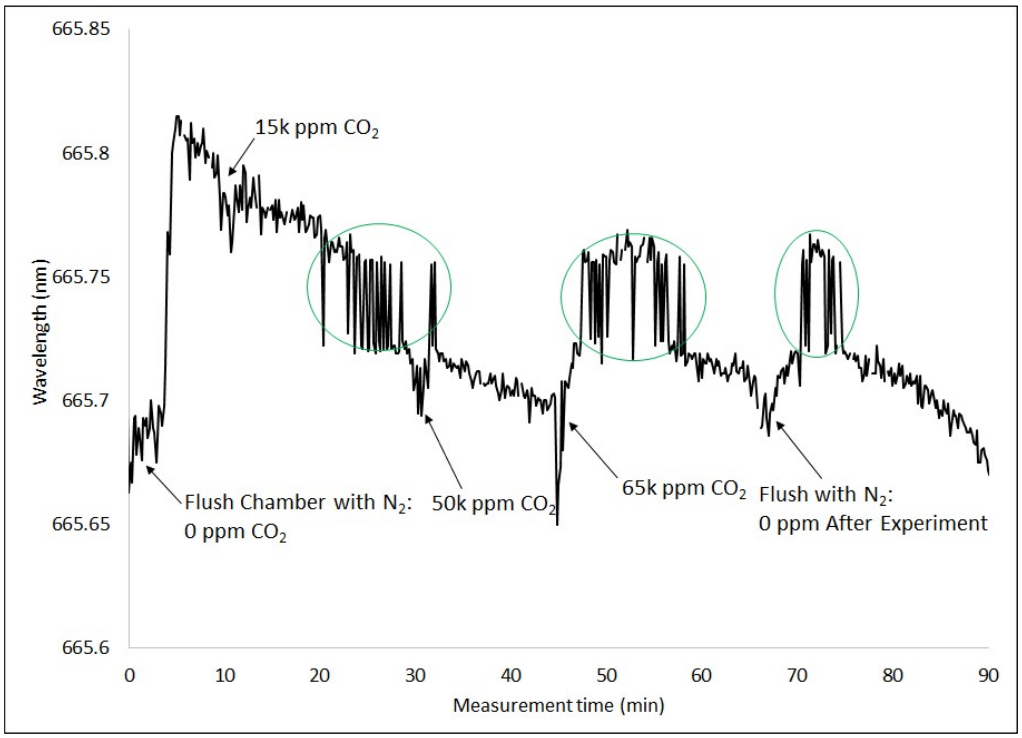


Figure 6-44: CO_2-sensor experiment results for fibre coated in-situ with TIFSIX at 85°C with 5 h reaction time. Measurement for the LP_{018}-band. During the measurement, several larger fluctuations of the wavelength have been observed (green).

Table 6-5: Measured wavelength during CO_2-sensor test with fibre coated with TIFSIX at 85°C and 5 h reaction time. Measured for the LP_{018}-band.

CO_2 concentration (ppm)	Wavelength (nm)
0	665.804
15k	665.745
50k	665.702
65k	665.713
0 after experiment	665.695

Table 6-6: Measured wavelength shift between varying CO_2-concentrations and sum of the wavelength shift for fibre coated with TIFSIX at 85°C and 5 h reaction time. Measured for the LP_{018}-band.

CO_2 concentration change (ppm)	Wavelength shift(nm)	Σ Wavelength shift (nm)
0 → 15k	-0.059	-0.059
15k → 50k	-0.043	-0.102
50k → 65k	+0.011	-0.091
65k → 0 after experiment	-0.018	-0.109

The results of the CO_2-measurement can be seen in Figure 6-44, whereas the measured wavelength and the wavelength difference between the varying CO_2-concentrations are shown in Table 6-5 and Table 6-6 respectively.

At the start of the experiment, the chamber was flushed with N_2 to reach a starting concentration in the chamber of 0 ppm CO_2. The measured wavelength has shifted during this step about ~0.2 nm, which might be caused by different effects like vibration by the N_2-flow and temperature reduction caused by gas expanding from a pressurized container to the chamber at ambient conditions (Joule-Thompson effect). After an additional ~10min

the temperature stabilized, and CO_2 was added, leading to a wavelength shift of -0.059 nm. The variation of the measured wavelength is noteworthy. The value measured at 0 ppm shows a relative low variation of the measured wavelength (665.804 ± 0.012 nm; σ = 0.0065 nm), while at higher concentrations fluctuations of the measured wavelength were observed (Figure 6-44, highlighted in green). After ~20 min measurement time, the CO_2-concentration was increased to 50k ppm, leading to a shift of -0.043 nm. Addition of more CO_2 and increasing the concentration to 65k ppm, surprisingly increased the measured wavelength by +0.011 nm. After flushing the chamber with N_2 to return the system to 0 ppm CO_2-concentration, the wavelength has decreased by -0.018 nm. However, both values are lower than the spectral resolution of the detector (0.02 nm) and it is concluded that after reaching 50k ppm CO_2 concentration, the measured wavelength has not changed further. In theory has the blank value at 0 ppm a relatively small standard derivation and a total shift of 0.065 nm (10 times the standard derivation) is needed to reach the LOQ. This value is reached between 15k ppm and 60k ppm CO_2, and the sensor might be able to measure accurate CO_2 concentration of >30k ppm CO_2. However, the observed fluctuations of the measured wavelength (Figure 6-44, highlighted in green) are problematic for an accurate sensor measurement.

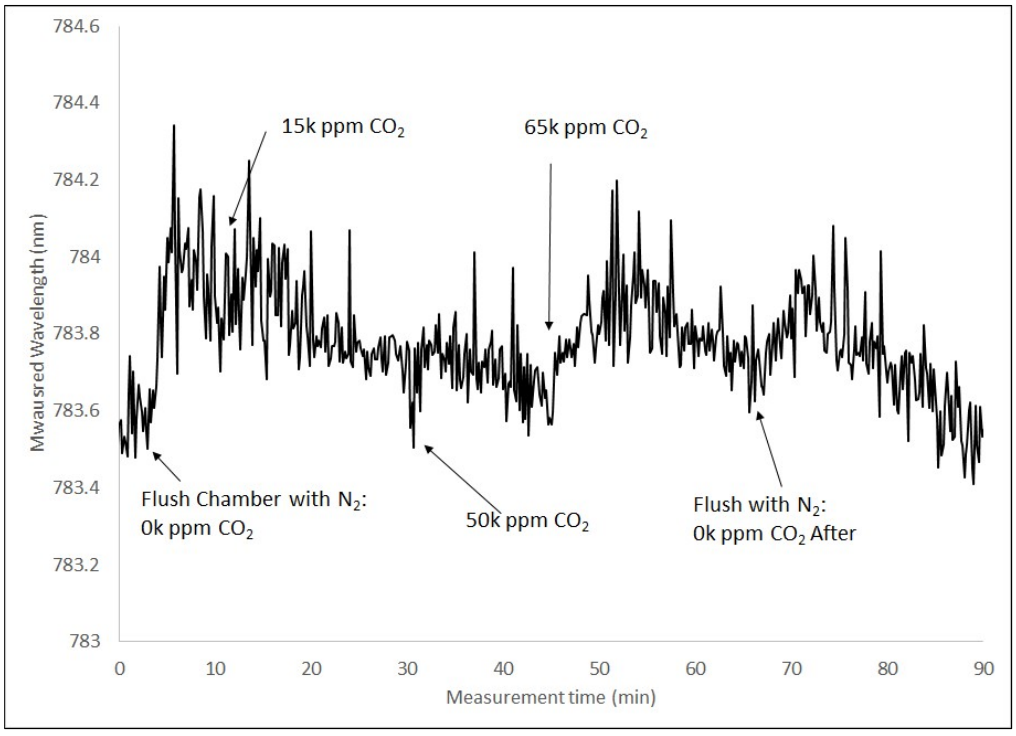


Figure 6-45: CO_2-sensor experiment results for fibre coated in-situ with TIFSIX at 85°C with 5 h reaction time. Measurement for the LP_{019L}-band.

Table 6-7: Measured wavelength during CO_2-sensor test with fibre coated with TIFSIX at 85°C and 5 h reaction time. Measured for the LP_{019L}-band.

CO_2 concentration (ppm)	Wavelength (nm)
0	783.998
15k	783.761
50k	783.677
65k	783.758
0 after experiment	783.682

Table 6-8: Measured wavelength difference between varying CO_2-concentrations and sum of the wavelength shift for fibre coated with TIFSIX at 85°C and 5 h reaction time. Measured for the LP_{019L}-band.

CO_2 concentration change (ppm)	Wavelength shift (nm)	Σ Wavelength shift (nm)
0 → 15k	-0.237	-0.237
15k → 50k	-0.084	-0.321
50k → 65k	+0.081	-0.240
65k→ 0 after experiment	-0.076	-0.316

The results for the LP_{019L}-band during the same measurement are shown in Figure 6-45. The measured wavelength and the resulting wavelength shift between the different concentrations are shown in Table 6-7 and Table 6-8. The results were recorded during the same measurement with the same fibre and hence show the measured wavelength during the measurement a similar pattern, but with larger fluctuations. For instance, was a wavelength shift after flushing the chamber observed at the start of the experiment as well (adding N_2 to reach 0 ppm CO_2), but this shift was with ~0.4 nm larger (for LP_{018}-band: 0.2 nm). During the first measurement step (changing the CO_2 concentration to 15k ppm), a shift of -0.237 nm was observed. At the subsequent steps of adding CO_2, the observed are with -0.084 nm and +0.081 nm smaller and have varying directions. For the last step of the process, changing the CO_2-concentration back to 0 ppm with N_2, the measured wavelength has not only returned to the starting value, but decreased even further. The results for the LP_{019L}-band verify larger wavelength shifts than for the LP_{018}-band, but with larger fluctuations and consequently larger standard derivation of the blank value (0 ppm of LP_{019L}-band: 783.998 ± 0.187 nm σ = 0.136 nm). This leads to the observation, that the LOQ was never reached and it is therefore not possible to quantify different CO_2-concentraion by the response of the for the LP_{019L}-band.

For MeOH sensor measurement, the same fibre studied for the CO_2-measuremnets was used. Prior to the MeOH sensing experiments, the fibre was heated at 100°C overnight to remove possible residues. The wavelength was measured after ~10 min to let the MeOH evaporate.

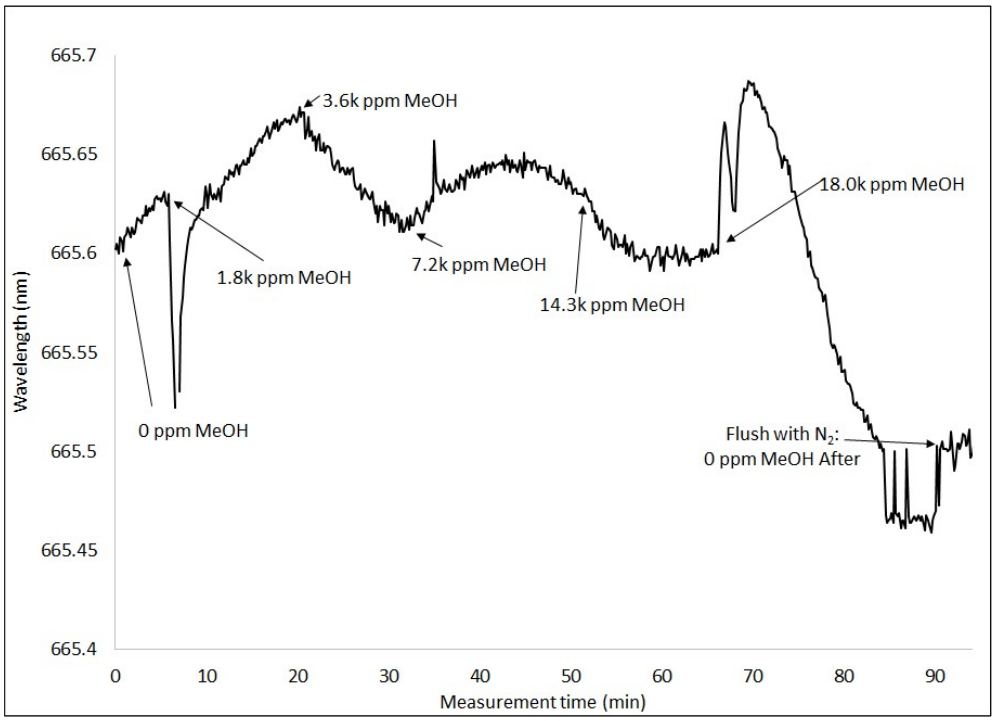


Figure 6-46: MeOH-sensor experiment results for fibre coated in-situ with TIFSIX at 85°C and 5 h reaction time. Measured for LP_{018}-band.

The results of the measurement for the LP_{018}-band can be seen in Figure 6-46. The measured wavelength and the difference between the individual CO_2-concentrations are shown in Table 6-9 and Table 6-10. After changing the concentration in the chamber to 1.8k ppm MeOH, the wavelength shifted by +0.040 nm. During the addition of the first sample of MeOH, the fibre moved slightly, leading to a sudden change of the wavelength at ~10 min, but after readjusting the fibre, the wavelength returned to the previous wavelength. After changing the MeOH concentration to 3.6k ppm, the wavelength dropped by -0.042 nm, followed by increase of +0.024 nm (at 7.2k ppm) and decrease of -0.044 nm (at 14.3k ppm). The final change to a MeOH concentration of 18.0k ppm has initially led to an increase in wavelength, but subsequently dropped even below the starting value. After flushing the chamber with N_2, returning the MeOH concentration in the chamber back to 0k ppm, the measured wavelength shifted again by +0.043 nm, but did not reach the original starting value. The wavelength shifts in opposing directions further imply that this fibre is not showing a quantifiable sensor response to MeOH.

Table 6-9: Measured wavelength during MeOH-sensor test with firer coated with TIFSIX at 85°C and 5 h reaction time. Measured for the LP_{018}-band.

MeOH concentration (ppm)	Wavelength (nm)
0	665.619
1.8k	665.659
3.6k	665.617
7.2k	665.641
14.3k	665.597
18.0k	665.461
0 after experiment	665.504

Table 6-10: Measured wavelength difference between varying MeOH-concentrations and sum of the wavelength shift for the fibre coated with TIFSIX at 85°C and 5h reaction time. Measured for the LP_{018}-band.

MeOH concentration (ppm)	Wavelength shift (nm)	Σ Wavelength shift (nm)
0 → 1.8k	+0.040	+0.040
1.8k → 3.6k	-0.042	-0.002
3.6k → 7.2k	+0.024	+0.022
7.2k → 14.3k	-0.044	-0.022
14.3k → 18.0k	-0.136	-0.158
18.0k → 0 after experiment	+0.043	-0.115

The results for the LP_{019L}-band (Figure 6-47) show similar response to LP_{018}-band, but with larger fluctuations of the measured wavelength and consequently a larger standard derivation of the blank (0 ppm MeOH: 783.055 ± 0.071 nm σ = 0.075 nm). The measured wavelength and the difference between the CO_2-concentrations are shown in Table 6-11 and Table 6-12, respectively. The wavelength drop after adding 1.8k ppm MeOH (at ~10 min, caused by movement of the fibre) and the large shift between 14.3k ppm and 18.0k ppm were observed again. Furthermore, the measured wavelength shifts in different directions and the sensor response ins lower than the LOQ. This implies no quantifiable sensor response to MeOH for the LP_{019}-band.

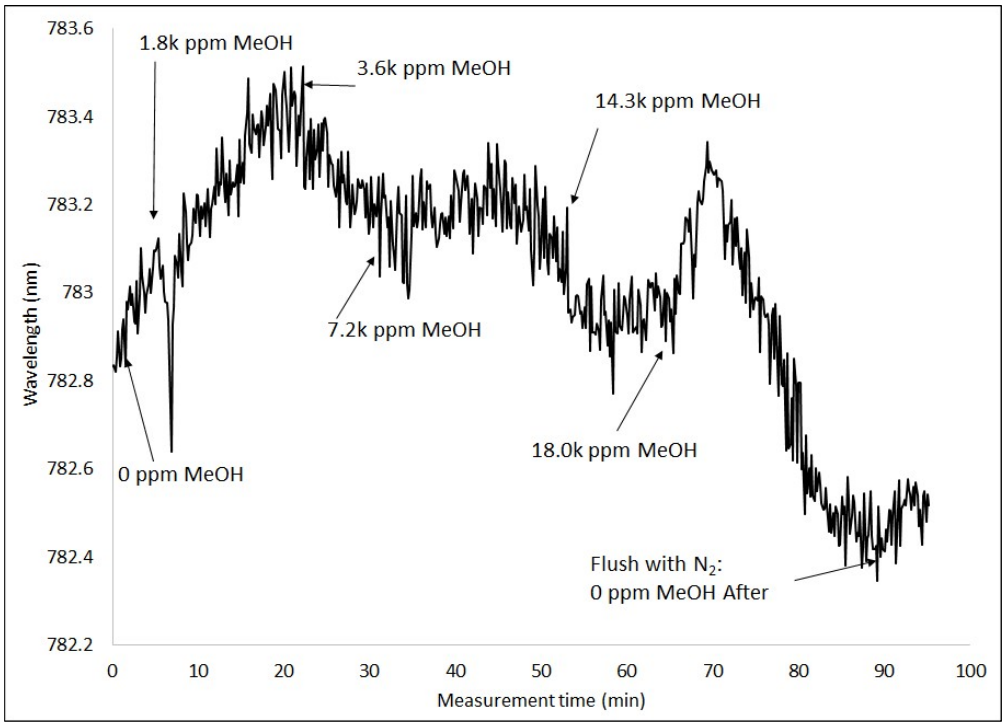


Figure 6-47: MeOH-sensor experiment results for of fibre coated in-situ with TIFSIX at 85°C and 5 h reaction time. Measured for LP_{019}-band.

Table 6-11: Measured wavelength during MeOH-sensor test with fibre coated with TIFSIX at 85°C and 5 h reaction time. Measured for the LP_{019L}-band.

MeOH concentration (ppm)	Wavelength (nm)
0	783.055
1.8k	783.398
3.6k	783.219
7.2k	783.233
14.3k	782.971
18.0k	782.422
0 after experiment	782.517

Table 6-12: Measured wavelength difference between varying MeOH-concentrations and sum of the wavelength shift for fibre coated with TIFSIX at 85°C and 5 h reaction time. Measured for the LP_{019L}-band.

MeOH concentration (ppm)	Wavelength shift (nm)	ΣWavelength shift (nm)
0 ppm → 1.8k	+0.343	+0.343
1.8k → 3.6k	-0.179	+0.164
3.6k → 7.2k	+0.014	+0.178
7.2k → 14.3k	-0.262	-0.084
14.3k → 18.0k	-0.549	-0.633
18.0k → 0 after experiment	+0.095	-0.538

6.5.2 In-situ coating; 15 h reaction time

An SEM image (Figure 6-48) of the fibre coated in-situ with 15 h reaction time shows a different morphology to that observed for the fibre coated using 5 h reaction time. The surface has a rough morphology and is covered with intergrown needle-shaped particles, whereas after using the shorter 5 h reaction time only a few needle-shaped particles are visible on the surface. This strongly suggests that the surface is completely covered with TIFSIX after 15 h reaction time. A spectrum of the LPG over the range 200-1100 nm (Figure 6-49) shows that both the LP_{018}- and LP_{019}-band are visible. In contrast to the spectrum for the 5 h LPG (Figure 6-38), the LP_{019R}-band at ~876 nm was clearly visible and will be used to investigate the sensor performance in response to CO_2 and MeOH and the wavelength difference between LP_{019L} and LP_{019R} with potentially high sensitivity can be utilised.

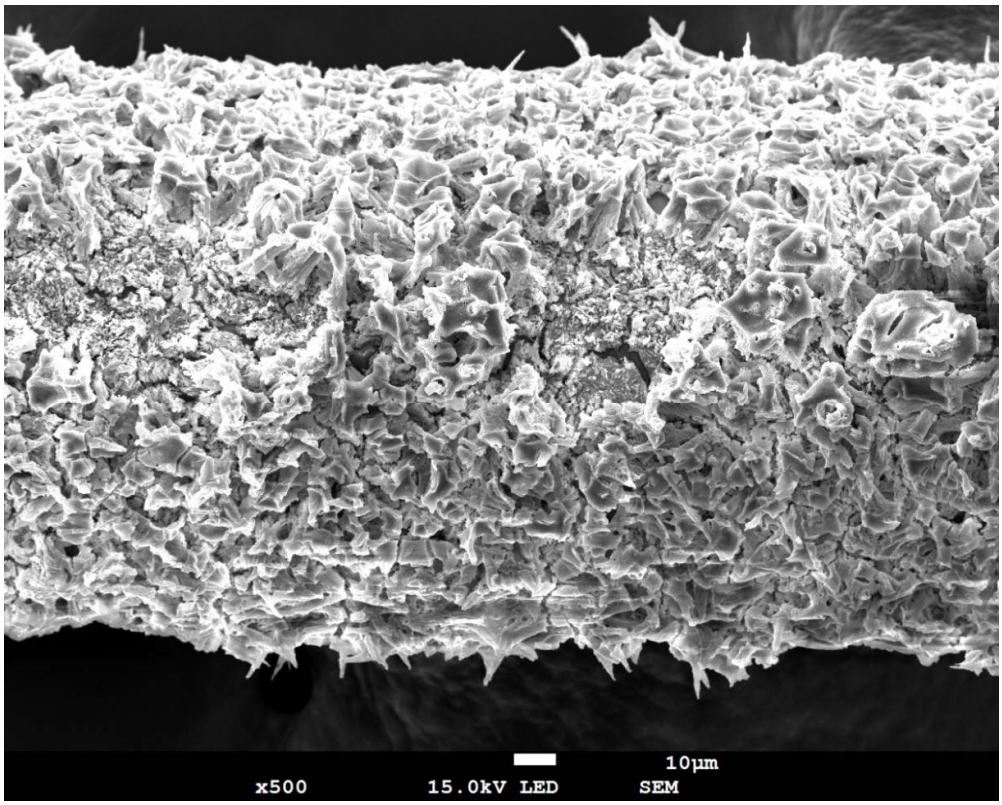


Figure 6-48: SEM image of the fibre coated in-situ with TIFSIX introduced at 85°C with 15 h reaction time.

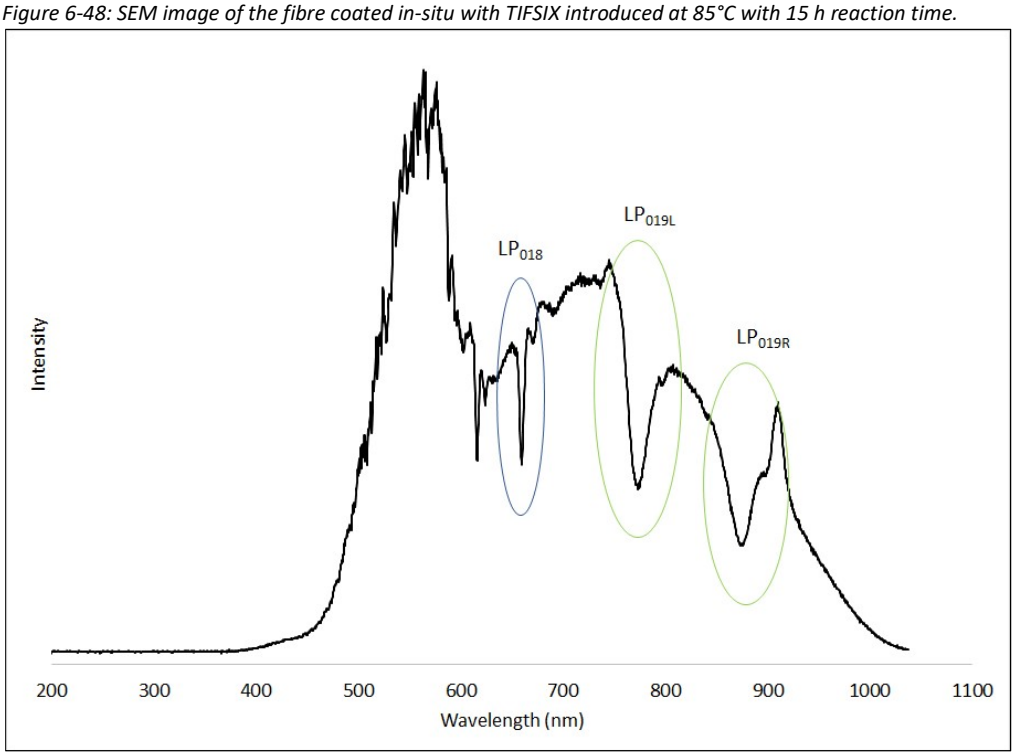


Figure 6-49: Spectrum recorded over the range 200-1100 nm of the LPG coated with TIFSIX in-situ at 85°C with 15 h reaction time. The LP_{018}-band (blue) and the split LP_{019}-band (green) can be seen in the spectrum and will be used for the investigation of the sensor performance.

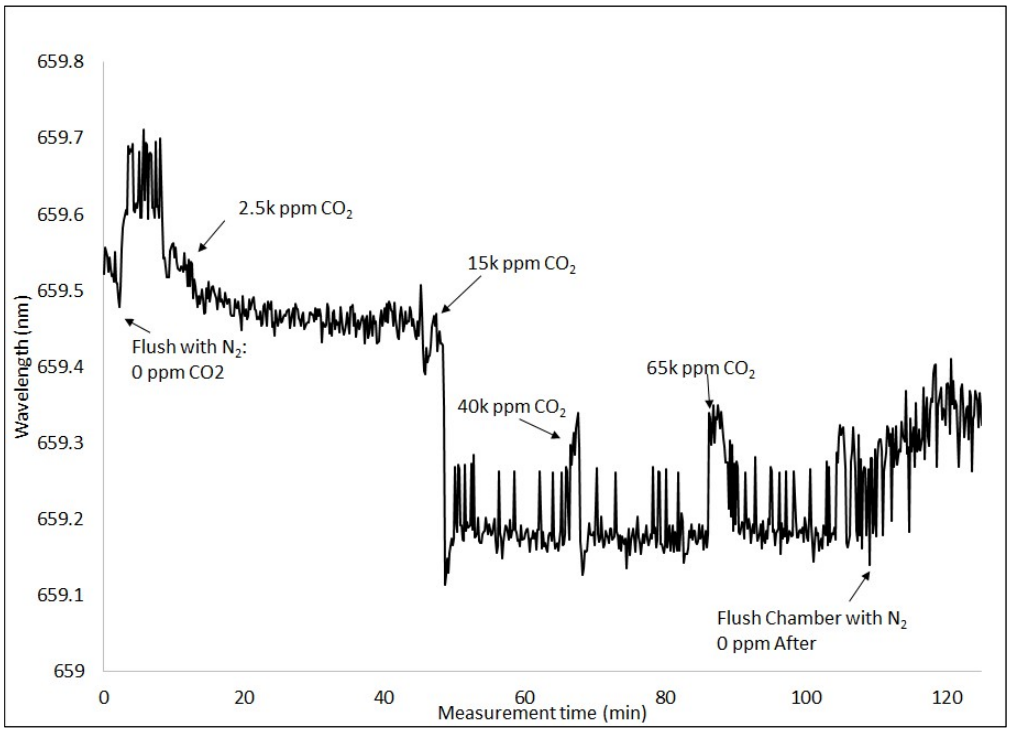


Figure 6-50: CO_2-sensor experiment results for fibre coated in-situ with TIFSIX at 85°C with 15 h reaction time. Results for LP_{018}-band.

The results of the CO_2-sensor measurement for the LP_{018}-band are shown in Figure 6-50, while the measured wavelength and the shifts between the different CO_2-concentrations are shown in Table 6-13 and Table 6-14, respectively.

After adding 2.5k ppm CO_2, the measured wavelength shifted by -0.057 nm and, after reaching 15k ppm CO_2-concentration, a wavelength drop of -0.279 nm was observed, but did not change further after reaching 40k ppm CO_2 (+ 0.002 nm). After flushing the chamber with N_2, returning the CO_2 concentration to 0 ppm, the wavelength shifted back to larger wavelength (+0.115 nm) but did not reach the starting value again.

Table 6-13: Measured wavelength during CO_2-sensor test with fibre coated with TIFSIX at 85°c and 15 h reaction time. Measured for the LP_{018}-band.

CO_2 concentration (ppm)	Wavelength (nm)
0	659.517
2.5k	659.460
15k	659.181
40k	659.183
65k	659.221
0 after experiment	659.336

Table 6-14: Measured wavelength shift between varying CO_2-concentrations and sum of the wavelength shift for fibre coated with TIFSIX at 85°C and 15 h reaction time. Measured for the LP_{018}-band.

CO_2 concentration change (ppm)	Wavelength shift (nm)	Σ Wavelength shift (nm)
0→ 2.5k	-0.057	-0.057
2.5k → 15k	-0.279	-0.336
15k → 40k	+0.002	-0.334
40k →65k	+0.038	-0.296
65k → 0 after experiment	+0.115	-0.191

A compareably large wavelength shift was observed between 2.5k ppm and 15k ppm CO_2, larger than the necessary LOQ of the blank value (0 ppm: 659.517 ± 0.025 nm; σ = 0.014 nm) and the sensor might be able to quantively measure CO_2-concentrations above 15k ppm. Therefore the reproducibility of the results was investigated.

Before this second measurement (Figure 6-51), the fibre was heated overnight at 100°C to remove possible residue from the coating. Even though recovery of the fibre was conducted, the starting wavelength of the first measurement (659.517 nm) could be not reached again and is with 659.361 nm lower. During the second CO_2-sensor measurement, after reaching 15k ppm, the wavelength shifted by only -0.026 nm. After changing the CO_2-concentration to 30k ppm and 55k ppm almost no change of wavelength was observed (-0.008 nm and +0.005 nm). In summary no response could be observed during the repetion of the CO_2-sensor experiment.

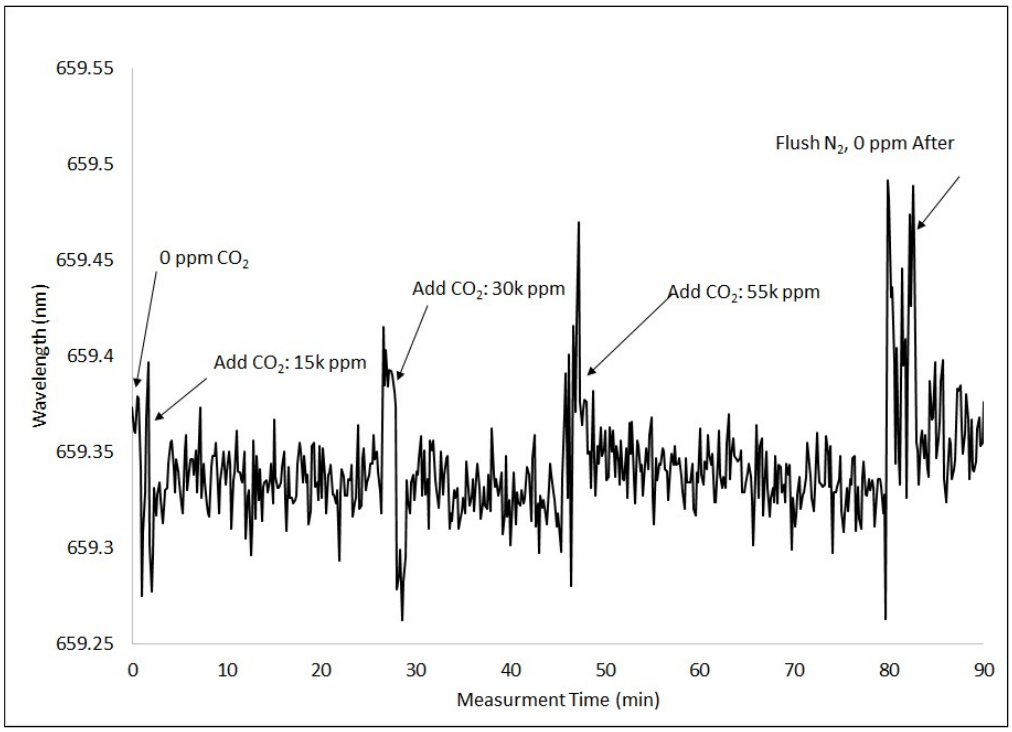


Figure 6-51: Results of repeated CO_2-sensor experiment for fibre coated in-situ with TIFSIX at 85°C with 15h reaction time. Measured for LP_{018}-band.

Table 6-15: Measured wavelength during repeated CO_2-sensor test for fibre coated with TIFSIX at 85°C and 15 h reaction time. Measured for the LP_{018}-band.

CO_2 concentration (ppm)	Wavelength (nm)
0	659.361
15k	659.335
30k	659.327
55k	659.332
0 after experiment	659.355

Table 6-16: Measured shift between varying CO_2-concentrations and sum of the wavelength shift for fibre coated with TIFSIX at 85°C and 15 h reaction time during the repeated CO_2-sensor test. Measured for the LP_{018}-band.

CO_2 concentration change (ppm)	Wavelength shift(nm)	Σ Wavelength shift (nm)
0→ 15k	-0.026	-0.026
15k→ 30k	-0.008	-0.034
30k→ 55k	+0.005	-0.029
55k → 0 after experiment	+0.023	-0.006

The CO_2-sensor results shown for the LP_{019L}-band on the TFISIX fibre coated in-situ with 15 h reaction time will be also shown here and compared with the response of the LP_{018}-band. The measured wavelength during the experiment for the LP_{019L}-band are visible in Figure 6-52, while the measured wavelength at different CO_2-concentrations and the resulting wavelength shift are shown in Table 6-17 and Table 6-18, respectively.

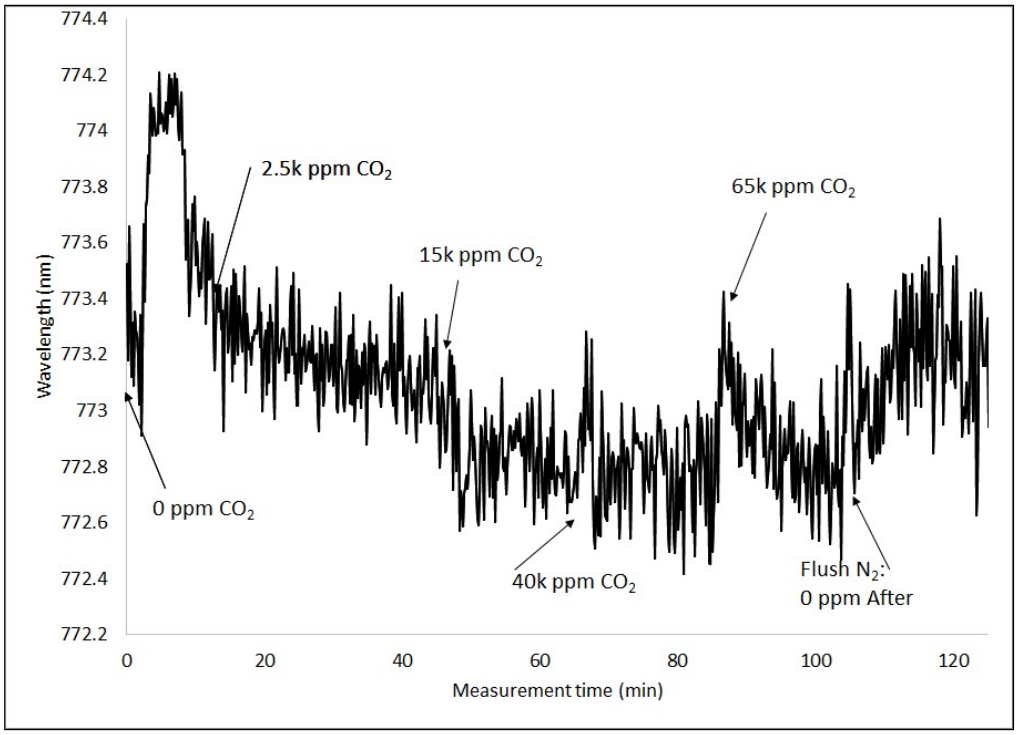


Figure 6-52: CO_2-sensor experiment results for fibre coated in-situ with TIFSIX at 85°C with 15 h reaction time. Measured for LP_{019L}-band.

Table 6-17: Measured wavelength during CO_2-sensor test for fibre coated with TIFSIX at 85°C and 15 h reaction time. Measured for LP_{019L}-band.

CO_2 concentration (ppm)	Wavelength(nm)
0	773.223
2.5k	773.114
15k	772.820
40k	772.791
65k	772.803
0 after experiment	773.284

Table 6-18: Measured shift between varying CO_2-concentrations and sum of the wavelength shift for fibre coated with TIFSIX at 85°C and 15 h reaction time. Measured for LP_{019L}-band.

CO_2 concentration change (ppm)	Wavelength shift (nm)	Σ Wavelength shift (nm)
0 → 2.5k	-0.109	-0.109
2.5k → 15k	-0.284	-0.393
15k → 40k	-0.049	-0.442
40k →65k	+0.022	-0.420
65k→ 0 after experiment	+0.481	+0.061

For the LP_{019L}-band a larger shift between 2.5k ppm CO_2 and 15k ppm CO_2 was observed. However, have bands at higher wavelength a normally larger fluctuations of the wavelength (0 ppm: 773.223 ± 0.147 nm, σ = 0.128 nm). As a result, the observed shift is smaller than the LOQ. At larger concentrations (> 15k ppm CO_2) the shift becomes smaller and has fluctuating directions. Another problem regarding the reliability of the results is that for the LP_{018}-band a large shift was observed between 15k ppm and 40k ppm, while for the LP_{019L}-band the shift was observed between 2.5k ppm and 15k ppm. If this is a response to CO_2, the shift should be visible for both bands at the same concentration change.

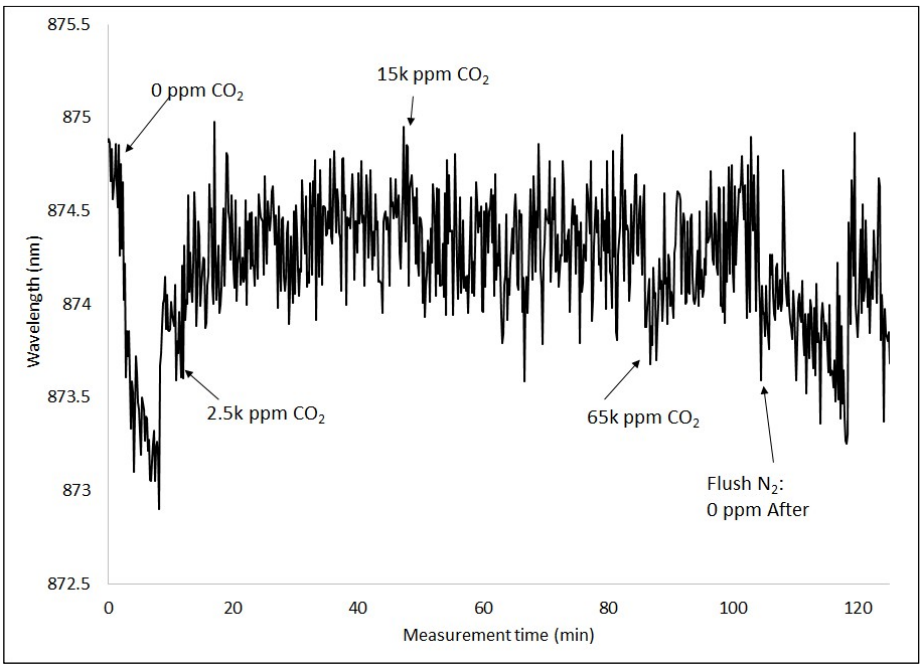


Figure 6-53: CO_2-sensor experiment results for fibre coated in-situ with TIFSIX at 85°C with 15 h reaction time. Measured for LP_{019R}-band.

Table 6-19: Measured wavelength during CO_2-sensor test with fibre coated with TIFSIX at 85°C and 15 h reaction time. Measured for LP_{019R}-band.

CO_2 concentration (ppm)	Wavelength(nm)
0	873.981
2.5k	874.229
15k	874.268
40k	874.346
65k	874.355
0 after experiment	874.034

Table 6-20: Measured shift between varying CO_2-concentrations and sum of the wavelength shift for fibre coated with TIFSIX at 85°C and 15 h reaction time. Measured for LP_{019R}-band.

CO_2 concentration (ppm)	Wavelength shift (nm)	Σ Wavelength shift (nm)
0→ 2.5k	+0.248	+0.248
2.5k → 15k	+0.039	+0.287
15k → 40k	+0.078	+0.365
40k →65k	+0.009	+0.374
65k → 0 after experiment	-0.321	+0.053

Table 6-21: Measured wavelength difference between the split ΔLP_{019}-band for fibre coated in-situ with TIFSIX at 85°C and 15 h reaction time.

CO_2 concentration change (ppm)	ΔWavelength LP_{019} (nm)
0→ 2.5k	0.357
2.5k → 15k	0.333
15k → 40k	0.117
40k →65k	0.013
65k → 0after experiment	0.802

The results for the LP_{019R}-band are shown in Figure 6-53, while the measured wavelength and the wavelength shift are shown in Table 6-19 and Table 6-20. In contrast to the LP_{019L}-band, the largest shift was not observed between 0 ppm and 2.5k ppm, but between 2.5k ppm and 15k ppm CO_2 and, as expected, the observed shifts have opposite directions than the LP_{019L}-band. In general, the observed absolute values of the observed shift and the fluctuations of the measured wavelengths are comparable (blank for the LP_{019R}-band at 0 ppm: 873.981 ± 0.295 nm σ = 0.129 nm). Consequently, the observed wavelength shift for theLP_{019R}-band and the wavelength difference between the two split ΔLP_{019}-bands are smaller than the LOQ.

This shift of the LP_{018}-band during the first experiment has shown a promising sensor response, which was higher the LOQ and a repetition of the CO_2-sensor experiment was conducted with the same fibre (Figure 6-51). Consequently, are CO_2-sensor responses for the $LP_{019L/R}$-bands for the repetition available, but the data for the repeated sensor response will not be discussed further. The results for the LP_{018}-band (Figure 6-51) have already confirmed, that the results are not repeatable.

For the investigation of the sensor response to MeOH, the same fibre used for the CO_2 sensor tests was used and heated overnight at 100°C to remove possible residues from the coating. The results for the LP_{018}-band are shown in Figure 6-54, while the measured wavelengths are shown in Table 6-22 and the observed wavelength shifts in Table 6-23. After changing the concentration to 1.8k ppm and 3.6k MeOH, the wavelength has slightly changed to smaller wavelength (-0.043 nm and -0.066 nm). However, after further increasing the concentration to 7.2k ppm MeOH, the wavelength has not decreased but increased by +0.189nm to 658.976 nm. After this larger wavelength shift at 7.2k ppm MeOH, the measured wavelength has nearly not changed for the rest of the experiment. The wavelength shift at 7.5k ppm MeOH exceeds the LOQ (0 ppm: 658.896 ± 0.031 nm σ = 0.0168 nm), but the wavelength shifts to smaller wavelength, followed by a sudden wavelength increase.

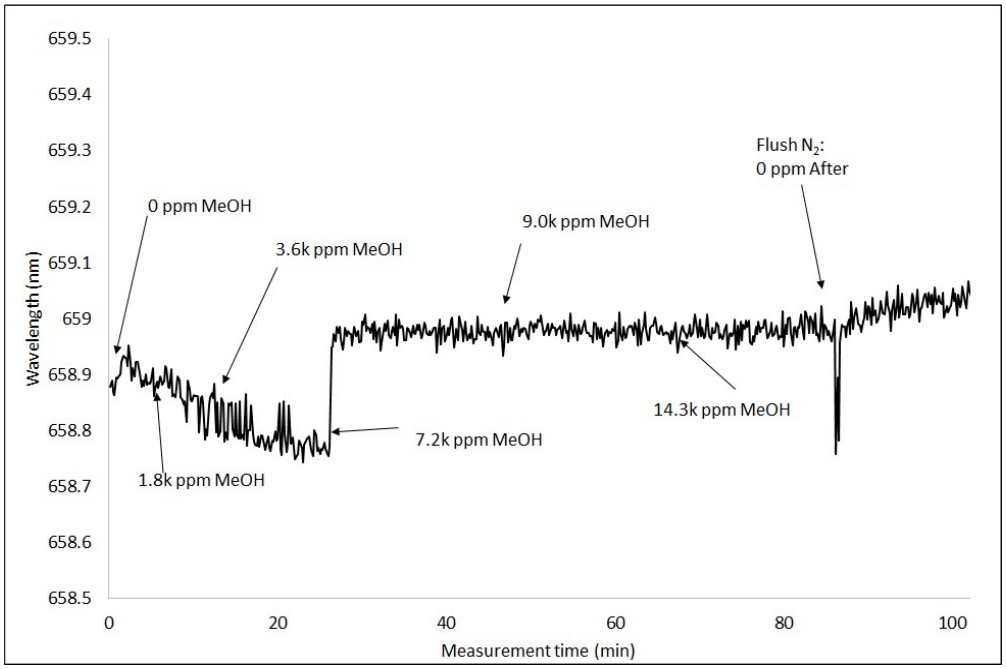


Figure 6-54: MeOH-sensor experiment results for fibre coated in-situ with TIFSIX at 85°C with 15 h reaction time. Measurement for LP_{018}-band.

Table 6-22: Measured wavelength during MeOH-sensor test for fibre coated with TIFSIX at 85°c and 15 h reaction time. Measurement for LP_{018}-band.

MeOH concentration (ppm)	Wavelength(nm)
0	658.896
1.8k	658.853
3.6k	658.787
7.2k	658.976
9.0k	658.978
14.3k	658.982
0 after experiment	659.030

Table 6-23 Measured wavelength shift between varying MeOH-concentrations and sum of the wavelength shift for fibre coated with TIFSIX at 85°C and 15 h reaction time. Measurement for LP_{018}-band.

MeOH concentration (ppm)	Wavelength shift (nm)	Σ Wavelength shift (nm)
0 → 1.8k	-0.043	-0.043
1.8k → 3.6k	-0.066	-0.109
3.6k → 7.2k	+0.189	+0.080
7.2k → 9.0k	+0.002	+0.082
9.0k → 14.3k	+0.004	+0.086
14.3k → 0 after experiment	+0.048	+0.134

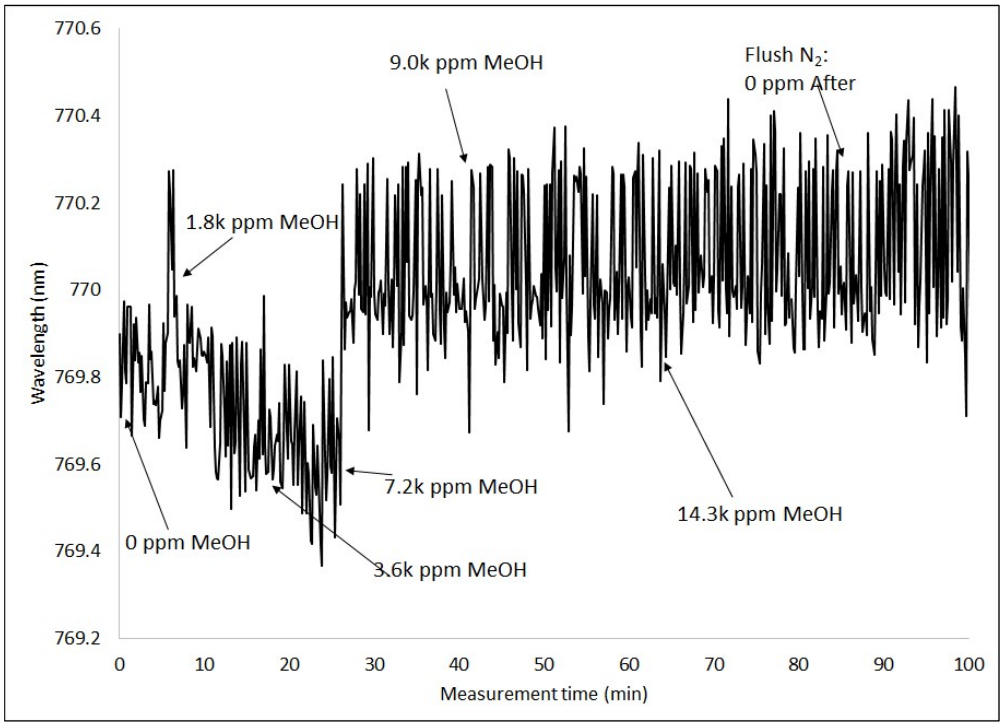


Figure 6-55: MeOH-sensor experiment results for fibre coated in-situ with TIFSIX at 85°C with 15 h reaction time. Measurement for LP_{019L}-band.

Table 6-24: Measured wavelength during MeOH sensor test for fibre coated with TIFSIX at 85°c and 15 h reaction time. Measured for the LP_{019L}-band.

MeOH concentration (ppm)	Wavelength(nm)
0	769.835
1.8k	769.702
3.6k	769.591
7.2k	770.033
9.0k	770.021
14.3k	770.048
0 after experiment	770.179

Table 6-25 Measured wavelength shift between varying MeOH-concentrations and sum of the wavelength shift for fibre coated with TIFSIX at 85°C and 15 h reaction time. Measured for LP_{019L}-band.

MeOH concentration (ppm)	Wavelength shift (nm)	Σ Wavelength shift (nm)
0→ 1.8k	-0.133	-0.133
1.8k → 3.6k	-0.111	-0.244
3.6k → 7.2k	+0.524	+0.280
7.2k → 9.0k	-0.012	+0.268
9.0k → 14.3k	+0.069	+0.337
14.3k → 0 after experiment	+0.131	+0.468

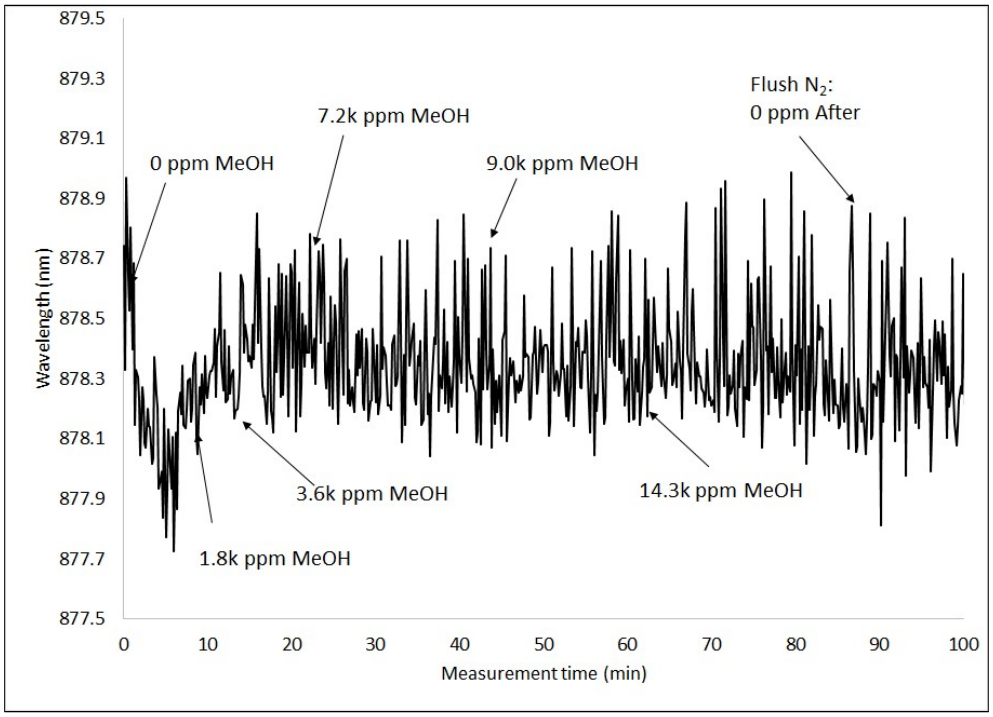


Figure 6-56: MeOH-sensor experiment results for fibre coated in-situ with TIFSIX at 85°C with 15 h reaction time. Measurement for LP_{019R}-band.

Table 6-26: Measured wavelength during MeOH sensor test for fibre coated with TIFSIX at 85°c and 15h reaction time. Measured for the LP_{019R}-band.

MeOH concentration (ppm)	Wavelength(nm)
0	878.199
1.8k	878.372
3.6k	878.438
7.2k	878.341
9.0k	878.400
14.3k	878.361
0 after experiment	878.330

Table 6-27 Measured wavelength shift between varying MeOH-concentrations and sum of the wavelength shift for fibre coated with TIFSIX at 85°C and 15 h reaction time. Measured for LP_{019R}-band.

MeOH concentration (ppm)	Wavelength shift (nm)	Σ Wavelength shift (nm)
0→ 1.8k	+0.173	+0.173
1.8k → 3.6k	+0.066	+0.239
3.6k → 7.2k	-0.097	+0.142
7.2k → 9.0k	+0.059	+0.201
9.0k → 14.3k	-0.039	+0.162
14.3k → 0after experiment	-0.031	+0.131

Table 6-28: Measured wavelength difference during MeOH sensor experiment between the split LP_{019}-band for LPG coated in-situ with TIFSIX at 85°C and 15 h reaction time.

MeOH concentration (ppm)	ΔWavelength LP_{019}(nm)
0 → 1.8k	0.306
1.8k → 3.6k	0.177
3.6k → 7.2k	0.621
7.2k → 9.0k	0.047
9.0k → 14.3k	0.108
14.3k → 0 after experiment	0.162

As observed during the CO_2-experiments, the shift for bands with larger wavelength increased, but at the same time the uncertainty of the results also increased for the MeOH sensor experiment. While for the LP_{018}-band, a shift was observed between 3.6k ppm and 7.2k ppm MeOH (+0.189 nm), this shift was smaller (in relation to the measured uncertainty of the blank value σ) for the LP_{019L}-band (0.524 nm) and could not be observed for the LP_{019R}-band. Due to the large standard deviation of the blank value (0 ppm MeOH) of the observed wavelength (LP_{019L}: 769.835 ± 0.122 nm σ = 0.102 nm; LP_{019R}: 878.199 ± 0.196 nm σ = 0.125 nm), the observed shift is always below the LOQ and the different directions of the shifts are problematic. Hence is the sensor response of the LPG to MeOH not reliable and no repetition of the sensor experiment to MeOH was conducted.

6.6 Conclusions and Future work

The work of this chapter can be separated into 3 steps, the powder synthesis, thin-film synthesis on glass and the LPG sensor measurements. Besides the only known synthesis protocol for TIFSIX several additional reaction conditions were investigated, derived from the literature synthesis of SIFSIX, a MOF with a very similar structure to TIFSIX.

The essential starting material $NiTiF_6$ could be prepared in good yields from H_2TiF_6 and $Ni(CO_3)_2$ in water. One problem with this reaction is the long preparation time, including a long drying step (3 days) at elevated temperature, which is required to produce a solid, non-hygroscopic product.

A direct one-step reaction, where the $NiTiF_6$ reacts in-situ from a nickel source and a TiF_6^{2-}-salt might therefore be able to speed up the synthesis of TIFSIX. Even though such a synthesis protocol exists in the literature for SIFSIX, it was not found to be possible to apply

this synthesis to TIFSIX. Under the applied conditions, nickel cations and pyrazine form a lattice where TiF_6^{2-} acts as a non-coordinated counterion and water was found binding to nickel in the nickel-pyrazine framework. This compound exhibits low porosity (with S_{BET} of 8.8 $m^2 g^{-1}$) and shows no tendency for CO_2-uptake.

For the two-step synthesis, variations regarding the ratio between $NiTiF_6$/pyrazine, solvents and reaction temperature were investigated to prepare TIFSIX. It was possible to prepare TIFSIX with the literature synthesis protocol in water [132] using a large excess of pyrazine (13.8 eq) in the reaction mixture, but the very low yield of less than 10% remains a problem, possibly caused by slow reaction rate in water. During the alternative attempts to prepare TIFSIX, the results imply that two compounds were prepared. Both compounds have a characteristic peak at ~12° in the XRD pattern. However, the second characteristic peak is slightly shifted between the two compounds. While TIFSIX has according to literature data [132] a peak at ~17.8°, the second compound shows a peak at ~18.2°. Besides the peak at 18.2°, a different relative intensity of the characteristic peaks was observed. In addition, nearly no porosity (2.9 $m^2 g^{-1}$) and a lower thermal stability were also observed. One possibility is that the second compounds (peak at ~18.2°) is a sample, which has not a primitive cubic topology, but a square grid topology. Different influences (*e.g.* higher humidity) can make the TiF_6^{2-} anion unable to work as a pillar in the framework of HUMs [397]. The low porosity of the sample and the lower thermal stability in comparison with TIFSIX might support this assumption. However, identification of the exact nature of this sample was not possible with the growth of single crystals of the sample being unsuccessful.

Hence it was investigated, whether it was possible to improve yield and product quality by changing the reaction solvent. Both DMF and acetone were investigated for this. While the use of acetone leads to decomposition of the starting materials, it was possible to improve the yield up to 61% by using DMF as solvent. However, the porosity of the sample remains a problem. While in the literature a porosity of 223 $m^2 g^{-1}$ was reported (for the SIFSIX derivative, for TIFSIX was no BET value is reported in the literature), for the TIFSIX samples prepared during this research much smaller values of 58 $m^2 g^{-1}$ (DMF as solvent) and 56 $m^2 g^{-1}$ (water as solvent) were observed, despite applying various activation techniques. These values are still higher in comparison to the As-synthesised samples (21 $m^2 g^{-1}$), implying that at least a partial activation of the samples was possible. The difference can be partly explained by the usage of CO_2-isotherms in the literature to calculate the porosity of HUMs. TIFSIX is known for a reduced N_2-adsoprtion capacity in comparison to CO_2-adsoprtion capacity [132], due to the larger kinetic diameter of N_2 in comparison with CO_2 (3.3 Å to 3.64 Å) [210]. However, it is questionable if the large difference between the surface areas measured by CO_2 and N_2-isotherms can be solely explained simply by the use of difference gases for the porosity measurement. It may be possible for the porosity of the samples in this research to be increased by using alternative activation methods, such as using supercritical CO_2[303].

The most promising TIFSIX powder synthesis, the two-step synthesis with excess of pyrazine in DMF as solvent, was used as the basis for the synthesis of thin-films on glass. Due to no known previous reports of the thin-film synthesis for SIFSIX and TIFSIX, a

screening was conducted with different techniques for growing thin-films like dip-coating, seeding and secondary growth or rapid-thermal deposition (RTD). While it was possible to coat the glass surface with TIFSIX by some techniques, like dip-coating or seeding and secondary growth, the surfaces coatings were often not homogeneous, and investigation of the morphology by SEM imaging showed large gaps in the coatings. For other techniques, like RTD or SAE, reactions were not successful. The XRD pattern of the samples was not matching the known TIFSIX pattern. From the different techniques investigated, it was only possible to coat a surface with a homogeneous film by the in-situ technique with 5 h and 15 h reaction time at 85°C in DMF as solvent. It is still possible that the properties of the thin-films could be further by optimising certain synthesis conditions.

The in-situ coating using 5 h or 15 h reaction times were chosen to investigate the performance of coated LPGs for sensing CO_2 and MeOH. However, it is often the case that coating a flat surface leads to slightly different results in comparison with a cylindrical surface such as an LPG. While a glass slide could be completely covered with cubic shaped TIFSIX particles, the LPG after in-situ coating with 5 h reaction time showed a less homogeneous coating. Several larger needle-shaped particles were visible on the surface, but between these particles the coating is incomplete and gaps in the coatings are visible. This may explain why the fibre studied did not show a reasonable sensor response to either CO_2 or MeOH.

In contrast, the LPG coated in-situ with 15 h reaction time showed a complete coating of the surface with needle-shaped particles. One disadvantage of the longer reaction time however, was the thicker coating (6.9 µm on the glass slide, see Figure 6-38), potentially reducing the sensitivity [59]. Consequently, the measured wavelength showed a large fluctuation and sensor response showed shifts in different directions or shifts which are lower than the LOQ. In some cases, a reasonable sensor response could be measured, but the repetition of the results was not possible. After recovery of the fibre at elevated temperature for 1 day, the sensitivity of the fibre could be not restored. Activation by heating the LPG at elevated temperature may be not sufficient for the recovery of the fibre (CO_2 is very strongly bond to TIFSIX). Another possibility is that the TIFSIX-coated LPG was not sensitive to CO_2 at all from the beginning and the shift was caused by other influences, such as a fibre bending while adding the CO_2 and was therefore not reproducible.

Hence, the response of the TIFSIX sensors to CO_2 and MeOH lack sensitivity and reproducibility. The low porosity of the thin-film on the surface and resulting low adsorption may lead to low response. Furthermore, the CO_2-capacity at low CO_2-pressures (~2000 ppm) for the prepared of TIFSIX samples was lower than expected. While literature reports for TIFSIX, a CO_2-capacity of ~40 $cm^3\ g^{-1}$ at low pressures, the sample prepared in DMF in this study showed a capacity of only 7.5 $cm^3\ g^{-1}$. For comparison, the data for HKUST-1 is shown here, because an HKUST-1 coated LPG sensor has been used successfully for CO_2 sensing [21]. Reports show uptakes of ~22 $cm^3\ g^{-1}$ [244],[245] at ~2000 ppm CO_2. However, further investigations are required to establish whether the lower CO_2-capacity for TIFSIX observed during this study is a result of problems during synthesis (some synthesis conditions might lead to lower porosity and CO_2-capacity) or incomplete activation (CO_2 is strongly bound to TIFSIX and is difficult to remove).

Another problem is the strong interaction and slow sorption kinetics in TIFSIX [389]. For comparison, CO_2-isotherms were measured with increased equilibrium time (60 s in comparison with the default value of 5 s) for each point (Figure 10-10) and the BET calculated from each isotherm. The BET value from the isotherm measured with increased equilibrium time is with 91 $m^2 g^{-1}$ higher than the isotherm measured with the default shorter equilibrium time (65 $m^2 g^{-1}$). It is therefore possible that further increasing of the equilibrium time may lead to further increase of the measured porosity. Still, the value of 91 $m^2 g^{-1}$ is much lower than the available literature value of ~223 $m^2 g^{-1}$. A similar discrepancy between N_2-BET and CO_2-BET was observed for other HUMs as well. In one of the most drastic cases, the N_2-isotherm gives a BET-value of 30 $m^2 g^{-1}$, while the CO_2-isotherm shows a porosity of 809 $m^2 g^{-1}$ [412].
Furthermore, the very high selectivity towards CO_2 may cause further problems. Even at CO_2-concentrations of 400 ppm, which is the average CO_2-concentration in the atmosphere [207], TIFSIX is already loaded by 46% of its total CO_2-capacity [132].

The next issue is the thickness of the film. Even with a reduced reaction time of 5 h (in comparison with the powder synthesis with 24 h), the film still has a thickness of 3.2 µm which might be too thick for a reasonable sensor response. An overly thick film may only adsorb target compound on the film surface and not reach the layer close to the core of the LPG. The light from the fibre has only a limited range and might only interact with MOF-film which is still "empty" leading to no observable shift. Overly thick coatings of LPG films can also lead to increased noise in the measured wavelength. We were unable to prepare a film of TIFSIX which is both homogeneous and thinner. However even very thick films might show a sensor response, which is dependent on the adsorption kinetics of the coatings used. For instance, a HKUST-1 film with a thickness of ~2 µm, prepared by the RTD approach, has been reported to shown a response of at least 0.76 nm at 40k ppm CO_2 [21], higher than any response measured during this research.

TIFSIX is a completely novel compound and none of the three targets investigated here, powder synthesis, thin-film synthesis, sensor application, have been comprehensively optimised. Numerous factors may reduce the sensitivity and response of a TIFSIX-coated LPG. At this point it seems that problems with the low CO_2-adsorption in comparison with the literature data and the slow CO_2-sorption kinetics must be solved. Even so, the sensitivity and selectivity towards CO_2 might be too high in TIFSIX for a sensor application. Even at ambient conditions, TIFSIX is already 46% saturated and so the usage of TIFSIX might be only plausible in inert atmospheres like cleanrooms to detect trace amounts of CO_2.

7 Conclusions and Future Work

During this study, MOFs as possible coatings for a sensor on an LPG have been investigated. MIL-53(Al) was identified as a promising candidate. One advantage of MIL-53(Al) is that it is a MOF, for which several thin-film syntheses are known. These acted as starting point for the development of a thin-film synthesis on glass surfaces in order to create a sensitive coating on an LPG fibre. Another advantage of this MOF is that MIL-53(Al) is an extremely versatile compound and MIL-53-compounds were already prepared with various linkers and from different metal sources while retaining the overall structure. It might be possible therefore that a thin-film coating of MIL-53(Al) on an LPG could be modified for different target compounds with only small changes in a successful synthesis protocol.

The synthesis of MIL-53(Al) with alternative solvents was thoroughly investigated and several aspects of the synthesis were improved for a more sustainable synthesis of MIL-53(Al). For instance, it was possible to prepare MIL-53(Al) using a 5 h reaction time at 150°C with water and DMF as solvent, in contrast to the standard synthesis protocol over 72 h and 220°C reaction temperature.

The use of the low-weight alcohol MeOH was shown to be a promising alternative to water and DMF. The yield was acceptable (~50%) and nanometer sized particles can be prepared. A possible reason for the smaller particle size was identified as the solubility of the starting materials in the solvent. Only when both metal and linker can be readily dissolved is the synthesis of nanometre sized particles possible. Another advantage is that MIL-53(Al)(MeOH) was highly porous even without an activation process. MIL-53(Al)(MeOH) furthermore displayed some unique properties. One effect was that MIL-53(Al)(MeOH) does not show a breathing effect, a reversible change of the pore dimensions upon appropriate stimuli, regardless of the applied synthesis conditions. This absence of the breathing effect was observed before in MIL-53(Al)(DMF) as a temperature dependent effect. Another peculiar effect was the fusing of particles at high humidity, which was not been reported for other MIL-53(Al) derivatives. This fusing is reversible and has not led to a sample degradation. However, the exact reason for the lack of breathing and fusing of the particles was not conclusively identified and further research has to be conducted. Additional identification methods might be able to answer some of these questions. The breathing in MIL-53 is caused by interaction of μ-OH framework atoms with adsorbed molecules in the pores like water and CO_2. Solid-state ^{1}H-NMR and ^{27}Al-NMR might be able to identify if these μ-OH are missing or have a different chemical environment [413].

Another interesting sample was prepared in DMSO. This was done to confirm the solubility theory, discussed above, as DMSO is able to dissolve the linker H_2BDC, but not $Al(NO_3)_3{\cdot}9H_2O$. This is in contrast to water, which dissolves the metal but has a low solubility for H_2BDC. Our results show that micrometre size particles are prepared in DMSO, but the XRD pattern does not match with other samples of MIL-53(Al). The sample prepared in DMSO could be identified as MIL-68(Al) by comparison of the XRD pattern of

calculated XRD powder pattern from existing crystal data of MIL-68(In). It known, that MIL-53(Al) and MIL-68(Al) can be interchanged into each other by a phase transformation. However, it still has to be identified why MIL-53(Al) has been prepared in water, DMF and MeOH as solvent, while MIL-68(Al) was prepared in otherwise similar reaction conditions with DMSO as solvent. It was also not possible to prepare a crystalline sample of MIL-53(Al) using ethanol as solvent. Future work is required to identify the reason for this and if longer chain alcohols exhibit similar effects.

For the subsequent application of a thin-film LPG fibre, the thin-film synthesis on glass slides has been investigated as test system. Numerous approaches have been applied for the formation of a homogenous thin-film with controllable thickness including possible candidates for the coating of the LPG. A straightforward in-situ coating has led to a film, which has a thickness of about 2 µm. Dip-coating from a suspension with 0.5 wt% MIL-53(Al)(DMF) in MeOH as solvent was able to completely coat the surface with a thickness of about 800 nm. Another advantage is that activated MIL-53(Al)(DMF) was used for the dip-coating, which may result in more straightforward activation of the thin-film before testing of the sensor performance. The newly developed solvent-assisted epitaxy, a thin-film synthesis in a saturated solvent atmosphere, led to a film which is with 4.1 µm thicker than other approaches, but the resulting coating was crack-free, highly homogenous and uniform.

Other approaches led to films with reduced quality. A coating performed by seeding and secondary approach was less homogenous and the application of the Layer-by-Layer approach did not led to a successful coating, probably due to weak interaction with the flat glass surface and low reaction rates of MIL-53(Al) at RT. The rapid-thermal deposition approach was tested for MIL-53(Al), but the glass slides were mostly covered with unreacted starting material possibly due to fast evaporation of the reaction solvent.

The most promising thin films (in-situ, dip-coating, solvent assisted epitaxy) were applied for coating of an LPG fibre and the results compared with a blank fibre. However, none of the MIL-53(Al) coated fibres showed a reasonable and repeatable sensor response to CO_2 or VOC. The LPG has shown shifts smaller than the spectral resolution of the spectrometer used, or the measured signal showed large fluctuations. In fact, only a blank fibre was able to show a reliable response to varying concentrations of VOCs and CO_2. Problematic was especially to prepare a thin-film of MIL-53(Al), which is at the same time homogenous, uniform and thinner than 1 µm (ideally a few hundred nm). As a possible additional coating technique was the spray-coating of a MOF containing suspension on the surface identified [173],[345]. However, has this technique exceeded the scope of this thesis, because custom-made equipment is often needed for the spray-coating technique. Another problem was the limited number of existing characterisation methods for the validation of thin-films on glass. During this research only SEM (identification of thin-film morphology and film thickness) and XRD (verification of MIL-53(Al) on the surface and phase purity of the coating) could be used. Additional characterisation techniques were not available during this research, but might help to better understand the properties of the MOF thin-film on glass. Such techniques might be ellipsometry [414] (measurement

of film-thickness), grazing incidence XRD [415] (measurement of XRD patter with increased sensitivity for thin-films and identification of the microstructure of the thin film) or krypton BET measurement [416] (krypton BET can improve the sensitivity especially for small surface areas in order to identify if the MOF thin-films are *e.g.* activated). Other techniques like EDX (chemical characterisation of the thin-film) could be not successfully applied to the MIL-53(Al) thin-films on glass. In case of EDX, was especially the background signal of the glass support problematic for the measurement.

Besides MIL-53(Al), another promising MOF candidate for a thin-film coating was identified. TIFSIX-3-Ni, a MOF composed of cubic nets made from nickel(II) cations and pyrazine linkers, bridged by TiF_6^- anions. This compound is part of the MOF-subclass of hybrid ultramicroporous materials (HUMs), which have smaller pore size than other commonly used MOFs such as HKUST-1 or ZIF-8. The combination of a pore size in the range of the kinetic diameter of CO_2 and strong interaction of anionic pillars to CO_2 led to a material with the highest known CO_2 capacities and selectivity at low CO_2-concentrations (~2000 ppm). This makes TIFSIX-3-Ni suited for CO_2 capture by direct-air capture, but at the same time a promising material for a CO_2 sensor, because in medical applications (*e.g.* monitoring of room air quality for comfort and productivity in offices) these low concentrations of CO_2 have to be detected.

As a novel material, no thin-film coatings and only sparse powder synthesis for TIFSIX-3-Ni are reported. The direct usage of the literature synthesis only led to the formation of a product with very low yields of less than 10%. Several alternative synthesis methods were adapted from the silicon derivative SIFSIX-3-Ni, but mostly products inconsistent with TIFSIX-3-Ni were isolated. One product could be identified as a crystalline compound with low-porosity, where nickel cations and pyrazine are bound in a *mer*-arrangement and the TiF_6^- anions acts as counterions in the framework. Another sample has an XRD pattern, which is slightly shifted with respect to that expected for TIFSIX-3-Ni pattern and reduced porosity. A possible reason for the formation of this alternative framework was interaction with humidity, leading to an incomplete formation of the framework, with coordinated water ligands blocking the bridging by the TiF_6^- anions. This assumption has however still to be confirmed *e.g.* by single-crystal measurement. However the formation of a single crystal from this compound was not possible yet.

The synthesis of TIFSIX-3-Ni could be successfully achieved by using a reaction mixture composed of $NiTiF_6$ and excess pyrazine in DMF as solvent and at 85°C reaction temperature which led to a 61% yield. Furthermore, it was possible to reduce the synthesis time from 72 h of the reported synthesis protocol to 15 h with DMF as solvent. However, a lower porosity was problematic probably caused by slow CO_2-adsorption kinetics. The porosity of HUMs is typically measured from CO_2-isotherms in the literature reports, because N_2 has a slightly larger kinetic diameter than CO_2 and does not fit into the pores. Although the measurement time for the CO_2-isotherms have also increased, but the porosity measured for the samples of TIFSIX-3-Ni herein were found to be lower than expected from literature data. Reasons for the discrepancy in the porosity between the literature data and the sample prepared during this research have still to be identified.

One possible method might be use of argon isotherms for the measurement of the porosity, (due to the smaller kinetic diameter of argon to N_2) and a further increase of the equilibrium time for the isotherm measurement to take possible slow adsorption kinetics in TIFSIX-3-Ni into account. The sample of TIFSIX-3-Ni prepared in DMF was used as the basis for thin-film synthesis. Several approaches were used for the formation of a TIFSIX-3-Ni thin-film, *e.g.* seeding and secondary growth or rapid-thermal deposition. The results confirmed the complexity of applying powder synthesis to thin-film synthesis. The different approaches led to films which are not homogenous or whose XRD pattern were not matching TIFSIX-3-Ni. The most promising approach was in-situ coating at 85°C with 5 h or 15 h reaction times, leading to homogenous coatings with thickness of 3.6 µm or 6.9 µm, respectively. The resulting coatings were applied for the formation of a thin-film on an LPG fibre and the sensor response to CO_2 and VOC was tested. Again, none of the LPG fibre showed a reasonable and repeatable sensor response. This may due to slow adsorption kinetics CO_2 and VOCs in TIFSIX-3-Ni, making this MOF unsuitable for an in-situ sensor system. Furthermore, the selectivity towards CO_2 may be even too high for a sensor system, because TIFSIX-3-Ni is already mostly saturated with CO_2 under ambient conditions. Similar to the thin-film coating of MIL-53(Al), the application of a spray-coating technique for thin-film preparation might be a promising alternative for the formation of a thin-film which is at the same time uniform, homogenous and has a thickness of ideally a few hundred nm. Furthermore, might the application of additional characterisation methods be of advantage for a better understanding of the coating process for TIFSIX-3-Ni.

In summary, the potential of new MOFs for the coating of LPG for the fabrication of selective and lightweight in-situ sensor for CO_2 and VOC has been investigated. However, none of the sensors were able to show a reasonable and repeatable sensor response. This might be caused by a combination of factors.

One problem is the sensor platform used, the LPG, which limits the number of possible thin-film coating techniques which could be used. This system is small and delicate with a diameter of less than 1 mm, but at the same has a length of over 80 cm. The system cannot be coiled up to fit inside a smaller reaction vessel and has to be kept straight during the coating process, due to the sensitivity of the fibre to strain. Due to the small diameter of the fibre is the use of alternative heating methods *e.g.* microwaves not possible, because these might melt the fibre even after short reaction times. Furthermore, the LPG has a cylindrical surface which makes the wetting of the surface with reaction mixture more complicated and several existing thin-film coating techniques, such as spin-coating, cannot be applied. In addition, the LPG is made from doped silica with an inert surface, which makes the attachment of MOF particles to the surface challenging.

Another challenge is the measurement principle of the LPG which is based on the measurement of an evanescence wave. The coating must be therefore be both homogenous, to have a signal with low background noise (the response of an LPG is depended on the film thickness and morphology of the coating), and at the same time the film must have a low thickness (ideally around 100 nm) and/or fast adsorption and

transfer kinetics for the desired target compound. The target compound must reach the layer close to the surface of the LPG in order to interact with the evanesce wave of the LPG. At the same time the MOF thin-film must be independent of additional coatings. In principle, the Layer-by-Layer approach is the best to be applied for LPG coating, because nanometre thin films can be prepared with atomic precision. However, SAMs are often needed, which act as a starting nucleation point for thin-film growth and to increase the interaction between the surface and the coating. However, these SAMs would reduce the response of the LPG to RI changes (by the gold coating required for SAM anchorage) and add a layer of non-sensitive material to the surface, further reducing the overall sensitivity. A Layer-by-Layer coating without the use of SAMs has not proven to be successful due to only weak interaction between coating and surface.

This study has therefore shown the complexity of MOF thin-film coating. A lot of different properties have to be considered and even with existing thin-film approaches, a transfer to different supports (*e.g.* from Al_2O_3 to glass) is not a trivial task.

Even though it was possible to create crack-free and homogeneous thin-films of MIL-53(Al) and TIFSIX-3-Ni during this research, these films have a thickness in the micrometre range, which makes them more promising for application in other fields such as gas separation.

Despite, the application of MIL-53(Al) or TIFSIX-3-Ni as a sensor coating was not possible, LPG coating with ZIF-8 and HKUST-1 have successfully acted as in-situ sensor systems in previous reports. MOFs are still promising materials for the coating of optical fibre optics due to their sensitivity and selectivity. Numerous MOFs are known only two of them could be investigated regarding their possible thin-film synthesis and application on optical fibre sensors. Other MOFs with known high sensitivity and selectivity towards CO_2 and VOCs and existing thin-film synthesis protocols like CPO-27(Mg) or UiO-66 might be therefore possible future MOFs for the coatings of LPGs.

8 References

1 A. Hulanicki, S. Glab and F. Ingman, *Pure Appl. Chem.*, 1991, **63**, 1247–1250.

2 E. Bowdan and G. A. Wyse, *Biol. Bull.*, 1996, **191**, 122–123.

3 National Research Council, *Expanding the Vision of Sensor Materials*, National Academies Press, Washington, D.C., 1995.

4 T. An, Y. Huang, G. Li, Z. He, J. Chen and C. Zhang, *Environ. Inter.*, 2014, **73**, 186–194.

5 C. A. Clayton, R. L. Perritt, E. Pellizzari, K. Thomas, R. W. Whitmore, L. Wallace, H. Ozkaynak and J. Spengler, *J. Expo. Anal. Environ. Epidemiol*, 1993, **3**, 227–250.

6 J. A. Leech, W. C. Nelson, R. T. Burnett, S. Aaron and M. E. Raizenne, *J. Expo. Anal. Environ. Epidemiol*, 2002, **12**, 427–432.

7 M. A. Sidheswaran, H. Destaillats, D. P. Sullivan, S. Cohn and W. J. Fisk, *Build. Environ.*, 2012, **47**, 357–367.

8 W.-T. Tsai, *Environments*, 2016, **3**, 23.

9 J. H. Shorter, D. D. Nelson, J. B. McManus, M. S. Zahniser, S. R. Sama and D. K. Milton, *J. Breath Res.*, 2011, **5**, 37108.

10 T. Graunke, K. Schmitt, S. Raible and J. Wöllenstein, *Sensors*, 2016, **16**, 1605.

11 A. A. Huurdeman, *The worldwide history of telecommunications*, Wiley-Interscience; IEEE Xplore, Hoboken, New Jersey, Piscataway, New Jersey, 2005.

12 R. Chen, F. Formenti, H. McPeak, A. N. Obeid, C. E. W. Hahn and A. D. Farmery, *IEEE Sensors J.*, 2014, **14**, 3358–3364.

13 N. Singh, P. K. Singh, M. Singh, P. Tandon, S. K. Singh and S. Singh, *J Mater Sci: Mater Electron*, 2019, **30**, 4487–4498.

14 C. Sun, P. R. Ohodnicki, P. Lu and R. Feng, in *Fiber Optic Sensors and Applications XV*, ed. H. H. Du, A. Mendez and C. S. Baldwin, p. 4.

15 Y. Xiao, J. Yu, L. Shun, S. Tan, X. Cai, Y. Luo, J. Zhang, H. Dong, H. Lu, H. Guan, Y. Zhong, J. Tang and Z. Chen, *Opt. Express*, 2016, **24**, 28290–28302.

16 T. Babeva, A. Andreev, J. Grand, M. Vasileva, E. Karakoleva, B. S. Zafirova, B. Georgieva, J. Koprinarova and S. Mintova, *Sensor Actuat B - Chem*, 2017, **248**, 359–366.

17 X. D. Wang and O. S. Wolfbeis, *Anal.Chem.*, 2016, **88**, 203–227.

18 J.-R. Li, R. J. Kuppler and H.-C. Zhou, *Chem Soc. Rev.*, 2009, **38**, 1477–1504.

19 J. Lee, O. K. Farha, J. Roberts, K. A. Scheidt, S. T. Nguyen and J. T. Hupp, *Chem Soc. Rev.*, 2009, **38**, 1450–1459.

20 P. A. Bayliss, I. A. Ibarra, E. Pérez, S. Yang, C. C. Tang, M. Poliakoff and M. Schröder, *Green Chem.*, 2014, **16**, 3796–3802.

21 J. Hromadka, B. Tokay, R. Correia, S. P. Morgan and S. Korposh, *Sensor Actuat B - Chem*, 2018, **255**, 2483–2494.

22 J. Hromadka, B. Tokay, S. James, R. P. Tatam and S. Korposh, *Sensor Actuat B - Chem*, 2015, **221**, 891–899.

23 M. Amann, Z. Klimont and F. Wagner, *Annu. Rev. Environ. Resour.*, 2013, **38**, 31–55.

24 E. Puhar, A. Einsele, H. Bühler and W. Ingold, *Biotechnol. Bioeng.*, 1980, **22**, 2411–2416.

25 Umweltbundesamt, *Bundesgesundheitsblatt, Gesundheitsforschung, Gesundheitsschutz*, 2008, **51**, 1358–1369.

26 Y. L. Boo, D. Stirling, L. Chi, L. Liu, K.-L. Ong, G. Williams, I. B. Arief-Ang, F. D. Salim and M. Hamilton, eds., *SD-HOC: Seasonal Decomposition Algorithm for Mining Lagged Time Series. Data Mining*, Springer Singapore, 2018.

27 O. Persson, C. Ostberg, J. Pagels and A. Sebastian, *J. Environ. Monit.*, 2006, **8**, 1111–1121.

28 F. Schuster, N. Roewer, D. Schneiderbanger and S. Johannsen, *TCRM*, 2014, 355–362.

29 J. W. Servinghaus and A. F. Bradly, *J. Appl. Phys.*, 1958, **13**, 515–520.

30 M. J. Tierney and H. O. L. Kim, *Anal. Chem.*, 2012, **65**, 3435–3440.

31 J. Zosel, W. Oelßner, M. Decker, G. Gerlach and U. Guth, *Meas. Sci. Technol.*, 2011, **22**, 72001.

32 J. Sipior, L. Randers-Eichhorn, J. R. Lakowicz, G. M. Carter and G. Rao, *Biotechnol. Prog.*, 1996, **12**, 266–271.

33 R. Zhou, S. Vaihinger, K. E. Geckeler and W. Göpel, *Sensor Actuat B - Chem*, 1994, **19**, 415–420.

34 N. Imanaka, M. Kamikawa and G.-Y. Adachi, *Anal. Chem.*, 2002, **74**, 4800–4804.

35 C. Wang, L. Yin, L. Zhang, D. Xiang and R. Gao, *Sensors*, 2010, **10**, 2088–2106.

36 A. Helwig, A. Hackner, G. Müller, D. Zappa and G. Sberveglieri, *Sensors*, 2018, **18**, 453.

37 S. Neethirajan, D. S. Jayas and S. Sadistap, *Food Bioprocess. Technol.*, 2009, **2**, 115–121.

38 G. F. Fine, L. M. Cavanagh, A. Afonja and R. Binions, *Sensors*, 2010, **10**, 5469–5502.

39 I. Elmi, S. Zampolli, E. Cozzani, F. Mancarella and G. C. Cardinali, *Sensor Actuat B - Chem*, 2008, **135**, 342–351.

40 U. Hoefer, G. Kühner, W. Schweizer, G. Sulz and K. Steiner, *Sensor Actuat B - Chem*, 1994, **22**, 115–119.

41 M.-S. Lee and J.-U. Meyer, *Sensor Actuat B - Chem*, 2000, **68**, 293–299.

42 G. Jasinski, P. Jasinski, B. Chachulski and A. Nowakowski, *Mat. Sci. Poland*, 2006, **24**, 261–268.

43 M. Hesse, H. Meier and B. Zeeh, *Spektroskopische Methoden in der organischen Chemie. 102 Tabellen*, Thieme, Stuttgart, 7th edn., 2005.

44 Sensair, *Sensair Website,* available at: https://senseair.com/, accessed 6 March 2019.

45 T. Yasuda, S. Yonemura and A. Tani, *Sensors*, 2012, **12**, 3641–3655.

46 S. Cui, M. Cohen, P. Stabat and D. Marchio, *Build. Environ.*, 2015, **84**, 162–169.

47 B. L. Upschulte, D. M. Sonnenfroh and M. G. Allen, *Appl. Opt.*, 1999, **38**, 1506.

48 T. Asakawa, N. Kanno and K. Tonokura, *Sensors*, 2010, **10**, 4686–4699.

49 M. D. Marazuela, M. C. Moreno-Bondi and G. Orellana, *Appl Spectrosc*, 2016, **52**, 1314–1320.

50 B. Mahmoudi, N. Gabouze, L. Guerbous, M. Haddadi, H. Cheraga and K. Beldjilali, *Mat. Sci. Engineer. B*, 2007, **138**, 293–297.

51 L. Liu, F. Hao, S. P. Morgan, R. Correia, A. Norris and S. Korposh, *Sens. Biosens. Res.*, 2019, **22**, 100254.

52 C. A. Redlich, J. Sparer and M. R. Cullen, *Lancet*, 1997, **349**, 1013–1016.

53 K.-H. Kim, S. A. Jahan and E. Kabir, *Environ. Inter.*, 2013, **59**, 41–52.

54 European Union, *VOC Solvents Emissions Directive and the Paints Directive.*, 1999, available at: https://eur-lex.europa.eu/legal-content/EN/TXT/?uri=LEGISSUM:l28029b.

55 United Stated Evironmental Protection Agency (EPA), *"Volatile Organic Compounds" Definition per 40 CFR Part 51.100(s)*, 2014.

56 United Stated Evironmental Protection Agency (EPA), *Technical Overview of Volatile Organic Compounds,* available at: https://www.epa.gov/indoor-air-quality-iaq/technical-overview-volatile-organic-compounds#references, accessed 19 March 2019.

57 G. Verreydt, M. D. Annable, S. Kaskassian, I. van Keer, J. Bronders, L. Diels and P. Vanderauwera, *Environ. Sci Pollut. Res.*, 2013, **20**, 4621–4634.

58 M. Marć, B. Zabiegała and J. Namieśnik, *Trend. Anal. Chem*, 2012, **32**, 76–86.

59 E. Gallego, F. J. Roca, J. F. Perales and X. Guardino, *J. Environ. Monit.*, 2011, **13**, 2612–2622.

60 N. Hudson and G. A. Ayoko, *Biores. Tech.*, 2008, **99**, 3993–4007.

61 P. Wolkoff, P. A. Clausen and P. A. Nielsen, *Indoor air*, 1995, **5**, 196–203.

62 X. Pang, H. Nan, J. Zhong, D. Ye, M. D. Shaw and A. C. Lewis, *Sci. Total Environ.*, 2019, **664**, 771–779.

63 L. Molhave, G. Clausen, B. Berglund, J. Ceaurriz, A. Kettrup, T. Lindvall, M. Maroni, A. C. Pickering, U. Risse, H. Rothweiler, B. Seifert and M. Younes, *Indoor air*, 1997, **7**, 225–240.

64 J. Hecht, *City of light. The story of fiber optics*, Oxford Univ. Press, Oxford, 2004.

65 S. R. Schmid and A. M. Toussaint, *Optical Fiber Coatings,* available at: https://www.semanticscholar.org/paper/Chapter-4-Optical-Fiber-Coatings-Schmid-Toussaint/e86ad8fcd1806783c497b9289491a069f642e3c0, accessed 31 March 2019.

66 Y.-J. Rao, *Opt. Fiber Technol.*, 2006, **12**, 227–237.

67 C.-H. Chen, C.-Y. Hsu, P.-H. Huang, J.-N. Wang and W.-T. Wu, *Int. J. Antenn. Propag.*, 2014, **2014**, 1–9.

68 A. M. Cubillas, S. Unterkofler, T. G. Euser, B. J. M. Etzold, A. C. Jones, P. J. Sadler, P. Wasserscheid and P. S. J. Russell, *Chem. Soc. Rev.*, 2013, **42**, 8629–8648.

69 D. Castelvecchi and A. Witze, *Einstein's gravitational waves found at last,* available at: https://www.nature.com/news/einstein-s-gravitational-waves-found-at-last-1.19361, accessed 28 March 2019.

70 B. H. Lee, Y. H. Kim, K. S. Park, J. B. Eom, M. J. Kim, B. S. Rho and H. Y. Choi, *Sensors*, 2012, **12**, 2467–2486.

71 T. Allsop, R. Reeves, D. J. Webb, I. Bennion and R. Neal, *Rev, Sci. Instrum.*, 2002, **73**, 1702–1705.

72 M. J. Kim, Y. H. Kim, G. Mudhana and B. H. Lee, *IEEE Photon. Technol. Lett.*, 2008, **20**, 1290–1292.

73 D. W. Kim, Y. Zhang, K. L. Cooper and A. Wang, *Appl. Opt.*, 2005, **44**, 5368–5373.

74 S.-I. Ohira, Y. Miki, T. Matsuzaki, N. Nakamura, Y.-K. Sato, Y. Hirose and K. Toda, *Anal. Chim. Acta*, 2015, **886**, 188–193.

75 X. Hong, J. Wu, C. Zuo, F. Liu, H. Guo and K. Xu, *Appl. Opt.*, 2011, **50**, 4333–4338.

76 S. Knudsen and K. Blotekjaer, *J. Lightwave Technol.*, 1994, **12**, 1696–1700.

77 M. R. Islam, M. M. Ali, M.-H. Lai, K.-S. Lim and H. Ahmad, *Sensors*, 2014, **14**, 7451–7488.

78 A. A. Veselov, B. G. Abraham, H. Lemmetyinen, M. T. Karp and N. V. Tkachenko, *Anal. Bioanal. Chem.*, 2012, **402**, 1149–1158.

79 S. M. Tseng and C. L. Chen, *Appl. Opt.*, 1992, **31**, 3438–3447.

80 G. J. Pendock, H. S. Mackenzie and F. P. Payne, *Appl. Opt.*, 1993, **32**, 5236–5242.

81 C. M. Bellot, M. Sangermano, M. Olivero and M. Salvo, *Materials*, 2019, **12**, 379.

82 H. A. Mohammed, N. A. Rahman, M. Z. Ahmad, M. H. Abu Bakar, S. B. A. Anas, M. A. Mahdi and M. H. Yaacob, *IEEE Access*, 2019, **7**, 5467–5476.

83 S. Yeoh, M. Z. Matjafri, K. N. Mutter and A. A. Oglat, *Sensor Actuat A - Phys*, 2019, **285**, 1–7.

84 V. Bhatia, D. K. Campbell, D. Sherr, T. D'Alberto, N. Zabaronick, G. A. Ten Eyck, K. A. Murphy and R. O. Claus, *Opt. Eng*, 1997, **36**, 1872–1878.

85 M. Partridge, S. W. James, J. Barrington and R. P. Tatam, *Opt. Express*, 2016, **24**, 22345–22356.

86 S. Savin, M. J. F. Digonnet, G. S. Kino and H. J. Shaw, *Opt. Lett.*, 2000, **25**, 710–712.

87 A. D. Kersey, *Opt. Fiber Technol.*, 1996, **2**, 291–317.

88 C. A. J. Gouveia, J. M. Baptista and P. A. S. Jorge, in *Current Developments in Optical Fiber Technology*, ed. S. W. Harun, InTech, 2013.

89 Y.-J. Rao, *Meas. Sci. Technol.*, 1997, **8**, 355–375.

90 A. M. Vengsarkar, P. J. Lemaire, J. B. Judkins, V. Bhatia, T. Erdogan and J. E. Sipe, *J. Lightwave Technol.*, 1996, **14**, 58–65.

91 L. Alwis, T. Sun and K. Grattan, *Measurement*, 2013, **46**, 4052–4074.

92 C. Cuadrado-Laborde, ed., *Current Trends in Short- and Long-period Fiber Gratings*, InTech, 2013.

93 M. N. Ng and K. S. Chiang, *Opt. Commn.*, 2002, **208**, 321–327.

94 S. W. James and R. P. Tatam, *Meas. Sci. Technol.*, 2003, **14**, R49-R61.

95 C. S. Cheung, S. M. Topliss, S. W. James and R. P. Tatam, *J. Opt. Soc. Am. B*, 2008, **25**, 897–902.

96 X. Shu, L. Zhang and I. Bennion, *J. Lightwave Technol.*, 2002, **20**, 255–266.

97 C. Liu, Q. Cai, B. Xu, W. Zhu, L. Zhang, J. Zhao and X. Chen, *Biosens Bioelectron*, 2017, **94**, 200–206.

98 T. R. Woliński, *Acta Phys. Pol. A*, 1999, **95**, 749–760.

99 T. M. Libish, M. C. Bobby, J. Linesh, S. Mathew, C. Pradeep, V. P. N. Nampoori, P. Biswas, S. Bandyopadhyay, K. Dasgupta and P. Radhakrishnan, *Laser Phys.*, 2013, **23**, 45112.

100 R. Falciai, A. Mignani and A. Vannini, *Sensor Actuat B - Chem*, 2001, **74**, 74–77.

101 N. D. Rees, S. W. James, R. P. Tatam and G. J. Ashwell, *Opt. Lett.*, 2002, **27**, 686.

102 J. Keith, L. C. Hess, W. U. Spendel, J. A. Cox and G. E. Pacey, *Talanta*, 2006, **70**, 818–822.

103 C. Li, L. Li, S. Yu, X. Jiao and D. Chen, *Adv. Mater. Technol.*, 2016, **1**, 1600127.

104 S. Korposh, S.-W. Lee, S. W. James and R. P. Tatam, in *21st International Conference on Optical Fibre Sensors (OFS21)*, SPIE, 2011, 77539A.

105 J. Hromadka, S. Korposh, M. C. Partridge, S. W. James, F. Davis, D. Crump and R. P. Tatam, *Sensor Actuat B - Chem*, 2017, **244**, 217–225.

106 L. Marques, F. U. Hernandez, S. W. James, S. P. Morgan, M. Clark, R. P. Tatam and S. Korposh, *Biosens Bioelectron*, 2016, **75**, 222–231.

107 S. Korposh, R. Selyanchyn, W. Yasukochi, S.-W. Lee, S. W. James and R. P. Tatam, *Mat. Chem. Phys.*, 2012, **133**, 784–792.

108 Y. Zhu, L. Chen, C. Zhang and Z. Guan, *Appl. Surf. Sci.*, 2018, **457**, 522–528.

109 C.-W. Wu, C.-C. Wu and C.-C. Chiang, *Inventions*, 2016, **1**, 21.

110 R. B. Queirós, C. Gouveia, J. R. A. Fernandes and P. A. S. Jorge, *Biosens Bioelectron*, 2014, **62**, 227–233.

111 O. K. Farha, I. Eryazici, N. C. Jeong, B. G. Hauser, C. E. Wilmer, A. A. Sarjeant, R. Q. Snurr, S. T. Nguyen, A. Ö. Yazaydın and J. T. Hupp, *J. Am. Chem. Soc.*, 2012, **134**, 15016–15021.

112 T. Ahnfeldt, D. Gunzelmann, T. Loiseau, D. Hirsemann, J. Senker, G. Férey and N. Stock, *Inorg. Chem.*, 2009, **48**, 3057–3064.

113 S. Achmann, G. Hagen, J. Kita, I. M. Malkowsky, C. Kiener and R. Moos, *Sensors*, 2009, **9**, 1574–1589.

114 R. C. Huxford, J. Della-Rocca and W. Lin, *Curr. Opin. Chem. Bio.*, 2010, **14**, 262–268.

115 T. Loiseau, C. Serre, C. Huguenard, G. Fink, F. Taulelle, M. Henry, T. Bataille and G. Férey, *Chem. Eur. J.*, 2004, **10**, 1373–1382.

116 S. S.-Y. Chui, S. M.-F. Lo, J. P. H. Charmant, A. G. Orpen and I. D. Williams, *Science*, 1999, **283**, 1148–1150.

117 O. Karagiaridi, M. B. Lalonde, W. Bury, A. A. Sarjeant, O. K. Farha and J. T. Hupp, *J. Am. Chem. Soc.*, 2012, **134**, 18790–18796.

118 N. Lock, Y. Wu, M. Christensen, L. J. Cameron, V. K. Peterson, A. J. Bridgeman, C. J. Kepert and B. B. Iversen, *J. Phys. Chem. C*, 2010, **114**, 16181–16186.

119 M. Rubio-Martinez, C. Avci-Camur, A. W. Thornton, I. Imaz, D. Maspoch and M. R. Hill, *Chem. Soc. Rev.*, 2017, **46**, 3453–3480.

120 Y.-R. Lee, J. Kim and W.-S. Ahn, *Korean J. Chem. Eng.*, 2013, **30**, 1667–1680.

121 P. Falcaro, R. Ricco, C. M. Doherty, K. Liang, A. J. Hill and M. J. Styles, *Chem. Soc. Rev.*, 2014, **43**, 5513–5560.

122 V. I. Isaeva and L. M. Kustov, *Russ. Chem. Bull.*, 2016, **65**, 2103–2114.

123 A. Laybourn, J. Katrib, R. S. Ferrari-John, C. G. Morris, S. Yang, O. Udoudo, T. L. Easun, C. Dodds, N. R. Champness, S. W. Kingman and M. Schröder, *J. Mater. Chem. A*, 2017, **5**, 7333–7338.

124 Anton-Paar, *Microwave-assisted synthesis,* available at: https://wiki.anton-paar.com/en/microwave-assisted-synthesis/#further-reading, accessed 26 March 2019.

125 H. Gong, T. H. Nguyen, R. Wang and T.-H. Bae, *J. Membrane Sci.*, 2015, **495**, 169–175.

126 Z.-Q. Li, L.-G. Qiu, T. Xu, Y. Wu, W. Wang, Z.-Y. Wu and X. Jiang, *Mat. Lett.*, 2009, **63**, 78–80.

127 T. Friscić, D. G. Reid, I. Halasz, R. S. Stein, R. E. Dinnebier and M. J. Duer, *Angew. Chem. Int. Ed.*, 2010, **49**, 712–715.

128 D. Crawford, J. Casaban, R. Haydon, N. Giri, T. McNally and S. L. James, *Chem. Sci.*, 2015, **6**, 1645–1649.

129 D. S. Sholl and R. P. Lively, *Nature*, 2016, **532**, 435–437.

130 J. Andraos, *Org. Process Res. Dev.*, 2005, **9**, 149–163.

131 O. K. Farha and J. T. Hupp, *Acc. Chem. Res.*, 2010, **43**, 1166–1175.

132 A. Kumar, C. Hua, D. G. Madden, D. O'Nolan, K.-J. Chen, L.-A. J. Keane, J. J. Perry and M. J. Zaworotko, *Chem. Commun.*, 2017, **53**, 5946–5949.

133 P. Rallapalli, D. Patil, K. P. Prasanth, R. S. Somani, R. V. Jasra and H. C. Bajaj, *J. Porous. Mater.*, 2010, **17**, 523–528.

134 C.-X. Yang, H.-B. Ren and X.-P. Yan, *Anal. Chem.*, 2013, **85**, 7441–7446.

135 A. P. Nelson, O. K. Farha, K. L. Mulfort and J. T. Hupp, *J. Am. Chem. Soc.*, 2009, **131**, 458–460.

136 E. Heidaryan, T. Hatami, M. Rahimi and J. Moghadasi, *J. Supercritical Fluids*, 2011, **56**, 144–151.

137 Y. Pan, B. Yuan, Y. Li and D. He, *Chem. Commun.*, 2010, **46**, 2280–2282.

138 M. Fischer, J. Schwegler, C. Paula, P. S. Schulz and M. Hartmann, *Dalton Trans.*, 2016, **45**, 18443–18446.

139 T. P. T. Pham, C.-W. Cho and Y.-S. Yun, *Water Res.*, 2010, **44**, 352–372.

140 S. Bhattacharjee, C. Chen and W.-S. Ahn, *RSC Adv*, 2014, **4**, 52500–52525.

141 G. Lu, O. K. Farha, W. Zhang, F. Huo and J. T. Hupp, *Adv. Mater.*, 2012, **24**, 3970–3974.

142 J. Hedlund, O. Öhrman, V. Msimang, E. van Steen, W. Böhringer, S. Sibya and K. Möller, *Chem. Eng. Sci.*, 2004, **59**, 2647–2657.

143 Y.-S. Li, F.-Y. Liang, H. Bux, A. Feldhoff, W.-S. Yang and J. Caro, *Angew. Chem. Int. Ed.*, 2010, **49**, 548–551.

144 G. Lu and J. T. Hupp, *J. Am. Chem. Soc.*, 2010, **132**, 7832–7833.

145 M. D. Allendorf, R. J. T. Houk, L. Andruszkiewicz, A. A. Talin, J. Pikarsky, A. Choudhury, K. A. Gall and P. J. Hesketh, *J. Am. Chem. Soc.*, 2008, **130**, 14404–14405.

146 Z. Liao, T. Xia, E. Yu and Y. Cui, *Crystals*, 2018, **8**, 338.

147 J. Liu and C. Wöll, *Chem. Soc. Rev.*, 2017, **46**, 5730–5770.

148 O. Shekhah, J. Liu, R. A. Fischer and C. Wöll, *Chem Soc. Rev.*, 2011, **40**, 1081–1106.

149 Z. Kang, L. Fan and D. Sun, *J. Mater. Chem. A*, 2017, **5**, 10073–10091.

150 B. Liu and R. A. Fischer, *Sci. China Chem.*, 2011, **54**, 1851–1866.

151 D. Zacher, O. Shekhah, C. Wöll and R. A. Fischer, *Chem. Soc. Rev.*, 2009, **38**, 1418–1429.

152 D. Bradshaw, A. Garai and J. Huo, *Chem. Soc. Rev.*, 2012, **41**, 2344–2381.

153 N. Rangnekar, N. Mittal, B. Elyassi, J. Caro and M. Tsapatsis, *Chem. Soc. Rev.*, 2015, **44**, 7128–7154.

154 R. Ameloot, F. Vermoortele, W. Vanhove, M. B. J. Roeffaers, B. F. Sels and D. E. de Vos, *Nature Chem.*, 2011, **3**, 382–387.

155 T.-S. Chung, L. Y. Jiang, Y. Li and S. Kulprathipanja, *Prog. Polym. Sci.*, 2007, **32**, 483–507.

156 Y. Liu, Z. Ng, E. A. Khan, H.-K. Jeong, C.-B. Ching and Z. Lai, *Micro. Meso. Mat.*, 2009, **118**, 296–301.

157 A. Bétard, D. Zacher and R. A. Fischer, *CrystEngComm*, 2010, **12**, 3768–3772.

158 S. Eslava, L. Zhang, S. Esconjauregui, J. Yang, K. Vanstreels, M. R. Baklanov and E. Saiz, *Chem. Mater.*, 2013, **25**, 27–33.

159 H. Bux, F. Liang, Y. Li, J. Cravillon, M. Wiebcke and J. Caro, *J. Am. Chem. Soc.*, 2009, **131**, 16000–16001.

160 M. N. Shah, M. A. Gonzalez, M. C. McCarthy and H.-K. Jeong, *Langmuir*, 2013, **29**, 7896–7902.

161 S. Y. Choi, Y.-J. Lee, Y. S. Park, K. Ha and K. B. Yoon, *J. Am. Chem. Soc.*, 2000, **122**, 5201–5209.

162 V. V. Guerrero, Y. Yoo, M. C. McCarthy and H.-K. Jeong, *J. Mater. Chem.*, 2010, **20**, 3938.

163 J. Gascon, S. Aguado and F. Kapteijn, *Micro. Meso. Mat.*, 2008, **113**, 132–138.

164 H. Fan, H. Xia, C. Kong and L. Chen, *Int. J. Hydrogen Ener.*, 2013, **38**, 10795–10801.

165 Y. Hu, X. Dong, J. Nan, W. Jin, X. Ren, N. Xu and Y. M. Lee, *Chem. Commun.*, 2011, **47**, 737–739.

166 N. Wang, A. Mundstock, Y. Liu, A. Huang and J. Caro, *Chem. Eng. Sci.*, 2015, **124**, 27–36.

167 T. Ben, C. Lu, C. Pei, S. Xu and S. Qiu, *Chemistry*, 2012, **18**, 10250–10253.

168 J. Zhang, T. Xia, D. Zhao, Y. Cui, Y. Yang and G. Qian, *Sensor Actuat B - Chem*, 2018, **260**, 63–69.

169 F. Zhang, X. Zou, F. Sun, H. Ren, Y. Jiang and G. Zhu, *CrystEngComm*, 2012, **14**, 5487–5492.

170 K. Tao, C. Kong and L. Chen, *Chem. Eng. J.*, 2013, **220**, 1–5.

171 H. T. Kwon and H.-K. Jeong, *Chem. Commun.*, 2013, **49**, 3854–3856.

172 A. Demessence, P. Horcajada, C. Serre, C. Boissière, D. Grosso, C. Sanchez and G. Férey, *Chem. Commun.*, 2009, 7149–7151.

173 B. N. Joshi, J.-G. Lee, S. An, D.-Y. Kim, J. S. Lee, Y. K. Hwang, J.-S. Chang, S. S. Al-Deyab, J.-C. Tan and S. S. Yoon, *Mat. & Des.*, 2017, **114**, 416–423.

174 R. Makiura, S. Motoyama, Y. Umemura, H. Yamanaka, O. Sakata and H. Kitagawa, *Nature Mat.*, 2010, **9**, 565–571.

175 L. Heinke, M. Tu, S. Wannapaiboon, R. A. Fischer and C. Wöll, *Micro. Meso. Mat.*, 2015, **216**, 200–215.

176 E. Biemmi, C. Scherb and T. Bein, *J. Am. Chem. Soc.*, 2007, **129**, 8054–8055.

177 J. C. Love, L. A. Estroff, J. K. Kriebel, R. G. Nuzzo and G. M. Whitesides, *Chem. Rev.*, 2005, **105**, 1103–1169.

178 M. Eddaoudi, J. Kim, N. Rosi, D. Vodak, J. Wachter, M. O'Keeffe and O. M. Yaghi, *Science*, 2002, **295**, 469–472.

179 O. Shekhah, R. Swaidan, Y. Belmabkhout, M. Du Plessis, T. Jacobs, L. J. Barbour, I. Pinnau and M. Eddaoudi, *Chem. Comm.*, 2014, **50**, 2089–2092.

180 D.-J. Lee, Q. Li, H. Kim and K. Lee, *Micro. Meso. Mat.*, 2012, **163**, 169–177.

181 O. Shekhah, H. Wang, M. Paradinas, C. Ocal, B. Schüpbach, A. Terfort, D. Zacher, R. A. Fischer and C. Wöll, *Nature Mat.*, 2009, **8**, 481–484.

182 B. Liu, M. Ma, D. Zacher, A. Bétard, K. Yusenko, N. Metzler-Nolte, C. Wöll and R. A. Fischer, *J. Am. Chem. Soc.*, 2011, **133**, 1734–1737.

183 H. K. Arslan, O. Shekhah, J. Wohlgemuth, M. Franzreb, R. A. Fischer and C. Wöll, *Adv. Funct. Mater.*, 2011, **21**, 4228–4231.

184 L. Heinke, Z. Gu and C. Wöll, *Nature Comm.*, 2014, **5**, 4562.

185 O. Shekhah, H. Wang, S. Kowarik, F. Schreiber, M. Paulus, M. Tolan, C. Sternemann, F. Evers, D. Zacher, R. A. Fischer and C. Woll, *J. Am. Chem. Soc.*, 2007, **129**, 15118–15119.

186 Z.-G. Gu, A. Pfriem, S. Hamsch, H. Breitwieser, J. Wohlgemuth, L. Heinke, H. Gliemann and C. Wöll, *Micro. Meso. Mat.*, 2015, **211**, 82–87.

187 R. Ameloot, L. Stappers, J. Fransaer, L. Alaerts, B. F. Sels and D. E. de Vos, *Chem. Mater.*, 2009, **21**, 2580–2582.

188 N. Campagnol, T. van Assche, T. Boudewijns, J. Denayer, K. Binnemans, D. de Vos and J. Fransaer, *J. Mater. Chem. A*, 2013, **1**, 5827–5830.

189 A. M. Joaristi, J. Juan-Alcañiz, P. Serra-Crespo, F. Kapteijn and J. Gascon, *Cryst. Grwoth Des.*, 2012, **12**, 3489–3498.

190 J.-F. Feng, S.-Y. Gao, J. Shi, T.-F. Liu and R. Cao, *Inorg. Chem.*, 2018, **57**, 2447–2454.

191 M. Li and M. Dincă, *Chem. Sci.*, 2014, **5**, 107–111.

192 H. T. Kwon and H.-K. Jeong, *J. Am. Chem. Soc.*, 2013, **135**, 10763–10768.

193 Y. Chen, S. Li, X. Pei, J. Zhou, X. Feng, S. Zhang, Y. Cheng, H. Li, R. Han and B. Wang, *Angew. Chem. Int. Ed.*, 2016, **55**, 3419–3423.

194 S. Rackley, *Carbon Capture and Storage*, Elsevier, Amsterdam, 1st edn., 2009.

195 J. Rockström, O. Gaffney, J. Rogelj, M. Meinshausen, N. Nakicenovic and H. J. Schellnhuber, *Science*, 2017, **355**, 1269–1271.

196 E. S. Sanz-Pérez, C. R. Murdock, S. A. Didas and C. W. Jones, *Chem. Rev.*, 2016, **116**, 11840–11876.

197 A. Goeppert, M. Czaun, G. K. Surya Prakash and G. A. Olah, *Energy Environ. Sci.*, 2012, **5**, 7833–7854.

198 C. Plötz, ed., *Sequestrierung von CO2:. Technologien, Potenziale, Kosten und Umweltauswirkungen*, Heidelberg, 2003.

199 D. M. D'Alessandro, B. Smit and J. R. Long, *Angew. Chem. Int. Ed.*, 2010, **49**, 6058–6082.

200 P. D. Vaidya and E. Y. Kenig, *Chem. Eng. Technol.*, 2007, **30**, 1467–1474.

201 X. Ma, X. Wang and C. Song, *J. Am. Chem. Soc.*, 2009, **131**, 5777–5783.

202 G. T. Rochelle, *Science*, 2009, **325**, 1652–1654.

203 D. Nikolaeva, I. Azcune, M. Tanczyk, K. Warmuzinski, M. Jaschik, M. Sandru, P. I. Dahl, A. Genua, S. Loïs, E. Sheridan, A. Fuoco and I. F. Vankelecom, *J Membrane Sci.*, 2018, **564**, 552–561.

204 A. Hart and N. Gnanendran, *Energy Proc.*, 2009, **1**, 697–706.

205 C.-H. Yu, C.-H. Huang and C.-S. Tan, *Aerosol Air Qual. Res.*, 2012, **12**, 745–769.

206 L. Riboldi and O. Bolland, *Energy Proc.*, 2017, **114**, 2390–2400.

207 S. Choi, J. H. Drese and C. W. Jones, *ChemSusChem*, 2009, **2**, 796–854.

208 J. A. Mason, K. Sumida, Z. R. Herm, R. Krishna and J. R. Long, *Energy Environ. Sci.*, 2011, **4**, 3030–3040.

209 D. W. Breck, *Zeolite molecular sieves. Structure, chemistry, and use*, Wiley, New York, 1974.

210 M. Tagliabue, D. Farrusseng, S. Valencia, S. Aguado, U. Ravon, C. Rizzo, A. Corma and C. Mirodatos, *Chem. Eng. J.*, 2009, **155**, 553–566.

211 C. M. Lew, R. Cai and Y. Yan, *Acc. Chem. Res.*, 2010, **43**, 210–219.

212 N. Konduru, P. Lindner and N. M. Assaf-Anid, *AIChE J.*, 2007, **53**, 3137–3143.

213 Y. Lin, Q. Yan, C. Kong and L. Chen, *Sci. Rep.*, 2013, **3**, 1859.

214 B. Arstad, H. Fjellvåg, K. O. Kongshaug, O. Swang and R. Blom, *Adsorption*, 2008, **14**, 755–762.

215 E. Stavitski, E. A. Pidko, S. Couck, T. Remy, E. J. M. Hensen, B. M. Weckhuysen, J. Denayer, J. Gascon and F. Kapteijn, *Langmuir*, 2011, **27**, 3970–3976.

216 P. Rallapalli, K. P. Prasanth, D. Patil, R. S. Somani, R. V. Jasra and H. C. Bajaj, *J. Porous. Mater.*, 2011, **18**, 205–210.

217 J. Kim, W. Y. Kim and W.-S. Ahn, *Fuel*, 2012, **102**, 574–579.

218 X. Y. Chen, V.-T. Hoang, D. Rodrigue and S. Kaliaguine, *RSC Adv.*, 2013, **3**, 24266–24279.

219 W. P. Mounfield III, M. Taborga Claure, P. K. Agrawal, C. W. Jones and K. S. Walton, *Ind. Eng. Chem. Res.*, 2016, **55**, 6492–6500.

220 M. Kandiah, M. H. Nilsen, S. Usseglio, S. Jakobsen, U. Olsbye, M. Tilset, C. Larabi, E. A. Quadrelli, F. Bonino and K. P. Lillerud, *Chem. Mater.*, 2010, **22**, 6632–6640.

221 D. G. Madden, H. S. Scott, A. Kumar, K.-J. Chen, R. Sanii, A. Bajpai, M. Lusi, T. Curtin, J. J. Perry and M. J. Zaworotko, *Phil. Trans. R. Soc.*, 2017, **375**, 20160025.

222 W. Liang, C. J. Coghlan, F. Ragon, M. Rubio-Martinez, D. M. D'Alessandro and R. Babarao, *Dalton Trans.*, 2016, **45**, 4496–4500.

223 M. Erkartal and U. Sen, *ACS Appl. Mater. Inter.*, 2018, **10**, 787–795.

224 H. Molavi, A. Eskandari, A. Shojaei and S. A. Mousavi, *Micro. Meso. Mat.*, 2018, **257**, 193–201.

225 P. Á. Szilágyi, P. Serra-Crespo, J. Gascon, H. Geerlings and B. Dam, *Front. Energy Res.*, 2016, **4**, 9.

226 P. Li, J. Chen, W. Feng and X. Wang, *J. Iran Chem. Soc*, 2014, **11**, 741–749.

227 X. Huang, J. Lu, W. Wang, X. Wei and J. Ding, *Appl. Surf. Sci.*, 2016, **371**, 307–313.

228 Y. Lin, C. Kong and L. Chen, *RSC Adv.*, 2012, **2**, 6417–6419.

229 A. Bajpai, M. Lusi and M. J. Zaworotko, *Chem. Commun.*, 2017, **53**, 3978–3981.

230 V. Zeleňák, Z. Vargová, M. Almáši, A. Zeleňáková and J. Kuchár, *Micro. Meso. Mat.*, 2010, **129**, 354–359.

231 R. Vaidhyanathan, S. S. Iremonger, K. W. Dawson and G. K. H. Shimizu, *Chem. Commun.*, 2009, 5230–5232.

232 N. H. Alsmail, M. Suyetin, Y. Yan, R. Cabot, C. P. Krap, J. Lü, T. L. Easun, E. Bichoutskaia, W. Lewis, A. J. Blake and M. Schröder, *Chemistry*, 2014, **20**, 7317–7324.

233 S. R. Caskey, A. G. Wong-Foy and A. J. Matzger, *J. Am. Chem. Soc.*, 2008, **130**, 10870–10871.

234 Z. Liang, M. Marshall and A. L. Chaffee, *Energy Fuels*, 2009, **23**, 2785–2789.

235 A. Kumar, D. G. Madden, M. Lusi, K.-J. Chen, E. A. Daniels, T. Curtin, J. J. Perry and M. J. Zaworotko, *Angew. Chem. Int. Ed.*, 2015, **54**, 14372–14377.

236 H. S. Scott, A. Bajpai, K.-J. Chen, T. Pham, B. Space, J. J. Perry and M. J. Zaworotko, *Chem. Commun.*, 2015, **51**, 14832–14835.

237 A. Cadiau, K. Adil, P. M. Bhatt, Y. Belmabkhout and M. Eddaoudi, *Science*, 2016, **353**, 137–140.

238 L. T. Ngyen, K. K. Le and N. T. Phan, *Chinese J. Catal.*, 2012, **33**, 688–696.

239 C. H. Hendon and A. Walsh, *Chem. Sci.*, 2015, **6**, 3674–3683.

240 A. R. Millward and O. M. Yaghi, *J. Am. Chem. Soc.*, 2005, **127**, 17998–17999.

241 P. Nugent, V. Rhodus, T. Pham, B. Tudor, K. Forrest, L. Wojtas, B. Space and M. Zaworotko, *Chem. Commun.*, 2013, **49**, 1606–1608.

242 O. Shekhah, Y. Belmabkhout, K. Adil, P. M. Bhatt, A. J. Cairns and M. Eddaoudi, *Chem. Commun.*, 2015, **51**, 13595–13598.

243 H. S. Scott, M. Shivanna, A. Bajpai, D. G. Madden, K.-J. Chen, T. Pham, K. A. Forrest, A. Hogan, B. Space, J. J. Perry Iv and M. J. Zaworotko, *ACS Appl. Mater. Inter.*, 2017, **9**, 33395–33400.

244 L. Ge, L. Wang, V. Rudolph and Z. Zhu, *RSC Adv*, 2013, **3**, 25360–25366.

245 N. Al-Janabi, P. Hill, L. Torrente-Murciano, A. Garforth, P. Gorgojo, F. Siperstein and X. Fan, *Chem. Eng. J.*, 2015, **281**, 669–677.

246 H. Cheng and M. Reinhard, *Environ. Sci. Technol.*, 2006, **40**, 7694–7701.

247 P. Liu, C. Long, Q. Li, H. Qian, A. Li and Q. Zhang, *J. Hazard. Mater.*, 2009, **166**, 46–51.

248 A. Aizpuru, L. Malhautier, J. C. Roux and J. L. Fanlo, *Biotechnol. Bioeng.*, 2003, **83**, 479–488.

249 D. Britt, D. Tranchemontagne and O. M. Yaghi, *P. Natl. Acad. Sci. USA*, 2008, **105**, 11623–11627.

250 K. Vellingiri, J. E. Szulejko, P. Kumar, E. E. Kwon, K.-H. Kim, A. Deep, D. W. Boukhvalov and R. J. C. Brown, *Sci. Rep.*, 2016, **6**, 27813.

251 K. Yang, Q. Sun, F. Xue and D. Lin, *J. Hazard. Mater.*, 2011, **195**, 124–131.

252 I. Ahmed and S. H. Jhung, *J. Hazard. Mater.*, 2015, **283**, 544–550.

253 Y.-H. Kim, P. Kumar, E. E. Kwon and K.-H. Kim, *Microchem. J.*, 2017, **132**, 219–226.

254 Y. Li, A.-S. Xiao, B. Zou, H.-X. Zhang, K.-L. Yan and Y. Lin, *Polyhedron*, 2018, **154**, 83–97.

255 L. A. Saari and W. R. Seitz, *Anal. Chem.*, 2002, **56**, 810–813.

256 M. Tu, S. Wannapaiboon, K. Khaletskaya and R. A. Fischer, *Adv. Funct. Mater.*, 2015, **25**, 4470–4479.

257 H. Yamagiwa, S. Sato, T. Fukawa, T. Ikehara, R. Maeda, T. Mihara and M. Kimura, *Sci. Rep.*, 2014, **4**, 6247.

258 Y. Takashima, V. M. Martínez, S. Furukawa, M. Kondo, S. Shimomura, H. Uehara, M. Nakahama, K. Sugimoto and S. Kitagawa, *Nature Comm.*, 2011, **2**, 168.

259 M. S. Hosseini, S. Zeinali and M. H. Sheikhi, *Sensor Actuat B - Chem*, 2016, **230**, 9–16.

260 G. Férey, M. Latroche, C. Serre, F. Millange, T. Loiseau and A. Percheron-Guégan, *Chem. Commun.*, 2003, **39**, 2976–2977.

261 F. Millange, N. Guillou, R. I. Walton, J.-M. Greneche, I. Margiolaki and G. Férey, *Chem. Commun.*, 2008, **44**, 4732–4734.

262 C. Volkringer, T. Loiseau, N. Guillou, G. Férey, E. Elkaim and A. Vimont, *Dalton Trans.*, 2009, **12**, 2241–2249.

263 J. Gascon, U. Aktay, M. Hernandez-Alonso, G. van Klink and F. Kapteijn, *J. Catal.*, 2009, **261**, 75–87.

264 L. Liu, X. Wang and A. J. Jacobson, *Dalton Trans.*, 2010, **39**, 1722–1725.

265 S. Biswas, T. Ahnfeldt and N. Stock, *Inorg. Chem.*, 2011, **50**, 9518–9526.

266 M. Mendt, B. Jee, N. Stock, T. Ahnfeldt, M. Hartmann, D. Himsl and A. Pöppl, *J. Phys. Chem. C*, 2010, **114**, 19443–19451.

267 J. Yang, X. Yan, T. Xue and Y. Liu, *RSC Adv*, 2016, **6**, 55266–55271.

268 S. Pourebrahimi, M. Kazemeini, E. Ganji Babakhani and A. Taheri, *Micro Meso Mat*, 2015, **218**, 144–152.

269 K. Akhbari and A. Morsali, *Mat. Lett.*, 2015, **141**, 315–318.

270 T. A. Vu, G. H. Le, C. D. Dao, L. Q. Dang, K. T. Nguyen, Q. K. Nguyen, P. T. Dang, H. T. K. Tran, Q. T. Duong, T. V. Nguyen and G. D. Lee, *RSC Adv*, 2015, **5**, 5261–5268.

271 J. Liu, F. Zhang, X. Zou, G. Yu, N. Zhao, S. Fan and G. Zhu, *Chem. Commun.*, 2013, **49**, 7430–7432.

272 H. Kim, S. Yang, S. R. Rao, S. Narayanan, E. A. Kapustin, H. Furukawa, A. S. Umans, O. M. Yaghi and E. N. Wang, *Science*, 2017, **256**, 430–434.

273 S. Biswas, T. Remy, S. Couck, D. Denysenko, G. Rampelberg, J. F. M. Denayer, D. Volkmer, C. Detavernier and P. van der Voort, *Phys. Chem. Chem. Phys.*, 2013, **15**, 3552–3561.

274 E. Haque, N. A. Khan, J. H. Park and S. H. Jhung, *Chemistry*, 2010, **16**, 1046–1052.

275 N. Stock and S. Biswas, *Chem. Rev.*, 2012, **112**, 933–969.

276 C. A. Redlich, W. S. Beckett, J. Sparer, K. W. Barwick, C. A. Riely, H. Miller, Sigal, Steohen L., Shalat, Stuard L. and M. R. Cullen, *Ann. Intern. Med.*, 1988, **108**, 680–686.

277 W. M. Haynes, *CRC Handbook of Chemistry and Physics, Version 2016). 96th Edition(Internet Version 2016)*, Boca Raton, 2016.

278 E. Tynan, P. Jensen, P. E. Kruger and A. C. Lees, *Chem. Commun.*, 2004, 776–777.

279 X. Cheng, A. Zhang, K. Hou, M. Liu, Y. Wang, C. Song, G. Zhang and X. Guo, *Dalton Trans.*, 2013, **42**, 13698–13705.

280 W. Lin, W. J. Rieter and K. M. L. Taylor, *Angew. Chem. Int. Ed.*, 2009, **48**, 650–658.

281 M. Sindoro, N. Yanai, A.-Y. Jee and S. Granick, *Acc. Chem. Res.*, 2014, **47**, 459–469.

282 T. Ahnfeldt, N. Guillou, D. Gunzelmann, I. Margiolaki, T. Loiseau, G. Ferey, J. Senker and N. Stock, *Angew. Chem. Int. Ed.*, 2009, **48**, 5163–5166.

283 W. P. Mounfield III and K. S. Walton, *J. Coll. Int. Sci.*, 2015, **447**, 33–39.

284 S. Biswas, D. E. P. Vanpoucke, T. Verstraelen, M. Vandichel, S. Couck, K. Leus, Y.-Y. Liu, M. Waroquier, V. van Speybroeck, J. F. M. Denayer and P. van der Voort, *J. Phys. Chem. C*, 2013, **117**, 22784–22796.

285 T. Düren, F. Millange, G. Férey, K. S. Walton and R. Q. Snurr, *J. Phys. Chem. C*, 2007, **111**, 15350–15356.

286 J. Rouquerol, P. Llewellyn and F. Rouquerol, in *Characterization of Porous Solids VII - Proceedings of the 7th International Symposium on the Characterization of Porous Solids (COPS-VII), Aix-en-Provence, France, 26-28 May 2005*, Elsevier, 2007, pp. 49–56.

287 M. Sánchez-Sánchez, N. Getachew, K. Díaz, M. Díaz-García, Y. Chebude and I. Díaz, *Green Chem*, 2015, **17**, 1500–1509.

288 S. Sorribas, B. Zornoza, P. Serra-Crespo, J. Gascon, F. Kapteijn, C. Téllez and J. Coronas, *Micro. Meso. Mat.*, 2016, **225**, 116–121.

289 A. S. Myerson, ed., *Handbook of industrial crystallization*, Butterworth-Heinemann, Boston, 2nd edn., 2002.

290 R.C. Dougherty and L. N. Howard, *J. Chem. Phys*, 1988, **109**, 7379–7393.

291 D. D. Perrin, *Dissociation Constants of Organic Acids and Bases*, Butterworths, London, 1965.

292 A. Apelblat, E. Manzurola and N. Abo Balal, *J. Chem. Thermo.*, 2006, **38**, 565–571.

293 N. Han, L. Zhu, L. Wang and R. Fu, *Sep. Purif. Tech.*, 1999, **16**, 175–180.

294 J. J. Harper and P. Janik, *J. Chem. Eng. Data*, 1970, **15**, 439–440.

295 P. Ma and M. Chen, *Chinese J. Eng.*, 2003, **11**, 334–337.

296 A. C. McKinnis and J. L. Bills, *US-Patent (2,741,633)*, 1956.

297 A. Seidel, R. E. Kirk and D. F. Othmer, eds., *Kirk-Othmer encyclopedia of chemical technology*, Wiley-Interscience, Hoboken, NJ, 4th edn., 1991-1996.

298 V. Chaudhary and S. Sharma, *J. Porous. Mater.*, 2017, **24**, 741–749.

299 F. J. Sotomayor, K. A. Cychosz and M. Thommes, *Acc. Mater. Surf. Res.*, 2018, **3**, 34–50.

300 B. C. Lippens and J. H. de Boer, *J. Catal.*, 1965, **4**, 319–323.

301 S. Storck, H. Bretinger and W. F. Maier, *Appl. Catal. A*, 1998, **174**, 137–146.

302 A. Galarneau, F. Villemot, J. Rodriguez, F. Fajula and B. Coasne, *Langmuir*, 2014, **30**, 13266–13274.

303 A. J. Howarth, A. W. Peters, N. A. Vermeulen, T. C. Wang, J. T. Hupp and O. K. Farha, *Chem. Mater.*, 2016, **29**, 26–39.

304 M. F. de Lange, T. J. Vlugt, J. Gascon and F. Kapteijn, *Micro. Meso. Mat.*, 2014, **200**, 199–215.

305 J. Canivet, A. Fateeva, Y. Guo, B. Coasne and D. Farrusseng, *Chem Soc. Rev.*, 2014, **43**, 5594–5617.

306 X. Qian, B. Yadian, R. Wu, Y. Long, K. Zhou, B. Zhu and Y. Huang, *Int. J. Hydrogen Ener.*, 2013, **38**, 16710–16715.

307 J. M. Salazar, G. Weber, J. M. Simon, I. Bezverkhyy and J. P. Bellat, *J. Chem. Eng. Data*, 2015, **142**, 124702.

308 P. Mishra, H. P. Uppara, B. Mandal and S. Gumma, *Ind. Eng. Chem. Res.*, 2014, **53**, 19747–19753.

309 B. van de Voorde, A. S. Munn, N. Guillou, F. Millange, D. E. de Vos and R. I. Walton, *Phys. Chem. Chem. Phys.*, 2013, **15**, 8606–8615.

310 S. Bourrelly, B. Moulin, A. Rivera, G. Maurin, S. Devautour-Vinot, C. Serre, T. Devic, P. Horcajada, A. Vimont, G. Clet, M. Daturi, J.-C. Lavalley, S. Loera-Serna, R. Denoyel, P. L. Llewellyn and G. Férey, *J. Am. Chem. Soc.*, 2010, **132**, 9488–9498.

311 B. C. Camacho, R. P. Ribeiro, I. A. Esteves and J. P. Mota, *Sep. Purif. Tech.*, 2015, **141**, 150–159.

312 A. Boutin, F.-X. Coudert, M.-A. Springuel-Huet, A. V. Neimark, G. Férey and A. H. Fuchs, *J. Phys. Chem. C*, 2010, **114**, 22237–22244.

313 D. Saha and S. Deng, *J. Phys. Chem. Lett.*, 2010, **1**, 73–78.

314 I. J. Kang, N. A. Khan, E. Haque and S. H. Jhung, *Chemistry*, 2011, **17**, 6437–6442.

315 C. Serre, F. Millange, C. Thouvenot, M. Noguès, G. Marsolier, D. Louër and G. Férey, *J. Am. Chem. Soc.*, 2002, **124**, 13519–13526.

316 AlumniumSulfate, *Alumnium Sulfate,* available at: https://aluminumsulfate.net/, accessed 13 January 2019.

317 Gaylord Chemical Company, *Dimethyl Sulfoxide (DMSO) Solubility Data. Bulletin # 102B*, 2007.

318 C. Volkringer, M. Meddouri, T. Loiseau, N. Guillou, J. Marrot, G. Férey, M. Haouas, F. Taulelle, N. Audebrand and M. Latroche, *Inorg. Chem.*, 2008, **47**, 11892–11901.

319 Z. Liu, Q. Li, H. Zhu, K. Lin, J. Deng, J. Chen and X. Xing, *Chem. Commun.*, 2018, **54**, 5712–5715.

320 A. Perea-Cachero, E. Romero, C. Téllez and J. Coronas, *CrystEngComm*, 2018, **20**, 402–406.

321 F. Millange, C. Serre and G. Férey, *Chem. Commun.*, 2002, **38**, 822–823.

322 S. H. Jhung, N. A. Khan and Z. Hasan, *CrystEngComm*, 2012, **14**, 7099–7109.

323 C. R. Das, *Trans. Indian Ceramic Soc.*, 2014, **24**, 12–23.

324 C.-H. Chen, S.-Y. Li, A. S. Chiang, A. T. Wu and Y. S. Sun, *Sol. Energ. Mat. Sol. C.*, 2011, **95**, 1694–1700.

325 H.-C. Flemming, *Appl. Microbiol. Biot.*, 2002, **59**, 629–640.

326 P. C. Lemaire, J. Zhao, P. S. Williams, H. J. Walls, S. D. Shepherd, M. D. Losego, G. W. Peterson and G. N. Parsons, *ACS Appl. Mater. Inter.*, 2016, **8**, 9514–9522.

327 A. Bétard and R. A. Fischer, *Chem. Rev.*, 2012, **112**, 1055–1083.

328 J. W. Maina, J. A. Schütz, L. Grundy, E. Des Ligneris, Z. Yi, L. Kong, C. Pozo-Gonzalo, M. Ionescu and L. F. Dumée, *ACS Appl. Mater. Inter.*, 2017, **9**, 35010–35017.

329 M. Zhou, B. Zhang and X. Liu, *Sci. Bull.*, 2008, **53**, 801–816.

330 E. Biemmi, A. Darga, N. Stock and T. Bein, *Micro. Meso. Mat.*, 2008, **114**, 380–386.

331 O. Duhem, A. DaCosta, J. F. Henninot and M. Douay, *Electron. Lett.*, 1999, **35**, 1014–1016.

332 D. M. Costantini, C. Muller, S. A. Vasiliev, H. G. Limberger and R. P. Salathe, *IEEE Photon. Technol. Lett.*, 1999, **11**, 1458–1460.

333 L. Srisombat, A. C. Jamison and T. R. Lee, *Colloid Surface A*, 2011, **390**, 1–19.

334 C. Scherb, A. Schödel and T. Bein, *Angew. Chem. Int. Ed.*, 2008, **120**, 5861–5863.

335 J.-R. Li, J. Sculley and H.-C. Zhou, *Chem. Rev.*, 2012, **112**, 869–932.

336 B. C. Punmia, A. K. Jain and A. K. Jain, *Basic civil engineering. For B.E. / B. Tech first year courses of various universities including M.D.U. and K.U., Haryana*, Laxmi Publications, New Delhi, 2003.

337 W. Vogel, *Glaschemie*, Springer, Berlin, 3rd edn., 1992.

338 A. Mitra, I. Kouzmina and M. Lopez, *Thermal Stability of the CPC Fiber Coating System*, Corning, 2010.

339 S. Sridevi, K. S. Vasu, S. Asokan and A. K. Sood, *Optics letters*, 2016, **41**, 2604–2607.

340 M. Konstantaki, S. Pissadakis, S. Pispas, N. Madamopoulos and N. A. Vainos, *Appl. Opt.*, 2006, **45**, 4567–4571.

341 F. Tian, A. M. Cerro, A. M. Mosier, H. K. Wayment-Steele, R. S. Shine, A. Park, E. R. Webster, L. E. Johnson, M. S. Johal and L. Benz, *J. Phys. Chem. C*, 2014, **118**, 14449–14456.

342 R. Ameloot, E. Gobechiya, H. Uji-i, J. A. Martens, J. Hofkens, L. Alaerts, B. F. Sels and D. E. de Vos, *Adv. Mater.*, 2010, **22**, 2685–2688.

343 H. Guo, M. Wang, J. Liu, S. Zhu and C. Liu, *Micro. Meso. Mat.*, 2016, **221**, 40–47.

344 J. Luo, S. Bae, M. Yuan, E. Schneider, M. T. Lanagan, C. G. Pantano and S. H. Kim, *J. Am. Ceram. Soc.*, 2018, **101**, 2951–2964.

345 M. Rismanchian, F. Golbabaei, Y. Mortazavi, G. Pourtaghi, A. Rahimi Foroushani and P. Nassiri, *Int. J. Photoenergy*, 2012, **2012**, 1–9.

346 H. R. Barzegar, F. Nitze, T. Sharifi, M. Ramstedt, C. W. Tai, A. Malolepszy, L. Stobinski and T. Wågberg, *J. Phys. Chem. C*, 2012, **116**, 12232–12239.

347 Y. Paz, Z. Luo, L. Rabenberg and A. Heller, *J. Mater. Res.*, 1995, **10**, 2842–2848.

348 K. H. Kim, Z. Akase, T. Suzuki and D. Shindo, *Mater. Trans.*, 2010, **51**, 1080–1083.

349 K. J. Seu, A. P. Pandey, F. Haque, E. A. Proctor, A. E. Ribbe and J. S. Hovis, *Biophys. J.*, 2007, **92**, 2445–2450.

350 M.-J. Yin, B. Huang, S. Gao, A. P. Zhang and X. Ye, *Biomed. Opt. Express*, 2016, **7**, 2067–2077.

351 D. Nagao, R. Kameyama, Y. Kobayashi and M. Konno, *Colloid Surface A*, 2007, **311**, 26–31.

352 D. Zacher, K. Yusenko, A. Betard, S. Henke, M. Molon, T. Ladnorg, O. Shekhah, B. Schupbach, T. de los Arcos, M. Krasnopolski, M. Meilikhov, J. Winter, A. Terfort, C. Woll and R. A. Fischer, *Chemistry*, 2011, **17**, 1448–1455.

353 S. Khanjani and A. Morsali, *Ultrason. Sonochem.*, 2014, **21**, 1424–1429.

354 R. Khajavian and K. Ghani, *CrystEngComm*, 2018, **20**, 1546–1552.

355 H. K. Arslan, O. Shekhah, D. C. F. Wieland, M. Paulus, C. Sternemann, M. A. Schroer, S. Tiemeyer, M. Tolan, R. A. Fischer and C. Wöll, *J. Am. Chem. Soc.*, 2011, **133**, 8158–8161.

356 N. A. Khan and S. H. Jhung, *Coordin. Chem. Rev.*, 2015, **285**, 11–23.

357 A. L. Semrau, S. Wannapaiboon, S. P. Pujari, P. Vervoorts, B. Albada, H. Zuilhof and R. A. Fischer, *Cryst. Grwoth Des.*, 2019, **19**, 1738–1747.

358 A. V. Makeenko, T. V. Larionova, O. G. Klimova-Korsmik, R. V. Starykh, V. V. Galkin and O. V. Tolochko, *Tech. Phys.*, 2017, **62**, 613–618.

359 G. Xomeritakis, A. Gouzinis, S. Nair, T. Okubo, M. He, R. M. Overney and M. Tsapatsis, *Chem. Eng. Sci.*, 1999, **54**, 3521–3531.

360 J. Grand, H. Awala and S. Mintova, *CrystEngComm*, 2016, **18**, 650–664.

361 C. S. Cundy and P. A. Cox, *Micro. Meso. Mat.*, 2005, **82**, 1–78.

362 N. D. Acha, J. Hromadka, B. Tokay, R. Correia, C. Elosua, I. R. Matías, F. J. Arregui, S. P. Morgan and S. Korposh, *Proceedings*, 2017, **1**, 474.

363 J. W. Maina, C. P. Gonzalo, A. Merenda, L. Kong, J. A. Schütz and L. F. Dumée, *Appl. Surf. Sci.*, 2018, **427**, 401–408.

364 Y. Pan, Y. Liu, G. Zeng, L. Zhao and Z. Lai, *Chem. Commun.*, 2011, **47**, 2071–2073.

365 J. Canivet, J. Bonnefoy, C. Daniel, A. Legrand, B. Coasne and D. Farrusseng, *New J. Chem.*, 2014, **38**, 3102.

366 G. Férey, *Chem. Soc. Rev.*, 2008, **37**, 191–214.

367 R. D. Deegan, O. Bakajin, T. F. Dupont, G. Huber, S. R. Nagel and T. A. Witten, *Nature*, 1997, **389**, 827–829.

368 S. Couck, J. F. M. Denayer, G. V. Baron, T. Remy, J. Gascon and F. Kapteijn, *J. Am. Chem. Soc.*, 2009, **131**, 6326–6327.

369 S. Korposh, S.-W. Lee, W. J. Batty, S. W. James, R. P. Tatam, S. Topliss and S. C. Cheung, *Opt. Express*, 2010, **18**, 666–669.

370 M. P. DeLisa, Z. Zhang, M. Shiloach, S. Pilevar, C. C. Davis, J. S. Sirkis and W. E. Bentley, *Anal. Chem.*, 2000, **72**, 2895–2900.

371 J. Zhang, X. Tang, J. Dong, T. Wei and H. Xiao, *Sensor Actuat B - Chem*, 2009, **135**, 420–425.

372 L. E. Kreno, J. T. Hupp and R. P. van Duyne, *Analytical chemistry*, 2010, **82**, 8042–8046.

373 K. Ashutosh, *Curr. Opin. Pulm. Med.*, 2000, **6**, 21–25.

374 D. Crump, *Proc. Ins. Civil. Eng.*, 2013, **166**, 94–103.

375 M. J. Thorpe, D. Balslev-Clausen, M. S. Kirchner and J. Ye, *Opt. Express*, 2008, **16**, 2387–2397.

376 F. U. Hernandez, R. Correia, S. Korposh, S. P. Morgan, B. R. Hayes-Gill, S. W. James, D. Evans and A. Norris, in *International Conference on Optical Fibre Sensors (OFS24)*, ed. H. J. Kalinowski, J. L. Fabris and W. J. Bock, SPIE, 2015, p. 963435.

377 A. Marzocca, A. Di Gilio, G. Farella, R. Giua and G. de Gennaro, *Environments*, 2017, **4**, 23.

378 J. Liesivuori and a. H. Savolainen, *Pharmacol. Toxicol.*, 1991, **69**, 157–163.

379 K. Bergmann, *Elektrische Messtechnik. Elektrische und elektronische Verfahren, Anlagen und Systeme*, Vieweg+Teubner Verlag, Wiesbaden, 6th edn., 2008.

380 E. R. Peck and B. N. Khanna, *J. Opt. Soc. Am.*, 1966, **56**, 1059–1063.

381 E. R. Peck and D. J. Fisher, *J. Opt. Soc. Am.*, 1964, **54**, 1362–1364.

382 A. Bideau-Mehu, Y. Guern, R. Abjean and A. Johannin-Gilles, *Opt. Commn.*, 1973, **9**, 432–434.

383 H. El-Kashef, *Physica B*, 2000, **279**, 295–301.

384 A. Zárate, R. A. Peralta, P. A. Bayliss, R. Howie, M. Sánchez-Serratos, P. Carmona-Monroy, D. Solis-Ibarra, E. González-Zamora and I. A. Ibarra, *RSC Adv*, 2016, **6**, 9978–9983.

385 J. Ge, L. Liu, L. Qiu, X. Jiang and Y. Shen, *J. Porous. Mater.*, 2016, **23**, 857–865.

386 J. Tao, X. Wang, T. Sun, H. Cai, Y. Wang, T. Lin, D. Fu, L. L. Y. Ting, Y. Gu and D. Zhao, *Sci. Rep.*, 2017, **7**, 41640.

387 A. C. Kizzie, A. G. Wong-Foy and A. J. Matzger, *Langmuir*, 2011, **27**, 6368–6373.

388 L. N. McHugh, M. J. McPherson, L. J. McCormick, S. A. Morris, P. S. Wheatley, S. J. Teat, D. McKay, D. M. Dawson, C. E. F. Sansome, S. E. Ashbrook, C. A. Stone, M. W. Smith and R. E. Morris, *Nature Chem.*, 2018, **10**, 1096–1102.

389 S. K. Elsaidi, M. H. Mohamed, H. T. Schaef, A. Kumar, M. Lusi, T. Pham, K. A. Forrest, B. Space, W. Xu, G. J. Halder, J. Liu, M. J. Zaworotko and P. K. Thallapally, *Chem. Commun.*, 2015, **51**, 15530–15533.

390 I. E. Ertas, M. Gulcan, A. Bulut, M. Yurderi and M. Zahmakiran, *Micro. Meso. Mat.*, 2016, **226**, 94–103.

391 B. Pato-Doldán, M. H. Rosnes and P. D. C. Dietzel, *ChemSusChem*, 2017, **10**, 1710–1719.

392 G. M. J. Schmidt, *Pure Appl. Chem.*, 1971, **27**, 647–678.

393 S. Subramanian and M. J. Zaworotko, *Angew. Chem. Int. Ed.*, 1995, **34**, 2127–2129.

394 X. Cui, K. Chen, H. Xing, Q. Yang, R. Krishna, Z. Bao, H. Wu, W. Zhou, X. Dong, Y. Han, B. Li, Q. Ren, M. J. Zaworotko and B. Chen, *Science*, 2016, **353**, 141–144.

395 O. Shekhah, Y. Belmabkhout, Z. Chen, V. Guillerm, A. Cairns, K. Adil and M. Eddaoudi, *Nature Comm.*, 2014, **5**, 4228.

396 A. Bajpai, D. O'Nolan, D. G. Madden, K.-J. Chen, T. Pham, A. Kumar, M. Lusi, J. J. Perry, B. Space and M. J. Zaworotko, *Chem. Commun.*, 2017, **53**, 11592–11595.

397 D. O'Nolan, A. Kumar and M. J. Zaworotko, *J. Am. Chem. Soc.*, 2017, **139**, 8508–8513.

398 M. H. Mohamed, S. K. Elsaidi, T. Pham, K. A. Forrest, B. Tudor, L. Wojtas, B. Space and M. J. Zaworotko, *Chem. Commun.*, 2013, **49**, 9809–9811.

399 K.-J. Chen, Q.-Y. Yang, S. Sen, D. G. Madden, A. Kumar, T. Pham, K. A. Forrest, N. Hosono, B. Space, S. Kitagawa and M. J. Zaworotko, *Angew. Chem. Int. Ed.*, 2018, **57**, 3332–3336.

400 X. Cui, Q. Yang, L. Yang, R. Krishna, Z. Zhang, Z. Bao, H. Wu, Q. Ren, W. Zhou, B. Chen and H. Xing, *Adv. Mater.*, 2017, **29**, 1606929.

401 M. Jiang, X. Cui, L. Yang, Q. Yang, Z. Zhang, Y. Yang and H. Xing, *Chem. Eng. J.*, 2018, **352**, 803–810.

402 K.-J. Chen, H. S. Scott, D. G. Madden, T. Pham, A. Kumar, A. Bajpai, M. Lusi, K. A. Forrest, B. Space, J. J. Perry and M. J. Zaworotko, *Chem*, 2016, **1**, 753–765.

403 O. V. Dolomanov, L. J. Bourhis, R. J. Gildea, J. A. K. Howard and H. Puschmann, *J. Appl. Crystallogr.*, 2009, **42**, 339–341.

404 G. M. Sheldrick, *Acta Cryst. C*, 2015, **71**, 3–8.

405 R. L. Davidovich, T. A. Kaidalova and T. F. Levchishina, *J. Struct. Chem.*, 1971, **12**, 166–168.

406 H. M. Cheung and R. L. Lichti, *J. Phys. Chem. C*, 1985, **18**, 6157–6167.

407 ThermoFisher Scientific, *Safety Data Sheet Nickel(II) carbonate (basic) hydrate*, 2017.

408 H. M. Wu, Master Thesis, 1984.

409 C. R. Choudhury, S. K. Dey, S. Sen, B. Bag, S. Mitra and V. Gramlich, *Z. Naturforsch*, 2002, **57**, 1191–1194.

410 J. Zheng, X. Cui, Q. Yang, Q. Ren, Y. Yang and H. Xing, *Chem. Eng. J.*, 2018, **354**, 1075–1082.

411 S. Kitagawa and R. Matsuda, *Coordin. Chem. Rev.*, 2007, **251**, 2490–2509.

412 P. S. Nugent, V. L. Rhodus, T. Pham, K. Forrest, L. Wojtas, B. Space and M. J. Zaworotko, *J. Am. Chem. Soc.*, 2013, **135**, 10950–10953.

413 C. Lieder, S. Opelt, M. Dyballa, H. Henning, E. Klemm and M. Hunger, *J. Phys. Chem. C*, 2010, **114**, 16596–16602.

414 D. E. Aspnes, J. B. Theeten and F. Hottier, *Phys. Rev. B*, 1979, **20**, 3292–3302.

415 D. Simeone, G. Baldinozzi, D. Gosset, S. Le Caer and J.-F. Bérar, *Thin Solid Films*, 2013, **530**, 9–13.

416 L. T. Zhuravlev, *Colloid Surface A*, 2000, **173**, 1–38.

9 Appendix A: Thin-Film synthesis of MIL-53(Al) on glass

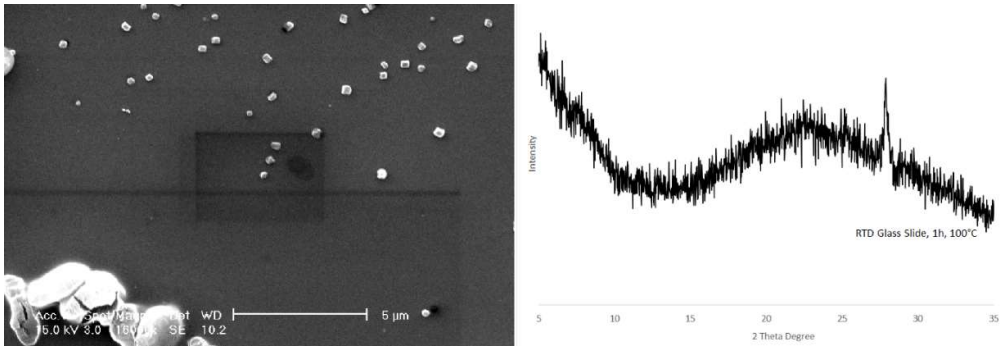


Figure 9-1: SEM image and XRD pattern of glass slide covered by RTD with NEq solution at 100°C with reaction time of 1 h.

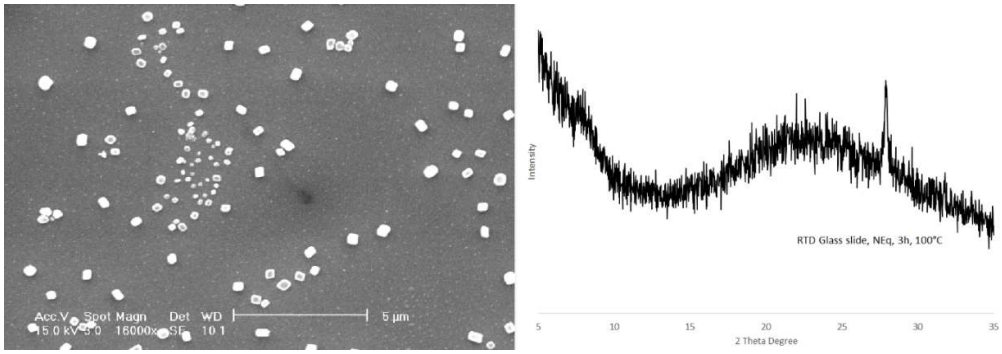


Figure 9-2: SEM image and XRD pattern of glass slide covered by RTD with NEq solution at 100°C with reaction time of 3 h.

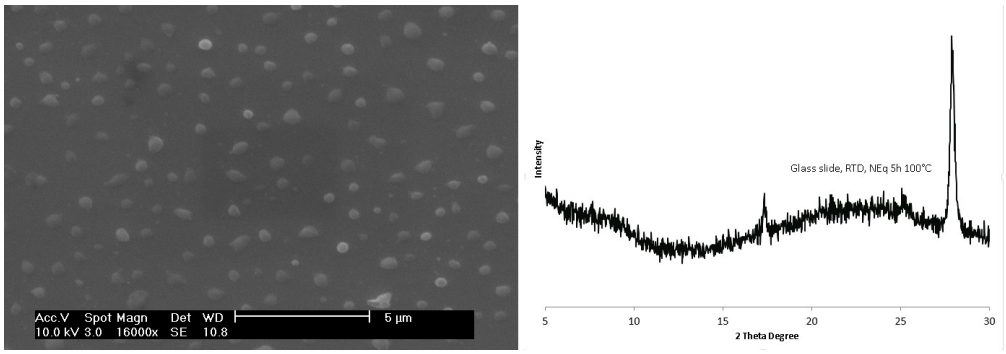


Figure 9-3: SEM image and XRD pattern of glass slide covered by RTD with NEq solution at 100°C with reaction time of 5 h.

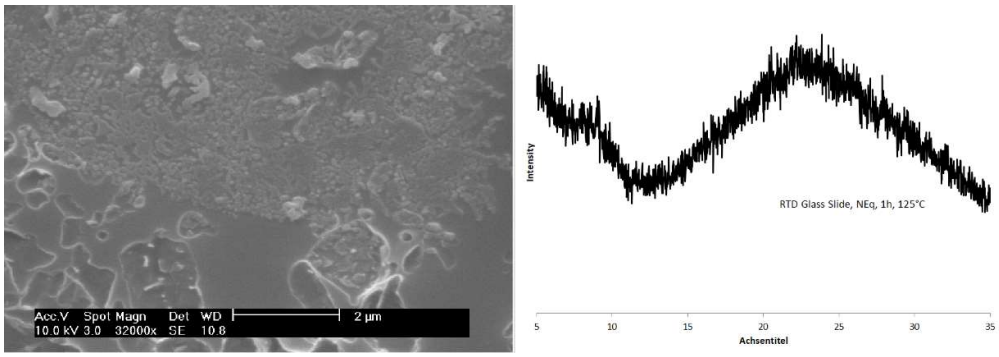


Figure 9-4: SEM image and XRD pattern of glass slide covered by RTD with NEq solution at 125°C with reaction time of 1 h.

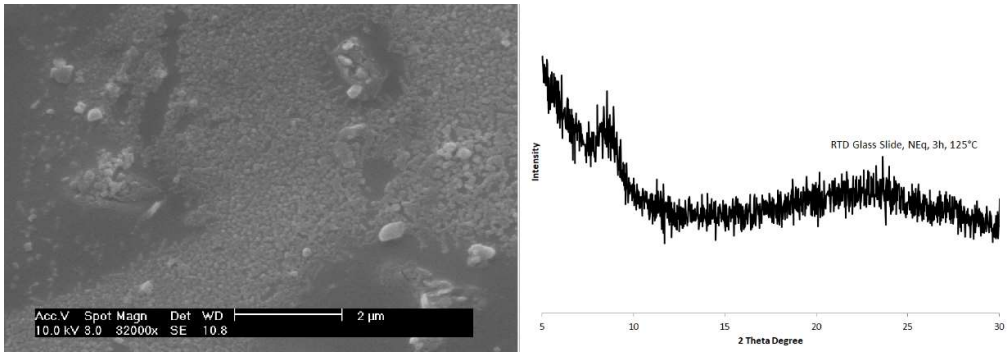


Figure 9-5: SEM image and XRD pattern of glass slide covered by RTD with NEq solution at 125°C with reaction time of 3 h.

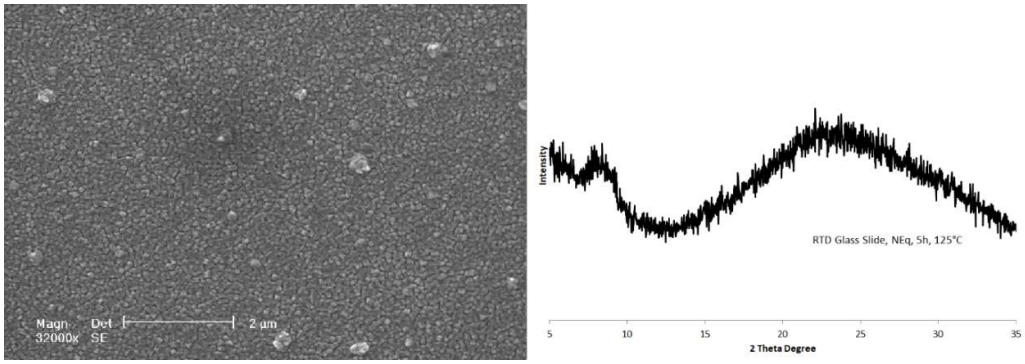


Figure 9-6: SEM image and XRD pattern of glass slide covered by RTD with NEq solution at 125°C with reaction time of 5 h.

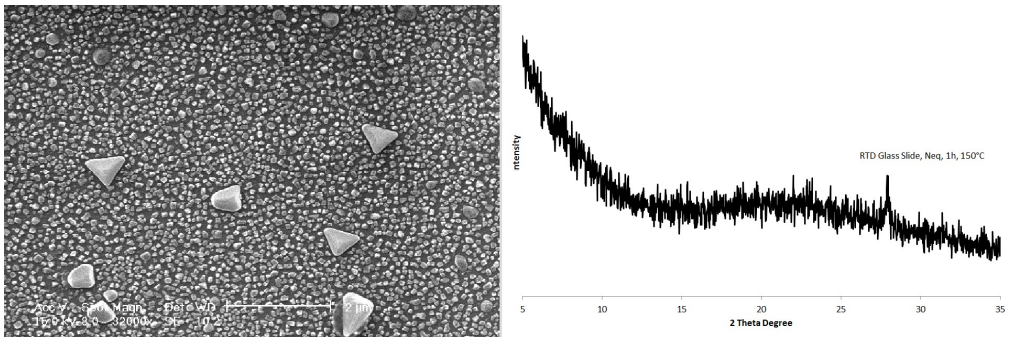


Figure 9-7: SEM image and XRD pattern of glass slide covered by RTD with NEq solution at 150°C with reaction time of 1 h.

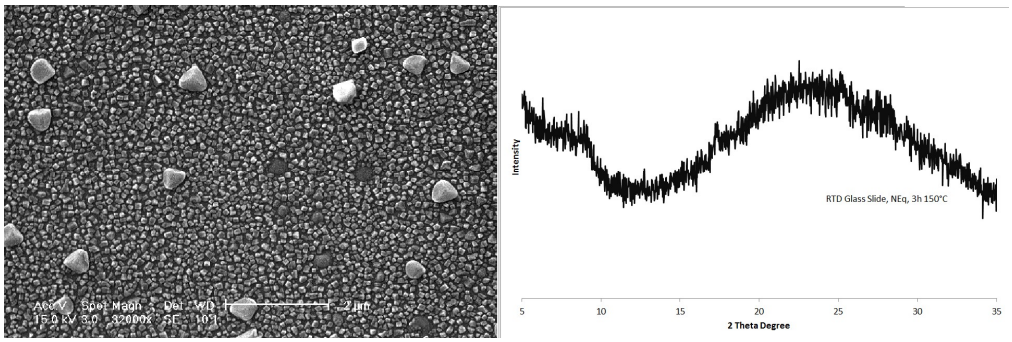


Figure 9-8: SEM image and XRD pattern of glass slide covered by RTD with NEq solution at 150°C with reaction time of 3 h.

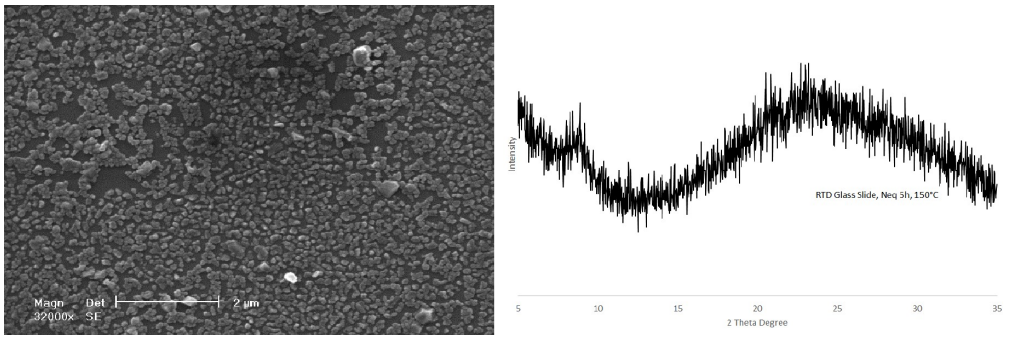


Figure 9-9: SEM image and XRD pattern of glass slide covered by RTD with NEq solution at 150°C with reaction time of 5 h.

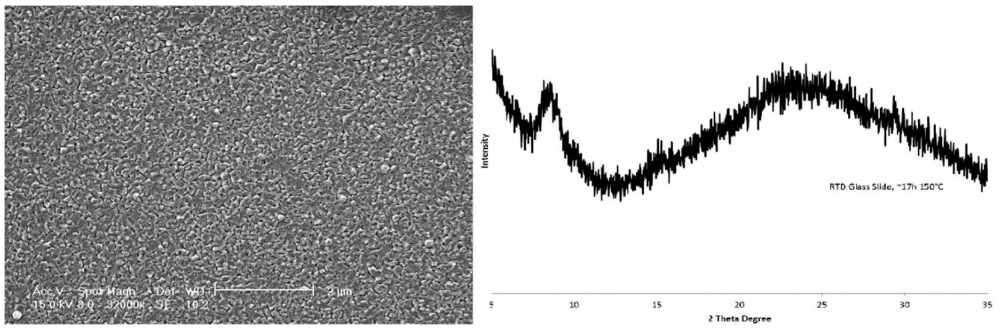


Figure 9-10: SEM image and XRD pattern of glass slide covered by RTD with NEq solution at 150°C with reaction time of ~17 h (overnight reaction).

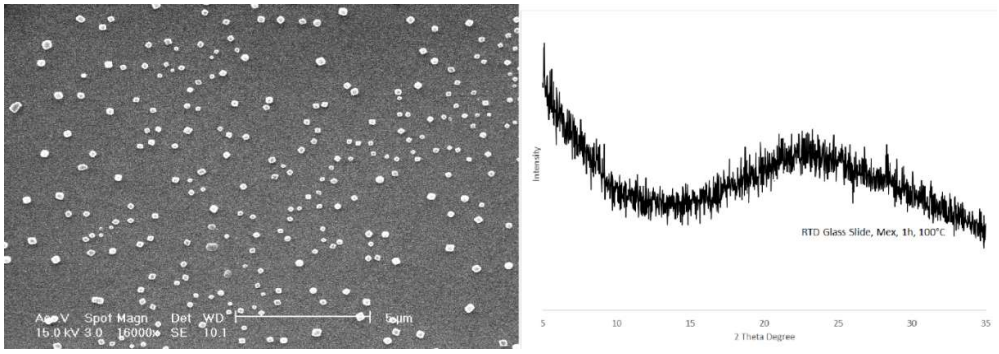


Figure 9-11: SEM image and XRD pattern of glass slide covered by RTD with Mex solution at 100°C with reaction time of 1 h.

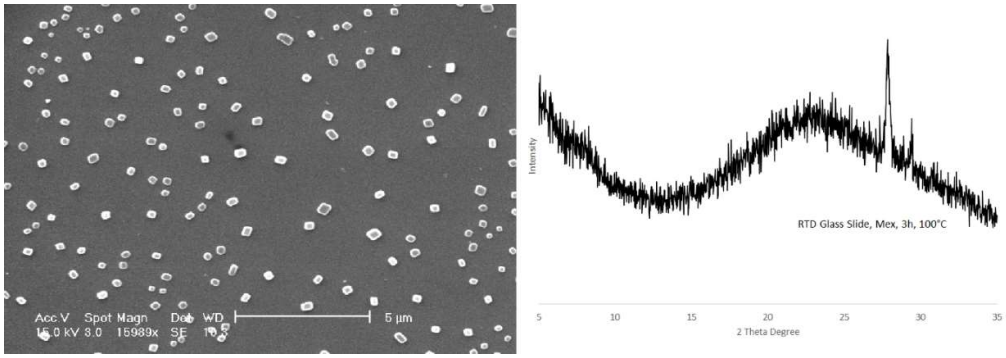


Figure 9-12: SEM image and XRD pattern of glass slide covered by RTD with Mex solution at 100°C with reaction time of 3 h.

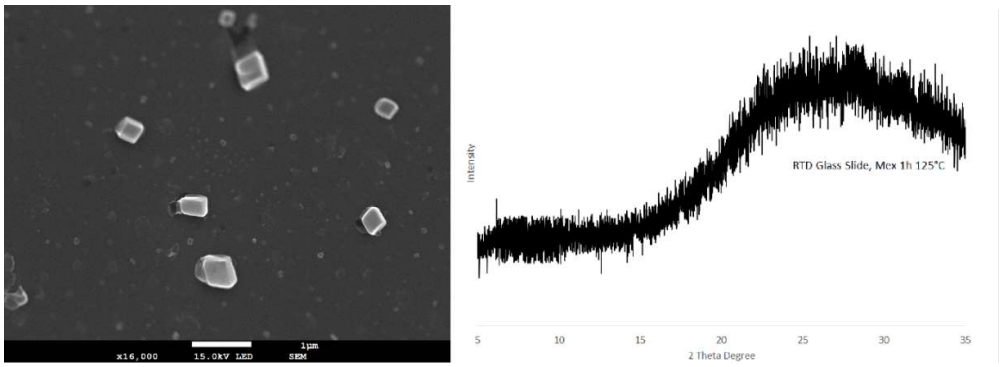


Figure 9-13: SEM image and XRD pattern of glass slide covered with Mex solution at 125°C with reaction time of 1 h.

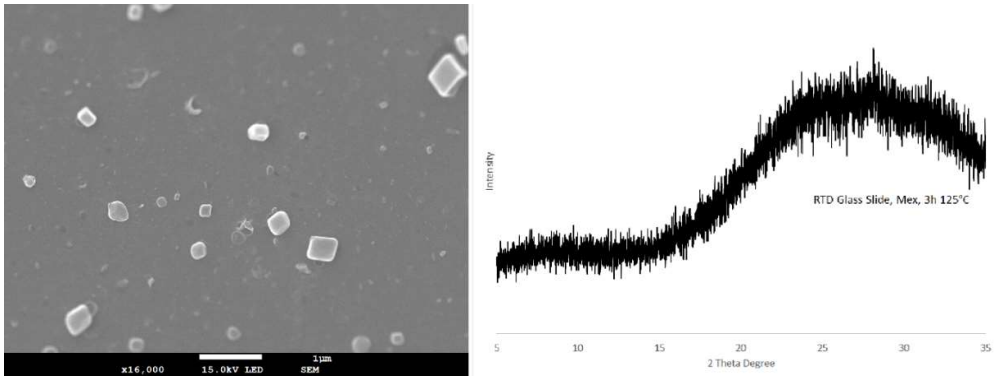


Figure 9-14: SEM image and XRD pattern of glass slide covered by RTD with Mex solution at 125°C with reaction time of 3 h.

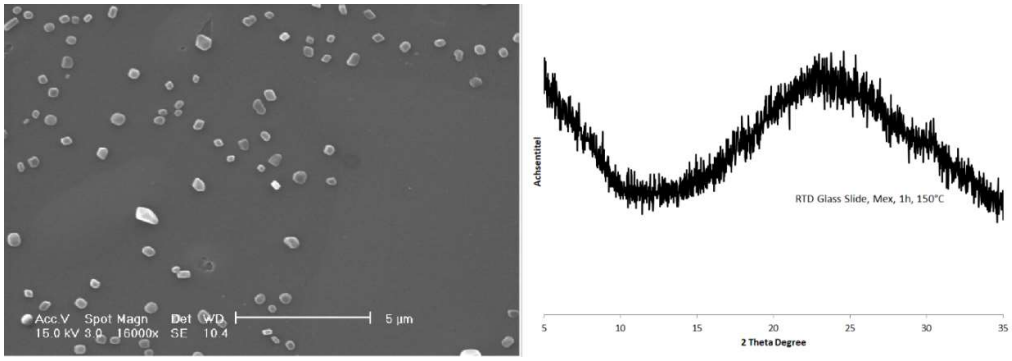


Figure 9-15: SEM image and XRD pattern of glass slide covered by RTD with Mex solution at 150°C with reacting time of 1 h.

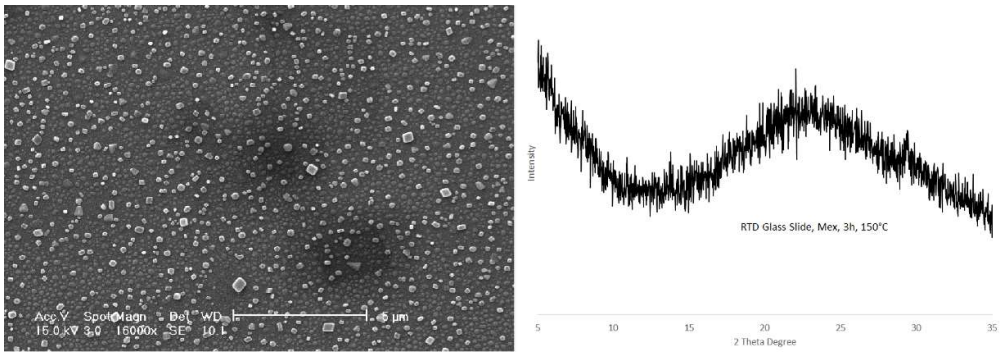


Figure 9-16: SEM image and XRD pattern of glass slide covered by RTD with Mex solution at 150°C with reaction time of 3 h.

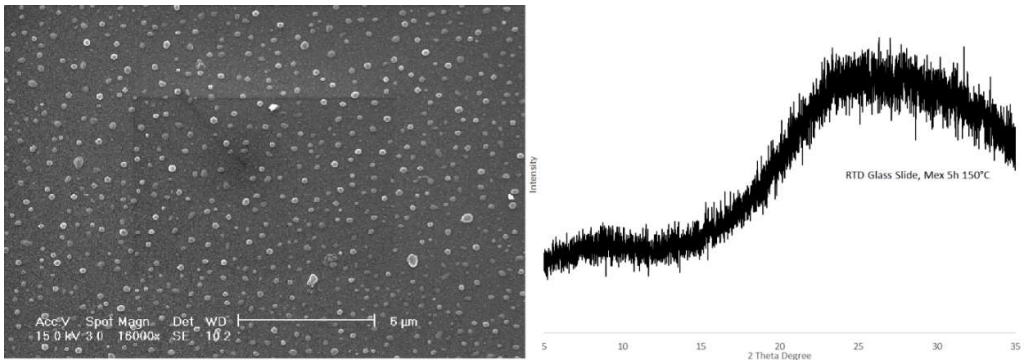


Figure 9-17: SEM image and XRD pattern of glass slide covered by RTD with Mex solution at 150°C with reaction time of 5 h.

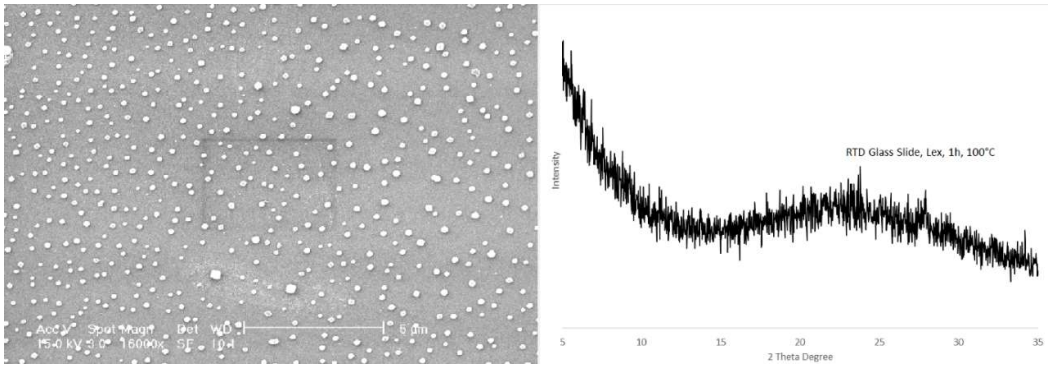


Figure 9-18: SEM image and XRD pattern of glass slide covered by RTD with Lex solution at 100°C with reaction time of 1 h.

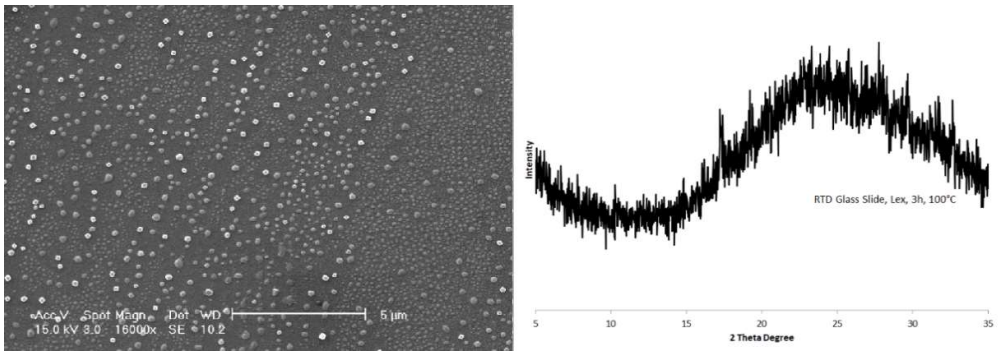


Figure 9-19: SEM image and XRD pattern of glass slide covered by RTD with Lex solution at 100°C with reaction time of 3 h.

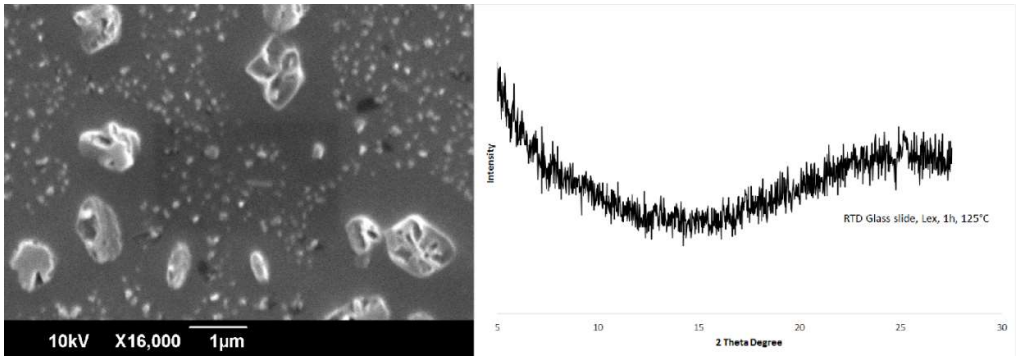


Figure 9-20: SEM image and XRD pattern of glass slide covered by RTD with Lex solution at 125°C with reaction time of 1 h.

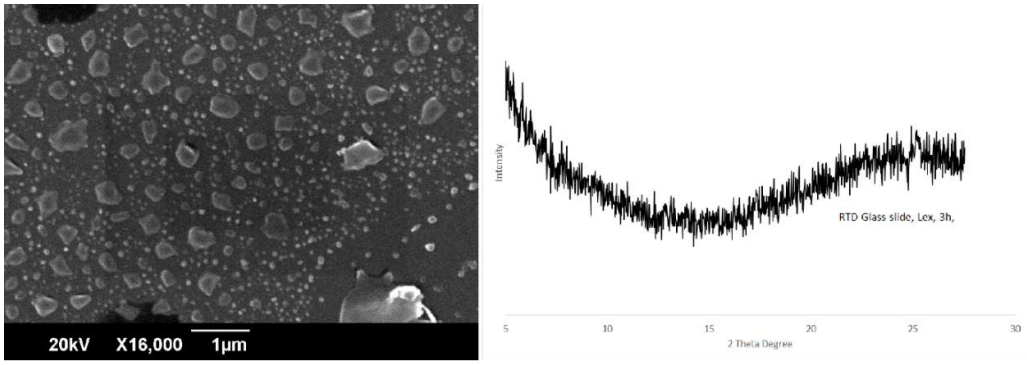


Figure 9-21: SEM image and XRD pattern of glass slide covered by RTD with Lex solution at 125°C with reaction time of 3 h.

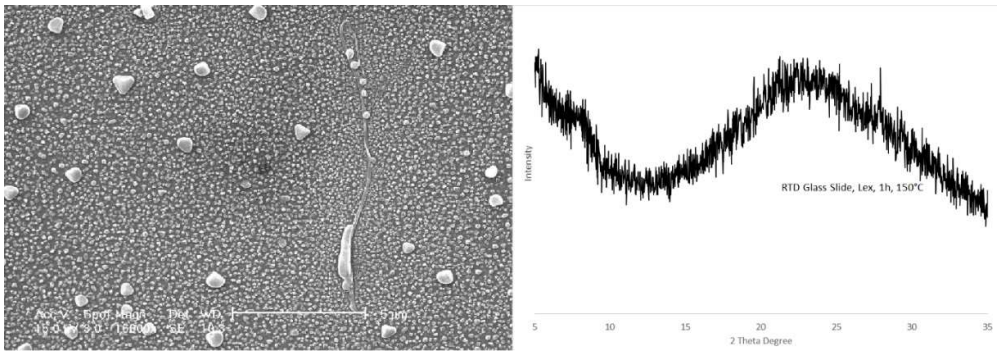


Figure 9-22: SEM image and XRD pattern of glass slide covered by RTD with Lex solution at 150°C with reaction time of 1 h.

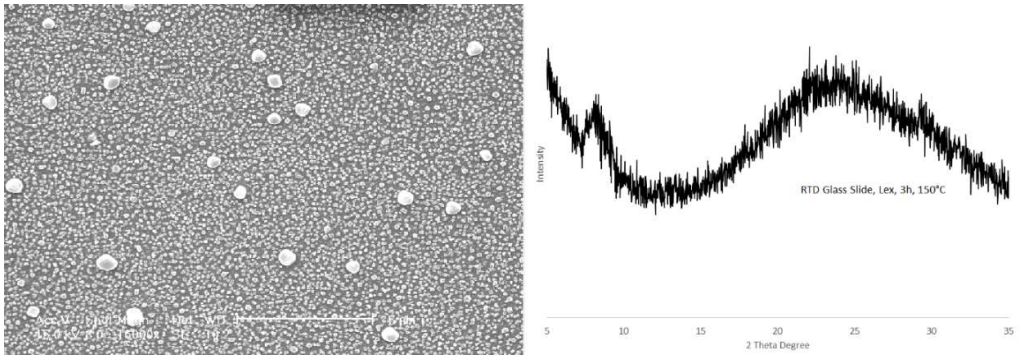


Figure 9-23: SEM image and XRD pattern of glass slide covered by RTD with Lex solution at 150°C with reaction time of 3 h.

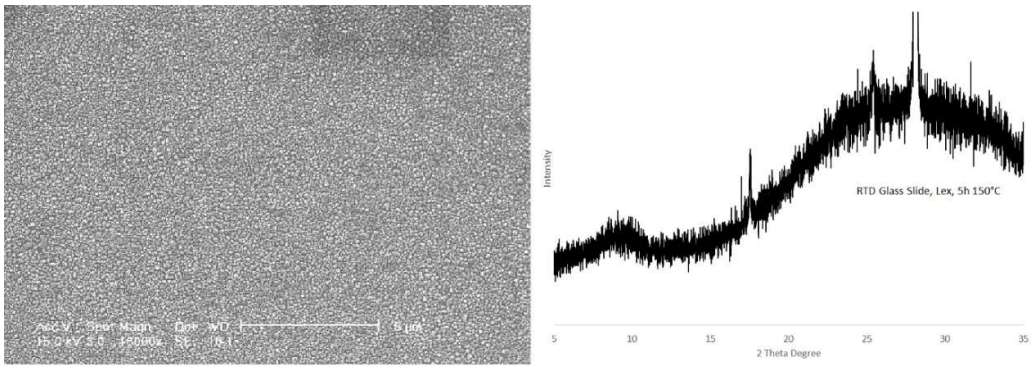


Figure 9-24: SEM image and XRD pattern of glass slide covered by RTD with Lex solution at 150°C with reaction time of 5 h.

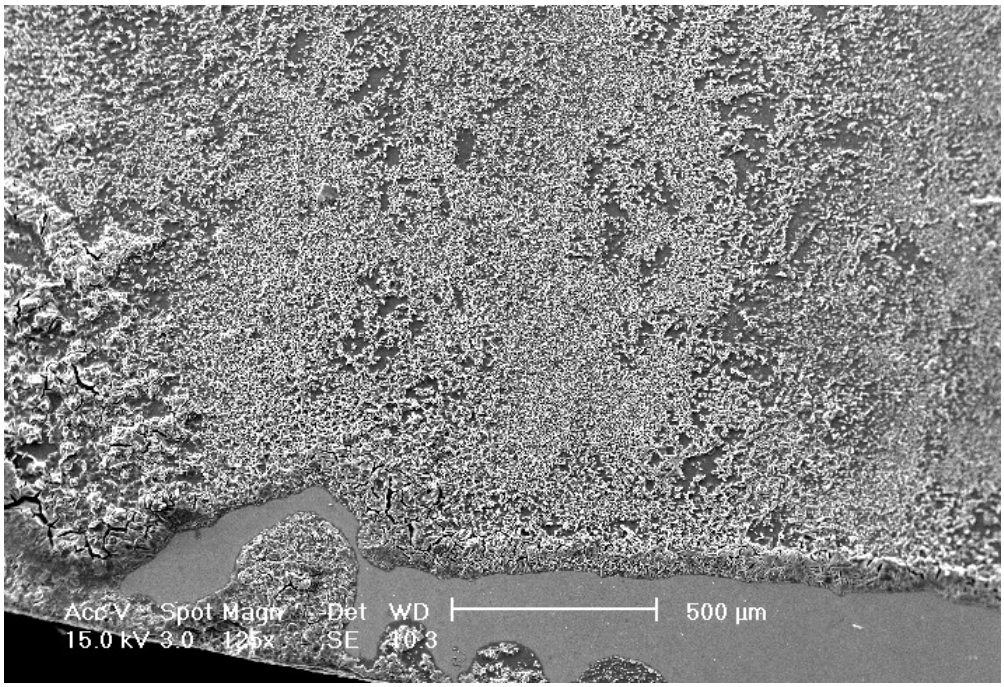


Figure 9-25: SEM image of glass slide covered with NEq reaction mixture at 150°C for 1 h. Only a small area at the bottom of this image is covered with agglomerated particles. Rest of the surface is covered with leaf-shaped of unreacted starting material (H_2BDC).

10 Appendix B: A novel hybrid ultramicroporous material as coatings on LPGs

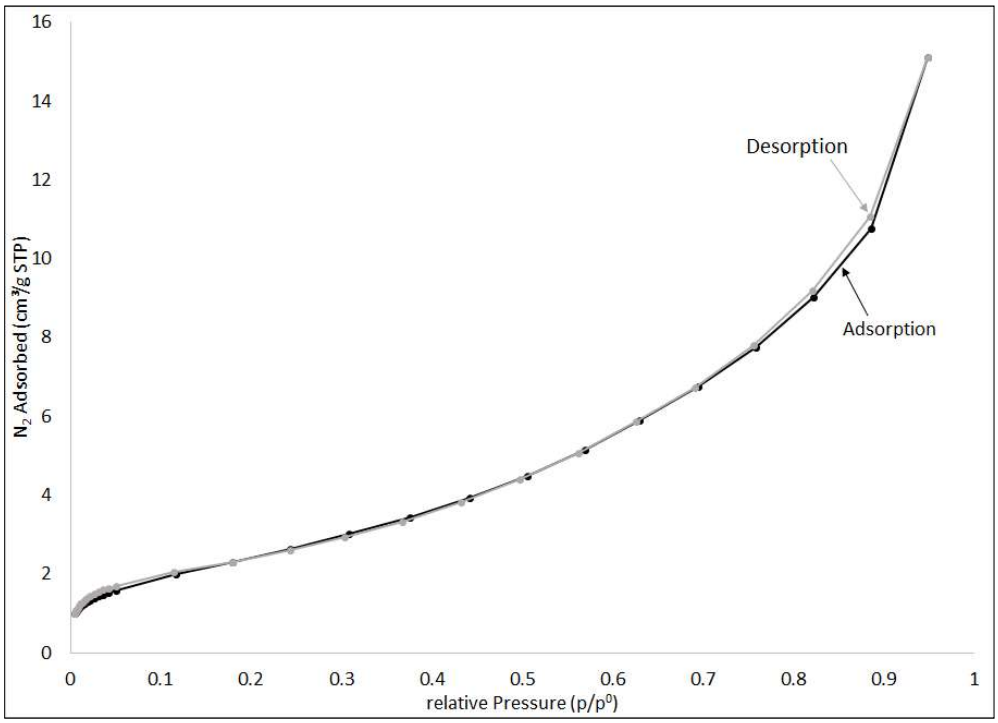


Figure 10-1: N_2-isotherm for TIFSIX prepared in one-step synthesis at RT with MeOH ($NiPyTiF_6$).

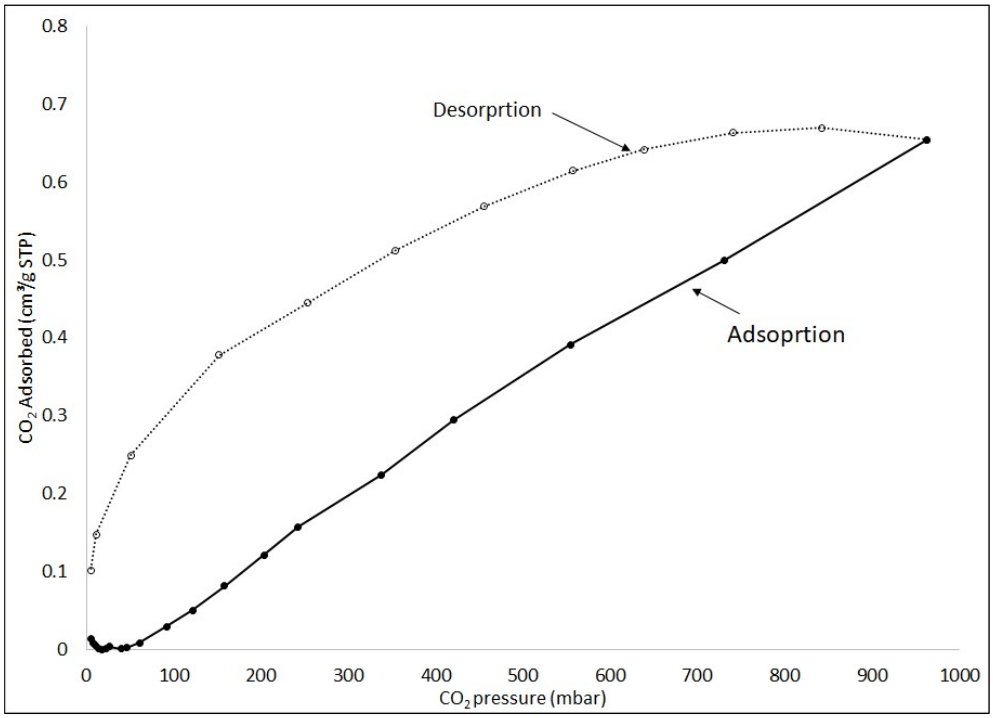


Figure 10-2: CO_2-isotherm of TIFSIX prepared in one-step synthesis at RT with MeOH ($NiPyTiF_6$).

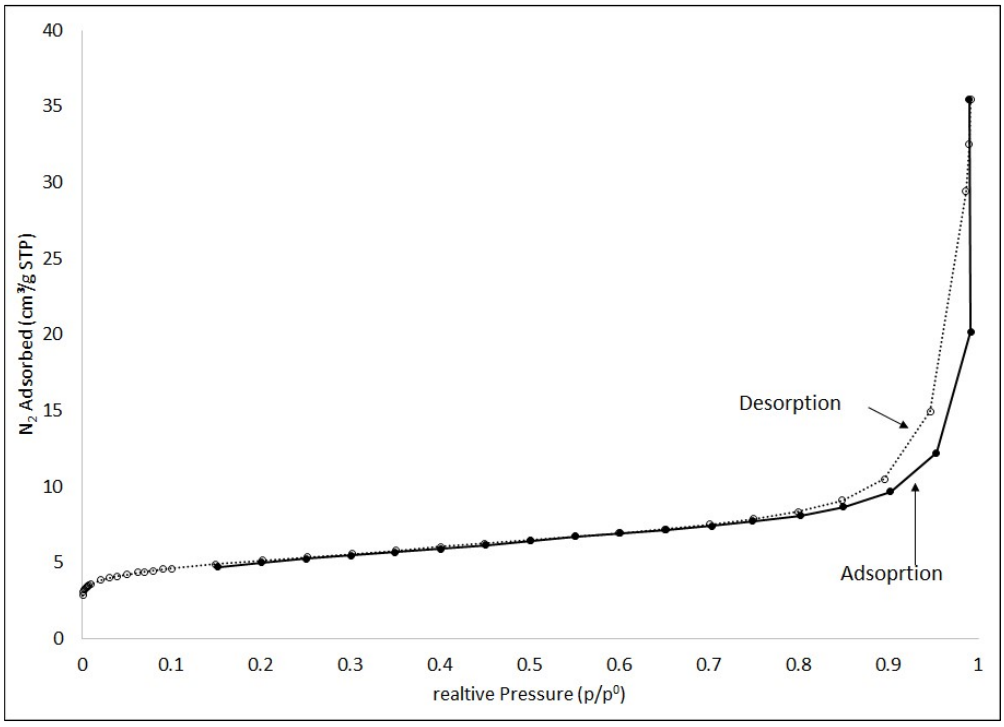


Figure 10-3: N_2-isotherm of TIFSIX prepared in acetone at 85°C in two-step reaction.

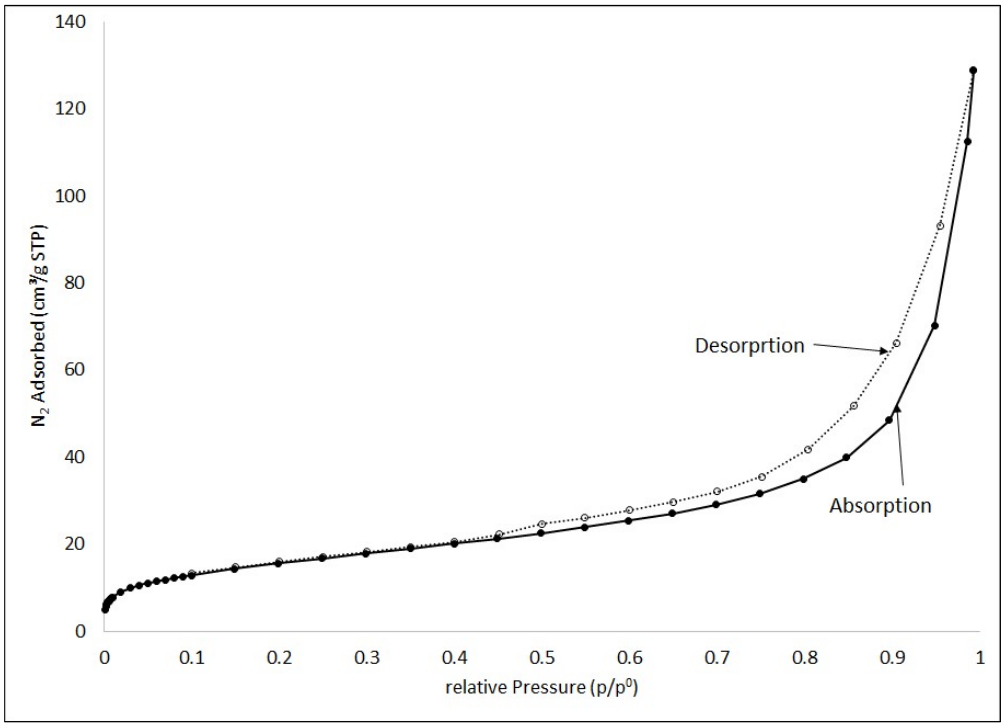


Figure 10-4: N_2-isotherm of TIFSIX prepared in DMF at 85°C in a two-step reaction with excess of pyrazine.

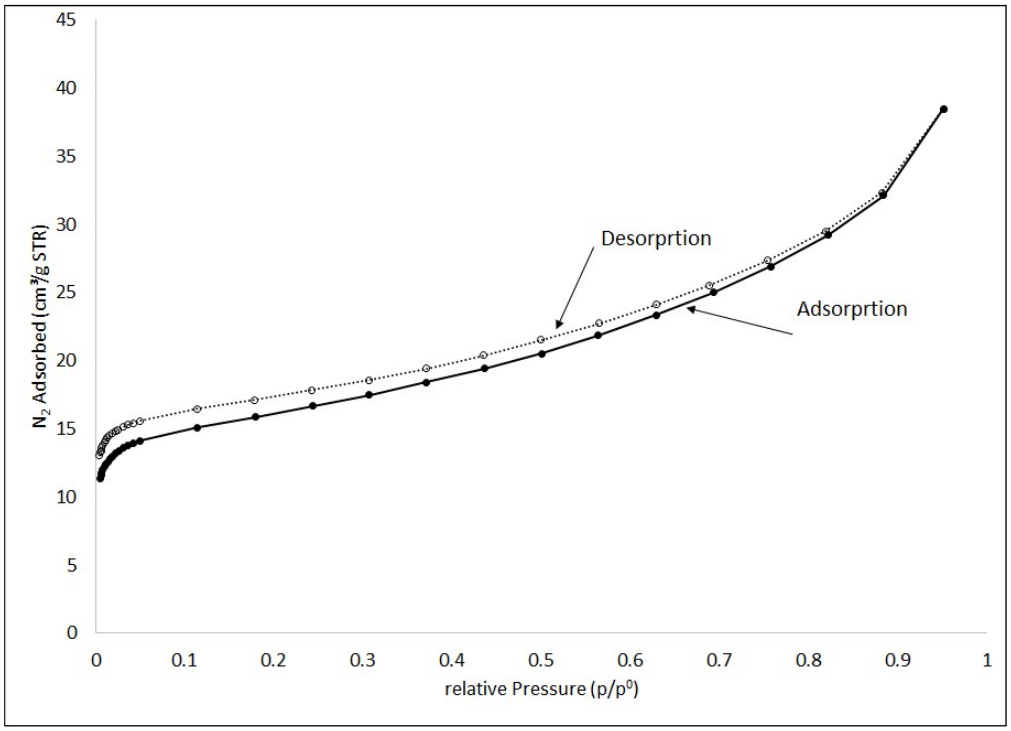


Figure 10-5: N_2-isotherm of TIFSIX prepared in water at RT in a two-step reaction with equimolar composition.

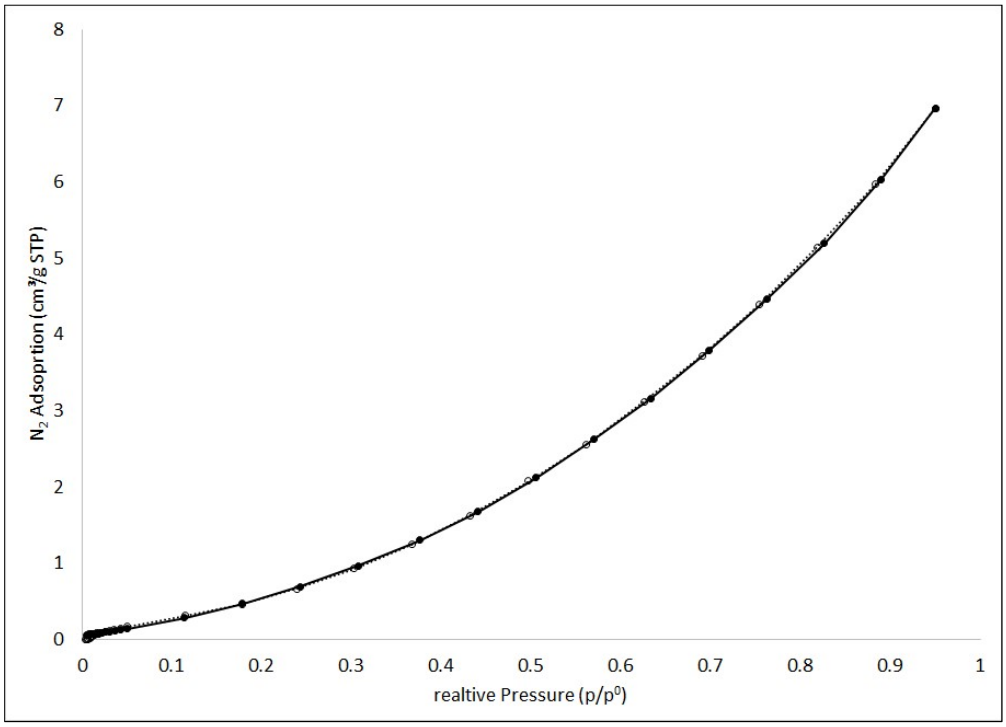


Figure 10-6: N_2-isotherm of sample prepared in one-step reaction in MeOH at 85°C.

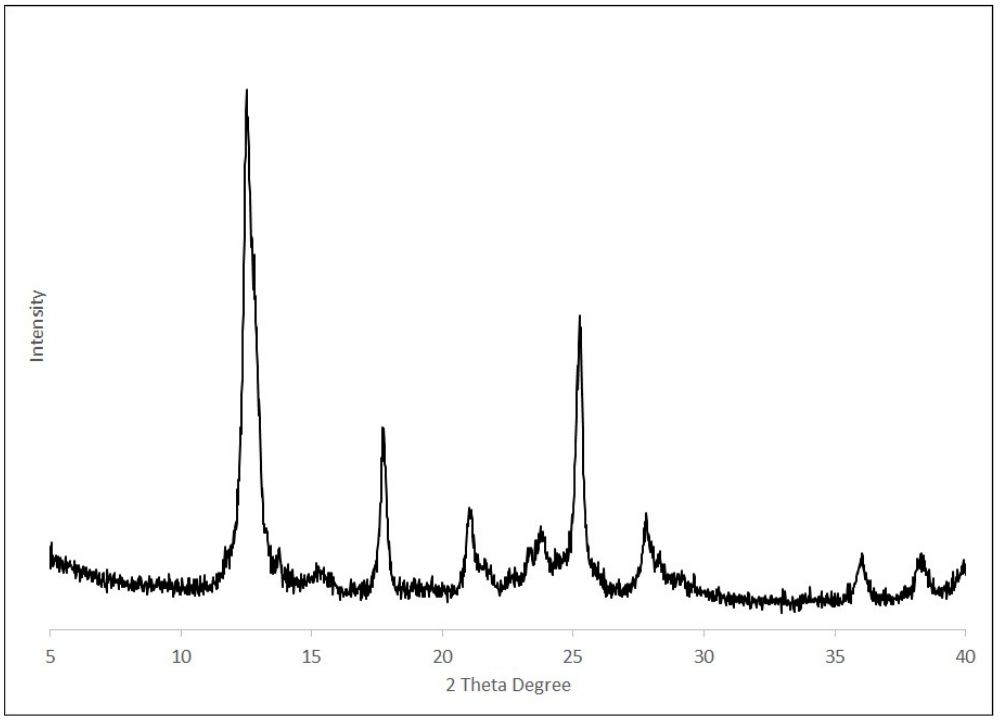


Figure 10-7: XRD pattern of TIFSIX prepared in DMF at 85°C with equimolar reaction mixture (0.5 g $NiTiF_6$ and 0.356 g pyrazine).

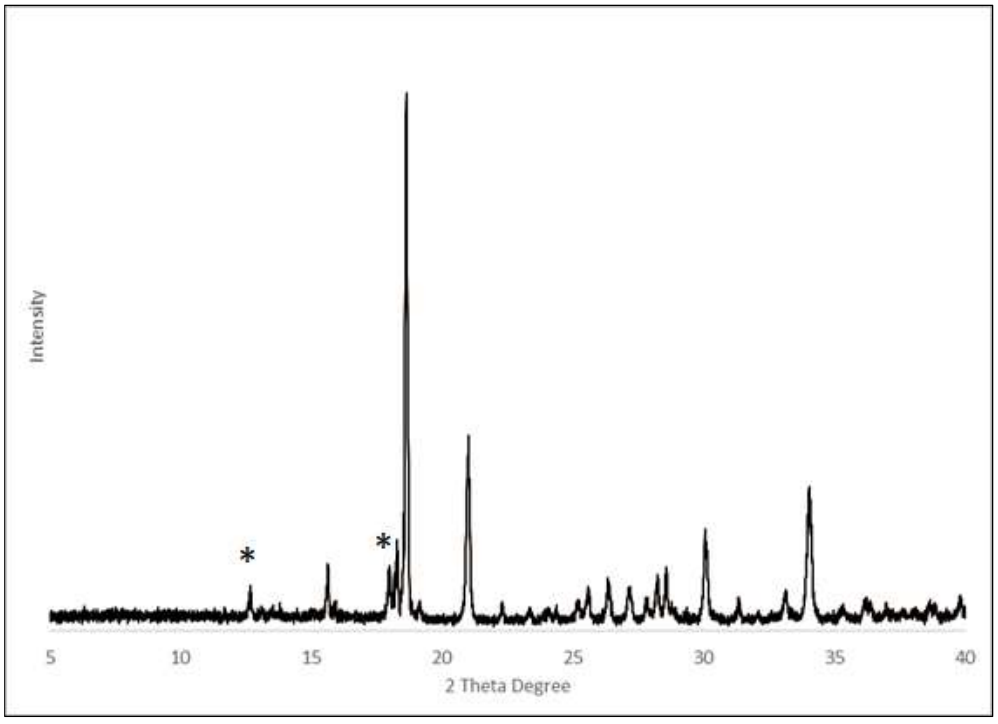


Figure 10-8: TIFSIX prepared in water at reduced concentration at 85°C. At 50% concentration (0.25 g NiTiF6 and 0.178 g pyrazine in 10 ml water), only starting material with a few small product peaks can be seen (highlighted by asterisks).

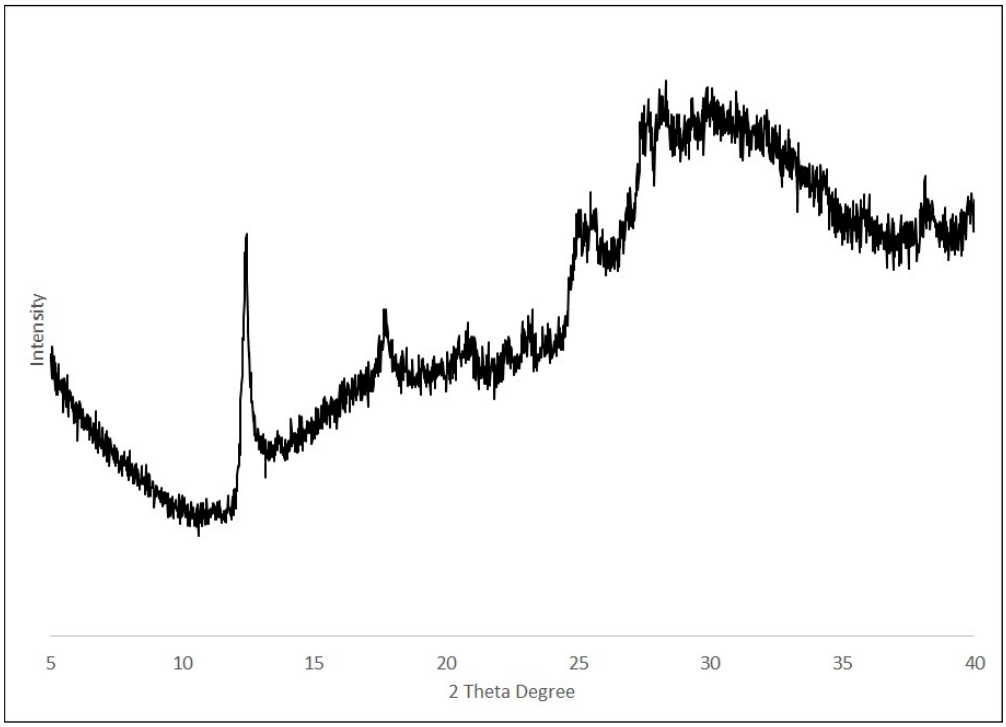


Figure 10-9: XRD pattern of TIFSIX, prepared in water at RT, after activation by solvent exchange in MeOH and heating in vacuum at 120°C. The peaks at 12.58° and 17.72° are matching TIFSIX, but pattern was measured with very small amount (~12 mg) of sample, leading to the pattern with low intensities.

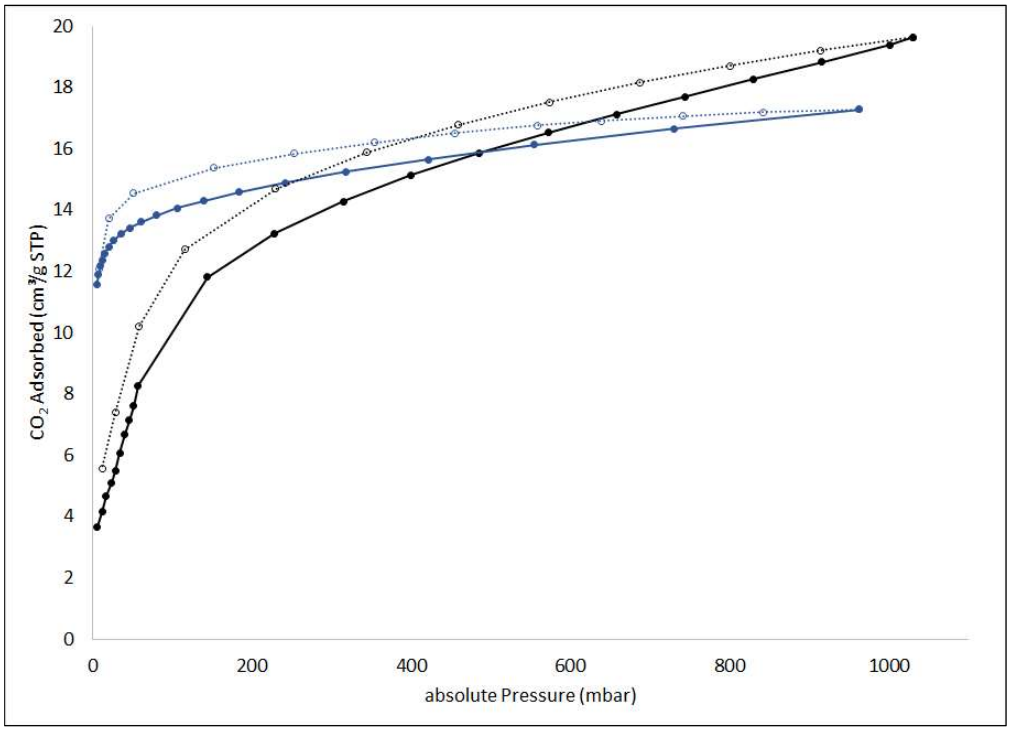


Figure 10-10: CO_2-isotherm of TIFSIX prepared in DMF at 85°C in a two-step synthesis. Measured with shorter (5 s, default, blue) and longer (60 s, black) equilibrium time for each point on the isotherm. Adsorption: solid line; Desorption: dotted line.

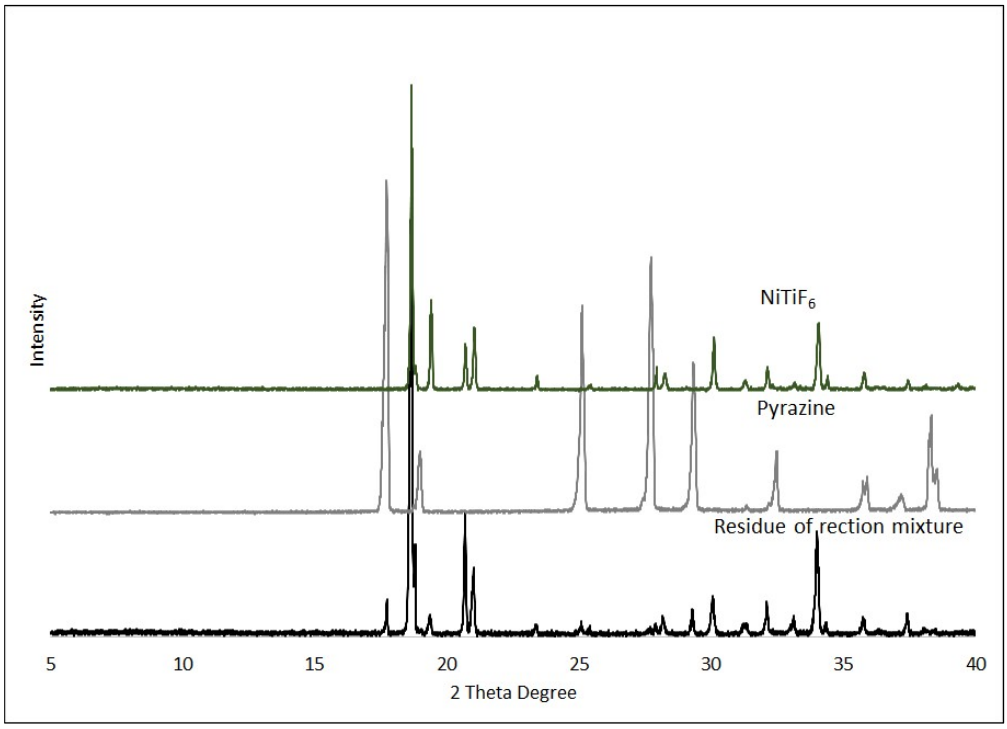


Figure 10-11: XRD of residue collected after evaporation of solvent from decanting process (black). Reaction was TIFSIX in two-step synthesis with excess of pyrazine at RT and water as solvent. XRD pattern of the starting material NiTiF6 (green) and pyrazine (grey) are shown for comparison.

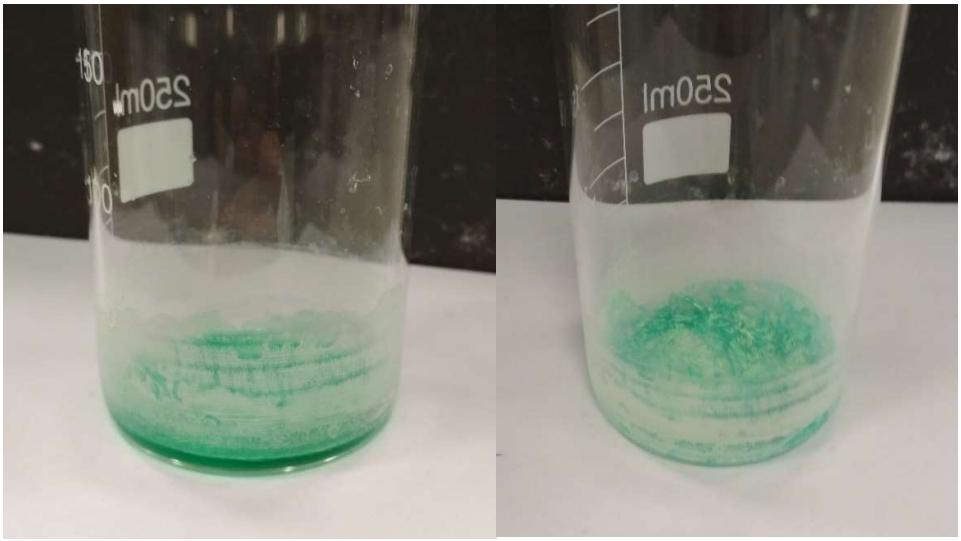


Figure 10-12: Sample of $NiTiF_6$ after 1 day drying (left) and after 3 days (right) at 90°C.